



Sodium Borohydride and Essential Oils as Reducing Agents for the Chemically and Green Synthesis of Silver Nanoparticles: A Comparative Analysis

Pelin ERKOC  

Faculty of Engineering and Natural Sciences, Bahcesehir University, Istanbul, Turkey.

Abstract: Silver nanoparticles (Ag-NPs) have gained immense attention among the variety of metallic nanoparticles during the past decades. In addition to the distinctive optical and electrical properties, Ag-NPs have been particularly employed for their biocidal features in industrial products, especially in biomedicine. Despite the wide range of studies and applications of Ag-NPs, yet serious limitations remained unsolved such as environmental toxicity caused by the reaction byproducts. In the present study, Ag-NPs synthesized by chemical synthesis as well by green synthesis method as a safer alternative considered as environmentally friendly, cost-effective and easy-to-handle. Sodium borohydride (NaBH_4) and the natural essential oils originating from rosemary (*Rosmarinus officinalis*) and grape seed (*Vitis vinifera*) were used as synthetic and bio-reducing agents, respectively. Ultraviolet-visible (UV-Vis) and X-ray Diffraction (XRD) spectroscopy analysis were performed, providing an insight into the composition of the Ag-NPs. Ultimately, the antimicrobial activity of the nanoparticles was tested on a gram-negative bacterium, *Escherichia coli* (*E. coli*). The results revealed that Ag-NPs can be synthesized by a sustainable alternative method with the usage of essential oils originating from rosemary and grape seed, and the resultant Ag-NPs exhibit enhanced the antimicrobial activity compared to the ones synthesized by the chemical reduction method.

Keywords: Silver nanoparticles, sodium borohydride, green synthesis, essential oils, antibacterial activity.

Submitted: May 14, 2020. **Accepted:** November 03, 2020.

Cite this: Erkoc P. Sodium Borohydride and Essential Oils as Reducing Agents for the Chemically and Green Synthesis of Silver Nanoparticles: A Comparative Analysis. JOTCSA. 2021;8(1):1-8.

DOI: <https://doi.org/10.18596/jotcsa.737566>.

***Corresponding author. E-mail:** pepin.erkoc@eng.bau.edu.tr.

INTRODUCTION

Recent advances in nanotechnology have paved the way for the development of nanoparticles for a broad range of applications including health-care, food, and consumer products (1). Among metallic nanoparticles, silver nanoparticles (Ag-NPs) have been widely used because of their unique properties such as large specific surface area, catalytic activity, and antimicrobial activity (2). Furthermore, Ag-NPs have special optical features that cause localized surface plasmon resonance (LSPR) phenomenon to occur. When exposed to a particular wavelength, the electrons at the surface of the NPs undergo a collective oscillation. Owe to their strong interactions with light, they often used for biosensing applications (3).

Ag-NPs can be synthesized by “top-down” and “bottom-up” approaches, in which size of bulk materials reduced into fine particles, and self-assembly of atoms occurs to form a new nuclei that grow into a nanoparticle, respectively (2). In bottom-up approach, the most common method for the synthesis of Ag-NPs is chemical reduction using sodium borohydride (NaBH_4) as a reducing agent (4). However, biological methods are environmentally benign and more cost-effective over synthetic methods (5). This comparatively new method, known as green synthesis route, utilizes non-toxic substances derived from bioresource varying from plant extracts to microorganisms (6-9). The secondary metabolites found in plants, especially the terpenoid-rich essential oils, have a substantial role in Ag-NPs synthesis and attracted considerable attention in

recent years (10). Essential oils can be extracted from plants such as rosemary, sage, thyme, and curcuma readily available worldwide as seasonings (6), and agricultural waste materials such as grape seeds (11). Moreover, these essential oils have been exhibited intrinsic anti-inflammatory, antioxidant, and antibacterial activities (12, 13). In this study, the aim was to conduct a comparative analysis on the synthesis routes of Ag-NPs. To achieve this goal, a study plan was developed including the synthesis of Ag-NPs by two different bottom-up approach, characterizations, and investigation of antibacterial activity on *Escherichia coli* (*E. coli*). The present work focuses more on the green synthesis route of Ag-NPs with a dual combination of essential oils originating from rosemary and grape seed, using a Y-junction glass equipment.

MATERIALS AND METHODS

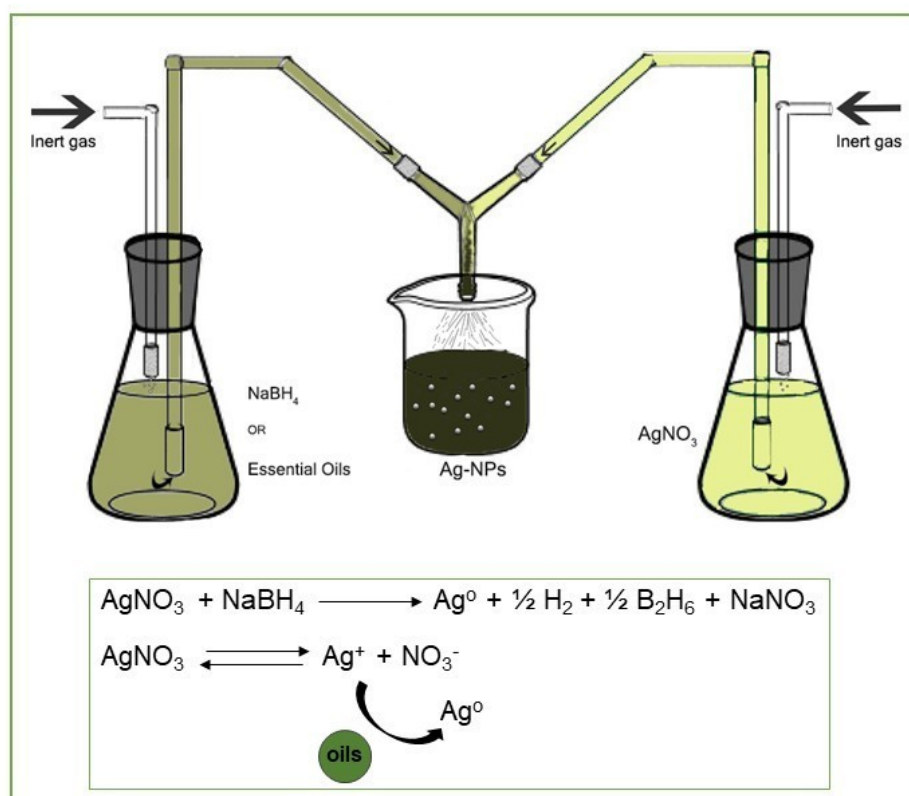
Synthesis of Ag-NPs

Silver nitrate (AgNO_3) of 99.9% purity (Sigma Aldrich) was the precursor for both synthetic routes. Deionized water (dH_2O) was used in all experiments.

Chemical synthesis of Ag-NPs

Aqueous solutions of 0.35 M AgNO_3 was prepared by dissolving in 50 mL of dH_2O . Then, an equal amount of dH_2O in a separate flask was degassed by N_2 gas for 30 minutes to provide an inert environment, and 1 M of NaBH_4 (%96, Sigma Aldrich) solution was prepared.

A custom-made Y-junction glass equipment was used in the reaction to increase the yield (14, 15). NaBH_4 and AgNO_3 solutions were repelled through the center of flow tubes by N_2 gas pressure, then a controlled molarity of chemical reacts when they encounter with each other. Reaction products at the neck were dropped into the collection beaker which contains the solvent (Scheme 1). The solvent used in reaction was added to the collection beaker and stirred with overhead stirrer (Thermomac) from start of the experiment to prevent aggregation. The product was then washed with acetone by centrifugation at 4100 rpm (Nuve NF400) for 10 minutes for 3 times and dried at room temperature under a laminar flow hood.



Scheme 1: Schematic representation of the synthesis of Ag-NP.

Green synthesis of Ag-NPs

In the present study, essential oil reduction method is first time used with a Y-junction glass equipment to synthesize silver nanoparticles (AgNPs). Grape seed and rosemary essential oil were together used to prepare a solution that both reduces and

stabilizes silver ions. Grape seed and rosemary essential oil mixture was prepared by diluting 1 mL of each oil together in 170 mL of acetone with 1 hour of constant stirring at room temperature. AgNO_3 solution (2.14×10^{-4} M, 50 mL) was heated until its boiling point and pH is adjusted to 7 with 4

M NaOH solution. Then, as similar with the procedure used in chemical reduction route, equal volumes of essential oil and AgNO₃ solutions were reacted in Y-junction tube (Scheme 1).

The color change from transparent to yellowish-brown represents the Ag-NP formation. The product was then washed with acetone by centrifuging at 15,000 rpm for 20 minutes for 3 times and dried at room temperature under a laminar flow hood.

Characterizations

UV-Vis absorbance measurement

UV-Vis absorption spectra of Ag-NPs in deionized water were measured in disposable polystyrene cuvettes (Isolab, Germany) by a T70 UV - Vis spectrophotometer (PG Instruments) with 0.5 nm spectral resolution.

XRD analysis

X-ray Diffraction (XRD) spectroscopic analysis of the air-dried samples were performed by a Bruker D2 Phaser XRD.

Antibacterial activity

The in vitro antibacterial efficacy of the synthesized Ag-NPs was studied by the disk diffusion method using Luria-Bertani (LB) agar with determination of inhibition zones. First, an overnight culture of StbI3™ *E. coli* strain (Thermo Fischer Scientific) was prepared from the isolated colonies selected from a 24-h grown LB agar plate (16), and optical density (OD) value was adjusted to 0.6, which approximately corresponds to 1.5 × 10⁸ colony-forming units (CFU) per milliliter of the bacteria suspension, by the spectrophotometric measurement at 600 nm (17). Afterwards, the antimicrobial susceptibility disks immersed in nanoparticle containing solutions (7.2 ng/mL in LB) were placed at on the agar dishes. Petri dishes were incubated at 37 °C for 24 hours.

RESULTS AND DISCUSSION

There are numerous approaches for the synthesis of silver nanoparticles of various shapes and sizes (18). In the present study, the antibacterial activity of silver nanoparticles, which were synthesized via reduction of silver nitrate, using both chemical and green reducing agents, were evaluated. NaBH₄ is utilized as a chemical reducing agent, whereas essential oils from two plant species, rosemary, and grape seed, were used as green reducing agents to combine their reducing capabilities. In contrast to current studies, here, a comparison-based methodology with a different experimental setup was carried out.

The methodology used in this work to obtain Ag-NPs is illustrated in Scheme 1. The reaction apparatus, a Y-junction flow tube, used for the particles synthesis is a previously optimized technique for the synthesis of iron nanoparticles (15). In this system the apparatus contains two distillation flasks for the silver salt and reducing agent. The reduction reaction started as soon as the two solutions react in the neck of the flow tube whose size was kept as small as possible (2 cm) to prevent agglomeration.

The formation of Ag-NPs was first visually observed by the color change of the reaction mixtures. The transparent color of the silver nitrate solution changed to brownish-yellow during the reaction, indicating the growth of silver particles (19).

Moreover, UV-Vis spectra of the colloidal solutions obtained from the two routes of synthesis were shown in Figure 1. The LSPR absorption band, which is characteristic to silver nanoparticles, were observed for both samples around 400 nm (5, 20, 21).

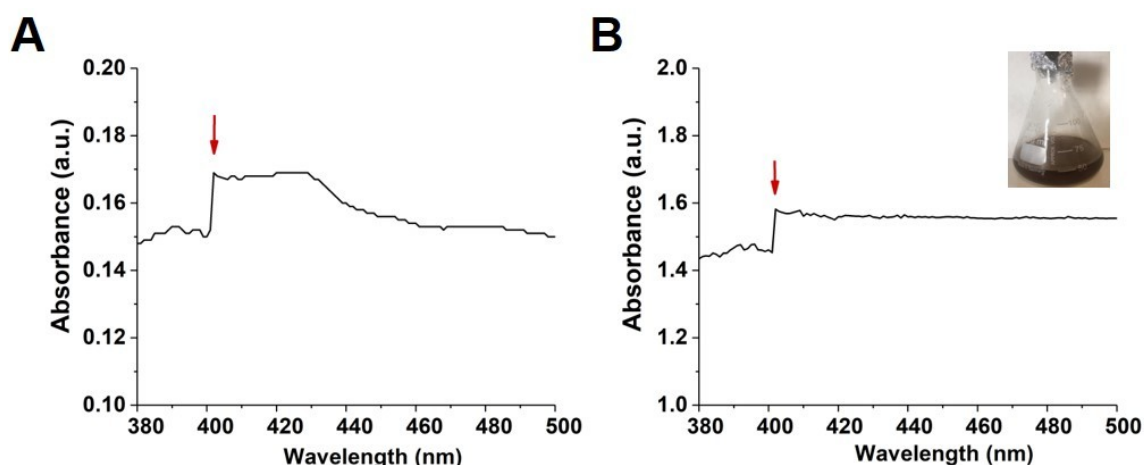


Figure 1. UV-Vis spectra. Silver nanoparticles synthesized by **A)** NaBH₄ reduction and **B)** green synthesis.

Besides, UV-Vis spectral analysis shows that the values of absorbance corresponding to the λ max

for each Ag colloid were different. Higher absorbance value of Ag colloid synthesized by the

chemical reduction method is thought to be resulted from the higher number of synthesized particles which highly depends on the differences in initial molar ratios of reactants used for these two methods.

The formation of the silver crystalline structures was evaluated by XRD spectroscopy. Figure 2

shows the XRD patterns of the formed Ag-NPs. The XRD peaks in the wide angle range of 2θ ($30^\circ < 2\theta < 80^\circ$) revealed that the peaks in 38.2° , 46.2° , 64.1° and 77.2° can be attributed to the 111, 200, 220, and 311 crystalline structures of the face centered cubic (fcc) synthesized silver nanocrystal, respectively (17).

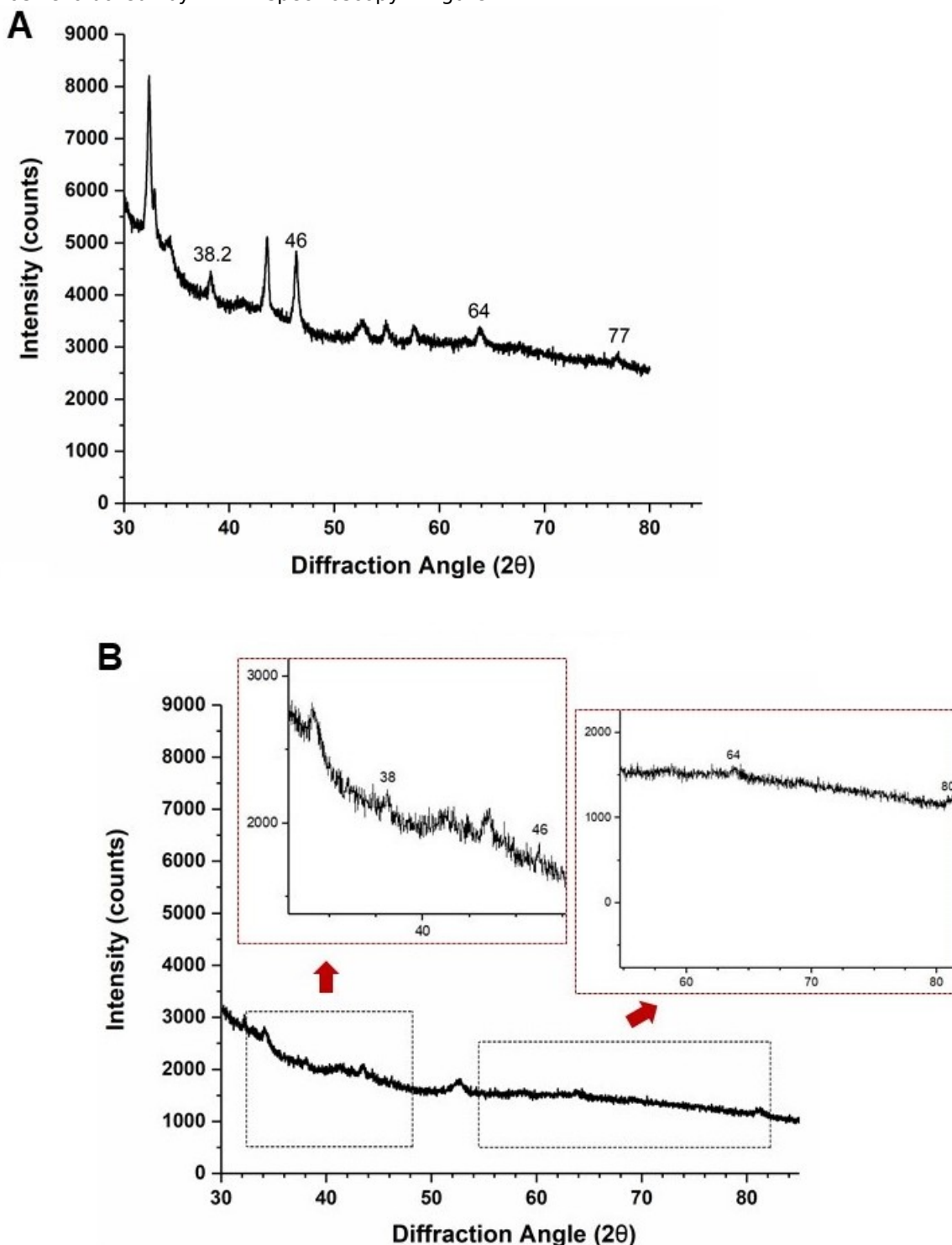


Figure 2. XRD patterns. Silver nanoparticles synthesized by **A)** NaBH_4 reduction and **B)** green synthesis.

Like the above discussed UV-Vis spectral analysis results, the corresponding XRD peaks were sharper and more visible for the particles synthesized by NaBH_4 reduction. Hence, the average size of Ag-NPs synthesized by this method was calculated using Debye-Scherrer equation:

$$D = \frac{K \times \lambda}{\beta \times \cos \theta} \quad \text{Eq. (1)}$$

where K is the Scherrer constant with value from 0.9 (shape factor), λ is the X-ray wavelength (1.5418 Å), β is the width of the XRD peak at half height and θ is the Bragg angle (14, 22). From the Scherrer equation, the average crystallite size of Ag-NPs is found to be around 10-22 nm.

As the final goal, the antibacterial activity of Ag-NPs was tested against a gram-negative bacterium, *E. coli*. Silver has already been known as an antibacterial agent since ancient times and it has been used in a variety of medical devices, such as catheters and in antimicrobial wound dressings (23). The antimicrobial activity of Ag, which lead to bacterial cell death, arises from the interaction of Ag^+ ions with thiol (-SH) groups of vital bacterial enzymes and proteins (3). In addition, free radicals of Ag are reported to react with the membrane lipids, causing damage to the membrane (23).

Disk diffusion or Kirby-Bauer susceptibility test is a routinely applied assay in clinical laboratories to detect the sensitivity or resistance of pathogenic bacteria to numerous antimicrobial compounds. In this assay, the presence or absence of microbial growth around the antimicrobial agent-soaked filter paper disk is an indirect technique to measure the ability of that agent to inhibit microbial growth on solid agar (24). Liquid medium assays are also preferred to determine the minimum inhibitory concentration (MIC) of an antimicrobial agent, which is the lowest concentration of the antimicrobial agent that inhibits growth (25). Utilization of disk diffusion on solid medium to determine zone of inhibition (zoi) remains as a widespread antimicrobial susceptibility testing tool, for being a standardized, easy, and low-cost method (25).

In this study, the antibacterial susceptibility was evaluated by the disk-diffusion assay (Figure 3). The results confirmed that *E. coli* exhibited sensitivity to Ag-NPs synthesized by the two techniques. Figure 3C shows that Ag-NPs synthesized by green synthesis method using

essential oils originating from rosemary and grape seeds demonstrated increased antibacterial activity in a concentration dependent manner, whereas the difference between the diameters of growth inhibition zones were insignificant for NPs synthesized by chemical reduction using NaBH_4 . Previously, Raza et al. reported that the smallest-sized spherical Ag-NPs demonstrated a better antibacterial activity against *E. coli* (26). The difference in the inhibition efficiency of the Ag-NPs synthesized here might be due to the alterations in size and shape of NPs. Furthermore, in addition to the bio-reductant roles of essential oils used in this synthesis route, they also possess a broad spectrum of pharmacological impacts, such as antibacterial and antifungal activity (12, 13, 27), which can contribute to the higher antibacterial activity of the Ag-NPs synthesized by green chemistry.

CONCLUSION

This study represents a comparative analysis on the synthesis of silver nanoparticles using the chemical reduction and greener approach. In the present study, rosemary and grape seed essential oils were successfully used as green and sustainable reducing agents to synthesize silver nanoparticles. The antibacterial susceptibility of the silver nanoparticles was approved by the disk-diffusion on solid agar, which could be further tested by MIC assay in a quantitative way. Moreover, our preliminary conclusions are open to be extended by elaborative investigation of size distribution by SEM or TEM characterizations in a future study.

In summary, the results reinforced the idea that organic substances such as essential oils in plant extracts can be used for the synthesis of Ag-NPs. Finally, this study could provide an understanding of the green synthesis reactions, and it could provide a new avenue for nanoscience community and pharmaceutical industry to develop simple, safer, economical, and environmentally friendly methods for Ag-NP incorporated therapeutics.

ACKNOWLEDGEMENTS

The author would like to thank undergraduate students Merve Begum Bacinoglu, Sude Beskardes, Huseyin Berkcan Isilgan, and Assoc. Prof. Dr. Ozan Akdogan for their technical supports, Chemistry and Molecular Biology research facilities of Bahçeşehir University as well.

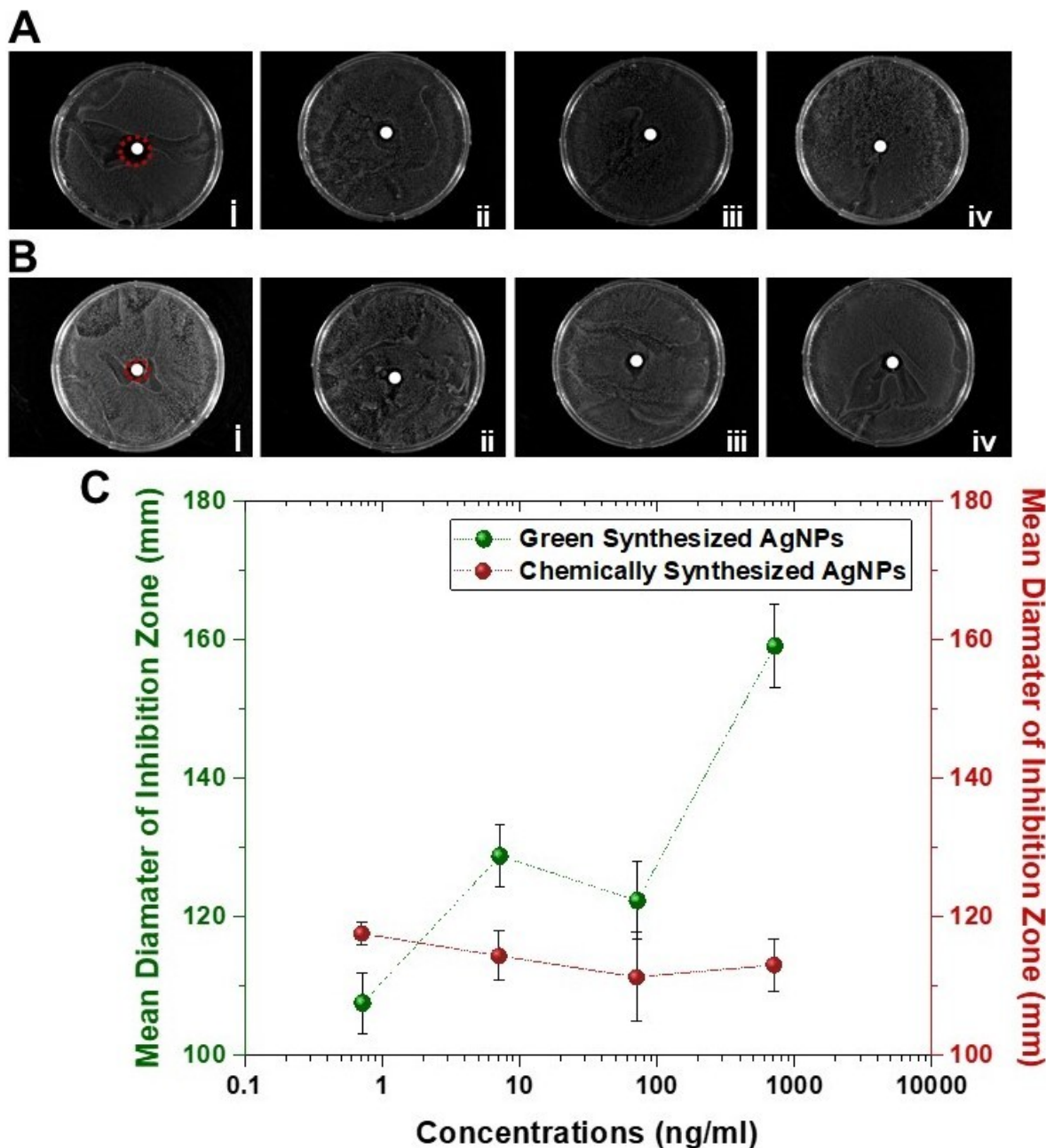


Figure 3. Disk diffusion assay. Antibacterial effect of silver nanoparticles synthesized by A) NaBH_4 reduction and B) green synthesis against *E. coli*. i-iv) Left to right increased concentrations of NPs are 720, 72, 7.2 and 0.72 ng/mL, respectively. C) Corresponding mean zone inhibition diameters. Diameters were manually measured by Image J software from 4 directions.

REFERENCES

- Zhang XF, Liu ZG, Shen W, Gurunathan S. Silver Nanoparticles: Synthesis, Characterization, Properties, Applications, and Therapeutic Approaches. *Int J Mol Sci*. 2016;17(9):1534-68.
- Rafique M, Sadaf I, Rafique MS, Tahir MB. A review on green synthesis of silver nanoparticles and their applications. *Artificial Cells Nanomedicine Biotechnology*. 2017;45(7):1272-91.
- Loiseau A, Asila V, Boitel-Aullen G, Lam M, Salmain M, Boujday S. Silver-Based Plasmonic Nanoparticles for and Their Use in Biosensing. *Biosensors (Basel)*. 2019;9(2):78-117.
- Zhang Z, Shen W, Xue J, Liu Y, Liu Y, Yan P, et al. Recent advances in synthetic methods and applications of silver nanostructures. *Nanoscale Research Letters*. 2018;13(1):54-72.
- Vilas V, Philip D, Mathew J. Essential oil mediated synthesis of silver nanocrystals for environmental, anti-microbial and antioxidant

applications. *Material Science and Engineering: C*. 2016;61:429-36.

6. González-Rivera J, Duce C, Ierardi V, Longo I, Spepi A, Tiné MR, et al. Fast and Eco-friendly Microwave-Assisted Synthesis of Silver Nanoparticles using Rosemary Essential Oil as Renewable Reducing Agent. *ChemistrySelect*. 2017;2(6):2131-8.

7. Korkmaz N. Bioreduction; The Biological Activity, Characterization and Synthesis of Silver Nanoparticles. *Turkish Journal of Chemistry*. 2020.

8. Sahin M, Gubbuk IH. Green Synthesis of Antioxidant Silver and Platinum Nanoparticles Using Ginger and Turmeric Extracts and Investigation of Their Catalytic Activity. *Journal of the Turkish Chemical Society A: Chemistry*. 2019;6(3):403-10.

9. Shelar A, Sangshetti J, Chakraborti S, Singh AV, Patil R, Gosavi S. Helminthocidal and Larvicidal Potentials of Biogenic Silver Nanoparticles Synthesized from Medicinal Plant *Momordica charantia*. *Med Chem*. 2019;15(7):781-9.

10. Mashwani ZU, Khan MA, Khan T, Nadhman A. Applications of plant terpenoids in the synthesis of colloidal silver nanoparticles. *Advances in Colloid and Interface Science*. 2016;234:132-41.

11. Ping Y, Zhang J, Xing T, Chen G, Tao R, Choo K-H. Green synthesis of silver nanoparticles using grape seed extract and their application for reductive catalysis of Direct Orange 26. *Journal of Industrial and Engineering Chemistry*. 2018;58:74-9.

12. Dzimitrowicz A, Berent S, Motyka A, Jamroz P, Kurcbach K, Sledz W, et al. Comparison of the characteristics of gold nanoparticles synthesized using aqueous plant extracts and natural plant essential oils of *Eucalyptus globulus* and *Rosmarinus officinalis*. *Arabian Journal of Chemistry*. 2019;12(8):4795-805.

13. Oroojalian F, Orafaee H, Azizi M. Synergistic antibacterial activity of medicinal plants essential oils with biogenic silver nanoparticles. *Nanomedicine Journal*. 2017;4(4):237-44.

14. Erkoc P, Odeh YN, Alrifai N, Zirhli O, Gunduz Akdogan N, Yildiz B, et al. Photocurable pentaerythritol triacrylate/lithium phenyl-2,4,6-trimethylbenzoylphosphinate-based ink for extrusion-based 3D printing of magneto-responsive materials. *Journal of Applied Polymer Science*. 2020:49043.

15. Khurshid H. Synthesis and Characterization of Iron Based Nanoparticles for Novel Applications [PhD]. UMI Dissertations Publishing: University of Delaware; 2011.

16. Elbing KL, Brent R. Recipes and Tools for Culture of *Escherichia coli*. *Current Protocols in Molecular Biology*. 2019;125(1):e83-97.

17. Shamel K, Ahmad MB, Jazayeri SD, Shabanzadeh P, Sangpour P, Jahangirian H, et al. Investigation of antibacterial properties silver nanoparticles prepared via green method. *Chemistry Central Journal*. 2012;6(1):73-83.

18. Mousavi-Khattat M, Keyhanfar M, Razmjou A. A comparative study of stability, antioxidant, DNA cleavage and antibacterial activities of green and chemically synthesized silver nanoparticles. *Artificial Cells, Nanomedicine, and Biotechnology*. 2018;46(sup3):S1022-S31.

19. Ga'al H, Fouad H, Mao G, Tian J, Jianchu M. Larvicidal and pupicidal evaluation of silver nanoparticles synthesized using *Aquilaria sinensis* and *Pogostemon cablin* essential oils against dengue and zika viruses vector *Aedes albopictus* mosquito and its histopathological analysis. *Artificial Cells Nanomedicine Biotechnology*. 2018;46(6):1171-9.

20. Junejo Y, Baykal A. Ultrarapid catalytic reduction of some dyes by reusable novel erythromycin-derived silver nanoparticles. *Turkish Journal of Chemistry*. 2014;38:765-74.

21. Singh AV, Bandgar BM, Kasture M, Prasad BLV, Sastry M. Synthesis of gold, silver and their alloy nanoparticles using bovine serum albumin as foaming and stabilizing agent. *J Mater Chem*. 2005;15(48):5115-21.

22. Kalishwaralal K, Deepak V, Ramkumarandian S, Nellaiah H, Sangiliyandi G. Extracellular biosynthesis of silver nanoparticles by the culture supernatant of *Bacillus licheniformis*. *Materials Letters*. 2008;62(29):4411-3.

23. Granbohm H, Larismaa J, Ali S, Johansson LS, Hannula SP. Control of the Size of Silver Nanoparticles and Release of Silver in Heat Treated SiO₂-Ag Composite Powders. *Materials* 2018;11(1):80-97.

24. Hombach M, Zbinden R, Böttger EC. Standardisation of disk diffusion results for antibiotic susceptibility testing using the sirscan automated zone reader. *BMC Microbiology*. 2013;13(1):225.

25. Flanagan JN, Steck TR. The Relationship Between Agar Thickness and Antimicrobial Susceptibility Testing. *Indian J Microbiol*. 2017;57(4):503-6.

26. Raza MA, Kanwal Z, Rauf A, Sabri AN, Riaz S, Naseem S. Size- and Shape-Dependent Antibacterial Studies of Silver Nanoparticles

Erkoc P. JOTCSA. 2021; 8(1): 1-8.

RESEARCH ARTICLE

Synthesized by Wet Chemical Routes. Nanomaterials-Basel. 2016;6(4):74-89.

grape seed extract on peri-implantitis microflora in craniofacial implants. Asian Pac J Trop Biomed. 2012;2(10):822-5.

27. Shrestha B, Theerathavaj MLS, Thaweboon S, Thaweboon B. In vitro antimicrobial effects of



Electrochemical and *in-situ* spectroelectrochemical behaviors of non-peripherally tetra substituted zinc(II) and magnesium(II) phthalocyanines

Duygu AKYÜZ *  

Department of Chemistry, Faculty of Science, Gebze Technical University, Kocaeli, Turkey.

Abstract: The electrochemical behaviors of non-peripherally tetra substituted zinc(II) and magnesium(II) phthalocyanines were studied at glassy carbon electrode in N,N-dimethylformamide using cyclic and square wave voltammetry techniques. Electrochemical mechanisms of complexes were illuminated by using the relationship between scan rate and peak current. The complexes exhibited reversible and diffusion controlled behaviors. The effect of metal center on redox properties of complexes were investigated and compared. Zinc and magnesium phthalocyanines showed three reduction redox pairs and one oxidation redox pair, which are similar with small differences in potential during electrochemical measurements. Electrochemical results were supported with *in-situ* spectroelectrochemical measurements. Moreover, the color changes were recorded and sharp color transitions were observed during the reduction and oxidation redox processes.

Keywords: Phthalocyanines, electrochemistry, spectroelectrochemistry.

Submitted: August 17, 2020. **Accepted:** November 03, 2020.

Cite this: Akyüz D. Electrochemical and *in-situ* spectroelectrochemical behaviors of non-peripherally tetra substituted zinc(II) and magnesium(II) phthalocyanines. JOTCSA. 2021;8(1):9-20.

DOI: <https://doi.org/10.18596/jotcsa.781748>.

***Corresponding author.** E-mail: dakyuz@gtu.edu.tr.

INTRODUCTION

Phthalocyanines are macrocyclic compounds, which have a large conjugated 18- π electron system (1). Numerous properties resulting from electronic delocalization make them valuable in different fields of science and technology (2). The most important advantage of phthalocyanines and metallo-derived phthalocyanines is that they can be modified with various functional groups and their physical, optical and electronic properties can be controlled (3). Metallo-phthalocyanines generally have been used as catalysts (4, 5), as organic semiconductors in transistors (6), as photo-active material in laser printers (7), as photosensitizers in dye sensitized solar cells (8) and photodynamic cancer therapy (9).

Recently, triazole substituted phthalocyanine complexes have attracted the attention due to their use in various applications fields such as materials science, agrochemistry, and medicinal chemistry (10, 11). We reported previously the

synthesis of tetra 4-(4-fluorophenyl)-5-(4-methoxyphenyl)-4H-1,2,4-triazole-3-thiol-substituted non-peripheral metal-free, zinc, lead, and copper phthalocyanines (12). Electrochemical and *in-situ* spectroelectrochemical responses of the compounds showed reversible and/or quasi-reversible redox processes and aggregation tendency in N,N-dimethylformamide. Electrochemical and spectroelectrochemical characterization of compounds are needed for determining redox properties, conductivity, color transition, and electron transfer ability and mechanism. The results of characterization provide information about the potential for use in potential application areas such as electrochromism, sensor, and photodynamic therapy. Although there are many studies on the synthesis and photophysical properties of triazole-substituted phthalocyanine complexes (13-16), there are a few studies about electrochemical and spectroelectrochemical properties of these phthalocyanines in literature (17, 18). The non-peripheral 4-(4,5-diphenyl)-4H-1,2,4-triazol-3-ylthio substituted Zn and Mg

phthalocyanine complexes were synthesized and photophysical and photochemical properties were reported by our research group (19).

In here, the electrochemical and *in-situ* spectroelectrochemical properties of synthesized the non-peripheral 4-(4,5-diphenyl-4H-1,2,4-triazol-3-ylthio) substituted Zn and Mg phthalocyanine complexes were studied for the first time. Redox properties, electron transfer mechanism, reversibility/irreversibility, the effect of metal center were determined by electrochemical characterization. The color transitions during the reduction and oxidation reactions, whether there is a by-product formed during the reaction, whether there is a chemical reaction accompanying the redox reaction, and peak assignments were determined by *in-situ* spectroelectrochemical measurements.

EXPERIMENTAL SECTION

The materials and methods for the synthesis of the non-peripheral 4-(4,5-diphenyl-4H-1,2,4-triazol-3-ylthio) substituted Zn and Mg phthalocyanine complexes were reported in previous study by our research group (19). Briefly, 3-nitrophthalonitrile, potassium carbonate, zinc acetate, and magnesium chloride was purchased from Sigma Aldrich (Darmstadt, Germany). During the synthesis, as solvents such as n-pentanol, 1,8-diazabicyclo [4.5.0] undec-7-ene (DBU), N,N-dimethylformamide (DMF), N,N-dimethylsulfoxide (DMSO), toluene, tetrahydrofuran, ethyl acetate, chloroform, dichloromethane, ethanol, methanol, acetone, 1,3-diphenylisobenzofuran (DPBF) were used and all solvent were purchased from Sigma Aldrich (Darmstadt, Germany).

The synthesized Zn and Mg phthalocyanines were characterized by ¹H-NMR spectra (Varian XL-400 NMR spectrometer), IR spectra (Perkin-Elmer Spectrum One FT-IR spectrometer), MS spectra (BRUKER Microflex LT by MALDI-TOF (Matrix Assisted Laser Desorption Ionization-Time-of-Flight)) and UV-Vis absorption spectra (Perkin Elmer Lambda 25 UV-Vis spectrophotometer). More detailed information has been reported in our previous publication(19).

The electrochemical measurements were carried out via cyclic voltammetry (CV) and square wave

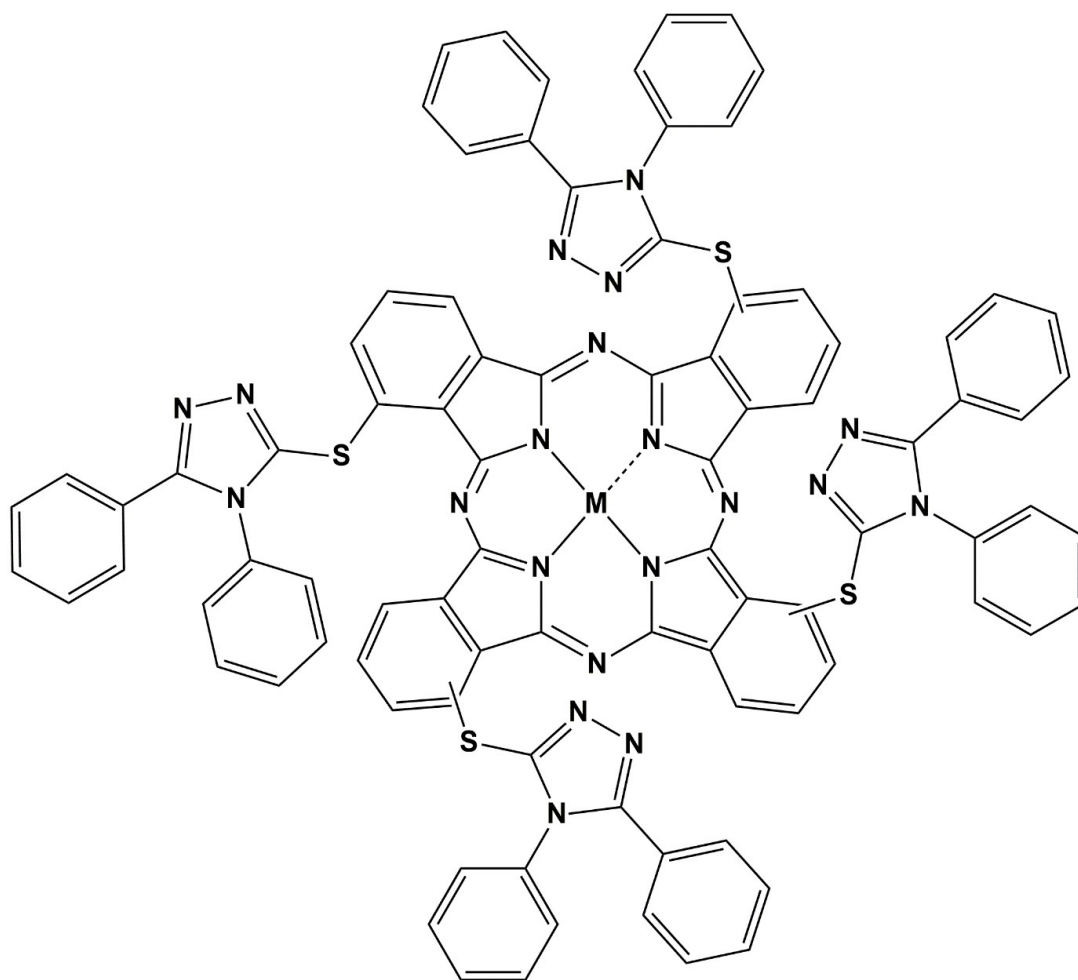
voltammetry (SWV) techniques using a potentiostat/galvanostat (Autolab PGSTAT 302N, Metrohm, Istanbul, Turkey). Electrochemical measurements were performed in three-electrode systems consisting of a glassy carbon (GC) electrode (BASi, 3.0 mm diameter, West Lafayette, USA) as the working electrode, a platinum wire as the counter electrode, and silver-silver chloride (Ag / AgCl) as the reference electrode. The tetrabutylammonium perchlorate (TBAP, Merck, Darmstadt, Germany) was used as supporting electrolyte. 5.0×10^{-4} M of the synthesized compounds dissolved in 2.0 mL dimethylformamide (DMF, Merck, Darmstadt, Germany). Electrochemical measurements were carried out under pure nitrogen gas.

The *in-situ* spectroelectrochemical experiments were performed in quartz UV-Vis cuvette. A potentiostat/galvanostat (Autolab PGSTAT 302N, Metrohm, Istanbul, Turkey) and a DH-mini UV-Vis-NIR Light source (Ocean Optics, Florida, USA) with a high-resolution spectrometer (Ocean Optics, Florida, USA) were used as *in-situ* during the spectroelectrochemical measurements. Pt gauze (working), platinum wire (counter) and Ag/AgCl electrode (reference) were used. All of measurements were performed in DMF/TBAP electrolyte system under nitrogen atmosphere.

RESULT AND DISCUSSIONS

Synthesis

The synthesis procedures of the non-peripheral 4-(4,5-diphenyl-4H-1,2,4-triazol-3-ylthio) substitute zinc and magnesium phthalocyanines were reported by our research group (19). Briefly, for the synthesis of Zn and Mg phthalocyanine compounds, 0.4 g of 1.05 mmol of phthalonitrile was placed in a flask in the presence of 5 mL of n-pentanol. Then, 5 drops of DBU were added as catalyst. Finally, an equivalent amount of anhydrous metal salt Zn(CH₃COO)₂ for ZnPc, MgCl₂ salt for MgPc was added. The reaction was continued at 160 °C for 24 hours and then the cooled mixture was poured into n-hexane. The crude solid product was refined by column chromatography after washing with ethanol, ethyl acetate and acetone. Figure 1 shows the structure of the synthesized non-peripherally tetra substituted zinc(II) and magnesium(II) phthalocyanines.



M= Zn, Mg

Figure 1. The schematic representation of the non-peripheral 4-(4,5-diphenyl-4H-1,2,4-triazol-3-ylthio) substituted zinc and magnesium phthalocyanines (19).

Electrochemical and *in-situ* spectroelectrochemical measurements

ZnPc

The electrochemical data of synthesized compounds (ZnPc and MgPc) were performed by CV and SWV measurements in DMF/TBAP electrolyte system. The peak to peak separation (ΔE_p), half-wave potential ($E_{1/2}$), the ratio of anodic to cathodic peak currents of redox couples ($I_{p,a}/I_{p,c}$) of each wave and separation of half-wave potential ($\Delta E_{1/2}$) for HOMO-LUMO gap value and were determined from plot of CV and SWV. The electrochemical data were given in Table 1. It is well known that the redox waves are associated with the metal atom at the center and the substituent of the compound (20). Therefore, the effect of metal center and substituent of phthalocyanine were investigated on electrochemical and spectroelectrochemical properties. It was reported that phthalocyanines having redox inactive metal center (Ni^{2+} , Zn^{2+} , Cu^{2+} , Mg^{2+}) generally show four redox couples, three reduction couples and one oxidation couple depending on the potential limit of the solvent being studied (12, 21, 22). Metal-free

phthalocyanine complexes generally show reduction couples at -0.63, -1.05 and -1.38 V and approximately at 0.86 V oxidation couple in DMF electrolyte solution (23, 24). The electrochemical responses of ZnPc were showed in Figure 2. ZnPc exhibited three reduction couples at -0.67, -1.08 and -1.77 V and one oxidation couple at 0.81 V and data are also tabulated in Table 1. The phthalocyanine ring of $[Zn^{II}Pc^{-2}]$ was first reduced to $[Zn^{II}Pc^{-3}]^-$ during the cathodic potential scan labeled as R_I , as seen in Figure 2a. The secondly, $[Zn^{II}Pc^{-3}]^-$ species in the electrolyte was reduced to $[Zn^{II}Pc^{-4}]^{2-}$ at more negative voltage labeled as R_{II} . Finally, the $[Zn^{II}Pc^{-4}]^{2-}$ species reduced to $[Zn^{II}Pc^{-5}]^{3-}$ species as labelled R_{III} . During the oxidation reaction, ZnPc oxidized to $[Zn^{II}Pc^{-1}]^+$ species as labelled O_I . When ZnPc was compared to with other triazole substituted zinc phthalocyanines in the literature, it showed more positive reduction potential to literature (24-26). This result can be stemmed from electron-releasing character of 4-(4,5-diphenyl-4H-1,2,4-triazol-3-ylthio) substituent. It is well known that while more electron-donating substituents make more difficult reduction process and more easy oxidation

process, more electron-releasing substituents make more easy reduction process and more difficult oxidation process (27). ΔE_p values was calculated using a formula $\Delta E_p = E_{pa} - E_{pc} = 0.0592/n$ V, which is the criterion of theoretical reversibility (28). ΔE_p values of ZnPc was obtained CV voltammogram at 100 mV/s and reduction and oxidation process indicated reversible character. The $E_{1/2}$ and E_p values of ZnPc are in agreement

with literature as seen in Table 1. $I_{pa}/I_{pc} \approx 1$ showed that the electrode reaction was not accompanied by chemical reactions and it carried out as a result of electrochemical reactions. SWV technique provides high sensitivity and reliable data at low concentration. SWV measurements of ZnPc was indicated in Figure 2b and SWV results supported CV data. The cyclic voltammograms were obtained at various scan rates from 25 to 1000 mV/s as shown in Figure 2a.

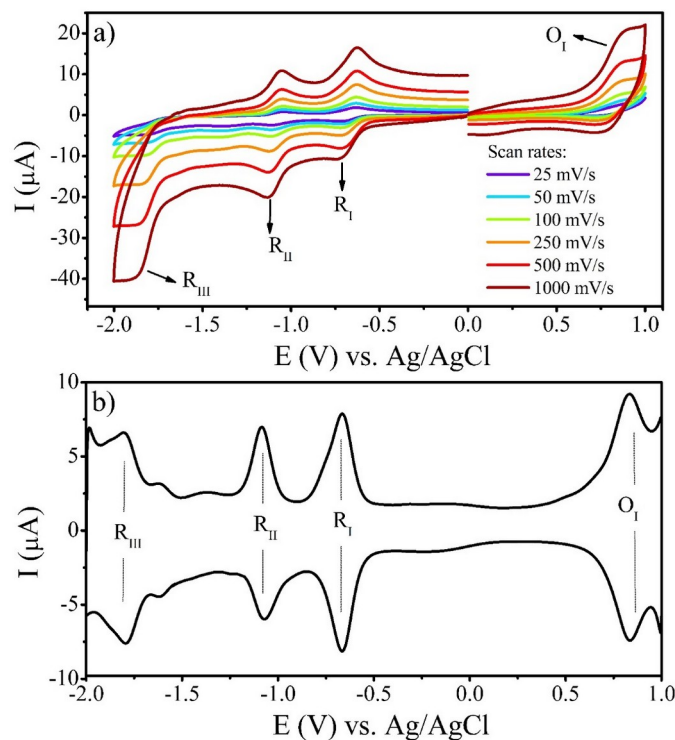
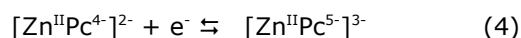
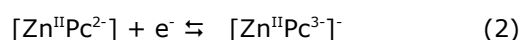


Figure 2. a) Cyclic voltammogram of ZnPc on GCE in DMF/TBAP at various scan rates b) The SWV voltammogram of the complex.

Scan rate studies have been carried out to determine whether the electron transfer is diffusion-controlled on GCE. The square root of scan rate versus the peak current for each redox couples was plotted and a linear line was obtained in the range of 0.025-0.25 mVs⁻¹ as shown in Figure 3. It was reported that $I_p/v^{1/2}$ must be constant in diffusion-controlled process (28, 29). This linear relationship shows that the redox reactions of ZnPc are diffusion-controlled. According to electrochemical results of ZnPc, proposed electron transfer mechanism is as the follows:

Oxidation reaction: $[Zn^{II}Pc^{2-}] \rightleftharpoons [Zn^{II}Pc^{-}] + e^-$ (1)

Reduction reactions:



The proposed oxidation mechanism (Equation 1) can be assigned to $[Zn^{II}Pc^{2-}]/[Zn^{II}Pc^{-}]$ redox couple labelled as O_I in Figure 2a and b. Reduction reactions can be assigned to $[Zn^{II}Pc^{2-}]/[Zn^{II}Pc^{3-}]$ as R_I (Equation 2), $[Zn^{II}Pc^{3-}]/[Zn^{II}Pc^{4-}]^{2-}$ as R_{II} (Equation 3) and $[Zn^{II}Pc^{4-}]^{2-}/[Zn^{II}Pc^{5-}]^{3-}$ redox couple as R_{III} (Equation 4). These assignments are in agreement with literature (30).

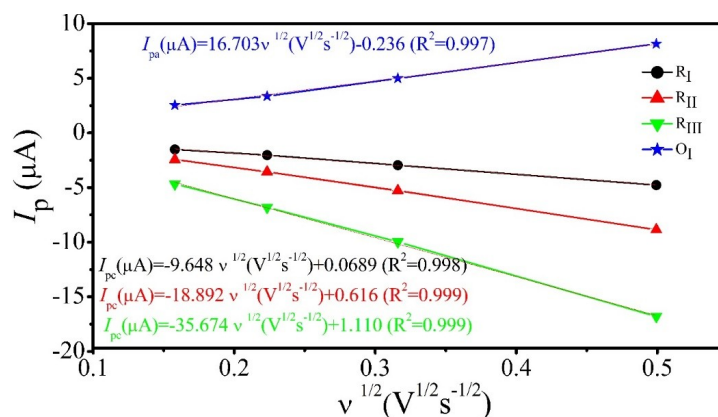


Figure 3. Dependence of anodic peak currents for oxidation, cathodic peak currents for reduction on the square root of scan rate for ZnPc.

In-situ spectroelectrochemical measurements were performed to illuminate the presence of intermediates formed during the reaction, chemical reactions or impurities accompanying the redox reactions, aggregation formation, color change, and assignment of redox couples. Figure 4 represents *in-situ* spectroelectrochemical measurements of ZnPc. During the first reduction process, the intensity of Q band, which is characteristic for phthalocyanines, at 700 nm with small shoulder at 631 nm decreases and new bands appear at 601 and 661 nm during constant potential electrolysis at -0.75 V. Decrease in the intensity of the Q band without any shifting and appearance of a peak in charge transfer region shows the characteristic ring based reduction process (31-33). This spectroelectrochemical changes support that $[\text{Zn}^{\text{II}}\text{Pc}^{-3}]^-$ occurs by a one-step electrode reaction as shown in Equation 1. Then, when applied more negative potential (-1.25 V), second electron transfer performed based on ligand reduction (Figure 4b). The intensity of the bands at 661 and 700 nm decreased and new bands at 552 and 586 nm appeared. Generally, it is difficult to observe the spectral changes of the third electron transfer. Figure 4c shows the spectral changes during the oxidation process. The intensity of the Q band decreased without shifting at 1.00 V. This change is a characteristic behavior for ligand-based oxidation reactions (33). Color changes of the ZnPc was recorded with *in-situ* electrocolorimetric measurements (Figure 4d). Before the reduction/oxidation reactions, the color of ZnPc is greenish blue ($x=0.3213$, $y=0.3525$).

During the reduction process, the color turns to light blue ($x=0.3012$, $y=0.3364$), which shows the presence of $[\text{Zn}^{\text{II}}\text{Pc}^{-3}]^-$ species and then blue color ($x=0.3065$, $y=0.3028$), which indicates presence of $[\text{Zn}^{\text{II}}\text{Pc}^{-4}]^{2-}$ species in solution. The color of ZnPc did not change much during the oxidation reaction ($x=0.3336$, $y=0.3458$).

MgPc

Figure 5 illustrates the electrochemical response of MgPc. MgPc exhibited similar electrochemical behavior with slight differences from that of ZnPc. These differences can stem from position of metal center. MgPc indicates three reversible reduction couples at $E_{1/2} = -0.69$ V, -1.17 V and -1.87 V, respectively and one reversible oxidation couple at $E_{1/2} = 0.80$ V. The redox couple labeled R_I in the Figure 5a and b corresponds to the ring reduction of $[\text{Mg}^{\text{II}}\text{Pc}^{-2}]/[\text{Mg}^{\text{II}}\text{Pc}^{-3}]^-$, R_{II} attributed to $[\text{Mg}^{\text{II}}\text{Pc}^{-3}]/[\text{Mg}^{\text{II}}\text{Pc}^{-4}]^{2-}$, R_{III} attributed to $[\text{Mg}^{\text{II}}\text{Pc}^{-4}]^{2-}/[\text{Mg}^{\text{II}}\text{Pc}^{-5}]^{3-}$ and O_I attributed to ring oxidation of $[\text{Mg}^{\text{II}}\text{Pc}^{-2}]/[\text{Mg}^{\text{II}}\text{Pc}^{-1}]^+$. Electrochemical data are given in Table 1. As shown in Figure 6, the peak current of the reduction and oxidation peaks is directly proportional to the square root of the scan rate. Therefore, the electrochemical reactions of MgPc performed as diffusion-controlled in the result of one-electron transfer. When the Table 1 is examined, MgPc is reduced at a more negative potential and is more easily oxidized than ZnPc. This difference can be stemmed from the effective nuclear charge differences between the magnesium and zinc metal centers in the phthalocyanine ring and radius of metal center.

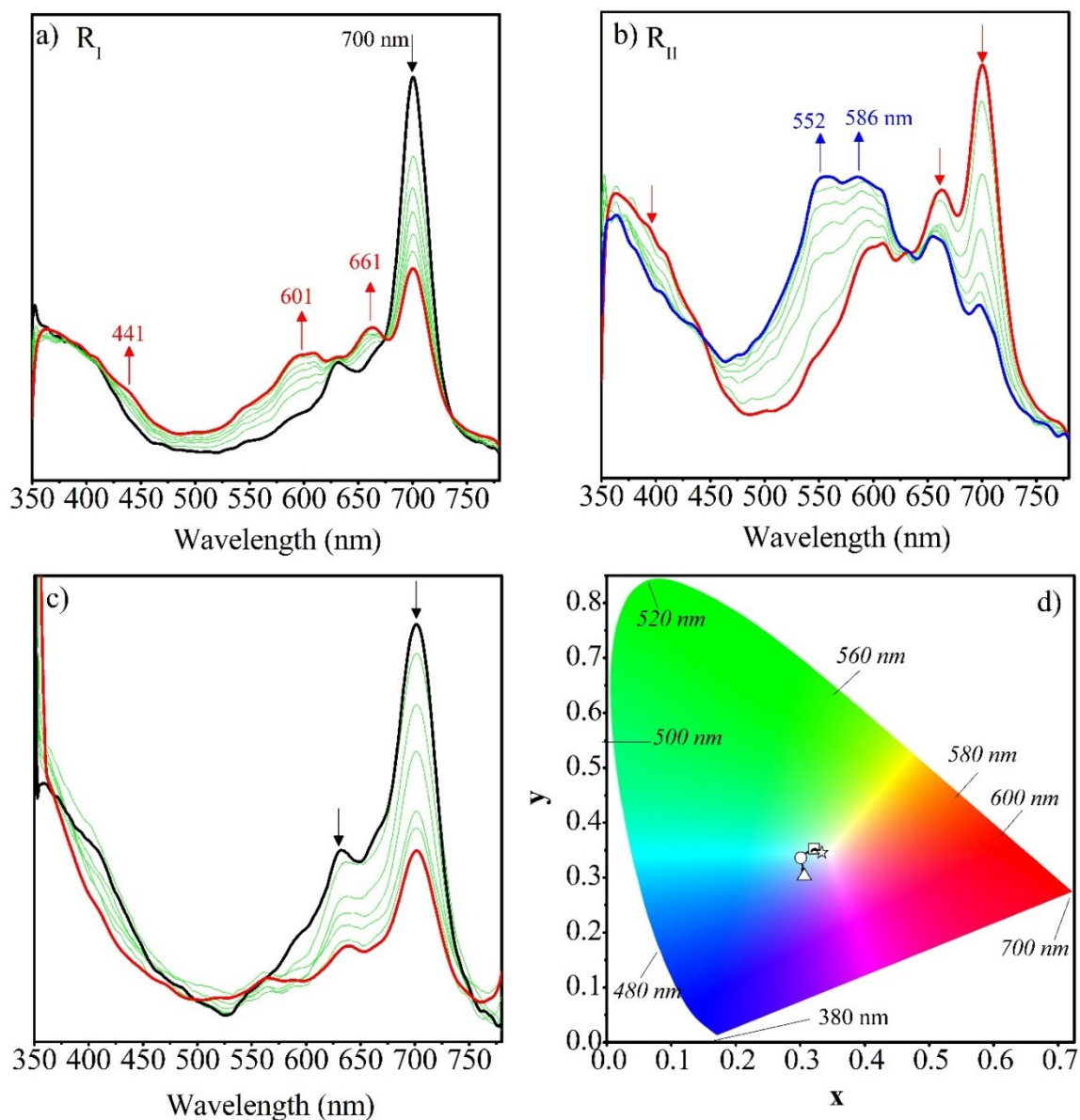


Figure 4. The *in-situ* spectroelectrochemical measurements of ZnPc **a)** during the first reduction reaction at -0.75 V, **b)** during the second reduction reaction at -1.25 V, **c)** during the oxidation reaction at 1.00 V, **d)** The symbols represent the color of occurred species in chromaticity diagram \odot : $[Zn^{II}Pc^{-2}]$; \square : $[Zn^{II}Pc^{-3}]$; \triangle : $[Zn^{II}Pc^{-3}]^{2-}$; \star : $[Zn^{II}Pc^{-1}]^+$.

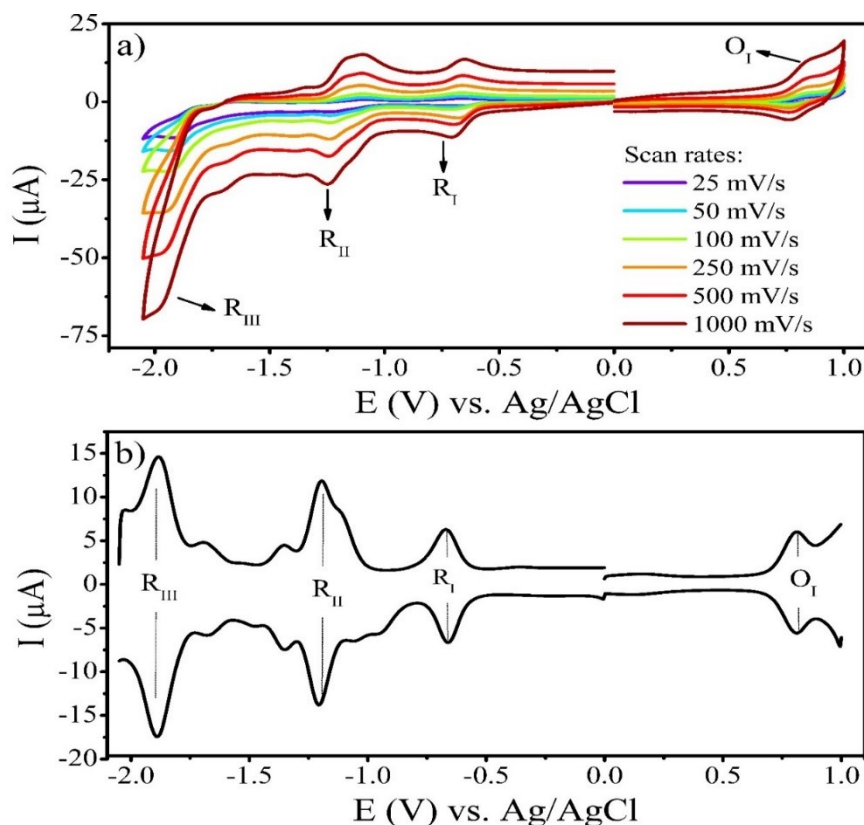


Figure 5. a) The cyclic voltammogram of MgPc on GCE in DMF/TBAP at various scan rates **b)** The SWV voltammogram.

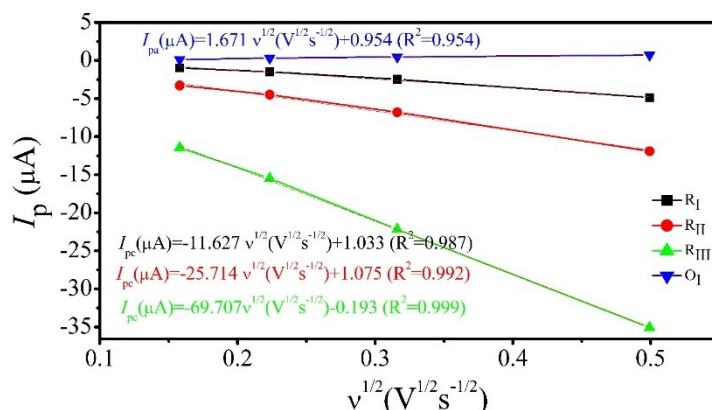
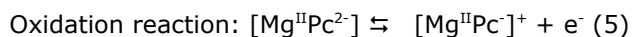
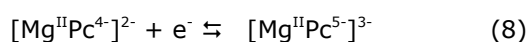
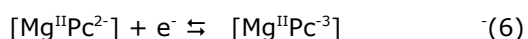


Figure 6. Dependence of anodic peak currents for oxidation, cathodic peak currents for reduction on the square root of scan rate for MgPc.

As a result of the electrochemical characterizations of MgPc in Figure 5, a typical ring-based reaction mechanism was proposed as follows:



Reduction reactions:



Spectroelectrochemical measurements of MgPc were recorded during electrochemical reduction and oxidation reactions (Figure 7). The Q band of MgPc complex observed at 703 nm with a small

shoulder at 631 nm. The intensity of characteristic Q band reduced without shifting and a new band appeared in the range of 530 - 620 nm at -0.90 V constant potential (Figure 7a). Figure 7a can be assigned to Equation 6. During the second reduction, the Q band disappeared and new peak increased at 548 nm under potential of -1.50 V (Figure 7b). Figure 7b can be assign to Equation 7. These spectral changes occurring without shift are characteristic for phthalocyanine ring reduction and thus the formation of $\text{Mg}^{\text{II}}\text{Pc}^{4-}$ species, corresponding to the redox couple in the CV labeled with R_{II} (31, 32, 34). The oxidation process was carried out with electrolysis of solutions including MgPc at 1.00 V constant potential (Figure 7c). The intensity of the Q band decreased, which can be assigned to Equation 5. The color changes in relation to the occurred redox species during the

redox reactions were recorded in Figure 7d. The light blue color ($x=0.3156$, $y=0.3487$) of MgPc at zero voltage turns to blue ($x=0.3162$, $y=0.3291$) and then the color does not change ($x=0.3167$,

$y=0.3009$) during the reduction process, respectively. The light blue color of MgPc turns to greenish blue ($x=0.3333$, $y=0.3602$) during the oxidation process.

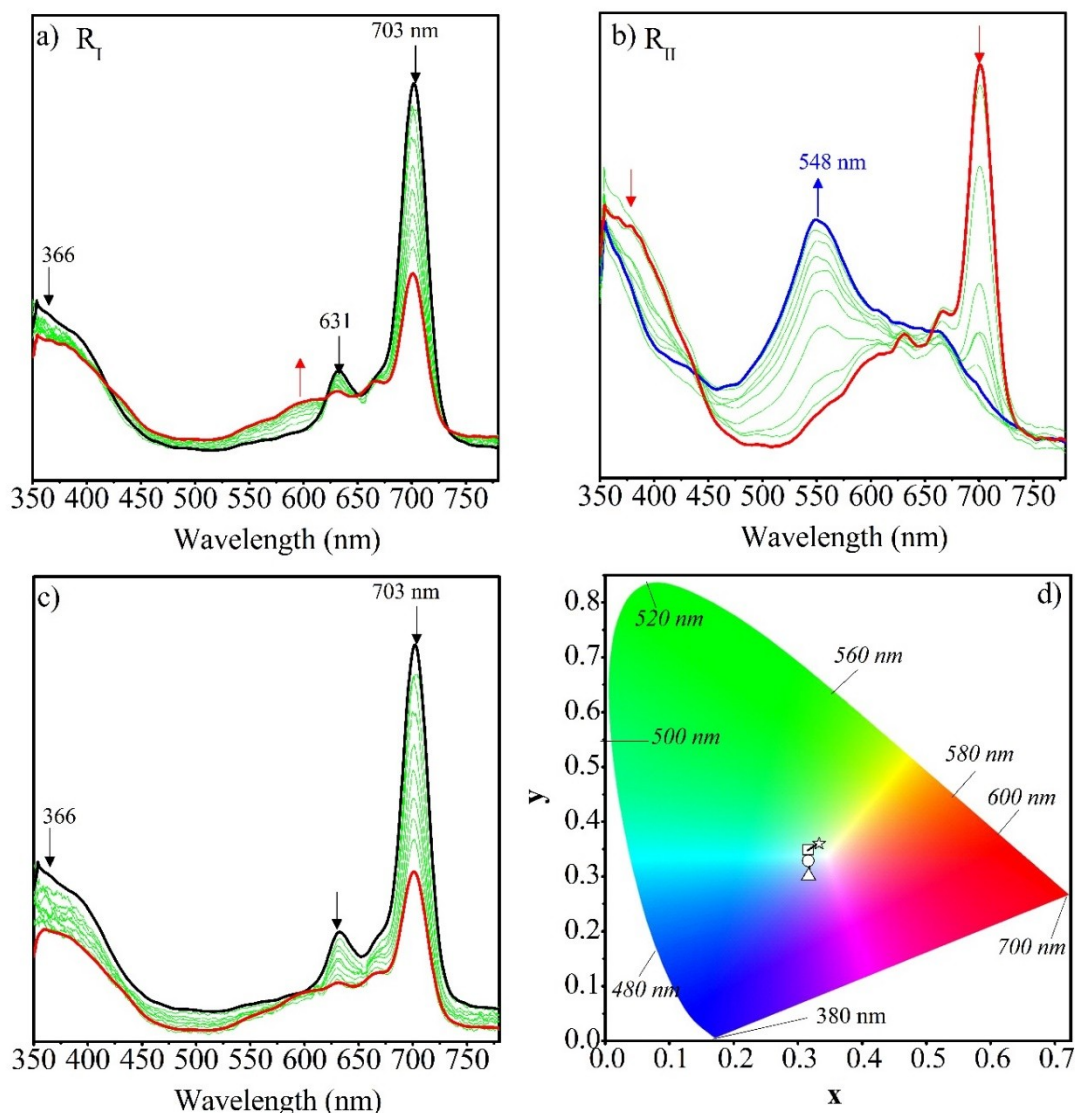


Figure 7. The *in-situ* spectroelectrochemical measurements of MgPc **a)** during the first reduction reaction at -0.90 V, **b)** during the second reduction reaction at -1.50 V, **c)** during the oxidation reaction at 1.00 V, **d)** The symbols represent the color of occurred species in chromaticity diagram \square : $[\text{Mg}^{\text{II}}\text{Pc}^{2-}]$; \circ : $[\text{Mg}^{\text{II}}\text{Pc}^{3-}]$; Δ : $[\text{Mg}^{\text{II}}\text{Pc}^{4-}]^{2-}$; \star : $[\text{Mg}^{\text{II}}\text{Pc}^{-1}]^{+}$.

CONCLUSION

The non-peripheral 4-(4,5-diphenyl-4H-1,2,4-triazol-3-ylthio) substituted Zn and Mg phthalocyanine complexes were characterized for the first time by electrochemical and *in-situ* spectroelectrochemical measurements. The electrochemical parameters such as $E_{1/2}$, ΔE_p , $I_{p,a}/I_{p,c}$ and $\Delta E_{1/2}$ determined and tabulated. Complexes showed electrochemically reversible behavior in DMF/TBAP electrolyte system. The electrochemical responses of ZnPc and MgPc are similar with small difference in reduction and oxidation potentials. The peak assignments of complexes and electron transfer mechanism was illuminated and reaction mechanisms were

purposed. Electrochemical responses are also supported *in-situ* spectroelectrochemical measurements. The effect of 4-(4,5-diphenyl-4H-1,2,4-triazol-3-ylthio) substituents of compounds on electrochemical responses was investigated. The non-peripheral 4-(4,5-diphenyl-4H-1,2,4-triazol-3-ylthio) substitution of the compounds with respect to other triazoles in the literature facilitated electrochemical reduction reactions. Electrochemical and *in-situ* spectroelectrochemical studies reveal that ligand based redox couples are generated during the *in-situ* electrolysis of the zinc and magnesium phthalocyanines. These compounds may have potential application due to rich redox properties as dual sensitizers in the photodynamic therapy and solar cell.

Table 1. The electrochemical data MgPc and ZnPc complexes and a brief summary of summary of triazole including phthalocyanine complexes the literature.

Compound		$E_{1/2}$	ΔE_p (mV)	$I_{p,a}/I_{p,c}$	$\Delta E_{1/2}$	References
ZnPc (in DMF)	R _I	-0.67	71	1.10		This work
	R _{II}	-1.08	60	1.02	1.48	
	R _{III}	-1.77	80	0.88		
	O _I	0.81	83	0.79		
MgPc (in DMF)	R _I	-0.69	60	0.99		This work
	R _{II}	-1.17	85	0.81	1.49	
	R _{III}	-1.87	80	0.75		
	O _I	0.80	60	0.70		
H₂Pc (in DMF)	R _I	-0.63	-	-		(23)
	R _{II}	-1.05	-	-	-	
	R _{III}	-1.38	-	-		
	O _I	0.86	-	-		
H₂Pc (in DMSO)	R _I	-0.52	74	-		(35)
	R _{II}	-0.97	72	-	-	
	R _{III}	-1.80	66	-		
	O _I	-	-	-		
ZnPc (in DMF)	R _I	-0.84	60	0.97		(36)
	R _{II}	-1.35	60	0.66	1.54	
	R _{III}	-	-	-		
	O _I	0.64	80	0.62		
ZnPc (in DMSO)	R _I	-0.82	60	1.00		(26)
	R _{II}	-1.26	63	1.06	-	
	R _{III}	-1.86	80	0.30		
	O _I	0.62	87	0.86		
MgPc (in DCM)	R _I	-1.70	61	-		(37)
	R _{II}	-2.17	78	-		
	O _I	0.09	136	-		
	O _{II}	0.63	80	-		
MgPc (in DMF)	R _I	-0.90	-	-	1.55	(34)
	R _{II}	-1.39	-	-		
	O _I	0.65	-	-		

$E_{1/2}$ values ($(E_{\text{anodic peak}} + E_{\text{cathodic peak}}) / 2$), $\Delta E_p = E_{\text{anodic peak}} - E_{\text{cathodic peak}} = E_{\text{pa}} - E_{\text{pc}}$ and $I_{\text{pa}}/I_{\text{pc}}$ is the rate of peak currents. $\Delta E_{1/2} = E_{1/2}$ (the first oxidation) – $E_{1/2}$ (the first reduction).

REFERENCES

- Lever AP. The phthalocyanines. *Advances in Inorganic Chemistry and Radiochemistry*. 7: Elsevier; 1965. p. 27-114.
- de la Torre G, Claessens CG, Torres T. Phthalocyanines: old dyes, new materials. Putting color in nanotechnology. *Chemical communications*. 2007(20):2000-15.
- Claessens CG, Hahn U, Torres T. Phthalocyanines: From outstanding electronic properties to emerging applications. *The Chemical Record*. 2008;8(2):75-97.
- Akyüz D, Dinçer H, Özkaya AR, Koca A. Electrocatalytic hydrogen evolution reaction with metallophthalocyanines modified with click electrochemistry. *International Journal of Hydrogen Energy*. 2015;40(38):12973-84.
- Özçesmeçi İ, Demir A, Akyüz D, Koca A, Gül A. Electrocatalytic hydrogen evolution reaction with a supramolecular cobalt(II) phthalocyanine carrying four cobaloxime moieties. *Inorganica Chimica Acta*. 2017;466:591-8.
- Zhang Y, Cai X, Bian Y, Jiang J. Organic semiconductors of phthalocyanine compounds for field effect transistors (FETs). *Functional Phthalocyanine Molecular Materials*: Springer; 2010. p. 275-321.
- Döring S, Otto T, Cehovski M, Charfi O, Caspary R, Kowalsky W, et al. Highly sensitive wide range organic photodiode based on zinc phthalocyanine: C60. *physica status solidi (a)*. 2016;213(9):2387-91.
- Yıldız B, Güzel E, Akyüz D, Arslan BS, Koca A, Şener MK. Unsymmetrically pyrazole-3-carboxylic acid substituted phthalocyanine-based photoanodes for use in water splitting photoelectrochemical and dye-sensitized solar cells. *Solar Energy*. 2019;191:654-62.
- Aliosman M, Angelov I, Mitrev Y, Iliev I, Durmuş M, Mantareva V. Novel Zn (II) phthalocyanine with tyrosine moieties for photodynamic therapy: Synthesis and comparative study of light-associated properties. *Polyhedron*. 2019;162:121-8.

10. Kaya M, Menteşe E, Sökmen BB, Akçay HT. The determination of molecular dynamic properties of Novel 5-oxo-1, 2, 4-triazole phthalocyanines and investigation of their urease inhibition properties. *Journal of Molecular Structure*. 2020;128870.
11. Arslan T, Çakır N, Keleş T, Biyiklioglu Z, Senturk M. Triazole substituted metal-free, metallo-phthalocyanines and their water soluble derivatives as potential cholinesterases inhibitors: Design, synthesis and in vitro inhibition study. *Bioorganic chemistry*. 2019;90:103100.
12. Demirbaş Ü, Akyüz D, Akçay HT, Koca A, Bekircan O, Kantekin H. Electrochemical and spectroelectrochemical study on novel non-peripherally tetra 1, 2, 4-triazole substituted phthalocyanines. *Journal of Molecular Structure*. 2018;1155:380-8.
13. Barut B, Yalçın CÖ, Demirbaş Ü, Özel A. Photochemical and in vitro phototoxic properties of Zn(II) phthalocyanine bearing piperidinium groups on different cell lines. *Journal of Organometallic Chemistry*. 2020:121358.
14. Demirbaş Ü, Pişkin M, Bayrak R, Durmuş M, Kantekin H. Zinc (II) and lead (II) phthalocyanines bearing thiadiazole substituents: Synthesis, characterization, photophysical and photochemical properties. *Journal of Molecular Structure*. 2019;1197:594-602.
15. Volov AN, Burtsev ID. New glycosylated platinum(II) phthalocyanine containing ribose moiety-synthesis and photophysical properties. *Journal of Organometallic Chemistry*. 2020:121372.
16. Baygu Y, Gök Y. A highly water-soluble zinc (II) phthalocyanines as potential for PDT studies: Synthesis and characterization. *Inorganic Chemistry Communications*. 2018;96:133-8.
17. Demirbaş Ü, Akyüz D, Akçay HT, Koca A, Kantekin H. Non-peripherally tetra substituted lead(II), nickel(II) and copper(II) phthalocyanines bearing [1,2,3] triazole moieties: Synthesis, characterization and investigation of electrochemical and spectroelectrochemical properties. *Journal of Molecular Structure*. 2019;1176:695-702.
18. Karaca H, Sezer S, Özalp-Yaman Ş, Tanyeli C. Concise synthesis, electrochemistry and spectroelectrochemistry of phthalocyanines having triazole functionality. *Polyhedron*. 2014;72:147-56.
19. Demirbaş Ü, Özçifçi Z, Akçay HT, Menteşe E. Novel phthalocyanines bearing 1, 2, 4 triazole substituents: Synthesis, characterization, photophysical and photochemical properties. *Polyhedron*. 2020:114470.
20. Lever ABP, Leznoff CC. *Phthalocyanines: properties and applications*: New York: VCH, 1989-c1996.; 1996.
21. Adebayo AI, Nyokong T. Synthesis, spectroscopic and electrochemical properties of manganese, nickel and iron octakis-(2-diethylaminoethanethiol)-phthalocyanine. *Polyhedron*. 2009;28(14):2831-8.
22. Kamiloğlu AA, Akyüz D, Koca A, Acar İ. Synthesis and investigation of spectroelectrochemical properties of peripherally tetra-substituted phthalocyanine bearing 3-(4-{[3-(trifluoromethyl) benzyl] oxy} phenyl) propan-1-ol and its metallo compounds. *Journal of Inclusion Phenomena and Macrocyclic Chemistry*. 2018;92(1-2):223-35.
23. Nar I, Gül A, Sivaev IB, Hamuryudan E. Cobaltacarborane functionalized phthalocyanines: Synthesis, photophysical, electrochemical and spectroelectrochemical properties. *Synthetic Metals*. 2015;210:376-85.
24. Alemdar A, Özkaya AR, Bulut M. Synthesis, spectroscopy, electrochemistry and in situ spectroelectrochemistry of partly halogenated coumarin phthalonitrile and corresponding metal-free, cobalt and zinc phthalocyanines. *Polyhedron*. 2009;28(17):3788-96.
25. Akyüz D, Demirbaş Ü, Akçay HT. Synthesis, characterization and electrochemistry of 1-phenoxypropan-2-yloxy substituted phthalocyanines. *Journal of Organometallic Chemistry*. 2020;923:121455.
26. Demirbaş Ü, Akyüz D, Akçay HT, Koca A, Menteşe E, Kantekin H. Novel 1, 2, 4-triazole substituted metallo-phthalocyanines: Synthesis, characterization and investigation of electrochemical and spectroelectrochemical properties. *Journal of Molecular Structure*. 2018;1173:205-12.
27. Orman EB, Arıbal A, Özkaya AR, Bulut M, Salan Ü. Synthesis, characterization and electrochemical properties of isoflavone substituted zinc(II), cobalt(II), and metal-free phthalocyanines. *Journal of Porphyrins and Phthalocyanines*. 2019;23(07n08):856-69.
28. Evans DH, O'Connell KM, Petersen RA, Kelly MJ. *Cyclic voltammetry*. ACS Publications; 1983.
29. Matsuda H, Ayabe Y. Zur Theorie der Randles-Sevčikschen Kathodenstrahl-Polarographie. *Zeitschrift für Elektrochemie, Berichte der Bunsengesellschaft für physikalische Chemie*. 1955;59(6):494-503.
30. Karaoğlu GK, Gümrükçü G, Koca A, Gül A. The synthesis, characterization, electrochemical and spectroelectrochemical properties of a novel,

cationic, water-soluble Zn phthalocyanine with extended conjugation. *Dyes and Pigments*. 2011;88(3):247-56.

31. Mack J, Stillman MJ. Photochemical formation of the anion radical of zinc phthalocyanine and analysis of the absorption and magnetic circular dichroism spectral data. Assignment of the optical spectrum of [ZnPc (-3)]. *Journal of the American Chemical Society*. 1994;116(4):1292-304.

32. Nyokong T, Gasyna Z, Stillman MJ. Phthalocyanine. pi.-cation-radical species: photochemical and electrochemical preparation of [ZnPc (-1).+ in solution. *Inorganic Chemistry*. 1987;26(4):548-53.

33. Alemdar A, Özkaya AR, Bulut M. Preparation, characterization, electrochemistry and in situ spectroelectrochemistry of novel α -tetra [7-oxo-3-(2-chloro-4-fluorophenyl) coumarin]-substituted metal-free, cobalt and zinc phthalocyanines. *Synthetic metals*. 2010;160(13-14):1556-65.

34. Ough EA, Creber KA, Stillman MJ. Electrochemistry and spectroscopy of magnesium octaethyltetraazaporphyrin and magnesium octakis (methylthio) tetraazaporphyrin. *Inorganica chimica acta*. 1996;246(1-2):361-9.

35. Rollmann LD, Iwamoto RT. Electrochemistry, electron paramagnetic resonance, and visible spectra of cobalt, nickel, copper, and metal-free phthalocyanines in dimethyl sulfoxide. *Journal of the American Chemical Society*. 1968;90(6):1455-63.

36. Akyüz D, Demirbaş Ü, Akçay HT. Synthesis, characterization and electrochemistry of 1-phenoxypropan-2-yloxy substituted phthalocyanines. *Journal of Organometallic Chemistry*. 2020:121455.

37. Kryjewski M, Rebis T, Milczarek G, Gdaniec Z, Goslinski T, Mielcarek J. Magnesium (ii) 1-(1-adamantylsulfanyl) phthalocyanine-synthesis, photochemical and electrochemical properties. *New Journal of Chemistry*. 2016;40(11):9774-80.



Chemical Constituents of *Rumex abyssinicus* Roots and Evaluation of Its Antimicrobial Activities

Muaz Shifa , Dele Abdissa , Tsegaye Girma Asere* 

Jimma University, College of Natural Sciences, Department of Chemistry, P.O.Box 378, Jimma, Ethiopia.

Abstract: Medicinal plants are usually screened for phytochemicals that may lead to further isolation, purification, and characterization of their active principles. The roots of *Rumex abyssinicus* are used traditionally in Ethiopia for treating different diseases such as hepatitis, hemorrhoids, gonorrhea, typhus, and wounds. Thus, this study was conducted to investigate the phytochemicals and *in vitro* antimicrobial activity of the roots of *R. abyssinicus* extracts. The roots were collected, chopped, and air-dried under shade in the laboratory. Then, the dried plant material was subjected to sequential extraction using the maceration technique by soaking 1 kg of the sample in petroleum ether, chloroform, acetone, and methanol. Meanwhile, the filtrates were concentrated under reduced pressure using a rotary evaporator. Afterward, the crude extracts were dried and screened for *in vitro* antimicrobial activity tests using four bacterial and two fungal strains. Based on its activity, the acetone extract was used for column chromatographic isolation. Herein, two known anthraquinones were isolated and characterized: chrysophanol and emodin. The microbial activity of both extracts and isolated compounds were evaluated against medically important strains by the agar disc diffusion method. The concentration of the extracts and isolated compounds was 100 mg/mL tested against *S. aureus* ATCC25903, *K. pneumoniae* NCTC13368, *E. coli* ATCC 25722, *P. aeruginosa* DSMZ 1117 and *C. albicans* and *S. cerevisiae*. The zone of growth inhibition of extracts and isolated compounds were compared with standard drugs like Gentamycin and Mancozeb. The results showed that the isolated compounds (**1** and **2**) have higher bacterial growth inhibition than the extracts. However, compound **2** was not active against *S. cerevisiae* strain.

Keywords: *Rumex abyssinicus*; chrysophanol; emodin

Submitted: September 20, 2020. **Accepted:** November 05, 2020.

Cite this: Shifa M, Abdissa D, Asere TG. Chemical Constituents of *Rumex abyssinicus* Roots and Evaluation of Its Antimicrobial Activities. JOTCSA. 2021;8(1):21-46.

DOI: <https://doi.org/10.18596/jotcsa.797560>.

***Corresponding author. E-mail:** tsegaye96@gmail.com.

INTRODUCTION

Medicinal plants (MPs) are the abundant bioresources of medical substances of traditional systems of medicine, modern medicines, nutraceuticals, food supplements, folk medicines, pharmaceutical intermediates, and chemical entities for synthetic drugs (1). Since time immemorial, different parts of medicinal herbs have been used to cure specific ailments (2). They are recognized for their ability to produce a wealth

of secondary metabolites, and mankind has used many species for centuries to treat a variety of diseases (1). Many of the natural products (NPs) have been shown to present interesting biological and pharmacological activities and serve as the starting point in the development of modern medicine (3).

A number of modern drugs have been derived from natural sources, many based on their traditional medicinal claims. The plant products used in the

treatment of diseases could be obtained from barks, leaves, flowers, roots, fruits, or seed parts of the plants (4). The use of biological resources for various therapies has been known in many different parts of the world, especially in remote regions where traditional medicines (TMs) provide an alternative to the modern health care system (5). Many people in developing countries still use TM due to its low cost and availability (6). Over 80% of people in developing countries rely on TM for primary health care needs, of which a major proportion corresponds to plant extracts (6,7). The phytochemicals isolated from these plants have shown *in vitro* and *in vivo* biological activities (8).

Ethiopia is the home of many plant species that are commonly used in many disease treatments by local healers (9). Some of the factors attributed to these facts are accessibility, affordability as compared to modern drugs, socio-cultural background, and their effectiveness against several health problems (1). For example, *R. abyssinicus* is a widely spread medicinal plant in the highlands of tropical Africa and is a common weed of cultivated lands or disturbed grounds ranging from North Africa to Ethiopia at altitudes between 1200 and 3300 m (10). It is a perennial herb, which grows up to 3 m tall, with a thick, fleshy rhizome. The plant is endemic to Ethiopia and it is referred to as *mekmeko* in the Amharic language (11,12).

The genus *Rumex* belongs to the family *Polygonaceae*, which consists of about 200 species. Most of the species of *Polygonaceae* contain a large number of bioactive compounds such as anthraquinones, flavonoids, terpenes, naphthalenes, stilbenoids, and steroids, flavonoid glycosides, leucoanthocyanidins, and phenolic acids (11). Traditionally, people use different parts of *Rumex* species to treat several health problems such as infections, diarrhea, constipation, mild diabetes, oedema, jaundice, skin, liver, and gallbladder disorders and inflammation, and as an antihypertensive, diuretic and analgesic preparation (9,13). The decoction of the leaves or root powder of *R. abyssinicus* is taken as a vermifuge. It is also used to treat malaria, gonorrhoea, poisoning, hepatitis, constipation, sciatic neuralgia, hypertension, migraine, rheumatism, breast cancer, stomach distention, earache, hepatic diseases, hemorrhoids, typhus, rabies, and wound (14). The roots of *R. abyssinicus* are reported to possess antibacterial activity against *Streptococcus pyogenes* (15). Its antifungal activities were also tested against several fungal pathogens (*Aspergillus fumigatus*, *Aspergillus flavus*, *Aspergillus versicolor*, *Aspergillus niger*, *Blastoschizomyces capitatus*, *Fusarium oxysporum*, *Fusarium moniliforme*, *Fusarium semitectum*, *Pythium sp.*, *Rhizopus sp.*,

Sporotrichum sp., and *Thermomyces ssp.*) and results showed its promising activity (16).

For this reason, medicinal plants are considered a chemical factory as it contains a multitude of chemical compounds which are suggested to be natural bioactive like alkaloids, glycosides, saponins, resins, oleoresins, sesquiterpene, lactones, anthraquinones, and essential oils and fixed oils (17). The emergence of antibiotic-resistant microbial strains (including bacterial and protozoan parasites) and the increasing failure of available chemotherapeutics (18) urge the search for microbiologically active MPs. Hence, the bioactive phytochemical constituents present in the plant play a significant role in the development of medicine and drug discovery. Therefore, herein it was aimed to carry out phytochemicals isolation and evaluation of their *in vitro* antimicrobial activities of extracts from the roots of *R. abyssinicus*.

EXPERIMENTAL SECTION

Chemicals

Chemicals used for this study were petroleum ether, chloroform, acetone, ethyl acetate, silica gel 60-120 mm mesh size. Dimethyl sulfoxide (DMSO), Mueller Hinton agar, and nutrient broth were used for the antimicrobial test. All chemicals and reagents used were of analytical grade.

Apparatus and Instruments

Apparatuses such as rotary evaporator (Heidolph, Germany, laboratory 4000), round bottom flasks, measuring cylinder, filter paper (cotton swab), weighing balance (model NWT100001X) oven (N50C GENLAB WIDNES, England) were used. Analytical Thin Layer Chromatography (TLC) was performed on precoated silica gel 60 F₂₅₄ plates. Incubator (Gene lab incubator) and Hood (CLB-201-04, vertical laminar cabinet) were used for the antimicrobial activity studies. Glass column chromatography (500 mm, B-34/35) and UV chamber (254 and 365 nm) were used for isolation of compounds. The NMR spectra were recorded on an Avance 600 MHz spectrometer (Bruker, Billerica, MA, USA) using the DMSO solvent.

Sample Collection and Preparation

The roots of *R. abyssinicus* were collected from Gomma District, Jimma Zone, Oromiya Regional State, Ethiopia, in July 2019. Then, it was roughly washed with tap water, chopped into smaller pieces, and air-dried under a shade at room temperature in the laboratory. The air-dried sample was homogenized into a suitable size to increase the rate of solvent penetration into the cells by using mechanical grinding. Finally, it was subjected to organic solvent extraction.

Extraction and Isolation

The air-dried root sample of *R. abyssinicus* (1 kg) was sequentially extracted by soaking in petroleum ether, chloroform, acetone, and methanol (2 x 2.5 L) each using a maceration technique at room temperature and was kept for 48 h. The extracts were filtered with filter paper, plugged in cotton, and concentrated using a rotary evaporator under reduced pressure; the yellowish crude extracts were kept in a desiccator until dryness for further experimental purposes. Then, the crude products weighing 5.45 g (0.55%), 8.50 g (0.85%), 14.50 (1.45%), and 14 g (1.40%), respectively were obtained. Meanwhile, the four extracts were applied for *in vitro* antimicrobial activity test and TLC analysis to continue the isolation of pure compounds, with the product having promising bioactivity against the selected bacterial and fungal strains.

Isolation of pure compounds was continued using the crude products demonstrating promising activity against the strains and good TLC profile. Among the four crude extracts, acetone extract has shown the highest zone of growth inhibition against bacterial and fungal strains. Thus, based on its bioactivity and TLC profile, it was subjected

to column chromatographic separation. Petroleum ether/ethyl acetate combination showed better separation of the compounds on TLC tests. Initially, the column chromatography was packed with silica gel (60-120 mesh size) just by activating in an oven at 100 °C for 2 h. Then, the fine powder of the sample acetone extract (14.5 g) was loaded to the column chromatography.

The elution was started with petroleum ether and increased the polarity using 1 up to 100% ethyl acetate. Meanwhile, a total of 148 fractions were collected in a 20 mL small beaker for each. The first 30 fractions were merged after TLC analysis. Using TLC and R_f value results, fractions with similar R_f values were combined. Fractions 52-65 were combined and washed repeatedly with n-hexane to afford compound **1** (0.40 g). The elution was continued by increasing the polarity of the solvent. The second pure compound **2** was obtained from fractions 66-81. It showed one spot and some impurities which were later purified by continuing washing it with n-hexane. Then, a crystalline orange color product of compound-**2** (0.38 g) was obtained. The isolated compounds were characterized by using $^1\text{H-NMR}$, $^{13}\text{C-NMR}$, and 2D NMR spectroscopy techniques.

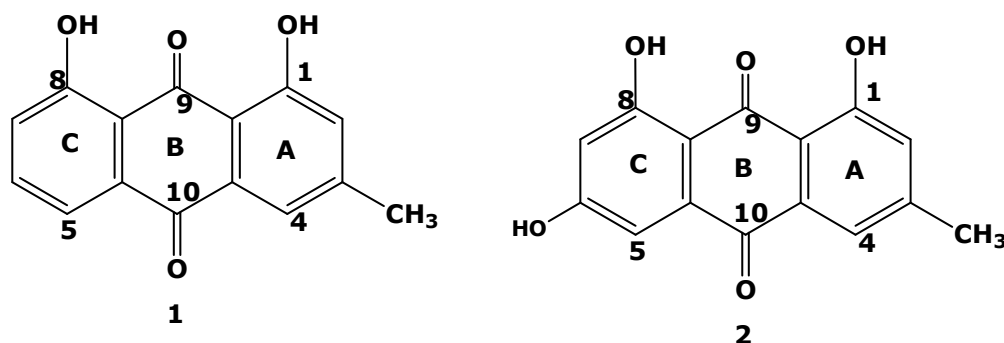


Figure 1. The proposed structure of compounds **1** and **2**.

Antimicrobial Activity Test

Test strains and preparation of test samples:

Microorganisms used for evaluation of *in vitro* antimicrobial activities were *S. aureus* ATCC25903, *K. pneumoniae* NCTC13368, *E. coli* ATCC 25722, *P. aeruginosa* DSMZ 1117, *C. albicans*, and *S. cerevisiae*. These strains were obtained from Jimma University Microbiology Research Laboratory, Biology Department. The *in vitro* antibacterial and antifungal activities of the crude extracts and isolated compounds were determined against four bacteria and two fungal strains mentioned above using the agar disc diffusion method and was carried out following a standard procedure as used earlier by Abdissa *et al.* (19). Then, bacterial and fungal stock cultures were incubated for 24 h at 37 °C on nutrient agar and potato dextrose agar (PDA) media following refrigeration storage at 4 °C. The bacterial strains were grown in Mueller-Hinton agar (MHA) plates at

37 °C (the bacteria were grown in the nutrient broth at 37 °C and maintained on nutrient agar slants at 4 °C), while the fungal strains were grown in PDA media at 28 °C. The stock cultures were maintained at 4 °C. The bacterial and fungal stock cultures were incubated for 24 h at 37 °C on nutrient agar and PDA medium.

Active cultures for this experiment were prepared by transferring a loop full of bacterial cells from the stock cultures to test tubes of Mueller-Hinton broth (MHB) that incubated without agitation for 24 h at 37 °C. A cell suspension of each organism was freshly prepared by transferring isolated colonies selected from a 24 h agar plate into a broth and the cell density was adjusted to turbidity equivalence of 0.5 McFarland turbidity standards (1×10^8 CFU/mL) in sterile saline solution. The bacterial and fungal cultures were then streaked onto MHA plate with a sterile cotton swab to obtain

a uniform thick lawn of growth. Meanwhile, the sterile paper discs (6 mm diameter, Whatman No.3) were separately soaked in pre-prepared crude extracts and pure compounds, whose stock solutions were prepared at a concentration of 100 mg/mL by dissolving 0.1 g (100 mg) of the crude extracts and pure compounds were separately dissolved in DMSO before aseptically placed on an already inoculated MHA plate. It was then allowed to diffuse for 5 min at ambient temperature and then incubated at 37 °C for 24 h. Gentamycin and Mancozeb (10 µg) were used as a standard positive control against bacterial and fungal strains, respectively, DMSO was used as a negative control. Finally, the zone of growth inhibition was reported by measuring diameter using a transparent ruler after 24 h of incubation.

RESULTS AND DISCUSSION

Characterization and Antimicrobial activities

Compound-**1** was isolated as a yellowish crystalline solid obtained from the fractions 52-65. Its R_f value was 0.65 using 70% petroleum ether in ethyl acetate as an eluent. The $^1\text{H-NMR}$ spectrum is given in supporting information (**SI1**), which showed that the presence of five aromatic protons at δ_{H} 7.22, 7.39, 7.55, 7.71, and 7.81 ppm (Table 1). Besides, hydroxyl proton (-OH) groups were observed at δ_{H} 11.93. And $^1\text{H-NMR}$ spectroscopic data of compound-**1** showed a singlet proton signal at δ_{H} 2.44 ppm representing three protons attached to C-3 of the aromatic ring A. The two broad singlet peaks observed at δ_{H} 7.22, 1H and 7.55, 1H represent the protons attached to C-2 and C-4 of the aromatic ring, respectively. The aromatic protons that are attached to C-5 and C-7 are a doublet of a doublet at δ_{H} 7.72, *dd*, $J=12$,

1H, and 7.39, *dd*, $J=6$, 1H, respectively. The *pseudo*-triplet proton was observed at δ_{H} 7.82, *t*, $J=6,12$ (m,1H). These three mutually coupled aromatic protons at C-5, C-6, and C-7 are in the ABX spin system. Moreover, there are two chelated protons at the *peri*-position (C-1 and C-8) of the aromatic ring, a highly deshielded proton at δ_{H} 11.93 ppm and downfield shifted carbonyl signals at δ_{C} 192.0 and 181.0 ppm (Table 1). Thus, the presence of a 1,8-dihydroxyanthraquinone moiety clearly indicates that as it is the chrysophanol (19). And its molecular formula is $\text{C}_{15}\text{H}_{10}\text{O}_4$ (12).

Its $^{13}\text{C-NMR}$ spectrum (**SI2**) showed 15 signals that represented 15 carbons including one methyl group at δ 22.0, five aromatic carbons at δ_{C} : C-2 (124.6), C-4 (120.0), C-5 (119.8), C-6 (137.8), and C-7 (124.9) as evidenced from HSQC data (**SI3**). Besides, the spectra showed two-hydroxyl carbons at δ_{C} 161.8 and 162.0, which represent carbons at *peri*-position and two aromatic carbonyl groups were also observed at δ_{C} C-9 (192.0) and C-10 (181.0). Therefore, based on the combined spectroscopic data (COSY (**SI4**), HSQC, HMBC (**SI5**), and $^1\text{H-}^{13}\text{C}$), the proposed structure was suggested chrysophanol (Compound **1**, 0.40 g). Based on this research finding and literature review reports (19,20), Compound-**1** was identified as 1,8-dihydroxy-3-methyl-9,10-anthraquinone (chrysophanol) (Table 2, Figure 1). It was reported from the roots of *R. abyssinicus*, where pure compounds were isolated using n-hexane, ethyl acetate, and methanol (20). Other studies reports also indicated that chrysophanol is present in *Polygonaceae*, *Rhamnaceae*, *Fabaceae*, *Liliaceae*, *Asphodelaceae*, *Buphorbiaceae*, *Meliaceae*, *Podocarpaceae*, *Picramniaceae*, and *Hemerocallidaceae* plant families (21–23).

Table 1. ^1H (600 MHz) and ^{13}C (150 MHz) NMR Spectral Data of Compounds **1** and **2** in DMSO-d_6 .

position	Compound-1		Compound-2	
	$\delta^1\text{H}$ (m, J in Hz)	$\delta^{13}\text{C}$	$\delta^1\text{H}$ (m, J in Hz)	$\delta^{13}\text{C}$
1	11.93, s	161.8	11.96, s	161.9
2	7.22, s	124.6	7.11, <i>b</i> , s	124.5
3	-	149.6	-	149.7
4	7.55, s	120.0	7.42, s	121.0
5	7.72 (<i>dd</i> , $J=12$)	119.8	7.06, s	109.2
6	7.82 (<i>t</i> , $J=6,12$)	137.8	-	164.9
7	7.39 (<i>dd</i> , $J=6$)	124.9	6.55, s	108.3
8	-	162.0	12.04, s	166.0
9	-	192.0	-	190.1
10	-	181.0	-	181.7
11	-	133.8	-	135.5
12	-	116.3	-	109.3
13	-	114.2	-	113.7
14	-	133.5	-	133.2
C-Me	2.44, s	22.1	H-Me 2.50, s	21.9

Compound-**2** (0.38 g) was isolated as an orange crystalline solid with R_f value 0.58 using 70% petroleum ether in ethyl acetate. The $^1\text{H-NMR}$ spectrum of the compound (**SI6**) shows the presence of four aromatic protons at δ_{H} 7.42, 7.11, 7.06, and 6.55 ppm. It has also revealed the presence of one set of methyl protons at δ_{H} 2.50 and two-hydroxyl protons at δ_{H} 11.96 and 12.04 ppm.

Its $^{13}\text{C-NMR}$ spectrum data shows (**SI7**) the presence of 15 carbon signals (Table 1). Among these carbons, there are four CH aromatic ring protons at δ_{C} : C-2 (124.5), C-4 (121.0), C-5 (109.2) and C-7 (108.3) ppm, two-carbonyl carbons that attached to benzene ring at δ_{C} C-9 (190.1) and C-10 (181.7) ppm, three oxygenated carbons of the aromatic ring at δ_{C} : C-1 (161.9), C-6 (164.9), C-8 (166.0) and five quaternary carbons indicated at C-3 (149.7), C-11 (135.5), C-12 (109.3), C-13 (113.7) and C-14 (133.2) ppm. The ^{13}C NMR spectrum also showed the presence of one methyl carbon at δ_{C} of 21.9 and one methyl-substituted carbon observed at δ_{C} 149.7(C-3). Furthermore, COSY (**SI8**), HMBC (**SI9**), and HSQC (**SI10**) spectrum correlation data have confirmed that the proposed compound structure was named as 3-methyl-1,6,8-trihydroxyanthraquinone (Emodin)(23–25) (Table 2, Figure 1). Emodin is found in *Rhamnus* and *Rumex* of higher plant species, and it is a metabolite of some *Penicillium* species (12,24,26).

From Table 2 above (compound **1**), the COSY correlation spectrum data show that there are three pairs of couplings between partner protons of 3J value observed at 7.72 (H-5) with H-6 (7.82), and H-6 (7.82) with H-7 (7.39) including the weak *meta*-coupled protons of 4J value of H-5 coupling with H-7. Similarly, a triplet proton for H-6, and a doublet of doublet for its partners. The other important heteronuclear multiple bonds correlation spectrum is HSQC, which correlates the carbon-proton of a single bond (1J). For instance, the correlation of H-2 (7.22) with C-2 (124.6), H-4 (7.55) with C-4 (120.0), H-5 (7.72) with C-5

(119.8), and H-6 (7.82) with C-6 (137.8). On the other hand, the HMBC spectrum shows the correlation of protons with carbon in two to four bond distances. For example, it is observed that at proton δ_{H} : H-2 (7.22) correlated with C-11 (133.8), C-4 (120.0), and the correlation with C-1 (161.8). The correlation at δ_{H} H-4 (7.55) showed a long-range correlation with C-10 (181.0), C-2 (124.6), and C-13 (114.2). Based on the combined spectroscopic data, the structure of compound **1** was proposed as Chrysophanol in Figure 1.

From Table 2 above (compound **2**), HMBC spectrum showed the correlations of protons H-2 (7.11) with C-1 (161.9), C-4 (121.0) C-11 (135.5) and C-Me (21.9) and H-4 (7.42) to C-1 (161.9), C-4 (121.0) C-13 (113.7) C-9 (190.1) and C-Me (21.9). These correlations give us the information of the partial aromatic structure of compound-**2** indicated as ring A. Correspondingly, the correlations of protons H-5 (7.06 ppm) to C-6 (164.9), C-9 (190.1), C-12 (109.3) and H-7 (6.55) to C-5 (109.2), C-8 (166.0) give us the presence of another partial aromatic cyclic structure of ring C.

The correlation of H-7 with C-8 and C-6 indicates the presence of two alcohols in this *meta* position of the aromatic cycle. The correlations of H-5 to the carbonyl signal C-10 and of H-2 (7.11 ppm) to carbonyl signal C-9 confirm the presence of anthraquinone. Moreover, the correlation of H-5 to C-6 (an oxygenated quaternary carbon) indicates the presence of an alcohol group (Figure 2). And the COSY correlation spectrum ($^1\text{H-}^1\text{H}$) helps to indicate the partner protons coupling each other like the two *meta*- coupling protons H-2 with H-4 (ring A) and H-5 with H-7 (ring C). Equally, the single bond coupling of the HSQC correlation spectrum ($^1\text{H-}^{13}\text{C}$) plays a vital role in suggesting the structure of the compound. The HSQC correlation of the aromatic ring A of H-2 to C-2 and H-4 to C-4 equivalently for ring B, H-5 correlated to C-5 and H-7 to C-7, which helps to propose the skeleton of the compound. Based on the combined NMR spectrum, compound **2** was proposed as Emodin.

Antibacterial and Antifungal Activity Evaluation

The *in vitro* antibacterial and antifungal activities of crude extracts and isolated compounds (**1** and **2**) were carried out using four human pathogenic bacterial strains: *P. aeruginosa*, *K. pneumoniae*, *S. aureus*, and *E. coli* and two fungal strains: *C. albicans* and *S. cerevisiae* by using agar disc diffusion method. The bioassay test was conducted using the petroleum ether, chloroform, acetone, and methanol extracts of *R. abyssinicus* roots. Its crude extracts have demonstrated a good yield of the antimicrobial zone of growth inhibition (**SI11**), but petroleum ether extract is not active against *S. aureus* and *K. pneumoniae*. The previous research report finding shows that the n-hexane extract of leaves, shoots, and roots of *Rumex dentatus* did not show any activity against several bacterial strains tested and the methanol extract has no prominent inhibition against fungal strains (27). Therefore, based on its promising antimicrobial activity in demonstrating a better zone of growth inhibition, good TLC profile, and a high percentage yield, the acetone extract was selected for the isolation of pure compounds. It has demonstrated zone of growth inhibition against *S. aureus* 21.0±1.4, *K. pneumoniae* 15.5±0.4, *P. aeruginosa* 22.5±0.7, and *E. coli* 18.0±0.4 mm and the positive standard (Gentamicin) has 34.5±0.7, 30.0±0.7, 30.0±0.1, and 32.0±0.1 mm, respectively (Table 3). The previous report also indicated that *R. abyssinicus* is used for wound healing purposes in Ethiopia (12).

The pure compound-**1** (Chrysophanol) and compound-**2** (Emodin) have also exhibited a diameter of better zone of growth inhibition against *S. aureus* (23.0±0.1 mm) and *K. pneumoniae* (22.5±0.4 mm) than *P. aeruginosa* (18.0±0.2 mm) and *E. coli* (18.0±0.4) in mm and the positive standard (Gentamicin) has 26.0±0.3 mm zone of growth inhibition (**SI11**). Compound-**2** has also shown a better zone of growth inhibition against *K. pneumoniae* (20.0±0.7) and *S. aureus* (20.0±0.2) than *P. aeruginosa* (19.0±0.3) and *E. coli* (17.0±0.7) in mm. The results indicated that compounds **1** and **2** have shown better

antibacterial activity against *K. pneumoniae* and *S. aureus* strains and their activity was close to the positive standard (Gentamicin). These anthraquinones themselves have little therapeutic activity and need to be in the form of water-soluble glycosides to exert their action (26). Similarly, the antifungal activity of compounds **1** and **2** (**SI12**), was active over *C. albicans* with a zone of inhibition 20.0±0.4 and 22.0±0.7 mm, respectively which is almost equal to the zone of inhibition exhibited by the positive standard (Mancozeb). Conversely, both compounds **1** and **2** were not active on the *S. cerevisiae* fungal strains (Table 3). Thus far, it was reported that chrysophanol (**1**) and emodin (**2**) are antimicrobial and wound healing active constituents isolated from the rhizomes of *R. abyssinicus* and other plant species (12,28).

CONCLUSION

The main objective of this study was to carry out a phytochemical constituent investigation and *in vitro* antimicrobial activity screening of the root extracts of *R. abyssinicus*. Based on its promising bioactivity and good TLC profile, the acetone crude extract was subjected to column chromatographic isolation packed with silica gel using petroleum ether. As a result, from the root extracts of *R. abyssinicus*, two compounds, Chrysophanol (Compound **1**) and Emodin (Compound **2**) anthraquinones were isolated and evaluated against four bacterial and two fungal strains. It was screened against *S. aureus*, *P. aeruginosa*, *E. coli*, *K. pneumoniae*, *C. albicans*, and *S. cerevisiae* using Gentamycin and Mancozeb as positive standards, and DMSO as negative standard. The antibacterial activity of isolated compound **1** showed higher activity against *S. aureus* 22.5±0.4 mm, *P. aeruginosa* 18.0±0.2 mm, *E. coli* 18.0±0.4 mm, *K. pneumoniae* 23.0±0.1 mm than **2**; while antifungal activity **2** is higher than *C. albicans* 22±0.7 mm than **1** for *C. albicans* 20±0.4 mm. On the contrary, compound **2** was not active against the *S. cerevisiae* strain. And the structures of these compounds were elucidated using 1D and 2D-NMR spectroscopic techniques.

Table 2. COSY, HSQC, and HMBC Correlation Data of Compounds **1** and **2** in DMSO.

	Position δ_C	Compound 1 δ_H	HSQC (1J)	COSY ($^3J, ^4J$)	HMBC (3J)
2	124.6	H-2 (7.22)	C-C-2 \leftrightarrow H-2	-	H-2 \rightarrow C-4, C-11
4	120.0	H-4 (7.55)	C-4 \leftrightarrow H-4	-	H-4 \rightarrow C-2, C-10
5	119.8	H-5 (7.72)	C-5 \leftrightarrow H-5	H-5 \leftrightarrow H-6	H-5 \rightarrow C-10, C-7, C-13
6	137.8	H-6 (7.82)	C-6 \leftrightarrow H-6	H-5 \leftrightarrow H-7	H-6 \rightarrow C-14, C-8
7	124.9	H-7 (7.39)	C-7 \leftrightarrow H-7	H-6 \leftrightarrow H-7	H-7 \rightarrow C-5, C-13
Me	22.1	H-Me (2.44)	-	-	H-Me \rightarrow C-2, C-4
Compound- 2					
2	124.5	H-2 (7.11)	H-2 \leftrightarrow C-2	-	H-2 \rightarrow C-4, C-13
4	121.0	H-4 (7.42)	H-4 \leftrightarrow C-4	-	H-4 \rightarrow C-2, C-10, C-13
5	109.2	H-5 (7.06)	H-5 \leftrightarrow C-5	-	H-5 \rightarrow C-7, C-10, C-12
7	108.3	H-7 (6.55)	H-7 \leftrightarrow C-7	-	H-7 \rightarrow C-5, C-12
8	166.0	H-8 (12.04)	OH-8 \leftrightarrow C-8	-	-
Me	21.9	H-Me (2.50)	H-Me \leftrightarrow C-Me	-	H-Me \rightarrow C-2, C-4

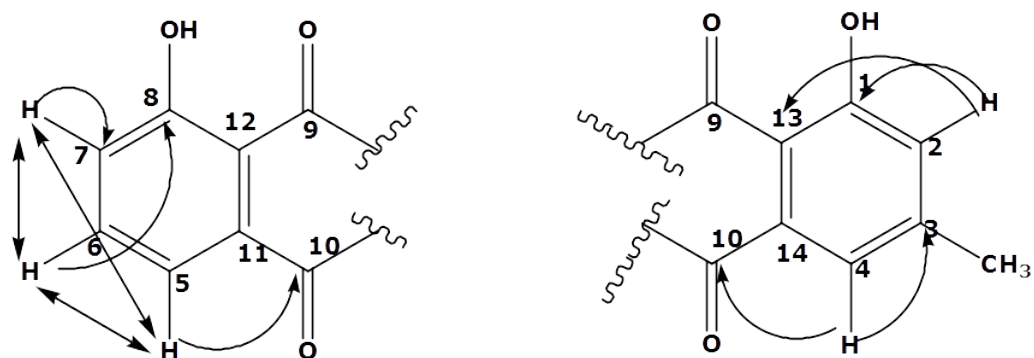
**Figure 2.** COSY, HSQC, and HMBC correlations of the aromatic cycle A, B, and C.

Table 3. *In-vitro* Antimicrobial Activities of Extracts and Isolated Compounds from Roots of *R. abyssinicus* in mm.

Bacterial strain	The diameter of zone of inhibition in mm (M±SD)				Gentamycin	DMSO	Isolated compounds	
	PE	CE	AE	ME			C-1	C-2
<i>S. aureus</i>	9.5±0.7	17.5±1.4	21.0±1.4	18.0±0.1	34.5±0.7	NI	23.0±0.1	20.0±0.2
<i>P. aeruginosa</i>	NA	12.5±0.7	15.5±0.4	13.0±0.1	30.5±0.7	NI	18.0±0.2	19.0±0.3
<i>E. coli</i>	10.5±0.7	14.0±0.2	18.0±0.4	13.5±0.7	32.0±0.1	NI	18.0±0.4	17.0±0.7
<i>K. pneumoniae</i>	NA	11.5±0.7	22.5±0.7	15.0±0.2	30.0±0.1	NI	22.5±0.4	20.0±0.7
Gentamycin	-	-	-	-	-	-	26.0±0.3	26.0±0.2
DMSO	-	-	-	-	-	-	NI	NI
Fungal strain					Mancozeb		C-1	C-2
<i>C. albicans</i>	9.0±1.4	12.0±0.1	17.5±0.7	13.0±3	20.5±.07	NI	20.0±0.4	22.0±0.7
<i>S. cerevisiae</i>	7.5±0.7	10.0±0.7	15.0±0.7	15.0±1.4	24.5±0.7	NI	NA	NA
Mancozeb	-	-	-	-	-	-	22.0±0.1	22.0±0.2
DMSO	-	-	-	-	-	-	NI	NI

Key :

PE= petroleum ether extract, CE=chloroform extract, AE=acetone extract, ME=methanol extract, C-1 Compound-1, C-2=Compound-2, NI=No inhibition, NA= Not active, DMSO = Dimethyl sulfoxide, M±SD = Mean ± Standard Deviation

ACKNOWLEDGMENTS

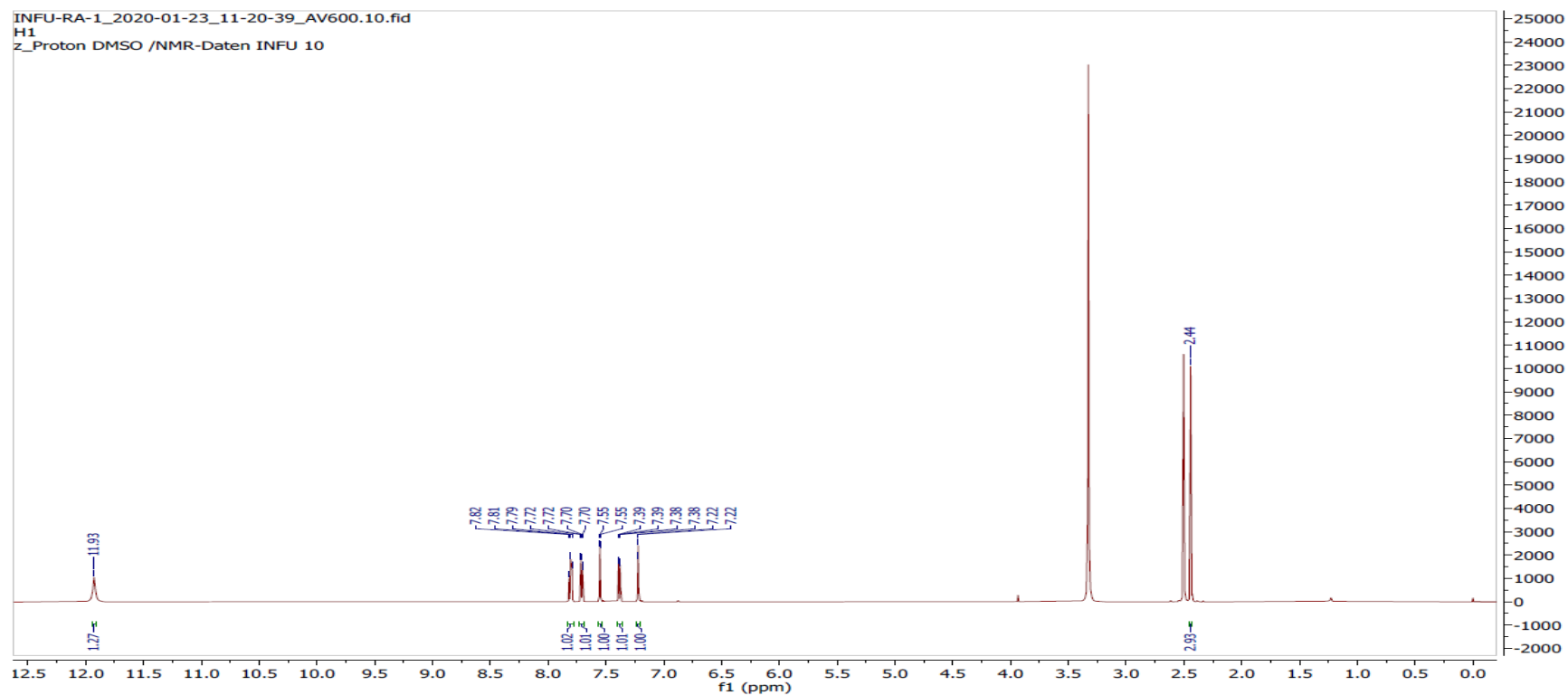
The authors wish to thank Jimma University, College of Natural Sciences for funding, and the Department of Biology for hosting us during the bioassay tests and professional support. We are also thankful to Dr. Kibrom Gebreheiwot, Institute of Environmental Research (INFU), TU Dortmund, Germany, for running the NMR data of the compounds.

REFERENCES

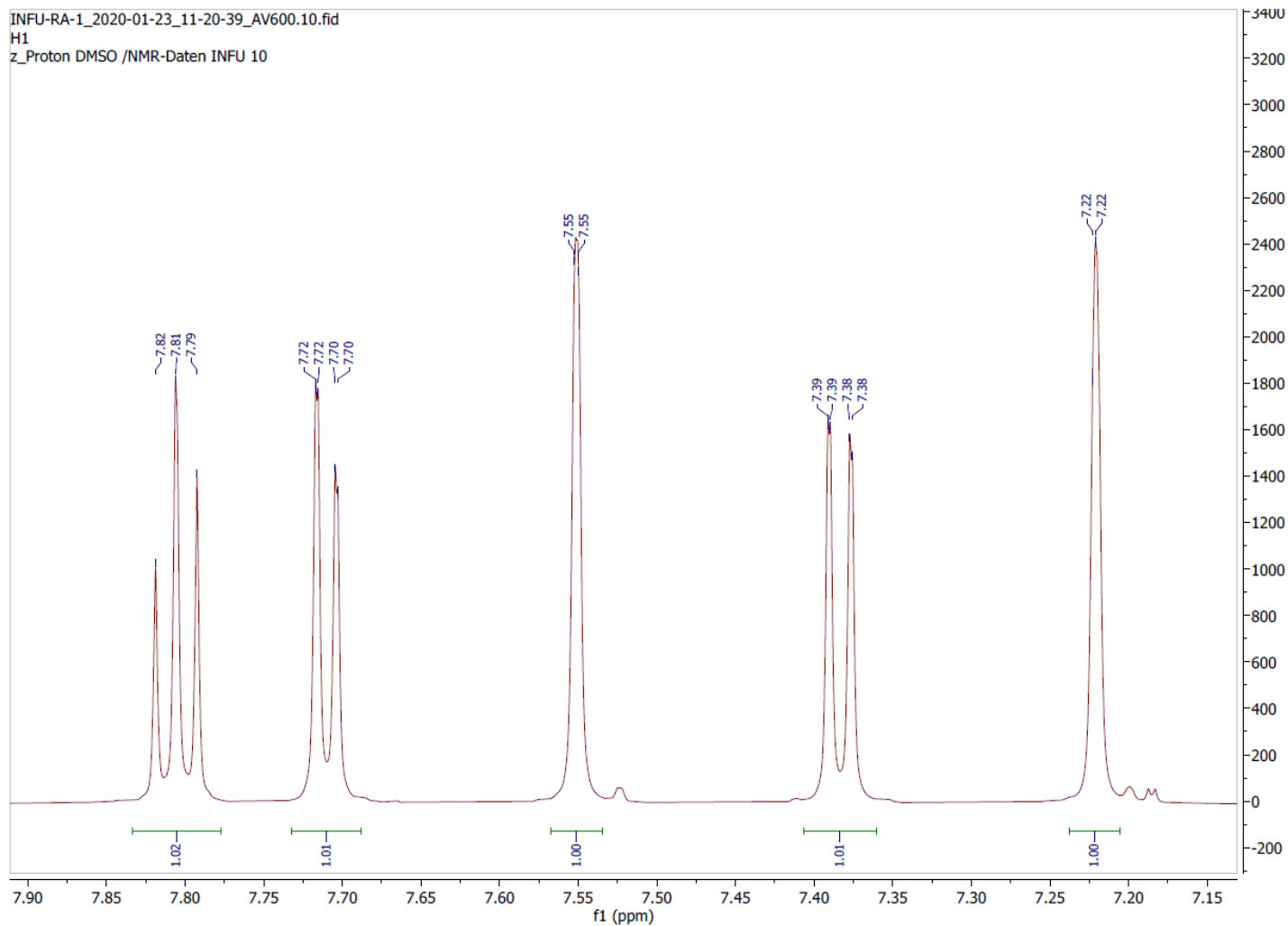
- Moges A. Ethiopian Common Medicinal Plants: Their Parts and Uses in Traditional Medicine - Ecology and Quality Control. In: Sağlam YME-AGE-MRE-NG, editor. Rijeka: IntechOpen; 2020. p. Ch. 7. Available from: <https://doi.org/10.5772/intechopen.86202>
- Cavalcante IHL, Martins ABG, Charles Johnson , Tim Raiford & Kristi Whitley. Int J Fruit Sci. 2005;5(4):39-46.
- Abubakar MG, Yerima MB, Zahriya AG, Ukwuani AN. Acute toxicity and antifungal studies of ethanolic leaves, stem and pulp extract of *Tamarindus indica*. Res J Pharm Biol Chem Sci. 2010;1(4):104-11.
- Yirga G. Use of traditional medicinal plants by indigenous people in mekele town, capital city of tigray regional state of Ethiopia. J Med Plants Res. 2010;4(17):1799-804.
- Tesfahuneygn G, Gebreegziabher G. Medicinal Plants Used in Traditional Medicine by Ethiopians: A Review Article OPEN ACCESS. J Respir Med Lung Dis. 2019;4(1):1-3.
- Muluye AB, Ayicheh MW. Medicinal plants utilized for hepatic disorders in Ethiopian traditional medical practices: a review. Clin Phytoscience. 2020;6(1).
- Yineger H, Yewhalaw D, Teketay D. Ethnomedicinal plant knowledge and practice of the Oromo ethnic group in southwestern Ethiopia. J Ethnobiol Ethnomed. 2008;4:1-10.
- Ekalu A, Gbekele-Oluwa Ayo R, Habila JD, Hamisu I. Bioactivities of phaeophytin a, α -amyrin, and lupeol from *Brachystelma togoense* Schltr. J Turkish Chem Soc Sect A Chem. 2019;6(3):411-8.
- Tesfaye S, Belete A, Engidawork E, Gedif T, Asres K. Ethnobotanical Study of Medicinal Plants Used by Traditional Healers to Treat Cancer-Like Symptoms in Eleven Districts, Ethiopia. Evidence-based Complement Altern Med. 2020;2020.
- Mekonnen T, Urga K, Engidawork E. Evaluation of the diuretic and analgesic activities of the rhizomes of *Rumex abyssinicus* Jacq in mice. J Ethnopharmacol. 2010;127(2):433-9.
- Mohammed SA, Madhan B, Demissie BA, Velappan B, Tamil Selvi A. *Rumex abyssinicus* (mekmeko) Ethiopian plant material for preservation of goat skins: Approach for cleaner leather manufacture. J Clean Prod [Internet]. 2016;133:1043-52. Available from: <http://dx.doi.org/10.1016/j.jclepro.2016.06.043>
- Mulisa E, Asres K, Engidawork E. Evaluation of wound healing and anti-inflammatory activity of the rhizomes of *Rumex abyssinicus* J. (Polygonaceae) in mice. BMC Complement Altern Med [Internet]. 2015;15(1):1-10. Available from: <http://dx.doi.org/10.1186/s12906-015-0878-y>
- Rouf ASS, Islam MS, Rahman MT. Evaluation of anti-diarrhoeal activity *Rumex maritimus* root. J Ethnopharmacol. 2003;84(2-3):307-10.
- Worku N, Mossie A, Stich A, Dauschies A, Trettner S, Hemdan NYA, et al. Evaluation of the In Vitro Efficacy of *Artemisia annua* , *Rumex abyssinicus* , and *Catha edulis* Forsk Extracts in Cancer and Trypanosoma brucei Cells . ISRN Biochem. 2013;2013:1-10.
- Sharma RS, Mishra V, Singh R, Seth N, Babu CR. Antifungal activity of some Himalayan medicinal plants and cultivated ornamental species. Fitoterapia [Internet]. 2008;79(7-8):589-91. Available from: <http://dx.doi.org/10.1016/j.fitote.2008.06.004>
- Getie M, Gebre-Mariam T, Rietz R, Höhne C, Huschka C, Schmidtke M, et al. Evaluation of the anti-microbial and anti-inflammatory activities of the medicinal plants *Dodonaea viscosa*, *Rumex nervosus* and *Rumex abyssinicus*. Fitoterapia. 2003;74(1-2):139-43.
- Kumar RS, Venkateshwar C, Samuel G, Rao SG. Phytochemical Screening of some compounds from plant leaf extracts of *Holoptelea integrifolia* (Planch .) and *Celestrus emarginata* (Grah .) used by Gondu tribes at Adilabad District. International Journal of Engineering Science Invention. 2013;2(8):65-70.
- Nithya Devi P, Kaleeswari S, Poonkothai M. Antimicrobial activity and phytochemical analysis of fruit extracts of *Terminalia Bellerica*. Int J Pharm Pharm Sci. 2014;6(5):639-42.
- Abdissa D, Geleta G, Bacha K, Abdissa N. Phytochemical investigation of *Aloe pulcherrima* roots and evaluation for its antibacterial and

- antiplasmodial activities. PLoS One. 2017;12(3):1–10.
20. Mohammed SA, Panda RC, Madhan B, Demessie BA. Rumex abyssinicus (mekmeko) extract as cleaner approach for dyeing in product manufacture: Optimization and modeling studies. Asia-Pacific J Chem Eng. 2018;13(2):1–19.
21. Prateeksha, Yusuf MA, Singh BN, Sudheer S, Kharwar RN, Siddiqui S, et al. Chrysophanol: A natural anthraquinone with multifaceted biotherapeutic potential. Biomolecules. 2019;9(2):1–24.
22. Van Wyk BE, Yenesew A, Dagne E. Chemotaxonomic survey of anthraquinones and pre-anthraquinones in roots of Aloe species. Biochem Syst Ecol. 1995;23(3):267–75.
23. Gizachew A, Legesse A, Berhanu, M. A. Natural Product Communications: Editorial. Nat Prod Commun. 2010;5(5):747–50.
24. Augustin N, Nuthakki VK, Abdullaha M, Hassan QP, Gandhi SG, Bharate SB. Discovery of Helminthosporin, an Anthraquinone Isolated from Rumex abyssinicus Jacq as a Dual Cholinesterase Inhibitor. ACS Omega. 2020;5(3):1616–24.
25. Zelalem GA, Dula DE. Isolation , Characterization and Antibacterial Activities Evaluation of Rumex abyssinicus Rootbark Extracts. Nat Prod Chem Res. 2019;7(1):1–8.
26. Dewick PM. Medicinal Natural Products: A Biosynthetic Approach. 3rd Edition. John Wiley & Sons, Ltd. 2009. 1–546 p.
27. Fatima N, Zia M, Riaz-ur-Rehman, Rizvi ZF, Ahmad S, Mirza B, et al. Biological activities of Rumex dentatus L: Evaluation of methanol and hexane extracts. African J Biotechnol. 2009;8(24):6945–51.
28. Tabin S, Gupta RC, Bansal G, Kamili AN. Comparative HPLC analysis of emodin , aloe emodin and rhein in Rheum emodi of wild and in vitro raised plants. Journal of Pharmacognosy and Phytochemistry. 2016;5(2):121–30.

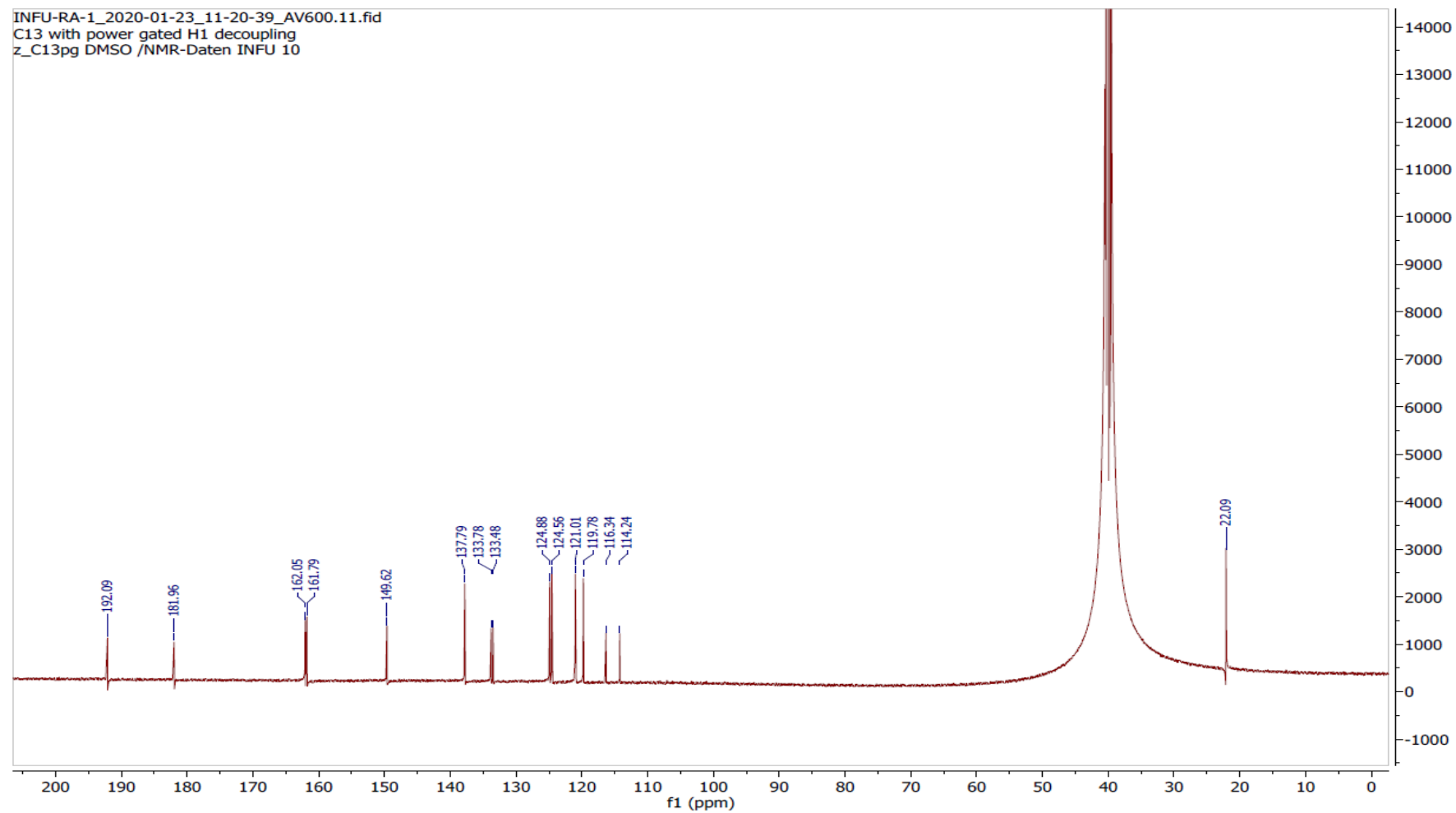
Supporting information
“Chemical Constituents of *Rumex abyssinicus* Roots and Evaluation of Its Antimicrobial Activities”
Muaz Shifa, Dele Abdissa, Tsegaye Girma Asere*



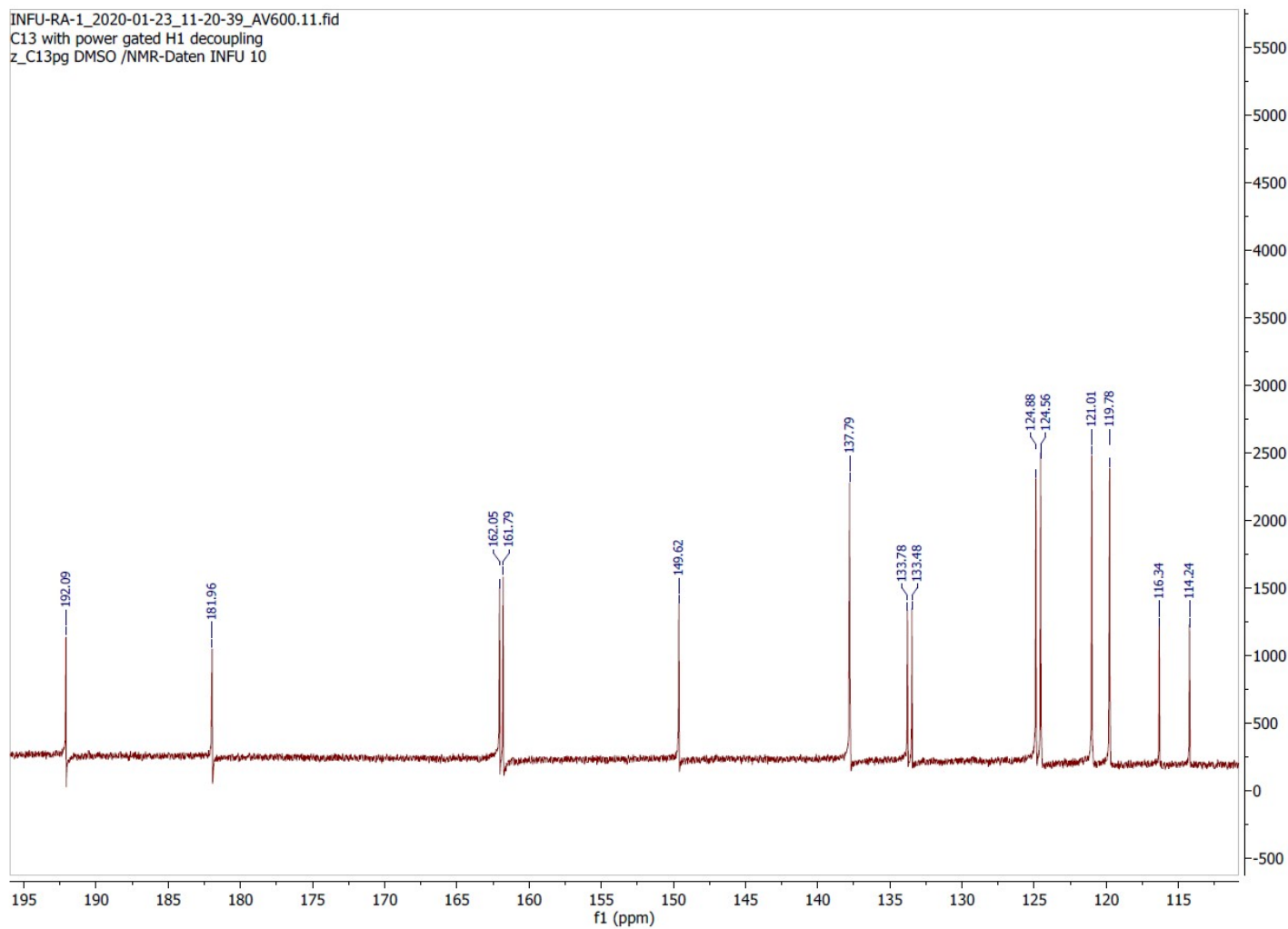
SI1a: ¹H-NMR spectral data of compound-1.



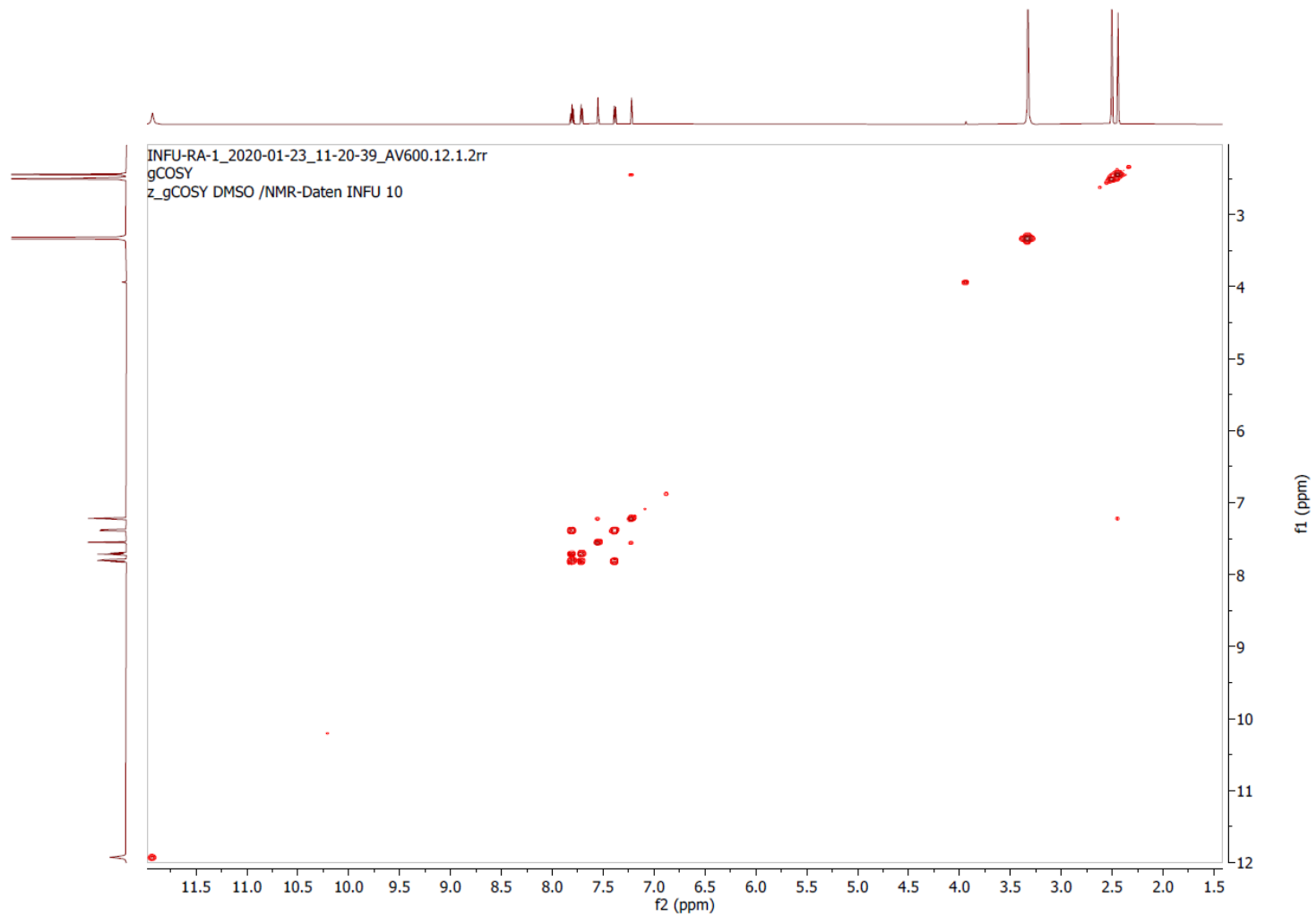
SI1b: Expanded ¹H NMR spectral data of compound-**1** from 7.15-7.90 ppm.



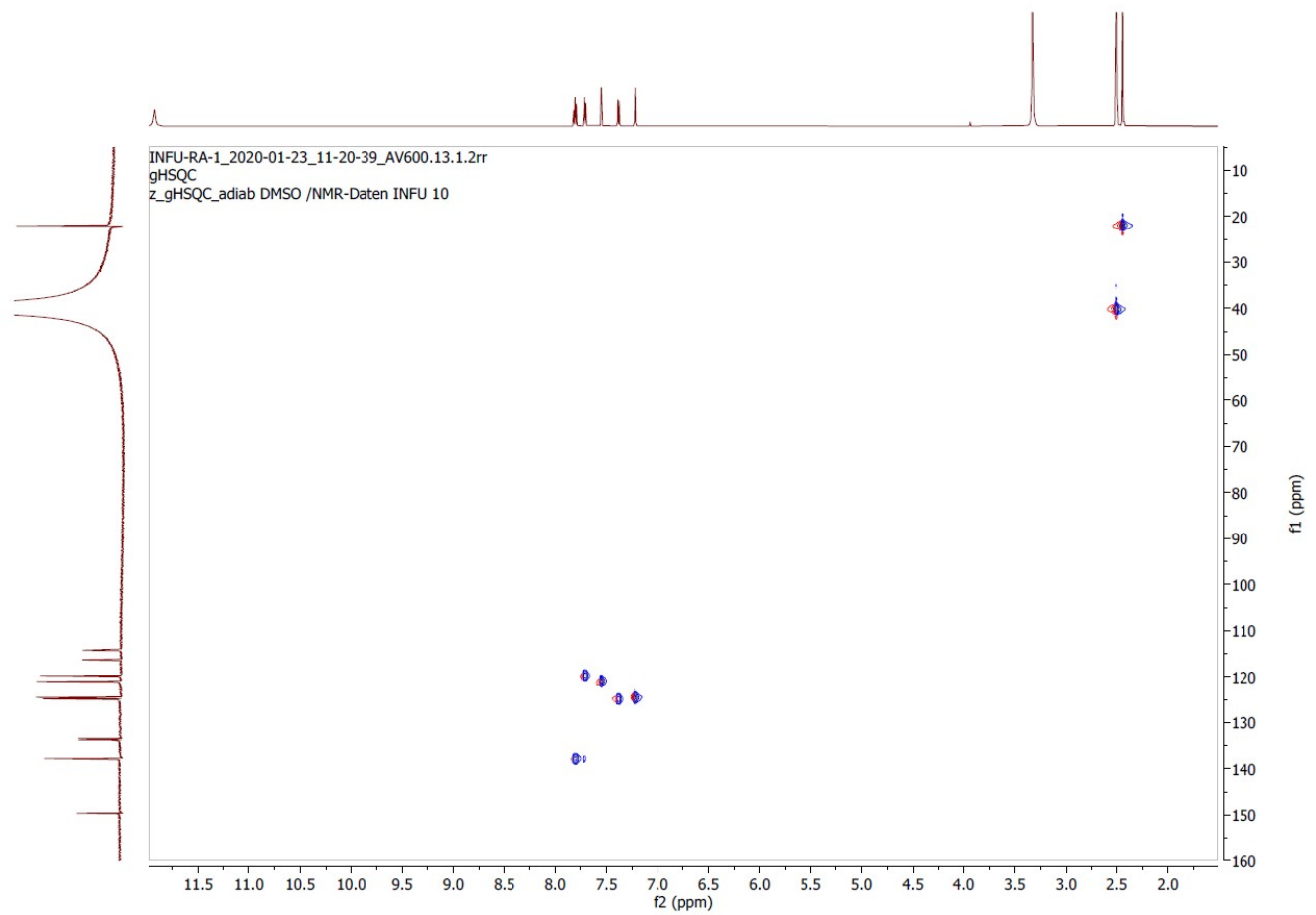
SI2a: ¹³CNMR spectral data of compound-1.



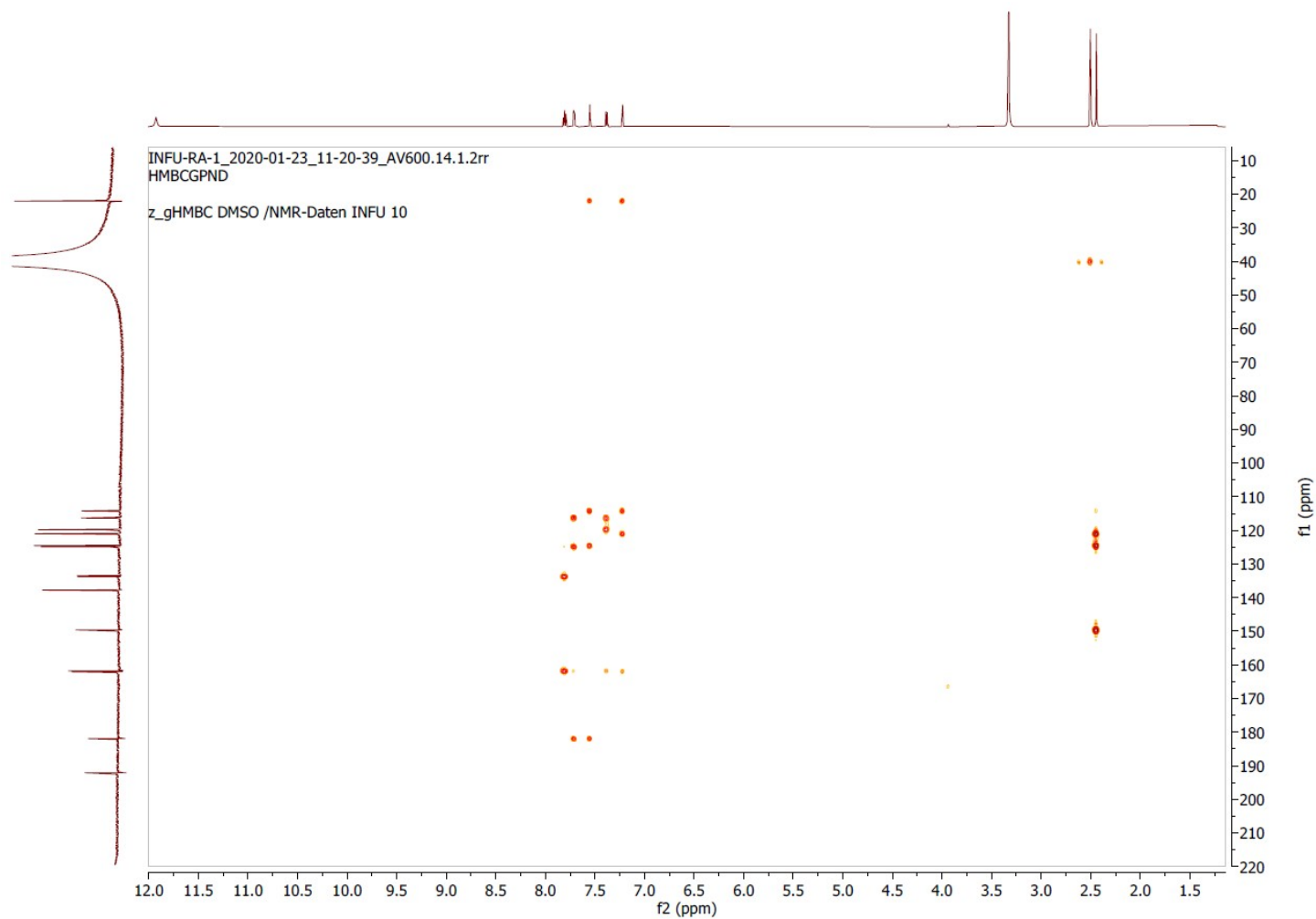
SI2b: Expanded ^{13}C NMR spectral data of compound-**1** from 115-195 ppm.



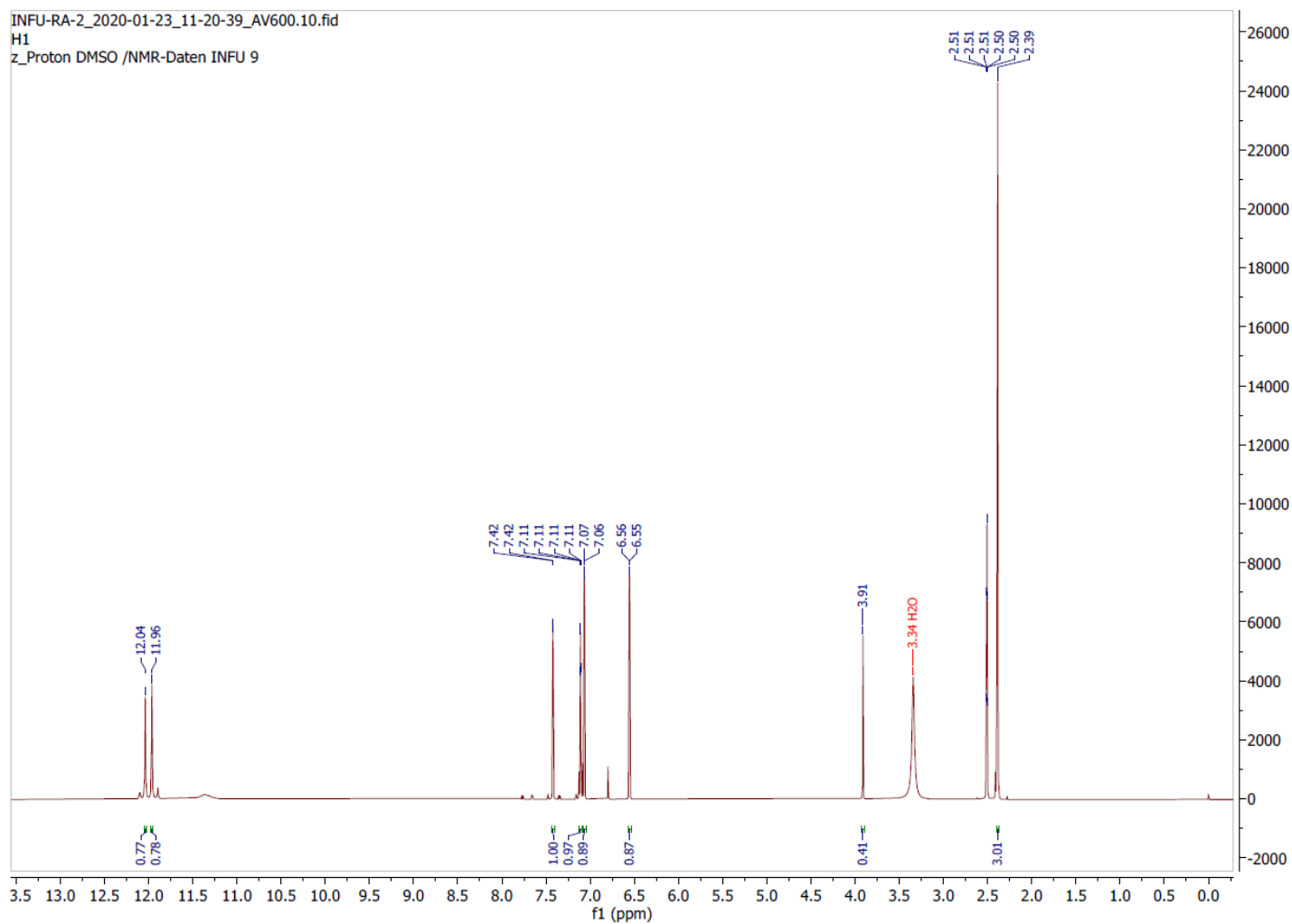
SI3: COSY spectral data of compound-**1**.



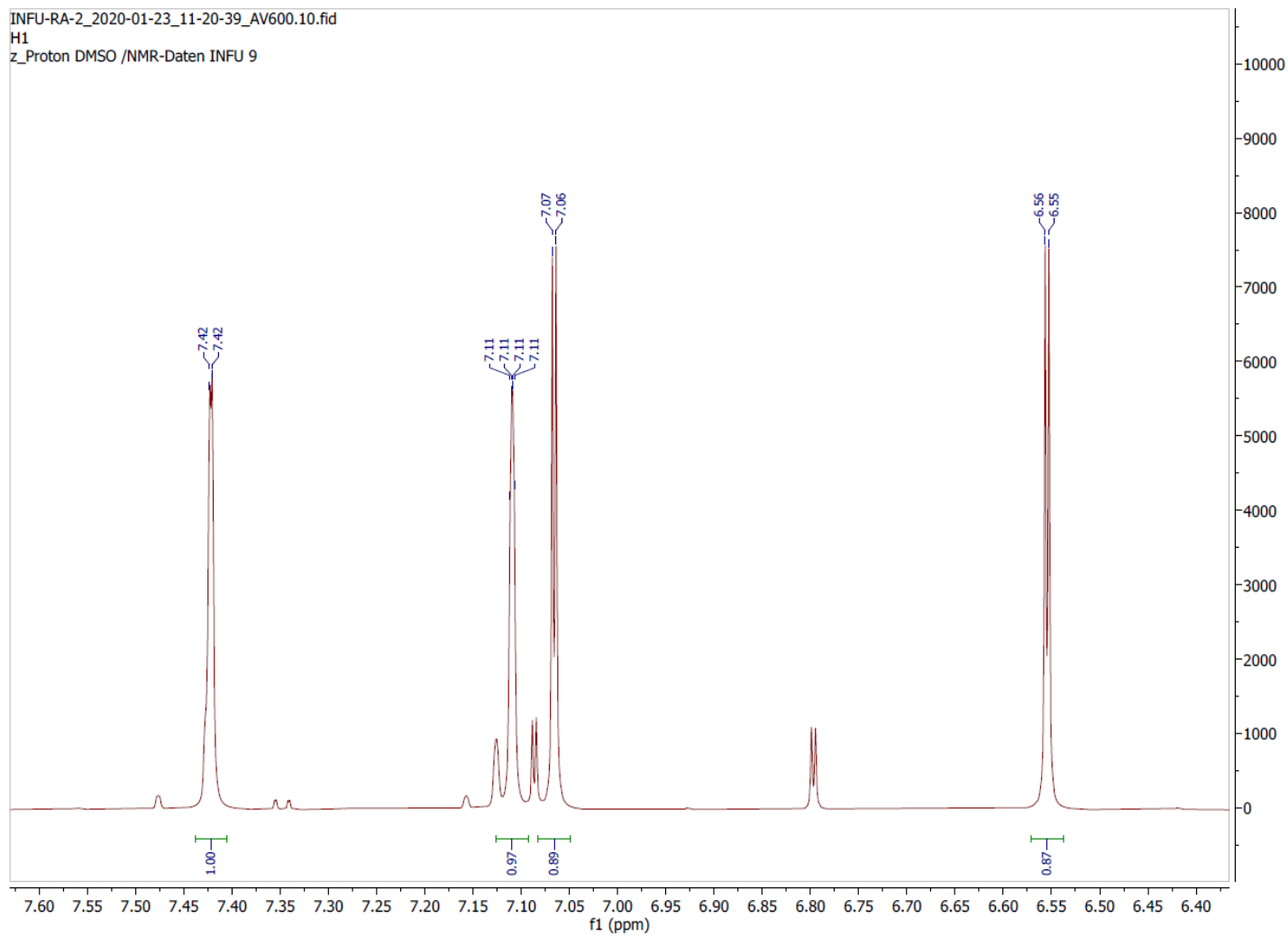
SI4: HSQC spectral data of compound-1.



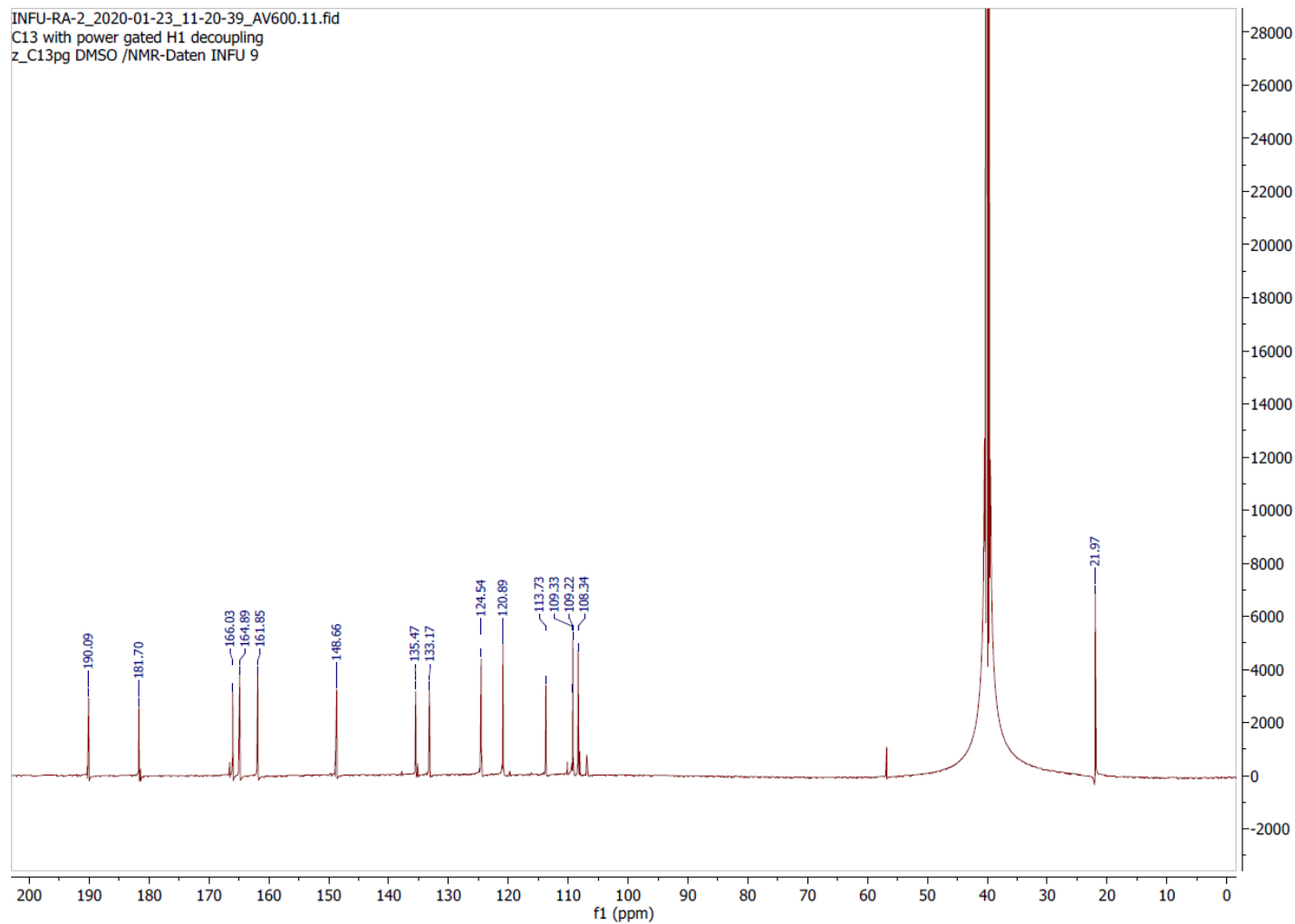
SI5: HMBC spectral data of compound-1.



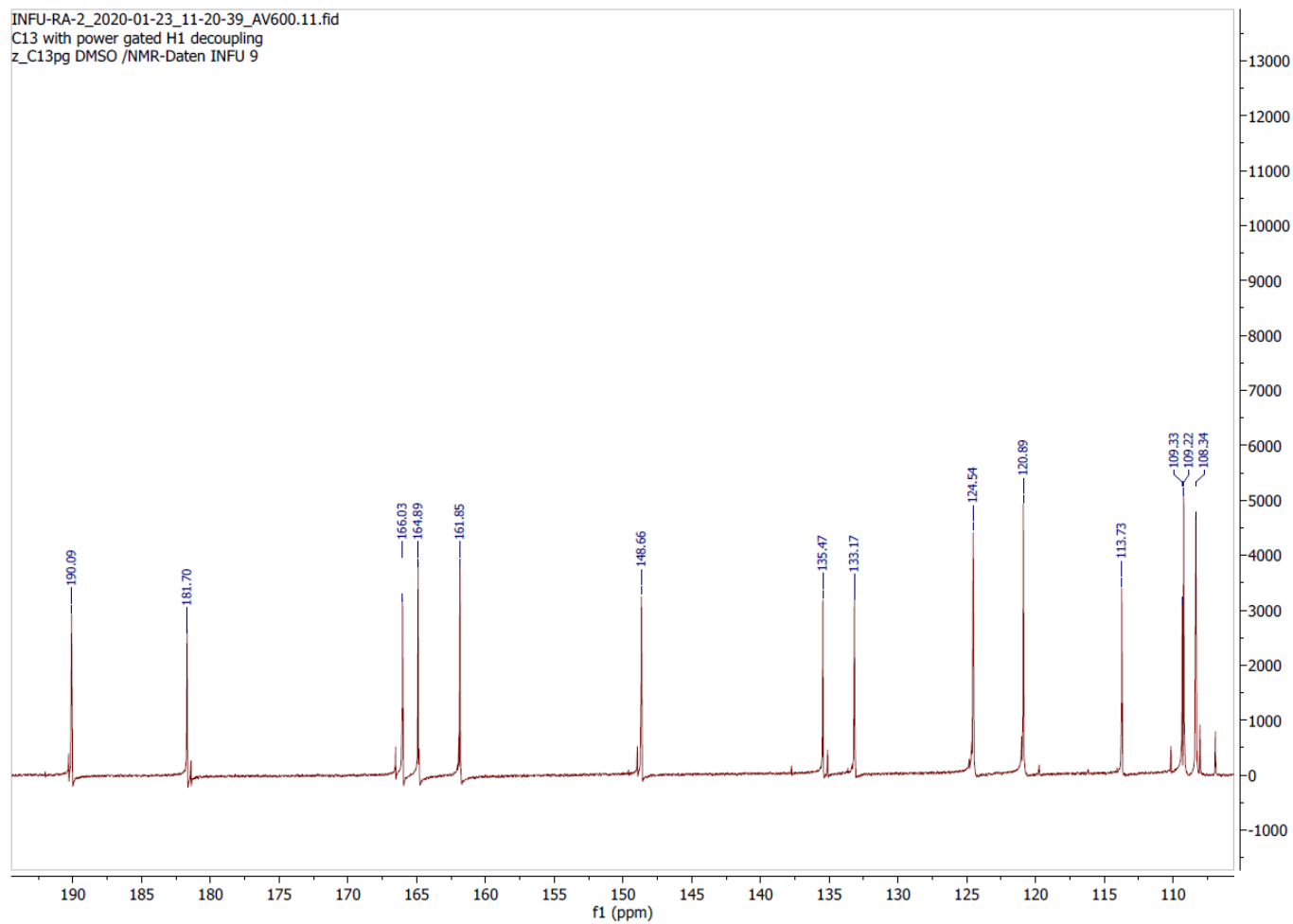
SI6a: ¹H NMR spectral data of compound-2.



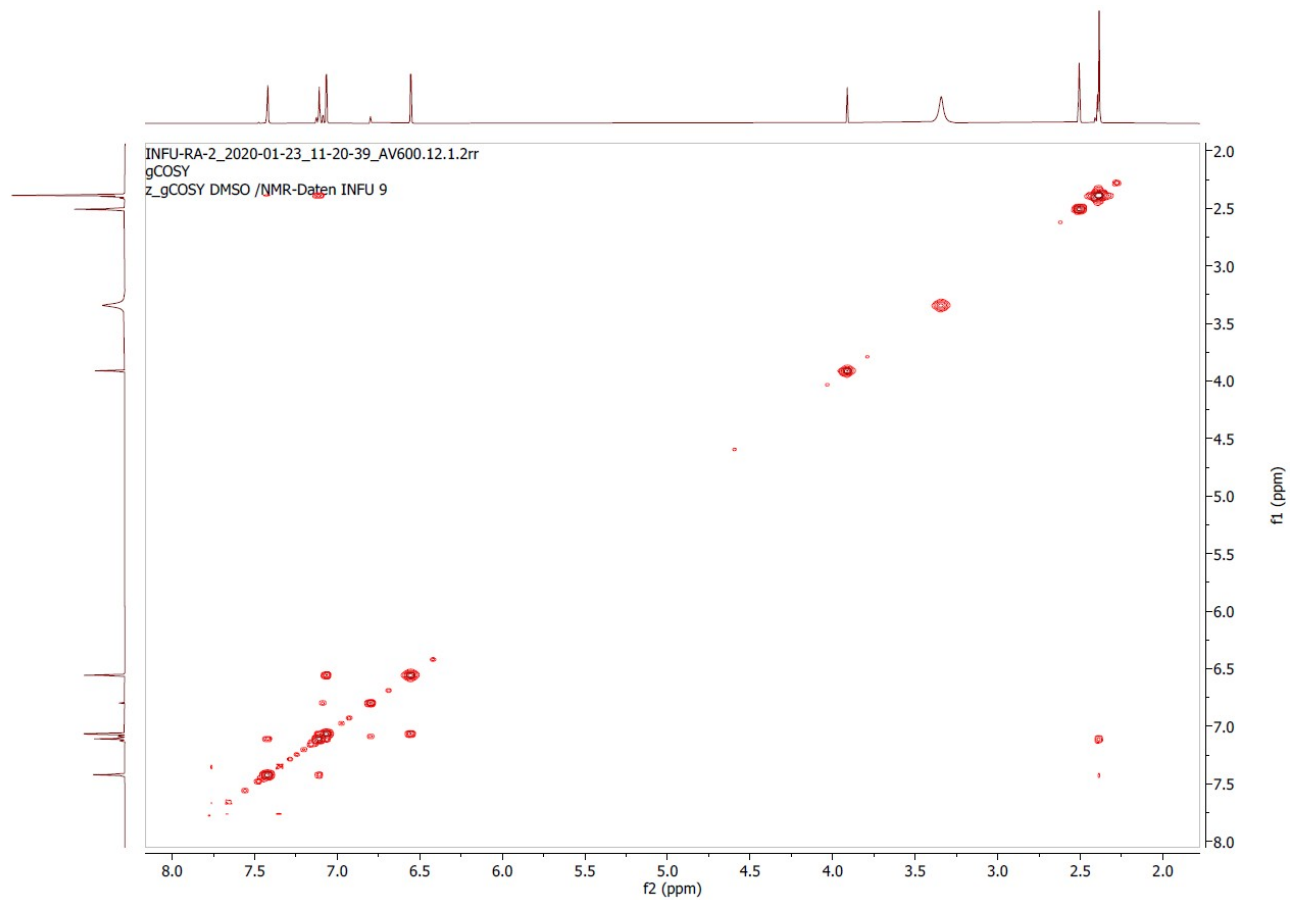
SI6b: Expanded ¹H NMR spectral data of compound-**2** from 6.40-7.60 ppm.



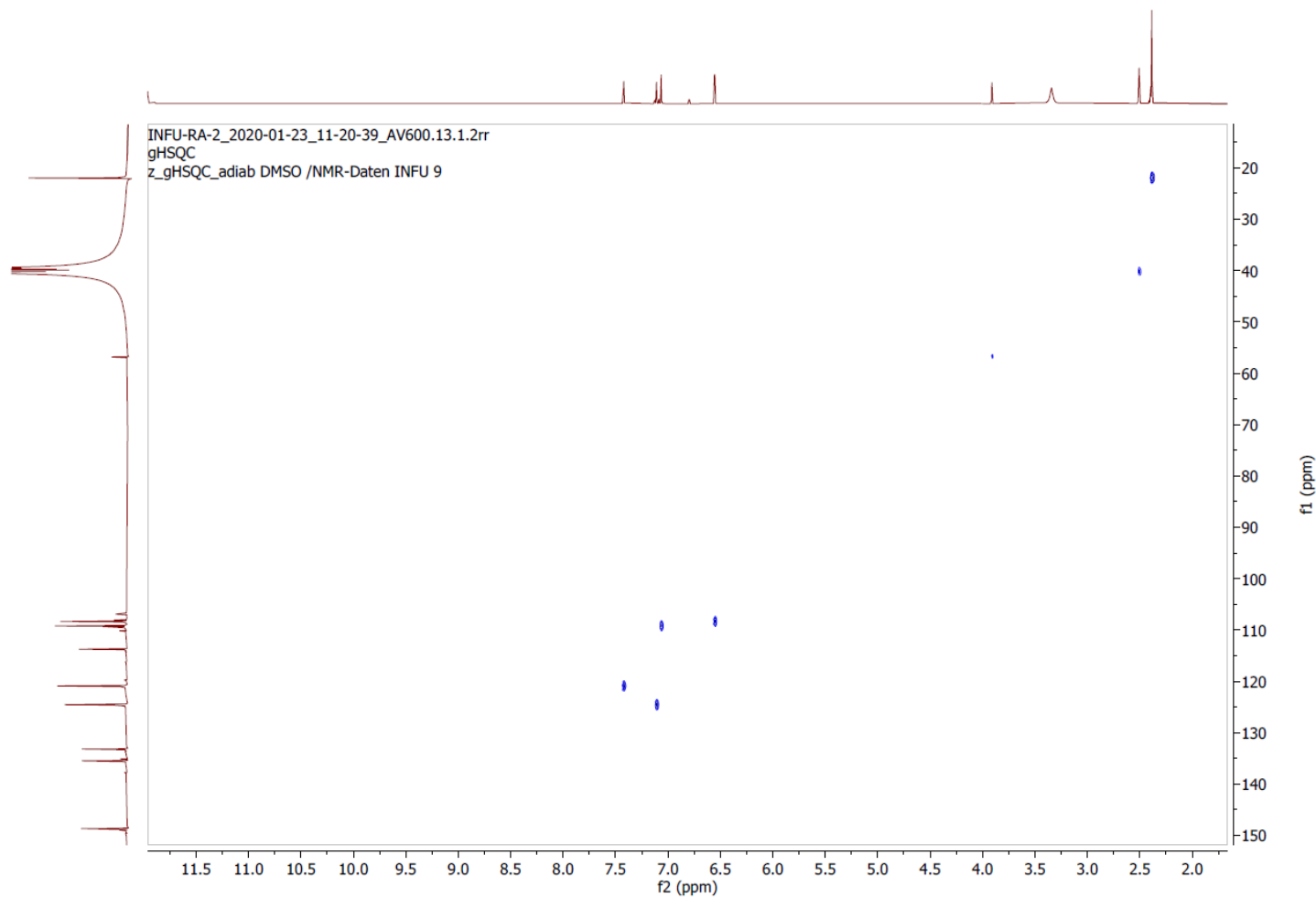
SI7a: ¹³CNMR spectral data of compound-2.



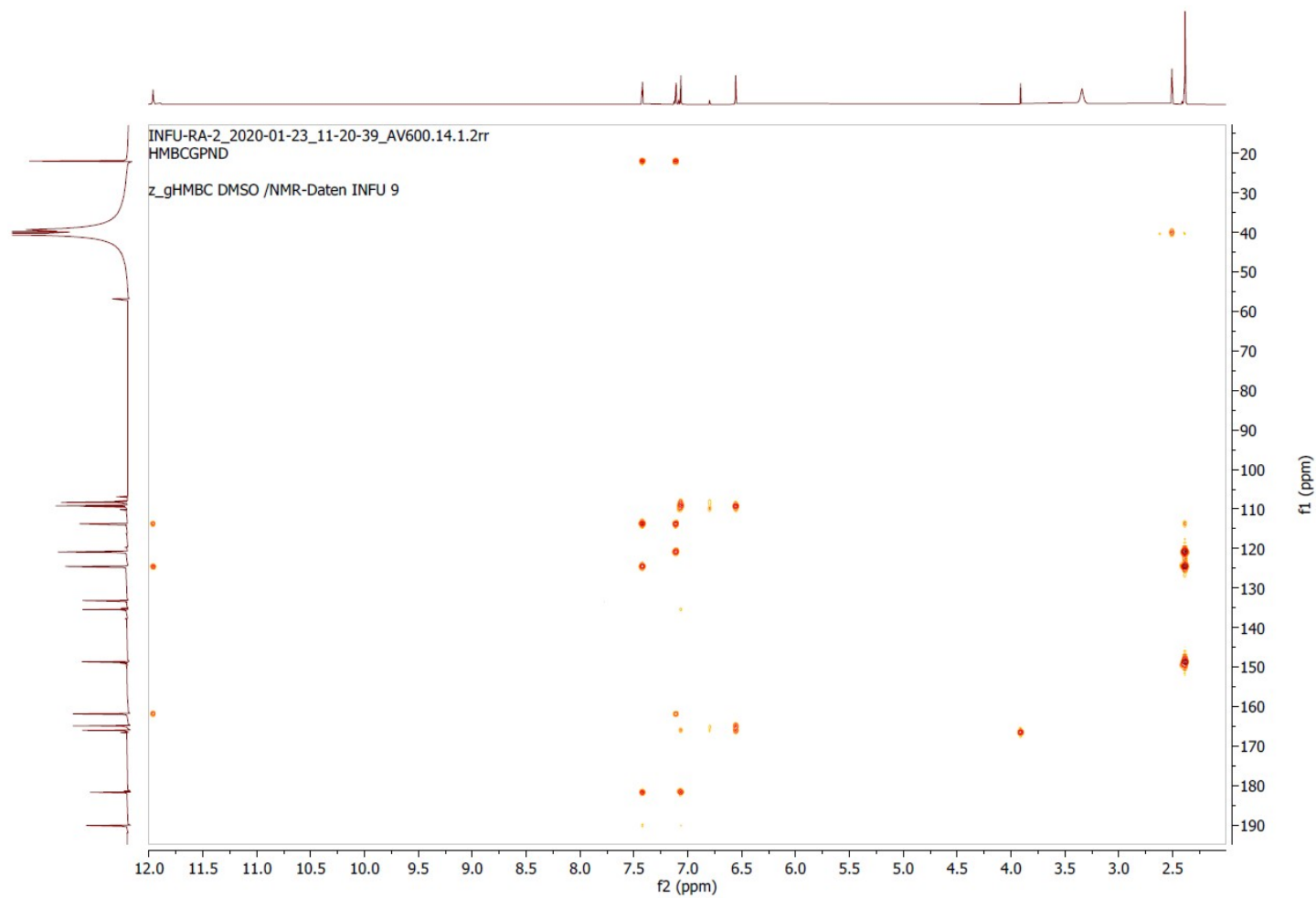
SI7b: Expanded ^{13}C NMR spectral data of compound-**2** from 110-190 ppm.



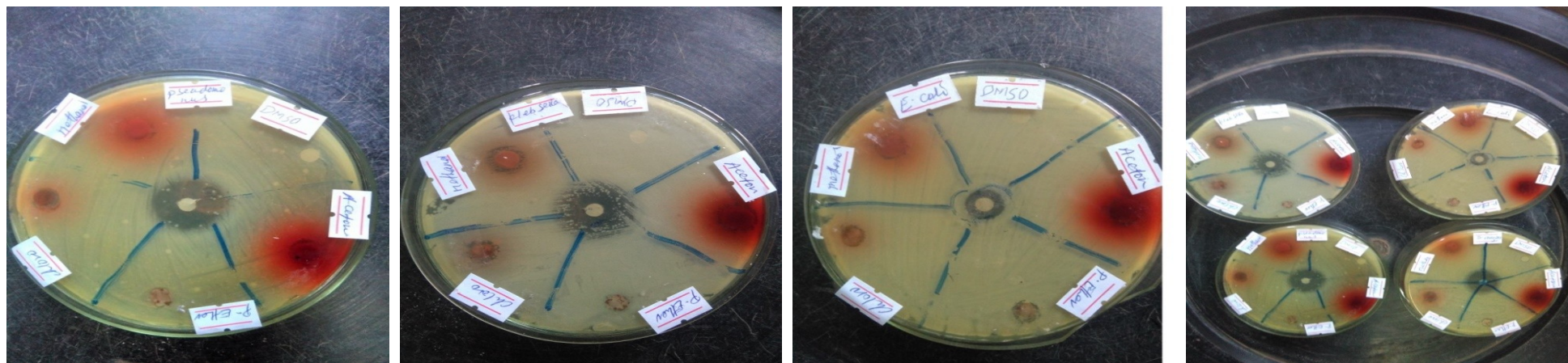
SI8: COSY spectral data of compound-**2**.



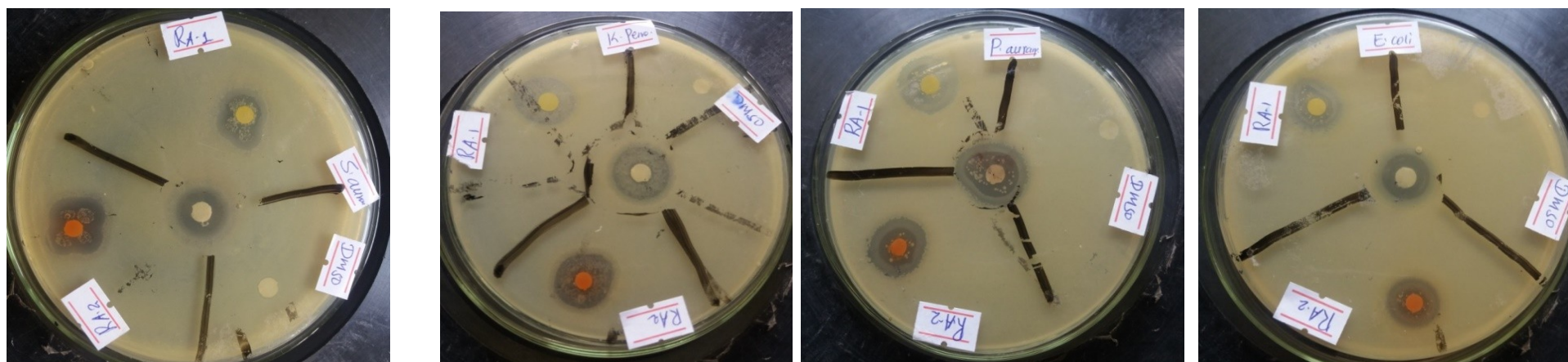
SI9: HSQC spectral data of compound-2.



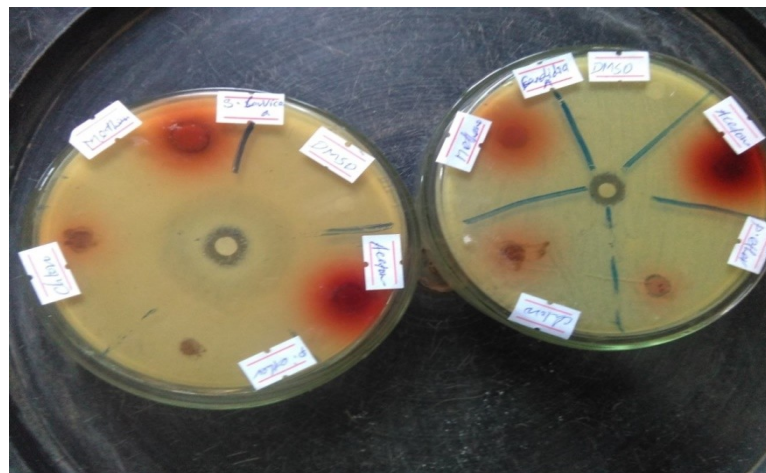
SI10: HMBC spectral data of compound-2.



SI11a: Antibacterial activity of crude extract of root of *R. abyssinicus*.



SI11b: Antibacterial activity of isolated compounds (**1** and **2**) from the root of *R. abyssinicus*.



SI12a: Antifungal activity of crude extract of root of *R. abyssinicus*.



SI12b: Antifungal activity of isolated compounds (**1** and **2**) from the root of *R. abyssinicus*.



Calcined Eggshell for the Removal of Victoria Blue R Dye from Wastewater Medium by Adsorption

İlknur Tosun Satır^{1*}  , Kadir Erol²  

¹University of Hitit, Faculty of Arts and Sciences, Department of Chemistry, 19040, Corum, Turkey.

²University of Hitit, Vocational School of Health Services, Medical Services and Techniques, 19030, Corum, Turkey

Abstract: In this study, the use of calcined eggshell (CE) as an adsorbent in removing Victoria Blue R (VBR) dyestuff from the solution medium was investigated. For this purpose, pH, interaction time, adsorbate concentration, amount of adsorbent, and salt effect parameters were studied to determine the appropriate adsorption conditions. The highest adsorption yield was obtained at pH 2, 2.0 g/L adsorbent, and a stirring time of 5 minutes. 97% of the dye was removed under optimum adsorption conditions. The results obtained from the experimental studies showed that the adsorption mechanism is compatible with the pseudo-second-order kinetic model and the Langmuir isotherm model. SEM and IR analysis were performed for the characterization of CE.

Keywords: Textile dye, calcined eggshell, water treatment, wastewater, adsorption, Victoria Blue R.

Submitted: June 29, 2020. **Accepted:** November 09, 2020.

Cite this: Tosun Satır İ., Erol K. Calcined Eggshell for the Removal of Victoria Blue R Dye from Wastewater Medium by Adsorption. JOTCSA. 2021;8(1):31-40.

DOI: <https://doi.org/10.18596/jotcsa.760083>.

***Corresponding author.** E-mail: (ilknurertosun@gmail.com), Tel: (+90364 227 7000 / 1642), Fax: (+90364 2277005).

INTRODUCTION

Synthetic dyes used in various industrial applications spread to the environment as a result of industrial activities (1). More than half of the dyes used in the textile industry disappear after dyeing and approximately 10 - 15% of the dyes are uptake with liquids. (2). Dyes are synthetic aromatic compounds widely used in textile industries (3,4). It is known that these dyes have mutagenic and carcinogenic effects for aqueous systems and human life. It has also known that some triphenylmethane dyes cause tumoral growth in some fish species (5-8). Also, triphenylmethane dyes have a strong coloring feature and reduce the transparency of the water and gaseous solubility in water (9). Fluids from the paint production industry have higher chemical and biochemical oxygen

demand and are significantly colorful (3). As this situation poses a serious risk to people and living organisms in the water, developing an effective method to get away these chemicals from the wastewater is becoming essential.

In order to remove triphenylmethane dyes or contaminants from wastewater; there are many methods, including adsorption, flocculation, electrochemical applications, photo-oxidation, and photocatalytic techniques (10-16). Biosorption is the kind of adsorption used as a biomass adsorbent, it has been widely demanded in recent years (17, 18). Victoria Blue R (VBR) is an essential member of the triphenylmethane family of dyes and is extensively used in the industry (19). The removal of the carcinogenic or mutagenic dye from wastewater is of great importance on the environment and human

health. Various adsorbents have been used from past to present to remove dye from wastewaters (20-23). One of the most commonly used is activated carbon (24,25). However, the regeneration of this material is due to the prolongation of processing times and additional costs. For this, it is necessary to develop alternative disposable adsorbents with no economic value. In line with this idea, eggshell as an agricultural waste has been preferred because it is no-cost and harmless to the environment. The high percentage of calcium carbonate in the eggshell makes it an effective adsorbent (26).

Within the scope of this work to remove the VBR paint from wastewaters, the calcined eggshell powder was used. It has been studied in both continuous and batch systems, and optimum adsorption conditions (pH, contact time, dye concentration, adsorbent dose, temperature, ionic strength) were provided.

EXPERIMENTAL SECTION

Preparation of Calcinated Eggshells

Eggshells purchased from a local market were first washed ultra-distilled water, then dried in an oven at 60 °C. Eggshells were calcined in the ash oven at 900 °C. After calcination, the adsorbent was ground with a laboratory grinder and sieved through a 150 µm sieve.

Instrumentation

After adsorption, the dye concentration remaining in the solution was measured using a Thermo Genesys 10S UV-VIS spectrophotometer at a wavelength of 615 nm. The surface morphology of CE was examined using Scanning Electron Microscopy (SEM); Carl Zeiss AG - EVO® 50 Series, Germany. With the help of double-sided carbon tape, CE was placed on the SEM sample holder surface. It was then coated with a thin layer of gold under vacuum and examined for surface morphology. The functional groups on the surface structure of CE were analyzed using a Fourier Transform Infrared Spectrometer (FTIR) (Thermo Nicolet iS10 FTIR Spectrometer, USA).

Adsorption Studies

The uptake of VBR dye from aqueous solutions with CE was investigated. To provide maximum removal, the effects of parameters such as adsorbent amount, contact time, pH, temperature, and ionic strength on adsorption capacity were investigated. The obtained data were evaluated with some kinetic and isotherm model parameters were calculated. In order to investigate the effect of pH on adsorption capacity, the pH of the dye solution was changed between 5-10, and adsorption capacity for CE was investigated. 50 mL of the dye solution at a concentration of 100 mg/L was treated with 0.1 g of adsorbent. The adsorbent amount was studied in the range of 0.02 to 0.3 g / 50 mL VBR dye at pH 9.0. The effect of contact time on adsorption capacity was investigated at 3 various temperatures (20, 30, and 40 °C) in the range of 5-90 minutes. Adsorption capacity and adsorption yield (%) were calculated by the following equations:

$$q_e = \frac{V(C_i - C_e)}{m} \quad (1)$$

$$\text{Adsorption yield (\%)} = \frac{C_i - C_e}{C_i} \times 100 \quad (2)$$

where

- q_e : Adsorption Capacity (mg/g)
- C_i : Initial adsorbate concentration (mg/L)
- C_e : Equilibrium adsorbate concentration (mg/L)
- V : The volume of dye solution (L)
- m : Amount of adsorbent (g)

RESULTS AND DISCUSSION

Characterization of Adsorbent

In the SEM micrograph of CE before adsorption (Fig.1a), a porous and coarse structure was observed, whereas after the adsorption (Fig. 1b), the porous structure became plate-like and the coarse appearance disappeared. This was interpreted as VBR adhering to the adsorbent surface and altering surface morphology.

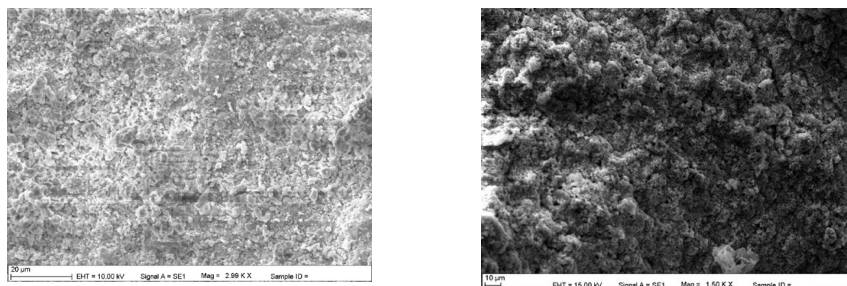


Figure 1: SEM pictogram a) before adsorption, b) after adsorption.

FTIR spectroscopy was performed in the range of 400–4000 cm^{-1} to study the biosorption of VBR on CE. On the FTIR spectrum of CE the peaks at 1403 and 869 cm^{-1} belong to the CO_3^{2-} anion (27).

Effect of pH

Within the scope of the study, firstly, the pH point where optimum adsorption capacity is optimum was investigated. Since VBR dye was dissolved in acidic pH regions, it was studied in regions higher than pH 5. Due to the possibility of interaction with the

electron density regions of VBR, the pH was not studied at points higher than 10. As can be seen from the figure, while the adsorption capacity increased in the range of pH 5-8, no significant increase was observed in the range of pH 8-10. According to these results, the optimum pH point was chosen as 9. Furthermore, considering the high calcium carbonate content of the eggshell, a primary point of pH 9 is considered to be an optimal choice.

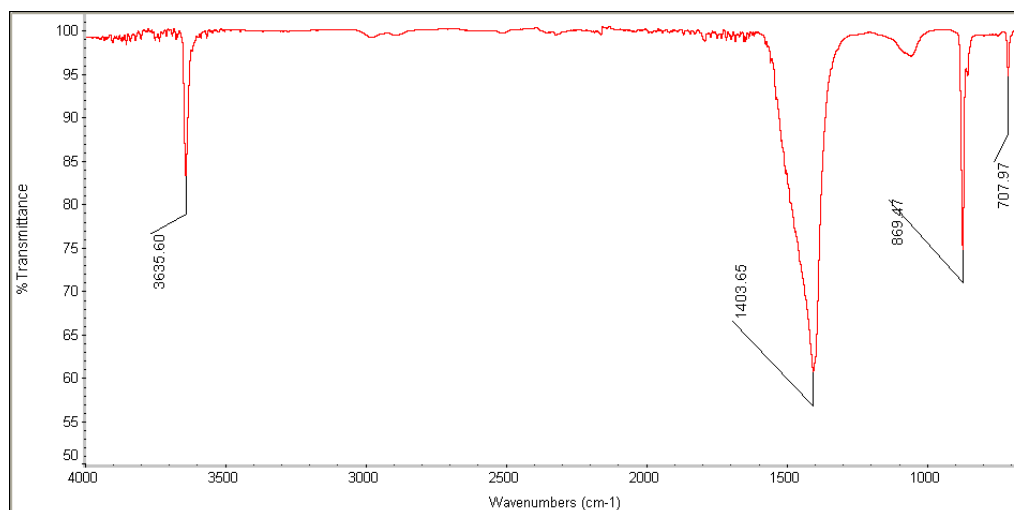


Figure 2: FT-IR Spectrum of calcinated eggshell.

Effect of Adsorbent Amount

To optimize adsorbent amount, the adsorbent amount of 0.4-0.6 g was investigated (Figure 3). A very high extraction rate of 94% was achieved, even at an adsorbent amount of 0.4 g. In the adsorbent amount higher than 3.0 g; a 100% removal was obtained.

Interaction Time

As seen in Figure 4, the effect of the interaction time was examined at 3 different temperatures (20, 30, 40 °C) in the range of 5-90 minutes. The adsorption capacity values remained almost constant when the interaction time was increased from 5 minutes to 90 minutes. q value showed a very low decrease from 26 to 25 with increasing

temperature. Optimum interaction time was determined as 5 minutes.

Adsorption Kinetics

The adsorption kinetics is a theoretical basis that determines the time required to establish an adsorption equilibrium. Many kinetic models have been developed to determine the mechanisms of adsorption, such as mass transfer and chemical reaction. The most common kinetic models in the literature are the pseudo-first-order kinetic model (Eq. 2) proposed by Lagergren (28) is the pseudo-second-order kinetic model (Eq. 3) proposed by Ho (29) and the interparticle diffusion equation model for Weber-Morris's (30) mass transfer mechanism (Eq. 4). The equations of kinetic models are as follows:

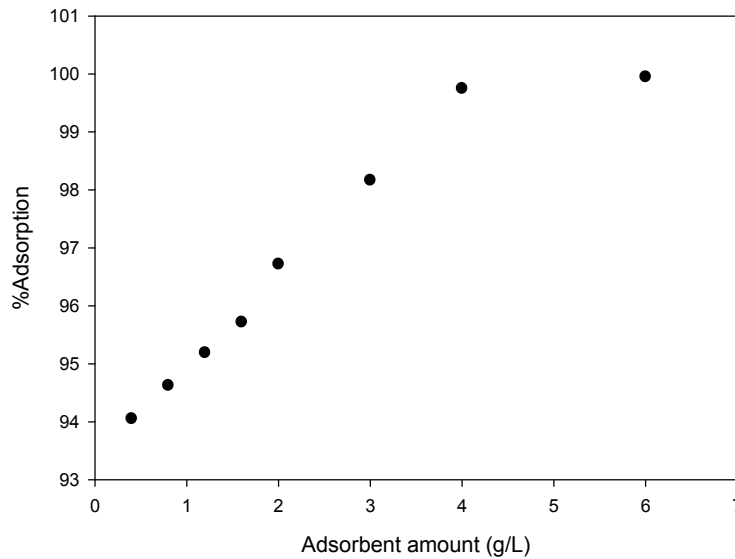


Figure 4: The effect of adsorbent amount on adsorption yield.

In this study, time-dependent data in the adsorption of calcined eggshell and VBR dye were evaluated by pseudo-first-order and pseudo-second-order kinetic models and intra-particle diffusion models. Some constants and r^2 values of the models are given in Table 1.

According to the results obtained from pseudo-first-order kinetic model studies; r^2 values (Table 1) are in the range of 0.959 - 0.997. According to the results obtained, it showed that the change was linear. But, q_e values calculated using y-intercept did not correspond to values obtained with Pseudo-First-Order

experimental data. These results showed that the adsorption process of the VBR dye on the calcined eggshell did not occur with the first-degree reaction.

When r^2 values (Table 1) of dye adsorption at three different temperatures were examined, it was seen that adsorption was compatible with the pseudo-second-order kinetic model at all temperatures (Fig. 5). Also, the calculated q values were in the acceptable range. As a result, it was determined that the adsorption of the dye onto the calcined eggshell was suitable for the pseudo-second-order kinetic model.

$$q_t = q_e (1 - \exp^{-k_1 t}) \quad (3)$$

Pseudo-Second-Order

$$q_e = \left(\frac{k_2 q_e^2 t}{1 + k_2 q_e t} \right) \quad (4)$$

Weber-Morris's mass transfer mechanism

$$q_t = k_p t^{1/2} + C \quad (5)$$

where:

- q_e Adsorption capacity at equilibrium (mg/g)
- q_t Adsorption capacity at different times (t) (mg/g)
- k_1 Pseudo-first-order equilibrium rate constant (1/min)
- k_2 Pseudo-second-order equilibrium rate constant (g/mg. min)
- k_p Intra-particle diffusion constant (g/mg. min^{1/2})
- C constant for any experiment (mg/g).

Table 1. Kinetic parameters for the adsorption of VBR dye onto CE.

Temperature	Pseudo-first-order			Pseudo-second-order			Intraparticle diffusion		
	K_1 (min^{-1})	q_e (mg g^{-1})	R^2 ($\text{g mg}^{-1} \text{min}^{-1}$)	k_2	q_e (mg g^{-1})	R^2	k_p ($\text{mg g}^{-1} \text{min}^{1/2}$)	C (mg g^{-1})	R^2
20 °C	6.69×10^{-2}	0.470	0.959	2.76×10^1	27.020	0.999	0.047	26.372	0.935
30 °C	5.50×10^{-2}	0.364	0.989	3.01×10^{-1}	25.641	0.999	0.043	25.135	0.938
40 °C	5.10×10^{-2}	0.324	0.997	3.08×10^{-1}	25.641	0.999	0.040	25.071	0.961

Table 2 Isotherm model parameters for the adsorption of VBR dye onto CE.

Temperature °C	Langmuir				Freundlich			Dubinin-Radushkevich (D-R)			
	q_{max} (mol g^{-1})	K_L (L mol^{-1})	r^2	R_L	n	K_F (L g^{-1})	r^2	q_m (mol g^{-1})	β ($\text{mol}^2 \text{kJ}^{-2}$)	r^2	E (kJ mol^{-1})
20	100	58.8×10^{-2}	0.919	0.99	1.052	63.68	0.964	50.95	5.645×10^{-8}	0.959	29.76×10^2
30	140	87.5×10^{-2}	0.917	0.99	1.584	51.62	0.912	31.75	1.663×10^{-8}	0.688	54.83×10^2
40	140	87.5×10^{-2}	0.937	0.99	1.675	53.96	0.969	34.32	1.585×10^{-8}	0.810	56.16×10^2

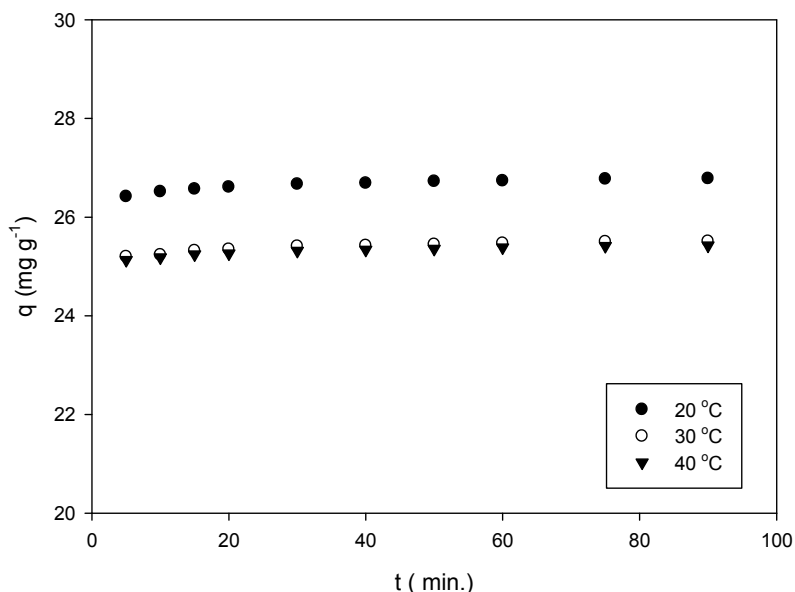


Figure 5: The effect of interaction time and temperature on adsorption yield.

Finally, experimental data was applied to the intraparticle diffusion model. According to the results obtained, it was found that this model does

not adapt to the adsorption of the VBR dye on calcined eggshells.

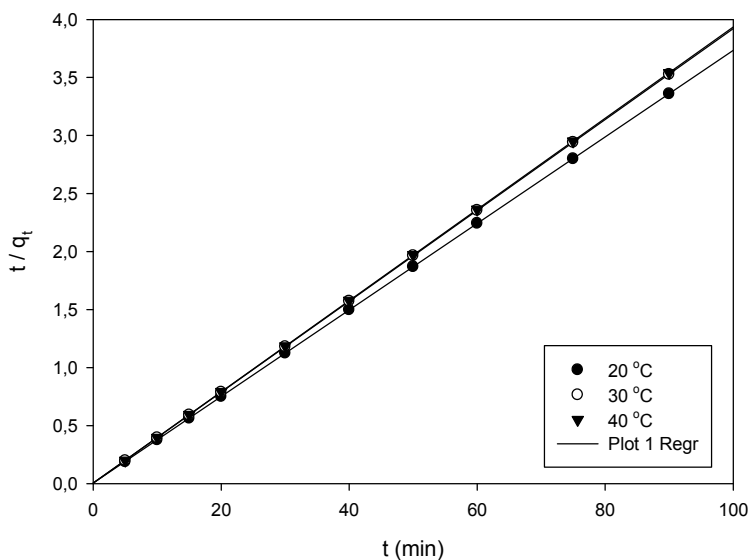


Figure 6: Pseudo-Second-order kinetic graphics.

Adsorption Isotherms

Adsorption in solution phase; temperature depends on concentration when adsorbent and adsorbate are kept constant. In this case, the equation showing the correlation of the amount of a

substance bound to the surface at a constant temperature with the concentration of that substance in solution is called adsorption isotherm. The most common isotherms in practice are

Langmuir, Freundlich, and Dubinin-Radushkevich (D-R) isotherms.

According to the Langmuir isotherm model (31), when a molecule is adsorbed to the surface, no more adsorption occurs in the same region. Therefore, the Langmuir equation is valid only for a single layer coating formed by adsorption of a single molecule on a completely homogeneous surface. Langmuir equation;

$$\frac{1}{q_e} = \frac{1}{q_{max}} + \left(\frac{1}{q_{max} K_L} \right) \times \frac{1}{C_e} \quad (6)$$

is calculated by equation (6).

According to the Freundlich isotherm model (32), the adsorption zones on the surface of an adsorbent are heterogeneous. The equation of this isotherm model is expressed as follows.

$$\ln q_e = \ln K_F + \frac{1}{n} \ln C_e \quad (7)$$

q_e : Amount of substance adsorbed in equilibrium (mg/g)

q_{max} : Max. single layer adsorption capacity (mg/g)

C_e : Amount of matter remaining without adsorption in equilibrium (mg/L)

K_F : Freundlich isotherm constant

K_L : Langmuir isotherm constant

ϵ : Polanyi potential

β : The activity coefficient related to biosorption energy

The D-R isotherm model (33) is used to understand whether adsorption occurring on heterogeneous surfaces is physical or chemical. D-R isotherm model equation:

$$\ln q_e = \ln q_m - \beta \epsilon^2 \quad (8)$$

In this study, the results obtained in equilibrium for the adsorption of VBR dyes to the CE surface were analyzed according to the Langmuir, Freundlich, and Dubinin-Radushkevich isotherm models, respectively. Constant values and r^2 values of all isotherm models are given in Table 2.

When the r^2 values of the adsorption data in Table 2 are compared, it is seen that the Freundlich isotherm model (Fig. 7) is the most suitable model for VBR adsorption.

The value of n appears to be higher than 1 for all 3 temperatures. It shows that the adsorption mechanism occurs voluntarily.

Salt Effect

In order to investigate the effect of ionic strength on adsorption capacity, dye solutions containing NaCl salt with concentrations ranging from 0.01 to 0.4 mol.L⁻¹ were prepared. The prepared solutions were mixed with the adsorbent during a 5 minute equilibrium period. The data obtained from the experiment are given in Fig.8.

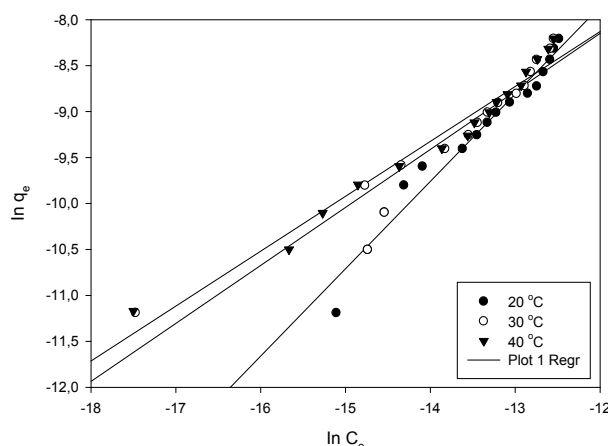


Figure 7: Freundlich isotherm graphics.

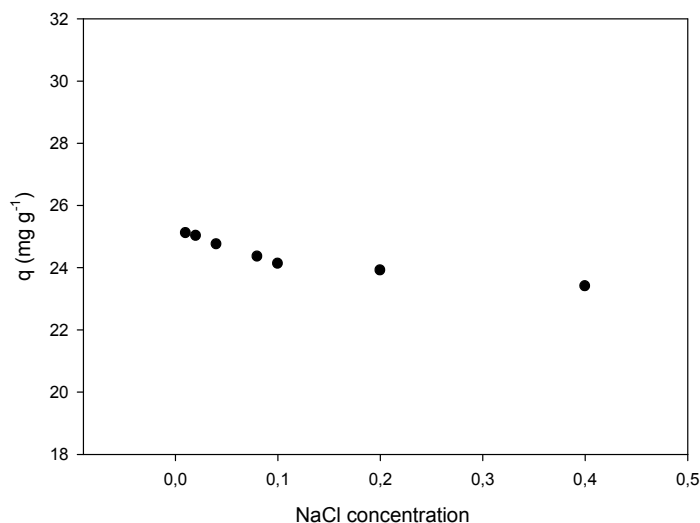


Figure 8: Salt effect on adsorption.

As it is understood from the figure, the increase of the concentration of salt in the medium, a small amount of adsorption capacity has been decreased. This situation indicates that ionic strength does not have a significant effect on the salt concentration range examined with calcined eggshell and VBR adsorption.

Real wastewater

The removal of the VBR dyestuff from the real wastewater environment was investigated in optimum conditions obtained by experimental studies. For this purpose, VBR dyestuff was added to the wastewater taken from the outlet water of a factory. In the adsorption study with real wastewater under optimum experimental conditions, 73.52% removal was observed. This value is very close to the efficiency obtained with synthetic solutions. This situation indicates that other components in the wastewater environment are not in competition with the VBR dyestuff to bind to the active sites on the adsorbent surface under the conditions under study. Thus, it has been revealed that the VBR dyestuff in wastewater can be removed from the environment with a small decrease in the adsorption efficiency with calcined eggshells.

CONCLUSION

In this study, the optimum pH value was determined as 6.0. The optimum pH value determined is also close to the initial pH of the dye solution (original dye solution pH = 5.62). Adsorption equilibrium has been established in a short time like 5 minutes. The adsorption process is best explained by the Freundlich isotherm model

and the pseudo-second-order kinetic model. 73.52% eggshell is thought to be a very effective adsorbent due to its abundance and waste in nature and high adsorption capacity. Removal was achieved under optimum adsorption conditions in a real wastewater environment.

ACKNOWLEDGMENTS

This study was supported by the Scientific Research Projects Department of Hitit University (Project no: FEF01.13.009)

REFERENCES

1. Chen C-Y, Wang G-H, Tseng I-H, Chung Y-C. Analysis of bacterial diversity and efficiency of continuous removal of Victoria Blue R from wastewater by using packed-bed bioreactor. *Chemosphere*. 2016;145:17-24.
2. Vaidya A. Environmental pollution during chemical processing of synthetic fibers. *Colourage*. 1982;14:3-10.
3. Ayed L, Chaieb K, Cheref A, Bakhrouf A. Biodegradation and decolorization of triphenylmethane dyes by *Staphylococcus epidermidis*. *Desalination*. 2010;260(1-3):137-46.
4. Azmi W, Sani RK, Banerjee UC. Biodegradation of triphenylmethane dyes. *Enzyme and microbial technology*. 1998;22(3):185-91.
5. Belpaire C, Reyns T, Geeraerts C, Van Loco J. Toxic textile dyes accumulate in wild European eel *Anguilla anguilla*. *Chemosphere*. 2015;138:784-91.

6. Black JJ, Holmes M, Dymerski PP, Zapisek WF. Fish tumor pathology and aromatic hydrocarbon pollution in a Great Lakes estuary. Hydrocarbons and halogenated hydrocarbons in the aquatic environment: Springer; 1980. p. 559-65.
7. Chen K, Lu C, Chang T, Lai Y, Wu C, Chen C. Comparison of photodegradative efficiencies and mechanisms of Victoria Blue R assisted by Nafion-coated and fluorinated TiO₂ photocatalysts. Journal of hazardous materials. 2010;174(1-3):598-609.
8. Cho BP, Yang T, Blankenship LR, Moody JD, Churchwell M, Beland FA, et al. Synthesis and characterization of N-demethylated metabolites of malachite green and leucomalachite green. Chemical research in toxicology. 2003;16(3):285-94.
9. Demirbaş O, Alkan M, Doğan M. The removal of Victoria blue from aqueous solution by adsorption on a low-cost material. Adsorption. 2002;8(4):341-9.
10. Rajabi HR, Khani O, Shamsipur M, Vatanpour V. High-performance pure and Fe³⁺-ion doped ZnS quantum dots as green nanophotocatalysts for the removal of malachite green under UV-light irradiation. Journal of hazardous materials. 2013;250:370-8.
11. Almeida LC, Silva BF, Zanoni MV. Photoelectrocatalytic/photoelectro-Fenton coupling system using a nanostructured photoanode for the oxidation of a textile dye: kinetics study and oxidation pathway. Chemosphere. 2015;136:63-71.
12. Huang S-T, Jiang Y-R, Chou S-Y, Dai Y-M, Chen C-C. Synthesis, characterization, photocatalytic activity of visible-light-responsive photocatalysts BiOxCl_y/BiO_mBr_n by controlled hydrothermal method. Journal of Molecular Catalysis A: Chemical. 2014;391:105-20.
13. Jiang Y-R, Chou S-Y, Chang J-L, Huang S-T, Lin H-P, Chen C-C. Hydrothermal synthesis of bismuth oxybromide-bismuth oxyiodide composites with high visible light photocatalytic performance for the degradation of CV and phenol. RSC Advances. 2015;5(39):30851-60.
14. Lee WW, Lu C-S, Chuang C-W, Chen Y-J, Fu J-Y, Siao C-W, et al. Synthesis of bismuth oxyiodides and their composites: characterization, photocatalytic activity, and degradation mechanisms. RSC Advances. 2015;5(30):23450-63.
15. Rajabi HR, Farsi M. Quantum dot based photocatalytic decolorization as an efficient and green strategy for the removal of anionic dye. Materials Science in Semiconductor Processing. 2015;31:478-86.
16. Roushani M, Mavaei M, Rajabi HR. Graphene quantum dots as novel and green nano-materials for the visible-light-driven photocatalytic degradation of cationic dye. Journal of Molecular Catalysis A: Chemical. 2015;409:102-9.
17. Geetha P, Latha M, Koshy M. Biosorption of malachite green dye from aqueous solution by calcium alginate nanoparticles: equilibrium study. Journal of Molecular Liquids. 2015;212:723-30.
18. Oguntimein GB. Biosorption of dye from textile wastewater effluent onto alkali treated dried sunflower seed hull and design of a batch adsorber. Journal of Environmental Chemical Engineering. 2015;3(4):2647-61.
19. Erol K, Köse K, Köse DA, Sızır Ü, Tosun Satır İ, Uzun L. Adsorption of Victoria Blue R (VBR) dye on magnetic microparticles containing Fe (II)-Co (II) double salt. Desalination and Water Treatment. 2016;57(20):9307-17.
20. Sun D, Zhang X, Wu Y, Liu X. Adsorption of anionic dyes from aqueous solution on fly ash. Journal of hazardous materials. 2010;181(1-3):335-42.
21. Madrakian T, Afkhami A, Ahmadi M. Adsorption and kinetic studies of seven different organic dyes onto magnetite nanoparticles loaded tea waste and removal of them from wastewater samples. Spectrochimica Acta Part A: Molecular and Biomolecular Spectroscopy. 2012;99:102-9.
22. Singh SA, Vemparala B, Madras G. Adsorption kinetics of dyes and their mixtures with Co₃O₄-ZrO₂ composites. Journal of Environmental Chemical Engineering. 2015;3(4):2684-96.
23. Gamoudi S, Srasra E. Adsorption of organic dyes by HDPy⁺-modified clay: Effect of molecular structure on the adsorption. Journal of Molecular Structure. 2019;1193:522-31.
24. Gupta K, Khatri OP. Fast and efficient adsorptive removal of organic dyes and active pharmaceutical ingredient by microporous carbon: Effect of molecular size and charge. Chemical Engineering Journal. 2019;378:122218.

25. Nyamukamba P, Tichagwa L, Okoh O, Petrik L. Visible active gold/carbon co-doped titanium dioxide photocatalytic nanoparticles for the removal of dyes in water. *Materials Science in Semiconductor Processing*. 2018;76:25-30.
26. Al-Ghouti MA, Salih NR. Application of eggshell wastes for boron remediation from water. *Journal of Molecular Liquids*. 2018;256:599-610.
27. Prabakaran K, Rajeswari S. Spectroscopic investigations on the synthesis of nano-hydroxyapatite from calcined eggshell by hydrothermal method using cationic surfactant as template. *Spectrochimica Acta Part A: Molecular and Biomolecular Spectroscopy*. 2009;74(5):1127-34.
28. Lagergren S, Lagergren S, Lagergren S, Sven K. Zurtheorie der sogenannten adsorption gelösterstoffe. 1898.
29. Ho Y, McKay G. Kinetic models for the sorption of dye from aqueous solution by wood. *Trans IChemE*. 1998;76(B):183-91.
30. Weber WJ, Morris JC. Kinetics of adsorption on carbon from solution. *Journal of the sanitary engineering division*. 1963;89(2):31-60.
31. Langmuir I. The adsorption of gases on plane surfaces of glass, mica and platinum. *Journal of the American Chemical society*. 1918;40(9):1361-403.
32. Freundlich H. Über die adsorption in lösungen. *Zeitschrift für physikalische Chemie*. 1907;57(1):385-470.
33. Radushkevich M. The equation of the characteristic curve of the activated charcoal USSR *Phys. Chem Sect*. 1947;55:331.



Ultrasound-Assisted Adsorption of Basic Blue 41 onto Salda mud: Optimization and Error Analysis

Elif Tüzün* , Selcan Karakuş 

Istanbul University Cerrahpasa, Faculty of Engineering, Department of Chemistry, Avcilar, Istanbul – Turkey.

Abstract: We investigated the ultrasound-assisted adsorption of Basic Blue 41 (BB41) dye from aqueous solutions using a green and low-cost adsorbent such as Salda mud (SM) in our study. BET, FTIR, and SEM techniques were used to determine the morphology and the functional groups of SM before and after dye adsorption. Furthermore, we calculated different adsorption kinetics, isotherms, and error models (SSE, HYBRID, and ARE) parameters to evaluate the optimum experimental conditions such as the initial dye concentration of BB41 (6.25 - 50 mg L⁻¹), SM dose (0.05 - 0.2 g), pH (3 - 10), and sonication time (400 - 3600 s). The value of uptake (%) of SM for BB41 was 94% at 50 mg L⁻¹, 25 °C at 3600 s. Following this, we found that the pseudo second-order (Type2) model of BB41 was the best fitted model with highest R² (0.973 - 0.999) values. We developed a simple, low-cost, and fast to remove BM41 from water using natural and efficient SM adsorbent, which exhibited superior adsorption performance in wastewater treatment under ultrasonic irradiation.

Keywords: Salda mud, ultrasonic-assisted adsorption, error analysis, isotherm models, Basic Blue 41.

Submitted: September 14, 2020. **Accepted:** November 12, 2020.

Cite this: Tüzün E, Karakuş S. Ultrasound-Assisted Adsorption of Basic Blue 41 onto Salda mud: Optimization and Error Analysis. JOTCSA. 2021;8(1):57-68.

DOI: <https://doi.org/10.18596/jotcsa.795083>.

***Corresponding author.** E-mail: (elif.tuzun@istanbul.edu.tr), Tel: (+90 212 473 7000), Fax: (+90 212 473 7180).

INTRODUCTION

Water pollutants such as chemical wastes, dyes, pesticides, radioactive pollutants, and heavy metals), originated from industrial activity and home waste, have become an increasingly global problem for environmental sustainability (1-3). Researchers study to solve accelerating water pollution problems such as physical, chemical, and biological pollution (4). Rapid population growth, unplanned urbanization, unplanned industrialization, and industrial wastewater are the main reasons for water pollution (5). For this reason, the importance of wastewater treatment has become vital for aquatic environments, animals, and humans (6-7). The low-cost based treatment, operation simplicity, and green chemistry play an important role in the treatment of textile-based dye wastewater (8-10). Studies have reported that different methods (oxidation, filtration, ion exchange, adsorption, coagulation-flocculation, and ultrasound-assisted

adsorption) can be used to remove textile dyes from aqueous medium (11-16). The ultrasound-assisted adsorption is an effective and rapid method used to remove textile dyes from aqueous medium using ultrasonic technology (16-18).

In recent years, interest in natural, effective and low-cost adsorbents such as microalgae (19), gum-based hydrogel (20), alginate (21), bentonite (22), sediment (23), activated carbon (24), and mud (25) increase to be used to remove dyes from wastewater. The adsorptive characteristics of different types of muds were proposed as natural, low-cost, available in large quantities, and efficient adsorbents for dye removal (26-28).

We preferred Salda mud (SM) as a green adsorbent which is obtained from Salda Lake region of Turkey, and consists of hydromagnesite stromatolites to remove BB41 from aqueous solution using the ultrasound-assisted adsorption method as a function

of the initial BB41 dye concentration, SM dose, temperature, and pH. Brunauer – Emmett – Teller (BET), Fourier-transfor infrared (FTIR), and Scanning Electron Microscopy (SEM) techniques were used to determine the morphology and the functional groups of SM before and after dye adsorption. According to reported studies on adsorption of dye, we have found that the ultrasound-assisted adsorption method is preferred to remove BB41 from aqueous solution, but there are limited studies on adsorption capacity of SM. In our study, the novelty was to research the ultrasonic-assisted adsorption of BB41 on the surface of SM due to the effect of sonic waves. According to our results, the value of uptake (%) of BB41 was calculated 94% at optimized ultrasound-assisted conditions (SM dose = 0.05 g, sonication time = 3600 s, pH = 7, the initial BB41 concentration = 50 mg L⁻¹ of BB41). We used different kinetic models such as first order, pseudo-second order (Type 1) and pseudo-second order (Type 2) models to find the kinetic parameters of models and adsorption capacity of SM. This ultrasound-assisted adsorption mechanism is in agreement with the Freundlich model (R²: 0.999) and pseudo-second-order (Type 2) (R²: 0.973 - 0.999) with high correlation constants (R²) and low error parameters. The experimental results showed that SM has great potential as a green adsorbent for the rapid removal of BB41 from the aqueous medium under ultrasonic power.

EXPERIMENTAL SECTION

Materials

BB41 (C₂₀H₂₆N₄O₆S₂, molecular weight: 482.57 g/mol) was purchased from Sigma Aldrich Company (Germany). SM was provided from Salda Lake (Burdur, Turkey), washed three times with water before use, then filtered and dried at 50 ± 1° C for 8 h in a vacuum oven until a constant weight of the sample. The powder was passed through a sieve (200 mesh) and then it was stored for use in the desiccator at room temperature.

Characterization

SEM device was a Hitachi SU3500, and FTIR was PerkinElmer®'s Spectrum 3™ Infrared Spectrometer and spectra were recorded in potassium bromide (KBr) powder within the spectral range 4000 to 600 cm⁻¹ with a resolution of 4 cm⁻¹ and 8 scans were averaged. Characterization of the samples was performed before and after dye adsorption. The ultraviolet-visible (double beam UV-visible) spectrophotometer (T80 & T80+ - PG Instruments) was used to view the absorbance. BET (Micromeritics ASAP 2020 analyzer) analysis was used to determine the specific surface area of SM.

Ultrasonic-Assisted Adsorption Experiments

In light of our experimental data, we investigated the selected operating parameters on the ultrasonic-

assisted adsorption study was performed to adsorption of BB41. Experimental runs were carried out at constant temperature with the initial BB41 concentration (6.25 - 50 mg L⁻¹), SM dose (0.05 - 0.2 g), and pH (3 - 10) in ultrasonic bath at 20 kHz. Before the measurement of absorbance, the samples were centrifuged at 10,000 rpm (rotor speed) for 5 min and measured at a certain wavelength (λ_{max}=617 nm) using a ultraviolet-visible spectrophotometer. All measurement runs were done in triplicate under the same experimental conditions.

Calculations Part

We calculated the value of equilibrium adsorption capacity of SM by the following formula (Eq. 1) (29-30):

$$q_e = (C_0 - C_e) \times \frac{V}{m} \quad (1)$$

where q_e: the equilibrium adsorption capacity of SM (mg g⁻¹), V: volume of BB41 solution (L), m: mass of the SM (g), C₀: the initial BB41 concentrations (mg L⁻¹), and C_e: the equilibrium BB41 concentrations (mg L⁻¹).

The kinetic experimental runs were performed at the similar optimized conditions (the initial BB41 concentration (6.25 - 50 mg L⁻¹), SM dose (0.05 - 0.2 g), and medium pH (3 - 10) in ultrasonic bath at 20 kHz). We used different kinetic models such as first order, pseudo-second order (Type 1) and pseudo-second order (Type 2) models to find the kinetic parameters of models and adsorption capacity of SM. The parameters of kinetic models were calculated by the following formulas (Eqs. 2-4) (31-33):

first order model:

$$\log(q_e - q_t) = \log q_e - \left(\frac{k_1}{2.303} \right) \times t \quad (2)$$

pseudo-second order model (Type 1):

$$\frac{t}{q_t} = \left(\frac{1}{h} \right) - \frac{t}{q_e} \quad (3)$$

pseudo-second order model (Type 2):

$$\frac{1}{q_t} = \left(\frac{1}{h} \right) \frac{1}{t} + \frac{1}{q_e} \quad (4)$$

Where q_t : the amount of measured adsorption capacity of SM (mg g⁻¹) at time t, t: time (min), k₁: the rate constant of the pseudo-first order model (min⁻¹), h: k₂q_e², k₂: the rate constant of the pseudo-second order model (g mg⁻¹ min⁻¹), and k_{ip}: the rate constant of intra-particle diffusion model (mg/g min^{1/2}).

Adsorption isotherms experiments were performed at initial dye (BB41) concentration (6.25-50 mg L⁻¹)

and SM dose (0.05 g) at solution pH 7.0. Different isotherm parameters (Langmuir, Freundlich, Temkin, Harkins - Jura, and Halsey parameters) were calculated using Eqs. 5-9, respectively (34-36).

$$\frac{1}{q_e} = \frac{1}{q_t} + \frac{1}{q_t K_L} \times \frac{1}{C_e} \quad (5)$$

$$\ln q_e = \ln K_F + n \ln C_e \quad (6)$$

$$q_e = K_T T \ln a_T + K T \ln C_e \quad (7)$$

$$\frac{1}{q_e^2} = \frac{B}{A} - \frac{1}{A} \log C_e \quad (8)$$

$$\ln q_e = \frac{1}{n} \ln k - \frac{1}{n} \ln C_e \quad (9)$$

Where, K_L : the Langmuir constant ($L \text{ mg}^{-1}$), K_F : the Freundlich constant (mg g^{-1}), $1/n$: the intensity of adsorption, K_T : the Temkin constant ($L \text{ g}^{-1}$), $K_T = R T / b$, T : the temperature (K), A and B : Halsey constant, and R : the universal gas constant (8.314 J / mol K).

We calculated the error analysis parameter to find the best fitted kinetic models. The formulas of the sum of squares of errors (SSE), the hybrid fractional error function (HYBRID), and the average relative error (ARE) models were given Eq. 10-12, respectively (37-38).

$$\sum_{i=1}^n (q_{cal} - q_e)_i^2 \quad (\text{Eq. 10})$$

$$\frac{100}{n-p} \sum_{i=1}^n \left(\frac{(q_e - q_{cal})_i^2}{q_e} \right) \quad (\text{Eq.11})$$

$$\frac{100}{n-p} \sum_{i=1}^n \left(\frac{q_e - q_{cal}}{q_e} \right)_i \quad (\text{Eq. 12})$$

Where q_e is the experimental capacity of the adsorbent, q_{cal} is the calculated capacity of the adsorbent, n is the number of data, and p is the number of parameters in the experiment.

RESULTS AND DISCUSSION

Characterizations of SM before and after BB41 adsorption

The main objective of this paper was to illuminate the adsorption behavior of SM for removal of BB41

dye using the ultrasonic-assisted adsorption method. Many previous studies have been reported about BB41 adsorption kinetics, but limited works have been reported on the adsorption characteristic of SM under the acoustic cavitation, but limited works have been reported on the adsorption characteristic of SM under the acoustic cavitation. The surface area of SM was given $20.12 \text{ m}^2/\text{g}$ (5) and the value of specific surface area was $0.022 \text{ m}^2/\text{g}$ of SM for after adsorption process. BET results demonstrated that BB41 was adsorbed onto SM. SEM images of the surface of SM before and after BB41 adsorption at different magnifications were given in Figure 1 (a-b). In Fig. 3.1, SEM results showed that the unloaded SM had an irregular and heterogeneous porous surface. After the adsorption process, the surface of SM was covered with BB41 dye and the surface of SM became smooth in a short time. According to results, we assumed there were physico-chemical adsorption mechanisms on the surface of SM. As a result of these differences between SEM results, we determined that BB 41 was physico-chemically adsorbed on the surface of SM and this result was supported by UV and FTIR results.

According to FTIR results of SM, we reported that the adsorbent had characteristic peaks at 3441.35 cm^{-1} (-OH), at 1477.21 cm^{-1} (CH_3 bending), at 1417.42 cm^{-1} (C-H asymmetric bending vibration), and at 1006.66 cm^{-1} (Si-O-Si), respectively. These results were similar with our previous FTIR results of the adsorbent (5). After the adsorption process, we noticed that the characteristic peaks of SM/BB41 were observed at 3441.35 cm^{-1} (-OH peak), at 1477.21 cm^{-1} (CH_3 bending), at 1416.46 cm^{-1} (C-H asymmetric bending vibration), at 1007.62 cm^{-1} (Si-O-Si), and 884.20 cm^{-1} (Si-O-Si), respectively. According to results of FTIR, we noticed that there was no prominent differences in peaks of before / after BB41 ultrasonic-assisted adsorption process. These FTIR results showed that the adsorption process was a physical one which was related to the weak electrostatic interaction and Van der Waals forces. It was determined that our results were consistent with similar studies (48).

Ultrasonic-assisted Adsorption Study Effect of the Initial BB41 Dye Concentration

During the last years, the ultrasound-assisted adsorption of textile dyes have been considered by some of researchers under ultrasound irradiation with 20 - 100 kHz ultrasonic waves at 25 - 40 °C for 5 - 60 min (39 - 42). The initial dye concentration has an impact on the adsorption characteristic of adsorbent under ultrasonic irradiation. The effect of the initial BB41 concentration on the uptake percentage was presented in Figure 3 (a-d).

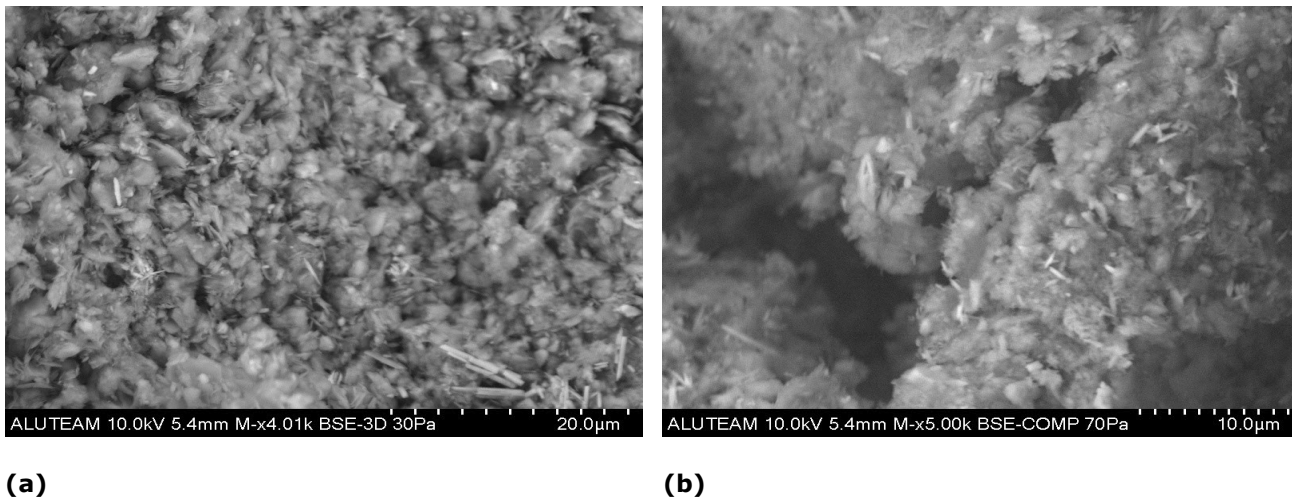


Figure 1: SEM images of SM (a) before and (b) after BB41 adsorption.

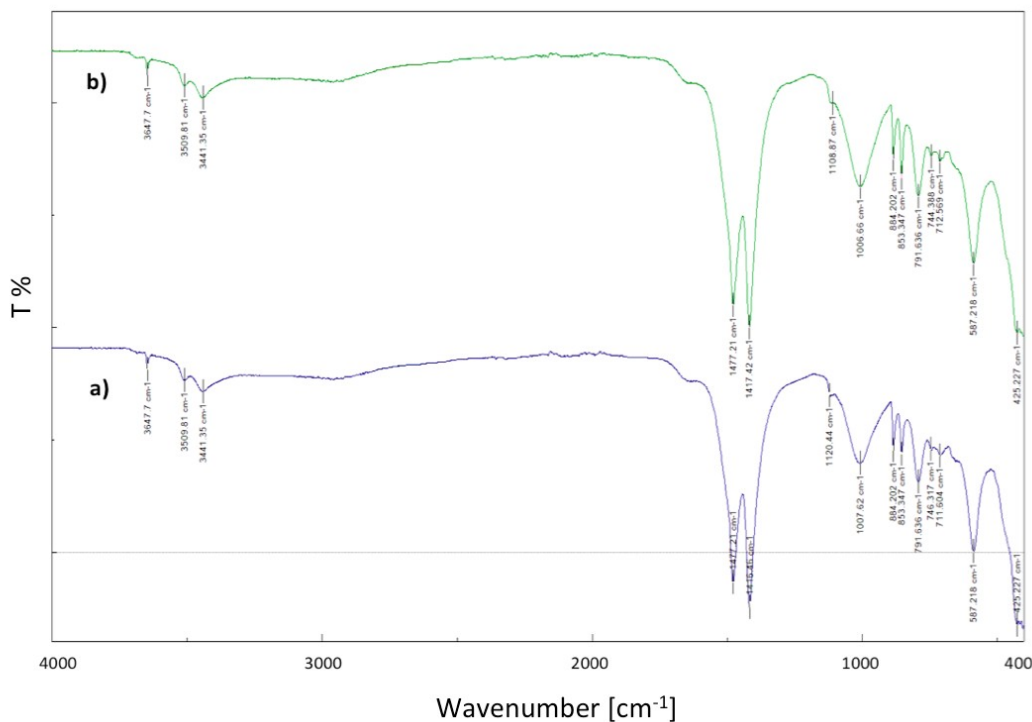


Figure 2: FTIR spectra of SM (a) before and (b) after BB41 adsorption.

In the present study, we used FTIR technique to shed light on the chemical structure and functional groups of SM on a) before and b) after BB41 ultrasonic-assisted adsorption process and FTIR graphs of samples were given in Figure 2.

In Figure 3, it was shown that the value of q_e of BB41 increased with increasing MB initial dye concentration (6.25-50 mg L⁻¹) at 25 °C, and the maximum equilibrium adsorption capacities of SM

were calculated to be 233 mg/g, 828 mg/g, 1862 mg/g, and 4699 mg/g for 6.25 mg L⁻¹, 12.5 mg L⁻¹, 25 mg L⁻¹ and 50 mg L⁻¹, respectively. We determined that the ultrasound irradiation played a major factor in the adsorption of the BB41 from the aqueous medium onto the surface of SM with 1 h sonication time. As a result, we assumed that q_e of SM increased with the initial BB41 concentration due to the amount of BB41 molecules adsorbed onto the active surface sites of SM (43).

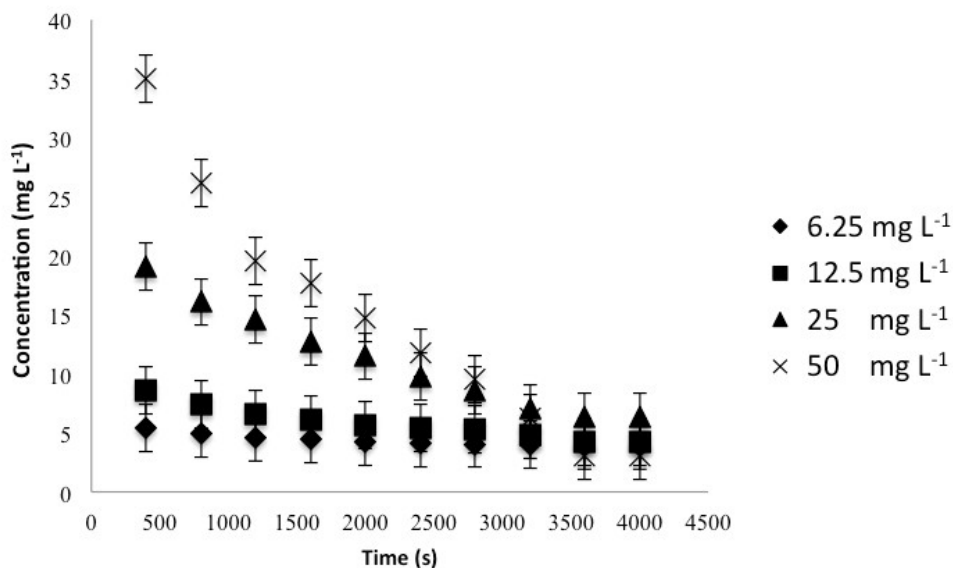


Figure 3: Effect of the initial dye concentration on the adsorption of BB41 onto SM (adsorbent dosage: 0.05 g, temperature: 25 °C, and pH: 7).

Effect of SM Dose

In this study, we investigated the different SM doses in the range of 0.05-0.2 g in the ultrasound-assisted

adsorption of BB41 from aqueous solutions (at pH 7, 25 °C and 20 kHz) and experimental results were given in Figure 4 (a-d).

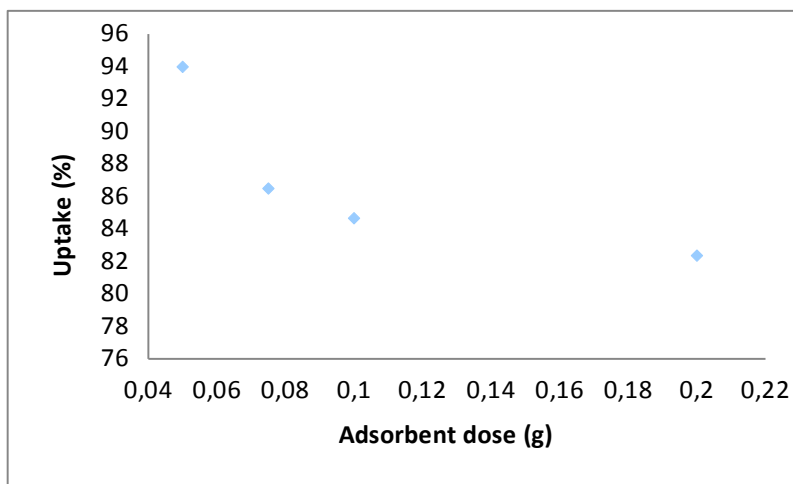


Figure 4: Effect of the adsorbent dose on the adsorption of BB41 onto SM (the initial dye concentration: 50 mg L⁻¹, temperature: 25 °C, and pH: 7).

According to the results, we showed that the adsorption capacities of SM were changed with the SM dose and adsorption was higher at low SM dose (uptake percentages: 93.97% for 0.05 g of SM) (44).

At lower the values of pH, the electrostatic repulsive force has an effect on the uptake percentages of SM and dyes removal efficiency due to the positive charges (45). Consequently, the optimum pH was 7.0 for adsorption experimental runs.

Effect of pH Medium

In this work, we investigated the effect of pH medium range of (3-10) on BB41 adsorption mechanism onto the surface of SM and results were given in **Fig. 3.5 (a-d)**. Depending on the results, the maximum uptake percentage of SM was measured at pH 7.

Effect of Sonication Time

In order to achieve the optimized operating conditions, we focused on the effect of the sonication time in the range of (400 - 3600 s) on adsorption process and evaluated the effects of the sonication time on the uptake percentages of SM. We compared the values of the uptake percentages of SM under ultrasonic irradiation in Figure 6.

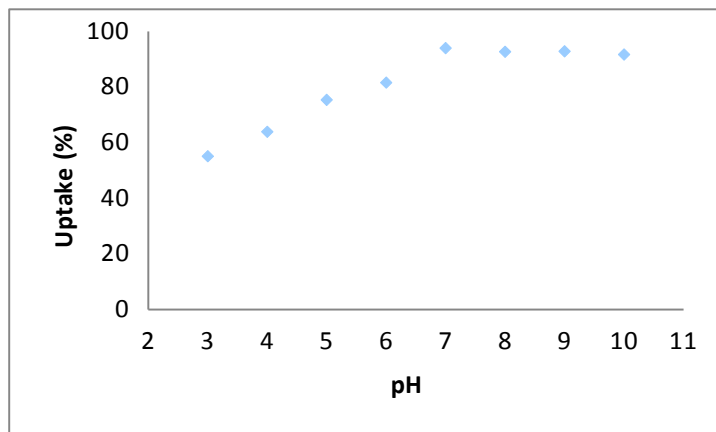


Figure 5: Effect of the pH on the adsorption of BB41 onto SM (the initial dye concentration: 50 mg L^{-1} , temperature: $25 \text{ }^\circ\text{C}$, and adsorbent dosage: 0.05 g).

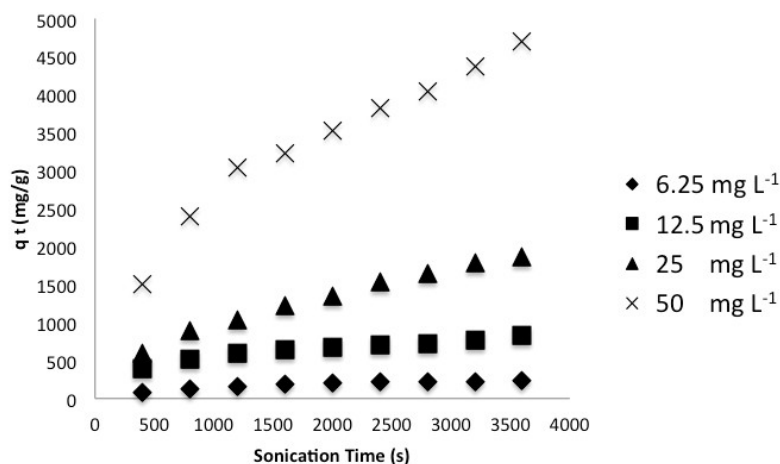


Figure 6: Effect of the sonication time on the adsorption of BB41 onto SM (temperature: $25 \text{ }^\circ\text{C}$, and adsorbent dosage: 0.05 g).

The initial BB41 concentration increased from 6.25 to 50 mg L^{-1} , while the dye adsorption capacity onto SM increased from 232.75 - 4698.66 mg/g . The results showed that the sonication time enhanced q_e of the adsorbent due to the synergic mechanism of the ultrasonic adsorption process (46).

Kinetic Studies

The kinetic model parameters of adsorption systems were calculated to understand the ultrasound-assisted adsorption mechanism and to optimize the adsorption process. For this purpose, several kinetic models such as first order, pseudo-second order (Type 1) and pseudo-second order (Type 2) models were compared to examine the ultrasound-assisted adsorption process of BB41 onto SM (0.05 g of adsorbent dosage) from the different initial dye concentrations in the range of 6.25 - 50 mg L^{-1} and at $25 \text{ }^\circ\text{C}$. Also we evaluated the mechanism of

ultrasound-assisted adsorption process consisting of the mass transfer, diffusion and chemical reaction with these models were calculated by Eqs. 2.2-2.4 kinetic models. The results of experimental kinetic studies of BB41 adsorption at different initial BB41 dye concentrations were indicated in Figure 7, and the corresponding kinetic model parameters obtained for each model were given in Table 1. According to the correlation coefficients ($R^2 > 0.99$) of models obtained for each kinetic model, the pseudo-second-order model (Type 2) was the most suitable to explain the BB41 adsorption reaction of SM. The linear graphs of the pseudo-second-order (Type 2) model for the BB41 adsorption onto the surface of SM were given in Figure 7. Consequently, the chemical reaction of BB41 dye with the surface of SM was the rate-limiting step in the ultrasound-assisted dye adsorption (47).

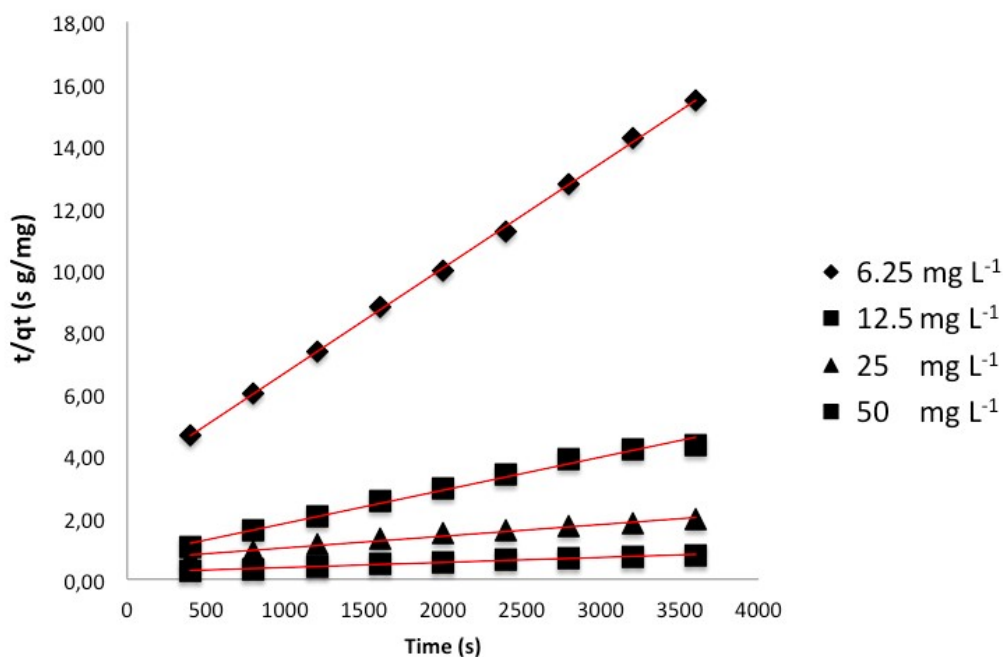


Figure 7: A pseudo-second order kinetic model (Type 2) of BB41 onto SM at different initial dye concentrations.

Table 1. Adsorption kinetic model parameters for the BB41 adsorption on SM at at different initial dye concentrations.

Adsorbent	C (g L ⁻¹)	Uptake (%)	q _e , exp (mg/g)	Second order model (Type 2)		Second order model (Type 1)	First order model	
				q _e , cal (mg/g)	k ₂	R ²	R ²	
SM	6.25	37.24	232.75	294.12	0.000040	0.999	0.662	0.696
	12.5	66.27	828.34	833.33	0.000020	0.990	0.665	0.682
	25.0	74.47	1861.76	1999.98	0.000015	0.986	0.896	0.891
	50.0	93.97	4698.66	4998.24	0.000012	0.982	0.895	0.890

Isotherm Models

We compared different adsorption isotherm models to explain a synergetic interaction between BB41 in the aqueous medium and the adsorbed BB41 concentration onto the surface of SM at equilibrium. The adsorption isotherm (Langmuir, Freundlich, Temkin, Harkins - Jura, and Halsey) parameters for the BB41 dye ultrasound-assisted adsorption onto SM were given in Table 2.

According to the experimental results, we found that the Freundlich isotherm model was best fitted with high correlation constants (R²) (0.999). The ultrasound-assisted adsorption of BB41 onto SM could better explain the mechanism of the heterogeneous system (Figure 8). Furthermore, we calculated the value of n (Freundlich isotherm constant) to show whether the mechanism of adsorption was chemical (n is smaller than 1) or

physical (n is greater than or equal to 1). In line with this information, the mechanism adsorption of BB41 dye onto the surface of SM was proven as a physical adsorption process under ultrasonic waves (48).

Optimization and Error Analysis

In our study, we calculated the different error parameters to optimize the ultrasound-assisted adsorption process of BB41 onto SM and compared different models parameters via SSE, HYBRID, and ARE models. All error results were given in Table 3, and accordingly we proved that the minimum error analysis results of ARE expression with high correlation constant of Freundlich isotherm were compatible. In Table 4, the comparison of the value of adsorption capacity of BB41 with the other adsorbents were given. Consequently, SM

demonstrate a efficient potential for removal of BB41 in a short time under ultrasound waves.

Table 2. Adsorption isotherm models parameters of BB41 on SM. (The initial dye concentration: 6.25-50 mg L⁻¹, SM dose: 0.05 g, pH 7, and temperature: 25 °C)

Models	Parameters	
Freundlich	n	1.100
	K _F (mg ^{1-1/n} L ^{1/n} /g)	100.01
	R ²	0.999
Langmuir	q _m (mg/g)	0.25
	K _L (mg/l) ⁻¹	4.67
	R ²	0.993
Temkin	K _T (kJ/mol)	1423.5
	a _T (Lm/g)	2.72
	R ²	0.907
Harkins - Jura	A _H	20.000
	B _H	0.00001
	R ²	0.751
Halsey	n _H	1.10
	K	100.02
	R ²	0.998

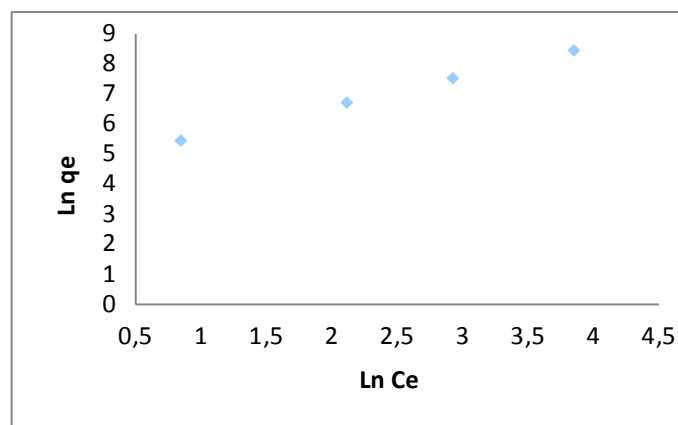


Figure 8: Freundlich isotherm model of BB41 on the adsorption of SM (The initial BB41 concentration: 6.25-50 mg L⁻¹, adsorbent dose: 0.05 g, pH 7, and temperature: 25 °C).

Table 3: The error results of adsorption isotherm of BB41 onto SM.

Models	Correlation constants (R ²)	SSE	HYBRID	ARE
Freundlich	0.999	0.994	0.996	0.998
Langmuir	0.993	0.988	0.989	0.995
Temkin	0.907	0.886	0.901	0.905
Harkins - Jura	0.751	0.742	0.745	0.749
Halsey	0.998	0.985	0.990	0.996

Table 4: The comparison of the adsorption capacities values of various adsorbents for BB41 adsorption.

Adsorbent	Adsorption Capacity	Ref
Pistachio shell	41.77 mg/g	(48)
Activated carbon	125 mg/g	(49)
Photobiocomposite bead	3.03 to 90.15 mg/g	(50)
Grape bagasse/Silica	268.1 mg/g	(51)
Brick waste	60-70 mg/g	(52)
Natural zeolitic tuff	192.31 mg/g	(53)
Nanoporous silica	345 mg/g	(54)
Salda mud	232.75-4698.66 mg/g	This study

CONCLUSIONS

In this work, we studied the rapid adsorption process of BB41 from aqueous solutions under ultrasonic waves in a short time using the low-cost and efficient adsorbent such as SM. Characteristic functional groups and surface morphologies of SM and SM/BB41 were analyzed using FTIR and SEM techniques. To examine the adsorption mechanism, we calculated the parameters of adsorption kinetic, adsorption isotherm and error models at different experimental conditions (SM dose, pH, and sonication time). According to the experimental results obtained, we proved that the best fitted kinetic model was a pseudo-second order kinetic model and the isotherm model was Freundlich (highest R^2 : 0.999 and lowest error data) model. Consequently, we determined that SM was a green, promising, and effective adsorbent and could be used in the environmental applications to remove BB41 dye.

Declaration of Competing Interest

The authors declare that they have no known competing financial interests or personal relationships that could have appeared to influence the work reported in this paper.

ACKNOWLEDGEMENTS

The authors would like to thank Fatih Özbaş for assistance of SEM analysis.

REFERENCES

1. Aksu Z. Application of biosorption for the removal of organic pollutants: a review. *Process biochemistry*. 2005;40(3-4):997-1026.
2. Zia Z, Hartland A, Mucalo M. Use of low cost biopolymers and biopolymeric composite systems for heavy metal removal from water. *International Journal of Environmental Science And Technology*. 2020; 17:4389-4406.
3. Madhav S, Ahamad A, Singh AK, Kushawaha J, Chauhan JS, Sharma S, et al. Water Pollutants: Sources and Impact on the Environment and Human Health. In: Pooja D, Kumar P, Singh P, Patil S, editors. *Sensors in Water Pollutants Monitoring: Role of Material*. Singapore: Springer Singapore; 2020;43-62.
4. Kulal DK, Loni PC, Dcosta C, Some S, Kalambate PK. Cyanobacteria: as a promising candidate for heavy-metals removal. In: *Advances in Cyanobacterial Biology*. Elsevier; 2020;291-300.
5. Karakuş S, Taşaltın N, Taşaltın C, Kilislioğlu A. Comparative study on ultrasonic assisted adsorption of Basic Blue 3, Basic Yellow 28 and Acid Red 336 dyes onto hydromagnesite stromatolite: kinetic, isotherm and error analysis. *Surfaces and Interfaces*. 2020;100528.
6. Sismanoglu T, Kismir Y, Karakus S. Single and binary adsorption of reactive dyes from aqueous solutions onto clinoptilolite. *Journal of Hazardous Materials*. 2010;184(1-3):164-9.
7. Gissawong N, Mukdasai S, Boonchiangma S, Sansuk S, Srijaranai S. A rapid and simple method for the removal of dyes and organophosphorus pesticides from water and soil samples using deep eutectic solvent embedded sponge. *Chemosphere*. 2020;260:127590.
8. Yashni G, Willy K, Al-Gheethi A, Mohamed R, Salleh SM, Hashim M. A Review on Green Synthesis of ZnO Nanoparticles Using Coriandrum Sativum Leaf Extract For Degrading Dyes in Textile Wastewater: A Prospect Towards Green Chemistry. *MS&E*. 2020;736(4):042003.
9. Joseph J, Radhakrishnan RC, Johnson JK, Joy SP, Thomas J. Ion-exchange mediated removal of cationic dye-stuffs from water using ammonium phosphomolybdate. *Materials Chemistry and Physics*. 2020;242:122488.
10. Goutam SP, Saxena G, Roy D, Yadav AK, Bharagava RN. Green synthesis of nanoparticles and their applications in water and wastewater treatment. In: *Bioremediation of Industrial Waste for Environmental Safety*. Springer; 2020;349-79.
11. Ma J, Tang X, He Y, Fan Y, Chen J. Robust stable MoS₂/GO filtration membrane for effective removal of dyes and salts from water with enhanced permeability. *Desalination*. 2020;480:114328.
12. Mukhlis MB, Khan MR, Islam M, Nazir M, Snigdha J, Akter R, et al. Decolorization of Reactive Dyes from Aqueous Solution Using Combined Coagulation-Flocculation and Photochemical Oxidation (UV/H₂O₂). *Sustainable Chemical Engineering*. 2020;51-61.
13. Jun BM, Kim S, Rho H, Park CM, Yoon Y. Ultrasound-assisted Ti₃C₂T_x MXene adsorption of dyes: Removal performance and mechanism analyses via dynamic light scattering. *Chemosphere*, 2020;126827.
14. Li J, Zhu K, Li R, Fan X, Lin H, Zhang H. The removal of azo dye from aqueous solution by oxidation with peroxydisulfate in the presence of granular activated carbon: Performance, mechanism and reusability. *Chemosphere*. 2020;259:127400.
15. Jawad AH, Abdulhameed AS, Mastuli MS. Acid-fractionalized biomass material for methylene blue dye removal: a comprehensive adsorption and

- mechanism study. *Journal of Taibah University for Science*. 2020;14(1):305–13.
16. Yu Q, Fan L, Li J. A novel process for asparagus polyphenols utilization by ultrasound assisted adsorption and desorption using resins. *Ultrasonics Sonochemistry*. 2020;63:104920.
17. Sharifpour E, Ghaedi M, Asfaram A, Farsadrooh M, Dil EA, Javadian H. Modeling and optimization of ultrasound-assisted high performance adsorption of Basic Fuchsin by starch-capped zinc selenide nanoparticles/AC as a novel composite using response surface methodology. *International Journal of Biological Macromolecules*. 2020;152:913–21.
18. Kifayatullah HM, Tahir H, Shah AR. Modeling and optimization of ultrasound-assisted adsorption of crystal violet dye by graphene oxide nanoparticles using response surface methodology. *International Journal of Environmental Analytical Chemistry*. 2020;1–17.
19. Chin JY, Chng LM, Leong SS, Yeap SP, Yasin NHM, Toh PY. Removal of Synthetic Dye by *Chlorella vulgaris* Microalgae as Natural Adsorbent. *Arabian Journal For Science And Engineering*. 2020.
20. Pandey S, Do JY, Kim J, Kang M. Fast and highly efficient removal of dye from aqueous solution using natural locust bean gum based hydrogels as adsorbent. *International Journal of Biological Macromolecules*. 2020;143:60–75.
21. Kazemi J, Javanbakht V. Alginate beads impregnated with magnetic Chitosan@ Zeolite nanocomposite for cationic methylene blue dye removal from aqueous solution. *International journal of biological macromolecules*. 2020;154:1426–37.
22. Al-Shahrani S. Phenomena of Removal of Crystal Violet from Wastewater Using Khulays Natural Bentonite. *Journal of Chemistry*. 2020;2020.
23. Tanji K, Arrahli A, Iboustaten EM, El Gaidoumi A, Kherchafi A, Benabdallah AC, et al. Valorization of Oued Sebou Natural Sediments (Fez-Morocco Area) as Adsorbent of Methylene Blue Dye: Kinetic and Thermodynamic Study. *The Scientific World Journal*. 2020;2020.
24. Rahimian R, Zarinabadi S. A review of studies on the removal of methylene blue dye from industrial wastewater using activated carbon adsorbents made from almond bark. *Progress in Chemical and Biochemical Research*. 2020;3(3):251–68.
25. Shi W, Ren H, Huang X, Li M, Tang Y, Guo F. Low cost red mud modified graphitic carbon nitride for the removal of organic pollutants in wastewater by the synergistic effect of adsorption and photocatalysis. *Separation and Purification Technology*. 2020;237:116477.
26. Zhu M-X, Lee L, Wang H-H, Wang Z. Removal of an anionic dye by adsorption/precipitation processes using alkaline white mud. *Journal of Hazardous Materials*. 2007;149(3):735–741.
27. Thakare SR, Thakare J, Kosankar P, Pal MR. A chief, industrial waste, Activated Red Mud for subtraction of Methylene blue dye from environment. *Materials Today: Proceedings*. 2020.
28. Babu AN, Reddy DS, Sharma P, Kumar GS, Ravindhranath K, Mohan GK. Removal of hazardous indigo carmine dye from waste water using treated red mud. *Materials Today: Proceedings*. 2019;17:198–208.
29. Foo KY, Hameed BH. Insights into the modeling of adsorption isotherm systems. *Chemical engineering journal*. 2010;156(1):2–10.
30. Markovski JS, \DJokić V, Milosavljević M, Mitrić M, Perić-Grujić AA, Onjia AE, et al. Ultrasonic assisted arsenate adsorption on solvothermally synthesized calcite modified by goethite, α -MnO₂ and goethite/ α -MnO₂. *Ultrasonics sonochemistry*. 2014;21(2):790–801.
31. Roosta M, Ghaedi M, Shokri N, Daneshfar A, Sahraei R, Asghari A. Optimization of the combined ultrasonic assisted/adsorption method for the removal of malachite green by gold nanoparticles loaded on activated carbon: experimental design. *Spectrochimica Acta Part A: Molecular and Biomolecular Spectroscopy*. 2014;118:55–65.
32. Jacques RA, Bernardi R, Caovila M, Lima EC, Pavan FA, Vaghetti JC, et al. Removal of Cu (II), Fe (III), and Cr (III) from aqueous solution by aniline grafted silica gel. *Separation Science and Technology*. 2007;42(3):591–609.
33. Bagheri AR, Ghaedi M, Asfaram A, Bazrafshan AA, Jannesar R. Comparative study on ultrasonic assisted adsorption of dyes from single system onto Fe₃O₄ magnetite nanoparticles loaded on activated carbon: experimental design methodology. *Ultrasonics sonochemistry*. 2017;34:294–304.
34. Zare-Dorabei R, Ferdowsi S, Barzin A, Tadjarodi A. Highly efficient simultaneous ultrasonic-assisted adsorption of Pb (II), Cd (II), Ni (II) and Cu (II) ions from aqueous solutions by graphene oxide modified with 2, 2'-dipyridylamine: central composite design optimization. *Ultrasonics sonochemistry*. 2016;2016(32):265–76.
35. Hamza W, Dammak N, Hadjltaief H, Eloussaief M, Benzina M. Sono-assisted adsorption of cristal

- violet dye onto tunisian smectite clay: Characterization, kinetics and adsorption isotherms. *Ecotoxicology and environmental safety*. 2018;2018(163):365–71.
36. Gülen J, Akin B, Özgür M. Ultrasonic-assisted adsorption of methylene blue on sumac leaves. *Desalination and water treatment*. 2016;20(57):9286–95.
37. Demirbas E, Kobya M, Konukman A. Error analysis of equilibrium studies for the almond shell activated carbon adsorption of Cr (VI) from aqueous solutions. *Journal of hazardous materials*. 2008;1–3(154):787–94.
38. Karakuş S. A Novel ZnO Nanoparticle as Drug Nanocarrier in Therapeutic Applications: Kinetic Models and Error Analysis. *JOTCSA*. 2019;6(2):119–32.
39. Amin M, Chetpattananondh P, Khan M. Ultrasound assisted adsorption of reactive dye-145 by biochars from marine *Chlorella* sp. extracted solid waste pyrolyzed at various temperatures. *Journal of Environmental Chemical Engineering*. 2009;16(4):557–63.
40. Milenković DD, Dašić PV, Veljković VB. Ultrasound-assisted adsorption of copper(II) ions on hazelnut shell activated carbon. *Ultrasonics Sonochemistry*. 2009;16(4):557–63.
41. Asfaram A, Ghaedi M, Goudarzi A, Rajabi M. Response surface methodology approach for optimization of simultaneous dye and metal ion ultrasound-assisted adsorption onto Mn doped Fe₃O₄-NPs loaded on AC: kinetic and isothermal studies. *Dalton Trans*. 2015;44(33):14707–23.
42. Wu Y, Han Y, Tao Y, Fan S, Chu D-T, Ye X, et al. Ultrasound assisted adsorption and desorption of blueberry anthocyanins using macroporous resins. *Ultrasonics Sonochemistry*. 2018;48:311–20.
43. Sirajudheen P, Nikitha MR, Karthikeyan P, Meenakshi S. Perceptive removal of toxic azo dyes from water using magnetic Fe₃O₄ reinforced graphene oxide–carboxymethyl cellulose recyclable composite: Adsorption investigation of parametric studies and their mechanisms. *Surfaces and Interfaces*. 2020;100648.
44. Noreen S, Mustafa G, Ibrahim SM, Naz S, Iqbal M, Yaseen M, et al. Iron oxide (Fe₂O₃) prepared via green route and adsorption efficiency evaluation for an anionic dye: kinetics, isotherms and thermodynamics studies. *Journal of Materials Research and Technology*. 2020;9(3):4206–17.
45. Jamshidi M, Ghaedi M, Dashtian K, Hajati S, Bazrafshan AA. Sonochemical assisted hydrothermal synthesis of ZnO: Cr nanoparticles loaded activated carbon for simultaneous ultrasound-assisted adsorption of ternary toxic organic dye: Derivative spectrophotometric, optimization, kinetic and isotherm study. *Ultrasonics Sonochemistry*. 2016;32:119–31.
46. Wen Z, Huang K, Niu Y, Yao Y, Wang S, Cao Z, et al. Kinetic study of ultrasonic-assisted uranium adsorption by anion exchange resin. *Colloids and Surfaces A: Physicochemical and Engineering Aspects*. 2020;585:124021.
47. Wei J, Xu J, Mei Y, Tan Q. Chloride adsorption on aminobenzoate intercalated layered double hydroxides: Kinetic, thermodynamic and equilibrium studies. *Applied Clay Science*. 2020;187:105495.
48. Şentürk İ, Alzein M. Adsorptive removal of basic blue 41 using pistachio shell adsorbent - Performance in batch and column system. *Sustainable Chemistry and Pharmacy*. 2020;16:100254.
49. Afshin S, Mokhtari SA, Vosoughi M, Sadeghi H, Rashtbari Y. Data of adsorption of Basic Blue 41 dye from aqueous solutions by activated carbon prepared from filamentous algae. *Data in Brief*. 2018;21:1008–13.
50. Nouri L, Hemidouche S, Boudjemaa A, Kaouah F, Sadaoui Z, Bachari K. Elaboration and characterization of photobiocomposite beads, based on titanium (IV) oxide and sodium alginate biopolymer, for basic blue 41 adsorption/photocatalytic degradation. *International Journal of Biological Macromolecules*. 2020;151:66–84.
51. Benvenuti J, Fisch A, dos Santos JHZ, Gutterres M. Silica-based adsorbent material with grape bagasse encapsulated by the sol-gel method for the adsorption of Basic Blue 41 dye. *Journal of Environmental Chemical Engineering*. 2019;7(5):103342.
52. Kooli F, Yan L, Al-Faze R, Al-Sehimi A. Removal enhancement of basic blue 41 by brick waste from an aqueous solution. *Arabian Journal of Chemistry*. 2015;8(3):333–42.
53. Humelnicu I, Băiceanu A, Ignat M-E, Dulman V. The removal of Basic Blue 41 textile dye from aqueous solution by adsorption onto natural zeolitic tuff: Kinetics and thermodynamics. *Process Safety and Environmental Protection*. 2017;105:274–87.
54. Zarezadeh-Mehrizi M, Badiei A. Highly efficient removal of basic blue 41 with nanoporous silica. *Water Resources and Industry*. 2014;5:49–57.



Evaluation of PVA/Chitosan Cryogels as Potential Tissue Engineering Scaffolds; Synthesis, Cytotoxicity, and Genotoxicity Investigations

Seda Ceylan^{1*}  , Burcu Alatepeli²  

¹Adana AlparslanTürkes Science and Technology University, Faculty of Engineering, Department of Bioengineering, Adana, Turkey.

²Çukurova University, Institute of Social Sciences, Department of Business Administration, Adana, Turkey.

Abstract: Cryogelation has become an advantageous method to obtain macro-porous materials with well-defined, interconnected pores for tissue engineering applications. Herein, polyvinyl alcohol and chitosan polymers (PVA-CHI) were used to produce cryogel scaffolds via cryogelation. Glutaraldehyde was used as a crosslinking agent and the effect of crosslinking amount on the properties of scaffolds investigated. Glutaraldehyde amount was divided into 5, 10, and 15% total amount of polymer concentration. The optimized pore morphology was obtained as a scaffold containing 5% glutaraldehyde amount. In addition to the FTIR, SEM, swelling, and degradation analyses, mechanical tests were performed to present the characterization properties of the cryogels. Direct and indirect cytotoxicity test and genotoxicity experiments were performed with Mouse Embryonic Fibroblasts (MEF). In addition, cell morphologies on scaffolds were analyzed with SEM. The results showed that PVA-CHI based cryogels had no genotoxic and cytotoxic effects on MEF cells and have a potential for tissue engineering applications.

Keywords: Polymeric scaffolds, PVA, chitosan, cryogel, genotoxicity.

Submitted: August 25, 2020. **Accepted:** November 17, 2020.

Cite this: Ceylan S, Alatepeli B. Evaluation of PVA/Chitosan Cryogels as Potential Tissue Engineering Scaffolds; Synthesis, Cytotoxicity, and Genotoxicity Investigations. JOTCSA. 2021;8(1):69–78.

DOI: <https://doi.org/10.18596/jotcsa.825115>.

***Corresponding author. E-mail:** sceylan@atu.edu.tr.

INTRODUCTION

Tissues have regeneration capacity, but large defects need grafts such as autografts, allografts, xenografts, and synthetic grafts to treat the restoration of tissue (1). Autografts, allografts, and xenografts have some problems, including the infection, pain, and immune rejection. In order to solve these problems, tissue engineers purpose to produce implantable synthetic grafts in laboratory conditions by using synthetic materials. In other words, tissue engineering aims to regenerate injured tissues by combining porous scaffold biomaterials with cells and body/growth factors, which act as a mold for tissue regeneration (2,3). Consequently, in recent years biodegradable polymeric grafts/scaffolds have been gained a great interest in tissue regeneration. In fact, these scaffolds are biocompatible substrates for cell growth, adhesion, proliferation, and formation of the

new tissue in defected areas (4,5). Both natural and synthetic polymers have been broadly utilized in different tissue engineering applications (6,7). Synthetic polymers can be tailored easily and have predictable properties. Moreover, natural polymers do not cause an immune reaction or inflammation. In addition, natural polymers are biocompatible and bioabsorbent (8). The main aim of blending natural and synthetic polymers is to fabricate ideal scaffolds for various tissue engineering applications.

In this work, synthetic polyvinyl alcohol (PVA) and natural chitosan (CHI) polymers were used to produce porous scaffolds. Glutaraldehyde (GA) was used as a crosslinking agent. GA amount is an important parameter for scaffold productions. There are several researches about the amount of GA. In addition, in several researches GA was used to produce scaffold and in vitro and in vivo experiments results show that produced scaffolds by

GA crosslinking agent supports cell viability and proliferation (9–12). PVA is a biodegradable polymer used in tissue engineering due to its biodegradability, crystallinity, and mechanical properties. PVA can be blended with starch, gelatin, polycaprolactone (PCL), and CHI to increase its biodegradability and biocompatibility (13–16). CHI is a non-toxic, biodegradable, and biocompatible polymer and has been extensively studied in the design of many different types of tissue engineering applications (17). Up to this time, different production techniques have been used such as electrospinning, freeze-thawing and solution casting, etc. to produce PVA / CHI scaffolds (18–20). Cryogelation is another technique to fabricate scaffolds with interconnected pores at sub-zero temperatures. The interconnected macropores are important for scaffold design because this property allows diffusion of solutes and mass transportation of micro and nanoparticles. The scaffolds fabricated by the cryogelation technique show a high degree of mechanical stability. In addition to this property, they represent high resistance to deformations such as torsion and elongation (21). Characteristic properties of cryogel scaffolds can be adjusted by freezing temperature, thawing period, polymer concentration, and crosslinking amount.

The aim of this study is to produce PVA / CHI porous cryogel scaffolds at subzero temperatures for the potential of different tissue engineering applications. In the literature, although there are different articles about PVA and CHI - based cryogels, to the best of authors' knowledge, there is no scientific study about the genotoxicity properties of scaffolds and comparison of those scaffolds' mechanical properties, in terms of using different crosslinking amount (GA) to fabricate them. The chemical composition of PVA / CHI cryogels was characterized by Fourier transform infrared analyses. In addition, water uptake, degradation, and mechanical properties were investigated. Indirect and direct cytotoxicity tests, cell

morphology investigations, and genotoxicity studies were also analyzed with mouse embryonic fibroblast (MEF) cell line.

MATERIAL and METHODS

Chemicals

Polyvinyl alcohol with a molecular weight of 89,000–98,000 g mol⁻¹ (99% hydrolyzed) and chitosan (low molecular weight) were obtained from Sigma-Aldrich (USA). Glutaraldehyde (25% (v/v), aqueous) was purchased from Merck (Germany).

Preparation of PVA-CHI Scaffolds

CHI solution (1% w/v) was prepared by dissolving 1 g of low molecular weight chitosan in 100 mL of 3% acetic acid solution under magnetic stirring and left for 6 hours for complete dissolution. 5% (w/v) of PVA was dissolved in deionized water at 90 °C with continuous mechanical stirring for 3 hours. PVA and CHI solutions were mixed in fixed amounts to obtain mixtures having CHI: PVA volume ratios of 1 : 1. Glutaraldehyde (GA, 5, 10, and 15% weight of total polymer amount) was slowly added to the mixtures under constant stirring. The detailed composition (w/w) of the cryogels and GA amount are listed in Table 1. After that, the solutions were put into the cryostat at -10 °C and allowed to undergo cryogelation for 4 h (Wisd Laboratory Instrument, WiseCircu WCR-P6, Korea). By this time, the color of the gels turned to yellow. The cryogels were transferred to the freezer at -16 °C and incubated for 20 h in the freezer. After the cryogelation period was finished, the cryogels were allowed to reach the room temperature to thaw for 1 h, and cryogels were immersed in deionized water to remove unreacted GA and polymer. Washing procedure continued for 6 hours and water was changed several times. All cryogels were freeze-dried (FreeZoneBenchtop Freeze DrySystem-7670531, Labconco, USA) before performing characterization investigations.

Table 1.Quantities of PVA and chitosan (w:w) used in the preparation scaffolds.

Scaffold Code	PVA	Chitosan	GA
PVA-CHI (GA) 5	83%	17%	5%
PVA-CHI (GA) 10	83%	17%	10%
PVA-CHI (GA) 15	83%	17%	15%

FTIR Instrumentation

Chemical analysis of the cryogels has been performed by using FTIR (PerkinElmer, FTIR/FIR/NIR Spectrometer Frontier-ATR, and USA). Each scaffold was scanned in the frequency region of 400 to 4000 cm⁻¹ using and the characteristic peaks of IR transmission spectra were recorded.

SEM Instrumentation

Scanning Electron Microscopy (FE-SEM Zeiss/Supra55, Quanta 400F Field Emission, USA) was used to analyze the surface morphology of

cryogels. Samples were coated with a thin layer of platinum. SEM was used at the acceleration of 5 kV and the magnification was 250x.

Swelling Ratio

The swelling ratio (SR%) of cryogels was determined in phosphate buffer saline (PBS) at 37 °C. The swelling ratio/water absorption capacity of the produced cryogels was calculated using Eq. 1. In order to calculate the average swelling ratio, three samples (0.5 cm height and 0.9 cm diameter) were used. Firstly, dry weights of cryogels were recorded.

Then, cryogels were immersed into deionized water. At certain times, the excess water from the surface of the cryogels was removed with filter paper and then cryogels were weighed. At different time intervals, this process was repeated and water uptake capacity of cryogels was calculated with respect to time. The swelling ratio/capacity of the cryogels was calculated using the equation below;

$$SR(\%) = \left[\frac{(M_f - M_i)}{M_i} \right] \times 100 \quad (1)$$

Where M_i is the initial dry weight of cryogel, M_f is the swollen weight of cryogel and SR is the swelling ratio.

Degradation Ratio

The weight loss or degradation ratio of cryogels was calculated using Eq. 2. Three scaffolds (0.5 cm height and 0.9 cm diameter) were used to investigate average weight loss.

The first step is weighing and recording dry cryogels. After that, cryogels were put into 15 mL tubes filled with PBS. The tubes were placed in water bath of which the temperature was adjusted to 37 °C (Daihan Scientific Co. Ltd., WiseBath WB-22, Korea). At certain times, cryogels were dried at room temperature and weighed. Finally, the weight loss of the cryogels was calculated by the equation below:

$$DD(\%) = \left[\frac{(W_i - W_f)}{W_i} \right] \times 100 \quad (2)$$

Where W_i is the initial dry weight of cryogel, W_f is the final dry weight of cryogel, and DD is the degree of degradation or degradation rate(15).

Mechanical Test

The compression measurement of scaffolds was investigated using a texture analyzer (TA.XT. Plus Texture Analyzer, Stable Micro Systems, Surrey, UK). The cylindrical cryogels ($r=1$ cm, $h=0.5$ cm) were put into the surface of the analyzer. After that, compression speed was adjusted 0.1 mm s^{-1} and the compression force was analyzed by a 5 kg load cell. The gels were compressed 2 mm in a longitudinal direction after having achieved a trigger load of 1 g. The compression tests of cryogels were performed at room temperature (22). Three samples were used to investigate the mechanical properties of cryogels.

Cells and Culture Conditions

Tests were carried out with mouse embryonic fibroblastic (CF-1), (ATCC1SCRC-1040™), (MEF) cell line. The MEF cells were obtained from Professor Devrim Gozuacik (Department of Molecular Biology Genetics and Bioengineering, Sabanci University,

Istanbul, Turkey). The cell line cultured with high glucose Dulbecco's Modified Eagle's medium (DMEM, Lonza, Belgium) added with 10% fetal bovine serum (FBS, Lonza) and $55 \mu\text{M}$ β -mercaptoethanol (Merck, Germany) in a humidified incubator (NUAIRE, NU-5800, USA) at 37 °C in which the CO_2 level was kept constant at 5%.

Direct & Indirect Cytotoxicity Studies

Sterilization of the scaffolds was performed by using 70% alcoholic solution and then washed 3 times with PBS. After that, the culture medium was used to wash scaffolds. Scaffolds were prepared at the same shape/volume ($r=6$ mm, $h=1$ mm) and transferred to the wells of a 6-well flat culture plate for the direct cytotoxicity assay. The cells were drop-seeded over the surface of the scaffolds at a density of 2.5×10^5 cells/10 μL . Meanwhile, as the control group, cells were drop-seeded into the 6-well flat culture plate at the same density for per well. The cultures were incubated for 1, 3 and 5 days. After this period, cell viabilities were examined by MTT protocol.

For the indirect assay, 25,000, 15,000, and 10,000 MEF cells per well were seeded into the 24-well plates. Control and test groups incubated with different media. The control group was incubated with normal medium (DMEM + 10% FBS + and $55 \mu\text{M}$ β -mercaptoethanol) and the test group was incubated with the medium which was designed with scaffold (scaffold degradation products with the medium).

For the 1 day incubation, 25,000 cells; 3 day incubation, 15,000 cells; and 5 day incubation 10,000 cells were transferred into the well at 37 °C in a humidified 5% CO_2 incubator. After the incubation period, the viabilities of cells were analyzed by MTT assay.

The first step of MTT assay was aspirating the culture medium and adding 1000 μL MTT solution (0,25 mg/mL) into each well. Then, the plates were incubated for 2 hours at 37 °C until the purple formazan crystals were formed. The second step was removing the medium and adding 1000 μL isopropanol (Merck, Germany) to each well to dissolve the formazan crystals. Plates were agitated for 30 minutes.

A spectrophotometer (Shimadzu UV-VIS, UVmini-1240, Japan) was used at 570 nm to read the dissolved formazan crystals of each well. Assays were processed in triplicate and cell viabilities were calculated with respect to the control groups.

Cell Morphology Analysis

For SEM measurement, MEF cells were seeded on scaffolds in six-well plates with 5×10^4 cells/well. After 5 days of incubation, the culture medium was aspirated and cells were fixed with 2.5%

glutaraldehyde for 2 hours in PBS at 4 °C. Before the SEM analyses, brief washing with PBS with three times were performed, followed by dehydrating with ethanol series incubation (70–80–90–100%, each for 3–5 min). After the dehydration process, critical point drying was performed and scaffolds were coated with thin layer of platinum was investigate cell morphologies.

Genotoxicity Assay

The first step was seeding 5×10^5 MEF into per well in a 24-well plate. The second step was giving the medium that was used in the indirect cytotoxicity assay to the test group cells. The standard medium was used for the control group. Test and control groups incubated with their media for 5 days.

After the incubation process, cells were harvested and DNA isolations were obtained. In the last step; isolated DNAs were loaded in the agarose gel electrophoresis for the investigation of DNA fragmentation (15).

Statistics

Statistical analysis was carried out with SPSS (Version 21.0 for MS Windows, SPSS Inc, Chicago, IL). The One-way ANOVA and Tukey's Multiple Comparison Test were performed to determine significant differences for cell viability tests. The lowest $p < 0.05$ was considered statistically significant.

RESULTS and DISCUSSION

Characterization of the Porosity of PVA-CHI Scaffolds

Scaffold characterization studies consist of collecting information that might elucidate how the scaffold will perform under different conditions. In this matter, techniques such as FTIR, SEM, swelling, and degradation profile and mechanic analyses will provide the characterization properties of scaffolds. In other words, the results of these tests will provide sufficient and relevant information about how the scaffold behaves and how the scaffold might interact with the surrounding.

In the first part of characterization studies, the samples were analyzed by FTIR to identify the chemical groups of PVA-CHI scaffolds and the results were compared with each other (Figure 1). The characteristic absorption peaks of PVA at 858 cm^{-1} and 1440 cm^{-1} were seen in the three spectra. In addition, the peak at 1325 cm^{-1} , which is characteristic of chitosan reported as III peaks (23). The peak located at the center of $3500\text{-}3000 \text{ cm}^{-1}$ for PVA-CHI scaffolds is corresponding to the overlapped stretching of the hydrogen bond between $-\text{OH}$ and $-\text{NH}_2$ (24). The similar FTIR spectra results of a glutaraldehyde cross-linked PVA - CHI scaffolds were also reported by Hu et al. (25).

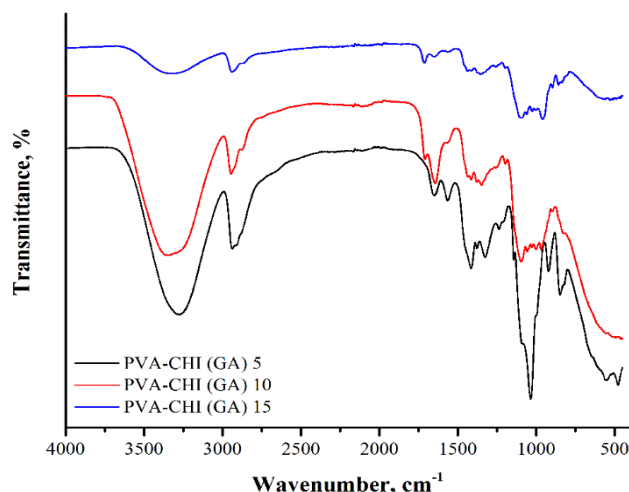


Figure 1. FTIR spectrum of PVA-CHI (GA) 5, PVA-CHI (GA) 10, PVA-CHI (GA) 15 scaffolds.

Figure 2 shows SEM images at cross section of scaffolds with different amounts of GA. For the PVA-CHI (GA) 5 and PVA-CHI (GA) 15 homogeneous pore size distribution is obtained, which occurs at all the areas of cross section, but at the sample PVA-CHI (GA) 10 pore size distribution is not uniform in

all the areas. Small pores of PVA-CHI (GA) 10 scaffold aggregate at most while bigger pores are found irregularly among them. In addition, SEM images of the PVA-CHI (GA) 5 scaffold showed more open and interconnected pore morphologies than the PVA-CHI scaffolds.

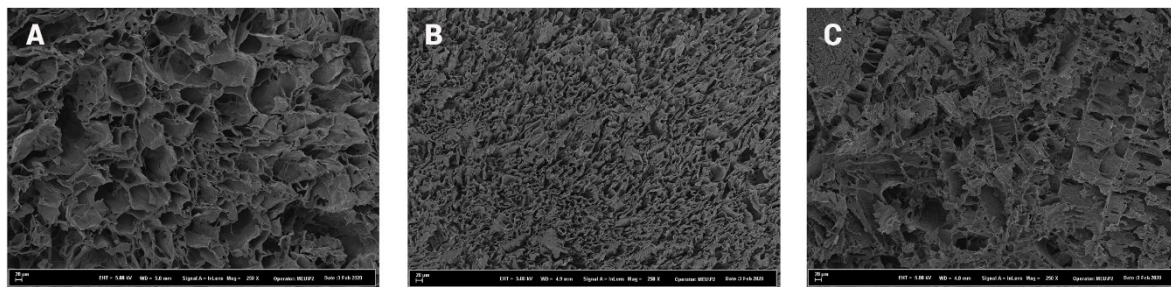


Figure 2. SEM photographs of PVA-CHI (GA) 5, PVA-CHI (GA) 10, PVA-CHI (GA) 15 scaffold (250x).

The swelling ratio or water absorption capacity is closely related to the porosity of biomaterial. As a result of a porous network, proper nutrition process and cell signaling can be achieved in scaffolds (26). The swelling ratio of PVA-CHI scaffolds is shown in Figure 3(A). The swelling ratio of PVA-CHI (GA) 5, PVA-CHI (GA) 10 and PVA-CHI (GA) 15 gels are 2000.3%, 654.4%, and 1468.04%, respectively. This result indicated that the water absorption capacity of PVA-CHI cryogels changed depending on the crosslinking amount in spite of using PVA and CHI solutions with fixed concentrations. This significant difference in swelling ratio is due to the basic difference in their pore morphology and wall thickness. Although the PVA-CHI (GA) 10 cryogels consist of a porous structure (the pore size is rather small), PVA-CHI (GA) 5 cryogels have pores that are

quite large and are interconnected through thin walls. This thin walls allows fast transport of water molecules within thin walls over short distances across the macroporous structure. In addition, pores of PVA-CHI (GA) 10 cryogels were close and were not interconnected. In addition, Figure 3(B) confirmed that the three scaffolds degraded at different rates. PVA-CHI (GA) 15 had significantly decreased by 3 days (57% \pm 2) and decreased to 63% \pm 1 by 9 days. PVA-CHI (GA) 5 degradation was slower than PVA-CHI (GA) 10 and PVA-CHI (GA) 15 scaffolds. In addition, as a result of 9 days incubation time the weight loss of PVA-CHI cryogels was increased regularly. The initial degradation ratio of scaffolds may have contributed to the wider pore size and high swelling ratio.

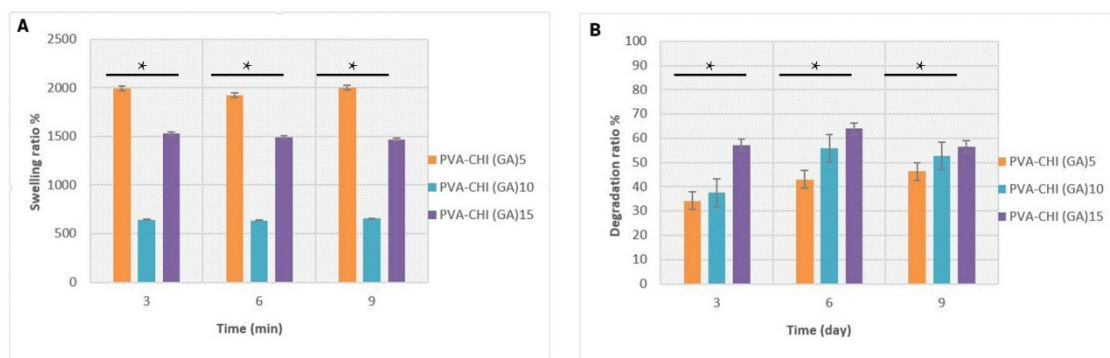


Figure 3. A) Swelling ratio of PVA-CHI cryogels and B) Degradation ratio of PVA-CHI cryogels. Here, asterisk (*) indicates significant statistical difference ($p \leq 0.05$, compared between cryogels).

The mechanical tests of PVA-CHI scaffolds were performed under compression in dry conditions and the results of the analysis are presented in Table 2. Compressive strength and young modulus of scaffolds were evaluated. The compressive strength of PVA-CHI (GA) 5 was measured as 128 ± 10 kPa with $8 \pm 1\%$ young modulus. The compression

strength of PVA-CHI (GA) 5, PVA-CHI (GA) 10 and PVA-CHI (GA) 15 scaffolds were determined as 128 ± 10 , 150 ± 13 and 150 ± 13 kPa under dry conditions, respectively. In the view of literature research, the young's modulus of the scaffolds was on the level of smooth muscle and demineralized bone (27).

Table 2. Mechanical properties of cryogels.

Sample	Compression strength, kPa	Young modulus, kPa/%
PVA-CHI (GA) 5	128±10	8±1
PVA-CHI (GA) 10	150±13	9±5
PVA-CHI (GA) 15	647±51	43±3

Cytotoxicity Studies

The amount of GA resulted difference in characteristic properties of scaffolds such as mean pore size, degradation, and swelling ratio. In addition to pore size properties, mechanical results show that compression strength and young modulus value of PVA-CHI based cryogels are changing with the crosslinking amount. PVA-CHI (GA) 5 formulated scaffold has uniform pore size distribution for cell interactions and mass or oxygen transportation. Mechanic properties were also acceptable for different tissue engineering applications. In the light

of characterization results, PVA-CHI (GA) 5 was chosen for future studies and cytotoxicity analysis was studied for this cryogel.

The MEF cells were treated with PVA-CHI (GA) 5 cryogel for 1, 3, and 5 days for direct and indirect tests. MTT assay was utilized to analyze the cell proliferation rates for PVA-CHI (GA) 5 cryogel scaffolds at the end of the incubation times. Figure 4(A) and 4(B) show the direct and indirect cell viability rate of MEF cells, respectively.

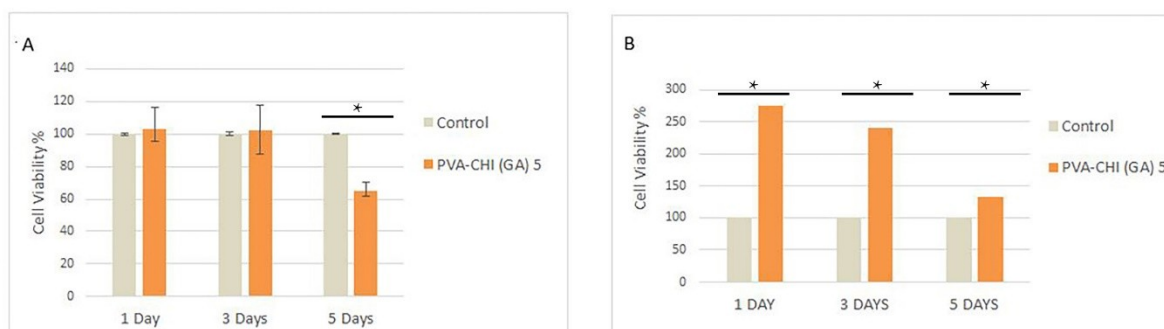


Figure 4. Evaluation graph of cytotoxicity potential of the PVA-CHI (GA) 5 cryogels ; A) direct test results, B) indirect test results. Here, asterisk (*) indicates significant statistical difference ($p \leq 0.05$, compared between control and cryogels).

It was determined that PVA-CHI (GA) 5 caused a slight decrease in MEF cell viability in the direct test ($103.19\% \pm 3.30\%$), except 5 days of incubation. The reason for this may be explained, based on the limiting area of the scaffold at the end of the 5 days incubation time. On the other hand, PVA-CHI (GA) 5 formulation significantly induced cell proliferation rate for indirect tests compared to control cells.

For the indirect test, cell viability percentage for PVA-CHI (GA) 5 scaffold decreased when the culture time increased from 1 to 5 days ($274.33\% \pm 4.40\%$ to $133.21\% \pm 4.40\%$). This result can be contributed to the limitation of area for cell proliferation and growth.

Different research studies show that PVA - CHI - based scaffolds have high blood compatibility and are good candidates for the use as matrices for tissue engineering applications (28). Alhosseini et al. evaluated the physicochemical, structural and physicochemical properties of PVA - CHI electrospun fibers and reported that PVA - CHI electrospun fibers enhance the viability and proliferation of PC12 neural cells. In addition, Peng et al. produced PVA - CHI hydrogels and combined with mesenchymal stem cells to analyze its application in articular cartilage repair and reported positive effects of PVA - CHI scaffold on cartilage healing (28).

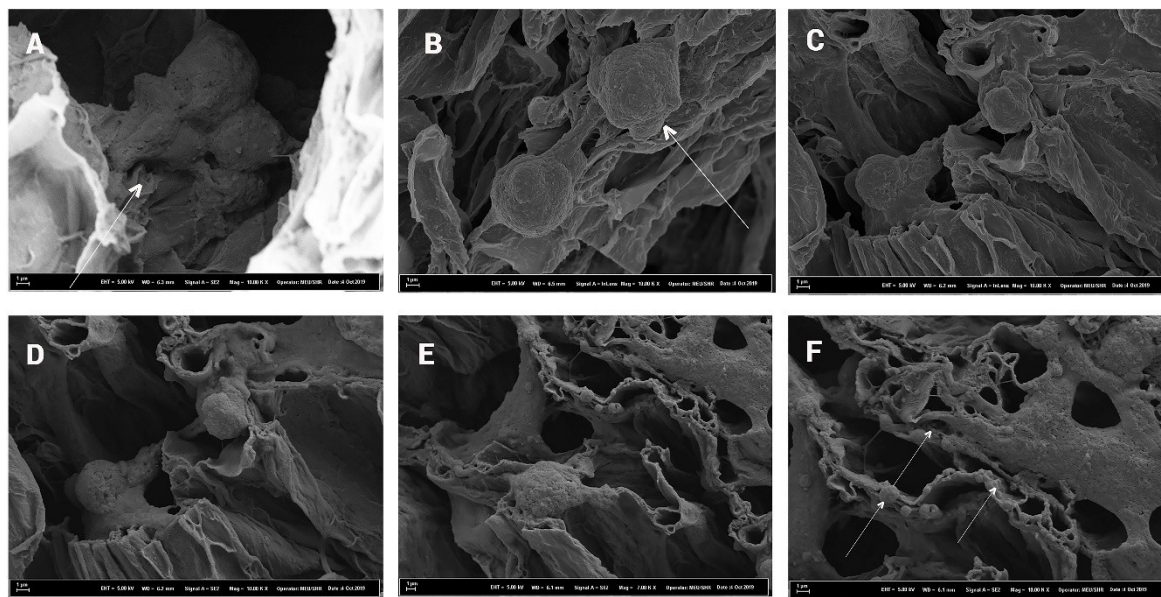


Figure 5. SEM photographs of MEF cells, cultured for 5 days on PVA-CHI (GA) 5 scaffold.

In addition to the cytotoxicity test, Figure 5 presents the SEM images of MEF cells cultured for 5 days on PVA-CHI (GA) 5 scaffold. It can be seen that MEF cells adhered well on the surface of all the scaffolds. Most of the cells on PVA-CHI (GA) 5 scaffolds were observed in normal morphology (Figure 5 A-D). On the other hand, a small number of blebblings and round-shaped cells were present

on the scaffolds. Also, elongated spindle-like morphology of MEF cells can be seen on PVA-CHI (GA) 5 scaffolds in SEM photographs (Figures 5 D). Figure 5 F among the SEM figures, shows the cells are piled up and to provide better cell proliferation. This figure also presents extracellular matrix formation beginning on the scaffold.

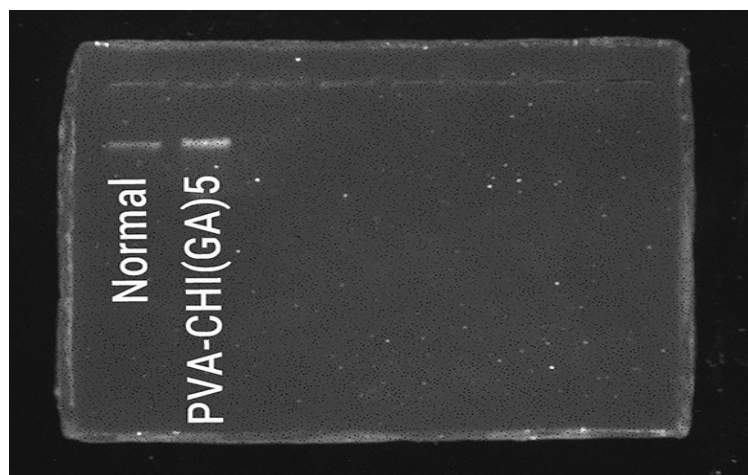


Figure 6. Genotoxicity tests results of the control group and PVA-CHI (GA) 5 scaffold (agarose gel electrophoresis, first line: control group DNA, second line: scaffold group DNA).

Results of the genotoxicity assay of control and PVA-CHI (GA) 5 scaffold are shown in Figure 6. The agarose gel electrophoresis results show that PVA-CHI (GA) 5 scaffolds did not create DNA fragmentation. So it can be said that the results of genotoxicity experiments indicate that PVA-CHI (GA) 5 scaffold formulation has no genotoxic potential. Similar observations have been made by Kelly et al. and Lima et al. who investigated a series

of PVA and chitosan based materials at different techniques and evidenced PVA-CHI biomaterials have no genotoxic potential (29,30).

CONCLUSION

PVA-CHI based cryogels were fabricated for different potential tissue engineering applications. In this study, the effects of GA into PVA-CHI based

scaffolds on physical, mechanical and cell proliferation properties were investigated. The SEM results demonstrated that all prepared cryogels were porous and mechanical strength increased with increasing GA amount. In addition, PVA-CHI (GA) 5 scaffold has a uniform and well-designed interconnected macroporous structure. In the light of characterization properties, PVA-CHI (GA) 5 formulated cryogel chosen for cell studies. In vitro results of cytotoxicity and genotoxicity studies confirmed that PVA-CHI (GA) 5 formulated scaffold has no toxic potential. Additionally, cell morphologies on the scaffold supported the MTT assay cytotoxicity experiment results. These results indicate that PVA-CHI based cryogels have a high potential as biomaterials for tissue engineering.

ACKNOWLEDGEMENT

This work was supported by the Scientific Research Projects Unit of Adana Alparslan Türkeş Science and Technology University (BAP-20103004).

REFERENCES

1. Shaltooki M, Dini G, Mehdikhani M. Fabrication of chitosan-coated porous polycaprolactone/strontium-substituted bioactive glass nanocomposite scaffold for bone tissue engineering. *Mater Sci Eng C* [Internet]. 2019;105(May):110138. Available from: <https://doi.org/10.1016/j.msec.2019.110138>
2. Marsich E, Bellomo F, Turco G, Travan A, Donati I, Paoletti S. Nano-composite scaffolds for bone tissue engineering containing silver nanoparticles: preparation, characterization and biological properties. *J Mater Sci Mater Med*. 2013;24(7):1799–807.
3. Mani MP, Jaganathan SK, Prabhakaran P, Nageswaran G, Krishnasamy NP. Electrospun polyurethane patch in combination with cedarwood and cobalt nitrate for cardiac applications. *J Appl Polym Sci*. 2019;136(47):48226.
4. Hutmacher DW. Scaffolds in tissue engineering bone and cartilage. 2000;21:2529–43.
5. Salgado AJ, Coutinho OP, Reis RL. Bone tissue engineering: State of the art and future trends. *Macromol Biosci*. 2004;4(8):743–65.
6. Lu DR, Xiao CM, Xu SJ. Starch-based completely biodegradable polymer materials. *Express Polym Lett*. 2009;3(6):366–75.
7. Hsieh WC, Liau JJ. Cell culture and characterization of cross-linked poly(vinyl alcohol)-g-starch 3D scaffold for tissue engineering. *Carbohydr Polym* [Internet]. 2013;98(1):574–80. Available from: <http://dx.doi.org/10.1016/j.carbpol.2013.06.020>
8. Gualandi C. Porous Polymeric Bioresorbable Scaffolds for Tissue Engineering. University Of Bologna, Italy; 2011.
9. Kemence N, Bölgen N. Gelatin- and hydroxyapatite-based cryogels for bone tissue engineering: synthesis, characterization, in vitro and in vivo biocompatibility. *J Tissue Eng Regen Med*. 2017;11(1):20–33.
10. Pinto R V, Gomes PS, Fernandes MH, Costa ME V, Almeida MM. Glutaraldehyde-crosslinking chitosan scaffolds reinforced with calcium phosphate spray-dried granules for bone tissue applications. *Mater Sci Eng C*. 2020;109:110557.
11. Mohammadzadehmoghadam S, Dong Y. Fabrication and characterization of electrospun silk fibroin/gelatin scaffolds crosslinked with glutaraldehyde vapor. *Front Mater*. 2019;6:91.
12. Ruijgrok JM, De Wijn JR, Boon ME. Optimizing glutaraldehyde crosslinking of collagen: effects of time, temperature and concentration as measured by shrinkage temperature. *J Mater Sci Mater Med*. 1994;5(2):80–7.
13. Yar M, Gigliobianco G, Shahzadi L, Dew L, Siddiqi SA, Khan AF, et al. Production of chitosan PVA PCL hydrogels to bind heparin and induce angiogenesis. *Int J Polym Mater Polym Biomater*. 2016;65(9):466–76.
14. Vrana NE, Cahill PA, McGuinness GB. Endothelialization of PVA/gelatin cryogels for vascular tissue engineering: Effect of disturbed shear stress conditions. *J Biomed Mater Res - Part A*. 2010;94(4):1080–90.
15. Ceylan S, Göktürk D, Demir D, Damla Özdemir M, Bölgen N. Comparison of additive effects on the PVA/starch cryogels: Synthesis, characterization, cytotoxicity, and genotoxicity studies. *Int J Polym Mater Polym Biomater*. 2017;1–10.
16. Chhatri A, Bajpai J, Bajpai AK. Designing polysaccharide-based antibacterial biomaterials for wound healing applications. *Biomater*. 2011;1(2):189–97.
17. Zargar V, Asghari M, Dashti A. A Review on Chitin and Chitosan Polymers: Structure, Chemistry, Solubility, Derivatives, and Applications. *ChemBioEng Rev* [Internet]. 2015;2(3):204–26. Available from: <http://doi.wiley.com/10.1002/cben.201400025>
18. Râpă M, Grosu E, Stoica P, Andreica M, Hetvary M. Journal of Environmental Research and Protection Polyvinyl alcohol and starch blends: properties and biodegradation behavior. *J Environ*

Res Prot. 2014;11(1):34.

19. Gomes ME, Ribeiro AS, Malafaya PB, Reis RL, Cunha AM. A new approach based on injection moulding to produce biodegradable starch-based polymeric scaffolds: morphology, mechanical and degradation behaviour. *Biomaterials*. 2001;22.

20. Silva GA, Coutinho OP, Ducheyne P, Shapiro IM, Reis RL. The effect of starch and starch-bioactive glass composite microparticles on the adhesion and expression of the osteoblastic phenotype of a bone cell line. *Biomaterials*. 2007;28(2):326-34.

21. Ozmen MM, Dinu MV, Dragan ES, Okay O. Preparation of macroporous acrylamide-based hydrogels: Cryogelation under isothermal conditions. *J Macromol Sci Part A Pure Appl Chem*. 2007;44(11):1195-202.

22. Syverud K, Pettersen SR, Draget K, Chinga-Carrasco G. Controlling the elastic modulus of cellulose nanofibril hydrogels—scaffolds with potential in tissue engineering. *Cellulose*. 2015;22(1):473-81.

23. Uslu İ, Atakol O, Aksu ML. Preparation of PVA / Chitosan Doped with Boron Composite Fibers and Their Characterization. *Hacettepe J Biol Chem [Internet]*. 2008;36(2):117-22. Available from: <http://www.hjbc.hacettepe.edu.tr/article/36/2/117> %5Cn<http://gazi.academia.edu/ibrahimUSLU>

24. Liang S, Liu L, Huang Q, Yam KL. Preparation of single or double-network chitosan/poly(vinyl alcohol) gel films through

selectively cross-linking method. *Carbohydr Polym [Internet]*. 2009;77(4):718-24. Available from: <http://dx.doi.org/10.1016/j.carbpol.2009.02.007>

25. Hu H, Hu H, Xin JH, Chan A, He L. Glutaraldehyde-chitosan and poly (vinyl alcohol) blends, and fluorescence of their nano-silica composite films. *Carbohydr Polym [Internet]*. 2013;91(1):305-13. Available from: <http://dx.doi.org/10.1016/j.carbpol.2012.08.038>

26. Mi Zo S, Singh D, Kumar A, Cho YW, Oh TH, Han SS. Chitosan-hydroxyapatite macroporous matrix for bone tissue engineering. *Curr Sci*. 2012;1438-46.

27. Reilly GC, Engler AJ. Intrinsic extracellular matrix properties regulate stem cell differentiation. *J Biomech [Internet]*. 2010;43(1):55-62. Available from: <http://dx.doi.org/10.1016/j.jbiomech.2009.09.009>

28. Peng L, Zhou Y, Lu W, Zhu W, Li Y, Chen K, et al. Characterization of a novel polyvinyl alcohol/chitosan porous hydrogel combined with bone marrow mesenchymal stem cells and its application in articular cartilage repair. *BMC Musculoskelet Disord*. 2019;20(1):1-12.

29. Kelly CM, DeMerlis CC, Schoneker DR, Borzelleca JF. Subchronic toxicity study in rats and genotoxicity tests with polyvinyl alcohol. *Food Chem Toxicol*. 2003;41(5):719-27.

30. De Lima R, Feitosa L, Pereira A do ES, De Moura MR, Aouada FA, Mattoso LHC, et al. Evaluation of the genotoxicity of chitosan nanoparticles for use in food packaging films. *J Food Sci*. 2010;75(6).



Can Soybean Lipoxygenases be Real Models for Mammalian Lipoxygenases? A Bioinformatics Approach

Sevilay CENGİZ ŞAHİN*  , Levent CAVAS  

¹University of Pamukkale, Faculty of Arts and Sciences, Department of Molecular Biology and Genetics, 20070, Kınıklı Campus, DENİZLİ-TURKEY.

²University of Dokuz Eylül, Faculty of Science, Department of Chemistry, Biochemistry Division, 35160, Kaynaklar Campus, İZMİR-TURKEY.

Abstract: Soybean lipoxygenase-1 is one of well-studied enzymes because it is considered as a model enzyme for mammalian lipoxygenases. In general, the soybean lipoxygenase-1 is used in the test of inhibitory activities of various compounds. The present study provides a bioinformatics approach for comparison of various lipoxygenases in the databases. Their various physical and chemical parameters such as molecular weight, theoretical pI, amino acid composition, aliphatic index, and grand average of hydropathicity and the multiple sequence alignments of the lipoxygenases were computed by using several bioinformatics tools. In order to see phylogenetic relationships among lipoxygenases, a phylogenetic tree was constructed. The first three most abundant amino acids in soybean lipoxygenase-1 and 15-lipoxygenase (human) are L (10.3 %), S (7.4 %), A (6.7 %) and L (13.3 %), G (7.4 %), V (7.1 %), respectively. According to the phylogenetic tree, the soybean lipoxygenases are within separate clade compared to the mammalian lipoxygenases. In conclusion, soybean lipoxygenase-1 may not fully characterize the human lipoxygenase-15 since there are remarkable sequence-based differences, which are obtained by using bioinformatics tools between soybean lipoxygenase-1 and lipoxygenases from other sources especially from human. In this context, the researchers, who are aware of the problems described above and who have similar concerns, have begun to use recombinant DNA technology to produce recombinant human lipoxygenase-15 enzyme.

Keywords: Bioinformatics, lipoxygenases, soybean lipoxygenase.

Submitted: August 25, 2020. **Accepted:** November 18, 2020.

Cite this: Cengiz Şahin S, Cavas L. Can Soybean Lipoxygenases be Real Models for Mammalian Lipoxygenases? JOTCSA. 2021;8(1):79-102.

DOI: <https://doi.org/10.18596/jotcsa.785109>.

***Corresponding author.** E-mail: scengiz@pau.edu.tr, Tel: [+902582963519](tel:+902582963519).

INTRODUCTION

Lipoxygenases (EC 1.13.11.12, linoleate:oxygen, oxidoreductases, LOXs) which are a large protein family are widely distributed in animals, plants and fungi. These enzymes are also found in cyanobacteria, although they are rarely found in other prokaryotes (1,2). Its general structure contained non-heme, non-sulfur iron atom which is responsible for enzymic activity. LOXs belong to dioxygenase family and they catalyze the oxidation of the polyunsaturated fatty acids (PUFA) such as linoleate, linolenate and arachidonate to form hydroperoxides utilizing Fe^{2+}/Fe^{3+} redox potential

and molecular oxygen (3,4). Mammalian LOXs are named as 5-LOX, 8-LOX, 11-LOX 12-LOX and 15-LOX, whereas it is 9-LOX and 13-LOX in plants based on the peroxidation position of PUFAs (5-7). Boyington et al (8) identified the first crystalline structure of LOXs from soybean that is previously named as soybean LOX-1. Although this enzyme was firstly characterized in 1947, the comprehensive analyses of soybean LOX-1 biochemistry were conducted following the structural identification in 1993 (9). Among LOXs, soybean LOX-1 is one of the well-studied LOX enzymes due to its ease of purification and activation stability (10,11) and also it has been considered as a model LOX for

mammalian LOXs, especially for human due to the insufficient purified human LOXs (5,8,12-19). According to the results of X-ray crystalline analysis, soybean LOX-1 has two domains: a smaller β -barrel domain and a much larger α -helix domain included the catalytic iron and substrate binding cavity (8,20,21). LOX enzymes generally have a highly conserved Fe-coordination sphere within the α -helix structure. Three His and one Ile ligands in the active site are also conserved in all lipoxygenases except from rat leukocyte 5-LOX (22,23). Minor et al (24) reported that the active site had two additional ligands as a water and Asn694 which can be responsible for the coordination flexibility of the active site. Although the highly conserved region in catalytic site motivate researchers to use soybean LOX-1 as a model for 15-LOX (human), it should be kept in mind that minor changes in conserved structure may lead significant functional differences between related enzymes (2). For instance, the reaction mechanism of 15-LOX (human) is considered to be similar to soybean LOX-1, but the k_{cat} value of 15-LOX (human) is approximately 45-fold lower than that of soybean LOX-1. The decrease in the k_{cat} value might have been caused by the change in redox potential of iron as a result of ligation difference (23).

LOXs have stimulated interests of many researchers so far because of the roles of these enzymes in many diseases such as bronchial asthma, allergic rhinitis, inflammatory bowel, rheumatoid arthritis, osteoporosis, stroke, cardiovascular diseases, Alzheimer's disease, and cancer. Moreover, LOX products, leukotrienes, and lipoxins, have a part in significant metabolic functions such as organelle degradation (25), transcription regulation (26), and possibly tumor cell metastasis (27). Therefore, the inhibition of LOXs is considered an important target for the treatment of LOX-related diseases (5-7,16,28-35). There are some reports which show the results of LOX inhibition studies in the literature. The inhibitory effects of three Malian plant extracts with different polarities on soybean 15-LOX were determined by Maiga et al (14). The inhibitory potential of substituted benzoic acids which is widely found in plants on soybean 15-LOX was studied by Russell et al (17). In another report conducted by Bouriche et al (36), the effects of *Cleome arabica* leaf extract, rutin, and quercetin on soybean LOX were examined. Mahesha et al (16) investigated the inhibitory effect of genistein and daidzein compounds against soybean LOX. Plant polyphenols known as sinapic acid, caffeic acid, chlorogenic acid, ferulic acid, naringenin, and chrysin were evaluated as an inhibitor of lipoxygenase and chlorogenic acid was determined

as the strongest inhibitor for soybean LOX with an IC_{50} values of 61.27 μ mol/L (37). The inhibitory effect of sesamol, the phenolic degradation product of sesamol, on lipoxygenase was determined in another investigation. It is reported that sesamol inhibited the soybean LOX-1 in a dose dependent manner with IC_{50} value of 51.84 μ M and the enzyme kinetic results indicated that the inhibition occurred in a competitive manner with the K_i value of 4.9 μ M (6). In above mentioned studies, soybean LOX has been used as a model enzyme for mammalian LOXs. On the other hand, the developments in bioinformatics and computational biology have provided a big contribution to understanding of proteins more comprehensively. Bioinformatics tools such as Clustal Omega (38,39), some tools in expasy.ch (40,41) such as PROTPARAM (41) and also phylogenetic tree construction (38,39) might help for a detailed comparison of LOXs.

This investigation aims at answering the following research questions:

- Is soybean LOX family phylogenetically close to mammalian LOX family?
- Are there any differences among various physical and chemical parameters of LOXs; such as molecular weight, theoretical pI, amino acid composition, aliphatic index and grand average of hydropathicity (GRAVY)?
- Is it reliable enough to use soybean LOXs in inhibition studies as a model for mammalian LOXs?

IN SILICO EXPERIMENTAL SECTION

The sequences and related biochemical reactions of the LOXs studied were retrieved from proteomics server of the Swiss Institute of Bioinformatics - Expasy (Expert Protein Analysis System) (40). LOXs analyzed and their corresponding codes were presented in Tables 1 and 2. Their various physical and chemical parameters such as molecular weight, theoretical pI, amino acid composition, aliphatic index, and GRAVY were computed by using PROTPARAM tool of Expasy.ch (40,41). These parameters were also shown in Tables 3 and 4. The multiple sequence alignments of the LOXs were also computed by using Clustal Omega (38,39). In order to understand the evolutionary relationship between the LOXs studied, a phylogenetic analysis was carried out. Phylogenetic tree was constructed via phylogenetic tool at Clustal Omega web tool (38,39). In order to achieve the secondary structure prediction of soybean LOX-1 and 15-LOX (human), the PSIPRED Protein Structure Prediction Server was used (42). Table 7 represents the conserved regions of the aligned sequences.

Table 1. Coding used for analyzed lipoxygenases and related database information.

Code	Protein Name	Abbreviation	Gene Name	Primary Accession Number in Swiss-Prot	Species
1	Polyunsaturated fatty acid 5-lipoxygenase	5-LO	ALOX5	P09917	<i>Homo sapiens</i> (Human)
2	Arachidonate 12-lipoxygenase, 12R-type	12R-LOX	ALOX12B	O75342	<i>Homo sapiens</i> (Human)
3	Polyunsaturated fatty acid 5-lipoxygenase	5-LO	Alox5	P12527	<i>Rattus norvegicus</i> (Rat)
4	Arachidonate 12-lipoxygenase, 12R-type	12R-LOX	Alox12b	O70582	<i>Mus musculus</i> (Mouse)
5	Polyunsaturated fatty acid lipoxygenase ALOX12	12S-LOX	ALOX12	P18054	<i>Homo sapiens</i> (Human)
6	Seed linoleate 13S-lipoxygenase-1	L-1	LOX1.1	P08170	<i>Glycine max</i> (Soybean)
7	Seed linoleate 9S-lipoxygenase-3	L-3	LOX1.3	P09186	<i>Glycine max</i> (Soybean)
8	Polyunsaturated fatty acid lipoxygenase ALOX15	15-LOX	ALOX15	P16050	<i>Homo sapiens</i> (Human)
9	Polyunsaturated fatty acid 5-lipoxygenase	5-LO	Alox5	P48999	<i>Mus musculus</i> (Mouse)
10	Arachidonate 12-lipoxygenase, 12R-type	12R-LOX	Alox12b	Q2KMM4	<i>Rattus norvegicus</i> (Rat)
11	Polyunsaturated fatty acid 5-lipoxygenase	5-LO	ALOX5	P51399	<i>Mesocricetus auratus</i> (Golden hamster)
12	Polyunsaturated fatty acid lipoxygenase ALOX15	15-LOX	ALOX15	P12530	<i>Oryctolagus cuniculus</i> (Rabbit)
13	Polyunsaturated fatty acid lipoxygenase ALOX15B	15-LOX-B	ALOX15B	O15296	<i>Homo sapiens</i> (Human)
14	Polyunsaturated fatty acid lipoxygenase ALOX8	8-LOX	Alox8	O35936	<i>Mus musculus</i> (Mouse)
15	Polyunsaturated fatty acid (12S)/(13S)-lipoxygenase, epidermal-type	12-LOX-e	Alox12e	P55249	<i>Mus musculus</i> (Mouse)
16	Polyunsaturated fatty acid lipoxygenase ALOX12	12S-LOX	Alox12	P39655	<i>Mus musculus</i> (Mouse)
17	Hydroperoxide isomerase ALOXE3	e-LOX-3	ALOXE3	Q9BYJ1	<i>Homo sapiens</i> (Human)
18	Seed linoleate 9S-lipoxygenase	-	LOX1.4	P24095	<i>Glycine max</i> (Soybean)
19	Seed linoleate 9S-lipoxygenase-2	L-2	LOX1.2	P09439	<i>Glycine max</i> (Soybean)
20	Polyunsaturated fatty acid lipoxygenase ALOX15	15-LOX	Alox15	P39654	<i>Mus musculus</i> (Mouse)
21	Polyunsaturated fatty acid lipoxygenase ALOX15	15-LOX	Alox15	Q02759	<i>Rattus norvegicus</i> (Rat)
22	Polyunsaturated fatty acid lipoxygenase ALOX15	15-LOX	ALOX15	P16469	<i>Sus scrofa</i> (Pig)
23	Linoleate 9S-lipoxygenase-4	L-4	LOX1.5	P38417	<i>Glycine max</i> (Soybean)
24	Polyunsaturated fatty acid lipoxygenase ALOX15B	15-LOX-B	Alox15b	Q8K4F2	<i>Rattus norvegicus</i> (Rat)
25	Polyunsaturated fatty acid lipoxygenase ALOX15	15-LOX	ALOX15	P27479	<i>Bos taurus</i> (Bovine)
26	Hydroperoxide isomerase ALOXE3	e-LOX-3	Aloxe3	Q9WV07	<i>Mus musculus</i> (Mouse)

RESULTS AND DISCUSSION

The functions and the catalytic activities of LOXs studied were summarized in Table 2. When the Table 2 is evaluated, it is very clear that LOXs from plants and vertebrates do not reveal completely same biochemical catalytic reactions.

Some chemical and physicochemical properties of LOXs studied such as number of amino acids, molecular weight (Da), theoretical pI, number of negatively and positively charged amino acids, aliphatic index and GRAVY were shown in Table 3. The molecular weight of soybean LOX-1 is higher than that of 15-LOX (human). The length of sequences for soybean LOXs are generally longer than those for mammalian ones. Although the soybean LOX have more amino acid residues in its general structure than mammalian LOX, approximately 200 amino acids, there is a little difference between the pI values of these species. The solubility characteristics of the proteins can be expressed via GRAVY index as the positive and negative values of it shows hydrophobic and hydrophilic characters, respectively (43). As it is seen in the Table 3, the value of GRAVY for soybean LOXs is more negative than those of mammals. So it can be said that soybean LOXs are more soluble in polar solvents. The minimum and maximum theoretical pI values were observed as 5.51 and 8.31 for polyunsaturated fatty acid 5-lipoxygenase and polyunsaturated fatty acid (12S)/(13S)-lipoxygenase, epidermal-type, respectively. It is well known that the amino acids in active site are responsible for the enzymic activity. Although these differences mentioned above exhibit the difference of evolutionary origins of these enzymes, the similarities in active site composition reveal convergent evolution. As can be seen from Table 3, the amino acid residues in active sites of all LOXs studied are very similar. Mogul et al (44) suggested that the active site of soybean LOX-1 and 15-LOX (human) is slightly different according to the results of inhibition studies conducted with alkenyl-sulfate substrates. It was reported that alkenyl-sulfates are not inhibitors for soybean LOX-1. They cannot inhibit

15-LOX (human) at low concentrations, either. But 15-LOX (human) is irreversibly inhibited by alkenyl-sulfates at high concentrations. Moreover, different enzymic activities were reported for LOXs from different origins in the scientific literature. For example, the activity of soybean LOX-1 was reported as 280 $\mu\text{mol}/\text{min}\cdot\text{mg}$ (45). On the other hand, the enzymic activity of 15-LOX from *Pseudomonas aeruginosa* (46) was reported to be 747130.2 IU/mg protein with linoleic acid. Therefore, there might be another parameter such as water or different ligand-substrate interactions except from the amino acid residues in active sites which can help researchers to a better understanding about the activity variations among LOXs. Iron atom in the active site of LOXs is essential for the enzymic activity and it is believed that the micro environment of this atom is crucial for the reaction (23,31). Iron in the active site has six coordinates which were identified as His499, His504, His690, Asn694, the terminal carboxylate of Ile839 and an additional water ligand (8,24). The enzymic activity (or the rate of the reaction) is affected by the various changes in this environment. For example, the Asn694 residue is converted His in mammalian LOX (15-LOX (rabbit)). As the His is a stronger ligand than Asn, the rate of the reaction is decreased as a result of the changes in the reduction potential of iron ion and the pKa value (23,31).

The amino acid compositions of LOXs are shown in Table 4. The first three most abundant amino acids in soybean LOX-1 and LOX-15 (human) are L (10.3 %), S (7.4 %), A (6.7 %) and L (13.3 %), G (7.4 %), V (7.1 %), respectively. It is known that the number of amino acids between plant and mammalian LOXs are significantly different. Mammalian LOXs have nearly 662-711 amino acids (in the range of 75-81 kDa for molecular weight) while plant LOXs have 838-923 amino acids (in the range of 94-103 kDa for molecular weight). It is very surprising that despite the difference between the amino acid number of plant and mammalian LOXs, the topologies and the catalytic site are highly conserved in LOX family (21,47).

Table 2. Comparison of functions and catalytic activities of lipoxygenases analyzed (40,41).

Protein Name	Function	Catalytic activity
Polyunsaturated fatty acid 5-lipoxygenase (Human)	It catalyzes the oxygenation of arachidonic acid to 5-hydroperoxyicosatetraenoic acid (5-HPETE) followed by the dehydration of the hydroperoxide into an epoxide, 5,6-oxidoicosatetraenoic acid (LTA4), thereby participates in the first step in leukotriene biosynthesis and in the inflammatory processes.	$(5Z,8Z,11Z,14Z)\text{-eicosatetraenoate} + O_2 = H_2O + \text{leukotriene } A_4$
Arachidonate 12-lipoxygenase, 12R type (Human)	It catalyzes the regio and stereo-specific incorporation of a single molecule of dioxygen into free and esterified polyunsaturated fatty acids generating lipid hydroperoxides that can be further reduced to the corresponding hydroxy species.	$(5Z,8Z,11Z,14Z)\text{-eicosatetraenoate} + O_2 = (12R)\text{-hydroperoxy-(5Z,8Z,10E,14Z)-eicosatetraenoate}$
Polyunsaturated fatty acid 5-lipoxygenase (Rat)	It catalyzes the oxygenation of arachidonic acid to 5-hydroperoxyicosatetraenoic acid (5-HPETE) followed by the dehydration of the hydroperoxide into an epoxide, 5,6-oxidoicosatetraenoic acid (LTA4), thereby participates in the first step in leukotriene biosynthesis and in the inflammatory processes.	$(5Z,8Z,11Z,14Z)\text{-eicosatetraenoate} + O_2 = H_2O + \text{leukotriene } A_4$
Arachidonate 12-lipoxygenase, 12R-type (Mouse)	It catalyzes the regio and stereo-specific incorporation of a single molecule of dioxygen into free and esterified polyunsaturated fatty acids generating lipid hydroperoxides that can be further reduced to the corresponding hydroxy species. Does not convert arachidonic acid to (12R)-hydroperoxyeicosatetraenoic acid/(12R)-HPETE.	$1\text{-O-methyl-(5Z,8Z,11Z,14Z)-eicosatetraenoate} + O_2 = 1\text{-O-methyl-(5Z,8Z,10E,12R,14Z)-hydroperoxyeicosatetraenoate}$
Polyunsaturated fatty acid lipoxygenase ALOX12 (Human)	It catalyzes the regio and stereo-specific incorporation of a single molecule of dioxygen into free and esterified polyunsaturated fatty acids generating lipid hydroperoxides that can be further reduced to the corresponding hydroxy species. Mainly converts arachidonic acid to (12S)-hydroperoxyeicosatetraenoic acid/(12S)-HPETE but can also metabolize linoleic acid.	$(5Z,8Z,11Z,14Z)\text{-eicosatetraenoate} + O_2 = (12S)\text{-hydroperoxy-(5Z,8Z,10E,14Z)-eicosatetraenoate}$
Seed linoleate 13S-lipoxygenase-1 (Soybean)	Plant lipoxygenase may be involved in a number of diverse aspects of plant physiology including growth and development, pest resistance, and senescence or responses to wounding. With linoleate as substrate, L-1 shows a preference for carbon 13 as the site for hydroperoxidation (in contrast to L-2 and L-3, which utilize either carbon 9 or 13).	$(9Z,12Z)\text{-octadecadienoate} + O_2 = (13S)\text{-hydroperoxy-(9Z,11E)-octadecadienoate}$
Seed linoleate 9S-lipoxygenase-3 (Soybean)	Plant lipoxygenase may be involved in a number of diverse aspects of plant physiology including growth and development, pest resistance, and senescence or responses to wounding. It catalyzes the hydroperoxidation of lipids containing a cis,cis-1,4-pentadiene structure.	$(9Z,12Z)\text{-octadecadienoate} + O_2 = (9S)\text{-hydroperoxy-(10E,12Z)-octadecadienoate}$
Polyunsaturated fatty acid lipoxygenase ALOX15 (Human)	It catalyzes the stereo-specific peroxidation of free and esterified polyunsaturated fatty acids generating a spectrum of bioactive lipid mediators. It converts arachidonic acid into 12-hydroperoxyeicosatetraenoic acid/12-HPETE and 15-hydroperoxyeicosatetraenoic acid/15-HPETE. Also converts linoleic acid to 13-hydroperoxyoctadecadienoic acid. May also act on (12S)-hydroperoxyeicosatetraenoic acid/(12S)-HPETE to produce hepxilin A3.	$(5Z,8Z,11Z,14Z)\text{-eicosatetraenoate} + O_2 = (12S)\text{-hydroperoxy-(5Z,8Z,10E,14Z)-eicosatetraenoate}$

Polyunsaturated fatty acid 5-lipoxygenase (Mouse)	It catalyzes the oxygenation of arachidonic acid to 5-hydroperoxyicosatetraenoic acid (5-HPETE) followed by the dehydration of the hydroperoxide into an epoxide, 5,6-oxidoicosatetraenoic acid (LTA4), thereby participates in the first step in leukotriene biosynthesis and in the inflammatory processes.	(5Z,8Z,11Z,14Z)-eicosatetraenoate + O ₂ = (5S)-hydroperoxy-(6E,8Z,11Z,14Z)-eicosatetraenoate
Arachidonate 12-lipoxygenase, 12R-type (Rat)	It catalyzes the regio and stereo-specific incorporation of a single molecule of dioxygen into free and esterified polyunsaturated fatty acids generating lipid hydroperoxides that can be further reduced to the corresponding hydroxy species.	(5Z,8Z,11Z,14Z)-eicosatetraenoate + O ₂ = (12R)-hydroperoxy-(5Z,8Z,10E,14Z)-eicosatetraenoate
Polyunsaturated fatty acid 5-lipoxygenase (Golden hamster)	It catalyzes the oxygenation of arachidonic acid to 5-hydroperoxyicosatetraenoic acid (5-HPETE) followed by the dehydration of the hydroperoxide into an epoxide, 5,6-oxidoicosatetraenoic acid (LTA4), thereby participates in the first step in leukotriene biosynthesis and in the inflammatory processes.	(5Z,8Z,11Z,14Z)-eicosatetraenoate + O ₂ = H ₂ O + leukotriene A ₄
Polyunsaturated fatty acid lipoxygenase ALOX15 (Rabbit)	It catalyzes the stereo-specific peroxidation of free and esterified polyunsaturated fatty acids generating a spectrum of bioactive lipid mediators. It converts arachidonic acid into 12-hydroperoxyeicosatetraenoic acid/12-HPETE and 15-hydroperoxyeicosatetraenoic acid/15-HPETE. Also converts linoleic acid to 13-hydroperoxyoctadecadienoic acid. May also act on (12S)-hydroperoxyeicosatetraenoic acid/(12S)-HPETE to produce hepoxilin A ₃ .	(5Z,8Z,11Z,14Z)-eicosatetraenoate + O ₂ = (12S)-hydroperoxy-(5Z,8Z,10E,14Z)-eicosatetraenoate
Polyunsaturated fatty acid lipoxygenase ALOX15B (Human)	It catalyzes the stereo-specific peroxidation of free and esterified polyunsaturated fatty acids (PUFAs) generating a spectrum of bioactive lipid mediators. It converts arachidonic acid to 15S-hydroperoxyeicosatetraenoic acid/(15S)-HPETE. Also acts on linoleic acid to produce 13-hydroxyoctadecadienoic acid/13-HPODE.	(5Z,8Z,11Z,14Z)-eicosatetraenoate + O ₂ = (15S)-hydroperoxy-(5Z,8Z,11Z,13E)-eicosatetraenoate
Polyunsaturated fatty acid lipoxygenase ALOX8 (Mouse)	It catalyzes the stereo-specific peroxidation of free and esterified polyunsaturated fatty acids (PUFAs) generating a spectrum of bioactive lipid mediators. It catalyzes the peroxidation of arachidonate and linoleate into (8S)-HPETE and (9S)-HPODE respectively.	(9Z,12Z)-octadecadienoate + O ₂ = (9S)-hydroperoxy-(10E,12Z)-octadecadienoate
Polyunsaturated fatty acid (12S)/(13S)-lipoxygenase, epidermal-type (Mouse)	It catalyzes the regio and stereo-specific incorporation of a single molecule of dioxygen into free and esterified polyunsaturated fatty acids generating lipid hydroperoxides that can be further reduced to the corresponding hydroxy species.	(5Z,8Z,11Z,14Z)-eicosatetraenoate + O ₂ = (12S)-hydroperoxy-(5Z,8Z,10E,14Z)-eicosatetraenoate
Polyunsaturated fatty acid lipoxygenase ALOX12 (Mouse)	It catalyzes the regio and stereo-specific incorporation of a single molecule of dioxygen into free and esterified polyunsaturated fatty acids generating lipid hydroperoxides that can be further reduced to the corresponding hydroxy species. Mainly converts arachidonic acid to (12S)-hydroperoxyeicosatetraenoic acid/(12S)-HPETE but can also metabolize linoleic acid. In contrast does not react towards methyl esters of linoleic and arachidonic acids.	(5Z,8Z,11Z,14Z)-eicosatetraenoate + O ₂ = (12S)-hydroperoxy-(5Z,8Z,10E,14Z)-eicosatetraenoate
Hydroperoxide isomerase ALOXE3 (Human)	Non-heme iron-containing lipoxygenase which is atypical in that it displays a prominent hydroperoxide isomerase activity and a reduced lipoxygenases activity. The hydroperoxide isomerase activity catalyzes the isomerization of hydroperoxides, derived	a hydroperoxyeicosatetraenoate = a hydroxy-epoxy-eicosatetraenoate

Seed linoleate 9S-lipoxygenase (Soybean)	<p>from arachidonic and linoleic acid by ALOX12B, into hepxilin-type epoxyalcohols and ketones. In presence of oxygen, oxygenates polyunsaturated fatty acids, including arachidonic acid, to produce fatty acid hydroperoxides.</p> <p>Plant lipoxygenase may be involved in a number of diverse aspects of plant physiology including growth and development, pest resistance, and senescence or responses to wounding. It catalyzes the hydroperoxidation of lipids containing a cis,cis-1,4-pentadiene structure.</p>	(9Z,12Z)-octadecadienoate + O ₂ = (9S)-hydroperoxy-(10E,12Z)-octadecadienoate
Seed linoleate 9S-lipoxygenase-2 (Soybean)	<p>Plant lipoxygenase may be involved in a number of diverse aspects of plant physiology including growth and development, pest resistance, and senescence or responses to wounding. It catalyzes the hydroperoxidation of lipids containing a cis,cis-1,4-pentadiene structure.</p>	(9Z,12Z)-octadecadienoate + O ₂ = (9S)-hydroperoxy-(10E,12Z)-octadecadienoate
Polyunsaturated fatty acid lipoxygenase ALOX15 (Mouse)	<p>It catalyzes the stereo-specific peroxidation of free and esterified polyunsaturated fatty acids generating a spectrum of bioactive lipid mediators. It converts arachidonic acid into 12-hydroperoxyeicosatetraenoic acid/12-HPETE and 15-hydroperoxyeicosatetraenoic acid/15-HPETE. Also converts linoleic acid to 13-hydroperoxyoctadecadienoic acid. May also act on (12S)-hydroperoxyeicosatetraenoic acid/(12S)-HPETE to produce hepxilin A3. Probably plays an important role in the immune and inflammatory responses.</p>	(5Z,8Z,11Z,14Z)-eicosatetraenoate + O ₂ = (12S)-hydroperoxy-(5Z,8Z,10E,14Z)-eicosatetraenoate
Polyunsaturated fatty acid lipoxygenase ALOX15 (Rat)	<p>It catalyzes the stereo-specific peroxidation of free and esterified polyunsaturated fatty acids generating a spectrum of bioactive lipid mediators. It converts arachidonic acid into 12-hydroperoxyeicosatetraenoic acid/12-HPETE and 15-hydroperoxyeicosatetraenoic acid/15-HPETE. Also converts linoleic acid to 13-hydroperoxyoctadecadienoic acid. May also act on (12S)-hydroperoxyeicosatetraenoic acid/(12S)-HPETE to produce hepxilin A3. Probably plays an important role in the immune and inflammatory responses.</p>	(5Z,8Z,11Z,14Z)-eicosatetraenoate + O ₂ = (12S)-hydroperoxy-(5Z,8Z,10E,14Z)-eicosatetraenoate
Polyunsaturated fatty acid lipoxygenase ALOX15 (Pig)	<p>It catalyzes the stereo-specific peroxidation of free and esterified polyunsaturated fatty acids generating a spectrum of bioactive lipid mediators. It converts arachidonic acid into 12-hydroperoxyeicosatetraenoic acid/12-HPETE and 15-hydroperoxyeicosatetraenoic acid/15-HPETE. Also converts linoleic acid to 13-hydroperoxyoctadecadienoic acid. May also act on (12S)-hydroperoxyeicosatetraenoic acid/(12S)-HPETE to produce hepxilin A3. Probably plays an important role in the immune and inflammatory responses.</p>	(5Z,8Z,11Z,14Z)-eicosatetraenoate + O ₂ = (12S)-hydroperoxy-(5Z,8Z,10E,14Z)-eicosatetraenoate
Linoleate 9S-lipoxygenase-4 (Soybean)	<p>Plant lipoxygenase may be involved in a number of diverse aspects of plant physiology including growth and development, pest resistance, and senescence or responses to wounding. It catalyzes the hydroperoxidation of lipids containing a cis,cis-1,4-pentadiene structure.</p>	(9Z,12Z)-octadecadienoate + O ₂ = (9S)-hydroperoxy-(10E,12Z)-octadecadienoate
Polyunsaturated fatty acid lipoxygenase ALOX15B (Rat)	<p>It catalyzes the stereo-specific peroxidation of free and esterified polyunsaturated fatty acids generating a spectrum of bioactive lipid mediators. It converts arachidonic acid to 15S-hydroperoxyeicosatetraenoic acid/(15S)-HPETE. Also acts on linoleic acid to produce 13-hydroxyoctadecadienoic acid/13-</p>	(5Z,8Z,11Z,14Z)-eicosatetraenoate + O ₂ = (15S)-hydroperoxy-(5Z,8Z,11Z,13E)-eicosatetraenoate

<p>Polyunsaturated fatty acid lipoygenase ALOX15 (Bovine)</p>	<p>HPODE. It catalyzes the stereo-specific peroxidation of free and esterified polyunsaturated fatty acids generating a spectrum of bioactive lipid mediators. It converts arachidonic acid into 12-hydroperoxyeicosatetraenoic acid/12-HPETE and 15-hydroperoxyeicosatetraenoic acid/15-HPETE. Also converts linoleic acid to 13-hydroperoxyoctadecadienoic acid. May also act on (12S)-hydroperoxyeicosatetraenoic acid/(12S)-HPETE to produce hepoxilin A3. Probably plays an important role in the immune and inflammatory responses.</p>	<p>(5Z,8Z,11Z,14Z)-eicosatetraenoate + O₂ = (12S)-hydroperoxy-(5Z,8Z,10E,14Z)-eicosatetraenoate</p>
<p>Hydroperoxide isomerase ALOXE3 (Mouse)</p>	<p>Non-heme iron-containing lipoygenase which is atypical in that it displays a prominent hydroperoxide isomerase activity and a reduced lipoygenases activity. The hydroperoxide isomerase activity catalyzes the isomerization of hydroperoxides, derived from arachidonic and linoleic acid by ALOX12B, into hepoxilin-type epoxyalcohols and ketones. In presence of oxygen, oxygenates polyunsaturated fatty acids, including arachidonic acid, to produce fatty acid hydroperoxides.</p>	<p>a hydroperoxyeicosatetraenoate = a hydroxy-epoxy-eicosatetraenoate</p>

Table 3. Protein characteristics of lipoxygenases analyzed.

Proteins	1	2	3	4	5	6	7	8	9	10	11	12	13	14	15	16
Number of amino acids	674	701	673	701	663	839	857	662	674	701	673	663	676	677	662	663
Molecular Weight (Da) x 10³	78.0	80.4	78.1	80.6	75.7	94.4	96.8	74.8	78.0	80.7	77.9	75.3	75.9	76.2	75.5	75.4
Theoretical pI	5.51	7.57	5.85	6.25	5.82	5.96	6.26	6.14	5.78	6.43	5.81	6.15	5.73	6.25	8.31	5.79
Number of negatively charged residues (Asp + Glu)	92	75	91	77	82	101	106	80	89	76	89	75	73	75	78	79
Number of positively charged residues (Arg + Lys)	74	76	77	69	69	86	96	72	74	70	75	68	58	66	82	65
Aliphatic index	87.06	89.17	85.75	86.66	88.60	89.73	89.42	94.70	86.93	85.82	86.92	93.95	90.47	89.62	95.53	90.75
Grand average of hydropathicity (GRAVY):	-0.278	-0.197	-0.337	-0.223	-0.268	-0.309	-0.337	-0.166	-0.281	-0.238	-0.285	-0.126	-0.173	-0.192	-0.210	-0.229
Active site residues	H ₃₆₈ H ₃₇₃ H ₅₅₁ N ₅₅₅ I ₆₇₄	H ₃₉₈ H ₄₀₃ H ₅₇₈ N ₅₈₂ I ₇₀₁	H ₃₆₇ H ₃₇₂ H ₅₅₀ N ₅₅₄ I ₆₇₃	H ₃₉₈ H ₄₀₃ H ₅₇₈ N ₅₈₂ I ₇₀₁	H ₃₆₀ H ₃₆₅ H ₅₄₀ N ₅₄₄ I ₆₆₃	H ₄₉₉ H ₅₀₄ H ₆₉₀ N ₆₉₄ I ₈₃₉	H ₅₁₈ H ₅₂₃ H ₇₀₉ N ₇₁₃ I ₈₅₇	H ₃₆₀ H ₃₆₅ H ₅₄₀ I ₆₆₂	H ₃₆₈ H ₃₇₃ H ₅₅₁ N ₅₅₅ I ₆₇₄	H ₃₉₈ H ₄₀₃ H ₅₇₈ N ₅₈₂ I ₇₀₁	H ₃₆₇ H ₃₇₂ H ₅₅₀ N ₅₅₄ I ₆₇₃	H ₃₆₁ H ₃₆₆ H ₅₄₁ H ₅₄₅ I ₆₆₃	H ₃₇₃ H ₃₇₈ H ₅₅₃ I ₆₇₆	H ₃₇₄ H ₃₇₉ H ₅₅₄ I ₆₇₇	H ₃₆₀ H ₃₆₅ H ₅₄₀ I ₆₆₂	H ₃₆₀ H ₃₆₅ H ₅₄₀ N ₅₄₄ I ₆₆₃

(TABLE CONTINUED)

Proteins	17	18	19	20	21	22	23	24	25	26
Number of amino acids	711	864	865	663	663	663	853	677	663	711
Molecular Weight (Da) x 10³	80.5	96.8	97.1	75.4	75.4	75.0	96.5	76.1	75.1	80.5
Theoretical pI	6.53	5.78	6.27	5.76	6.15	5.86	5.71	5.86	6.09	6.35
Number of negatively charged residues (Asp + Glu)	69	107	102	79	77	80	115	78	81	72
Number of positively charged residues (Arg + Lys)	65	92	93	67	70	67	99	64	72	66
Aliphatic index	84.92	89.59	90.05	87.93	87.06	93.68	86.89	89.48	93.24	87.26
Grand average of hydropathicity (GRAVY):	-0.188	-0.280	-0.293	-0.211	-0.188	-0.153	-0.361	-0.170	-0.190	-0.148
Active site residues	H ₄₀₈ H ₄₁₃ H ₅₈₈ N ₅₉₂ I ₇₁₁	H ₅₂₅ H ₅₃₀ H ₇₁₆ N ₇₂₀ I ₈₆₄	H ₅₂₇ H ₅₃₂ H ₇₁₈ N ₇₂₂ I ₈₆₅	H ₃₆₁ H ₃₆₆ H ₅₄₁ I ₆₆₃	H ₃₆₁ H ₃₆₆ H ₅₄₁ I ₆₆₃	H ₃₆₁ H ₃₆₆ H ₅₄₁ I ₆₆₃	H ₅₁₃ H ₅₁₈ H ₇₀₄ N ₇₀₈ I ₈₅₃	H ₃₇₄ H ₃₇₉ H ₅₅₄ I ₆₇₇	H ₃₆₁ H ₃₆₆ H ₅₄₁ I ₆₆₃	H ₄₀₈ H ₄₁₃ H ₅₈₈ N ₅₉₂ I ₇₁₁

Table 4. The amino acid composition of lipoxygenases analyzed.

Protein Amino acids (aa)	1		2		3		4		5		6		7		8		9	
	Number of aa	%	Number of aa	%	Number of aa	%	Number of aa	%	Number of aa	%	Number of aa	%	Number of aa	%	Number of aa	%	Number of aa	%
Ala (A)	43	6.4	44	6.3	40	5.9	40	5.7	52	7.8	56	6.7	49	5.7	46	6.9	43	6.4
Arg (R)	36	5.3	46	6.6	34	5.1	44	6.3	42	6.3	37	4.4	46	5.4	40	6.0	32	4.7
Asn (N)	26	3.9	23	3.3	26	3.9	29	4.1	18	2.7	40	4.8	41	4.8	16	2.4	25	3.7
Asp (D)	44	6.5	33	4.7	43	6.4	37	5.3	38	5.7	46	5.5	50	5.8	36	5.4	42	6.2
Cys (C)	13	1.9	16	2.3	13	1.9	20	2.9	17	2.6	4	0.5	7	0.8	13	2.0	12	1.8
Gln (Q)	31	4.6	22	3.1	30	4.5	27	3.9	40	6	27	3.2	25	2.9	33	5.0	30	4.5
Glu (E)	48	7.1	42	6	48	7.1	40	5.7	44	6.6	55	6.6	56	6.5	44	6.6	47	7.0
Gly (G)	33	4.9	43	6.1	33	4.9	41	5.8	39	5.9	53	6.3	61	7.1	49	7.4	33	4.9
His (H)	17	2.5	22	3.1	20	3	21	3	18	2.7	25	3	26	3	17	2.6	20	3.0
Ile (I)	44	6.5	43	6.1	46	6.8	43	6.1	29	4.4	54	6.4	50	5.8	26	3.9	46	6.8
Leu (L)	59	8.8	77	11	59	8.8	75	10.7	83	12.5	86	10.3	96	11.2	88	13.3	59	8.8
Lys (K)	38	5.6	30	4.3	43	6.4	25	3.6	27	4.1	49	5.8	50	5.8	32	4.8	42	6.2
Met (M)	16	2.4	14	2	14	2.1	17	2.4	18	2.7	15	1.8	12	1.4	16	2.4	15	2.2
Phe (F)	35	5.2	33	4.7	34	5.1	33	4.7	26	3.9	30	3.6	37	4.3	26	3.9	35	5.2
Pro (P)	34	5.0	50	7.1	32	4.8	49	7	43	6.5	51	6.1	51	6	41	6.2	33	4.9
Ser (S)	33	4.9	34	4.9	34	5.1	34	4.9	29	4.4	62	7.4	56	6.5	32	4.8	36	5.3
Thr (T)	30	4.5	41	5.8	33	4.9	40	5.7	30	4.5	46	5.5	47	5.5	26	3.9	31	4.6
Trp (W)	15	2.2	13	1.9	14	2.1	13	1.9	19	2.9	14	1.7	15	1.8	17	2.6	15	2.2
Tyr (Y)	30	4.5	36	5.1	33	4.9	36	5.1	17	2.6	37	4.4	31	3.6	17	2.6	32	4.7
Val (V)	49	7.3	39	5.6	44	6.5	37	5.3	34	5.1	52	6.2	51	6	47	7.1	46	6.8
Pyl (O)	0	0	0	0	0	0	0	0	0	0	0	0	0	0	0	0	0	0
Sec (U)	0	0	0	0	0	0	0	0	0	0	0	0	0	0	0	0	0	0

(TABLE CONTINUED)

Protein Amino acids (aa)	10		11		12		13		14		15		16		17		18	
	Number of aa	%	Number of aa	%	Number of aa	%	Number of aa	%	Number of aa	%	Number of aa	%	Number of aa	%	Number of aa	%	Number of aa	%
Ala (A)	39	5.6	46	6.8	41	6.2	49	7.2	49	7.2	34	5.1	46	6.9	46	6.5	50	5.8
Arg (R)	43	6.1	34	5.1	36	5.4	35	5.2	37	5.5	46	6.9	39	5.9	40	5.6	41	4.7
Asn (N)	32	4.6	26	3.9	19	2.9	22	3.3	18	2.7	15	2.3	19	2.9	26	3.7	35	4.1
Asp (D)	35	5.0	42	6.2	31	4.7	28	4.1	33	4.9	37	5.6	37	5.6	34	4.8	53	6.1
Cys (C)	20	2.9	13	1.9	15	2.3	11	1.6	10	1.5	12	1.8	14	2.1	24	3.4	2	0.2
Gln (Q)	26	3.7	31	4.6	37	5.6	36	5.3	27	4.0	34	5.1	41	6.2	34	4.8	24	2.8
Glu (E)	41	5.8	47	7.0	44	6.6	45	6.7	42	6.2	41	6.2	42	6.3	35	4.9	54	6.2
Gly (G)	39	5.6	32	4.8	45	6.8	46	6.8	43	6.4	41	6.2	41	6.2	40	5.6	64	7.4
His (H)	22	3.1	19	2.8	15	2.3	19	2.8	24	3.5	14	2.1	19	2.9	18	2.5	19	2.2
Ile (I)	41	5.8	46	6.8	29	4.4	32	4.7	34	5.0	26	3.9	25	3.8	32	4.5	64	7.4
Leu (L)	75	10.7	58	8.6	86	13.0	84	12.4	80	11.8	91	13.7	87	13.1	85	12.0	83	9.6
Lys (K)	27	3.9	41	6.1	32	4.8	23	3.4	29	4.3	36	5.4	26	3.9	25	3.5	51	5.9
Met (M)	18	2.6	15	2.2	17	2.6	11	1.6	14	2.1	17	2.6	18	2.7	16	2.3	10	1.2
Phe (F)	34	4.9	34	5.1	30	4.5	32	4.7	30	4.4	27	4.1	27	4.1	30	4.2	39	4.5
Pro (P)	50	7.1	31	4.6	38	5.7	53	7.8	48	7.1	42	6.3	44	6.6	48	6.8	56	6.5
Ser (S)	33	4.7	35	5.2	39	5.9	41	6.1	51	7.5	39	5.9	29	4.4	47	6.6	59	6.8
Thr (T)	40	5.7	30	4.5	27	4.1	37	5.5	33	4.9	31	4.7	35	5.3	51	7.2	59	6.8
Trp (W)	13	1.9	15	2.2	18	2.7	16	2.4	17	2.5	13	2.0	17	2.6	15	2.1	14	1.6
Tyr (Y)	35	5.0	32	4.8	18	2.7	18	2.7	19	2.8	17	2.6	16	2.4	30	4.2	35	4.1
Val (V)	38	5.4	46	6.8	46	6.9	38	5.6	39	5.8	49	7.4	41	6.2	35	4.9	52	6.0
Pyl (O)	0	0	0	0	0	0	0	0	0	0	0	0	0	0	0	0	0	0
Sec (U)	0	0	0	0	0	0	0	0	0	0	0	0	0	0	0	0	0	0

(TABLE CONTINUED)

In order to obtain genetic relationships among LOXs studied, a phylogenetic tree is constructed in Figure 1. According to phylogenetic tree, soybean LOXs are within separate clade compared to mammalian LOXs. The human LOXs are in the same clade with the mouse, rat and golden hamster. The sequence identity between the plant and mammalian LOXs are reported as 21%-27% only while it is 43%-86% for plant LOXs and 39%-93% for mammalian ones (47). The phylogenetic tree shows that soybean LOXs are different compared to mammalian LOXs.

The similarities among sequences of LOXs studied are analyzed by Clustal Omega for multiple alignments. According to these results, the best similarities are observed with the score of 98 between 5-LO (rat) – 5-LO (mouse). Besides, 5-LO (rat), 5-LO (mouse) and 5-LO (golden hamster) can be a better model for 5-LO (human) as the scores of Clustal Omega are observed 93. 12R-LOX (human) can be best represented by 12R-LOX (mouse) and 12R-LOX (rat) with the score of 86. 12S-LOX (human) can be best represented by 12S-LOX (mouse) with the score of 86. 15-LOX (human) can be best represented by 15-LOX (pig or bovine) with the score of 87 (Table 5).

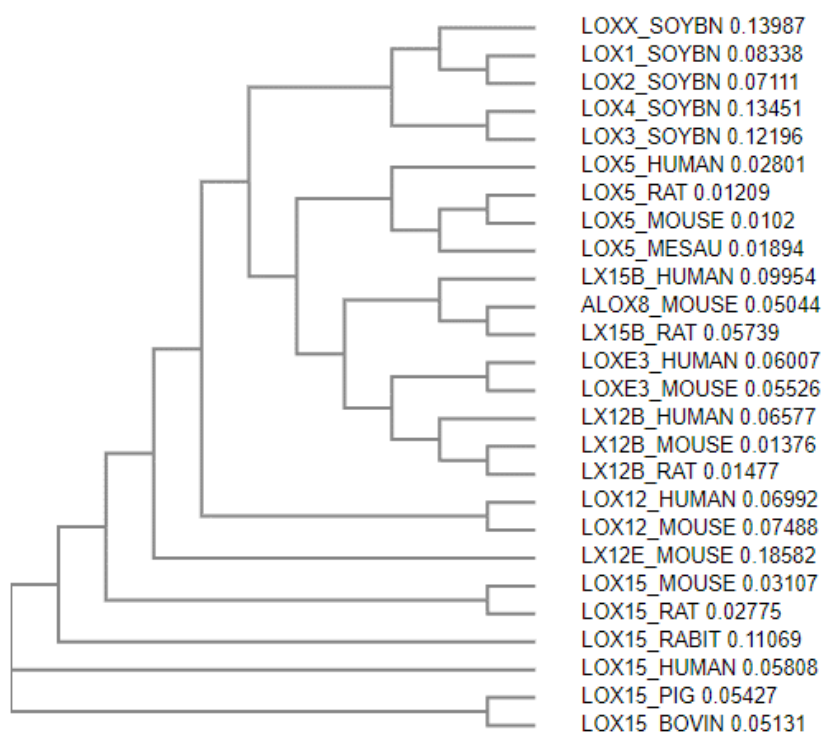


Figure 1. Phylogenetic tree of lipoxygenases examined.

Table 5. The similarity scores of lipoxygenases obtained from Clustal Omega analysis.

		1	2	3	4	5	6	7	8	9	10	11	12	13
1	LOXX_SOYBN	100	67.84	71.09	70.3	71.93	26.4	26.4	26.79	25.51	25.04	24.42	25.86	26.44
2	LOX4_SOYBN	67.84	100	74.35	66.51	67.45	24.73	24.73	26.68	23.83	24.14	23.52	24.49	25.39
3	LOX3_SOYBN	71.09	74.35	100	72.25	75.03	26.36	27.75	27.99	25.93	25.78	25.78	26.28	27.17
4	LOX1_SOYBN	70.3	66.51	72.25	100	84.55	24.53	24.69	27.12	25.2	24.57	24.26	25.24	25.98
5	LOX2_SOYBN	71.93	67.45	75.03	84.55	100	26.13	25.82	27.77	26.17	25.23	24.77	25.43	26.64
6	LOX12_HUMAN	26.4	24.73	26.36	24.53	26.13	100	85.52	59.76	57.4	58.61	61.78	65.51	65.71
7	LOX12_MOUSE	26.4	24.73	27.75	24.69	25.82	85.52	100	60.06	58.16	58.16	60.57	63.69	64.35
8	LX12E_MOUSE	26.79	26.68	27.99	27.12	27.77	59.76	60.06	100	59.52	59.67	62.39	66.41	65.86
9	LOX15_MOUSE	25.51	23.83	25.93	25.2	26.17	57.4	58.16	59.52	100	94.12	71.49	73.72	70.74
10	LOX15_RAT	25.04	24.14	25.78	24.57	25.23	58.61	58.16	59.67	94.12	100	71.79	74.77	71.79
11	LOX15_RABIT	24.42	23.52	25.78	24.26	24.77	61.78	60.57	62.39	71.49	71.79	100	81.27	79.34
12	LOX15_HUMAN	25.86	24.49	26.28	25.24	25.43	65.51	63.69	66.41	73.72	74.77	81.27	100	86.56
13	LOX15_PIG	26.44	25.39	27.17	25.98	26.64	65.71	64.35	65.86	70.74	71.79	79.34	86.56	100
14	LOX15_BOVIN	26.28	24.92	27.33	25.51	26.17	65.11	64.35	66.31	72.25	73	78.73	86.86	89.44
15	LOX5_HUMAN	28.91	28.96	29.08	25.97	27.99	42.86	42.69	40.43	41.69	41.69	40.03	41.2	42.19
16	LOX5_RAT	27.37	28.42	27.22	24.54	26.53	40.85	41.01	38.93	40.55	40.24	38.26	40.09	40.85
17	LOX5_MOUSE	27.79	28.53	27.63	24.96	26.95	40.94	41.1	39.02	40.79	40.49	38.36	40.18	40.79
18	LOX5_MESAU	27.68	28.57	27.52	24.69	26.84	41.31	41.16	38.47	40.24	40.09	38.11	39.48	40.7
19	LX15B_HUMAN	27.37	26.19	27.33	25.42	26.07	38.05	38.66	36.28	38.36	38.2	37.75	38.36	38.66
20	ALOX8_MOUSE	27.63	26.91	27.59	25.38	26.19	38.05	38.81	36.89	38.36	38.66	36.99	38.05	38.2
21	LX15B_RAT	26.56	25.54	26.37	24.77	25.88	37.6	37.9	35.82	37.44	37.29	36.07	36.99	37.14
22	LOXE3_HUMAN	27.22	26.71	27.33	25.34	26.41	37.78	37.48	35.71	37.63	37.63	37.78	37.48	37.78
23	LOXE3_MOUSE	27.96	27	27.47	26.23	27.45	38.09	37.48	37.08	38.54	38.09	37.48	37.78	37.63
24	LX12B_HUMAN	25.98	26.05	25.34	23.6	25	38.09	37.18	34.65	35.96	36.12	35.05	35.51	34.6
25	LX12B_MOUSE	25.08	25	24.89	23.3	24.7	37.33	36.57	34.5	35.36	35.36	35.36	35.05	34.6
26	LX12B_RAT	25.08	25.15	24.74	23.3	24.55	37.03	36.42	34.5	35.2	35.36	35.05	34.75	33.99

(TABLE CONTINUE)

		14	15	16	17	18	19	20	21	22	23	24	25	26
1	LOXX_SOYBN	26.28	28.91	27.37	27.79	27.68	27.37	27.63	26.56	27.22	27.96	25.98	25.08	25.08
2	LOX4_SOYBN	24.92	28.96	28.42	28.53	28.57	26.19	26.91	25.54	26.71	27	26.05	25	25.15
3	LOX3_SOYBN	27.33	29.08	27.22	27.63	27.52	27.33	27.59	26.37	27.33	27.47	25.34	24.89	24.74
4	LOX1_SOYBN	25.51	25.97	24.54	24.96	24.69	25.42	25.38	24.77	25.34	26.23	23.6	23.3	23.3
5	LOX2_SOYBN	26.17	27.99	26.53	26.95	26.84	26.07	26.19	25.88	26.41	27.45	25	24.7	24.55
6	LOX12_HUMAN	65.11	42.86	40.85	40.94	41.31	38.05	38.05	37.6	37.78	38.09	38.09	37.33	37.03
7	LOX12_MOUSE	64.35	42.69	41.01	41.1	41.16	38.66	38.81	37.9	37.48	37.48	37.18	36.57	36.42
8	LX12E_MOUSE	66.31	40.43	38.93	39.02	38.47	36.28	36.89	35.82	35.71	37.08	34.65	34.5	34.5
9	LOX15_MOUSE	72.25	41.69	40.55	40.79	40.24	38.36	38.36	37.44	37.63	38.54	35.96	35.36	35.2
10	LOX15_RAT	73	41.69	40.24	40.49	40.09	38.2	38.66	37.29	37.63	38.09	36.12	35.36	35.36
11	LOX15_RABIT	78.73	40.03	38.26	38.36	38.11	37.75	36.99	36.07	37.78	37.48	35.05	35.36	35.05
12	LOX15_HUMAN	86.86	41.2	40.09	40.18	39.48	38.36	38.05	36.99	37.48	37.78	35.51	35.05	34.75
13	LOX15_PIG	89.44	42.19	40.85	40.79	40.7	38.66	38.2	37.14	37.78	37.63	34.6	34.6	33.99
14	LOX15_BOVIN	100	41.69	40.85	40.94	40.24	39.57	38.05	37.6	37.63	37.94	35.51	35.05	34.6
15	LOX5_HUMAN	41.69	100	92.99	93.16	93.31	43.64	44.46	43.8	41.22	42.36	40.07	39.74	39.57
16	LOX5_RAT	40.85	92.99	100	97.77	96.14	42.53	43.59	42.23	40.63	41.83	40.03	40.18	40.03
17	LOX5_MOUSE	40.94	93.16	97.77	100	96.58	42.92	43.52	42.47	41.02	42.22	40.27	40.42	40.27
18	LOX5_MESAU	40.24	93.31	96.14	96.58	100	42.68	43.74	42.53	40.93	42.13	39.73	39.73	39.73
19	LX15B_HUMAN	39.57	43.64	42.53	42.92	42.68	100	78.11	80.77	55.07	54.63	50.9	50.75	51.04
20	ALOX8_MOUSE	38.05	44.46	43.59	43.52	43.74	78.11	100	89.22	53.73	53.58	50.3	49.1	49.4
21	LX15B_RAT	37.6	43.8	42.23	42.47	42.53	80.77	89.22	100	52.09	52.39	50.6	49.7	50.15
22	LOXE3_HUMAN	37.63	41.22	40.63	41.02	40.93	55.07	53.73	52.09	100	88.47	54.92	53.78	53.21
23	LOXE3_MOUSE	37.94	42.36	41.83	42.22	42.13	54.63	53.58	52.39	88.47	100	55.49	54.21	53.64
24	LX12B_HUMAN	35.51	40.07	40.03	40.27	39.73	50.9	50.3	50.6	54.92	55.49	100	86.02	86.59
25	LX12B_MOUSE	35.05	39.74	40.18	40.42	39.73	50.75	49.1	49.7	53.78	54.21	86.02	100	97.15
26	LX12B_RAT	34.6	39.57	40.03	40.27	39.73	51.04	49.4	50.15	53.21	53.64	86.59	97.15	100

The sequence alignments may present the deletion and conserved amino acids residues during the evolution process. According to the results from the sequence alignments, a deletion site which consists of 177 amino acids is observed in 15-LOX (human) compared to soybean LOX-1 (Table 6a). On the other hand, the high similarities are seen between 15-LOX (human) and 15-LOX (rabbit). There is only one amino acid deletion which is localized at 90th position of the 15-LOX (human) compared to 15-LOX (rabbit). There are 535 conserved residues, 70 residues with very similar physical characteristics, 21 residues with similar physical characteristics in LOXs analyzed which is presented in Table 6b. The results presented in Table 7 that there is an important structural similarity between soybean LOX-1 and 15-LOX (human) enzymes and the alpha-helical structure is more common model than β -strand. It is important to note that the enzymes compared have remarkable similarity, although there is quite a difference between the amino acid residues of these sequences. As can be seen from that figure the same structured regions contained 135 conserved amino acid residues. Moreover, all of the amino acid residues replaced in active site have the same secondary structure prediction (Table 7). Amagata et al (48) investigated the inhibitory activities and the selectivity of some compounds

isolated from marine sponge on soybean LOX-1 and 15-LOX (human). The different IC_{50} values obtained for these compounds and the variations in selectivity presented that the structures of studied enzymes were different. Prigge et al (49) use the identified molecular structure of soybean LOX-1 as a model in order to develop the possible structures of human 5-, 12-, and 15- LOXs. Although the structures of human enzymes were not identified fully, the molecular models of active sites that are highly conserved of these enzymes were studied by Prigge et al (49). Besides, the differences among sequences were analyzed in details. There has not been any report which identified the 3D structure of 15-LOX (human). The known 3D structure of LOX from mammals is only reticulocyte-type 15-LOX (rabbit). According to alignments between the sequences of soybean LOX-1, 15-LOX (human) and 15-LOX (rabbit), the 3D structure of 15-LOX (rabbit) can be a better model for 15-LOX (human) than that of soybean LOX-1. The Clustal Omega score was 81 between 15-LOX (human) and 15-LOX (rabbit). These results are well in line with the results of Gillmor et al (50) and Choi et al (51) who reported that the crystal structure of 15-LOX (rabbit) had an important role for understanding the properties of mammalian LOXs.

Table 6a. Sequence alignments between Soybean LOX-1 – 15-LOX (human) ((*) conserved, (:) very similar, (.) somewhat similar physicochemical character).

SP P08170 LOX1_SOYBN	MFSAGHKIKGTVVLMPKNELEVNPDSAVDNLNAFLGRVSLSQLISATKADAHGKGVK	60
SP P16050 LOX15_HUMAN	-----MGLYRIRVSTGA-----SLYAGSNQVQLW---LVGQHGEAALGK	37
	* : : * : * . : * . . . * . . . * . . : * *	
SP P08170 LOX1_SOYBN	DTFLEGINTSLPTLGAGESAFNIH-FEWDGSMGIPGAFYIKNYMQVEFFLKSILTLEAISN	119
SP P16050 LOX15_HUMAN	RLWPA-----RGK-ETELKVEVPEYLGPLL FVKLRKRHLLKDDAWFCNWISVQGGPA	88
	: * * : : : * : * : : : : : * : : : : : . .	
SP P08170 LOX1_SOYBN	QGTIRFVCNSWVYNTKLYKSVRIFFANHTYVPESETPAPLV-SYREEELKSLRNGTGERK	178
SP P16050 LOX15_HUMAN	GDEVRFPFCYRWVEGVLSLPE---GTGRTVGEDPQGLFQKHREEE-----LE	133
	. : * * * * * : * * * * * : * * * * * : * * * * * : *	
SP P08170 LOX1_SOYBN	EYDRIYDYDVYNDLGNPDKSEKLARPVLGGSSFPYPRRGRTGRGPTVTDPNTEKQGEVF	238
SP P16050 LOX15_HUMAN	ERRKLYRWGNWKDGLI-----LNMAGA-----KLY	158
	* : : * . . : * : : * : : * : : * : : * : : * : : * : : * : : *	
SP P08170 LOX1_SOYBN	YVPRDENLGHLSKDALEIGTKSLSQIVQPAFESAFDLKSTPIEFHSFQDVHDLYEGGIK	298
SP P16050 LOX15_HUMAN	DLPVDERFLED-----KRVDFEVSLAKG---LADLAIK	188
	: * * : : * . : * * : * *	
SP P08170 LOX1_SOYBN	LPRDVISTIIPVIKELYRTDQGHILKFPQPHVQVSQSAWMTDEEFAREMIAGVNPCV	358
SP P16050 LOX15_HUMAN	DSLNVLTC-----WKDL---DDFNRIFWCGQSKLAERVRDWSKEDALFGYQFLNGANPVV	240
	: * : : * : : * : : : * : : : * : : : * : : : * : : : * : : *	
SP P08170 LOX1_SOYBN	IRGLEEFPPKSNLDPAIYGDQSSKITADSLDLGYTMDEALGSRRLFMLDYHDFMPPYVR	418
SP P16050 LOX15_HUMAN	LRRSAHLPARLVFPPGMEELQAQ-----LEKELEGGTLFEADFSLLD-GIKA	286
	: * . : * : : * : : * : : . . : : * . * * * * : :	
SP P08170 LOX1_SOYBN	QINQLNSAKTYATRITLFLREDGLKPVAIELS LPHSAGDLSAAVSQVVLPAKEGVVESTI	478
SP P16050 LOX15_HUMAN	NVILCSQQHLAAPLVMKLPDQDGKLLPMVIQLQLPRTGSPPPP----LFLPT---DPPMA	339
	: : . . : * . : * * : * * * * : * : * * * : : : * * :	
SP P08170 LOX1_SOYBN	WLLAKAYVIVNDSCYHQLMSHWLNTHAAMEPFVIATHRHLSVLHPYKLLTPHYRNMNI	538
SP P16050 LOX15_HUMAN	WLLAKCWRVSSDFQLHELQSHLLRGHLMAEVIVVATMRCLPSIHPIFKLIIPHLRYTLEI	399
	* * * * : * * * * * * * * * * * * : * * * * * * * * * * * * : * *	
SP P08170 LOX1_SOYBN	NALARQSLINANGIETTFLPSKYS-VEMSSAVYKNWVFTDQALPADLIKRGVAIKDPST	597
SP P16050 LOX15_HUMAN	NVRARTGLVSDMGIFDQIMSTGGGGHVQLLKQAGFLTYSFCPPDDLADRGL-----	452
	* . * * . * : * * : : : . . : * : : . . . : . . * * * . * * :	
SP P08170 LOX1_SOYBN	PHGVRLIEDYPYAADGLEIWAAIKTWVQYEVPLYYARDDVDKNDSELQHWKEAVEKGH	657
SP P16050 LOX15_HUMAN	-----LGVKSSFYAQDALRLWEIIYRYVEGIVSLHYKTDVAVKDDPELQTWCREITEIGL	507
	* : : . * * * * . : * * * : : *	
SP P08170 LOX1_SOYBN	GDLKDKPWPKLQTLLEDLVEVCLIIWIASALHAAVNFGQYPYGLIMNRPTASRRLPE	717
SP P16050 LOX15_HUMAN	QGAQDRGFVSLQARDQVCHFVTMCIFTCTGQHASVHLGQLDWYSWVPNAPCTMRLPPPT	567
	. : * : : . * * : : : . . . : * : : . * * : * * : * * : : . : * * : * *	
SP P08170 LOX1_SOYBN	KGTPEYEEMINNHEKAYLRITSKLPTLISL---VIEILSTHASDEVYLGQRDNPHWT	773
SP P16050 LOX15_HUMAN	TKDATLE-----TVMATLPNFHQASLQMSITWQLGRRQPVMVAVGQHEEE-YF	614
	. * : * : * * : . * : * : * : * * : : * * : : * * * : : :	
SP P08170 LOX1_SOYBN	SDSKALQAFQKFGNKLKEIEEKLVRNNDPSLQGNRLGVPQLPYTYLLPSSEELTFRGI	833
SP P16050 LOX15_HUMAN	SGPEPKAVLKFFREELAALDKIEIERN-----AKLDMPYEYLRPSVVENSV----	660
	* . : . : * * * * : * * : : : * * . : : * * * * * * * * . .	
SP P08170 LOX1_SOYBN	PNSISI 839	
SP P16050 LOX15_HUMAN	----AI 662	
	: *	

Table 6b. Sequence alignments between 15-LOX (rabbit) – 15-LOX (human) ((*) conserved, (:) very similar, (.) somewhat similar physicochemical character).

```

SP|P16050|LOX15_HUMAN MGLYRIRVSTGASLYAGSNNQVQLWLVGQHGEAALGKRLWPARGKETELKVEVPEYLGPL 60
SP|P12530|LOX15_RABIT MGVYRVCVSTGASIVYAGSKNKVELWLVGQHGEVELGSLRPTNRKEEEFKVNVSKYLGSL 60
    **:***: *****:*****:*.:.*****. ** . * * . ** * :*** * :*** *
SP|P16050|LOX15_HUMAN LFKVLRKRHLKDDAWFCNWISVQGGGAG-DEVRFPCYRWVEGNVLSLPEGTGRTVGED 119
SP|P12530|LOX15_RABIT LFKVLRKRHLKDDAWFCNWISVQALGAAEDKYWFPCYRWVVDGQVSLPVGTCCTTVGD 120
    **:***:*.:.*****:*****:*.:.*****. ** . * * . ** * :*** * :*** *
SP|P16050|LOX15_HUMAN PQGLFQKHREEELEERRKLYRWGNWGDGLILNMAGAKLYDLPVDERFLEDKRVDFEVSLSLA 179
SP|P12530|LOX15_RABIT PQGLFQKHREQELEERRKLYQWGSWKEGLILNVAGSKLTDLPVDERFLEDKIDFEASLSLA 180
    *****:*****:*.:.*****:*.:.*****. ** . * * . ** * :*** * :*** *
SP|P16050|LOX15_HUMAN KGLADLAIKDSLNLVLTCKWDLDDFNRIFWCGQSKLAERVRSWKEDALFGYQFLNGANPV 239
SP|P12530|LOX15_RABIT WGLAELALKNSLNILAPWKTLDDFNRIFWCGRSKLARRVRSWQEDSLFGYQFLNGANPM 240
    **:***:*.:.*****:*.:.*****. ** . * * . ** * :*** * :*** *
SP|P16050|LOX15_HUMAN VLRRSAHLPARLVFPPGMEELQAQLEKELEGGTLFEADFSLLDGIKANVILCSQQHLAAP 299
SP|P12530|LOX15_RABIT LLRRSVQLPARLVFPPGMEELQAQLEKELKAGTLFEADFALLDNIKANVILYCOQYLAAP 300
    **:***:*.:.*****:*****:*.:.*****. ** . * * . ** * :*** * :*** *
SP|P16050|LOX15_HUMAN LVMLKQLPDGKLLPMVIQLQLPRTGSPPPPLFLPTDPPMAWLLAKCWRSSDFQLHELQS 359
SP|P12530|LOX15_RABIT LVMLKQLPDGKLLPMVIQLHLPKIGSSPPPLFLPTDPPMVWLLAKCWRSSDFQVHELNS 360
    *****:*****:*.:.*****. ** . * * . ** * :*** * :*** *
SP|P16050|LOX15_HUMAN HLLRGHLMAEVIVVATMRCLPSIHPIFKLIIPHLRYTLEINVRARTGLVSDMGIFDQIMS 419
SP|P12530|LOX15_RABIT HLLRGHLMAEVFTVATMRCLPSIHPVFKLIVPHLRYTLEINVRARNGLVSDFGIFDQIMS 420
    *****:*.:.*****:*****. *****. *****:***:*****
SP|P16050|LOX15_HUMAN TGGGGHVQLLQAGAFITYSSFCPPDDLADRGLLGVKSSFYAQDALRLWEIYRYVEGIV 479
SP|P12530|LOX15_RABIT TGGGGHVQLLQAGAFITYRSFCPPDDLADRGLLGVESSEFYAQDALRLWEIISRYVQGIM 480
    *****:*****. *****. *****. *****. *****. *****. *****:***:***:
SP|P16050|LOX15_HUMAN SLHYKTDVAVKDDPELQTWCREITEIGLQGAQDRGFPVSLQARDQVCHFVTCIFTCTGQ 539
SP|P12530|LOX15_RABIT GLYYKTDEAVRDDLELQSWCREITEIGLQGAQKQGFPTSLQSAQACHFVTCIFTCTGQ 540
    .*:*** **:* ***:*****:***:***: * .*****
SP|P16050|LOX15_HUMAN HASVHLGQLDWYSWVPNAPCTMRLPPPTTKDATLETVMATLPNFHQASLQMSITWQLGRR 599
SP|P12530|LOX15_RABIT HSSIHLGQLDWFTWVPNAPCTMRLPPPTTKDATLETVMATLPNLHQSSLQMSIVWQLGRD 600
    *:.*****:*****. *****. *****:***:*****. *****
SP|P16050|LOX15_HUMAN QPVMVAVGQHEEEYFSGPEPKAVLKKFREELAALDKEIEIRNAKLDMPEYLRPSVENS 659
SP|P12530|LOX15_RABIT QPIMVPLGQHQQEYFSGPEPRAVLEKFREELAIMDKIEIEVRNEKLDIPYEYLRPSIVENS 660
    **:***:*.:.*****:*****:*.:.*****. *****. ** . * * . ** * :*** * :*** *
SP|P16050|LOX15_HUMAN VAI 662
SP|P12530|LOX15_RABIT VAI 663
    ***

```

Table 7. Sequence alignments and secondary structure predictions for Soybean LOX-1 and 15-LOX (human). Residues estimated to be in coil conformation shown in yellow; residues estimated to be in β -sheet conformation shown in blue and residues estimated to be in alpha-helical conformation shown in green.

SP P16050 LOX15_HUMAN	-----MGLYRIRVSTGA-----SLYAGSNQVQLW---LVGQHGEAALGK	37
SP P08170 LOX1_SOYBN	MFSAGHKIKGTVVLMPKNELEVPDGS AVDNLNAFLGR SVSLQLISATK ADAHGKGVK 60	
	* : * : * : * : * : * : * : * : * : * : * : *	
SP P16050 LOX15_HUMAN	RLWPA-----RGK-ETELKVEVPEYLGP LLFVKLRKRHLLKDDAWFCNWISVQGPGA	88
SP P08170 LOX1_SOYBN	DTFLEGINTSLPTLGAGESAFNIH-FEWDGSMGIPGAFYIKNYMQVEFFLKSLTLEAISN	119
	: * * * : : : : * : * : : : : : * : : : : : *	
SP P16050 LOX15_HUMAN	GDEVRFPCYR WVEGNGVLSLPE----GTGRTVGEDPQGLFQKHREEE-----LE	133
SP P08170 LOX1_SOYBN	QGTIRFVCNSWYNTKLYKSVRIFFANHTYVPSETPAPLV-SYREEELKSLRGNGTGERK	178
	: * * * * * : : : : : * * * * * : : : : : *	
SP P16050 LOX15_HUMAN	ERRKLYRWGNWKDGLI-----LNMAGA-----KLY	158
SP P08170 LOX1_SOYBN	EYDRIYDYVDYNDLGNPDKSEK LARPVLGSSSTFPYPRRGRTGRGPTVTDPNTEKQGEVF	238
	* : * : * : : : * : * : : : * : * : : : *	
SP P16050 LOX15_HUMAN	DLPVDERFLED-----KR VDFEVSLAKG---LADLAIK	188
SP P08170 LOX1_SOYBN	YVPRDENLGH LKSKDALEIGTKSLSQIVQPAFESAFDLKSTPIEFHSFQDVHDLYEGGIK	298
	: * * * : : : * : : * : : * : : * : : * : : *	
SP P16050 LOX15_HUMAN	DSLNLVLC-----WKDL--DDFNRIFCWGSKLAERVRDSWKEDALFGYQFLNGANPVV	240
SP P08170 LOX1_SOYBN	LPRDVISTIIP LPIKELVRTDGQHILKFPQPHVVQS QSAWMTDEEFAREMIAGVNPCV	358
	: * : * : * : * : * : * : * : * : * : * : *	
SP P16050 LOX15_HUMAN	LRRSAHLPARLVFPPGMEELQAQ-----LEKELEGGTLF EADFSLLD-GIKA	286
SP P08170 LOX1_SOYBN	IRGLEEFPPKSNLDPAIYGDQSSKITADSLDLGYSMDEALGSRRLFMLDYHDIFMPYVR	418
	: * : * : * : * : * : * : * : * : * : * : *	
SP P16050 LOX15_HUMAN	NVILCSQQHLAAPLVMLKIQPDGKLLPMVIQLQLPRTGSPPPP----LFLPT---DPPMA	339
SP P08170 LOX1_SOYBN	QINQLNSAKTYATRILFLREDGTLKPVAI ELSLPHSAGDL SAAVSQVVLP AKEGVESTI	478
	: : : * : * * : * : * : * : * : * : * : * : *	
SP P16050 LOX15_HUMAN	WLLAKCWVRSDFQLHELQSHLRGHLMAEVIVVATMRCLPSIHPIFKLIIPHLYRTLEI	399
SP P08170 LOX1_SOYBN	WLLAKAYVIVNDSCYHQLS HLNTHAAMEPFVIATHRHLSVLHPIYKLLTPHYRNMMNI	538
	* * * * * : * : * : * * * : * : * : * : * : * : *	
SP P16050 LOX15_HUMAN	NVRARTGLVSDMGIFDQIMSTGGGGHVQLLKQAGAF LTYSSFCPPDDLAD RGL-----	452
SP P08170 LOX1_SOYBN	NALARQSLINANGI IETTF LPSKYS-VEMSSAVYKNWVF TDQALPADLIKRGVAIKDPST	597
	* : * * * : * : * : * : * : * : * : * : * : *	
SP P16050 LOX15_HUMAN	----LGVKSSFYAQDALRLWEIYRYVEGIVSLHYKT DVAVKDDPELQ TWCREITEIGL	507
SP P08170 LOX1_SOYBN	PHGVRLIEDYPPAADGLIWA AIKTWVQEYVPLYYARDD DVKNDSELQHWWKEAVEKGH	657
	* : : * * * * * : * : * : * : * : * : * : *	
SP P16050 LOX15_HUMAN	QGAQDRGFVPSLQARDQVCHFVTMCIFTC TGQHASVHLGQLDWYSWVPNAPCTMRLPPPT	567
SP P08170 LOX1_SOYBN	GDLKDKPWWPKLQTLLEDLVEVCLIIIIWIASALHAAVNFGQYPYGG LIMNRPTASRRLLPE	717
	: * : : * * : : * : * : * : * : * : * : * : *	
SP P16050 LOX15_HUMAN	TKDATLE-----TVMATLPNFHQASLQMSITWQLGRRQPV MVAVGQHEEE-YF	614
SP P08170 LOX1_SOYBN	KGTPEYEEMIN NHEKAYLRTITSKLPTLISLS----VIEILSTHASDEVYLGQRDNPHWT	773
	: * : * * : * : * : * : * : * : * : * : * : *	
SP P16050 LOX15_HUMAN	SGPEPKAVLKKFREELAALDKEIEIRN-----AKLDMPEYLRPSV VENSVD	660
SP P08170 LOX1_SOYBN	SDSKALQAFQKFGNKLKEIEEKLVRRNNDPSLQGNRLG PVLQPYLL YPSSEGLTFRGI	833
	* : : * * : * : * : : * : * : : * * * * *	
SP P16050 LOX15_HUMAN	----AI 662	
SP P08170 LOX1_SOYBN	PNSISI 839	
	: *	

CONCLUSION

Soybean LOX-1 might not be accepted as a model enzyme for 15-LOX from other sources as mentioned by several researchers that soybean LOX-1 used as a model enzyme for 15 LOX (human) (14,16-18,52) since there are remarkable sequence-based differences which are obtained by using bioinformatics tools between soybean LOX-1 and LOXs from other sources especially from human. The future works are strongly warranted by using newly developed bioinformatics tools to find the appropriate enzyme model for human LOX. At this point, various genetic methods can be introduced and developed. The relevant enzymes can be produced in large scale by micro-organisms with the help of recombinant DNA technology for instance. Recently, the use of recombinant human lipoxygenase enzymes has become increasingly common due to such sensitivities in lipoxygenase inhibition studies (35,48,53,54).

ACKNOWLEDGMENTS

We thank Prof. Dr. Theodore Holman from Chemistry and Biochemistry Department of UC Santa Cruz for sharing his valuable comments about LOXs.

REFERENCES

- Jacquot C, McGinley CM, Plata E, Holman TR, van der Donk WA. Synthesis of 11-thialinoleic acid and 14-thialinoleic acid, inhibitors of soybean and human lipoxygenases. *Organic and Biomolecular Chemistry*. 2008 Dec;6(22):4242-52.
- Newcomer ME, Brash AR. The structural basis for specificity in lipoxygenase catalysis. *Protein Science*. 2015 Mar;24(3):298-309.
- Skrzypczak-Jankun E, McCabe NP, Selman SH, Jankun J. Curcumin inhibits lipoxygenase by binding to its central cavity: theoretical and X-ray evidence. *International Journal of Molecular Medicine*. 2000 Nov;6(5):521-6.
- Simona V, Chedea VS, Dulf F, Socaciu C. The influence of quercetin concentration on its intermolecular interaction with soybean lipoxygenase-1. *Bulletin USAMV-CN*. 2006;62:376-80.
- Shrivastava SK, Srivastava P, Bandresh R, Tripathi PN, Tripathi A. Design, synthesis, and biological evaluation of some novel indolizine derivatives as dual cyclooxygenase and lipoxygenase inhibitor for anti-inflammatory activity. *Bioorganic and Medicinal Chemistry*. June 2017;25(16):4424-32.
- Yashaswini PS, Appu Rao AG, Singh SA. Inhibition of lipoxygenase by sesamol corroborates its potential anti-inflammatory activity. *International Journal of Biological Macromolecules* 2017 Jan;94(Pt B):781-7.
- ElBordiny HS, El-Miligy MM, Kassab SE, Daabees H, Mohamed Ali WA, El-Hawash SAM. Design, synthesis, biological evaluation and docking studies of new 3-(4,5-dihydro-1H-pyrazol/isoxazol-5-yl)-2-phenyl-1H-indole derivatives as potent antioxidants and 15-lipoxygenase inhibitors. *European Journal of Medicinal Chemistry*. 2018 Feb;145:594-605.
- Boyington JC, Gaffney BJ, Amzel LM. The three-dimensional structure of an arachidonic acid 15-lipoxygenase. *Science*. 1993 Jun;260(5113):1482-6.
- Ivanov I, Heydeck D, Hofheinz K, Roffeis J, O'Donnell VB, Kuhn H, Walther M. Molecular enzymology of lipoxygenases. *Archives of Biochemistry and Biophysics*. 2010 Nov;503(2):161-74.
- Segraves EN, Holman TR. Kinetic Investigations of the Rate-Limiting Step in Human 12- and 15-Lipoxygenase. *Biochemistry*. 2003 May;42(18):5236-43.
- Neidig ML, Wecksler AT, Schenk G, Holman TR, Solomon EI. Kinetic and Spectroscopic Studies of N694C Lipoxygenase: A Probe of the Substrate Activation Mechanism of a Nonheme Ferric Enzyme. *Journal of the American Chemical Society*. 2007 Jun;129(24):7531-7.
- Gardner HW. Recent investigations into the lipoxygenase pathway of plants. *Biochimica et Biophysica Acta (BBA) - Lipids and Lipid Metabolism*. 1991 Jul;1084(3):221-39.
- Yamamoto S. Mammalian lipoxygenases: molecular structures and functions. *Biochimica et Biophysica Acta (BBA) - Lipids and Lipid Metabolism*. 1992 Oct;1128(2-3):117-31.
- Maiga A, Malterud KE, Diallo D, Paulsen BS. Antioxidant and 15-lipoxygenase inhibitory activities of the Malian medicinal plants *Diospyros abyssinica* (Hiern) F. White (Ebenaceae), *Lannea velutina* A. Rich (Anacardiaceae) and *Crossopteryx febrifuga* (Afzel) Benth. (Rubiaceae). *Journal of Ethnopharmacology*. 2006 Mar;104(1-2):132-7.
- Kuhn H, Walther M, Kuban RJ. Mammalian arachidonate 15-lipoxygenases structure, function, and biological implications. *Prostaglandins and Other Lipid Mediators*. 2002 Aug;68-69:263-90.
- Mahesha HG, Singh SA, Appu Rao AG. Inhibition of lipoxygenase by soy isoflavones: Evidence of isoflavones as redox inhibitors. *Archives of Biochemistry and Biophysics*. 2007 May;461(2):176-85.
- Russell WR, Scobbie L, Duthie GG, Chesson A. Inhibition of 15-lipoxygenase-catalysed oxygenation of arachidonic acid by substituted benzoic acids. *Bioorganic and Medicinal Chemistry*. 2008 Apr;16(8):4589-93.

18. Nguyen MD, Nguyen DH, Yoo JM, Myung PK, Kim MR, Sok DE. Effect of endocannabinoids on soybean lipoxygenase-1 activity. *Bioorganic Chemistry*. 2013 Aug;49:24-32.
19. Oso BJ, Karigidi KO. Inhibitory action of dried leaf of *Cassia alata* (Linn.) Roxb against lipoxygenase activity and nitric oxide generation. *Scientia Agropecuaria*. 2019 Mar;10(2):185-90.
20. Jonsson T, Glickman MH, Sun S, Klinman JP. Experimental Evidence for Extensive Tunneling of Hydrogen in the Lipoxygenase Reaction: Implications for Enzyme Catalysis. *Journal of the American Chemical Society*. 1996 Oct;118(42):10319-20.
21. Gousiadou C, Kouskoumvekaki I. LOX1 inhibition with small molecules. *Journal of Molecular Graphics and Modelling*. 2016 Jan;63:99-109.
22. Sigal E, Craik CS, Highland E, Grunberger D, Costello LL, Dixon RA, Nadel JA. Molecular cloning and primary structure of human 15-lipoxygenase. *Biochemical and Biophysical Research Communications*. 1988 Dec;157(2):457-64.
23. Holman TR, Zhou J, Solomon EI. Spectroscopic and Functional Characterization of a Ligand Coordination Mutant of Soybean Lipoxygenase-1: First Coordination Sphere Analogue of Human 15-Lipoxygenase. *Journal of the American Chemical Society*. 1998 Nov;120(48):12564-72.
24. Minor W, Steczko J, Stec B, Otwinowski Z, Bolin JT, Walter R, Axelrod B. Crystal structure of soybean lipoxygenase L-1 at 1.4 Å resolution. *Biochemistry*. 1996 Aug;35(33):10687-701.
25. van Leyen K, Duvoisin RM, Engelhardt H, Wiedmann M. A function for lipoxygenase in programmed organelle degradation. *Nature*. 1998 Sep;395(6700):392-5.
26. Kuhn H, Thiele BJ. The diversity of the lipoxygenase family. Many sequence data but little information on biological significance. *FEBS Letters*. 1999 Apr;449(1):7-11.
27. Honn KV, Tang DG, Gao X, Butovich IA, Liu B, Timar J, Hagmann W. 12-lipoxygenases and 12(S)-HETE: role in cancer metastasis. *Cancer and Metastasis Reviews*. 1994 Dec;13(3-4):365-96.
28. Werz O. Inhibition of 5-lipoxygenase product synthesis by natural compounds of plant origin. *Planta Medica*. 2007 Oct;73(13):1331-57.
29. Mhater M. The role of the 5-lipoxygenase pathway in Alzheimer's disease. *Drugs of the Future*. 2006 Jan;31(1):83-9.
30. Praticò D, Zhukareva V, Yao Y, Uryu K, Funk CD, Lawson JA, Trojanowski JQ, Lee VMY. 12/15-Lipoxygenase is increased in Alzheimer's disease - Possible involvement in brain oxidative stress. *American Journal of Pathology*. 2004 May;164(5):1655-62.
31. Schenk G, Neidig ML, Zhou J, Holman TR, Solomon EI. Spectroscopic Characterization of Soybean Lipoxygenase-1 Mutants: the Role of Second Coordination Sphere Residues in the Regulation of Enzyme Activity. *Biochemistry*. 2003 Jun;42(24):7294-302.
32. Cengiz S, Cavas L, Yurdakoc K, Pohnert G. The sesquiterpene caulerpenyne from *Caulerpa* spp. is a lipoxygenase inhibitor. *Marine Biotechnology*. 2011 Apr;13(2):321-6.
33. Richter P, Schubert G, Schaible AM, Cavas L, Werz O, Pohnert G. Caulerpenyne and Related Bis-enol Esters Are Novel-Type Inhibitors of Human 5-Lipoxygenase. *ChemMedChem*. 2014 Aug;9(8):1655-9.
34. Omar YM, Abdu-Allah HHM, Abdel-Moty SG. Synthesis, biological evaluation and docking study of 1,3,4-thiadiazolethiazolidinone hybrids as anti-inflammatory agents with dual inhibition of COX-2 and 15-LOX. *Bioorganic Chemistry*. 2018 Oct;80:461-71.
35. van der Vlag R, Guo H, Hapko U, Eleftheriadis N, Monjas L, Dekker FJ, Hirsch AKH. A combinatorial approach for the discovery of drug-like inhibitors of 15-lipoxygenase-1. *European Journal of Medicinal Chemistry*. 2019 Jul;174:45-55.
36. Bouriche H, Miles EA, Selloum L, Calder PC. Effect of *Cleome arabica* leaf extract, rutin and quercetin on soybean lipoxygenase activity and on generation of inflammatory eicosanoids by human neutrophils. *Prostaglandins Leukotrienes and Essential Fatty Acids*. 2005 Mar;72(3):195-201.
37. Zhang YY, Thakur K, Wei CK, Wang H, Zhang JG, Wei ZJ. Evaluation of inhibitory activity of natural plant polyphenols on Soybean lipoxygenase by UFLC-mass spectrometry. *South African Journal of Botany*. 2019 Jan;120:179-85.
38. Sievers F, Wilm A, Dineen DG, Gibson TJ, Karplus K, Li W, Lopez R, McWilliam H, Remmert M, Söding J, Thompson JD, Higgins DG. Fast, scalable generation of high-quality protein multiple sequence alignments using Clustal Omega. *Molecular Systems Biology*. 2011 Oct;7:539.
39. Madeira F, Park YM, Lee J, Buso N, Gur T, Madhusoodanan N, Basutkar P, Tivey ARN, Potter SC, Finn RD, Lopez R. The EMBL-EBI search and sequence analysis tools APIs in 2019. *Nucleic Acids Research*. 2019 Jul;47(W1):W636-W641.
40. Gasteiger E, Hoogland C, Gattiker A, Duvaud S, Wilkins MR, Appel RD, Bairoch A. Protein Identification and Analysis Tools on the ExPASy Server. In: Walker JM (eds) *The Proteomics Protocols Handbook*. Humana Press, 2005;pp 571-607.

41. Gasteiger E, Gattiker A, Hoogland C, Ivanyi I, Appel RD, Bairoch A. ExPASy: the proteomics server for in-depth protein knowledge and analysis. *Nucleic Acids Research*. 2003 Jul;31(13):3784-8.
42. Jones DT. Protein secondary structure prediction based on position-specific scoring matrices. *Journal of Molecular Biology*. 1999 Sep;292(2):195-202.
43. Kyte J, Doolittle RF. A simple method for displaying the hydropathic character of a protein. *Journal of Molecular Biology*. 1982 May;157(1):105-32.
44. Mogul R, Holman TR. Inhibition Studies of Soybean and Human 15-Lipoxygenases with Long-Chain Alkenyl Sulfate Substrates. *Biochemistry*. 2001 Apr;40(14):4391-7.
45. Galliard T, Chan HWS. Lipoxygenases. In: Stumpf PK, Conn EE (eds) *The Biochemistry of Plants*. Academic Press, New York, 1980;pp 4:131-61.
46. Vidal-Mas J, Busquets M, Manresa A. Cloning and expression of a lipoxygenase from *Pseudomonas aeruginosa* 42A2. *Antonie Van Leeuwenhoek*. 2005 Apr;87(3):245-51.
47. Sadeghian H, Jabbari A. 15-Lipoxygenase inhibitors: a patent review. *Expert Opinion on Therapeutic Patents*. 2016;26(1):65-88.
48. Amagata T, Whitman S, Johnson TA, Stessman CC, Loo CP, Lobkovsky E, Clardy J, Crews P, Holman TR. Exploring Sponge-Derived Terpenoids for Their Potency and Selectivity against 12-Human, 15-Human, and 15-Soybean Lipoxygenases. *Journal of Natural Products*. 2003 Feb;66(2):230-5.
49. Prigge ST, Boyington JC, Gaffney BJ, Amzel LM. Structure Conservation in Lipoxygenases: Structural Analysis of Soybean Lipoxygenase-1 and Modeling of Human Lipoxygenases. *Proteins Structure Function and Bioinformatics*. 1996 Mar;24(3):275-91.
50. Gillmor SA, Villasenor A, Fletterick R, Sigal E, Browner MF. The structure of mammalian 15-lipoxygenase reveals similarity to the lipases and the determinants of substrate specificity. *Nature Structural Biology*. 1997 Dec;4(12):1003-9.
51. Choi J, Chon JK, Kim S, Shin W. Conformational flexibility in mammalian 15S- lipoxygenase: Reinterpretation of the crystallographic data. *Proteins*. 2008 Feb;70(3):1023-32.
52. Serpen A, Gökmen V. Effects of β -carotene on soybean lipoxygenase activity: kinetic studies. *European Food Research and Technology*. 2007 Apr;224(6):743-8.
53. Eleftheriadis N, Thee S, te Biesebeek J, van der Wouden P, Baas BJ, Dekker FJ. Identification of 6-benzyloxysalicylates as a novel class of inhibitors of 15-lipoxygenase-1. *European Journal of Medicinal Chemistry*. 2015 Apr;94:265-75.
54. Guo H, Verhoek IC, Prins GGH, van der Vlag R, van der Wouden PE, van Merkerk R, Quax WJ, Olinga P, Hirsch AKH, Dekker FJ. Novel 15-Lipoxygenase-1 Inhibitor Protects Macrophages from Lipopolysaccharide-Induced Cytotoxicity. *Journal of Medicinal Chemistry*. 2019 May;62(9):4624-37.



Mg-Al Layered Double Hydroxide (LDH) as an Adsorbent for Removal of Itaconic Acid from Aqueous Solutions: Equilibrium and Kinetic Study

Melisa LALIKOĞLU*  

Istanbul University-Cerrahpasa, Faculty of Engineering, Department of Chemical Engineering, 34320, Istanbul, Turkey.

Abstract: This study aims to remove itaconic acid, one of the important members of carboxylic acids, from its aqueous solutions by using an adsorption method. Recently the Layered Double Hydroxide (LDH), which has attracted attention in many areas, was synthesized by the co-precipitation method and used as an adsorbent. The effects of the adsorption time, LDH amounts, adsorption temperature, and initial acid concentration changes on the adsorption efficiency were examined. In one-stage batch adsorption experiments performed under different conditions, approximately 70% of itaconic acid was removed from the aqueous phase using 1 g of LDH. Various adsorption isotherm models such as Langmuir, Freundlich, and Temkin were applied to the obtained experimental data. Since R^2 values are greater than 0.98, it can be said that the experimental data fit all three isotherm models. Kinetic studies were carried out using time-dependent measurements. Adsorption behavior was kinetically investigated using pseudo-first-order, pseudo-second-order, and Elovich models. The kinetics of the adsorption of itaconic acid by LDH was found to be the best defined by the pseudo-second-order model.

Keywords: Itaconic acid, adsorption, layered double hydroxide.

Submitted: September 05, 2020. **Accepted:** December 04, 2020.

Cite this: Lalikoğlu M. Mg-Al Layered Double Hydroxide (LDH) as an Adsorbent for Removal of Itaconic Acid from Aqueous Solutions: Equilibrium and Kinetic Study. JOTCSA. 2021;8(1):103-116.

DOI: <https://doi.org/10.18596/jotcsa.790865>.

*Corresponding author. E-mail: melisad@istanbul.edu.tr.

INTRODUCTION

Itaconic acid, also called methylene succinic acid, is an unsaturated dicarboxylic acid with the molecular formula of $C_5H_6O_4$. It is used as a monomer in plastic, resin, coating, thickener, adhesive, paint, and synthetic fibers in the chemical industry. Conjugated double bonds and two carboxyl groups in the structure activate this acid for many chemical reactions such as esterification with alcohols, complexing with metal ions, anhydride production and polymerization. It can be used in the food and pharmaceutical industry as a biomonomer instead of petrochemical-based acrylic or methacrylic acid. Itaconic acid is soluble in ethanol, acetone, and water and slightly soluble in organic solvents (1). Its chemical structure is shown in Figure 1.

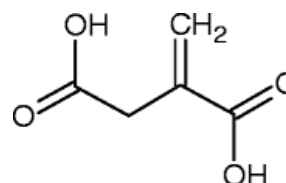


Figure 1: Itaconic acid's molecular structure.

Itaconic acid can be obtained by synthetic and biotechnological methods. Synthetic methods have considerable disadvantages, such as high chemical consumption and high energy requirements. Besides, in recent years, developments affecting the world, such as depleting fossil fuel reserves and global warming, reveal the importance of sustainable production. In this sense, the chemical industry has turned towards the biotechnological process for clean production via fermentation, which will ensure the use of natural resources as raw materials and minimize waste. This method has revealed a

renewable and environmentally friendly alternative to petrochemical-based (synthetic) production (2). However, there are two main problems with fermentation technology. The first one is acid inhibition. As the amount of acid formed in the fermentation medium increases, the pH decreases, which causes the death of microorganisms. Therefore, the continuation of the process will be feasible by removing the acid in the medium or adding an agent to neutralize the fermentation media. Another problem is that the acid formed from fermentation is found in a dilute aqueous solution of about 10% (w/w) (3,4).

Recovery of the acid from the aqueous medium accounts for approximately 50% of the total cost. Therefore, the separation part is an essential step in the economic evaluation of the process. The development and implementation of a low cost and effective separation method will make biotechnological acid production preferable. For this purpose, many different methods have been investigated in the literature to separate carboxylic acids from their aqueous solutions (5-7). Among these methods, membrane processes (8,9), electrodialysis processes (10,11), crystallization processes (12,13), and reactive extraction processes (14-18) have been used to remove itaconic acid from the aqueous solution. However, when these methods were compared with each other, it is possible to mention of various drawbacks. Membrane and crystallization processes are expensive processes due to high energy costs (19). Conventional solvents used in the reactive extraction method has a harmful effect on both human health and ecological balance. Besides, extraction systems have several disadvantages, such as high energy consumption and large equipment size requirement. One of the most crucial advantages of the adsorption process over the extraction is the ease of separation of the adsorbent. Magalhaes et al. conducted an economic analysis of the purification and recovery process of itaconic acid by fermentation. They indicated that the adsorption method is the most economical process compared to other separation methods (crystallization, extraction, and electrodialysis). The adsorption process is generally preferred due to its low cost, easy applicability, high efficiency, simplicity of equipment and easy regeneration of the adsorbent, and it is considered one of the promising methods (20).

The properties of adsorbent, which is to be used to separate carboxylic acids from their aqueous solutions, can be listed as having high selectivity, high adsorption capacity, being chemically and thermally stable, regenerable, biologically compatible with microorganisms, and being low-cost. In recent years, researches showed that synthetic polymeric and inorganic adsorbents had gained importance. Many modifications of adsorbent properties, such as functionality, surface area, polarity, and porosity, enable these materials to

behave selectively. Thus, an effective separation can be realized (21).

Layered double hydroxide (LDH), $[M^{II}_{1-x} M^{III}_x (OH)_2]^{x+} [A^{n-}_{x/n} \cdot yH_2O]^x$ denoted by the general formula. M^{II} and M^{III} represent divalent and trivalent metal cations, respectively. A^{n-} indicate inorganic or organic interlayer anion with the n electrical charge, and x defines the trivalent metal ratio $[M^{III} / (M^{II} + M^{III})]$ (22). It is an anionic clay classified as an inorganic nanomaterial. According to the application, layered double hydroxides can be designed in many ways with their various compositions and different synthesis methods. They are used as catalysts, additives for polymers, ion exchangers, and drug carriers (23). It has physical and chemical properties similar to clay minerals and is used as adsorbent. The most important feature of these inorganic materials; the adsorption capacity is high due to their high ion exchange capacity. Also, it is cheap and easily synthesized (24-27). In recent research, different carboxylic acids have been successfully removed from aqueous solutions using LDH (28-30).

Limited numbers of scientific studies have been conducted on separating itaconic acid from aqueous solutions by the adsorption method. Gulicovski et al. investigated the parameters affecting the adsorption of itaconic acid onto alumina (31). Magalhaes et al. reported that the adsorption process using strong basic ion exchange resin (Purolite A-500P and PFA-300) was more effective and faster than crystallization and evaporation processes in the industry (32).

This study aims to separate itaconic acid from aqueous solutions by adsorption using Mg-Al-Cl LDH. Various adsorption isotherm models such as Langmuir, Freundlich, and Temkin were applied to the obtained experimental data. Adsorption behavior was kinetically investigated using pseudo-first-order, pseudo-second-order, and Elovich models.

EXPERIMENTAL SECTION

Chemicals

Aluminum chloride hexahydrate ($AlCl_3 \cdot 6H_2O$), magnesium chloride hexahydrate ($MgCl_2 \cdot 6H_2O$), and sodium hydroxide (NaOH) were all purchased from Sigma-Aldrich (Germany). Itaconic acid was purchased from Merck (Germany). All chemicals used in experimental studies were provided as high purity products, and solution forms were prepared using deionized water.

Synthesis of Mg-Al-LDH

In our study, Mg-Al-LDH was synthesized using the co-precipitation method under an inert atmosphere at room temperature in accordance with the procedure in the literature (33,34). Briefly, salt solutions of $MgCl_2 \cdot 6H_2O$ (3 mmol) and $AlCl_3 \cdot 6H_2O$ (1 mmol) were dissolved in 10 mL of deionized water

and rapidly poured into 40 mL of NaOH solution (6 mmol). The prepared solution in slurry form was stirred for 1 hour; after aging for 2 hours, it was subjected to centrifugation for 5 minutes, at 4500 rpm. The LDH was prepared for adsorption by drying in a vacuum atmosphere at room temperature before using.

Batch Adsorption Experiments

Among the parameters affecting the adsorption processes, adsorbent amount, time, initial acid concentration and temperature were selected and examined experimentally. Batch adsorption experiments were carried out in a 50 mL glass flask. First, to determine the equilibrium time (optimum time) in the adsorption of itaconic acid with LDH, 5 mL of acid solution with an initial acid concentration of 80.50 g L⁻¹ onto 0.1 g adsorbent were added. This mixture was agitated in a Nuve Shaker ST30 thermostat bath at a constant speed (150 rpm) and temperature (298 K). The samples were taken from the shaker every 15 minutes and centrifuged at 4000 rpm for 10 minutes. The aqueous phase was analyzed using an automatic titrator with 0.1 M NaOH solution and phenolphthalein indicator. (± 0.01 uncertainty). The point at which the acid percentage did not change with time was defined as equilibrium time. To examine the effect of adsorbent amount, experiments were carried out by adding 5 mL of the itaconic acid solution with a concentration of 80.50 g L⁻¹ to the flasks containing 0.05-1.0 g of LDH. In order to investigate effect of temperature on adsorption, experiments were conducted at three different temperatures of 298, 308, and 318 K. For this aim, 0.1 g of adsorbent and acid solutions having 20.06, 40.12, 60.35, and 80.50 g L⁻¹ initial acid concentrations were investigated at these temperatures according to the experimental procedure described above.

The adsorption capacity (q_e) and removal efficiency (R%) was calculated using the following equations (1) and (2), respectively:

$$q_e = \frac{C_0 - C_e}{M} \times V \quad (1)$$

$$R\% = \frac{C_0 - C_e}{C_0} \times 100 \quad (2)$$

where C_0 represents the initial acid concentration of itaconic acid (mg L⁻¹); C_e shows the equilibrium acid concentration of itaconic acid (mg L⁻¹); V and M signify the volume of solution (L) and the amount of LDH (g).

RESULTS AND DISCUSSIONS

The effects of the adsorption time, LDH amounts, initial acid concentration, and adsorption temperature changes on the adsorption efficiency were examined and reported.

The Effect of Adsorption Time

To determine the equilibrium adsorption time, the experiments were carried out at 298 K using an initial acid concentration of 80.50 g L⁻¹ in the presence of 0.1 grams of the adsorbent. The results are shown in Figure 2. It was seen that the amount of acid adsorbed increased as the contact time increased over time, and the acid concentration remained constant after a certain time. Thus, the optimum equilibrium adsorption time was determined as 180 minutes.

The Effect of Adsorbent Amount

In order to examine the effect of different LDH amounts on adsorption; 0.05, 0.10, 0.15, 0.20, 0.30, 0.40, 0.50, 0.60, 0.80, and 1.0 g of adsorbent was used with an initial acid concentration of 80.5 g L⁻¹ at 298 K. The experimental data were given in Table 1 and Figure 3. It was observed from Figure 3 that the adsorption capacity decreased with the amount of adsorbent increase. Previous studies in the literature explain the decrease in adsorption capacity by the presence of a large number of unsaturated active sites on the adsorbent surface (29). As shown in Table 1, the itaconic acid removal efficiency increased from 10.8% to 69.1%.

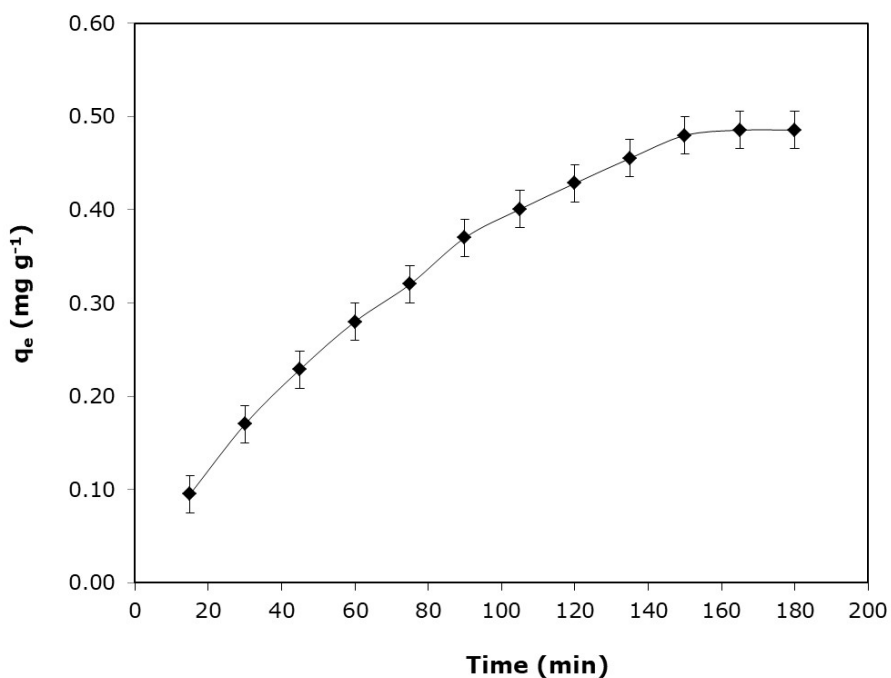


Figure 2: Equilibrium time for the adsorption of itaconic acid by LDH. ($C_0 = 80.50 \text{ g L}^{-1}$, $M = 0.1 \text{ g LDH}$, and $T = 298 \text{ K}$)

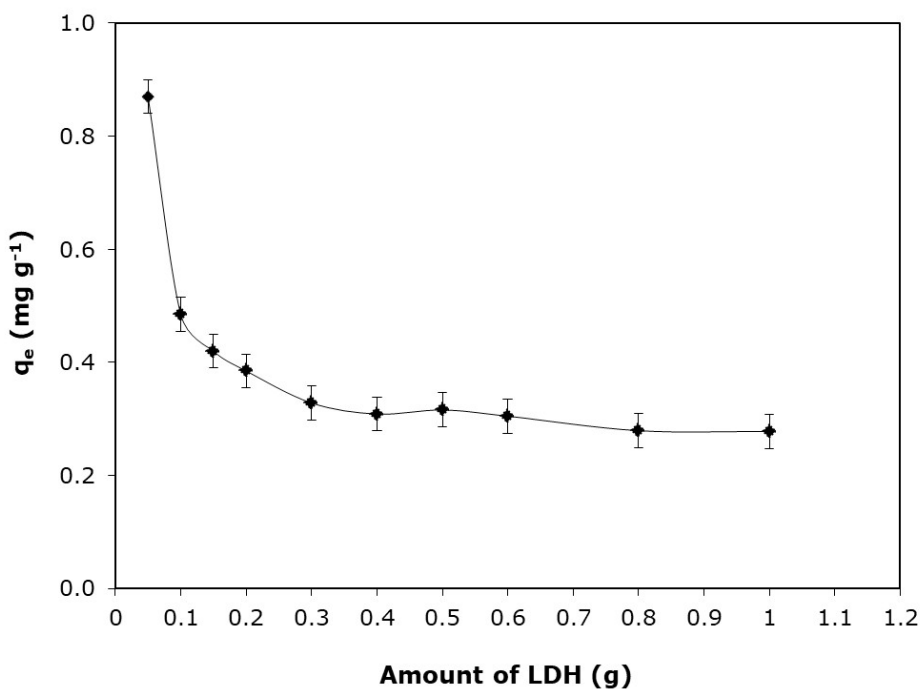


Figure 3: The effect of amounts of LDH on itaconic acid adsorption. ($C_0 = 80.50 \text{ g L}^{-1}$, $T = 298 \text{ K}$, $t = 180 \text{ min}$)

Table 1: The effect of amounts of LDH on itaconic acid adsorption. ($C_0 = 80.5 \text{ g}\cdot\text{L}^{-1}$, $T = 298 \text{ K}$, and $t = 180 \text{ min}$)

Amount of LDH (g)	Equilibrium concentration, C_e (g L^{-1})	Amount of adsorbed acid, q_e (mg g^{-1})	Removal efficiency (%)
0.05	71.8	0.870	10.8
0.10	70.8	0.485	12.1
0.15	67.9	0.420	15.6
0.20	65.1	0.385	19.1
0.30	60.8	0.328	24.5
0.40	55.8	0.309	30.7
0.50	48.9	0.316	39.2
0.60	43.9	0.305	45.5
0.80	35.8	0.279	55.5
1.00	24.9	0.278	69.1

The Effect of Initial Itaconic Acid Concentration

To investigate the effect of initial acid concentration on adsorption, itaconic acid solution concentrations were determined as 20.06, 40.12, 60.35, and 80.50 g L^{-1} . The experiments were executed at three different temperatures (298, 308, and 318 K) and the predetermined adsorption equilibrium time with an adsorbent amount of 0.1 grams. The results of the experiments were given in Table 2. The adsorbed acid amount (q_e) values increased with increasing initial acid concentration.

The Effect of Temperature

The effect of temperature on the adsorption of itaconic acid onto LDH was investigated at three different temperatures of 298, 308 and 318 K, and four different initial acid concentrations (20.06, 40.12, 60.35, and 80.50 g L^{-1}). The obtained experimental results were demonstrated in Figure 4. It was seen from Figure 4, the adsorption capacity increased with the increase in temperature. It was observed that the adsorption capacity increased from 0.358 mg g^{-1} to 0.485 mg g^{-1} at 298 K, from 0.368 mg g^{-1} to 0.630 mg g^{-1} at 308 K, from 0.395 mg g^{-1} to 0.740 mg g^{-1} at 318 K. As a result of these data, it was revealed that the adsorption of itaconic acid with LDH is an endothermic process.

Adsorption Isotherms

Adsorption isotherms are mathematical models used to explain the adsorption process. The models indicate at a constant temperature that the relationship between the amount of material adsorbed by the adsorbent and the equilibrium concentration. In this study, Langmuir, Freundlich and Temkin isotherm models were used to explain the adsorption process. Equations for the isotherm models were presented below (35):

Langmuir Isotherm

The Langmuir isotherm model is an experimental model showing that adsorption is single layer adsorption and formulated as:

$$q_e = \frac{q_0 K_L C_e}{1 + K_L C_e} \quad (3)$$

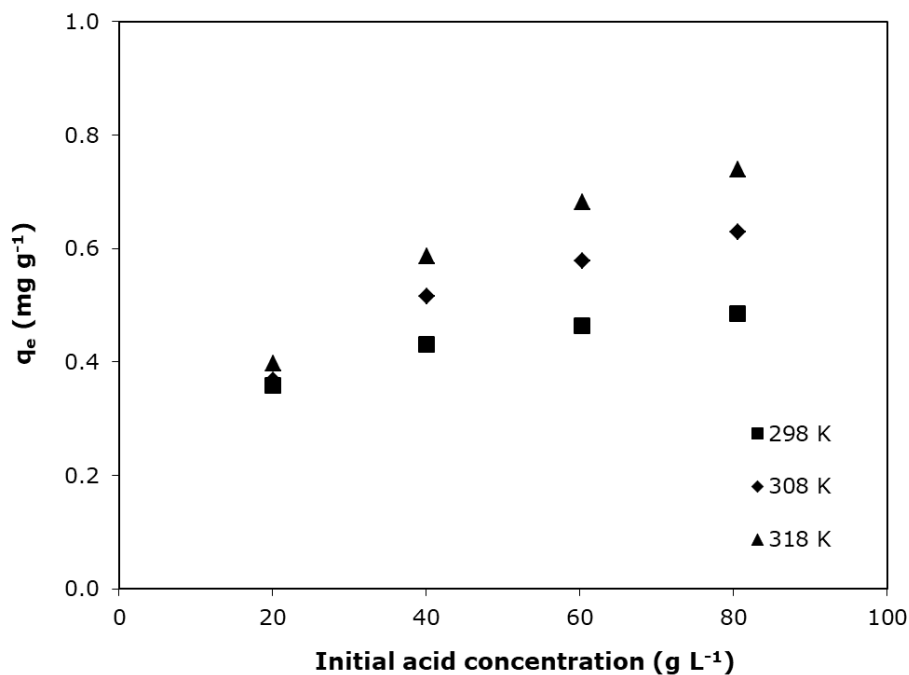
Linear expression of the Langmuir isotherm model can be stated as (Eq. 4):

$$\frac{C_e}{q_e} = \frac{1}{K_L q_0} + \frac{C_e}{q_0} \quad (4)$$

In this equation, C_e (mg L^{-1}) shows the equilibrium concentration of itaconic acid, q_e (mg g^{-1}) signifies adsorption capacity, q_0 (mg g^{-1}) and K_L denotes saturation capacity and Langmuir isotherm coefficient, respectively.

Table 2: The Effects of initial acid concentration at different temperatures (M=0.1 g, t=180 min)

Temperature (K)	Initial acid concentration, C_0 (g L ⁻¹)	Equilibrium concentration, C_e (g L ⁻¹)	Amount of adsorbed acid, q_e (mg g ⁻¹)
298	20.06	12.9	0.358
	40.12	31.5	0.431
	60.35	51.1	0.463
	80.50	70.8	0.485
308	20.06	12.7	0.368
	40.12	29.8	0.516
	60.35	48.8	0.578
	80.50	67.9	0.630
318	20.06	12.1	0.398
	40.12	28.4	0.586
	60.35	46.7	0.683
	80.50	65.7	0.740

**Figure 4:** The effect of temperature on itaconic acid adsorption by LDH for different initial acid concentration. (M=0.1 g, t=180 min)*Freundlich Isotherm*

The Freundlich isotherm is generally used to define adsorption properties for the heterogeneous surfaces and the adsorption characteristics of adsorbents. The

non-linear mathematical equation form of the Freundlich isotherm can be expressed as follows:

(5)

Equation (6) is obtained by linearizing Equation (5):

$$q_e = K_f \times C_e^{\frac{1}{n}} \quad (5)$$

$$B = \frac{RT}{b} \quad (8)$$

$$\log q_e = \log K_f + \frac{1}{n} \log C_e \quad (6)$$

The linear form of the equation of Temkin is given in Equation (9).

where $1/n$ and K_f represent heterogeneity factor and Freundlich coefficient related to adsorption capacity and adsorption intensity, respectively.

$$q_e = B(\ln K_T) + B(\ln C_e) \quad (9)$$

Temkin Isotherm

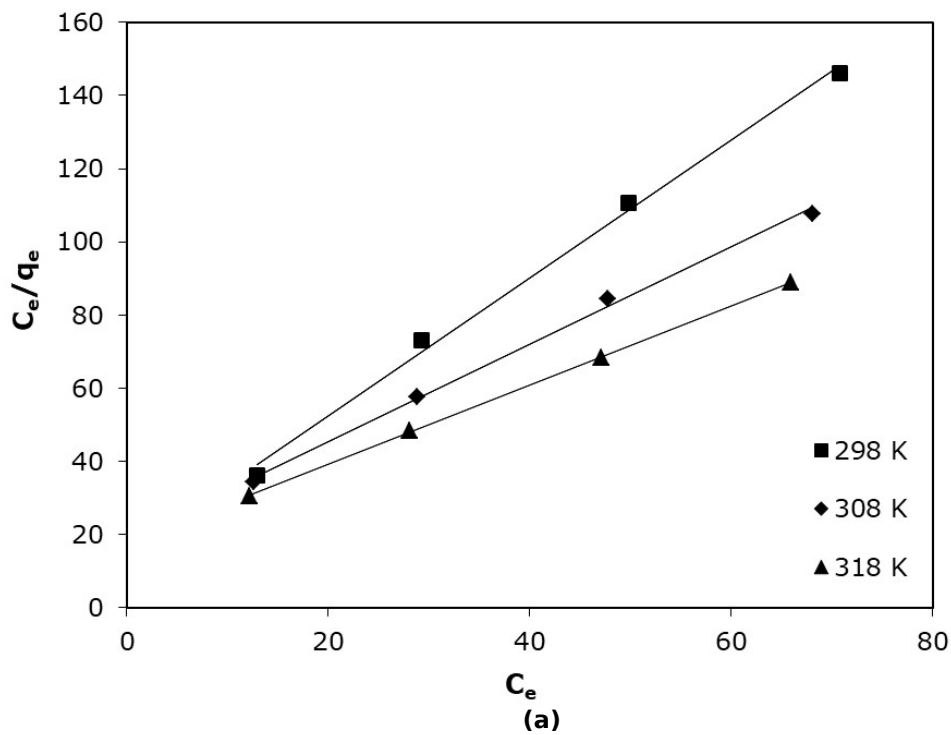
The Temkin isotherm is used to explain the adsorption behavior. It reveals that the adsorption energy in the molecular layer is a result of adsorbent-adsorbate interactions. The Temkin isotherm assumes that the decrease in adsorption energy is linear.

in this equation, b ($J \text{ mol}^{-1}$) is Temkin constant is related to the adsorption heat. K_T ($L \text{ g}^{-1}$) Temkin isotherm constant, R is ideal gas constant ($8.314 \text{ J mol}^{-1}K^{-1}$), and T (K) is temperature.

Temkin isotherm model equations are signified as below:

The compatibility of the experimental results of itaconic acid adsorption onto LDH with the Langmuir, Freundlich and Temkin isotherm models are shown in Figure 5 (a,b,c). Langmuir, Freundlich and Temkin isotherm constants and regression coefficients (R^2) were calculated, and the results are summarized in Table 3.

$$q_e = b \ln(K_T C_e) \quad (7)$$



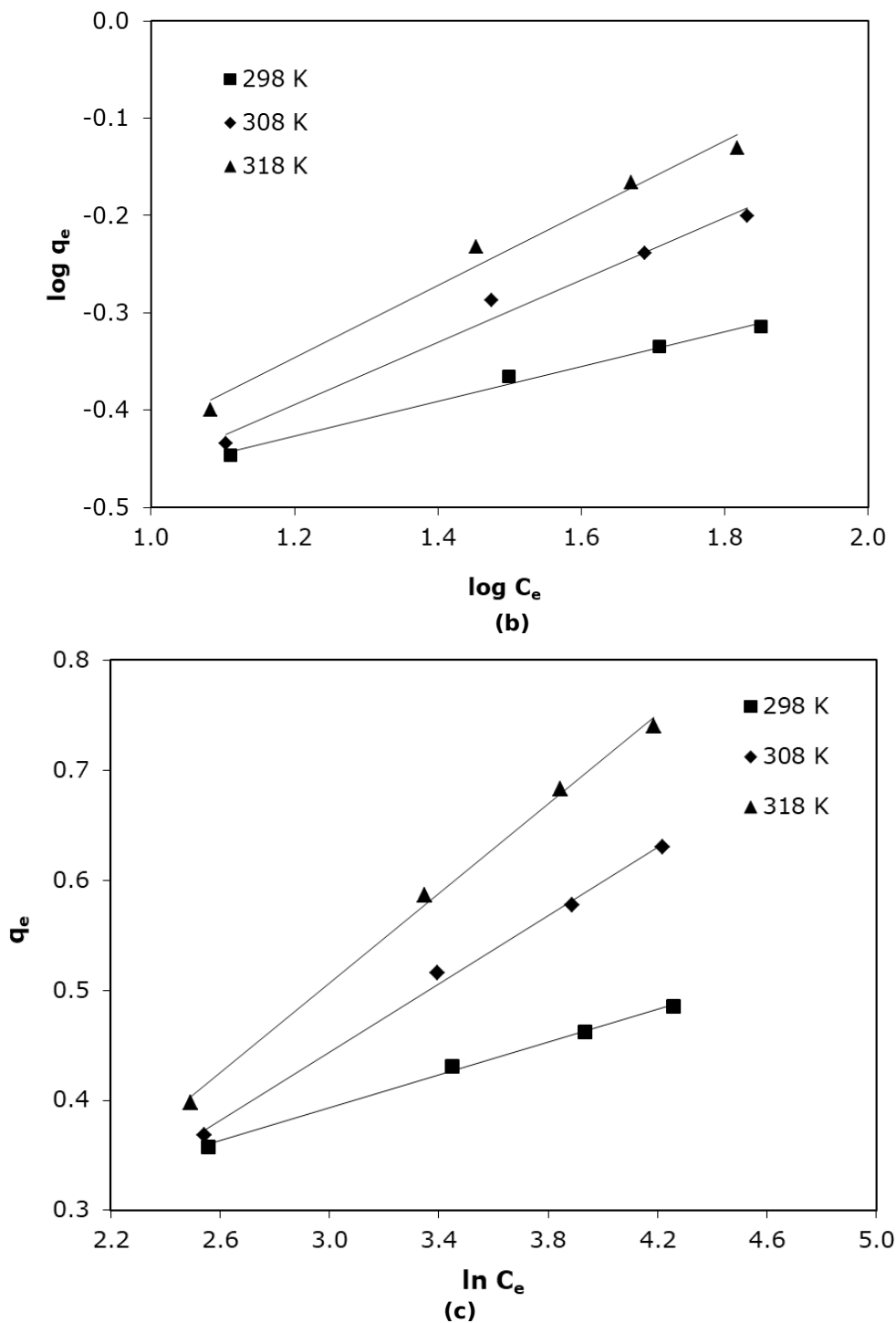


Figure 5: Equilibrium of itaconic acid adsorption onto LDH at different temperatures, (a) Langmuir isotherm; (b) Freundlich isotherm; (c) Temkin isotherm.

Table 3: Isotherm parameters for adsorption of itaconic acid by LDH

Isotherm	Temperature (K)	q_0 (mg g ⁻¹)	K_L (g L ⁻¹)	R^2
Langmuir	298	0.5307	0.1318	0.9960
	308	0.7541	0.0698	0.9972
	318	0.9236	0.0618	0.9998
	Temperature (K)	n	K_f (g L ⁻¹)	R^2
Freundlich	298	5.58	0.2429	0.9913
	308	3.12	0.1664	0.9833
	318	2.69	0.1616	0.9828
	Temperature (K)	B	K_T (g L ⁻¹)	R^2
Temkin	298	0.0746	9.6800	0.9970
	308	0.1550	0.8716	0.9957
	318	0.2037	0.5987	0.9972

As shown in Table 3, the regression coefficient (R^2) values of all the isotherm models were higher than 0.98. So, all the isotherm models used in the study showed high compatibility with the experimental data. This situation indicated that there is more than one mechanism for the adsorption of itaconic acid by LDH (36).

Adsorption Kinetics

Explanation of the adsorption mechanism is very important for the design of the adsorption process. The kinetic models were used to reveal the adsorption mechanism. Pseudo-first-order, pseudo-second-order and Elovich kinetic models were applied to the adsorption equilibrium data to evaluate the adsorption of itaconic acid by LDH at 298 K (37). The kinetic model equations used to determine the rate of adsorption are presented as follows:

Pseudo-first-order (Lagergren) kinetic model;

$$\log(q_e - q_t) = \log q_e - \frac{k}{2.303} \times t \quad (10)$$

Pseudo-second-order kinetic model;

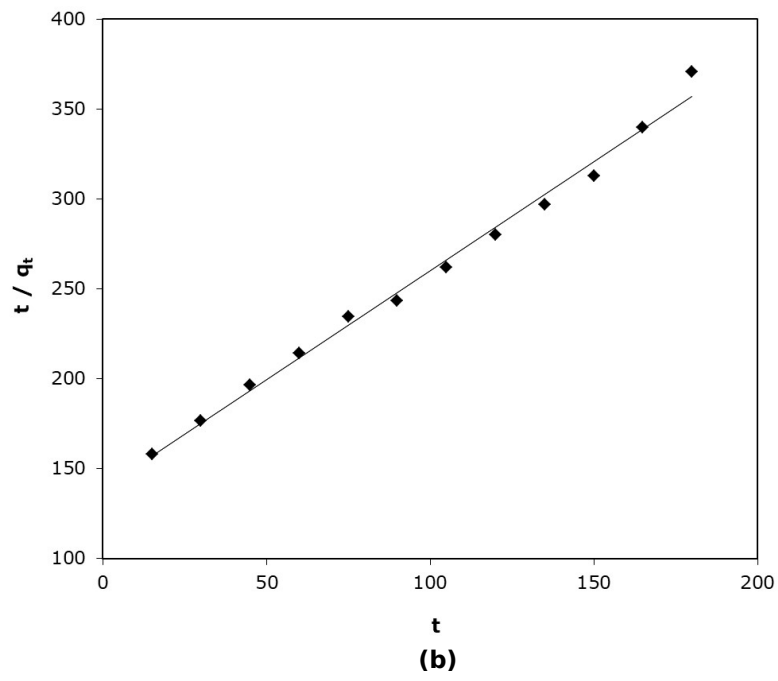
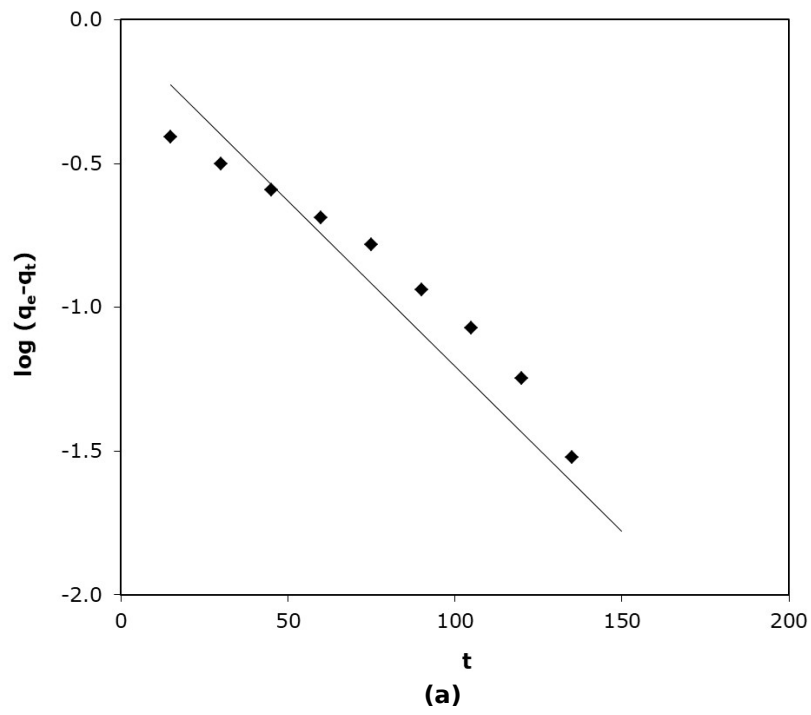
$$\frac{t}{q_t} = \frac{1}{k_2 q_e^2} + \frac{1}{q_e} t \quad (11)$$

Elovich kinetic model

$$q_t = \frac{1}{\beta} \ln(\alpha\beta) + \frac{1}{\beta} \ln(t) q_t \quad (12)$$

q_e (mg g⁻¹): is the adsorption capacity at equilibrium,
 q_t (mg g⁻¹): is the adsorption capacity at any time (t),
 k_1 (min⁻¹): pseudo-first-order kinetic rate coefficient,
 k_2 (g mg⁻¹ min⁻¹): pseudo-second-order kinetic rate coefficient,
 α (mg g⁻¹ min⁻¹): is the initial adsorption rate,
 β (g mg⁻¹) adsorption capacity; is the constant of desorption.

Figure 6 (a,b,c) gives the kinetic model plots for the LDH, and the model parameters are represented in Table 4.



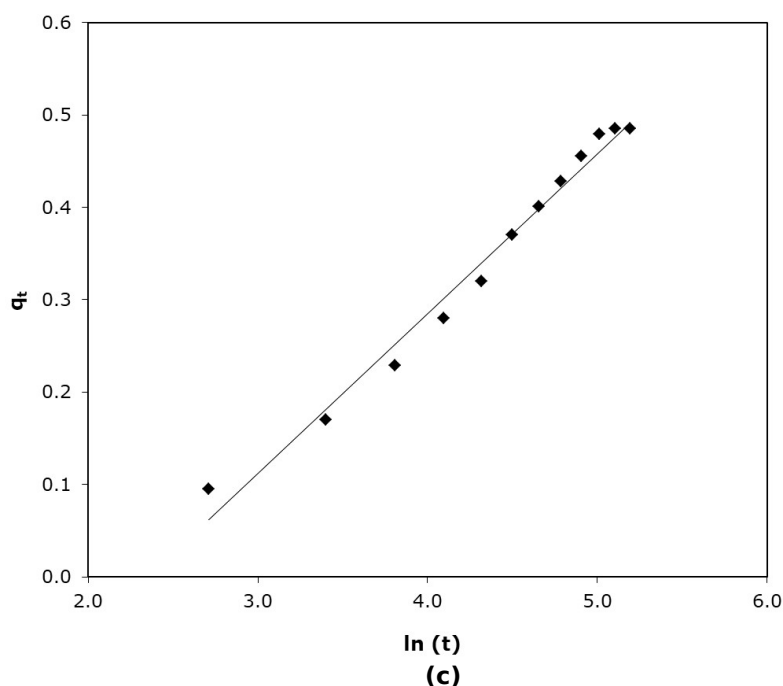


Figure 6 : Adsorption kinetics of itaconic acid by LDH at different temperatures, (a) Pseudo-first order equation; (b) Pseudo-second-order equation; (c) Elovich equation.

Table 4: Kinetic parameters for adsorption of itaconic acid by LDH (T= 298 K).

Pseudo-first-order			Pseudo-second-order			Elovich		
k_1	q_0	R^2	k_2	q_e	R^2	α	β	R^2
0.0265	0.8841	0.8587	0.0105	0.8256	0.9919	0.016	5.78	0.9824

When the R^2 values in Table 4 were evaluated, it was seen that the pseudo-second-order kinetic model was the most suitable kinetic model with a value of $R^2 = 0.9919$. This model shows that the adsorption of itaconic acid onto LDH is a chemisorption process (38,39).

CONCLUSIONS

LDH was used to as an adsorbent to recover itaconic acid from aqueous solutions due to their high ion exchange capacity. In the study, the optimum adsorption time was determined and the effect of initial acid concentration, adsorbent amount, and temperature parameters on the adsorption capacity was investigated. The adsorption process and mechanism was revealed by analyzing the equilibrium and kinetic data after examining the parameters affecting the adsorption of itaconic acid onto LDH. The maximum recovery efficiency was about 70% at the condition of 80.50 g L⁻¹ initial acid concentration, 1 g of adsorbent, and 298 K. When the isotherm results defining the chemical equilibrium process were examined, it was seen that all the isotherm models were fitted the equilibrium data. This result showed that the adsorption of itaconic acid by LDH was a monolayer process. It was

revealed that the model specifying the kinetic process is the pseudo-second-order model with the highest regression coefficient ($R^2 = 0.9919$). This work showed that LDH, a cheap and easily synthesis clay, can remove itaconic acid from the aqueous solutions. This study will also lead to further investigation of the adsorption behavior in the separation of itaconic acid from aqueous solutions using LDH with different Mg/Al ratios.

REFERENCES

1. Willke T, Vorlop KD. Biotechnological production of itaconic acid. Appl Microbiol Biotechnol. 2001;56:289-95.
2. Kaur G, Elst K. Development of reactive extraction systems for itaconic acid: A step towards in situ product recovery for itaconic acid fermentation. RSC Adv. 2014; 4 (85): 45029-39.
3. Lalikoglu M, Bilgin M. Ternary phase diagrams for aqueous mixtures of butyric acid with several solvents: Experimental and correlated data. Fluid Phase Equilib. 2014;371:50-6.
4. Datta D, Aşçi YS, Tuyun AF. Extraction Equilibria of

- Glycolic Acid Using Tertiary Amines: Experimental Data and Theoretical Predictions. *J Chem Eng Data*. 2015;60(11):3262-7.
5. Baylan N, Çehreli S. Experimental and modeling study for the removal of formic acid through bulk ionic liquid membrane using response surface methodology. *Chem Eng Commun*. 2020; 207(10):1426-39.
 6. Gemici A, Uslu H, Gök A, Kirbaşlar SI. Effect of diluents on the extraction of fumaric acid by tridodecyl amine (TDA). *J Chem Eng Data*. 2015;60(3):919-24.
 7. López-Garzón CS, Straathof AJJ. Recovery of carboxylic acids produced by fermentation. *Biotechnol Adv*. 2014;32(5):873-904.
 8. Carstensen F, Klement T, Büchs J, Melin T, Wessling M. Continuous production and recovery of itaconic acid in a membrane bioreactor. *Bioresour Technol*. 2013; 137: 179-87.
 9. Li A, Sachdeva S, Urbanus JH, Punt PJ. In-stream itaconic acid recovery from *Aspergillus terreus* fedbatch fermentation. *Ind Biotechnol*. 2013;9(3):139-45.
 10. Stodollick J, Femmer R, Gloede M, Melin T, Wessling M. Electrodialysis of itaconic acid: A short-cut model quantifying the electrical resistance in the overlimiting current density region. *J Memb Sci*. 2014;453:275-81.
 11. Fidaleo M, Moresi M. Application of the Nernst-Planck approach to model the electrodialytic recovery of disodium itaconate. *J Memb Sci*. 2010;349(1-2):393-404.
 12. Dwiarti L, Otsuka M, Miura S, Yaguchi M, Okabe M. Itaconic acid production using sago starch hydrolysate by *Aspergillus terreus* TN484-M1. *Bioresour Technol*. 2007; 98 (17) :3329-37.
 13. Hogle BP, Shekhawat D, Nagarajan K, Jackson JE, Miller DJ. Formation and recovery of itaconic acid from aqueous solutions of citraconic acid and succinic acid. *Ind Eng Chem Res*. 2002;41(9):2069-73.
 14. Kreyenschulte D, Heyman B, Eggert A, Maßmann T, Kalvelage C, Kossack R, et al. In situ reactive extraction of itaconic acid during fermentation of *Aspergillus terreus*. *Biochem Eng J*. 2018;135:133-41.
 15. Kumar S, Babu BV. Process Intensification for Separation of Carboxylic Acids from Fermentation Broths using Reactive Extraction. *i-manager's J Futur Eng Technol*. 2008;3(3):21-8.
 16. Wasewar KL, Shende D, Keshav A. Reactive extraction of itaconic acid using quaternary amine Aliquat 336 in ethyl acetate, toluene, hexane, and kerosene. *Ind Eng Chem Res*. 2011;50(2):1003-11.
 17. Bressler E, Braun S. Separation mechanisms of citric and itaconic acids by water-immiscible amines. *J Chem Technol Biotechnol*. 1999;74(9):891-896.
 18. Aşçı YS, İnci İ. A novel approach for itaconic acid extraction: Mixture of trioctylamine and tridodecylamine in different diluents. *J Ind Eng Chem*. 2012;18(5):1705-9.
 19. Magalhães AI, de Carvalho JC, Medina JDC, Soccol CR. Downstream process development in biotechnological itaconic acid manufacturing. *Appl Microbiol Biotechnol*. 2017;101(1):1-12.
 20. Magalhães AI, de Carvalho JC, Thoms JF, Medina JDC, Soccol CR. Techno-economic analysis of downstream processes in itaconic acid production from fermentation broth. *J Clean Prod*. 2019;206:336-48.
 21. Pan B, Pan B, Zhang W, Lv L, Zhang Q, Zheng S. Development of polymeric and polymer-based hybrid adsorbents for pollutants removal from waters. *Chem Eng J*. 2009;151:19-29.
 22. Gasser MS, Mohsen HT, Aly HF. Humic acid adsorption onto Mg/Fe layered double hydroxide. *Colloids Surfaces A Physicochem Eng Asp*. 2008;331(3):195-201.
 23. Zümreoglu-Karan B, Ay AN. Layered double hydroxides - Multifunctional nanomaterials. *Chem Pap*. 2012;66(1):1-10.
 24. Das NN, Konar J, Mohanta MK, Srivastava SC. Adsorption of Cr(VI) and Se(IV) from their aqueous solutions onto Zr⁴⁺-substituted ZnAl/MgAl-layered double hydroxides: effect of Zr⁴⁺ substitution in the layer. *J Colloid Interface Sci*. 2004;270(1):1-8.
 25. Centi G, Perathoner S. Catalysis by layered materials: A review. *Microporous Mesoporous Mater*. 2008;107(1):3-15.
 26. Nedim Ay A, Konuk D, Zümreoglu-Karan B. Prolate spheroidal hematite particles equatorially belt with drug-carrying layered double hydroxide disks: Ring Nebula-like nanocomposites. *Nanoscale Res Lett*. 2011;6(1):116.
 27. Ay AN, Zümreoglu-Karan B, Temel A. Boron removal by hydrotalcite-like, carbonate-free Mg-Al-NO₃-LDH and a rationale on the mechanism. *Microporous Mesoporous Mater*. 2007;98(1):1-5.
 28. Gök A, Gök MK, Aşçı YS, Lalikoğlu M. Equilibrium, kinetics and thermodynamic studies for separation of malic acid on layered double hydroxide (LDH). *Fluid Phase Equilib*. 2014 Jun;372:15-20.

29. Gök A. Enhanced adsorption of nicotinic acid by different types of Mg/Al layered double hydroxides: synthesis, equilibrium, kinetics, and thermodynamics. *J Dispers Sci Technol.* 2020 Apr 15;41(5):779-86.
30. Lalikoğlu M, Gök A, Gök MK, Aşçı YS. Investigation of Lactic Acid Separation by Layered Double Hydroxide: Equilibrium, Kinetics, and Thermodynamics. *J Chem Eng Data.* 2015 ;60(11):3159-65.
31. Gulicovski JJ, Čerović LS, Milonjić SK, Popović IG. Adsorption of itaconic acid from aqueous solutions onto alumina. *J Serbian Chem Soc.* 2008;73(8-9):825-34.
32. Magalhães AI, De Carvalho JC, Ramírez ENM, Medina JDC, Soccol CR. Separation of Itaconic Acid from Aqueous Solution onto Ion-Exchange Resins. *J Chem Eng Data.* 2016;61(1):430-7.
33. Ladewig K, Niebert M, Xu ZP, Gray PP, Lu GQ (Max). Controlled preparation of layered double hydroxide nanoparticles and their application as gene delivery vehicles. *Appl Clay Sci.* 2010;48:280-9.
34. Özgümüş S, Gök MK, Bal A, Güçlü G. Study on novel exfoliated polyampholyte nanocomposite hydrogels based on acrylic monomers and Mg-Al-Cl layered double hydroxide: Synthesis and characterization. *Chem Eng J.* 2013;223:277-86.
35. Baylan N. Removal of levulinic acid from aqueous solutions by clay nano-adsorbents: equilibrium, kinetic, and thermodynamic data. *Biomass Convers Biorefinery.* 2020; In press.
36. Özcan Ö, İnci İ, Aşçı YS. Multiwall Carbon Nanotube for Adsorption of Acetic Acid. *J Chem Eng Data.* 2013;58(3):583-7.
37. Aşçı YS. Removal of textile dye mixtures by using modified Mg-Al-Cl layered double hydroxide (LDH). *J Dispers Sci Technol.* 2017;38(7):923-9.
38. Du B, Shan R, Yang K, Hao Y, Yan L. Adsorption of Cd(II) by Mg-Al-CO₃- and magnetic Fe₃O₄/Mg-Al-CO₃-layered double hydroxides: Kinetic, isothermal, thermodynamic and mechanistic studies. *J Hazard Mater.* 2015;299:42-9.
39. Rasoulpoor K, Poursattar Marjani A, Nozad E. Competitive chemisorption and physisorption processes of a walnut shell based semi-IPN bio-composite adsorbent for lead ion removal from water: Equilibrium, Kinetic and Thermodynamic studies. *Environ Technol Innov.* 2020; 20: 101133.



Polymorphic Phase Change of Calcium Carbonate with Glutamic Acid as an Additive

Sevgi POLAT* , Tuba Nur ÖZALP , Perviz SAYAN 

Marmara University, Department of Chemical Engineering, Istanbul, Turkey

Abstract: The calcium carbonate (CaCO_3) crystals were successfully synthesized in the presence of glutamic acid used as an additive at 30 °C and at a pH of 8.5. The synthesized product was characterized in detail by X-ray diffraction (XRD), Fourier transform infrared (FTIR) spectroscopy and scanning electron microscopy (SEM) to identify the structure and habit of the crystals. Moreover, the size and surface charge of the crystals were measured by particle size and zeta potential analyzer. XRD and FTIR results showed that both calcite and vaterite in forms of apparently CaCO_3 crystals were obtained in the presence of 50 ppm additive concentration at $t=30$ min. When increasing the glutamic acid concentration in the suspension, the formed CaCO_3 were only in the vaterite form. The SEM analysis results pointed out that the addition of the glutamic acid significantly changed the shape of the CaCO_3 . At $t=30$ min the resulting product sample was found to contain two types of polymorphs; larger cubic shaped calcite crystals and smaller spherical-like vaterite crystals. Further addition of high concentrations of the additive enhanced the adsorption of the glutamic acid, resulting in the smaller spherical-like ellipsoidal vaterite crystals. Investigation of the zeta potential analysis indicated that higher additive concentration (100 ppm) resulted in a positive surface charge of the crystals, whereas lower concentration (50 ppm) gave negative electrical charge. Moreover, filtration analysis pointed out that adding glutamic acid additive resulted in a less specific cake resistance value (5.01×10^{11} m/kg) than that in pure media, which was 1.03×10^{12} m/kg.

Keywords: Calcium carbonate, polymorphism, crystal morphology, additive.

Submitted: October 16, 2020. **Accepted:** December 04, 2020.

Cite this: Polat S, Özalp TN, Sayan P. Polymorphic Phase Change of Calcium Carbonate with Glutamic Acid as an Additive. JOTCSA. 2021;8(1):117-24.

DOI: <https://doi.org/10.18596/jotcsa.811283>.

INTRODUCTION

There is significant research interest in calcium carbonate (CaCO_3) because of its industrial importance, diversity as a biomineral, and crystalline complexity (1,2). CaCO_3 typically takes one of three crystal polymorph forms: calcite, aragonite, or vaterite (3). Calcite is the most thermally stable polymorph. The vaterite phase can be converted into the stable calcite phase under appropriate conditions (4,5). The properties of CaCO_3 crystals are determined by the crystal polymorph, size, and shape (6). CaCO_3 is important in the oil/petrochemicals, water treatment, and energy production. Calcium carbonate is among the most common fillers applied in the pulp and paper industry because of its easy dispersibility and low

propensity for agglomeration. Furthermore, CaCO_3 particles in the micrometer size range are used in the production of plastics to reinforce polymers, improve their properties, and reduce production costs. In addition, fillers and pigments made using CaCO_3 crystals with small particle size have wide-ranging applications in the pharmaceutical and cosmetics industries, for example, as colorants, abrasives in toothpaste, and coatings for therapeutic delivery (7). Thus, the precise polymorphic and morphological control of CaCO_3 crystals is crucial for industrial processes and is the subject of great research interest. Despite being present in small quantities, additives can have a drastic effect on the quality of the final crystalline product (8). Additives influence particular parts of the crystallization process through their close structural relationship

with the target system. The effects of additives including metal ions (9), carboxylic acids (10), polyelectrolytes (11), biopolymers (12), polysaccharides (13), and amino acids (14) on the phase transformation of CaCO_3 have recently been investigated by several research groups. However, to date, the effects of glutamic acid on the CaCO_3 transformation process and the morphological and filtration characteristics have not been investigated in detail.

The aim of this study was therefore to investigate the effects of glutamic acid as a crystal modifier on CaCO_3 crystal structure, morphology, and size. Glutamic acid is a biodegradable and non-toxic as well as being an effective crystal modifier at low concentrations. In this study, we investigated the effects of glutamic acid on the polymorphic transformation of CaCO_3 from calcite to vaterite form, considering the morphology, phase structure, particle size distribution, and filtration characteristics of the end products. The use of glutamic acid as an additive was found to give a

significant reduction in the crystal particle size as well as significantly improving the filtration characteristics. The results reported here will be invaluable for ensuring adequate control of product characteristics in industrial processes.

MATERIALS AND METHOD

Materials

Calcium chloride dihydrate ($\text{CaCl}_2 \cdot 2\text{H}_2\text{O}$), sodium carbonate (Na_2CO_3), and glutamic acid ($\text{C}_5\text{H}_9\text{NO}_4$) used in the experiment were all analytically pure and were purchased at Merck. All solutions were prepared using distilled water. All experiments were conducted at least in triplicate.

Method

The polymorphic phase change of CaCO_3 was performed using the setup shown in Figure 1. The synthesis process is as follows. CaCO_3 was prepared by the reaction between $\text{CaCl}_2 \cdot 2\text{H}_2\text{O}$ and Na_2CO_3 in a glass crystallizer with an active volume of 1.0 L at $30 \pm 0.1^\circ\text{C}$.

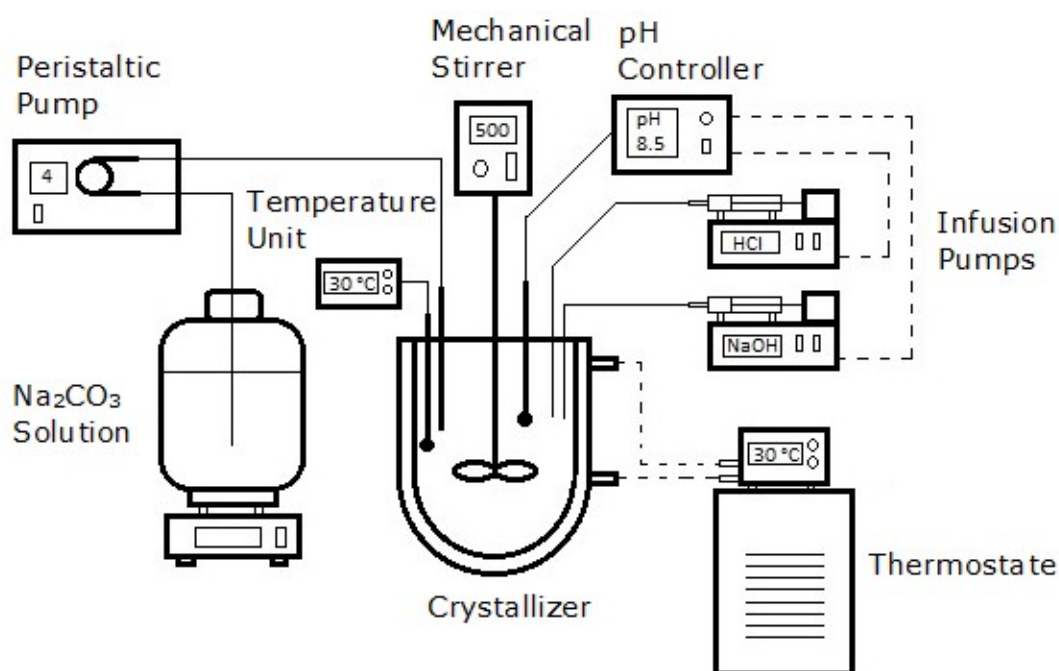


Figure 1. The experimental setup.

At the beginning of the experiment, 0.2 M CaCl_2 solution (400 mL) was placed into the crystallizer. Once the temperature was stabilized, 400 mL of Na_2CO_3 solution with a concentration of 0.2 M was added into the crystallizer at a rate of 4 mL/min using a peristaltic pump. The suspension in the crystallizer was stirred at a rate of 500 rpm. The pH value of the suspension was kept at pH 8.5 using 0.1 N HCl (aq) and 0.1 N NaOH (aq). At 30 and 100 mins, 20-mL aliquots of the suspension were removed and used for crystal structure and morphology analysis.

The influence of glutamic acid and its concentrations on the polymorphic change of CaCO_3 was investigated in this study. The specific amount of the glutamic acid (corresponding to 50 ppm and 100 ppm) was added into the crystallizer at the beginning of the experiment. The obtained crystals were filtered by 0.45 μm membrane filters connected to a vacuum pump. The crystals were washed thoroughly with distilled water and the remaining crystals were dried at room temperature.

X-ray diffraction (XRD) was used to determine the crystal polymorph of the sample. The XRD pattern of

the powder sample was collected by a Bruker D2 Phaser Table-top Diffractometer. X-ray radiation $\text{Cu K}\alpha$ ($\lambda = 1.542 \text{ \AA}$) was set at 30 kV and 10 mA. Meanwhile, the polymorphic transformation was monitored by Fourier transform infrared spectroscopy (FTIR; Shimadzu IR Affinity-1). The crystal habit and particle size distribution were observed by scanning electron microscopy (SEM; Zeiss EVO LS 10) and Malvern Mastersizer 2000 instrument, respectively. Zeta potential

measurements were performed using a Malvern Zeta Sizer Nano Series Nano-ZS.

RESULTS AND DISCUSSION

XRD Analysis

Figure 2 illustrates the XRD patterns of CaCO_3 crystals with and without glutamic acid in which C represents peaks from calcite, while V denotes peaks from vaterite within the range of $10\text{-}70^\circ$.

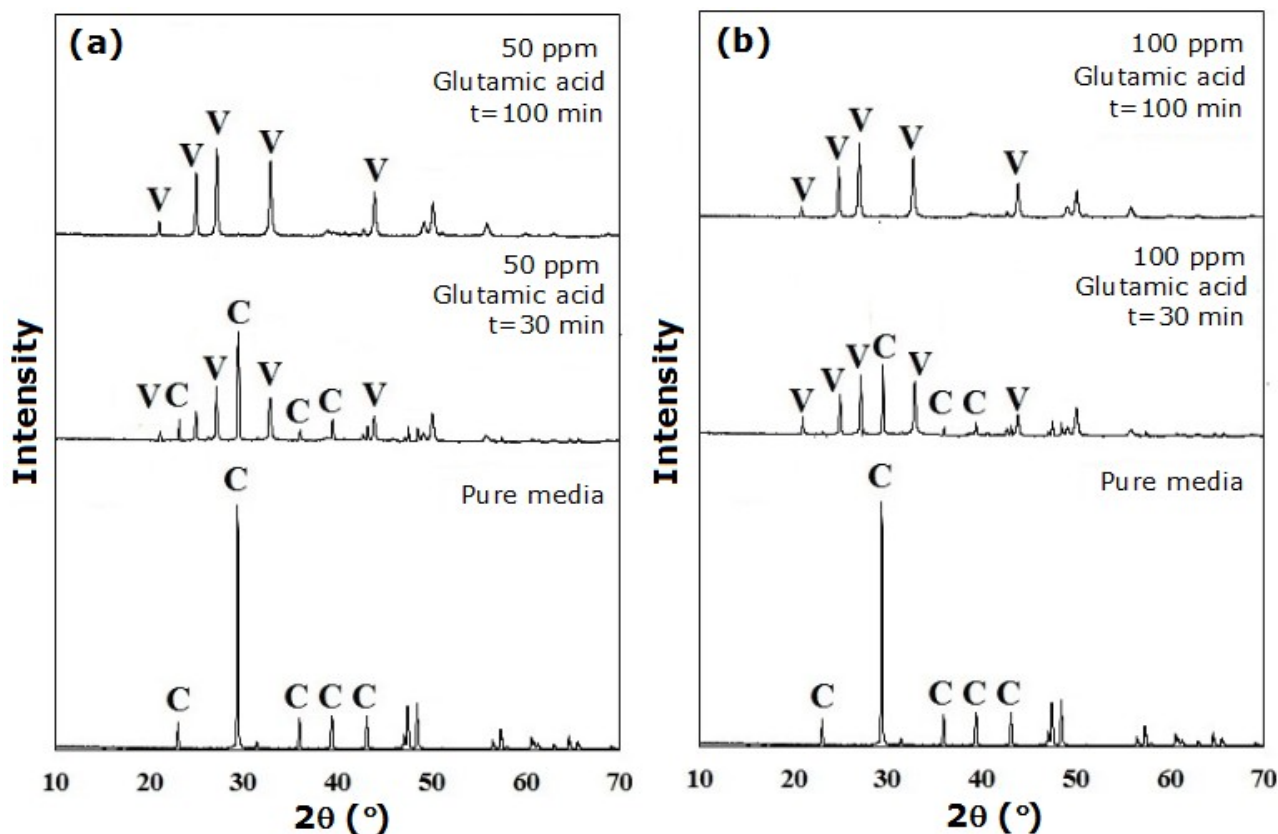


Figure 2. XRD patterns for CaCO_3 crystals acquired in pure media and media supplemented with 50 ppm (a) and 100 ppm (b) glutamic acid.

XRD patterns of the crystals acquired in pure media showed that calcite was the only major crystallization product. All the main characteristic peaks of the crystal products with corresponding faces (012), (104), (110), (113) and (022) were the standard pattern of calcite form (JCPDS: 05-0586). The addition of glutamic acid to the solution led to significant changes in crystal structure and new crystallization products were formed. In addition to the characteristic diffraction peaks of calcite, the new diffraction peaks of vaterite were detected at $2\theta = 21.0^\circ, 24.9^\circ, 27.1^\circ, 32.7^\circ,$ and 50.1° (JCPDS: 33-0268). For the solid sample obtained at 30 min, the characteristics peaks of both calcite and vaterite were seen together. As time goes by, the characteristic peak intensity of vaterite enhanced,

while that of the calcite weakened. At $t=100$ min, the calcite peaks disappeared completely and the vaterite was the only crystallization product at each characteristic point of the system. The XRD results showed that glutamic acid altered the crystal form of CaCO_3 .

FTIR Analysis

The calcite and vaterite polymorphs could be distinguished according to FTIR spectra. The spectra of calcite and vaterite are obviously different. Thus, except for XRD analysis, FTIR analysis was performed to follow the polymorphic phase transformation of CaCO_3 . The FTIR spectra for CaCO_3 crystals with and without glutamic acid are given in Figure 3.

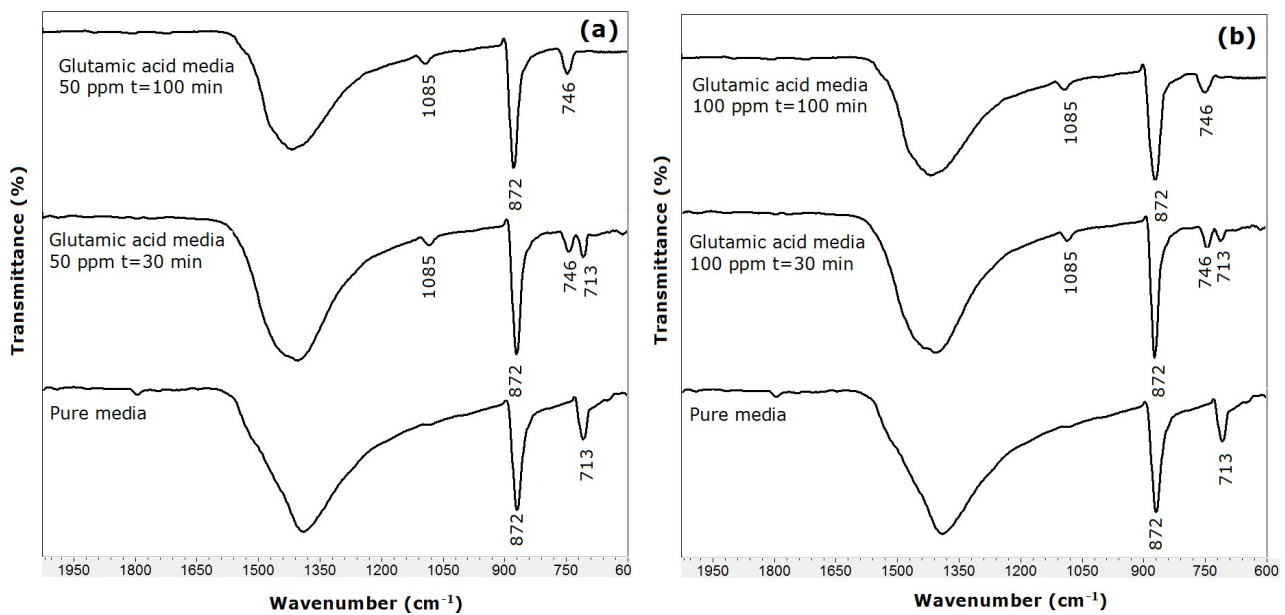


Figure 3. FTIR results for CaCO₃ crystals acquired in pure media and media supplemented with 50 ppm (a) and 100 ppm (b) glutamic acid.

The FTIR spectrum of the CaCO₃ crystals acquired in pure media is very similar in the intensity and position of the main characteristic absorption peak (712 cm⁻¹) with that of calcite form reported by the previous studies (15-17). When the FTIR spectra for the crystals with 50 and 100 ppm glutamic acid at 30 min were examined, new additional absorption bands not in the spectrum of the crystals acquired in pure media were detected at 1085 cm⁻¹ and 746 cm⁻¹ belonged to the vaterite polymorph. The crystal products acquired in the presence of 50 ppm additive concentration were mixtures of calcite and vaterite, and the intensity of the calcite peaks was weaker than the intensity of the vaterite peaks. At higher additive concentration, intensity of the peaks of the calcite was very weak while the

corresponding main absorption peak of vaterite was very strong. FTIR spectra for the crystals acquired at t=100 min showed that the crystal products were all vaterite purely. These results are supported by the XRD patterns.

SEM Analysis

SEM analysis was conducted to explore the effect of glutamic acid and its concentration on the surface character of CaCO₃ crystals. The CaCO₃ crystals acquired in pure media consisted mainly of smooth and uniform cubic-shaped calcite crystals with the mean particle size of 32.0 μm as shown in Figure 4a. The similar morphology of CaCO₃ crystals was observed in the recent studies (18,19).

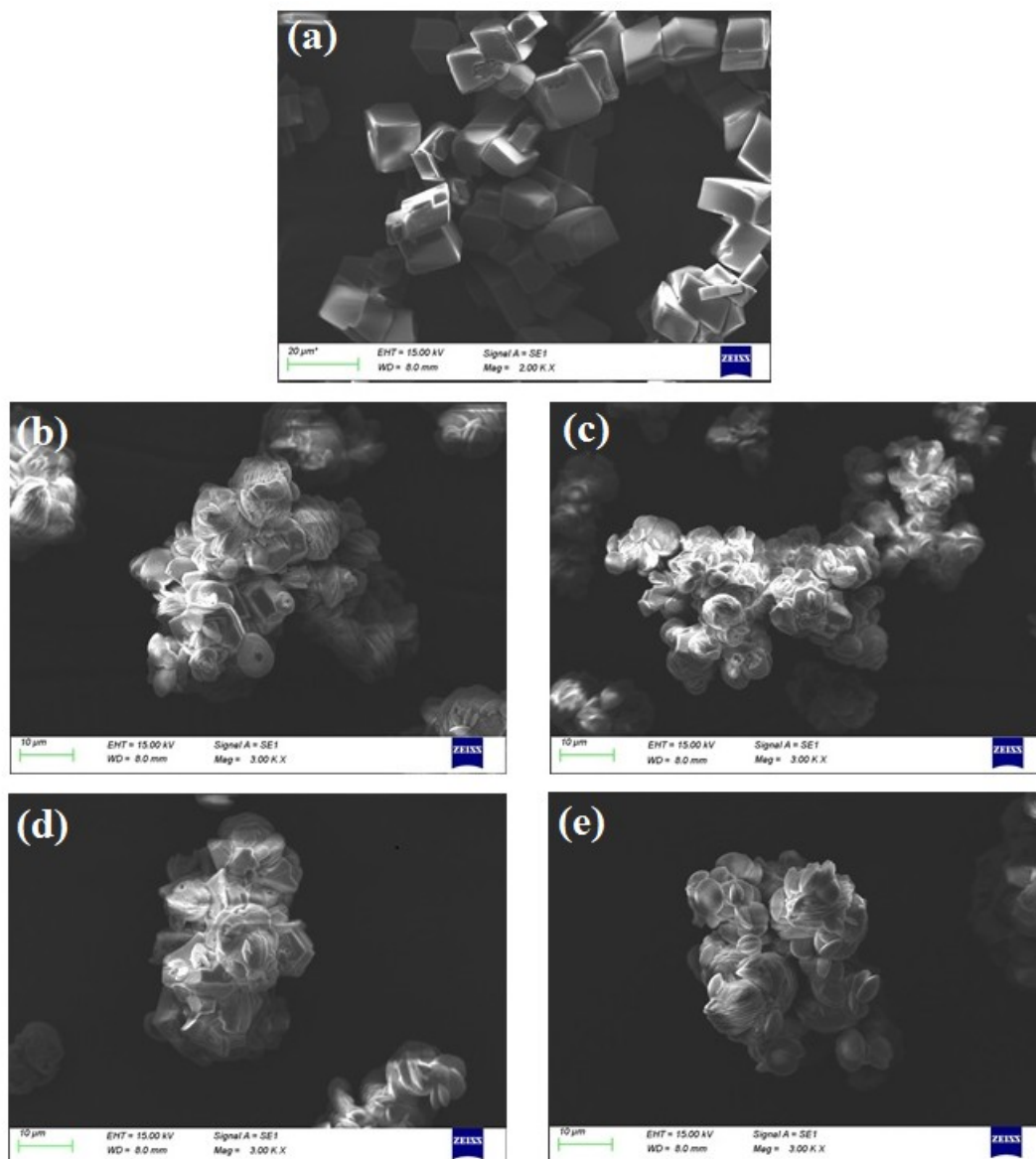


Figure 4. SEM images for CaCO_3 crystals acquired in pure media (a) and media supplemented with 50 ppm glutamic acid at $t = 30$ min (b) and at $t = 100$ min (c) and with 100 ppm glutamic acid at $t = 30$ min (d) and at $t = 100$ min (e).

As can be seen from Figure 4(b-d), the morphological characteristics of the CaCO_3 crystals were directly related to the transformation time and glutamic acid concentration. Examining the SEM image of the crystals with 50 ppm glutamic acid at 30 min (Figure 4b), the cubic-shaped calcite crystals started to change. Alongside the cubic calcite crystals, vaterite crystals with a round appearance started to form. The formed crystals consisted of highly robust agglomerates. As the transformation process continued, the cubic calcite crystals were no longer formed, and all of the crystals were spherical-like vaterite crystals with the rough surface aggregated by many particles (Figure 4c). Moreover, there was a significant increment in the counts of small particles. When the SEM image of the crystal products acquired with 100 ppm additive at 30 min

(Figure 4d) was examined, it was determined that there was more transformation of calcite into vaterite crystals in comparison to the concentration of 50 ppm. However, the two polymorphs were still found together in the same medium, and the obtained crystals had an irregular shape, and some of the crystals formed irregular aggregates. The vaterite crystals grown on the surfaces of the untransformed calcite crystals were in an ellipsoidal form with a plate structure. As the transformation process progressed, the calcite crystals completely transformed to the vaterite and gained a spherical and ellipsoidal appearance (Figure 4e). The surface of the crystals was rough and included a lot of spherical-like particles aggregated. It was also detected that the mean particle size of the final products was smaller in comparison to both pure

and 50 ppm additive media. As shown in Figure 5, the mean particle size of CaCO₃ decreased from 17.9 to 14.6 μm as the glutamic acid concentration increased from 50 to 100 ppm. It can be concluded

that the glutamic acid had a profound effect on the controlling the polymorph, habit, and particle size of the crystals due to its adsorption on the active site of CaCO₃.

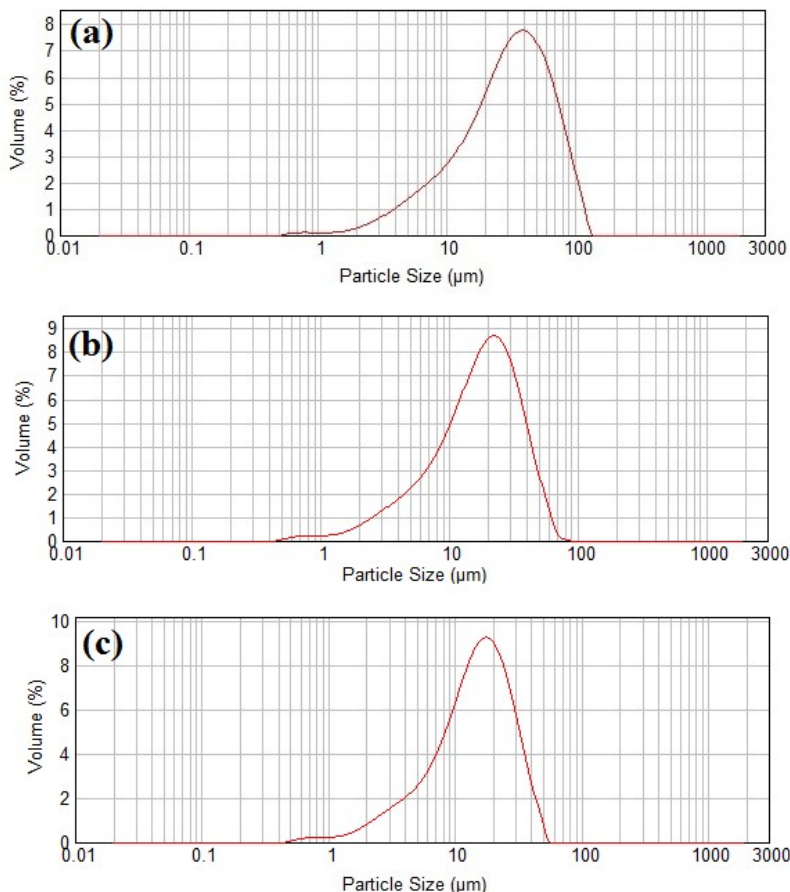


Figure 5. Particle size distributions for CaCO₃ crystals acquired in pure media (a) and media supplemented with 50 ppm glutamic acid (b) and with 100 ppm glutamic acid (c) at t = 100 min.

Zeta Potential Analysis

The zeta potential of the CaCO₃ crystals with and without glutamic acid was investigated to determine

the surface charge of the samples. The results are given in Figure 6. The zeta potential of CaCO₃ crystals acquired in pure media was -8.1 ± 2.1 mV.

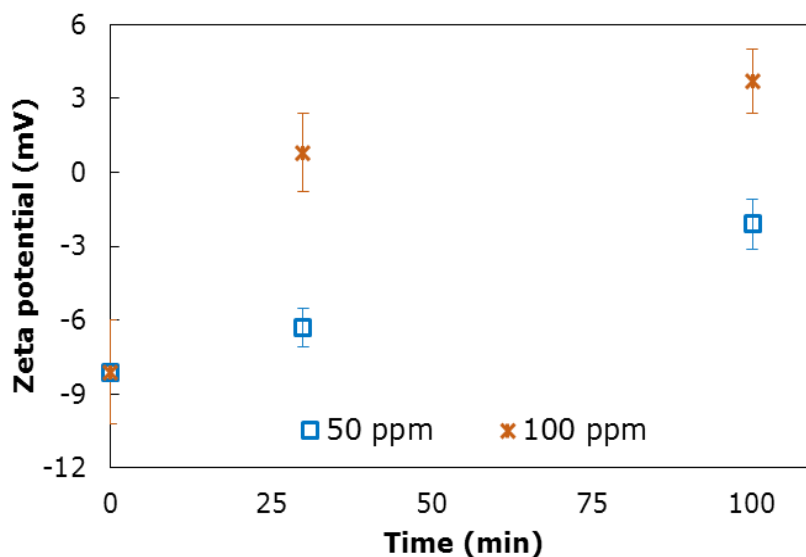


Figure 6. The change of zeta potential with time.

The addition of glutamic acid to the crystallization media led to a distinctive change in surface charge and the zeta potential value at 50 ppm reached -6.3 ± 0.8 and -2.1 ± 1.0 mV for $t=30$ and 100 mins, respectively. The zeta potential value of CaCO_3 crystals acquired in 100 ppm additive media showed a rising tendency and the electrical surface charge was more positive.

Filtration Analysis

Filtration characteristics of CaCO_3 is important for economic considerations, since this characteristic is closely related with energy consumption during the filtration process. Therefore, the filtration property of the CaCO_3 crystals with and without additive was evaluated by Darcy's Law under 700 mbar constant pressure. The average specific cake resistance and the average cake porosity of the CaCO_3 crystals acquired without glutamic acid were 1.03×10^{12} m/kg and 0.548, respectively.

When 50 ppm glutamic acid was added to the crystallization media, the average specific cake resistance decreased to 8.26×10^{11} m/kg. Increasing the additive concentration to 100 ppm caused to significantly reduce the effect on the specific cake resistance (5.01×10^{11} m/kg). This decreasing trend in specific cake resistance can be explained by the changes in the morphology and particle size of the CaCO_3 crystals. In the same time, the average cake porosity increased from 0.589 to 0.703 as the glutamic acid concentration increased from 50 to 100 ppm. Glutamic acid exhibited good performance in promoting the acceleration of filtration and improving the filtration properties of the CaCO_3 crystals.

CONCLUSION

The present study investigated the effect of the glutamic acid on the polymorphic change of CaCO_3 . Specific conclusions drawn from this work include the following:

- The XRD and FTIR results showed that although a calcite structure was created in pure media, a vaterite structure was produced in the presence of glutamic acid.
- According to the SEM and particle size analysis, the additive significantly reduced the size of the crystal and changed its morphology. The mean size of the crystals decreased from 32.0 to 14.6 μm with the use of the additive. It can be suggested that glutamic acid could be used as a crystal size and morphology modifier.
- The results of the zeta potential measurement suggested that glutamic acid increased the positivity of the surface charge of the CaCO_3 crystals.
- The values of the average specific cake resistance were calculated in the range of 1.03×10^{12} to 5.01×10^{11} m/kg.
- It can be concluded that glutamic acid is important for better understanding and controlling the polymorph, size, and morphology of CaCO_3 crystals.

ACKNOWLEDGMENT

Authors would like to acknowledge the Marmara University Scientific Research Projects Commission for financial support. (Project number: FYL-2020-10025)

REFERENCES

1. Zhao Z, Zhang L, Dai H, Du Y, Meng X,

- Zhang R, et al. Surfactant-assisted solvo- or hydrothermal fabrication and characterization of high-surface-area porous calcium carbonate with multiple morphologies. *Microporous Mesoporous Mater.* 2011;138:191-199.
- Butler MF, Frith WJ, Rawlins C, Weaver AC, Heppenstall-Butler M. Hollow calcium carbonate microsphere formation in the presence of biopolymers and additives. *Cryst Growth Des.* 2009;9:534-545.
 - Koga N, Kasahara D, Kimura T. Aragonite crystal growth and solid-state aragonite-calcite transformation: A physico-geometrical relationship via thermal dehydration of included water. *Cryst Growth Des.* 2013;13:2238-2246.
 - Zhang J, Zhou X, Dong C, Sun Y, Yu J. Investigation of amorphous calcium carbonate's formation under high concentration of magnesium: The prenucleation cluster pathway. *J Cryst Growth.* 2018;494:8-16.
 - Trushina DB, Bukreeva T V., Kovalchuk M V., Antipina MN. CaCO₃ vaterite microparticles for biomedical and personal care applications. *Mater Sci Eng C.* 2014;45:644-658.
 - Saulat H, Cao M, Khan MM, Khan M, Khan MM, Rehman A. Preparation and applications of calcium carbonate whisker with a special focus on construction materials. *Constr. Build. Mater.* 2020;236:117613.
 - Aghajanian S, Koironen T. Dynamic modeling and semibatch reactive crystallization of calcium carbonate through CO₂ capture in highly alkaline water. *J CO₂ Util.* 2020;38:366-374.
 - Ševčík R, Pérez-Estébanez M, Viani A, Šašek P, Mácová P. Characterization of vaterite synthesized at various temperatures and stirring velocities without use of additives. *Powder Technol.* 2015; 284:265-271.
 - Jung GY, Shin E, Park JH, Choi BY, Lee SW, Kwak SK. Thermodynamic Control of Amorphous Precursor Phases for Calcium Carbonate via Additive Ions. *Chem Mater.* 2019; 31:7547-7557.
 - Miyashita M, Yamada E, Kawano M. Influence of low-molecular-weight dicarboxylic acids on the formation of calcium carbonate minerals in solutions with Mg²⁺ ions. *J Mineral Petrol Sci.* 2018; 113:207-217.
 - Wang T, Cölfen H, Antonietti M. Nonclassical crystallization: Mesocrystals and morphology change of CaCO₃ crystals in the presence of a polyelectrolyte additive. *J Am Chem Soc.* 2005; 127:3246-3247.
 - Kirboga S, Oner M, Akyol E. The effect of ultrasonication on calcium carbonate crystallization in the presence of biopolymer. *J Cryst Growth.* 2014; 401:266-270.
 - Yang L, Zhang X, Liao Z, Guo Y, Hu Z, Cao Y. Interfacial molecular recognition between polysaccharides and calcium carbonate during crystallization. *J Inorg Biochem.* 2003; 97:377-383.
 - Yao Y, Dong W, Zhu S, Yu X, Yan D. Novel morphology of calcium carbonate controlled by poly(L-lysine). *Langmuir.* 2009; 25:13238-13243.
 - Zheng T, Zhang X, Yi H. Spherical vaterite microspheres of calcium carbonate synthesized with poly (acrylic acid) and sodium dodecyl benzene sulfonate. *J Cryst Growth.* 2019; 528:125275.
 - Wei Y, Xu H, Xu S, Su H, Sun R, Huang D, et al. Synthesis and characterization of calcium carbonate on three kinds of microbial cells templates. *J Cryst Growth.* 2020;547:125755.
 - Abeywardena MR, Elkaduwe RKWHMK, Karunarathne DGGP, Pitawala HMTGA, Rajapakse RMG, Manipura A, et al. Surfactant assisted synthesis of precipitated calcium carbonate nanoparticles using dolomite: Effect of pH on morphology and particle size. *Adv Powder Technol.* 2020;31:269-278.
 - Zheng T, Yi H, Zhang S, Wang C. Preparation and formation mechanism of calcium carbonate hollow microspheres. *J Cryst Growth.* 2020; 549:125870.
 - Fujiwara M, Shiokawa K, Kubota T, Morigaki K. Preparation of calcium carbonate microparticles containing organic fluorescent molecules from vaterite. *Adv Powder Technol.* 2014; 25:1147-1154.



Hirshfeld Surface Analysis, Interaction Energy Calculations of Metal (II) 4-Cyanobenzoate with Nicotinamide / N,N'-Diethylnicotinamide Complexes

Füreyâ Elif Öztürkkan^{1*}, Mustafa Sertçelik¹, Mustafa Yüksek²,
Hacali Necefoğlu³, Tuncer Hökelek⁴

¹Kafkas University, Engineering and Architecture Faculty, Department of Chemical Engineering, Kars, Turkey.

²Iskenderun Technical University, Faculty of Engineering and Natural Sciences, Department of Electrical and Electronics Engineering, Iskenderun, Hatay, Turkey.

³ Kafkas University, Art and Science Faculty, Department of Chemistry, Kars, Turkey.

⁴ Hacettepe University, Faculty of Science, Department of Physics, Ankara, Turkey.

Abstract: Hirshfeld surface analysis, a suitable tool for investigating intermolecular interactions, has been widely used in crystallography in recent years. A breakdown of related fingerprint graphics is presented as a color chart, allowing a quantitative analysis of intermolecular interaction types. In this study, the intermolecular interactions of diaqua-bis(4-cyanobenzoato- κO)bis(nicotinamide- κN^2)cobalt(II) (I), diaquabis(4-cyanobenzoato- κO)bis(nicotinamide- κN^2)copper(II) (II), diaquabis(4-cyanobenzoato- κO)bis(nicotinamide- κN^2)nickel(II) (III), triaqua(4-cyanobenzoato- $\kappa^2 O, O$)(nicotinamide- κN)zinc(II) 4-cyanobenzoate (IV), diaquabis(4-cyanobenzoato- κO)bis(N,N'-diethylnicotinamide- κN)cadmium(II) (V), diaquabis(4-cyanobenzoato- κO)bis(N,N'-diethylnicotinamide- κN)zinc(II) (VI) and *catena-poly*[[aquabis(4-cyanobenzoato- κO)copper(II)]- μ -N,N'-diethylnicotinamide- $\kappa^2 N^2:O$] (VII) complexes, crystal structures were previously determined and investigated by using Hirshfeld surface analysis via CrystalExplorer Program Version 17.5. In addition, the intermolecular interaction energies of the complexes were calculated using CE-HF/3-21G and CE-B3LYP/6-31G (d,p) energy models that involved in CrystalExplorer (CE) software. Related to the obtained Hirshfeld surface analysis results, H \cdots H, H \cdots C/C \cdots H, H \cdots O/O \cdots H, H \cdots N/N \cdots H, C \cdots C, C \cdots N/N \cdots C and C \cdots O/O \cdots C constitute the intermolecular interactions of the complexes. Additionally, N \cdots O/O \cdots N and N \cdots N interactions only in I, II, III, IV and VII complexes, H \cdots Cu/Cu \cdots H, O \cdots Cu/Cu \cdots O only in complexes II and VII and O \cdots O interactions only in complexes II, V and VI were also found. The most significant interactions of all of the complexes were found as the H \cdots H interactions. These results support the existence of π - π interactions between benzene and pyridine rings and medium strength hydrogen bonds which contribute to the stability of the crystal packing of the complexes that are determined by single crystal X-ray diffraction method. Depending on the intermolecular interactions and the energy-framework analysis the O-H \cdots O and N-H \cdots O hydrogen bonds, and π - π stacking and C-H \cdots π interaction energies are the most significant forces in the crystal packaging. The estimation of the intermolecular interactions and electrostatic energy values of the complexes are very important for the classification of them for their electrical, magnetic and optical properties.

Keywords: 4-Cyanobenzoate complex, Nicotinamide, N,N'-Diethylnicotinamide, Hirshfeld surface analysis, Energy Calculations.

Submitted: November 11, 2020. **Accepted:** December 07, 2020.

Cite this: Öztürkkan F, Sertçelik M, Yüksek M, Necefoğlu H, Hökelek T. Hirshfeld Surface Analysis, Interaction Energy Calculations of Metal (II) 4-Cyanobenzoate with Nicotinamide / N,N'-Diethylnicotinamide Complexes. JOTCSA. 2021;8(1):125-36.

DOI: <https://doi.org/10.18596/jotcsa.824551>.

*Corresponding author. E-mail: fozturkkan36@gmail.com.

INTRODUCTION

Non-covalent interactions such as hydrogen bonds, halogen bonds, $\text{CH}\cdots\pi$ and $\pi\cdots\pi$ interactions play important roles in chemical, catalytic, photochemical, crystal engineering, and supramolecular processes (1-4). Particularly, hydrogen bonding interactions such as the $\text{O}\cdots\text{H}$ and $\text{N}\cdots\text{H}$ interactions lead to an increase in the stability of crystal packaging (5). Van der Waals interactions also play a key role in the formation of the supramolecular structures. To understand the nature of non-covalent interactions, many theoretical and experimental researches have been carried out in recent years (3). As a new trend, many of studies were done in the field of theoretical chemistry to investigate the structural, physical and biological properties of materials (6). The CrystalExplorer software is a theoretical calculation program that has been widely used in crystallography for the last decade. Hirshfeld surface analysis presents a visual picture and 2D fingerprint plots of crystalline packaging types and intermolecular interactions (7). Thanks to Hirshfeld Surface analysis, by determining a surface, it is possible to partition the electron density of the crystal into molecular parts and to describe the region in which the molecule is located. In this way, the differences among the complexes related to their intermolecular interactions can be determined. With this analysis, both of the contribution of intermolecular interactions to crystal packaging and whether there are the differences at the intermolecular interactions depending on the crystal structures of the complexes can be identified (8). Besides, a new feature has been added to the Crystal Explorer 17.5 software for calculating the pair-wise interaction energies within a crystal. Energy models of the software can be used at the calculations of the interaction energies of neutral organic molecules, organic salts, solvates, coordination compounds, and radicals (9-11). Herein, the Hirshfeld Surface analysis and Interaction Energy Analysis of diaquabis(4-cyanobenzoato- κO)bis(nicotinamide- κN1)cobalt(II) (**I**) (12), diaquabis(4-cyanobenzoato- κO)bis(nicotinamide- κN^2)copper(II) (**II**) (13), diaquabis(4-cyanobenzoato- κO)bis(nicotinamide- κN^2)nickel(II) (**III**) (13), triqua(4-cyanobenzoato- $\kappa^2\text{O},\text{O}'$)(nicotinamide- κN)zinc(II) 4-cyanobenzoate (**IV**) (14), diaquabis(4-cyanobenzoato- κO)bis(*N,N'*-diethylnicotinamide- κN)cadmium(II) (**V**) (15), diaquabis(4-cyanobenzoato- κO)bis(*N,N'*-diethylnicotinamide- κN)zinc(II) (**VI**) (16) and *catenapoly*[[aquabis(4-cyanobenzoato- κO)copper(II)]- μ

N,N'-diethylnicotinamide- $\kappa^2\text{N}^2:\text{O}$] (**VII**) (17) complexes, which we previously synthesized them and determined their crystal structures, were performed using the CrystalExplorer software. In order to interpret the intermolecular interactions of the complexes, d_{norm} , shape-index, curvedness, 2D fingerprint, and fragment patches of the molecules were plotted. For the energy frameworks analysis of the complex, electrostatic energy (E_{ele}), polarization energy (E_{pol}), dispersion energy (E_{dis}), exchange-repulsion energy (E_{rep}), and total intermolecular energy (E_{tot}) were calculated using two energy models, which were notified as CE-HF/3-21G and CE-B3LYP/6-31G (d,p).

MATERIALS AND METHOD

Hirshfeld surface analysis (9,11) was performed to investigate the visualization of intermolecular interactions of the complexes that we previously synthesized and characterized (see Figure 1 for the structures) (18). Hirshfeld surface (7, 10), 2D fingerprint (11) plots, and interaction energy analysis were obtained using CrystalExplorer Version 17.5 software based on the input crystallographic information file (CIF) (7). The Tonto Quantum Chemistry package involving in the CrystalExplorer (CE) software was used to achieve more accuracy on intermolecular interactions with energy frame analysis (8,19,20). The intermolecular interaction energies of the complexes were calculated using CE-HF/3-21G and CE-B3LYP/6-31G (d,p) energy models in CrystalExplorer software.

RESULTS AND DISCUSSION

Hirshfeld Surface Analysis

Hirshfeld surface analysis, short or long contacts, and intermolecular interactions are visualized by different colors and color intensity (11). The d_{norm} maps of the complexes were given in Figure 2. On the d_{norm} map of the complexes, contacts with a distance shorter than the Van der Waals radii (in close contact) and longer than the Van der Waals radii (in distant contact) were seen as red and blue surfaces, respectively. In addition, distances equal to the sum of the Van der Waals radii were observed as white surfaces (11). 3D Hirshfeld surfaces of the complexes were mapped over d_{norm} in the range of -0.5248-1.5120 a.u (for **I**), -0.6299-1.4753 a.u (for **II**), -0.5207-1.4833 a.u (for **III**), -0.6210-1.4544 a.u (for **IV**), -0.6169-1.6478 a.u (for **V**), -0.5667-1.5939 a.u (for **VI**) and -0.7415-1,5447 a.u (for **VII**) (21).

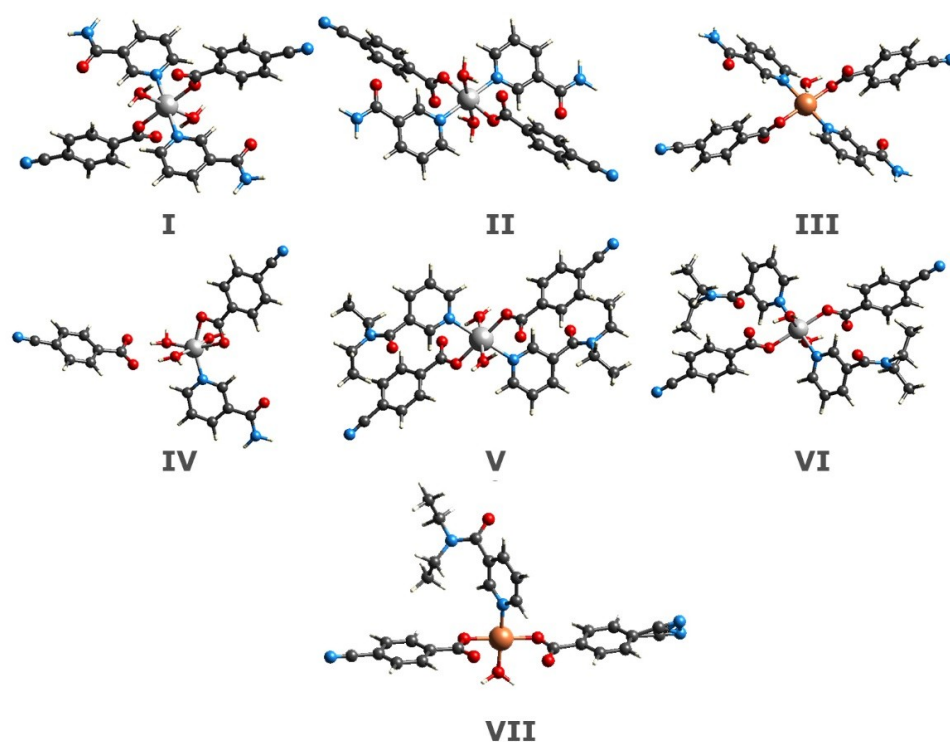


Figure 1. Crystal structure of the complexes.

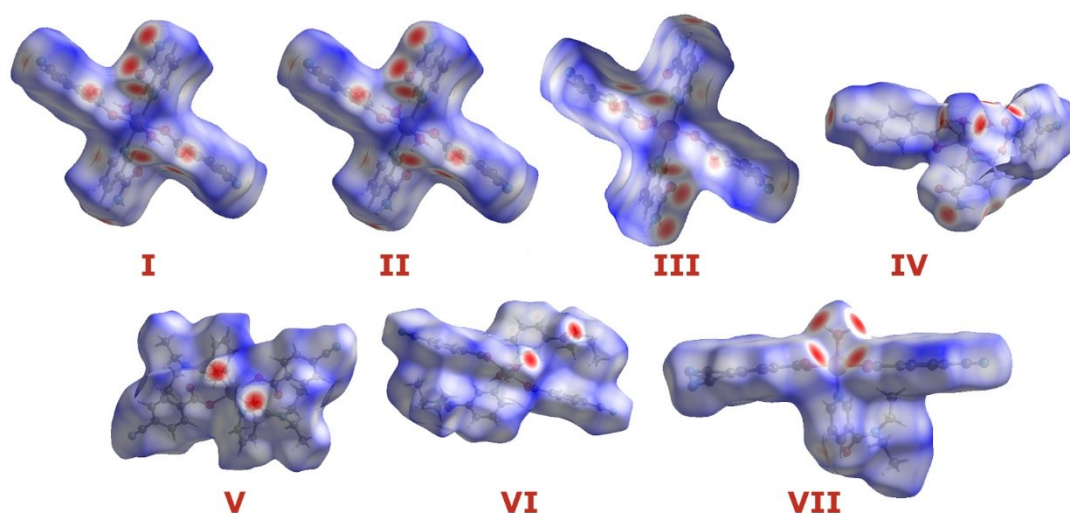


Figure 2. View of the 3D Hirshfeld surfaces of the complexes which were mapped over d_{norm} .

In the shape indexes of the complexes, the acceptor and donor groups have been represented by red and blue regions, respectively (Figure 3). As seen from Figure 3, adjacent red and blue triangles confirm the existence of interactions resulting from π - π stacking among the aromatic rings in the crystal structures of the complexes (21).

In the Hirshfeld surface analysis of the complexes, in Curvedness maps, relatively large green planes

separated by blue edges were observed in the regions where benzene rings of 4-cyanobenzoate ligands and pyridine rings of nicotinamide/*N,N'*-diethylnicotinamide ligands are located. These green planes give us an idea of the flatness of complexes related to π - π stacking and C...C interactions of the rings. The larger green planes were seen in complex **VII** with a monoclinic crystal system compared to complexes **I-VI** that crystallize in the triclinic system (Figure 4) (21).

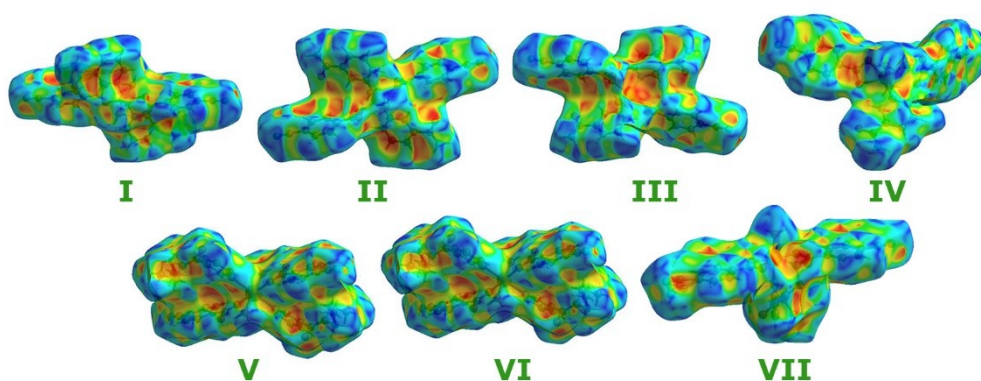


Figure 3. Hirshfeld surface of the complex plotted over shape-index

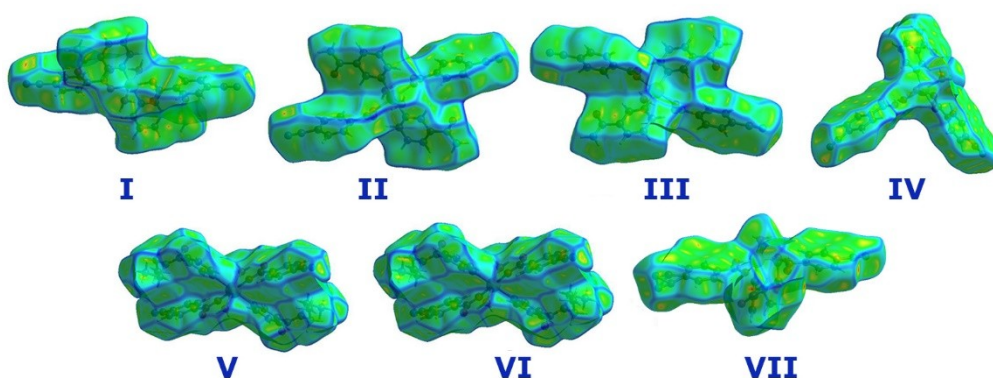


Figure 4. Curvedness maps of the complexes.

2D fingerprint plots for all of the investigated complexes were given in Figure 5. Complexes **I**, **II** and **III** are isostructure. Intermolecular interactions that contribute to the crystal packaging of these three complexes were almost similar (Table 1). The main interaction contribution to the stability of these structures were causing by the $H\cdots C/C\cdots H$ contacts with 27.2 at %. $H\cdots H$ and $H\cdots O/O\cdots H$ were the second and third major interactions, and they contributed to the interactions by approximately 24.0 at % and 19 at %, respectively. According to the crystal structure analysis, $C-H\cdots O$ and $O-H\cdots O$ hydrogen bonds linked the layers together in three dimension networks. As a result, these findings present matchings. The contribution ratios of intermolecular interaction of the three complexes to the crystal package were very close. Differently, only in the complex **III**, the interactions of $H\cdots Cu/Cu\cdots H$ and $O\cdots Cu/Cu\cdots O$ were observed with very small proportion. The most important interaction in complex **IV**, which was another complex with nicotinamide ligand, whose structure was different from these three complexes, is $H\cdots H$ interactions with 32.6 at %. $H\cdots O/O\cdots H$ and $H\cdots N/N\cdots H$ interactions contributed with 20.5 at % (second important interaction) and with 16.2 at % (third important interaction) to the intermolecular interactions in complex **IV**, respectively. These results support the presence of $N-H\cdots O$, $O-H\cdots O$ hydrogen bonds, which bind molecular components

in the crystal structure and make the crystal structure more stable. It was estimated that the $H\cdots C/C\cdots H$ interactions were the most dominant interaction in the other three complexes containing nicotinamide ligand, and these interactions are the fourth major interaction with 13.3 at % in complex **IV**. All of the other interaction percentages that contribute to the crystal architecture were given in Table 1 and plotted in Figures 6 and 7. Although the structures of the three complexes containing *N,N'*-diethylnicotinamide ligand were different from each other, the most important intermolecular interactions for all of the three complexes were the $H\cdots H$ interactions (46.8 at % (for **V**), 45.9 at % (for **VI**) and 33.2 at % (for **VII**)). In the complexes 5 and 6, the second important interactions were the $H\cdots O/O\cdots H$ interactions with 18.4 at % and 19.2 at %, respectively, while the second important interactions in the complex **VII** were the $H\cdots N/N\cdots H$ interactions with 19.5 at % . $H\cdots N/N\cdots H$ interactions with 15.2 at % and 15.3 at % were third important interactions for complex **V** and **VI**, respectively. $H\cdots C/C\cdots H$ interactions with 16.7 at % were third important interactions for complex **VII**. The fourth important interactions were $H\cdots C/C\cdots H$ interactions for the complexes **V** and **VI** and $H\cdots O/O\cdots H$ interactions for the complex **VII**. In complex **VII**, just like complex **III**, the central atom was copper. Similarly, in the complex **VII**, $H\cdots Cu/Cu\cdots H$ and $O\cdots Cu/Cu\cdots O$

interactions were also found. $\text{H}\cdots\text{N}/\text{N}\cdots\text{H}$ and $\text{H}\cdots\text{O}/\text{O}\cdots\text{H}$ interactions confirm the existence of $\text{N}-\text{H}\cdots\text{O}$ and $\text{O}-\text{H}\cdots\text{O}$ hydrogen bonds in crystal structures, while

$\text{H}\cdots\text{C}/\text{C}\cdots\text{H}$ interactions support the interaction of benzene and pyridine rings and $\pi-\pi$ stacking for all investigated complexes.

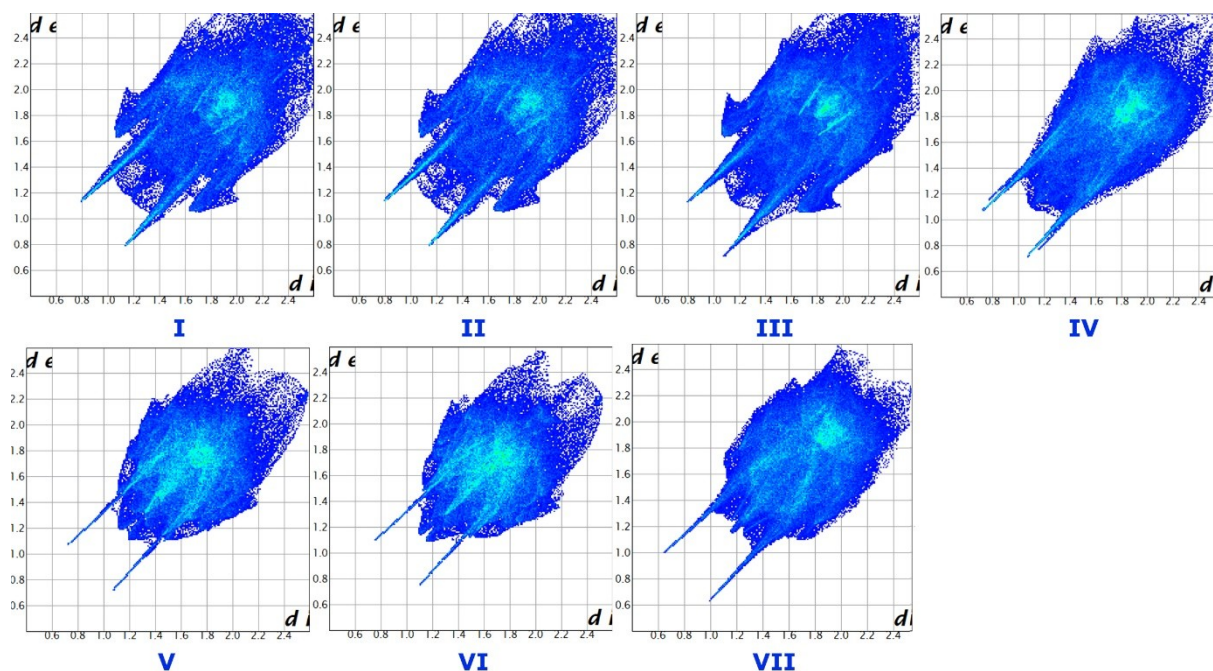


Figure 5. All interactions of two-dimensional fingerprint plots for the complexes I-VII.

Table 1. Intermolecular Interactions of the Complex I-VII.

Interaction	Complex						
	I	II	III	IV	V	VI	VII
$\text{H}\cdots\text{O}/\text{O}\cdots\text{H}$	18.5	20.2	18.6	20.5	18.4	19.0	16.7
$\text{N}\cdots\text{O}/\text{O}\cdots\text{N}$	0.6	0.5	0.5	0.5			0.2
$\text{C}\cdots\text{O}/\text{O}\cdots\text{C}$	1	1.1	0.9	3.4	0.2	0.2	0.6
$\text{H}\cdots\text{H}$	25.4	23.5	25.6	32.6	46.8	45.9	33.2
$\text{H}\cdots\text{N}/\text{N}\cdots\text{H}$	16.3	16.1	16.2	16.2	15.2	15.3	19.5
$\text{H}\cdots\text{C}/\text{C}\cdots\text{H}$	27.2	27.4	27.1	13.3	14.3	14.7	17.7
$\text{N}\cdots\text{N}$	2.0	1.8	1.9	0.4			0.8
$\text{C}\cdots\text{N}/\text{N}\cdots\text{C}$	3.6	4.1	3.8	4.4	2.3	2.2	2.7
$\text{C}\cdots\text{C}$	5.4	4.6	5.4	8.7	2.6	2.6	6.3
$\text{O}\cdots\text{Cu}/\text{Cu}\cdots\text{O}$		0.4					1.4
$\text{H}\cdots\text{Cu}/\text{Cu}\cdots\text{H}$		0.2					0.2
$\text{O}\cdots\text{O}$		0.1			0.2	0.1	0.8

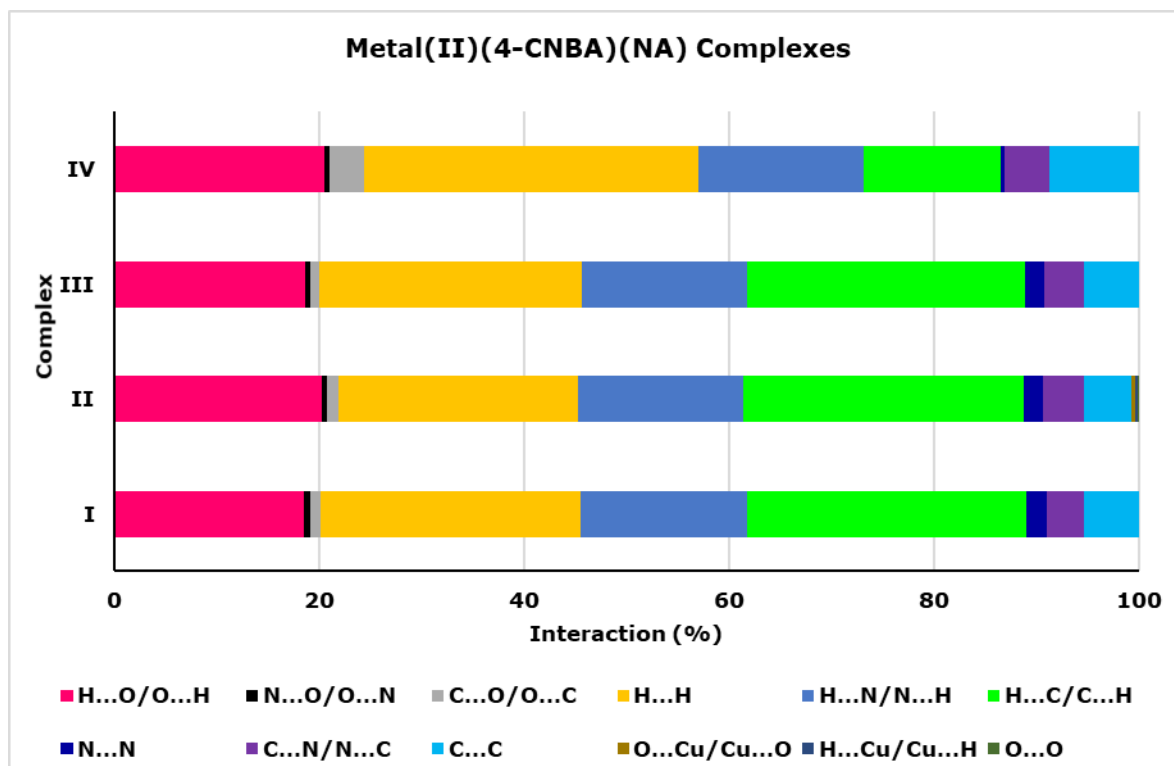


Figure 6. Comparison of the intermolecular interactions of the complex I-IV.

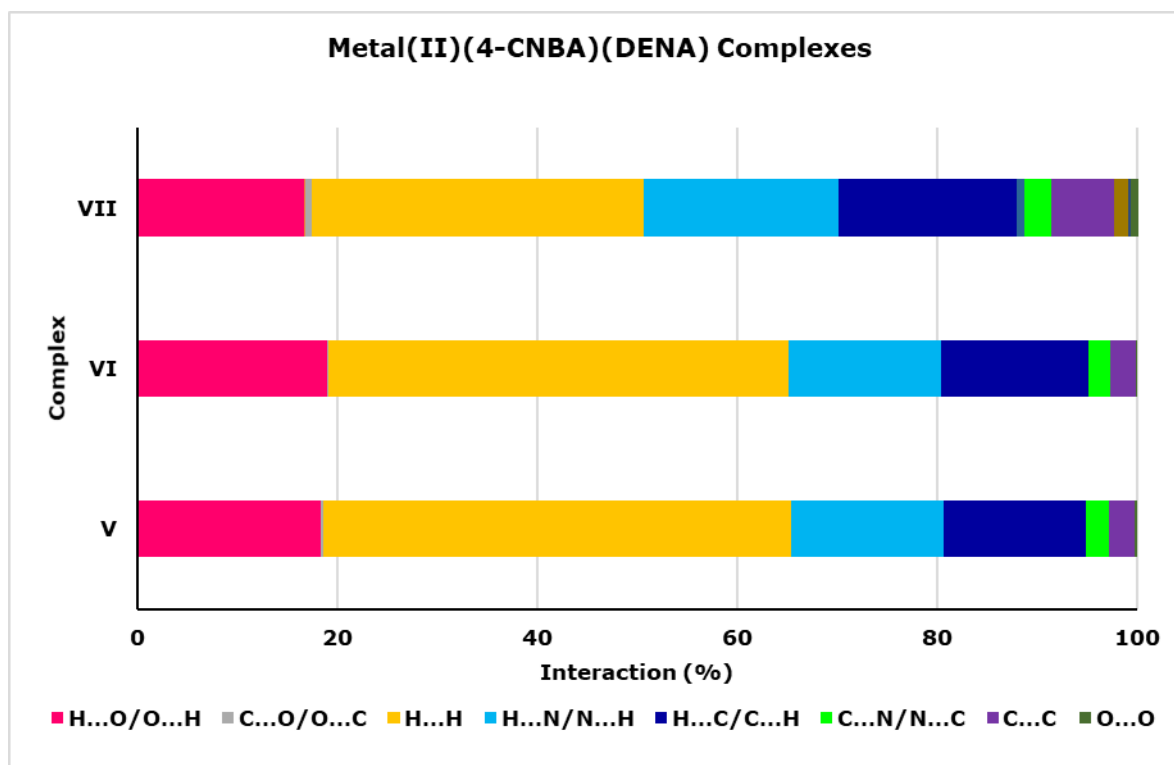


Figure 7. Comparison of the intermolecular interactions of the complex V-VII.

Interactions Energy Analysis

The total intermolecular energy E_{tot} (kJ/mol), which correlative to the reference molecule, is the sum of four main energy component comprising

electrostatic (E_{ele}), polarization (E_{pol}), dispersion (E_{dis}) and exchange-repulsion (E_{rep}). Scale factors, k_{ele} , k_{pol} , k_{disp} , k_{rep} , for B3LYP/6-31G(d,p) electron densities and HF/3-21G electron

densities are used as: 1.057, 0.740, 0.871 and 0.618 kJ/mol and 1.019, 0.651, 0.901 and 0.811 kJ/mol, respectively. As seen from Table 3, energy calculations were made by using CE-HF/3-21G, and CE-B3LYP/6-31G(d,p). Two different energy models of the CrystalExplorer software were used to increase the accuracy of the estimation of the energy values. E_{tot} values of each energy model have shown very similar results in themselves. For complex **V**, the Tonto Quantum Chemistry package could not calculate the B3LYP/6-31G(d,p) model. It was clearly seen from Table 2 that the dispersion (E_{dis}), polarization (E_{pol}) and exchange-repulsion (E_{rep}) and total intermolecular energy (E_{tot}) values have close for all of the models for isostructural complexes **I** and **III**. The total energy values which were calculated for the complex **II**, which have the same structure as these complexes, are different from those of the **I** and **III** complexes. This difference in E_{tot} value can be attributed to the similarity of the electron configuration of the Co and Ni central atoms in complexes **I** and **III**, respectively. While the values of the two energy models are close to each other for the **IV** complex,

these values are very different from those of the other three complexes which have got nicotinamide ligands. In the **VI** complexes which involved *N,N*-diethylnicotinamide ligand, the energy values were calculated in both models, and they revealed close values with each other (Table 3). The agreement at the values of different models for each molecule can be explained by the stability of the reference molecule. However, these values differ significantly in the **VII** complex. According to the results of previous studies, we consider that the results of the B3LYP model are more accurate for this complex, which has a polymeric structure. On the other hand, it was determined that electrostatic energy (E_{ele}) values affect the total energy values. In previous studies, it was reported that the hydrogen bonds contributed to the electrostatic energy. In this study, N-H...O and O-H...O hydrogen bonds and weak C-H... π interactions significantly contribute to electrostatic energy. Like the structures of the three complexes containing *N,N*-diethylnicotinamide ligand, their energy values are also different from each other (20,22-24).

Table 2. Interaction energy values of the complexes **I-IV**.

	N	Symop	R	Electron Density	E _{ele}	E _{pol}	E _{dis}	E _{rep}	E _{tot}	
I	2	x, y, z	13.42	B3LYP/6-31G(d,p)	-31.6	-10.7	-38.3	35.8	-52.6	
	2	x, y, z	14.32	B3LYP/6-31G(d,p)	-69.8	-17.5	-21.0	66.5	-64.0	
	2	x, y, z	7.65	B3LYP/6-31G(d,p)	-73.9	-20.8	-58.7	91.0	-88.5	
	2	x, y, z	10.28	B3LYP/6-31G(d,p)	-2.8	-5.8	-55.2	27.1	-38.6	
	2	x, y, z	9.93	B3LYP/6-31G(d,p)	-67.4	-28.3	-82.6	87.6	-110.0	
					-245.5	-83.1	-255.8	308	-353.7	
	1	x, y, z	13.42	HF/3-21G	-34.4	-12.6	-38.3	26.5	-56.3	
	0	x, y, z	14.32	HF/3-21G	-66.7	-20.5	-21.0	48.2	-61.1	
	1	x, y, z	7.65	HF/3-21G	-91.3	-29.3	-58.7	66.6	-110.9	
	1	x, y, z	10.28	HF/3-21G	1.1	-6.1	-55.2	20.4	-35.9	
0	x, y, z	9.93	HF/3-21G	-73.3	-35.9	-82.6	68.0	-117.3		
				-264.6	-104.4	-255.8	229.7	-381.5		
II	1	-	2.49	B3LYP/6-31G(d,p)	-107.4	-30.9	-21.3	118.6	-81.6	
	1	-	2.49	HF/3-21G	-106.7	-44.7	-21.3	77.2	-94.3	
III	2	x, y, z	7.64	B3LYP/6-31G(d,p)	-71.0	-20.4	-59.8	94.3	-84.0	
	2	x, y, z	14.24	B3LYP/6-31G(d,p)	-70.5	-17.6	-21.3	64.7	-66.1	
	2	x, y, z	10.25	B3LYP/6-31G(d,p)	-2.4	-6.1	-55.4	27.4	-38.4	
	2	x, y, z	9.86	B3LYP/6-31G(d,p)	-71.4	-30.8	-82.9	89.6	-115.1	
	2	x, y, z	13.41	B3LYP/6-31G(d,p)	-32.4	-11.0	-38.8	35.5	-54.2	
	Total					-247.7	-85.9	-258.2	311.5	-357.8
	2	x, y, z	7.64	HF/3-21G	-90.6	-29.3	-59.8	68.4	-109.8	

	2	x, y, z	14.24	HF/3-21G	-67.7	-20.5	-21.3	46.7	-63.7
	2	x, y, z	10.25	HF/3-21G	1.7	-6.0	-55.4	20.6	-35.5
	2	x, y, z	9.86	HF/3-21G	-75.1	-37.9	-82.9	69.7	-119.3
	2	x, y, z	13.41	HF/3-21G	-34.5	-12.7	-38.8	26.3	-57.0
	Total				-266.2	-106.4	-258.2	231.7	-385.3
IV	1	-	8.55	B3LYP/6-31G(d.p)	-94.7	-15.0	-13.4	181.3	-11.0
	1	-	8.55	HF/3-21G	-82.7	-31.6	-13.4	121.0	-18.8

E:interaction energies components, Symop: rotational symmetry operations with respect to the reference molecule, R: the centroid-to-centroid distance between the reference molecule N: interacting molecules as well as the number of pair(s) of interacting molecules with respect to the reference molecule (20).

Table 3. Interaction energy values of the complexes **V-VII**

	N	Symop	R	Electron Density	E_ele	E_pol	E_dis	E_rep	E_tot	
V	2	x, y, z	7.51	HF/3-21G	-47.2	-16.5	-110.3	50.0	-117.7	
	2	x, y, z	8.67	HF/3-21G	-28.4	-10.4	-111.9	48.4	-97.3	
	2	x, y, z	15.3 7	HF/3-21G	-0.3	-1.2	-9.8	1.5	-8.7	
	2	x, y, z	9.86	HF/3-21G	-91.4	-28.1	-33.3	65.7	-88.1	
	2	x, y, z	17.1 6	HF/3-21G	-0.2	-1.6	-20.4	4.3	-16.1	
	Total					-167.5	-57.8	-285.7	169.9	-327.9
VI	2	x, y, z	7.49	B3LYP/6-31G(d.p)	-41.5	-14.3	-112.2	72.7	-107.2	
	2	x, y, z	8.59	B3LYP/6-31G(d.p)	-29.1	-7.9	-112.2	65.1	-94.1	
	2	x, y, z	15.0 7	B3LYP/6-31G(d.p)	0.1	-0.9	-10.7	3.0	-8.1	
	2	x, y, z	9.76	B3LYP/6-31G(d.p)	-73.9	-17.9	-35.7	70.8	-78.7	
	2	x, y, z	16.8 2	B3LYP/6-31G(d.p)	-0.1	-1.7	-20.8	6.2	-15.6	
	Total					-144.5	-42.7	-291.6	217.8	-303.7
	2	x, y, z	7.49	HF/3-21G	-45.0	-16.6	-112.2	54.3	-113.7	
	2	x, y, z	8.59	HF/3-21G	-29.7	-9.9	-112.2	52.3	-95.4	
	2	x, y, z	15.0 7	HF/3-21G	0.4	-1.3	-10.7	2.0	-8.5	
	2	x, y, z	9.76	HF/3-21G	-84.7	-25.6	-35.7	54.1	-91.2	
	2	x, y, z	16.8 2	HF/3-21G	0.3	-1.6	-20.8	4.6	-15.8	
Total					-158.7	-55	-291.6	167.3	-324.6	
	1	-x, -y, -z	6.75	B3LYP/6-31G(d,p)	-554331.1	-189.8	-103.5	-3606.6	-588552.7	

VII	2	-x+1/2, y+1/2, -z+1/2	7.40	B3LYP/6-31G(d,p)	-443441.9	-246.6	-83.9	-4100.8	-471639.7
	2	x, y, z	16.67	B3LYP/6-31G(d,p)	-357281.4	-59.7	-22.7	8301.7	-372689.6
	1	-x, -y, -z	7.51	B3LYP/6-31G(d,p)	-577535.4	-67.8	-44.5	-27937.6	-627974.2
	2	x+1/2, -y+1/2, z+1/2	12.04	B3LYP/6-31G(d,p)	-343411.2	-33.3	-8.0	-524.5	-363444.2
	2	-x+1/2, y+1/2, -z+1/2	14.47	B3LYP/6-31G(d,p)	-461902.7	-48.9	-12.9	-990.7	-489029.1
	2	x, y, z	14.62	B3LYP/6-31G(d,p)	-373681.0	-68.7	-14.4	-1281.6	-395947.9
	1	-x, -y, -z	13.07	B3LYP/6-31G(d,p)	-344634.1	-38.8	-54.8	-679.6	-364877.9
	1	-x, -y, -z	16.99	B3LYP/6-31G(d,p)	-256442.5	-3.0	-10.8	-1855.2	-272294.2
	2	x, y, z	8.02	B3LYP/6-31G(d,p)	-475586.0	-40.5	-28.7	-4542.8	-505698.1
	Total					-4188247,3	-797,1	-384,2	-37217,7
1	-x, -y, -z	6.75	HF/3-21G	-297.8	-100.1	-103.5	235.3	-271.1	
2	-x+1/2, y+1/2, -z+1/2	7.40	HF/3-21G	-38.1	-35.3	-83.9	79.2	-73.1	
2	x, y, z	16.67	HF/3-21G	-1.4	-7.9	-22.7	10.5	-18.5	
1	-x, -y, -z	7.51	HF/3-21G	-40.9	-23.6	-44.5	9.5	-89.4	
2	x+1/2, -y+1/2, z+1/2	12.04	HF/3-21G	2.6	-4.0	-8.0	2.4	-5.2	
2	-x+1/2, y+1/2, -z+1/2	14.47	HF/3-21G	15.2	-6.2	-12.9	3.1	2.4	
2	x, y, z	14.62	HF/3-21G	-3.0	-4.1	-14.4	2.2	-17.0	
1	-x, -y, -z	13.07	HF/3-21G	15.2	-13.0	-54.8	23.4	-23.4	
1	-x, -y, -z	16.99	HF/3-21G	1.1	-3.3	-10.8	4.3	-7.3	
2	x, y, z	8.02	HF/3-21G	1.5	-4.7	-28.7	12.8	-17.0	
Total					-345,6	-202,2	-384,2	382,7	-519,6

E:interaction energies components, Symop: rotational symmetry operations with respect to the reference molecule, R: the centroid-to-centroid distance between the reference molecule N: interacting molecules as well as the number of pair(s) of interacting molecules with respect to the reference molecule (20).

CONCLUSION

In this study, Hirshfeld surfaces and the relationship 2D fingerprint plots of seven complexes, metal(II) 4-cyanobenzoate nicotinamide/*N,N'*-diethylnicotinamide, were investigated. According to Hirshfeld Surface Analysis results, H \cdots O/O \cdots H, C \cdots O/O \cdots C, H \cdots H, H \cdots N/N \cdots H, H \cdots C/C \cdots H, C \cdots N/N \cdots C and C \cdots C interactions are found in Hirshfeld surface of all of the complexes. H \cdots H interactions provide a significant contribution to the crystal packaging of the complexes. H \cdots O/O \cdots H and H \cdots N/N \cdots H interactions also provide a key contribution to the intermolecular interactions of the complexes, and they support the presence of hydrogen bonds in the crystal structures. On the shape-index of the complexes, presences of adjacent red and blue triangles were supported the weak C-H \cdots π and π - π stacking interactions between the benzene and pyridine rings in crystal structures. As a result, it can be said that the results obtained from single crystal X-ray analysis and Hirshfeld surface analysis have supported each other. The polarization (E_{pol}), dispersion (E_{dis}), and exchange-repulsion (E_{rep}) energies were calculated by using two different models of the CrystalExplorer (CE) software. The E_{tot} values calculated for **I**, **II**, **III**, **IV**, **VI**, and **VII** complexes with the B3LYP/6-31G(d,p) energy model were found to be -353.7, 81.6, -357.8, -11.0, -303.7 and -4452147.6 kJ/mol, respectively. These values were also calculated for **I**, **II**, **III**, **IV**, **V**, **VI** and **VII** complexes by using the HF/3-21G energy model, and they were also found to be -381.5, 94.3, -385.3, -18.8, -327.9, -324.6 and 519.6 kJ/mol, respectively. While the E_{tot} values of **I** and **III** complexes which have similar structures are close to each other in both models, it is thought that the different E_{tot} values of the complex **II**, which has isostructural with these complexes, cause by the nature of metal cation. As a result, it was found that the complexes with different structures showed different energy values.

ACKNOWLEDGMENT

The authors would like to thank Ömer Aydoğdu and Gamze Yılmaz Nayir for their valuable contributions.

REFERENCES

- Philp D, Stoddart JF. Self-Assembly in Natural and Unnatural Systems. *Angew Chem Int Ed Engl*. 1996;35(11):1154-96.
- Głowacki ED, Irimia-Vladu M, Bauer S, Sariciftci NS. Hydrogen-bonds in molecular solids - from biological systems to organic electronics. *J Mater Chem B*. 2013;1(31):3742.
- Seth SK, Manna P, Singh NJ, Mitra M, Jana AD, Das A, vd. Molecular architecture using novel types of non-covalent π -interactions involving aromatic neutrals, aromatic cations and π -anions. *CrystEngComm*. 2013;15(7):1285.
- Martin AD, Britton J, Easun TL, Blake AJ, Lewis W, Schröder M. Hirshfeld Surface Investigation of Structure-Directing Interactions within Dipicolinic Acid Derivatives. *Crystal Growth & Design*. 2015;15(4):1697-706.
- Maity T, Mandal H, Bauzá A, Samanta BC, Frontera A, Seth SK. Quantifying conventional C-H \cdots π (aryl) and unconventional C-H \cdots π (chelate) interactions in dinuclear Cu(II) complexes: experimental observations, Hirshfeld surface and theoretical DFT study. *New J Chem*. 2018;42(12):10202-13.
- Kirste B. Applications of Density Functional Theory to Theoretical Organic Chemistry. *Chem Sci J*. 2016 ;7(2).
- M. J. Turner, J. J. McKinnon, S. K. Wolff, D. J. Grimwood, P. R. Spackman, D. Jayatilaka and M. A. Spackman, *CrystalExplorer17* (2017). University of Western Australia.
- Tan SL, Jotani MM, Tiekink ERT. Utilizing Hirshfeld surface calculations, non-covalent interaction (NCI) plots and the calculation of interaction energies in the analysis of molecular packing. *Acta Crystallogr E Cryst Commun*. 2019;75(3):308-18.
- Hirshfeld FL. Bonded-atom fragments for describing molecular charge densities. *Theoret Chim Acta*. 1977;44(2):129-38.
- McKinnon JJ, Jayatilaka D, Spackman MA. Towards quantitative analysis of intermolecular interactions with Hirshfeld surfaces. *Chem Commun*. 2007;(37):3814.
- Spackman MA, Jayatilaka D. Hirshfeld surface analysis. *CrystEngComm*. 2009;11(1):19-32.
- Aşkın GŞ, Necefoğlu H, Yılmaz Nayir G, Çatak Çelik R, Hökelek T. Crystal structure of trans - diaquabis(4-cyanobenzoato- κ O)bis(nicotinamide- κ N 1)cobalt(II). *Acta Crystallogr E Cryst Commun*. 2015;71(5):561-3.
- Özbek FE, Sertçelik M, Yüksek M, Necefoğlu H, Çelik RÇ, Nayir GY, vd. Cu(II) and Ni(II) 4-cyanobenzoate complexes with nicotinamide: Synthesis, spectral, structural and optical characterization and thermal behavior. *Journal of Molecular Structure*. 2017;1150:112-7.
- Aşkın GŞ, Necefoğlu H, Yılmaz Nayir G, Çatak Çelik R, Hökelek T. Crystal structure of triaqua(4-cyanobenzoato- κ 2 O , O ')(nicotinamide- κ N 1)zinc 4-cyanobenzoate. *Acta Crystallogr E Cryst Commun*. 2015;71(6):684-6.
- Akduran N, Sertçelik M, Aydoğdu Ö, Necefoğlu H, Hökelek T. Crystal structure of trans -diaquabis(4-cyanobenzoato- κ O)bis(N , N -diethylnicotinamide- κ

- N)cadmium. *Acta Crystallogr E Cryst Commun.* 2016;72(12):1827-9.
16. Akduran N, Necefoğlu H, Aydoğdu Ö, Hökelek T. Crystal structure of trans -diaquabis(4-cyanobenzoato-κ O)bis(N , N -diethylnicotinamide-κ N)zinc(II). *Acta Crystallogr E Cryst Commun.* 2016;72(10):1374-6.
17. Akduran N, Necefoğlu H, Aydoğdu Ö, Hökelek T. Crystal structure of catena -poly[[aquabis(4-cyanobenzoato-κ O)copper(II)]-μ- N , N -diethylnicotinamide-κ 2 N 1: O]. *Acta Crystallographica Section E Crystallographic Communications.* 2016;72(8):1183-6.
18. Özbek FE, Sertçelik M, Yüksek M, Uğurlu G, Tonbul AM, Necefoğlu H, vd. Synthesis and Crystallographic, Absorption and Emission Studies of 4-Pyridine Carboxamide of Zn(II) 4-Chlorophenylacetate. *J Fluoresc.* 2019;29(5):1265-75.
19. Jayatilaka D, Grimwood DJ. Tonto: A Fortran Based Object-Oriented System for Quantum Chemistry and Crystallography. in: Sloot PMA, Abramson D, Bogdanov AV, Gorbachev YE, Dongarra JJ, Zomaya AY, Eds. *Computational Science — ICCS 2003* [Internet]. Berlin, Heidelberg: Springer Berlin Heidelberg; 2003. p. 142-51.
20. Mackenzie CF, Spackman PR, Jayatilaka D, Spackman MA. CrystalExplorer model energies and energy frameworks: extension to metal coordination compounds, organic salts, solvates and open-shell systems. *IUCrJ.* 2017;4(5):575-87.
21. Spackman MA, McKinnon JJ, Jayatilaka D. Electrostatic potentials mapped on Hirshfeld surfaces provide direct insight into intermolecular interactions in crystals. *CrystEngComm.* 2008;10(4):377-88.
22. Caracelli I, Zukerman-Schpector J, Schwab RS, Silva EM da, Jotani MM, Tiekink ERT. 2-Methyl-4-(4-nitrophenyl)but-3-yn-2-ol: crystal structure, Hirshfeld surface analysis and computational chemistry study. *Acta Crystallogr E Cryst Commun.* 2019;75(8):1232-8.
23. Etse KS, Lamela LC, Zaragoza G, Pirotte B. Synthesis, crystal structure, Hirshfeld surface and interaction energies analysis of 5-methyl-1,3-bis(3-nitrobenzyl)pyrimidine-2,4(1H,3H)-dione. *Eur J Chem.* 2020;11(2):91-9.
24. Madan Kumar S. 3D energy frameworks of dimethylbenzophenone tetramorphs. *Heliyon.* 2019;5(2):e01209.



Hydrothermal Synthesis of Fluorescent Schiff Base Functionalized Carbon Dot Composite for The Removal of Cd(II) Ions from Aqueous Solution: Optical, Equilibrium and Kinetic Studies

Nworie Felix Sunday^{1*}  and Eburnoha Jane Ifeoma¹ 

¹Department of Industrial Chemistry, Ebonyi State University,
PMB 053 Abakaliki, Ebonyi State, Nigeria.

Abstract: The search for nanoparticle metal chelator biomarker has been on the rise in recent years. In this study, bis(salicylidene)ethylenediamine (SALEN) functionalized carbon dot derived from waste banana peels was synthesized using facile hydrothermal technique and the optical biomarker and adsorption properties of the highly fluorescent red nanomaterial was studied. The carbon dot and its functionalized counterpart were characterized using FTIR, SEM/EDX, and UV-Visible spectrophotometry. Evaluation of the optical properties of the yellowish brown carbon dot and reddish highly luminescent functionalized carbon dot indicated band gap energy values of 1.85 and 2.04 eV, respectively. Extraneous variables such as effect of initial metal ion concentration, pH, and contact time were studied in the batch extraction process for the sorption of Cd(II) ions from aqueous solution. The sorption of Cd(II) ion was observed to be highest at pH 5 with 99.3 % removal efficiency. The adsorption isotherm and kinetic models indicated interplay of physisorption and chemisorption processes. The mechanism for the chelation of Cd(II) ions onto the surface of the functionalized carbon dot was mainly governed by inner sphere chelation and ion exchange. Reusability of the material was evaluated using adsorption-desorption experiments. Results of the study indicated the potential of the functionalized carbon dot as (i) semiconductor materials with strong photoluminescence at the visible region which could be used as environmental biomarker and as sensor, and (ii) effective, efficient and low cost adsorbent for remediating Cd(II) ions contaminated environment.

Keywords: Adsorption studies, carbon dot nanoparticle, cadmium, adsorption mechanism, optical biomarker.

Submitted: July 29, 2020. **Accepted:** December 13, 2020.

Cite this: Nworie FS, Eburnoha JI. Hydrothermal Synthesis of Fluorescent Schiff Base Functionalized Carbon Dot Composite for The Removal Of Cd(II) Ions From Aqueous Solution: Optical, Equilibrium and Kinetic Studies. JOTCSA. 2021;8(1):137-54.

DOI: <https://doi.org/10.18596/jotcsa.775739>.

***Corresponding author, e-mail:** nworie.sunday@ebsu.edu.ng, Tel: +234 8034813342.

INTRODUCTION

Deleterious heavy metals such as cadmium pose serious harmful health and environmental hazard as they are regarded as destructive contaminant due to their bio-accumulative and non-degradable properties (1). The anthropogenicity, teratogenicity, and carcinogenicity of cadmium and its implicative role in renal failure and cancer-related deformities have been

widely reported (2). As a result of the health and environmental problems associated with ingestion of cadmium in its bioaccumulation in the ecosystem, its removal from environmental matrices using an eco-friendly technique has remained an enormous task. Recently, researchers have employed several techniques for the removal of heavy metals cadmium inclusive from environmental matrices (3). The commonly used techniques include electrolysis, ion

exchange, chemical precipitation, and adsorption (3-6). The techniques listed are faced with one limitation or the other such as high cost, waste of time, secondary waste generation, and lack of equipment (7). The evolution of nanomaterial technology as an alternative to the techniques has succeeded in proffering solution to the myriads of problems hitherto observed in heavy removal processes (8-9). Nanoparticles is currently the preferred adsorption material due to their unique properties like high surface area, high chemical stability, rapid adsorption potentials, and high adsorption capacity (8). As a consequence, nanoparticles have greater potentials to adsorb metal ions with high adsorption capacity in a rapid batch or column modulated process. There has been rising concern all over the world on waste management practices that is environmentally benign. Carbon dots from waste pectin and alginate sources have been recently researched on (10). A majority of carbon dots have been applied in theranostic purposes and other medical, photocatalytic and fluorescence studies (11). The use of carbon dots in the removal of metal ions from aqueous matrices started lately with current research on the modification in the structural, magnetic and molecular moiety using different conjugants (10,12). The development of excellent functionalized carbon quantum dot nanomaterial for the adsorption of cadmium from aqueous solution has been reported, however, carbon quantum dot is potentially toxic compared to carbon dot (7). The use of hydrothermal synthetic technique in the preparation of carbon dot is advantageous because of relatively mild operating conditions (reaction temperatures < 300 °C), one-step synthetic procedure, environmental friendliness, and good dispersion in solution (1). Studies have noted that carbon dots with surface immobilization exhibit high fluorescent properties whereas the non-functionalized carbon nanoparticles are weakly fluorescent. Consequently, fluorescence results due to surface charge separation with cations and anions (holes and electrons) trapped causing radiative recombination. Carbon dots have been shown to exhibit excellent properties not limited to photostability, chemical inertness, bio-consistency, nontoxicity, bright fluorescence, photodynamic and photo induced redox (electron donor- acceptor) properties (7,13).

Optical properties of nanomaterial and functionalized counterparts have attracted much attention and concern in recent time because of the myriads of their important technological applications, like bioimaging, biosensing, optoelectronics, photocatalysis and water splitting for energy conversion (7, 14). Carbon dots nanomaterial are fluorescent with the functionalized counterpart exhibiting greater fluorescence over the visible spectrum region and little or no extension into

the near-infrared region (15). Carbon dots and its functionalized counterpart have recently emerged as a new hybrid nanoparticle of high fluorescence and gradually replacing the conventional semiconductor quantum dots. This new field of research is rapidly advancing with countless researchers on the synthesis and applications of the non-toxic, low cost and environmentally benign nanomaterial in different technological processes and investigations.

In the work reported in this paper, carbon dot was synthesized from waste banana peels and thereafter functionalized using a bis Schiff base bis(salicylidene)ethylenediamine (SALEN). The SALEN functionalized carbon dot was then characterized using ultraviolet-visible, Fourier transform infrared, scanning electron microscopy, and energy dispersive X-ray to obtain the optical properties, functional group, structural and elemental compositions, respectively. The functionalized carbon dot nanomaterial was further applied for the adsorptive removal of cadmium(II) ions from aqueous solution. The mechanism of the removal of cadmium was investigated using equilibrium and kinetic data after studying the influence of extraneous variables of time, pH and initial metal ion concentration. The chelation mechanism of Cd(II) ions onto the functionalized carbon dot was proposed based on the result from pH analysis.

EXPERIMENTAL SECTION

Materials and methods

Reagents: The following analytical grade reagents were obtained from Merck Germany and used for the synthesis: Cadmium sulfate, hydrochloric acid, aqueous ammonia, salicylaldehyde, ethylenediamine, sodium hydroxide, ethanol.

Apparatus: The following apparatuses were used for measurement and characterization: Drying oven (model DHG) for drying of samples, Buck 205 Scientific Atomic Absorption Spectrophotometer for measurement of concentration of samples, Phenomprox by Phenom world Eindhoven, The Netherlands for structural morphology and elemental composition measurement, Cary 630 Agilent Technologies, USA for functional group determination, UV-Vis Spectrophotometer (model Genesis 10S) was used to obtain electronic spectra of the nanoparticle and functionalized counterpart. Rotary shaker (RF-12 Remi equipment) was used for all equilibrations and shakings.

Methods

Synthesis of the carbon dot from banana peel: Fresh banana peel was obtained from Abakpa main market in Abakaliki, Ebonyi State, Nigeria using polyethylene bags. Carbon dot was prepared using a modified literature method (1). It was washed repeatedly with distilled water, air-dried and the juice extracted using a grinder. In the synthesis, 150 g of the washed banana peel was ground to a paste and squeezed to extract the juice. Exactly 30 mL of the banana peel juice was mixed with 8.0 mL of deionized water and 10 mL of 25% (v/v) NH_4OH solution. The mixture was then transferred into a 250 mL conical flask and heated using a domestic microwave oven for 6 min. Immediately after cooling to room temperature, the mixture was centrifuged at 600 rpm for 30 min and washed several times with double distilled water to remove all the unreacted molecules. Then the carbon dots-based nanoparticle obtained by evaporation was collected and dried at a temperature of 60 °C for 30 min.

Synthesis of bis(salicylidene) ethylenediamine (SALEN): This was prepared according to the literature procedure (16). Ethylenediamine (22.475 g) was gradually added with stirring to 91.336 g of salicylaldehyde in a 500 cm^3 beaker. The yellow crystal formed was recrystallized twice from carbon tetrachloride to give the golden yellow crystals [64.45% yield, mp 121 ± 1 °C].

Synthesis of SALEN functionalized carbon dot: SALEN functionalized carbon dot nanoparticle was obtained by weighing 2.94 g of carbon dot into a 250 mL beaker and 10 mL of the 0.5% SALEN solution added. The mixture was stirred for 6 h at ambient temperature and the SALEN functionalized carbon dot was separated by filtration, washed several times with distilled water to remove unreacted SALEN, and then dried at a temperature of 90 °C for 1 h.

Adsorption studies with the SALEN functionalized carbon dot nanoparticle: Batch experiments were performed to elucidate the metal chelation properties of the SALEN functionalized carbon dot for the preconcentration of Cd(II) ions from aqueous solution. The experiment was conducted to obtain the requisite data by varying different conditions of time of contact, pH and initial metal ion concentration. The metal chelation properties was investigated by adding 0.1 g of the SALEN functionalized carbon dot to 10 mL of different concentrations of cadmium (II) solution (0.0448, 0.448 and 4.48 mg) and the mixture equilibrated at room temperature (30 ± 1 °C) for 3 min using mechanical shaker at 100 rpm and the resulting solution was filtered. The sorption kinetics

was studied by varying the time between 2-6 min while pH was varied between 2-11. To determine the maximum time needed for adsorption and pH of maximum adsorption, 0.1 g of the functionalized carbon dot was mixed with 10 mL of 0.01 M Cd(II) ion in the vessel. In both cases, the mixture was equilibrated at room temperature (30 ± 1 °C) for 3 min using a mechanical shaker at 100 rpm and resulting solution filtered and kept for analysis. Regeneration and reusability experiment was performed to access the economical and eco-friendliness of the composite. In the study, 5 mL of different concentrations of HCl (1, 0.1, 0.01, 0.001 M) were equilibrated with 0.1 g of the Cd(II) loaded nanocomposite at different time intervals of 5, 10, 15, 20, 25, and 30 min. The Cd(II) ion in the combined filtrate after triplicate analysis was determined using AAS. The distribution coefficient (K_d), dosage concentration (S), the adsorption capacity (" α "), percentage of metal chelated (%) of Cd(II) ion and quantity of cadmium chelated (q_t) at time t were evaluated using Equations 1-5 respectively.

$$K_d = \frac{\text{Amount of metal, adsorbent}}{\text{amount of metal, solution}} \times \frac{1}{S} \quad (1)$$

$$S = \frac{m}{V} \quad (2)$$

$$\alpha = \frac{(C_0 - C_e)V}{m} \quad (3)$$

$$\% \text{cadmium, chelated} = \frac{C_0 - C_e}{C_0} \times 100 \quad (4)$$

$$q_t = \frac{(C_0 - C_t)V}{m} \quad (5)$$

C_0 (mg/L), C_e (mg/L), C_t (mg/g), V (L) and m(g) stands for the initial Cd(II) concentration, final concentration of the cadmium(II) ion, concentration of Cd(II) ion at time t, volume of aqueous solution, and weight of SALEN functionalized carbon dot respectively. The simulation of the metal chelation properties was modeled using linear adsorption models of Langmuir and Freundlich. The mass transfer and kinetics of chelation of Cd(II) onto SALEN-functionalized carbon dot was studied by plotting the equation of line of best fit using the simulated data applied to pseudo-first order and pseudo-second order models. The adequacy cum applicability of the design in relation with the best fit model for the process was evaluated using the

coefficient of determination (R^2). To ensure the adequacy, accuracy, and reproducibility of the process, triplicate experiments were conducted and mean values which are reproducible were used for further data simulation.

RESULTS AND DISCUSSION

To assess the nature, composition, structure, optical and adsorbent characteristics of the SALEN functionalized carbon dot and the Cd adsorption from aqueous solution AAS, FTIR, SEM/EDX, and UV-Vis analysis were performed.

EDX Analysis

The percentage elemental composition of the SALEN functionalized carbon dot before and after adsorption as given by EDX analysis is shown in (Table 1 and 2) and (Fig 1 and 2) respectively. The percentage weight concentration of the elements in the SALEN functionalized carbon dot could be seen to be 66.20 % carbon, 15.24 % oxygen, 5.22 % potassium, 3.27 % nitrogen, 1.72 % cadmium, 1.46 % calcium, 1.28 % silicon, 1.15 % chlorine, 0.96 % sulfur, 0.95 % aluminum, 0.91 % iron, 0.78 % phosphorus, 0.58 % magnesium, and 0.29 % sodium. For the cadmium loaded SALEN functionalized carbon dot, the weight concentration of the elements are 57.33% carbon,

11.49% oxygen, 0.48% potassium, 0.83% of nitrogen, 19.19% cadmium, 1.63% calcium, 1.02% silicon, 2.96% chlorine, 1.70% sulfur, 0.87% iron, 0.59% phosphorus, 0.30% sodium, 0.84% aluminum, and 0.31% magnesium. From the result, it could be observed that the weight of Cd increased from 1.72% before adsorption to 19.19% after adsorption indicating the entrapment of the element onto the microporous nanoparticle.

Table 3 shows the surface polar functional group, hydrophobicity, and cation exchange capacity of the SALEN functionalized and unfunctionalized carbon dot nanomaterial. The result indicated higher atomic ratios of (O+N)/C for the SALEN functionalized carbon dot nanomaterial than the unfunctionalized counterpart. The implication is that the functionalized carbon dot has greater surface polar groups and would lead to greater adsorption capacity compared to the unfunctionalized counterpart as more binding sites are exposed for conjugation and entrapment of both anionic and cationic species. The high O/C atomic ratios of the functionalized carbon dot in relation to the unfunctionalized counterpart indicated high cation exchange capacity, low hydrophobicity of the functionalized nanomaterial and greater metal chelation ability (4).

Table 1: EDX of SALEN functionalized carbon dot (CD2) showing elemental composition (%).

Atomic Number	Element Name	Atomic Conc.	Weight Conc.
6	Carbon	77.59	66.20
8	Oxygen	13.41	15.24
19	Potassium	1.88	5.22
7	Nitrogen	3.29	3.27
48	Cadmium	0.22	1.72
20	Calcium	0.51	1.46
14	Silicon	0.64	1.28
17	Chlorine	0.46	1.15
16	Sulfur	0.42	0.96
13	Aluminum	0.49	0.95
26	Iron	0.23	0.91
15	Phosphorus	0.35	0.78
12	Magnesium	0.34	0.58
11	Sodium	0.18	0.29

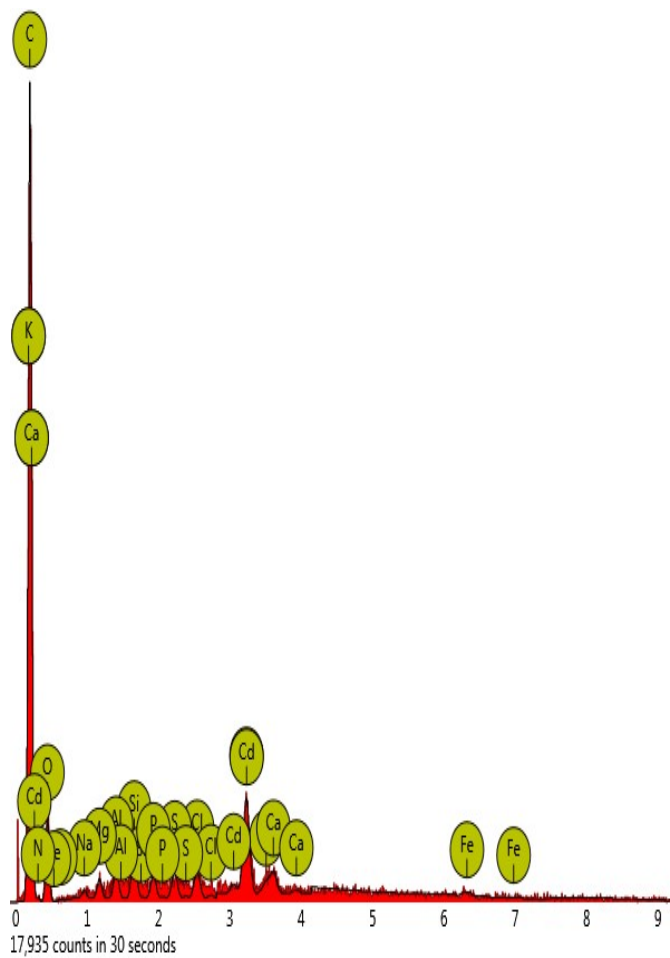


Figure 1: EDX of SALEN functionalized carbon dot(CD2)showing elemental composition.

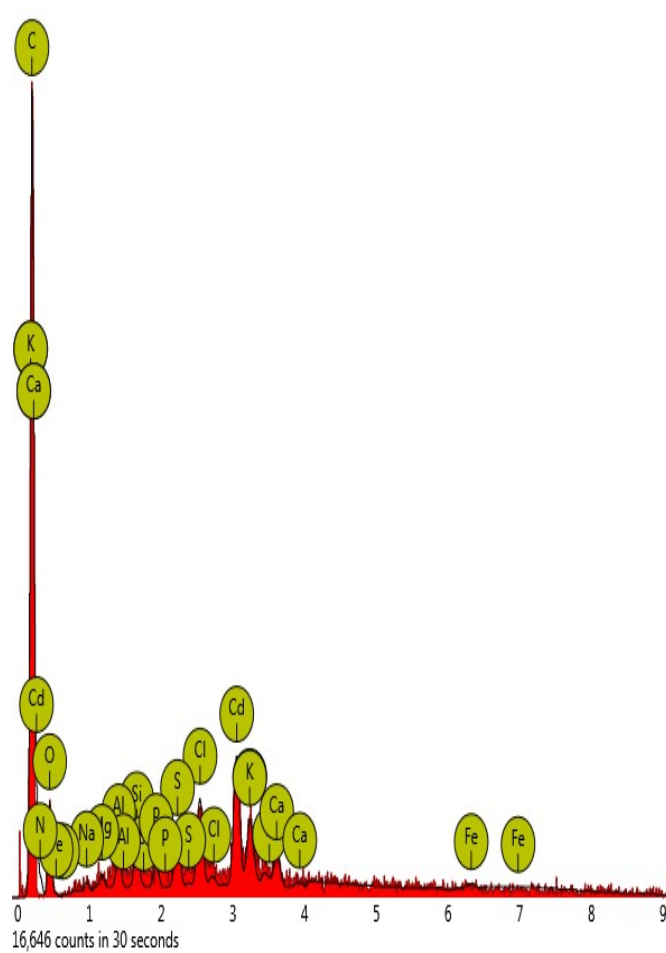


Figure 2: EDX of cadmium loaded SALEN functionalized carbon dot showing elemental composition.

Table 2: EDX of cadmium-loaded carbon dot (CD3) showing elemental composition (%)

Atomic Name	Element	Atomic Conc.	Weight Conc.
6	Carbon	78.68	57.33
48	Cadmium	2.81	19.19
8	Oxygen	12.29	11.94
17	Chlorine	1.38	2.96
16	Sulfur	0.87	1.70
20	Calcium	0.67	1.63
14	Silicon	0.60	1.02
26	Iron	0.26	0.87
13	Aluminum	0.51	0.84
7	Nitrogen	0.98	0.83
15	Phosphorus	0.31	0.59
19	Potassium	0.20	0.48
12	Magnesium	0.21	0.31
11	Sodium	0.22	0.30

Table 3: Comparison of the surface polar functional group, cation exchange capacity and hydrophobicity of SALEN functionalized and unfunctionalized carbon dot.

	Carbon (C)	Oxygen (O)	Nitrogen (N)	(O+N)/C	O/C
Functionalized carbon dot	77.59	13.41	3.29	0.22	0.17
Unfunctionalized carbon dot	78.68	12.21	0.98	0.17	0.15

SEM Analysis

The surface morphology of the SALEN functionalized and cadmium loaded SALEN-functionalized carbon dot nanoparticle was characterized using SEM/EDX and the micrograph shown in Figures 3 and 4, respectively. The microporous structure was observed with 10000 X resolution and the image was taken with a particle size of 10 μm . The SEM images of carbon dot from banana peel showed that it contained an irregular porous surface. Figures 3 and 4 represent SEM micrograph of the CD2 and CD3, respectively, at different magnifications. From the SEM image of CD2 it could be observed that the surface morphology is rough, irregular and highly corrugated providing enough micropores that could enhance adsorption. Similar observations have been made on related agricultural biowaste of saw dust and brewers spent grain (5, 17). The SEM image of CD3 could be seen as clusters of small particles not originally present on CD2. This could be the indication of Cd ions adsorbed to the surface of the nanoparticle. Similar observation have been made previously on the utilization of agrowaste material for the toxic hexavalent chromium removal (18).

FTIR Analysis

The result on FTIR indicating the surface functional groups as in Figures 5-7 revealed a number of absorption peaks characteristic of a complex structure. A broad band representing hydroxyl group(-OH) was observed at 3265.1 cm^{-1} for carbon dot nanoparticle which shifted to 3261.4 cm^{-1} upon immobilization with SALEN and then to 3251.7 cm^{-1} after adsorption with Cd. This band was attributed to O-H stretching vibration present in polymeric species such as lignin and is due to intra and intermolecular hydrogen bonding (17). This is an indication of free hydroxyl groups at the surface of the functionalized carbon dot nanoparticle and its functionalized counterpart (16). The bands observed at 2926.0, 2922.2, and 2926.0 cm^{-1} for CD1, CD2 and CD3, respectively, could be that of aliphatic C-H groups (5).

The band observed at 1625.1, 1606.5, and 1606.0 cm^{-1} for CD1, CD2, and CD3, respectively, could be attributed to the carbonyl group (C=O) of unionized carboxylate stretching of carboxylic group while the peaks observed at 1028.7, 1021.3 and 1025.0 cm^{-1} for CD1, CD2 and CD3, respectively, could be assigned to C=C phenolic ring stretching vibration from lignin (17). The band observed at 1371.7, 1371.7 and 1375.4 cm^{-1} for CD1, CD2, and CD3 respectively could be assigned to C-N stretching of the amine group (5, 17). The intense band of 1244.9 and 1148.0 cm^{-1} observed between 2000-400 cm^{-1} region for CD1 and CD2 could have probably arisen from polysaccharide and could be assigned to C-O, C=C or C-C-O stretching vibration of ether group of cellulose, hemicellulose or lignin (5, 17). The band that extends from 887.1 and 887.1 cm^{-1} to 738.0 cm^{-1} respectively for CD2 and CD3 could be ascribed to ester vibration of mono-substituted aromatic rings (17). Spectral band shift as observed in CD1, CD2 and CD3 is a confirmation of the immobilization of SALEN to the carbon dot and adsorption of Cd to the SALEN functionalized carbon dot nanoparticle.

Optical / biomarker properties of the nanoparticle

The UV-Visible spectra of the CD1 and CD2 is displayed in Figures 8 and 9. The carbon dot has a single absorption peak at 332 nm attributed to $\pi \rightarrow \pi^*$ transition of C=C characteristic of all carbon dot nanoparticles (15). The absorption band of the carbon dots upon immobilization with a dopant SALEN was centred at 370 nm assigned to $n \rightarrow \pi^*$ transition of C=O characteristic of N doped carbon dot nanomaterials (19-20). The cadmium loaded carbon dot showed strong reddish color which is attributed to tuneable photoluminescence character of amine moiety bonded carbon dots resulting from nucleophilic substitution and orbital resonance of the nitrogen conjugated system (15). The absorption coefficient, refractive index, reflectance, transmittance and dielectric constant values were evaluated using Eqs 6-10 (15).

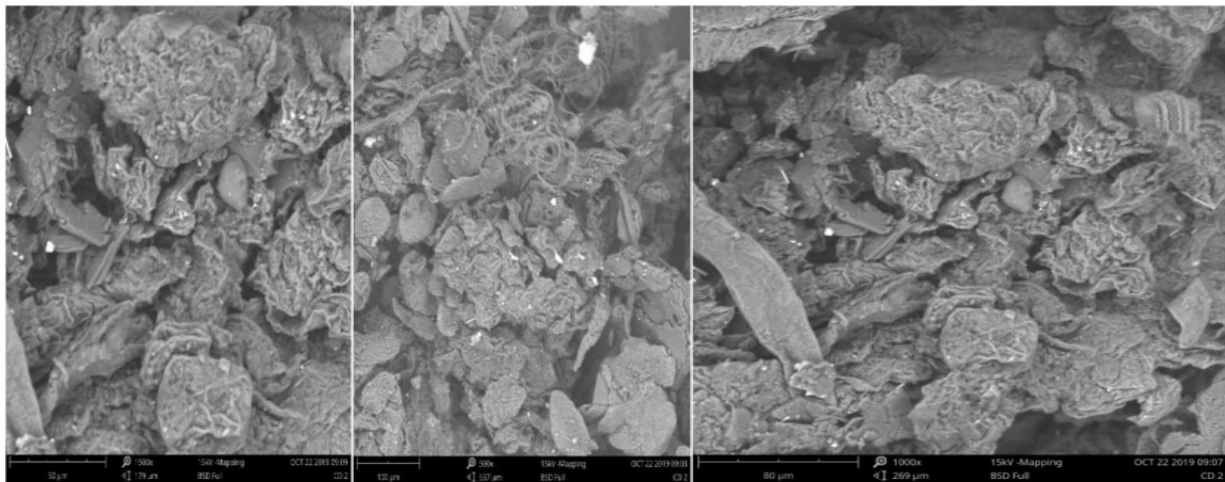


Figure 3: SEM Micrographs of SALEN functionalized carbon dot nanoparticle at different magnifications.

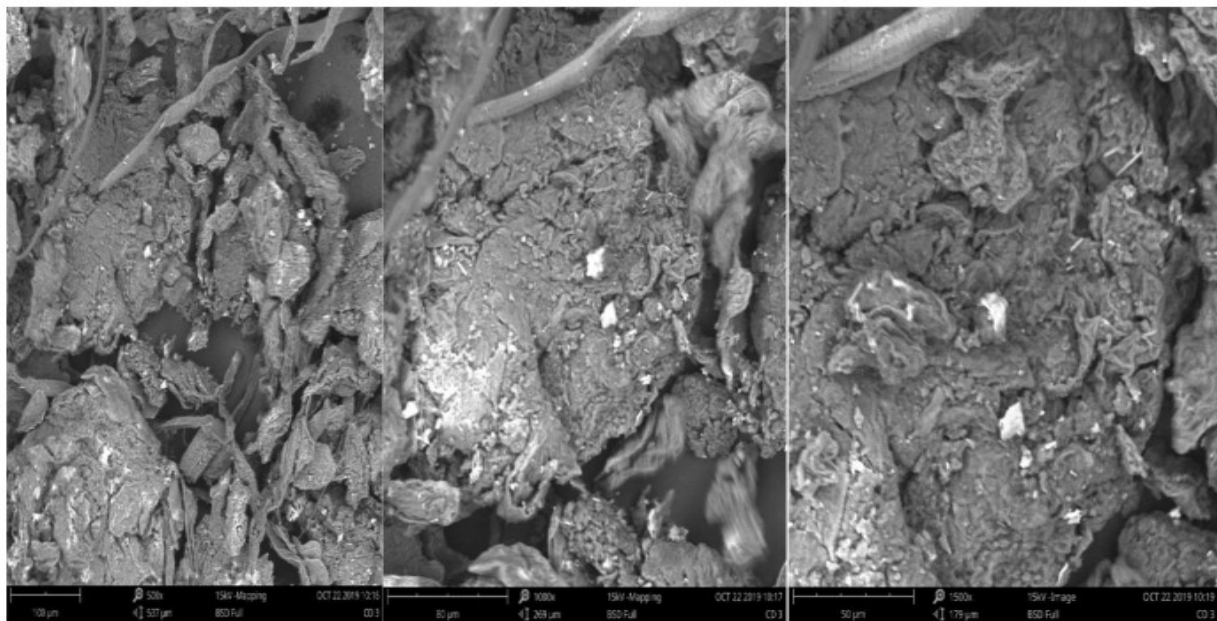


Figure 4: SEM Micrographs of cadmium loaded SALEN functionalized carbon dot nanoparticle at different magnifications.

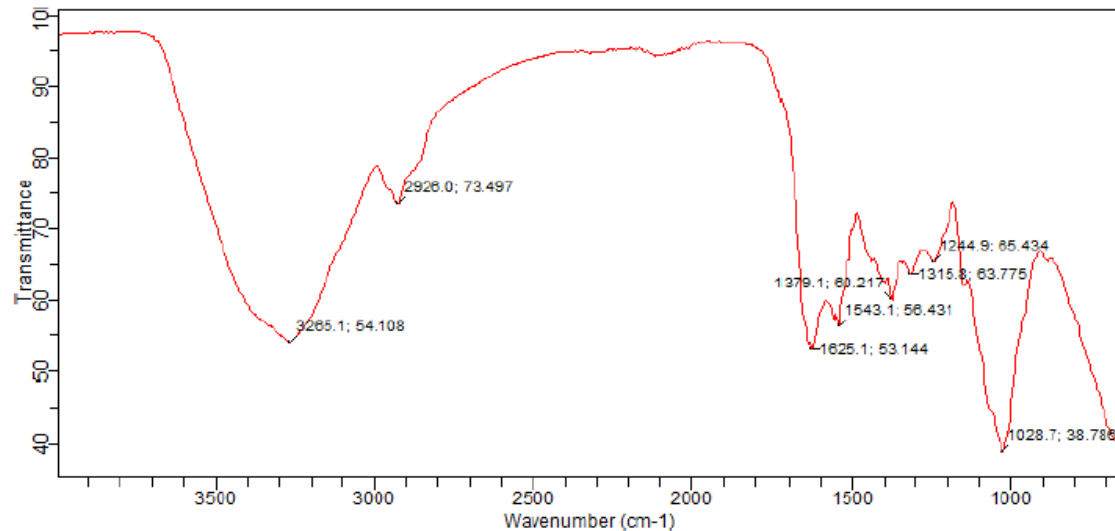


Figure 5: FTIR Absorption Bands (cm⁻¹) of carbon dot nanoparticle (carbon dot = CD1).

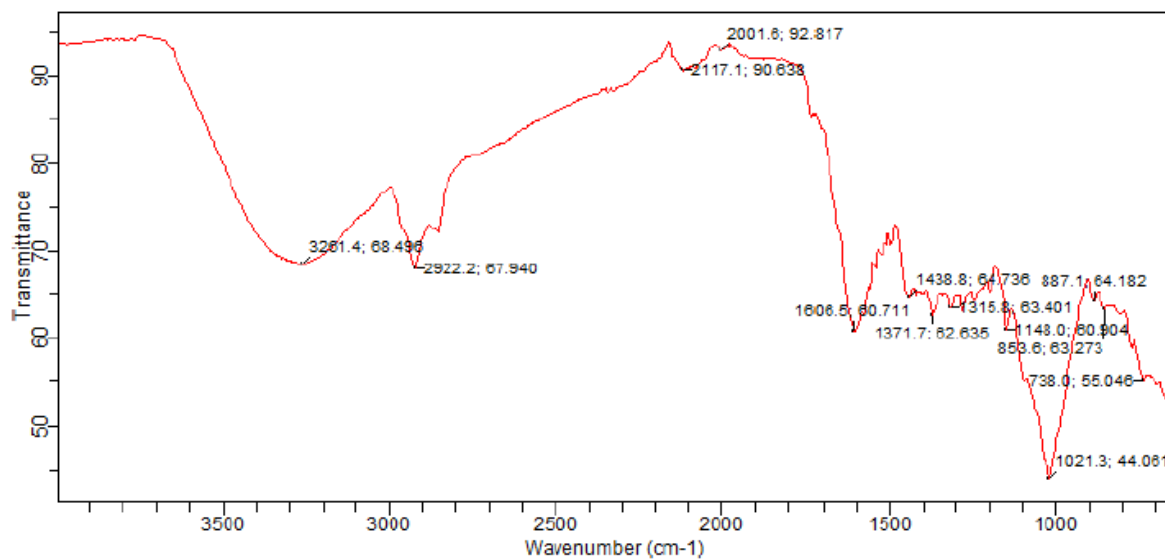


Figure 6: FTIR Absorption Bands (cm⁻¹) of SALEN-functionalized carbon dot (CD2).

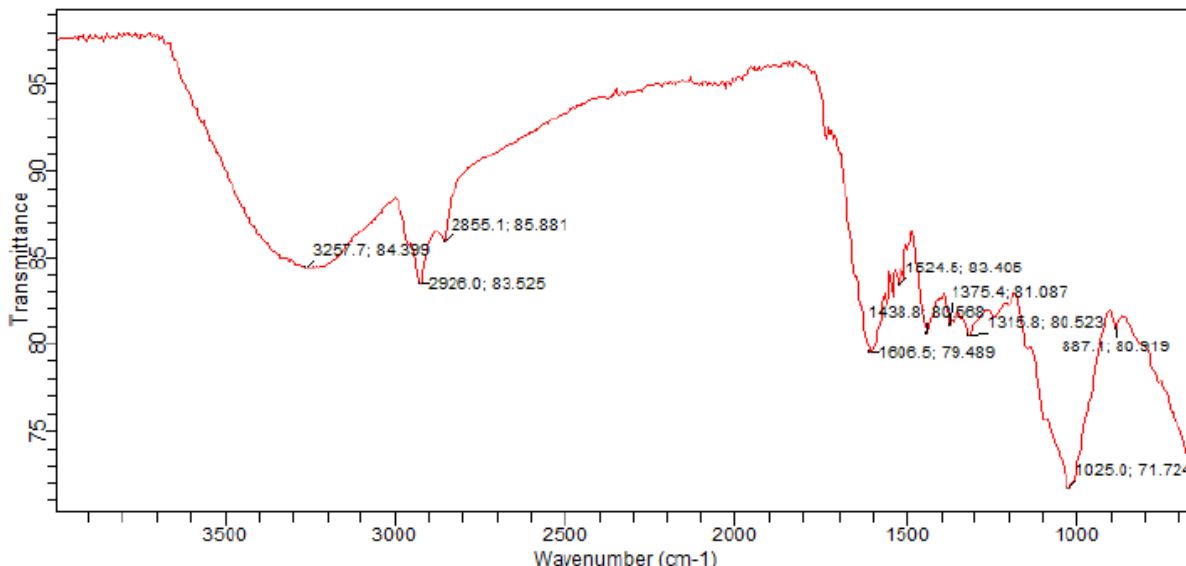


Figure 7: FTIR Absorption Bands (Cm⁻¹) of Cadmium loaded SALEN functionalized carbon dot (CD3).

$$\alpha = 2.303 \times \frac{A}{T} \tag{6}$$

$$n = \frac{1+R^{1/2}}{1-R^{1/2}} \tag{7}$$

$$R = 1 - (A+T) \tag{8}$$

$$A = \log\left(\frac{1}{T}\right) \tag{9}$$

$$\epsilon = n^2 \tag{10}$$

Where α , A, T, R, n, and ϵ represent absorption coefficient, absorbance, transmittance, reflectance, refractive index, and dielectric constant, respectively. The absorption coefficient of the functionalized and unfunctionalized carbon dot was evaluated to be 0.03347 and 0.00167, respectively. The result indicated that the functionalized carbon dot is a better optical material as the presence of the N-dopant (SALEN) has increased the orbital resonance effect of the nanomaterial. The refractive index value of 3.44 and 3.52 of the functionalized and unfunctionalized carbon dot indicated a direct forbidden transition of the nanomaterial and its N doped counterpart (19). The reflectance, refractive index and dielectric constant of 0.302, 0.688, and 11.86, respectively, of

the functionalized and 0.3044, 0.6906 and 12.39, respectively, of the unfunctionalized counterpart indicated that they are strong sensing nanodot and could be used in bioimaging and biotracking especially in theranostic studies. The band gap energy (E_g) was determined using the Herve-Vandamme relations (Eq 11) (19).

$$n^2 = 1 + \left(\frac{A}{E_g + B}\right)^2 \tag{11}$$

Where A and B are constants with values of 13.6 eV and 3.34 eV, respectively, and n the refractive index.

The band gap energy of the functionalized carbon dot was obtained to be 2.04 eV and the unfunctionalized carbon dot was evaluated to be 1.85 eV characteristic of luminescence semiconductor materials with strong photoluminescence at the visible region (15, 21). The band gap energy of the functionalized nanomaterial was observed to be greater than the unfunctionalized probably because of optical band enhancement due to increased chelation or functionalization of the amine group and introduction of SALEN moiety impurity which modified the state of the carbon dot surface. The unfunctionalized carbon dot that is UV excited at 332 nm was strongly yellowish brown in color with tunable photoluminescence character from brownish to reddish emission and tunable band gap energy after conjugation through nucleophilic substitution with imine of Schiff base to form the functionalized highly luminescent carbon nanodot.

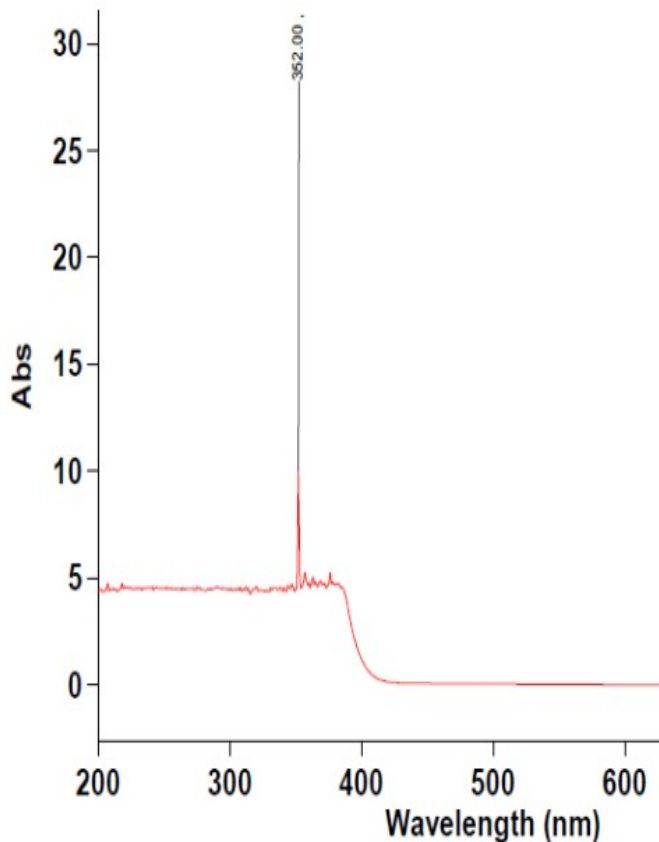


Figure 8: UV-Visible spectrum of banana peel carbon dot nanoparticle.

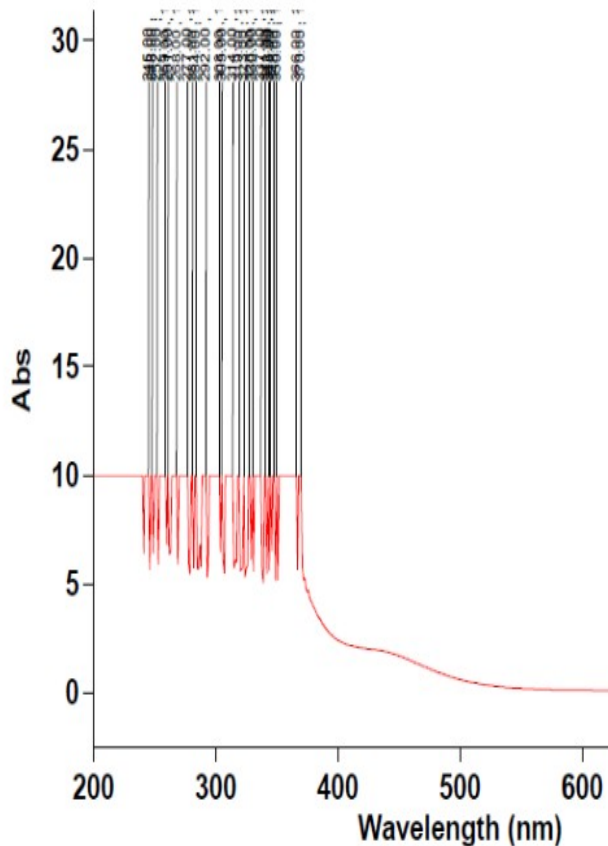


Figure 9: UV-Visible spectrum of SALEN-functionalized carbon dot.

Effect of initial amount of Cd(II) ions

The effect of initial amount of Cd(II) ions captured on the surface of the functionalized carbon dot is illustrated in Fig 10. The study employed initial amounts of 0.0448, 0.448, and 4.48 mg. The percentage amount of Cd(II) ions adsorbed onto the functionalized carbon dot increased to maximum at

4.48 mg from 0.0448 mg at pH 5 and equilibration for 3 min. The adsorptive sites of functionalized carbon dot were gradually filled up due to increase in the amount of Cd(II) ions adsorbed onto the surface until no more exposed surface resulting from intermolecular hydrogen bonding and hence regress in the amount adsorbed (22).

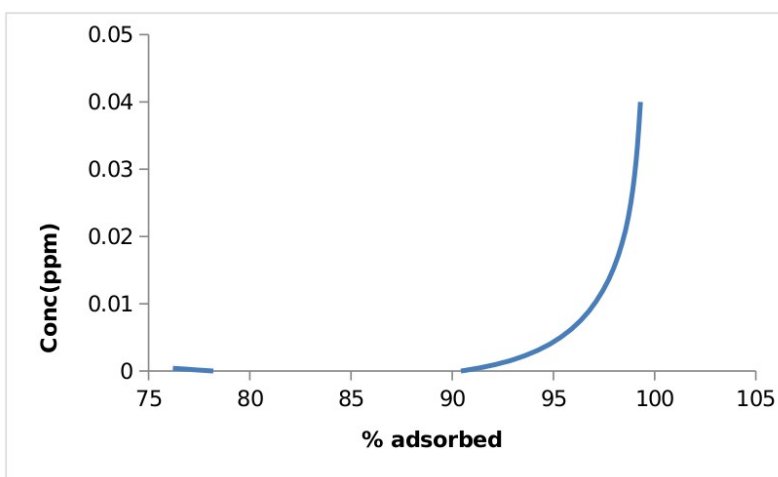


Figure 10: The effect of initial metal ion concentration on the percentage amount of Cd(II) chelated on the surface of the functionalized carbon dot at pH 5.

Effect of contact time

The adsorption of Cd(II) ions onto the functionalized carbon dot at the pH of 5 and initial Cd(II) ion concentration of 0.0448 mg was varied at different contact time as shown in Figure 11. As observed in the plot of percentage amount (%) of Cd(II) ions adsorbed on the functionalized carbon dot against time, there was increase in contact time until equilibrium was attained at 3 min. As time of contact was further increased, there was no significant change in the percentage amount of Cd(II) adsorbed.

Reaching equilibrium for the functionalized nanosized adsorbent was rapid and remained fairly constant, implying the presence of uniform adsorption site which upon saturation by the adsorbate through hydrogen bonding and dipole-dipole interactions was filled up without more spaces or binding sites to occupy (22-23). The maximum adsorption indicating saturation point was observed at equilibrium and for a nano-based material it has been observed in similar study to lie at the same range (23-25).

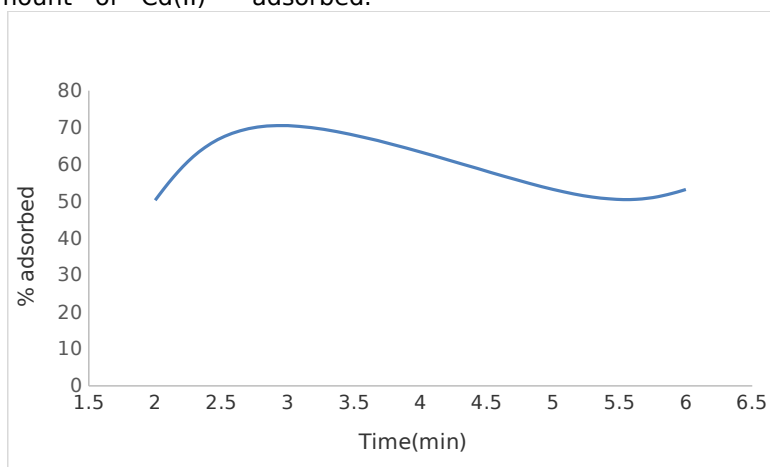


Figure 11: The effect of contact time on the percentage amount of Cd(II) chelated on the surface of the functionalized carbon dot at pH 5 .

Effect of pH on the sorption of Cd(II) ions

The effect of pH on the percentage amount of Cd(II) ions chelated is shown in Fig 12 at equilibration time of 3 min and initial Cd(II) ion concentration of 0.0448 mg. The characteristics of every sorbent and the chemical nature of the metal ion to be chelated by the sorbent is greatly influenced by the pH of the solution.

As observed in Fig 10 there was an increase in the percentage amount of Cd(II) ions adsorbed at pH 2-3 with a regress at pH 4. The highest amount of Cd(II) ion adsorbed was observed at the optimal pH of 5. The observed increase in the percentage amount of Cd(II) ions adsorbed at pH 10 - 11 could be as a result of the formation of metal hydroxo species. Increased

adsorption at pH 5 could be as a result of the formation of protonated cationic complex between SALEN functionalized carbon dot and the metal species.

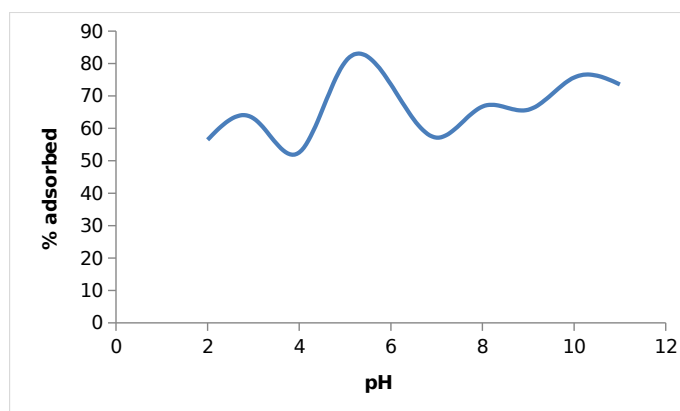


Figure 12: The effect of pH on the percentage amount of Cd(II) chelated on the surface of the functionalized carbon dot at 3 min equilibration.

Adsorption isotherm and kinetic studies

Adsorption isotherm models of Langmuir and Freundlich (22) were used to investigate the mechanistic behavior and relationship between the mass of Cd(II) ions adsorbed onto the surface of the SALEN-functionalized carbon dot and the processes that control the adsorption of the divalent metal cation on the functionalized carbon dot nanomaterial at constant pH and ambient temperature (303 ± 1 K). The kinetics of the adsorption process was investigated using pseudo-first-order and pseudo-second-order kinetic (1).

Langmuir and Freundlich isotherms

The plot of Langmuir and Freundlich isotherm models are shown in Figures 13 and 14, respectively, while Table 4 gives a summary of the isotherm parameters and regression coefficients at 303 ± 1 K.

The maximum adsorption capacity (q_{max}) of the adsorption of Cd(II) ions onto the functionalized carbon dot was obtained as 0.97 mg/g. The Langmuir constant (K_L) was obtained as 0.24 mL/mg and describes the binding site affinity of Cd(II) ions onto the functionalized carbon dot. The equilibrium parameter (R_L) was evaluated using the Langmuir constant (K_L) as shown in Equation 12 and predictively shows the degree of affinity of the sorbent and the sorbate in sorption processes.

$$R_L = \frac{1}{1 + K_L C_0} \quad (12)$$

Here, C_0 represents initial Cd(II) ions concentration and K_L the Langmuir constant.

The value of R_L determines the nature of Langmuir isotherms and generally when $R_L=0$, the isotherm is irreversible, if $R_L > 1$, then it is unfavorable, if $R_L =1$, then it is linear but if $0 < R_L < 1$ then it is favorable (22). Evaluating R_L from the experimental data revealed that the values are in the range of 0.009 to 0.405 indicating a favorable adsorption process of Cd(II) ion on the functionalized carbon dot. The regression coefficient (R^2) of 0.985 obtained from the plot suggested that experimental data fitted well into the Langmuir isotherm. Based on the value of the regression coefficient and dimensionless constant equilibrium parameter, the experimental data could be said to conform to the Langmuir isotherm model. The implication is that monolayer coverage of the finite number of adsorption sites on the functionalized carbon dot is prominent with uniform and equivalent adsorption sites. Interaction between the adsorbed molecules is impaired and the adsorption of Cd(II) ions onto the functionalized carbon dot is inconsequential of the occupied nearby sites (1, 22, 26). The implication is that at the point of saturation or maximum adsorption at the adsorptive site of the functionalized carbon dot, further adsorption is quenched or hindered.

Freundlich adsorption capacity (K_f) value was determined at 303 ± 1 K to be 13.24 mg/g. The Freundlich adsorption strength (n) which indicates the degree of nonlinearity between the adsorption process and concentration of solution was 0.229. Consequently, if $n=1$, adsorption process was linear, if $n < 1$, adsorption process was chemisorption while if $n > 1$, adsorption process was physisorption (22). Based on the value of n , the adsorption process is basically physisorption. The regression coefficient (R^2) value was 0.950 which suggested close fit of the experimental data into the Freundlich isotherms.

The experimental data fitted well into both Langmuir and Freundlich isotherm models which is consistent with other studies on carbon dot nanomaterials (1) though a close consideration of the R^2 values indicated higher values for Langmuir (0.985) than for Freundlich (0.950). This implies that the nanomaterial is versatile and adsorption involves both monolayer and multilayer processes.

Pseudo-first-order and Pseudo-second-order kinetic models

The plot of $\log(q_e - q_t)$ against time (t) for pseudo-first-order kinetic model is shown in Figure 15 while the plot of t/q_t against t for pseudo-second-order kinetic model is shown in Figure 16. The equilibrium rate constants K_1 (min^{-1}) and K_2 ($\text{g/mg}\cdot\text{min}$) and calculated

adsorption capacity values are shown in Table 4. Based on the regression coefficients and kinetic parameters, the adsorption kinetics could be said to follow the pseudo-second-order kinetics. A clear investigation indicated that the K_1 (min^{-1}) is 25.609 but q_e (mg/g) was negative (-1.055), indicating the undesirability of the kinetic model even though the R^2 value was high (0.996). The equilibrium rate constant of the linearized pseudo-second-order kinetic model (K_2) ($\text{g/mg}\cdot\text{min}$) and adsorption capacity (q_e) were obtained to be 0.544 and 11.49 respectively with R^2 value of 0.993. The adsorption process shows an interplay of physisorption and chemisorption common among carbon dots nanomaterials (1) with rate controlling step likely to involve electron pair donor-acceptor interactions, hydrogen bonding and dipole-dipole interactions.

Table 4: Isotherms, kinetic parameters, and regression constants.

Models	Parameter 1	Parameter 2	R^2
Langmuir	q_m (mg g^{-1}) = 0.97	b (L mg^{-1}) = 0.24	0.9850
Freundlich	n = 0.299	K_F ($\text{mg}^{1-1/n} \text{L}^{1/n} \text{g}^{-1}$) = -13.24	0.9500
Langmuir	q_e (mg g^{-1}) = 25.609	K_1 (min^{-1}) = 25.609	0.9960
Freundlich	q_e (mg g^{-1}) = 11.49	K_2 (g/mg min) = 0.544	0.9930

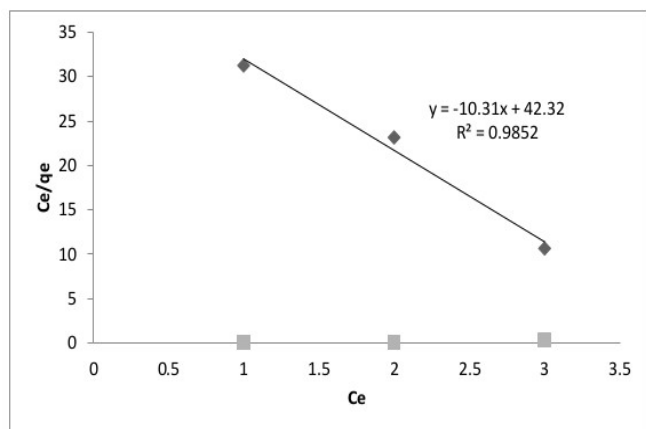


Figure 13: Langmuir adsorption isotherm plot of (C_e/q_e) versus C_e for the adsorption of Cd(II) ions onto Functionalized carbon dot at pH 5 and 303 ± 1 K.

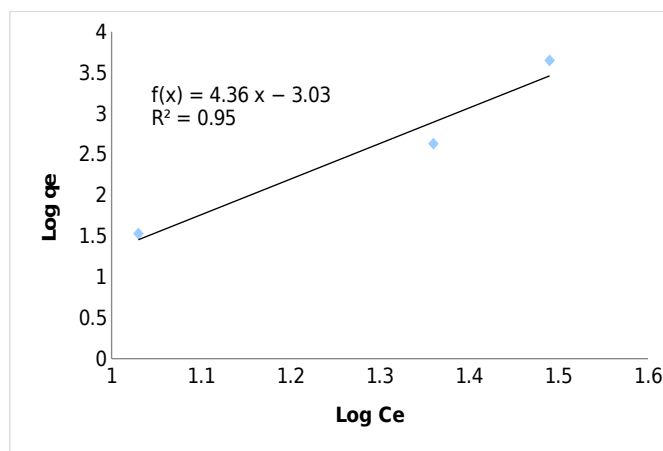


Figure 14: Freundlich adsorption isotherm plot of $\log q_e$ versus $\log C_e$ for the adsorption of Cd(II) ions onto Functionalized carbon dot at pH 5 and 303 ± 1 K.

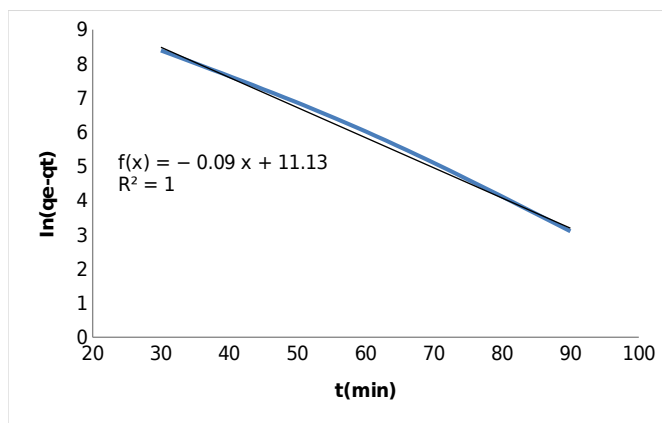


Figure 15: Pseudo-first-order kinetic plot of $\ln(q_e - q_t)$ versus t for the adsorption of Cd(II) ions onto the functionalized carbon dot at pH 5 and 303 ± 1 K.

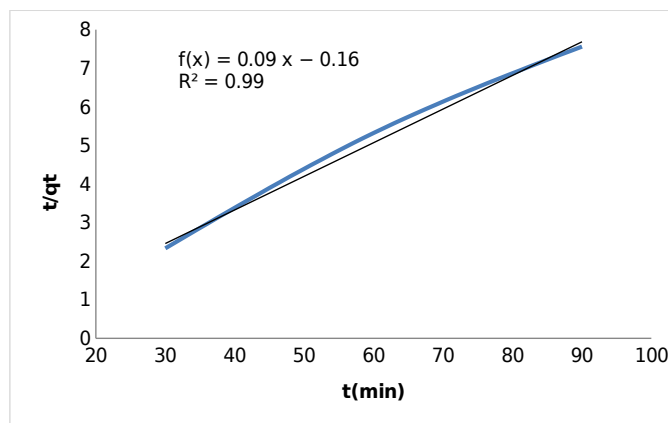


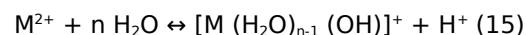
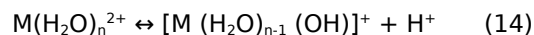
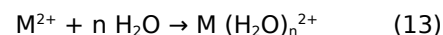
Figure 16: Pseudo-second-order plot of t/q_t versus t for the adsorption of Cd(II) ions onto functionalized carbon dot at pH 5 and 303 ± 1 K.

Possible mechanism of Cd(II) chelation and removal using the functionalized carbon dot

Previous work (27) suggests that Cd(II) forms extractable complex of the type $\text{Cd}(\text{H}_2\text{SAL})$ in the mole ratio of ligand to metal of 1:1. The quantitative removal of cadmium(II) from aqueous solution of pH 10-11 could be as a result of chelation with the dissociated HSAL^- and SAL^{2-} on the surface of the functionalized carbon dot nanoparticle. At higher pH and in the dissociated form, H_2SAL on the biointerface of the functionalized carbon dot is chelated with Cd(II) ions in solution through the lone electron pair resident on the oxygen and nitrogen atoms of the H_2SAL moiety and imine group, respectively. At lower pH, and in the protonated form, $[\text{H}_4\text{SAL}]^{2+}$ or $[\text{H}_3\text{SAL}]^+$, the H_2SAL on the biointerface of the functionalized carbon dot may exist as protonated cationic complex with Cd(II) ions.

The competition between the Cd(II) ions in solution and the hydronium ions formed at pH 2-4 resulted in instability of the cationic complex formed and consequent regress in the amount of Cd(II) adsorbed (28). At pH 5, increase in the competition between the Cd(II) ions and the hydronium ions in solution disappears and stable cationic complex is formed leading to increase in the amount of Cd(II) removed. The pK_a of Cd(II) is 10.1 with M^{2+} and $\text{M}(\text{OH})^+$ as the dominant species at pH 5 and as shown in equations 13-15. At higher pH of 10-11, possibility of increase in the quantity of Cd(II) adsorbed due to formation of stable metal hydroxo species exist. Cadmium(II) ions

tend to hydrolyze at pH 10-11 and formation of stable hydroxo complexes of cadmium with the ligand exist leading to increased extraction of cadmium from solution. Precipitation of $\text{Cd}(\text{OH})_2$ lowers adsorption, but in this case chelation and formation of stable hydroxo complexes of Cd(II) ions could have likely won over the former process.



Comparison with other adsorbents

Table 5 shows the adsorption capacity of some biomaterials in comparison with carbon dot. The initial concentration of the metal used is lower for carbon dot sorption as surveyed from various studies. However, carbon dot exists in nano form as against some of the adsorbent. The adsorption capacity of the SALEN functionalized carbon dot seems to be lowest for the carbon dot in comparison to the listed biomaterials. Possible influence of extraneous variables may be a factor. However, the concentrations of initial cadmium for the studied biosorbents was not available for effective comparison. Other studies for the sorption of lead using carbon dot used low lead concentration without evaluation of sorption capacity (1).

Table 5: Comparison of the adsorption capacity of impregnated biomaterials for the sorption of Cd(II) ions from aqueous solution.

S/N	Biochar source	Dopant	Adsorption capacity	Reference
1	Corn straw	MnFe ₂ O ₄	127.83 mg/g	(29)
2	Spent coffee	sodium dodecyl sulfate	10.67 mg/g	(30)
3	Wheat straw	CS ₂ /NaOH	N/A	(31)
4	Bamboo	NH ₃ /ZnCl ₂	44.54 mg/g	(32)
5	Plantain peel	SALEN	8220 mg/kg	(33)
6	Banana waste	SALEN	0.97 mg/g	This work

Regeneration/Reusability of the used nanocomposites

The reusability of the SALEN functionalized adsorbent was evaluated after regeneration of the used composite using different concentrations of HCl. Variation of concentrations of HCl from 1-0.0001 M, equilibration time between 5-30 min and volume of solution between 5-10 cm³ indicated that equilibration of 0.1 g of used sorbent with 5 cm³ solution at HCl concentration of 1M and time of contact of 10 min gave maximum desorption of used sorbent. Single extraction was applied and result shows that at high acid concentration, demetallation, and ligand degradation of the SALEN-carbon dot composite occurred freeing the metal from the sorbent. To ensure the reusability of composite, desorption - adsorption study was conducted and result obtained after four times of batch processes decreased only by 9-15 %.

CONCLUSION

A facile method was used for the preparation of highly fluorescent functionalized carbon dot nanoparticle for application in optical sensors and in extraction of Cd(II) ion from aqueous solution. The parameters for estimating the optical sensitivity of nanomaterials as applied to the newly synthesized nanoparticle indicated that the carbon dot and its SALEN functionalized counterpart are highly optically sensitive and of strong photoluminescence ability. The metal chelation and removal property studied indicated that the nanosized material is highly efficient, versatile and effective in the removal of Cd(II) ions (99.3%) and could be extended for the removal of other heavy metals and environmental toxicants from matrices. The results obtained indicated the preparation of an environmentally friendly carbon based nanomaterial that is safe, highly fluorescent, versatile and reusable nanocomposite that could serve as biomarkers for tracing and removal of environmental cadmium contamination.

CONFLICT OF INTEREST

The authors declare no conflict of interest in the manuscript submission

ACKNOWLEDGMENT

The authors are grateful to Ebonyi State University, Abakaliki for TETFund grant (Ref No:EBSU/TETFund/IBR/2015/10) financial assistance.

REFERENCES

- Musa YP, Zurina Z A, Suraya A R, Faizah M, Noor A S M, Mohammed A I. Eco-Friendly Sustainable Fluorescent Carbon Dots for the Adsorption of Heavy Metal Ions in Aqueous Environment. *Nanomaterials*. 2019; 10:315. <https://doi.org/10.3390/nano10020315>
- Waalkes M P (2000) Cadmium carcinogenesis in review. *J. Inorg. Biochem.* 2000; 79(1-4): 241-4. [https://doi.org/10.1016/S0162-0134\(00\)00009-X](https://doi.org/10.1016/S0162-0134(00)00009-X)
- Scimeca M, Feola M, Romano L, Rao C, Gasbarra E, Bonanno E. Heavy metals accumulation affects bone microarchitecture in osteoporotic patients. *Environ Toxicol.* 2017;32: 1333-42. <https://doi.org/10.1002/tox.22327>
- Ghorbani M, Eisazadeh H. Removal of COD, color, anions and heavy metals from cotton textile waste water by using polyaniline and polypyrrole nanocomposites coated on rice husk ash. *Composites B: Eng.* 2015; 45(1): 1 <https://DOI: 10.1016/j.compositesb.2012.09.035>
- Banerjee S, Chattopadhyaya MC. Adsorption characteristics for the removal of a toxic dye, tartrazine from aqueous solutions by a low cost agricultural by-product. *Arabian Journal of*

- Chemistry.2017; 10:S1629-S1638. <https://doi.org/10.1016/j.arabjc.2013.06.005>
6. Moyakhe D, Waanders F.B, Le Roux M, Campbell M.Q. The Journal of the Southern African Institute of Mining and Metallurgy. 2019 ; 119 : 607-12.
7. Khan A S, Dhevagi, P, Chitdeshwari P, Avudainayagam S (2018) Bio-sorption of cadmium from Aqueous solutions by banana peel powder. Madras Agric Journal.2018; 105(1- 3): 24-9. <https://DOI: 10.29321/MAJ.2018.000096>
8. Abdolali A, Ngo HH, Guo W, Lu S, Chen SS, Nguyen NC, Zhang X, Wang J, Wu Y.A breakthrough biosorbents in removing heavy metals: equilibrium, kinetic, thermodynamic and mechanism analyses in a lab-scale study. Sci Total Environ.2016;542:603–11. <https://doi.org/10.1016/j.scitotenv.2015.10.095>
9. Tao S, Lu S, Geng Y, Zhu S, Redfern SAT, Song Y, Feng T, Xu W, Yang B. Design of metal-free polymer carbon dots: a new class of room-temperature phosphorescent materials Angew. Chem. Int. Ed. 2018; 57: 2393–8. <https://doi.org/10.1002/anie.201712662>
10. Kong W. Quantitative and real-time effects of carbon quantum dots on single living HeLa cell membrane permeability. Nanoscale.2014; 6: 5116–20. <https://doi.org/10.1039/C3NR06590A>
11. Chen Y, Zheng M, Xiao Y, Dong H, Zhang H, Zhuang J, Hu H, Lei B, Liu Y. (2016). A self-quenching-resistant carbon-dot powder with tuneable solid-state fluorescence and construction of dual-fluorescence morphologies for white light-emission. Adv. Mater.2016; 28: 312–8. <http://doi.org/10.1002/adma.201503380>
12. Hu S. Tunable photoluminescence across the entire visible spectrum from carbon dots excited by white light. Angew. Chem. Int. Ed.2015; 54: 2970–4. <https://DOI: 10.1002/anie.201411004>
13. Ge J. Red-emissive carbon dots for fluorescent, photoacoustic, and thermal theranostics in living mice. Adv. Mater.2015; 27: 4169–77. <https://DOI:10.1002/adma.201500323>
14. Young AT. Neuro-nano interfaces: Utilizing nano-coatings and nanoparticles to enable next-generation electrophysiological recording, neural stimulation, and biochemi-cal modulation. Adv. Funct. Mater. 2018; 28: 1700239. <https://doi.org/10.1002/adfm.201700239>
15. Hola K. Graphitic nitrogen triggers red fluorescence in carbon dots. ACS Nano. 2017; 11: 12402–10. <https://DOI: 10.1021/acsnano.7b06399>
16. Nworie FS, Nwabue FI. Synthesis, Optimization, Characterization and Antimicrobial Studies of Cu (II) and Co (III) Complexes of Bis(2,2-methylidene phenol) diaminoethane. Chemistry Journal of Moldova, General, Industrial and Ecological Chemistry.2017; 12(2): 41-9. <https:// DOI: 10.19261/cjm.2017.392>
17. Kezerle A, Velic N, Hasenay K D(2018) Lignocellulosic materials as adsorbents: Adsorption of MEB and Congo red on brewers spent grain. Croat. Chem. Acta.2018; 91:53-64. <https://doi.org/10.1016/j.jhazmat.2019.120897>
18. Mokkalapati RP, Ratnakaram VN, Mokkalapati JS. Utilization of agro-waste for removal of toxic hexavalent chromium: surface interaction and mass transfer studies. Int.J. Environ. Sci. Technol. 2017; 10:017-037. <https://DOI:10.1007/s13762-017-1443->
19. Li H. Water-soluble fluorescent carbon quantum dots and photocatalyst design. Angew. Chem. Int. Ed. 2010; 49: 4430–4. <https://doi.org/10.1002/anie.200906154>
20. Chen BC, Li CD, Zhang J, Kan JF, Jiang TT, Zhou J, Ma HM. Sensing and imaging of mitochondrial viscosity in living cells using a red fluorescent probe with a long lifetime. Chem Commun.2019; 55:7410-3. <https://doi.org/10.1039/C9CC03977E>
21. Arcudi F. Rationally designed carbon dots nanodots towards pure white light emission. Angew. Chem. Int. Ed.2016; 56: 4170–3. <https://doi.org/10.1002/anie.201612160>
22. Nworie FS, Nwabue F, Ikelle I, Ogah A, Elom N, Ilochi N, Itumoh E, Oroke C. Activated plantain peel biochar as adsorbent for sorption of Zinc (II) ions: Equilibrium and kinetic studies. Journal of the Turkish Chemical Society, Section A.2018; 5(3), 1257-70. <http://dx.doi.org/10.18596/jotcsa.438332>.
23. Zhao G, Li J, Ren X, Chen C, Chen X. Few-layered graphene oxide nanosheets as superior sorbents for heavy metal ion pollution management. Environ.

Sci.Technol.2011; 45(24): 10454-62. [https:// doi: 10.1021/es203439v](https://doi.org/10.1021/es203439v).

24. Ghaedi M, Montazerzohori M, Soyak M. Solid phase extraction method for selective determination of Pb(II) in water samples using 4-(4-methoxybenzylideneimine) thiophenole. *Journal of Hazardous Materials*.2017; 142: 368-73. <https://doi.org/10.1016/j.jhazmat.2006.08.033>

25. Haruna A, Abdulkadir I, Idris S O. Synthesis, Characterization and Photocatalytic Properties of Bi_{0.85}-XMXBa_{0.15}FeO₃ (M = Na and K, X= 0, 0.1) Perovskite-like Nanoparticles Using the Sol-gel Method. *Journal of King Saud University - Science* .2020; 32(1): 896-903.

26. Haruna A, Abdulkadir I, Idris S O. Photocatalytic activity and doping effects of BiFeO₃ nanoparticles in model organic dyes. *Heliyon*. 2020; e03237.

27. Nworie FS. Spectral, Thermal and In Vitro Antibacterial Studies on Cadmium(II)-bis(2,2'-methylidenephenol)diaminoethane. *Journal of the Turkish Chemical Society Section A: Chemistry*.2018;5 (3): 1029-36. <https://doi.org/10.18596/jotcsa.423508>

28. Nworie FS, Nwabue FI. Synthesis, Optimization, Characterization and Antimicrobial Studies of Cu (II) and Co (III) Complexes of Bis(2,2'-methylidenephenol) diaminoethane. *Chemistry Journal of Moldova, General, Industrial and Ecological Chemistry*.2017; 12(2): 41-9 .[https:// DOI: 10.19261/cjm.2017.392](https://doi.org/10.19261/cjm.2017.392)

29. Zhang L, Guo J, Huang X, Wang W, Sun P, Lib Y, Han J. Functionalized Biochar-Supported Magnetic MnFe₂O₄ Nanocomposite for the Removal of Pb(II) and Cd(II). *RSC Adv*. 2019; 9: 365 DOI: 10.1039/c8ra09061k

30. Moyakhe D, Waanders FB, Le Roux M, Campbell Q P. Hydrothermal Preparation of Biochar from Spent Coffee Grounds, and its Application for the Removal of Cadmium from Coal Tailings Leachate. *The Journal of the Southern African Institute of Mining and Metallurgy*.2019; 119: 607-12 DOI: 10.17159/2411-9717/449/2019.

31. Chen D, Wang X, Wang X, Feng K, Su J, Dong J. The mechanism of cadmium sorption by sulphur-modified wheat straw biochar and its application cadmium contaminated soil. *Science of The Total Environment*. 2020; 714:136550 <https://doi.org/10.1016/j.scitotenv.2020.136550>

32. Tang W, Cai N, Xie H, Liu Y, Wang Z, Liao Y, Wei T, Zhang C, Fu Z, Yin D. Efficient Adsorption Removal of Cd²⁺ from Aqueous Solutions by HNO₃ Modified Bamboo-Derived Biochar. *Materials Science and Engineering*. 2020; 729: 012081

33. Nworie F S, Nwabue F I, Oti W, Omaka N O, Igwe H. Hydrothermal Synthesis of Multifunctional Biochar-supported SALEN Nanocomposite for Adsorption of Cd(II) Ions: Function, Mechanism, Equilibrium and Kinetic Studies. *Anal. Bioanal. Chem. Res*.2020; 8(1): 91-112.



A Study on the Optoelectronic Parameters of 4-Chloromethyl-7-Hydroxy Coumarin in Various Solvents and Concentrations

Adnan Kurt^{1,*}  , Bayram Gündüz²  , Murat Koca³  

¹Department of Chemistry, Faculty of Science and Arts, Adiyaman University, Adiyaman/Turkey

²Department of Engineering Basic Sciences, Faculty of Engineering and Natural Sciences, Malatya Turgut Özal University, Malatya, Turkey

³Department of Pharm. Chemistry, Pharmacy Faculty, Adiyaman University, Adiyaman/Turkey

Abstract: A coumarin derivative, namely 4-chloromethyl-7-hydroxy coumarin (CMEHC), was synthesized in order to test the concentration and solvent effect on its optical properties. The spectral characterization of this compound was accomplished by FTIR and ¹H-NMR techniques. The UV absorption spectra of CMEHC compound in various solvents (THF, DMSO, DMF) were recorded with a UV-VIS spectrophotometer. The optical parameters such as maximum peak position, absorption band edge, and direct allowed bandgap were reported for these solvents and also various concentrations. The lowest direct allowed bandgap was obtained with THF. The absorbance spectra of CMEHC compound were dominant at the near ultraviolet region. The refractive index values were compared with each other using Moss, Ravindra, Herve-Vandamme, Reddy and Kumar-Singh relations.

Keywords: Coumarin derivative, optoelectronic parameters, concentration and solvent effect, absorption band edge, optical bandgap, refractive index.

Submitted: March 04, 2020. **Accepted:** December 15, 2020.

Cite this: Kurt A, Gündüz B, Koca M. A Study on the Optoelectronic Parameters of 4-Chloromethyl-7-Hydroxy Coumarin in Various Solvents and Concentrations. JOTCSA. 2021;8(1):155-62.

DOI: <https://doi.org/10.18596/jotcsa.698612>.

***Corresponding author: e-mail:** akurt@adiyaman.edu.tr, Tel: +90416 2233800.

INTRODUCTION

As is well known, coumarins are important members of oxygen-containing heterocyclic compounds. They are included in the class of lactones containing benzopyrone skeletal framework (1). The chemical structure of the basic coumarin ring consisting of the combination of benzene and pyrone rings at second position of the pyrone carbonyl (2). Coumarins establish one of the major classes of naturally occurring compounds and are widely isolated from plants. The synthesis of these natural or novel synthetic coumarins and their derivatives with various functional groups in the laboratory are also possible (3). Especially, the characteristics of the main coumarin compounds vary considerably by connecting the appropriate components into them. Thus, they may be converted to more useful and relevant products in different fields of science and

technology (4). Because of their π -conjugated structures, coumarins and derivatives exhibit significant and unique photophysical and spectroscopic properties (5). They have been extensively used in electronically, optically, and photonic applications such as organic light-emitting diodes (6), electroluminescence (7), fluorescent materials (8), nonlinear optical materials (9), photoalignment of liquid crystalline molecules (10), charge-transfer agents (11), two-photon absorption materials (12), organic-inorganic hybrid materials (13), and laser dyes (14).

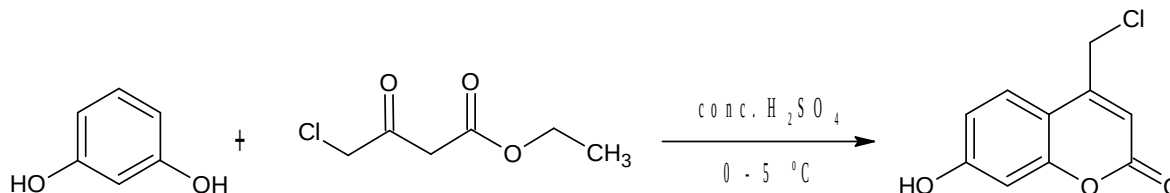
Besides, the investigation of optical parameters of organic compounds is essential for many applications, as highlighted above. These compounds are usually characterized by their UV-visible absorption spectra (15) to measure some optical parameters such as refractive index,

absorption band edge, optical bandgap, etc. (16-19). For this purpose, some papers have been published on the optical properties of coumarins (2,5,20,21). In one of these studies, Tasior and coworkers (5) reported a review involved the synthesis mechanisms, comparison and analysis of linear optical properties and possible applications in the current technology of some π -expanded coumarins. Bai and coworkers (20) investigated the synthesis, characterization, optical properties and theoretical calculations of 6-fluoro coumarin compound. They reported that it absorbed UV-VIS light at 319, 269, and 215 nm and exhibited blue-purple fluorescence emission at 416 nm. Skowronski and coworkers (2) reported that the optical properties of coumarin-containing copolymers thin films by means of spectroscopic ellipsometry combined with transmittance measurements and atomic force microscopy. In another study reported by Rabahi and coworkers (21), the synthesis and optical properties of coumarins and iminocoumarins were investigated in different solvents by UV/vis absorption and fluorescence spectroscopy at room temperature. Ground-state and excited-state dipole moments were estimated from a solvatochromic shift and theoretical methods.

As it is explained above, although the optical properties of some coumarin compounds have been investigated, these properties are mainly focused on the investigation of transmittance or emission properties. Based on our literature knowledge, there are not enough works on the optical parameters such as the maximum peak position, absorption band edge, refractive index, and direct allowed bandgap reported for 4-chloromethyl-7-hydroxy coumarin. Therefore, we aim to investigate some optical parameters in different solvents and concentrations of a coumarin derivative compound, 4-chloromethyl-7-hydroxy coumarin. The obtained results show that 4-chloromethyl-7-hydroxy coumarin exhibits a semiconductor behavior and it may be an important candidate for many optoelectronic devices such as diodes, photo-diodes, and sensors.

EXPERIMENTAL

Materials



Scheme 1. Synthesis of CMEHC compound.

RESULTS AND DISCUSSIONS

Spectral Characterization

Resorcinol (99%), ethyl-4-chloroacetoacetate (95%) and sulfuric acid (H₂SO₄, ACS reagent, 95.0-98.0%) were purchased from Sigma-Aldrich. The used solvents tetrahydrofuran (THF, anhydrous $\geq 99.9\%$), N,N-dimethylformamide (DMF, anhydrous 99.8%), dimethyl sulfoxide (DMSO, anhydrous $\geq 99.9\%$) were also purchased from Sigma-Aldrich.

Instrumental Techniques

Proton nuclear magnetic resonance spectrum (¹H-NMR) of the coumarin compound was recorded on a Bruker 300 Mhz Ultrashield TM instrument at room temperature using deuterated DMSO solvent and TMS as an internal standard. The infrared characterization was carried out by a Perkin Elmer Spectrum 100 FTIR spectrometer with ATR accessory. The UV measurements of the CMEHC solutions for different solvents and molarities were recorded with a Shimadzu model UV-1800 spectrophotometer using a cylindrical bathtub (Hellma QS-100) in the wavelength 1100-190 nm at room temperature. The CMEHC compound samples weighed with an analytical balance (AND-GR-200 Series) were homogeneously dissolved in 12-mL volumes of THF, DMF, and DMSO solvents. Besides, the solutions at different molarities of 28.65, 0.358, 0.054, 0.013, and 0.007 mM of this compound were also prepared using the same amount of DMSO solvent (12 mL).

Synthesis of 4-Chloromethyl-7-Hydroxy Coumarin (CMEHC)

The synthesis of CMEHC was carried out according to the pathway reported in previous studies (22,23). Briefly, CMEHC compound was synthesized as follows: Powdered resorcinol (11.011 g) and ethyl-4-chloroacetoacetate (16.459 g) were dissolved in a 50- mL beaker and this solution was added dropwise to 40 mL of concentrated sulfuric acid in a reaction balloon at the temperature of 0-5 °C. The reaction mixture was stirred continuously on a magnetic stirrer for two hours. Then, the obtained dark brown solution was poured into the excess ice-cold water. Thus, the product of 4-chloromethyl-7-hydroxy coumarin (CMEHC) was precipitated as white sediments, filtered, and dried (Scheme 1). The yield of CMEHC synthesis reaction was found to be 81%.

Figure 1 shows the FTIR spectrum of CMEHC in which the most characteristic bands are observed at 3286 cm⁻¹ (-OH stretching vibration), 3092-3018 cm⁻¹ and 2989-2880 cm⁻¹ (aromatic and aliphatic C-H

stretching vibrations, respectively), 1694 cm^{-1} (lactone C=O stretching in coumarin ring), 1621 cm^{-1} (lactone C=C stretching) and 1605 cm^{-1} (aromatic C=C stretching). $^1\text{H-NMR}$ spectrum of CMEHC compound was shown in Figure 2. A singlet signal at 10.6 ppm is attributed to O-H proton in coumarin ring. The chemical shifts observed between 7.7 ppm

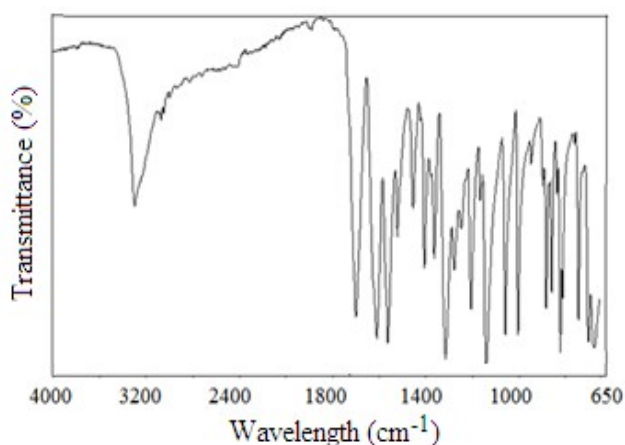


Figure 1. FTIR spectrum of CMEHC.

and 6.7 ppm are characteristics for aromatic =CH- protons. The signal at 6.4 ppm is also attributed to aliphatic =CH- proton in coumarin ring. The singlet signal for $-\text{CH}_2\text{Cl}$ protons is observed at the chemical shift 4.9 ppm . The signals at 3.3 and 2.5 ppm are due to DMSO solvent.

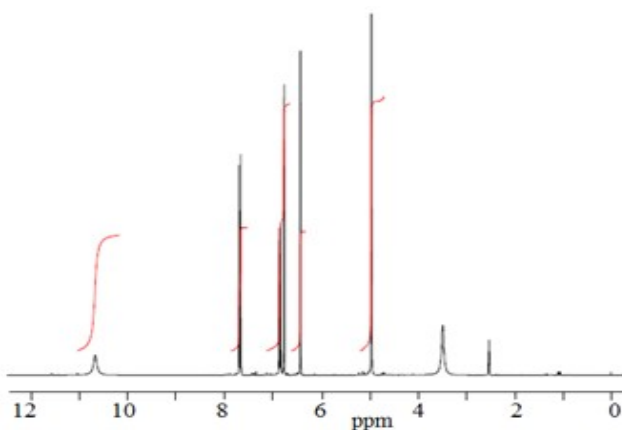


Figure 2. $^1\text{H-NMR}$ spectrum of CMEHC compound.

Optical Properties

Absorbance is the amount of light absorbed by a sample and is important in the determination of optical properties. Figure 3(a,b) indicates the

absorbance spectra of the CMEHC coumarin compound for different solvents (THF, DMF, and DMSO) and different molarities using DMSO (28.65 , 0.358 , 0.054 , 0.013 , and 0.007 mM), respectively.

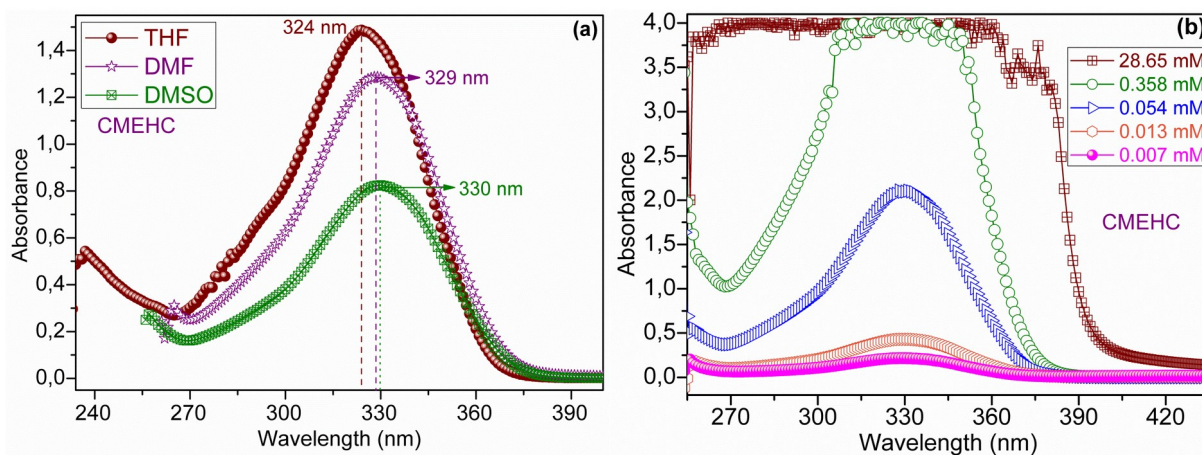


Figure 3. The absorbance spectra: **(a)** for THF, DMF and DMSO solvents and **(b)** for 28.65 , 0.358 , 0.054 , 0.013 and 0.007 mM in DMSO.

As seen in Figure 3a, CMEHC exhibits the maximum absorbance peaks at 324 , 329 and 330 nm for THF, DMF and DMSO solvents, respectively. Obtained results show that the position of the maximum absorbance peak can be changed with the solvents, and also, the absorbance for THF solvent is the highest while the absorbance for DMSO solvent is the lowest. As seen in Figure 3b, the absorbance of

the CMEHC has not been observed at higher molarities than 0.358 mM and that decreases with decreasing molarity. The absorbance spectra of the CMEHC compound are dominant at the near ultraviolet (NUV) region. Besides, THF, DMF and DMSO have a significant effect on absorbance of CMEHC.

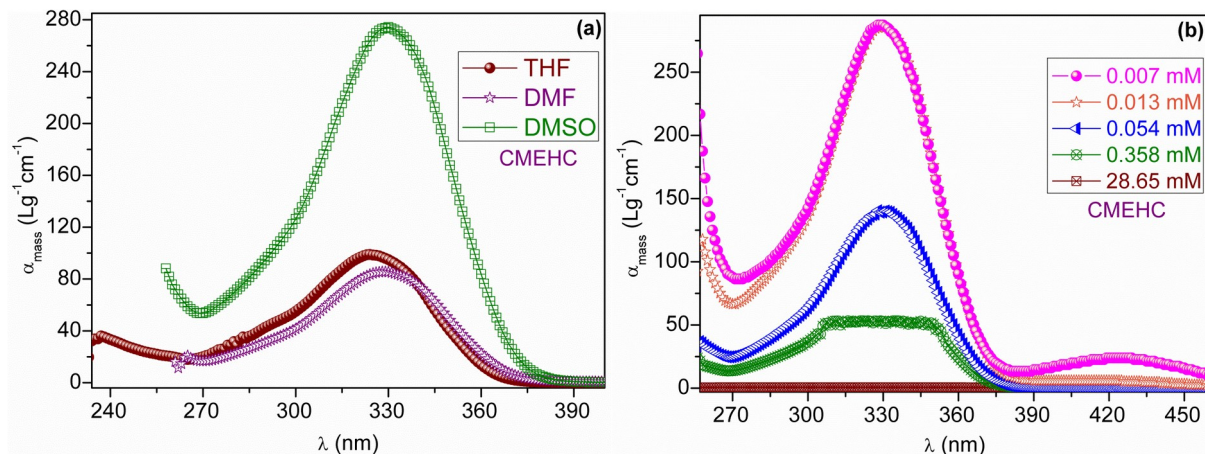


Figure 4. The mass extinction coefficient (α_{mass}) plot vs. wavelength (λ) **(a)** for THF, DMF and DMSO and **(b)** for 28.65, 0.358, 0.054, 0.013 and 0.007 mM in DMSO.

The mass extinction coefficient (α_{mass}) is investigated for optoelectronic applications and is given in (18, 24).

$$\alpha_{mass} = \frac{Abs}{C \times l \times M_A} \quad (1)$$

where Abs is the absorbance, C is the molar concentration, l is the length of the optical path of the used cylindrical bathtub and M_A is the molecular mass. The M_A values of the CMEHC is 210.560 g/mol. The α_{mass} values of the CMEHC for different solvents and molarities were calculated from Eq. (1). Figure 4(a,b) shows the plots of the α_{mass} vs. wavelength (λ) of the CMEHC for THF, DMF and DMSO solvents and for the concentrations of 28.65, 0.358, 0.054, 0.013 and 0.007 mM, respectively. As seen in Figure 4a,

the highest α_{mass} value of the CMEHC is calculated as 274.296 $Lg^{-1}cm^{-1}$ for DMSO solvent and it varies with solvents. In Figure 4b, the α_{mass} of the CMEHC increases with decreasing molarities, and the highest α_{mass} value of which is found to be 287.264 $Lg^{-1}cm^{-1}$ at 0.007 mM.

The transmittance (T) spectra of the CMEHC for THF, DMF and DMSO solvents are shown in Figure 5a where the transmittance values of the CMEHC are at high levels in the visible region while they have pits in the NUV region and vary with solvents. The T spectra of the CMEHC for 28.65, 0.358, 0.054, 0.013 and 0.007 mM are shown in Figure 5b. As seen in Figure 5b, the transmittance of the CMEHC continuously increases with decreasing molarity, and after about from 325 nm to 390 nm, the transmittance sharply increases.

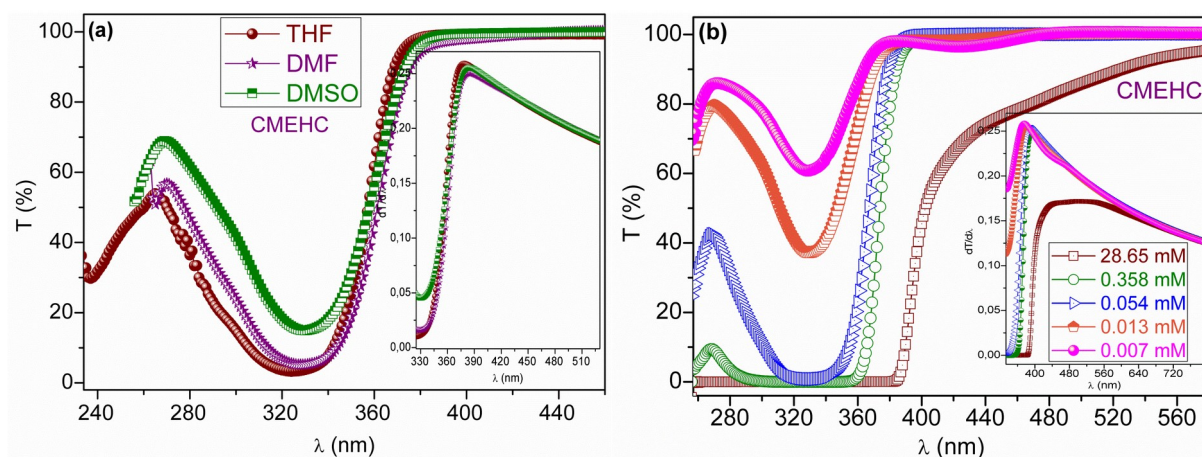


Figure 5. The transmittance (T) spectra: **(a)** for THF, DMF and DMSO solvents and **(b)** for 28.65, 0.358, 0.054, 0.013 and 0.007 mM in DMSO.

Table 1. The maximum peak position (λ_{\max}), absorption band edge ($E_{\text{Abs-be}}$), and direct allowed bandgap (E_{gd}) parameters for different solvents (a) and molarities (b) of CMEHC.

	Solvents	λ_{\max} (nm)	$E_{\text{Abs-be}}$ (eV)	E_{gd} (eV)
(a)	THF	384	3.229167	3.295
	DMSO	383	3.237598	3.313
	DMF	379	3.271768	3.357
	Molarities (mM)	λ_{\max} (nm)	$E_{\text{Abs-be}}$ (eV)	E_{gd} (eV)
(b)	28.65	459	2.702	2.778
	0.358	395	3.139	3.202
	0.054	389	3.188	3.238
	0.013	380	3.263	3.319
	0.007	376	3.298	3.355

To determine the absorption band edge ($E_{\text{Abs-be}}$) values of the CMEHC, we plotted the first derivative ($dT/d\lambda$) vs. λ . The $E_{\text{Abs-be}}$ values of the CMEHC for THF, DMF and DMSO solvents and for 28.65, 0.358, 0.054, 0.013 and 0.007 mM are calculated from the maximum peak position (λ_{\max}) of the $dT/d\lambda$ plots vs. λ as seen in insets of Figs. 5(a,b), respectively. The λ_{\max} and $E_{\text{Abs-be}}$ values of the CMEHC coumarin compound for THF, DMF and DMSO solvents and for 28.65, 0.358, 0.054, 0.013 and 0.007 mM are given in Table 1(a,b). As seen in Table 1a, the $E_{\text{Abs-be}}$ value (3.229 eV) of the CMEHC for THF is the lowest, while the $E_{\text{Abs-be}}$ value (3.272 eV) of the CMEHC for DMF is the highest. As seen in Table 1b, the $E_{\text{Abs-be}}$ of the CMEHC increases with decreasing molarity and varies from 2.702 to 3.298 eV.

The optical bandgap (E_g) is a fundamental optical parameter, and the E_g of optical transitions can be obtained using Tauc relation (25,26);

$$(\alpha h \nu) = A (h \nu - E_g)^n \quad (2)$$

where α is absorption coefficient, A is a constant, $h\nu$ is photon energy, and n is a parameter, which measures the type of bandgaps. For CMEHC, the type of bandgap (26) is the direct allowed bandgap (E_{gd}). For this, we plotted the $(\alpha h \nu)^2$ plot vs E of the CMEHC for THF, DMF and DMSO solvents and for 28.65, 0.358, 0.054, 0.013 and 0.007 mM as seen in Figure 6(a,b). We calculated the E_{gd} values from the linear regions of the Figure 6(a,b) and obtained E_{gd} values of the CMEHC for THF, DMF, and DMSO solvents and also for 28.65, 0.358, 0.054, 0.013 and 0.007 mM were given in Table 1(a,b). As seen in Table 1a, the E_{gd} value (3.295 eV) of the CMEHC for THF is the lowest while the E_{gd} value (3.357 eV) of the CMEHC for DMF is the highest. As seen in Table 1b, the E_{gd} value (2.778 eV) of the CMEHC for 28.65 mM is the lowest while the E_{gd} value (3.355 eV) of the CMEHC for 0.007 mM is the highest. Obtained these results show that the lowest direct allowed bandgap of the CMEHC can be obtained with THF solvent and the E_{gd} is decreased with increasing molarity.

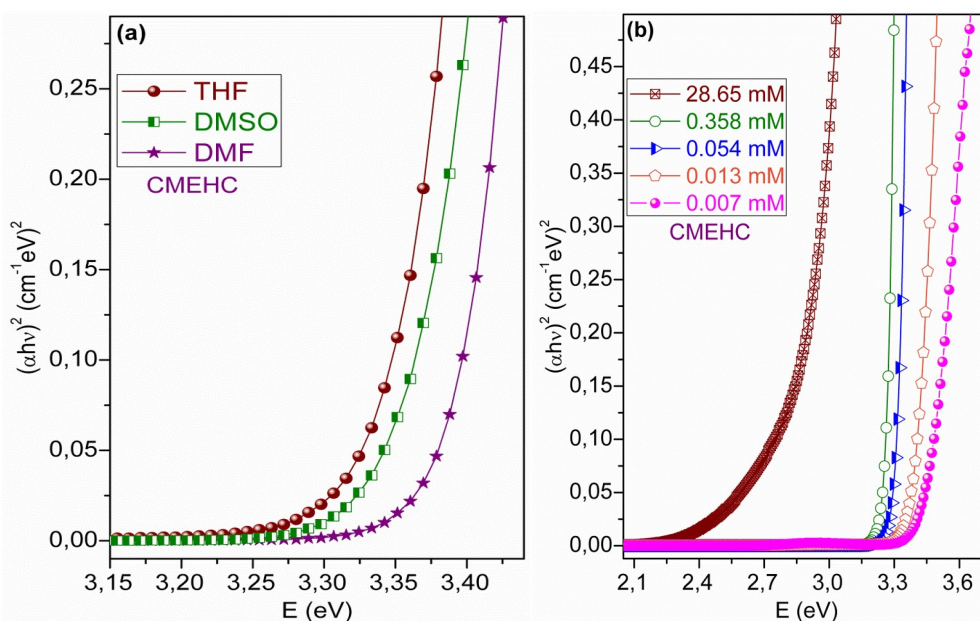
**Figure 6.** The $(\alpha h \nu)^2$ plot vs. photon energy (E): (a) for THF, DMF and DMSO solvents and (b) for 28.65, 0.358, 0.054, 0.013 and 0.007 mM in DMSO.

Table 2. The refractive index (n) parameters obtained from experimental (Exp) results, Moss (M), Ravindra (Ra), Herve-vandamme (H-V), Reddy (Re) and Kumar-Singh (K-S) relations for different solvents (a) and molarities (b) of the CMEHC.

(a)	Solvents	Exp	M	Ra	H-V	Re	K-S
	THF	2.174	2.317	2.0411	2.245	2.693	2.292
	DMSO	2.099	2.314	2.030	2.241	2.688	2.288
	DMF	2.023	2.306	2.003	2.229	2.679	2.279
(b)	Molarities (mM)	Exp	M	Ra	H-V	Re	K-S
	28.65	2.532	2.418	2.362	2.395	2.827	2.422
	0.358	2.242	2.334	2.099	2.271	2.714	2.314
	0.054	2.293	2.327	2.076	2.261	2.706	2.305
	0.013	2.289	2.313	2.026	2.239	2.687	2.287
	0.007	2.269	2.307	2.004	2.230	2.679	2.279

The refractive index or index of refraction (n) is a fundamental optical parameter for optoelectronic applications. The n values can be obtained by (16,24).

$$n = \left\{ \left[\frac{4R}{(R-1)^2} - k^2 \right]^{1/2} - \frac{R+1}{R-1} \right\} \quad (3)$$

The n values calculated experimentally of the CMEHC compound for THF, DMF, and DMSO solvents and for 28.65, 0.358, 0.054, 0.013, and 0.007 mM were given in Table 2(a,b). As seen in Table 2(a,b), the lowest refractive index of the CMEHC can be obtained with DMF solvent and the n of the CMEHC is decreased with decreasing molarity.

The relation between the optical bandgap and refractive index can be explained with many relations such as Moss, Ravindra, Herve-vandamme, Reddy, and Kumar-Singh (27). These are represented in the following equations:

Moss relation is given by:

$$n = \left(\frac{95}{E_g (eV)} \right)^{1/4} \quad (4)$$

Ravindra relation is given by:

$$n = 4.084 - 0.62 E_g \quad (5)$$

Herve-vandamme relation is given by:

$$n^2 = 1 + \left(\frac{A}{E_g + B} \right)^2 \quad (6)$$

where A is the hydrogen ionization energy 13.6 eV and B = 3.47 eV is a constant.

Reddy relation is given by:

$$n = \left(\frac{154}{(E_g - 0.365)} \right)^{1/4} \quad (7)$$

Kumar-Singh relation is given by

$$n = \frac{3.3688}{E_g^{0.32234}} \quad (8)$$

Consequently, the refractive index values of the CMEHC were obtained from experimental results of Moss, Ravindra, Herve-vandamme, Reddy, and Kumar-Singh relations. The refractive index curves derived from these equations for CMEHC compound in different solvents (THF, DMF, DMSO) and concentrations (28.65, 0.358, 0.054, 0.013, 0.007 mM) were illustrated in Figure 7(a,b). Their values were also given in Table 2(a,b). As seen in Table 2(a,b), the n values of the CMEHC obtained for THF solvent and from Reddy relation are the highest, while the n values of the CMEHC obtained for DMF solvent and from Ravindra relation are the lowest. Obtained results suggest that the related solvents have a higher effect on the refractive index of the CMEHC and also the refractive index can be controlled with different solvents and molarities.

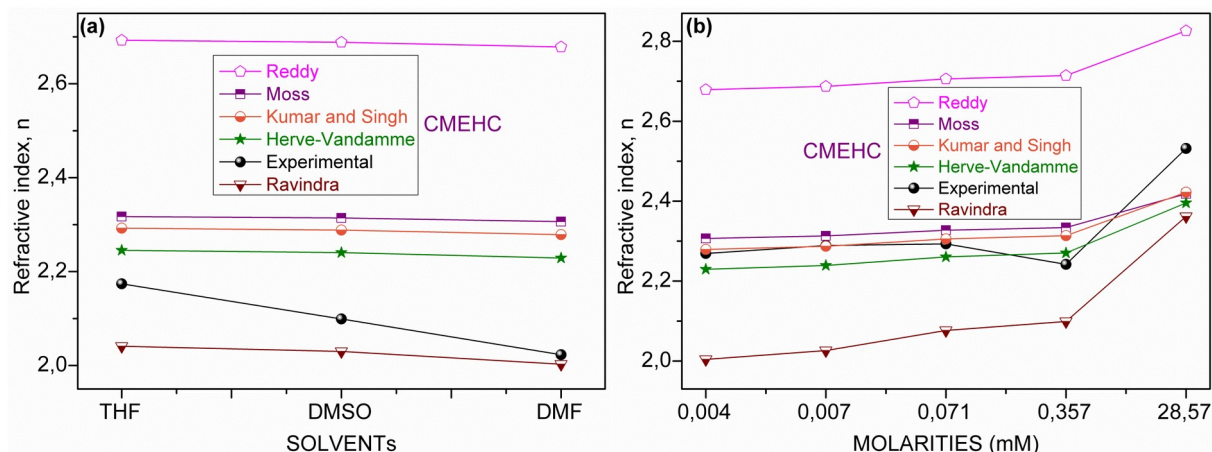


Figure 7. The refractive index plots obtained from various relations **(a)** for THF, DMF and DMSO solvents and **(b)** for 28.65, 0.358, 0.054, 0.013 and 0.007 mM in DMSO.

CONCLUSION

Effects of the solvents and molarities on the optical properties of the CMEHC coumarin compound were investigated. The absorbance spectra of the CMEHC are dominant in the NUV region. The mass extinction coefficient of the CMEHC increases with decreasing molarities. THF, DMF and DMSO solvents have a role in the absorption band edge of the CMEHC compound. The lowest direct allowed bandgap can be obtained with THF solvent. The E_{gd} of the CMEHC is also decreased with increasing molarity. The lowest refractive index can be obtained with DMF solvent, and the n of the CMEHC is decreased with decreasing molarity. The n values obtained for THF and Reddy relation are the highest whereas those are the lowest values for DMF and Ravindra relation. The obtained results show that 4-chloromethyl-7-hydroxy coumarin exhibits a semiconductor behavior and it may be an important candidate for many optoelectronic devices such as diodes, photo-diodes, and sensors.

REFERENCES

- Sahoo SS., Shukla S, Nandy S, Sahoo HB. Synthesis of Novel Coumarin Derivatives and its Biological Evaluations. *European Journal of Experimental Biology*. 2012;2(4):899-908.
- Skowronski L, Krupka O, Smokal V, Grabowski A, Naparty M, Derkowska-Zielinska B. Optical properties of coumarins containing copolymers. *Optical Materials*. 2015;47:18-23.
- Olayinka AO, Obinna NC. Microwave-assisted synthesis and evaluation of antimicrobial activity of 3-{3-(s-aryl and s-heteroaromatic)acryloyl} -2H-chromen-2-one derivatives. *Journal of Heterocyclic Chemistry*. 2010;47(1):179-87.
- Brahnbhatt DI, Gajera JM, Pandya VP, Patel MA. Synthesis of 3-(6-aryl-pyridin-2-yl)- and 8-(6-aryl-pyridin-2-yl) coumarins. *Indian Journal of Chemistry*. 2007;46(B):869-71.
- Tasior M, Kim D, Singha S, Krzeszewski M, Ahn KH, Gryko DT. pi-Expanded coumarins: synthesis, optical properties and applications. *Journal of Materials Chemistry C*. 2015;3:1421-46.
- Swanson SA, Wallraff GM, Chen JP, Zhang WJ, Bozano LD, Carter KR, Salem JR, Villa R, Scott JC. Stable and Efficient Fluorescent Red and Green Dyes for External and Internal Conversion of Blue OLED Emission. *Chemistry of Materials*. 2003;15(12):2305-12.
- Zhang H, Yu T, Zhao Y, Fan D, Qian L, Yang C, Zhang K. Syntheses, characterization and fluorescent properties of two triethylene-glycol dicoumarin-3-carboxylates. *Spectrochimica Acta Part A: Molecular and Biomolecular Spectroscopy*. 2007;68(3):725-27.
- Jones G, Rahman MA, Fluorescence properties of coumarin laser dyes in aqueous polymer media. chromophore isolation in poly(methacrylic acid) hypercoils. *J. Phys. Chem.*, 1994;98(49):13028-37.
- Gindre D, Iliopoulos K, Krupka O, Evrard M, Champigny E, Sallé M. Coumarin-Containing polymers for high density non-linear optical data storage. *Molecules*, 2016;21(2):147.
- Kim C, Trajkovska A, Wallace JU, Chen SH. New insight into photoalignment of liquid crystals on coumarin-containing polymer films. *Macromolecules*. 2006;39 (11):3817-23.
- Donovalova J, Cigan M, Stankovicova H, Gaspar J, Danko M, Gaplovsky A, Hrdlovic P. Spectral properties of substituted coumarins in solution and polymer matrices. *Molecules*. 2012;17:3259-76.

- 12 Gindre D, Iliopoulos K, Krupka O, Champigny E, Morille Y, Sallé M. Image storage in coumarin-based copolymer thin films by photoinduced dimerization. *Optics Letters*. 2013;38(22):4636-9.
- 13 Chen W, Tong US, Zeng T, Streb C, Song YF. Reversible photodimerization of coumarin-modified Wells-Dawson anions. *Journal of Materials Chemistry C* 2015;3:4388-93.
- 14 Bakhtiari G, Moradi S, Soltanali S. A novel method for the synthesis of coumarin laser dyes derived from 3-(1H-benzimidazol-2-yl) coumarin-2-one under microwave irradiation. *Arabian Journal of Chemistry*. 2014;7(6):972-5.
- 15 Liu X, Xu Z, Cole JM. Molecular design of UV-vis absorption and emission properties in organic fluorophores: toward larger bathochromic shifts, enhanced molar extinction coefficients, and greater stokes shifts. *The Journal of Physical Chemistry C*. 2013;117(32):16584-95.
- 16 Kurt A. Influence of $AlCl_3$ on the optical properties of new synthesized 3-armed poly(methyl methacrylate) films. *Turkish Journal of Chemistry*. 2010;34(1):67-69.
- 17 Kurt A, Koca M. Blending of poly(ethyl methacrylate) with poly(2-hydroxy-3-phenoxypropyl methacrylate): thermal and optical properties. *The Arabian Journal for Science and Engineering*. 2014;39:5413-20.
- 18 Gunduz B. Investigation of the spectral, optical and surface morphology properties of the N,N'-Dipentyl-3,4,9,10-perylenedicarboximide small molecule for optoelectronic applications. *Polymers For Advanced Technologies*. 2016;27:144-55.
- 19 Gunduz B. Surface morphology properties of the 5,5'-di(4-biphenyl)-2,2'-bithiophene (PPTTP) nanofiber film and calculations of the optical parameters of the PPTTP nanofiber optoelectronic devices. *Journal of Nanoelectronics and Optoelectronics*. 2015;10(1):1-8.
- 20 Bai Y, Du J, Weng X. Synthesis, characterization, optical properties and theoretical calculations of 6-fluoro coumarin. *Spectrochimica Acta Part A: Molecular and Biomolecular Spectroscopy*. 2014;126:14-20.
- 21 Rabahi A, Makhloufi-Chebli M, Hamdi SM, Silva AMS, Kheffache D, Kheddis BB, Hamdi M. Synthesis and optical properties of coumarins and iminocoumarins: Estimation of ground- and excited-state dipole moments from a solvatochromic shift and theoretical methods. *Journal of Molecular Liquids*. 2014;195:240-7.
- 22 Abd-El-Aziz AS, Mohamed HM, Mohammed S, Zahid S, Ata A, Bedair AH, El-Agrody AM, Harvey PD. Synthesis of novel coumarin and benzocoumarin derivatives and their biological and photophysical studies. *Journal of Heterocyclic Chemistry*, 2007;44:1287-1301.
- 23 Kurt A, Kaya M, Koca M. Synthesis and characterization of coumarin derived surface active monomer. *Adiyaman University Journal of Science*. 2016; 6:110-21.
- 24 Gündüz B. Optical properties of poly[2-methoxy-5-(3',7'-dimethyloctyloxy)-1,4-phenylenevinylene] light-emitting polymer solutions: effects of molarities and solvents. *Polymer Bulletin*. 2015;72(12):3241-67.
- 25 Tauc J. *Amorphous and Liquid Semiconductors*, Plenum Press, New York, 1974.
- 26 Gündüz B. Effects of molarity and solvents on the optical properties of the solutions of tris[4-(5-dicyanomethylidenemethyl-2-thienyl)phenyl]amine (TDCV-TPA) and structural properties of its film. *Optical Materials*. 2013;36(2):425-36.
- 27 Tripathy SK. Refractive indices of semiconductors from energy gaps. *Optical Materials*. 2015;46:240-46.



Voltammetric and spectrophotometric pathways for the determination of total antioxidant capacity in commercial turnip juice

Merve Ozturk^a  , Ersin Demir^{b*}  , Tugba Ozdal^{*b}  

^a Department of Food Engineering, Faculty of Engineering, Istanbul Okan University, Istanbul, 34959, Turkey

^b Afyonkarahisar Health Sciences University, Faculty of Pharmacy, Department of Analytical Chemistry, 03030, Afyonkarahisar, Turkey

Abstract: In this study, total flavonoid substances, total phenolic substances, and total antioxidant capacity in turnip juice which made from the turnip (*Brassica rapa*), a plant belonging to the family of "Turpgiller" (*Brassicaceae*), and also a drink specific to the Çukurova, were investigated. The turnip juice samples, taken from the turnip juice (A sample) and hot turnip juice (B) sample in local market, prepared in the laboratory were performed as two different parallel assays. In addition, electrochemical method was used to evaluate total antioxidant capacity (TAC) of turnip juice and hot turnip juice. By the square wave stripping voltammetry (SWSV) method, under the optimized experimental conditions was applied for quercetin determination with a limit of detection (LOD) and limit of quantification (LOQ) of 0.017 and 0.057 µg/L, respectively. These values are satisfactory for application to real food samples for the evaluation of TAC. According to the results carried out by spectrophotometric methods, the highest total phenolic and flavonoid contents and TAC were observed as 13.049±0.40 g GAE/mL, 37.850±0.70 mg QE/mL and 81.831±3,24 mg TE/100 mL, respectively. In addition, the TAC in turnip juice and hot turnip juice were calculated as 573.05±0.43 mg/L and 854.98±9.9 mg/L by SWSV, respectively. The results obtained by voltammetric and spectrophotometric methods for determinations of TAC were in correlation and found to be compatible for the determination of TAC.

Keywords: Antioxidant; Turnip juice, Voltammetry, Spectrophotometry

Submitted: June 15, 2020. **Accepted:** December 15, 2020.

Cite this: Ozturk M, Demir E, Ozdal T. Voltammetric and spectrophotometric pathways for the determination of total antioxidant capacity in commercial turnip juice. JOTCSA. 2021;8(1):163-72.

DOI: <https://doi.org/10.18596/jotcsa.752982>.

* **Corresponding authors: Email:** ersindemir@aku.edu.tr; tugba.ozdal@okan.edu.tr

INTRODUCTION

Antioxidants can be classified mainly in two groups, primary and chain-breaking. In addition, it can be divided into 5 groups as primary antioxidants, secondary antioxidants, enzymatic antioxidants, oxygen cleaners and chelating agents (1). Phenolic compounds directly contribute to the antioxidant capacity amount in foods (2). The most important effect of antioxidant compounds on human health inhibits the damage caused by free radicals in the body or prevents complete damage. The source of

free radicals (unpaired electrons) can be events such as prolonged exposure to X-rays, excessive smoking, intensely polluted air, and exposure to toxic industrial chemicals (3). It is recommended to consume food products with high antioxidant capacity against diseases such as cancer, cardiovascular disease, carcinogenesis, aging and Alzheimer's caused by free radicals (3, 4).

Turnip juice is produced from the turnip (*Brassica rapa*), a plant belonging to the family of *Brassicaceae*. Turnip juice consumption is very common in Turkey

although it is a drink specific to the Cukurova province. Although there are some differences in its production, purple carrots, radishes, bulgur flour, sour dough, salt, water and red powdered pepper are used in making turnip juice (5). Generally, two methods are dominant for the production of turnip juice. The first is the traditional method and the other is the direct method, which can vary locally (6). Turnip juice is a functional beverage with a very strong antioxidant activity due to its rich phenolic and anthocyanin content. Functional properties of turnip juice can be listed as cleaning the respiratory tract, regulating the digestive system, preventing cardiac and vascular diseases, and influencing the immune system in a positive direction (7). In turnip juice, the color comes from the black carrot, rich in phenolic content of the anthocyanins. During turnip juice fermentation lactic acid fermentation takes place that make a great influence on taste and odor characteristics of the product.

Turnip is one of the most effective antioxidant substances against cutaneous diseases thanks to its abundant vitamin C content. Turnip juice can also support the immune system by increasing blood cell function due to its rich content. Moreover, it inhibits free radicals caused blockages. It can also reduce the severity and duration of the common cold by reducing histamine levels. Thanks to glucosinolates, another important ingredient in turnip juice, it plays an important role in cancer treatment. Carrot, which is one of the raw materials of turnip juice, is an excellent source of antioxidants due to its abundant phenolic content, flavonoids and pro-vitamins. They detected abundant purple pigments and Cyanidine-3-glucoside derivatives, which can exhibit abundant purple pigments and chemopreventive and chemotherapeutic activity (8). Furthermore, purple carrots are known to contain more antioxidant, vitamin, carotenoid and phenolic compounds than colored carrot varieties such as orange, yellow and white (9). In conclusion, it is very important to investigate the amount of antioxidants of turnip juices, which is an important and natural drink for human health.

The various methods have been used to measure the *in vitro* antioxidant capacities of fruits and vegetables in the literature. Methods such as cupric ion reducing antioxidant capacity (CUPRAC) and 2,2-diphenyl-1-picrylhydrazyl (DPPH) are simple, cost-effective, easily interpreted and show either reduction capacity (CUPRAC) or direct free radical inhibition (DPPH) (10). While evaluating antioxidant capacity of a food or beverage, at least two of these assays should be combined to have a more reliable conclusion of the total antioxidant capacity (11). Furthermore, in routine antioxidant analyses, cheap, fast, sensitive, environmentally friendly, and reliable

new methods are needed. Electrochemical measurements draw great attention in this respect, especially since they are cheap, reliable, and environmentally friendly. Therefore, antioxidant studies with electrochemical methods have been concentrated in the last decade.

In this study, total antioxidant capacities (TAC) in commercial turnip juices were evaluated by voltammetric and spectrophotometric methods. In order to compare with the voltammetric and traditional analytical methods for the TAC, quercetin was chosen as a reference standard substance. Moreover, gallic acid, quercetin, and trolox were used to investigate for the total phenolic content analysis, total flavonoid analysis and total antioxidant capacities in spectrophotometric methods, respectively. In the electrochemical study, square wave stripping voltammetry (SWSV) was used under the optimum experimental conditions such as pH medium, accumulation time, frequency, and step potential, etc. were researched on carbon paste electrode (CPE). Thus, TAC values obtained by different methods were evaluated statistically. Consequently, TAC values of turnip juices were analyzed for the first time using both electrochemical and conventional analytical methods.

EXPERIMENTAL

Electrochemical Instrumentation

For the electrochemical measurements, Gamry Reference 600 Electrochemical Analyzer was used. The analyzer consists of triple electrode systems which is a platinum wire, a Ag/AgCl reference electrode and carbon paste electrode (CPE) (BASi MF 2010; Ø 3 mm, diameter) as working electrode. In addition, a voltammetric cell with 10 mL capacity was used for collecting the voltammetric data. The working electrode was performed using carbon nanotube powder (MER Corporation, mesh size < 53 µm) and mineral oil at a mass ratio of 70% and 30%, respectively. The carbon paste powder was plugged into the hollow part of the BASi MF 2010 electrode attached. After that, the electrode surface was polished on a polishing cloth. The pH measurements were performed by digital a pH meter (Mettler Toledo, S220).

Reagents and solutions

The analytical standard of quercetin (≥98.0%) was purchased from Sigma-Aldrich. A 500 ppm stock solution of quercetin was prepared daily by dissolving it in water. All other reagents were provided analytical grade and used without further purification. 0.04 M Britton-Robinson (B-R) solutions were used as a supporting electrolyte by mixing of 2.7 mL of orthophosphoric, 2.5 g of boric, and 2.3 mL of acetic acids in distilled water. B-R buffer solutions were

prepared from pH 2.0 to 10.0 by adding the required amount of 5 M NaOH in this triple acid mixture and monitoring with a pH meter. All stock solutions were stored in a refrigerator at 4.0 °C. All electrochemical data were carried out at a comfortable ambient temperature 25 ± 2 °C.

Food samples assay procedure

The commercial turnip juice samples were purchased from a local market. 0.1 mL of the real sample solution was directly placed into 10.0 mL of pH 7.0 B-R buffer solution without any purification and pretreatment food samples. Then, the SWSV measurements from - 0.2 to 1.3 V were obtained to determine the antioxidant capacity of food samples under optimum conditions (step potential (E_s) 3 mV; frequency (f) 300 Hz; pulse amplitude (E) 110 mV; accumulation potential (E_{acc}) 200 mV; accumulation time (t_{acc}) 30 s and pH 7.0 B-R buffer solutions). For all the food samples, the measurements were performed in triplicate and the validation parameters were calculated.

Spectrophotometric Methods

Two types of turnip juice (hot turnip juice and basic turnip juice) were purchased from local market. According to the results of 1,1-diphenyl-2-picrylhydrazyl (DPPH) and cupric reducing antioxidant capacity (CUPRAC) methods, total phenolics, total flavonoids, and antioxidant capacities in turnip juice samples were determined.

Sample preparation

Two different turnip juice samples (hot and basic) were diluted 1/10 and 1/100 using 80% methanol and samples were subjected to vortex mixer for 30 seconds in sterile sample containers and then stored in a refrigerator at -18 °C. Examples in the research were carried out by spectrophotometry in the food engineering laboratory of Okan University.

Determination of total phenolic content

Total phenolics determination was performed colorimetrically as developed slightly by Shahidi and Naczka (12). For this, Folin-Ciocalteu's phenol reagent and gallic acid solutions were prepared with 7.5% Na_2CO_3 in milli-Q water and distilled water, respectively. The phenol reagent of Folin-Ciocalteu was kept in the dark when not in use. 50 μL of diluted phenolic extract, in 1.5 mL of 7.5% sodium carbonate solution and 1.5 mL of Folin-Ciocalteu's Phenol Reagent was homogeneously mixed with vortex in test tubes. A standard calibration graph was created for gallic acid at a concentration of 0.01 to 0.8 g/L in 80% methanolic solution. Absorbance measurements were obtained at 765 nm using the Beckman Coulter DU 730 Life Science UV/Vis Spectrophotometer. The measured blank solution's absorbance was removed from the absorbance of the sample and standard

substances. The measurements taken for each turnip juice sample were repeated three times. As a result, the content of phenolics was calculated as mg gallic acid equivalent (GAE)/100 g of dry weight.

Determination of total flavonoid content

Total flavonoids in turnip juice were measured colorimetrically as described by Dewanto et al. (2002), Zhishen et al. (1999) and Lee et al. (2003) (13-15). Firstly, stock solutions such as 5% sodium nitrite (NaNO_2), 1 M sodium hydroxide (NaOH), 10% aluminum chloride hexahydrate ($\text{AlCl}_3 \cdot 6\text{H}_2\text{O}$) and quercetin (1 g/L) were prepared very precisely. 1 mL of diluted turnip sample was mixed with 0.3 mL of 5% NaNO_2 . Then 0.6 mL of 10% $\text{AlCl}_3 \cdot 6\text{H}_2\text{O}$ and 2 mL of 1 M NaOH were added. Finally, 2.4 mL of water was added quickly and vortexed immediately. Calibration graphic for quercetin was created in different concentrations between 0.01 g/L and 0.8 g/L in 80% methanolic solution. Absorbance data were obtained in 80% methanol solution at 510 nm using Shimadzu UV-1700 Pharmospec UV-Visible Spectrophotometer and all analyses were also performed in triplicate. The content of flavonoids in turnip juices was calculated as mg quercetin/100 mL sample.

Determination of antioxidant capacity according to DPPH method

For the amount of antioxidant in turnip juices, colorimetric method was used as described by Kumaran (2006) and Rai et al. (2006) (16, 17). 1 mM DPPH solution was prepared from methanol. The absorbances of turnip juice samples were collected against the methanol blank solution at 517 nm using Shimadzu UV-1700 Pharmospec UV-Visible Spectrophotometer. The calibration plot for Trolox was obtained between 0.01 g/L and 0.8 g/L in 80% methanol solution. All analyses were performed three times for each turnip sample, and the results were calculated in mg Trolox equivalent (TEAC).

Determination of antioxidant capacity according to CUPRAC method

Antioxidant capacities of turnip juice samples were analyzed colorimetrically by CUPRAC method developed by Apak et al. (2004) (18). In the first stage of the study, solutions of copper (II) chloride at a concentration of 0.01 M, neocuproine (Nc) in ethanol at a concentration of 7.5×10^{-3} M, and ammonium acetate (NH_4Ac) buffer at pH 7.0 was prepared very precisely. Moreover, the solutions used in the whole experiment were prepared daily. 1 mL of copper (II) chloride solution, 1 mL of ammonium acetate buffer and 1 mL of neocuproine were added to 100 μL of the turnip samples. Absorbance data were obtained in 80% methanol solution at 450 nm using Shimadzu UV-1700 Pharmospec UV-Visible Spectrophotometer and all analyses were performed in triplicate. Calibration graph for Trolox was created in different

concentrations between 0.01 and 0.8 g/L in 80% methanol solution. All analyses were performed in triplicate for each turnip sample, and the results were calculated in mg trolox equivalent (TEAC).

Statistical Analysis

Student's t-test was performed to understand if there are statistically significant ($p < 0.05$) differences between total flavonoid contents and total phenolics, total antioxidant capacities of two turnip juice samples in spectrophotometric method. Electrochemical analysis results for total antioxidant capacities in turnip juice samples were obtained on the standard calibration chart. Results were calculated as mean and standard deviation.

RESULTS AND DISCUSSION

Electrochemical Analysis

In analytical chemistry, electrochemical methods are used for investigating a huge scale of substances. For example, metal ions and organic compounds are discovered in pesticides, food, and medicine. They are generally quick and cheap. The using of electrochemical methods, investigations of antioxidant in food sources have been analyzed by some groups (19-23). Cyclic voltammetry (CV) and differential pulse voltammetry (DPV) and square wave voltammetry (SWV) have been mostly used for electrochemical species, because the results give very fast and reliable results in total antioxidant capacity (TAC) analysis (24-26). It is imaginable to have quantitative analysis of antioxidant present in the samples. The different groups of antioxidants compound such as phenolics and ascorbic acid show

different oxidation potential which shows the results in different regions of antioxidants, a mignon number of electrochemical methods can be discovered in the literature.

Optimization of the Parameters

The influence of step potential (E_s) was studied by step potentials from 1 mV to 6 mV. The peak current increased at between 1 mV and 3 mV and then it shows stability after 3 mV for step potentials. Hence, 3 mV was chosen as the optimum step potential for the subsequent experiments. The effect of pulse amplitude (E) was also determined various amplitudes from 10 mV to 110 mV. The oxidation peak signal increased until 90 mV linearly. That is why 110 mV was chosen as the optimum pulse amplitude because the maximum result is obtained from 110 mV. In addition to these steps, accumulation time (t_{acc}) was determined from 10 s to 70 s. Until 30 s, the oxidation peak current was increased. After this point, accumulation time was not depended on peak current of quercetin because electrode surface is saturated fully. Therefore, optimum accumulation time was chosen as 30 s. The next step is accumulation potential (E_{acc}) was studied from 100 mV to 600 mV. The increase of peak current started at 100 mV and after 200 mV, it showed stability until 600 mV. The available accumulation potential is 200 mV. The impact of frequency (f) was evaluated between 20 Hz and 300 Hz. The peak current gradually increased between 20 and 300 Hz. Therefore, the optimum frequency was used as a 300 Hz at subsequent measurements. The optimized parameters for the SWSV in 1 mg/L quercetin were shown in **Figure 1** and **Table 1**.

Table 1. Optimized parameters of SWSV for the determination of quercetin.

Parameters	Optimized values/unit
Step potential (E_s)	3 mV
Pulse amplitude (E)	110 mV
Accumulation potential (E_{acc})	200 mV
Accumulation time (t_{acc})	30 s
Frequency (f)	300 Hz
Supporting electrolyte	pH 7.0 B-R Buffer solution
Peak Potential	+200 mV

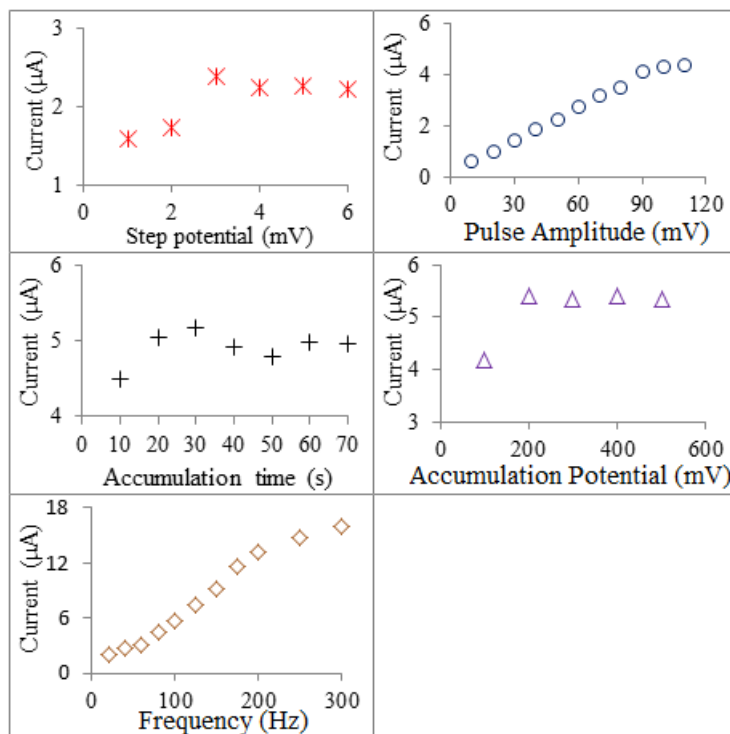


Figure 1. Optimized parameters for the SWSV in 1 mg/L quercetin.

Influence of pH

In the electrochemical studies, supporting electrolyte is one of most important parameters due to the effects on peak potential, current intensity can also affect the electrode kinetics in the charge transfer process. Hence, the effects of the supporting electrolyte anodic signal of quercetin at various pH values on the carbon paste electrode (CPE) were investigated. In order to determine the pH effect, square wave stripping (SWS) voltammograms were taken in the Britton-Robinson buffer solutions between pH 2.0 and pH 10.0 for the 1 mg/L quercetin. SWS experiments that the highest signals were obtained in moderate medium at pH 7.0 were found to be dependent on the below $\text{pH} \leq 10.00$ buffer solutions. In addition, the oxidation peak potential of quercetin

gradually increased linearly between potential from pH 3 to pH 7 per unit pH changes. Significant decreasing in the quercetin peak current of quercetin was observed pH 7.0 then to up pH 10.0. Also, peak potential of the quercetin was a change as 65.28 mV by increasing as unit pH. This is the evidence that consumption of hydrogen ions contains in the electrochemical oxidation process. Britton-Robinson buffer solution at pH 7.0, where maximum peak flow was obtained for the determination of quercetin on the CPE, was determined as the ideal support electrolyte. Figure 2 shows the influence of pH for the peak I. (1 mg/L of quercetin from pH 2.0 to pH 10.0)

$$E_p \text{ (mV)} = - 65.28 \text{ pH} + 635.97 \text{ (mV)} \text{ (} R^2 = 0.9919 \text{)}$$

$$E_p \text{ (mV)} = - 50.85 \text{ pH} + 990.6 \text{ (mV)} \text{ (} R^2 = 0.9996 \text{)}$$

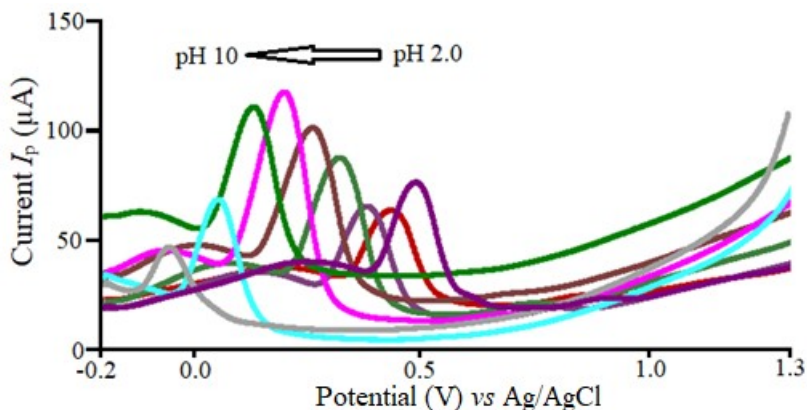


Figure 2. The pH effects on the peak I in 1 mg/L of quercetin by SWSV.

Quantitative evaluation and validation of Quercetin

Peak current values against concentration were evaluated for anodic peak I of quercetin by using CPE. The peak intensities changed in a way to increase linearly as a result of increasing quercetin concentrations by SWSV on CPE in pH 7.0 (**Figure 3**). As a result of this change, a linear working range between 0.04 µg/L and 10 µg/L was obtained on the calibration graph. The limit of determination (LOD) and limit of detection (LOQ) were calculated as 0.017

µg/L and 0.057 µg/L, respectively. In calculating LOD and LOQ values, $LOD = 3 s/m$ and $LOQ = 10 s/m$ equations were preferred. The “m” is the slope of the calibration equation of the quercetin and the “s” is the standard deviation of the point where the concentration in the calibration equation is zero. Validation parameters of the calibration chart for quercetin determination are summarized in Table 2.

$$I_p (\mu A) = 0.203 (C, \mu g/L) - 0.032 \quad r = 0.9934$$

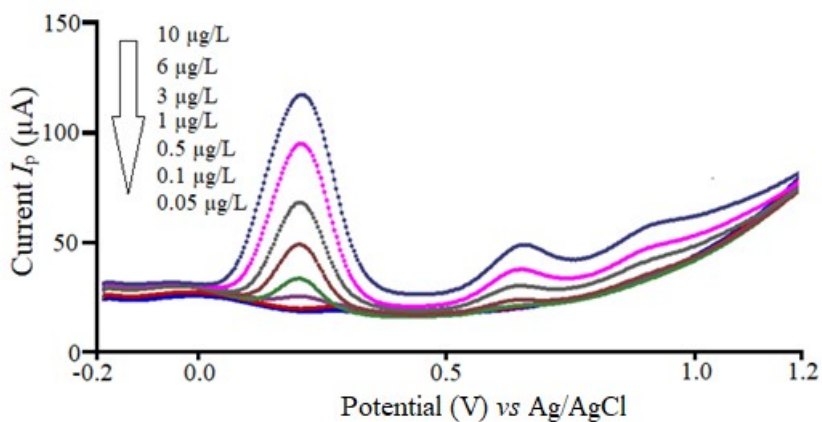


Figure 3. SWS voltammograms for the calibration graph of quercetin on CPE in pH 7.0.

Table 2. Validation parameters for determination of quercetin by SWS on CPE.

Parameter	Value
Peak potential (E_p) (mV)	+ 200
Working range (µg/L)	0.04 – 10.0
Slope (µA L/µg)	0.203
Intercept (µA)	- 0.032
Limit of determination (LOD) (µg/L)	0.017
Limit of detection (LOQ) (µg/L)	0.057
Correlation coefficient	0.9934

The determination TAC in turnip juices on CPE by SWSV

With the increasing importance of antioxidant substances in recent years, scientists are researching new analytical methods for antioxidant capacity determinations. A standard method for the determination of antioxidants, especially in complex samples such as food, has not yet been fully developed. Analytical methods such as chromatography, spectrophotometry, capillary electrophoresis, and spectrofluorometric analyses have been widely preferred in determining antioxidant capacity. However, the working principles of these methods are very different from each other. The common problems of these methods are them being expensive, analysis times are long and they are using too many chemicals. In addition, using less organic solvent is an important indicator for environmentally friendly methods. For these reasons, electrochemical methods, which are a fast, cheap, and reliable method that require less solution, are of great interest in antioxidant determinations. Furthermore, electrochemical methods are included not only in the determination of antioxidants, but also in the analysis

of many different substances such as drugs, pesticides, metals, vitamins and amino acids.

In this study, the total antioxidant capacity of turnip juices purchased from the local market was examined for the first time with a CPE using quercetin as the reference compound. Firstly, turnip juice samples were diluted 10 times with methanol and analyzed directly by SWSV method in buffer solutions at pH 7.0. SWS voltammograms were obtained in turnip samples under the optimization conditions for standard quercetin solutions. Then, by adding standard quercetin as a 0.5 µg/L in the turnip juice samples, the total antioxidant capacity was calculated as equivalent quercetin from the peak current increase. Figures 4a and 4b represent the electrochemical analysis on carbon paste electrode for the total antioxidant capacity of turnip juice as sample A and sample B by SWSV, respectively determination of the total antioxidant capacity in turnip juices with SWSV is given in Table 3. Consequently, TAC values found by electrochemical method are mostly compatible with the results of total flavonoid contents.

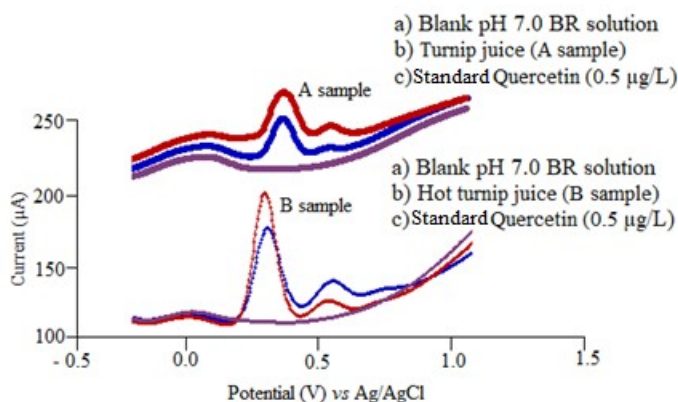


Figure 5. Electrochemical determination pathway of total antioxidant capacity for the turnip juice samples by SWSV on carbon paste electrode.

Table 3. The determination of the total antioxidants capacity (TAC) for the turnip juices by SWSV on carbon paste electrode.

Sample	Total antioxidant capacity Equivalent Quercetin	RDS,%
A	573±0.43 mg/L	0.07
B	854±9.90 mg/L	1.16

Spectrophotometric Analysis

Total Phenolic and Flavonoid Contents

The concentrations of phenolic compounds in a sample can vary. In addition, phenolic compounds are very rare to be found in the samples in free form. It is generally more likely to exist in the form of glycosides or ester forms with carboxylic acid. Moreover, there is a possibility that phenolic compounds bind to fatty

acids, sterols and cellular walls. The amount of total phenolic of sample A and sample B were found as 11.361±0.49 mg GAE/mL and 13.049±0.40 mg GAE/mL, respectively (**Table 4**). According to the results of the total phenolic content, it was determined that the total phenolic content in the B sample as hot turnip juice was higher than the A sample as turnip juice. Moreover, the total flavonoid

content of sample B (37.850 ± 0.70 mg QE/mL turnip juice) was also found to be higher than sample A (23.894 ± 0.55 mg QE/mL turnip juice) about 58.41% as shown in Table 4. Furthermore, the total flavonoid content in turnip samples was very close to the

electrochemical results in percent. Compared to sample A with electrochemical methods, there was 49.04 percent increase in sample B, while this ratio was 58.41 percent with total flavonoid content.

Table 4. The total phenolic and flavonoid contents of turnip juice samples.

Sample	Total Phenolic Contents (mg GAE/mL turnip juice)	Total Flavonoid Contents (mg QE/mL turnip juice)
A (Turnip Juice)	11.361 ± 0.49^a	23.894 ± 0.55^a
B (Hot Turnip Juice)	13.049 ± 0.40^a	37.850 ± 0.70^a

In the study of Ekinci et al. (2016), the total phenolic content of turnip juice was found as 0.000517 ± 0.072 mg GAE/mL (27). Our results for total phenolic content were higher than their result. However, Öztan (2006) was found the total phenolic content of turnip juice as 15.5 mg GA/mL which is in accordance with our results (28).

Antioxidant capacity according to DPPH and CUPRAC Analyses

The antioxidant activity of turnip juice samples were investigated as TE (mg TE/g mL) by DPPH and CUPRAC

methods. The antioxidant activity in sample B was higher than those of sample A using both methods. Antioxidant activities in turnip juice and hot turnip juice were found as 57.634 ± 3.01 mg TE /100 mL and 81.831 ± 3.24 mg TE /100 mL, respectively by the DPPH assay (Table 5). On the other hand, antioxidant activity of turnip juice samples were found as 561.18 ± 45.72 mg TE / 100 mL for sample A and 619.94 ± 186.58 mg TE /100 mL for sample B by CUPRAC analysis (Table 5).

Table 5. Antioxidant capacities of turnip juice samples according to DPPH and CUPRAC analyses.

Sample	DPPH (mg TE/100 mL turnip juice)	CUPRAC (mg TE/100 mL turnip juice)
A (Turnip Juice)	57.634 ± 3.01^b	561.18 ± 45.72^a
B (Hot Turnip Juice)	81.831 ± 3.24^a	619.94 ± 186.58^a

Statistical Analysis

According to *t*-test, *t* values were found to be 0.438 and 1.238 for total phenolic and total flavonoid analyses, respectively. Therefore, there were no statistically significant difference between two turnip juice samples according to their total phenolic and flavonoid contents. However, there were statistically significant differences between amounts of antioxidant of two samples according to DPPH analysis ($p < 0.05$) as *t* value was found to be 0.0003. There were no statistically significant differences (t -value=0.312; $p > 0.05$) between two samples according to their antioxidant capacities measured by CUPRAC analysis.

CONCLUSION

Herein, flavonoid contents, phenolic contents, and total antioxidant capacities in turnip juices were investigated. Since the above methods are different from each other in terms of analysis principles and reaction conditions, a single method is not sufficient to show all antioxidant properties. For this reason, this study compared the four most commonly used spectrophotometric tests. The highest phenolic and flavonoid components and antioxidant activities were obtained from hot turnip juice (B sample). This study was carried out by electrochemical analysis except for

spectrophotometric tests. A sensitive SWSV method was applied using the carbon paste electrode for the direct development of total antioxidant capacity (TAC) in turnip juices. Using the SWSV method developed for standard quercetin as antioxidant agent determine the total antioxidant amounts in turnip samples were carried out with the standard addition method. To ensure the accuracy and feasibility of the method, the optimized SWS voltammetric procedure was used directly, without any pre-treatment to samples. Consequently, the data obtained by new SWSV electrochemical method which is fast, easy, portable for the determination of antioxidants is compatible with the results of the total flavonoid content most among other spectrophotometric methods. According to all analytical methods, it has been proved that the antioxidant capacity of hot turnip juice is higher than that of normal turnip juice.

REFERENCES

1. Bartosz G. Food oxidants and antioxidants: chemical, biological, and functional properties: CRC press; 2013.
2. Algarra M, Fernandes A, Mateus N, de Freitas V, da Silva JCE, Casado J. Anthocyanin profile and antioxidant capacity of black carrots (*Daucus carota* L.

- ssp. sativus var. atropurpureus Alef.) from Cuevas Bajas, Spain. *Journal of Food Composition and Analysis*. 2014;33(1):71-6.
3. Lobo V, Patil A, Phatak A, Chandra N. Free radicals, antioxidants and functional foods: Impact on human health. *Pharmacognosy reviews*. 2010;4(8):118.
 4. Nizamlioglu N, Nas S. The phenolic compounds in vegetables and fruit; structures and their importance. *Electronic Journal of Food Technologies*. 2010;5(1):20-35.
 5. Erten H, Tanguler H, Canbař A. A traditional Turkish lactic acid fermented beverage: Shalgam (Salgam). *Food Reviews International*. 2008;24(3):352-9.
 6. Tanguler H, Erten H. Occurrence and growth of lactic acid bacteria species during the fermentation of shalgam (salgam), a traditional Turkish fermented beverage. *LWT-Food Science and Technology*. 2012;46(1):36-41.
 7. Tanguler H. Identification of predominant lactic acid bacteria isolated from shalgam beverage and improvement of its production technique. Doctor of Philosophy thesis, Cukurova University, Adana, Turkey. 2010.
 8. Gläβgen WE, Wray V, Strack D, Metzger JW, Seitz HU. Anthocyanins from cell suspension cultures of *Daucus carota*. *Phytochemistry*. 1992;31(5):1593-601.
 9. Alasalvar C, Grigor JM, Zhang D, Quantick PC, Shahidi F. Comparison of volatiles, phenolics, sugars, antioxidant vitamins, and sensory quality of different colored carrot varieties. *Journal of Agricultural and Food Chemistry*. 2001;49(3):1410-6.
 10. Wootton-Beard PC, Moran A, Ryan L. Stability of the total antioxidant capacity and total polyphenol content of 23 commercially available vegetable juices before and after in vitro digestion measured by FRAP, DPPH, ABTS and Folin-Ciocalteu methods. *Food Research International*. 2011;44(1):217-24.
 11. Contreras-Calderón J, Calderón-Jaimes L, Guerra-Hernández E, García-Villanova B. Antioxidant capacity, phenolic content and vitamin C in pulp, peel and seed from 24 exotic fruits from Colombia. *Food research international*. 2011;44(7):2047-53.
 12. Shahidi F, Naczki M. Antioxidant properties of food phenolics. *Phenolics in food and nutraceuticals*. CRC Press; 2004.
 13. Dewanto V, Wu X, Adom KK, Liu RH. Thermal processing enhances the nutritional value of tomatoes by increasing total antioxidant activity. *Journal of agricultural and food chemistry*. 2002;50(10):3010-4.
 14. Zhishen J, Mengcheng T, Jianming W. The determination of flavonoid contents in mulberry and their scavenging effects on superoxide radicals. *Food chemistry*. 1999;64(4):555-9.
 15. Lee KW, Kim YJ, Lee HJ, Lee CY. Cocoa has more phenolic phytochemicals and a higher antioxidant capacity than teas and red wine. *Journal of agricultural and food chemistry*. 2003;51(25):7292-5.
 16. Kumaran A. Antioxidant and free radical scavenging activity of an aqueous extract of *Coleus aromaticus*. *Food chemistry*. 2006;97(1):109-14.
 17. Rai S, Wahile A, Mukherjee K, Saha BP, Mukherjee PK. Antioxidant activity of *Nelumbo nucifera* (sacred lotus) seeds. *Journal of ethnopharmacology*. 2006;104(3):322-7.
 18. Apak R, Güçlü K, Özyürek M, Karademir SE. Novel total antioxidant capacity index for dietary polyphenols and vitamins C and E, using their cupric ion reducing capability in the presence of neocuproine: CUPRAC method. *Journal of agricultural and food chemistry*. 2004;52(26):7970-81.
 19. Demir E, Senocak A, Tassembledo-Koubangoye MF, Demirbas E, Aboul-Enein HY. Electrochemical Evaluation of the Total Antioxidant Capacity of Yam Food Samples on a Polyglycine-Glassy Carbon Modified Electrode. *Current Analytical Chemistry*. 2018;14:1-8.
 20. Pastor FT, Šegan DM, Gorjanović SŽ, Kalušević AM, Sužnjević DŽ. Development of voltammetric methods for antioxidant activity determination based on Fe (III) reduction. *Microchemical Journal*. 2020;155:104721.
 21. García-Carvajal E, Blandón-Naranjo L, Villa-Montoya V, Vázquez MV, Peláez-Jaramillo C. Electrochemical Approach to the Study of the Antioxidant Capacity of *Vaccinium Meridionale* Swart at Different Ripening Stages. *Portugaliae Electrochimica Acta*. 2019;37(1):71-82.
 22. Alcalde B, Granados M, Saurina J. Exploring the Antioxidant Features of Polyphenols by Spectroscopic and Electrochemical Methods. *Antioxidants*. 2019;8(11):523.
 23. Giovagnoli-Vicuña C, Pizarro S, Briones-Labarca V, Delgadillo Á. A Square Wave Voltammetry Study on the Antioxidant Interaction and Effect of

Extraction Method for Binary Fruit Mixture Extracts. Journal of Chemistry. 2019;2019.

24. de Araújo Rodrigues I, Gomes SM, Fernandes IPG, Oliveira-Brett AM. Phenolic Composition and Total Antioxidant Capacity by Electrochemical, Spectrophotometric and HPLC-EC Evaluation in Portuguese Red and White Wines. Electroanalysis. 2019;31(5):936-45.

25. Demir E. Sensitive and Selective Pathway of Total Antioxidant Capacity in Commercially Lemon, Watermelon and Mango-pineapple Cold Teas by Square Wave Adsorptive Stripping Voltammetry. Gazi University Journal of Science. 2019;32(4):1123-36.

26. Vilas-Boas Â, Valderrama P, Fontes N, Geraldo D, Bento F. Evaluation of total polyphenol content of

wines by means of voltammetric techniques: Cyclic voltammetry vs differential pulse voltammetry. Food chemistry. 2019;276:719-25.

27. Ekinci FY, Baser GM, Özcan E, Üstündağ ÖG, Korachi M, Sofu A, et al. Characterization of chemical, biological, and antiproliferative properties of fermented black carrot juice, shalgam. European Food Research and Technology. 2016;242(8):1355-68.

28. Öztan T. Antioxidant activities and phenolic substance profile of purple carrot, its concentrate, shalgam beverage, pomegranate juice and sour pomegranate concentrate products. International Information System For The Agricultural Science And Technology (AGRIS). 2006.



Poly(glutamic acid) Modified Pencil Graphite Electrode for the Voltammetric Determination of Bisphenol A

Ozge Gorduk*  

Yildiz Technical University, Faculty of Arts and Science, Department of Chemistry, 34210, Istanbul, Turkey.

Abstract: Bisphenol A (BPA), which is an endocrine-disrupting substance, is often utilized as beverage and food packing material, and it may accumulate in nutrition and water sources, which is why it is important to monitor. In this study, for the determination of bisphenol A, electro-polymerization of glutamic acid (GA) was performed on a pencil graphite electrode (PGE). The performance of the sensor (PGA/PGE) for determining bisphenol A was examined utilizing the cyclic voltammetric (CV) and differential pulse voltammetric (DPV) methods. Electrochemical characterization process of the PGA/PGE was carried out by the electrochemical impedance spectroscopy (EIS) and CV methods. The morphological property of the PGA/PGE was investigated by scanning electron microscopy (SEM). The presence of functional groups in the PGA/PGE composition was characterized by Fourier transform infrared spectroscopy (FTIR). The electrochemical behavior of BPA was observed with the bare PGE and the PGA/PGE. Based on the findings, the response of BPA was considerably raised with PGA/PGE. With the optimized parameters and based on the findings from DPV, the BPA oxidation current was linear in a concentration interval of 1.0 to 100 μM ($R=0.9992$), and the detection limit was found to be 0.37 μM . Detection of BPA in the plastic bottled drinking water sample using PGA/PGE was performed successfully, and the recoveries were in the range of 89.3 to 104.7%. This strategy can provide several prospects in electrochemically determining BPA in practical applications.

Keywords: Glutamic acid, Electro-polymerization, Bisphenol A, Pencil Graphite Electrode, Voltammetric determination.

Submitted: April 28, 2020. **Accepted:** December 15, 2020.

Cite this: Gorduk O. Poly(glutamic acid) Modified Pencil Graphite Electrode for the Voltammetric Determination of Bisphenol A. JOTCSA. 2021;8(1):173-86.

DOI: <https://doi.org/10.18596/jotcsa.728165>.

***Corresponding author.** E-mail: ozgekyn34@gmail.com, okoyun@yildiz.edu.tr, Tel: +90(212)3834150.

INTRODUCTION

Bisphenol A (BPA), with its International Union of Pure and Applied Chemistry (IUPAC) name called 4,4'-(propane-2,2-diyl)diphenol, is among the most frequently utilized substances around the world to produce epoxy and polycarbonate resins employed for packaging, food storage, bottles and beverage cans (1-3). The common usage of BPA has led it to infiltrate into food and water from packaging materials, causing human and aquatic organisms to be exposed to it (4). The existence of phenolic compounds in the composition of BPA is like the compounds in endocrine hormones, especially estradiol and diethylstilbestrol and causes binding to estrogen receptors (5, 6). Therefore, BPA is recognized as an endocrine-disrupting compound

(EDC) (1, 5). It is also thought to be related to the emergence of various health effects like diabetes, birth defects, infertility, cardiovascular disease, and developmental neurotoxicity. Even more crucially, BPA can lead to an increase in the prevalence of some types of cancer (6, 7).

The main origin of BPA contact in humans is water, beverages, and food because of its transfer from plastic vessels to nutrition products (4). When the negative effects of BPA reported on human health are evaluated, it has become very important to determine the concentration of BPA, which can contaminate foods and beverages (8). With the increasing momentum in recent years, studies on BPA determination have begun to enter the literature. When the literature is examined, it is seen

that there are many analytical methods used for BPA determination. These methods include high-performance liquid chromatography (9), electrochemical methods (1, 10), gas chromatography (11), enzyme-linked immunosorbent (12), molecular suppression (13) and fluorimetry (14). Among these methods, electrochemical methods have several benefits such as speed, minimal cost, simple usage, good sensitivity, and satisfactory selectivity. Therefore, electrochemical methods are very attractive for BPA determination (15-17).

In the last few decades, using the electropolymerization method is of great significance in the construction of electrochemical sensors and biosensors due to its practical benefits like modification of the electrode, selectivity, good repeatability, electrochemical recycling, stability and low cost (18, 19). To reinforce this, there is much literature on the use of these modified electrodes for qualitatively and quantitatively determining BPA. A PGE is novel kind of carbon electrode and has been widely used recently (20-22). PGE has been utilized to identify a broad diversity of analytes using different voltammetric methods (23). PGE has many benefits over other carbon-based electrodes like low cost, surface polishing and no need for time-consuming processes due to characteristics as disposability (18). The surface may be modified effortlessly, and it has high electrochemical reactivity and surface area (19).

Glutamic acid (GA) is among twenty widespread amino acids that may be effortlessly electropolymerized on the electrode surface to create poly(glutamic acid) (PGA) (24, 25). PGA includes glutamate repeat units and free protonated carboxylic groups ($pK_a = 4.45$) by linking α -amino and δ -carboxylic acid functional substances, which show enhanced properties in electrochemical applications (26). Studies on the electropolymerization of GA on different electrode platforms are included in the literature (26-32).

Herein, a polymer-based electrode, which can be fabricated in one step, was prepared by the electropolymerization process using the cyclic voltammetric method. The PGA/PGE displayed effective catalytic properties in the electrochemical determination of bisphenol A. The sensor (PGA/PGE) was effectively utilized to determine BPA alongside potential interferences. The sensitivity, linear range, LOD, LOQ, and measurements in the plastic bottled drinking water sample were additionally shown. The presented electrochemical sensor offers chances for creating a simple, cost-efficient and effortless method in water quality observation.

MATERIAL AND METHODS

Chemicals and Apparatus

All the chemical materials (bisphenol A, potassium hexacyanoferrate(II) trihydrate, L-glutamic acid, potassium hydroxide, lithium perchlorate, potassium

hexacyanoferrate(III), and phosphoric acid) used in the experimental processes were purchased from the Sigma-Aldrich Company. Besides, potassium hydrogen phosphate and potassium dihydrogen phosphate chemicals used in the preparation of phosphate buffer solution (PBS) were obtained from Merck Company. All of the chemicals used during this study are of analytical grade. The plastic bottled drinking water sample was bought from a local shop. Distilled water used during experimental studies was obtained from a Millipore Milli-Q Direct 16 device ($18 \text{ M}\Omega\text{cm}^{-1}$).

Voltammetric measurements were performed using the Autolab PGSTAT128N instrument. Gamry Reference 3000 Potentiostat/Galvanostat system was used for electrochemical impedance spectroscopy (EIS) measurements. During the experiments, the conventional 3-electrode system was used. In this context, pencil graphite (Tombow 0.5 HB), Ag/AgCl, and Pt wire are used as working electrode, reference electrode, and counter electrode, respectively. The pH measurements were carried out with a Mettler Toledo pH meter at room temperature. FTIR data was recorded using the Perkin Elmer spectrophotometer with ATR sampling accessory. Ultraviolet-visible measurements were performed with the Agilent 8453 UV/Vis spectrophotometer. For the investigation of the surface morphology, SEM Zeiss Evo LS 10 device was made use of.

Fabrication of poly(glutamic acid) modified pencil graphite electrode

The fabrication of the PGA/PGE to be utilized in the electrochemical detection of the bisphenol A was performed in one step. Firstly, electrodes with 10 cycles of film thickness in PBS pH 7.0 containing different concentrations of glutamic acid monomer (0.001, 0.01 and 0.1 M) were prepared to optimize the monomer concentration. The performances of the prepared electrodes were compared using both CV and DPV methods in the solution containing 100 μM BPA and it was observed that the highest oxidation response belongs to the concentration of 0.01 M glutamic acid. Therefore, the optimized monomer concentration was chosen as 0.01 M. Then, polymerization of 0.01 M GA in PBS at different pHs (4.0, 5.0, 6.0, 7.0, and 8.0) was investigated to examine the pH effect on the polymerization solution. The optimum pH value for the controlled growth of the film thickness was found to be 7.0. The modification was carried out in 0.01 M L-glutamic acid solution which was arranged in 0.1 M PBS pH 7.0 at scan rate of 50 mV/s. CV method was employed to carry out the electropolymerization procedure. According to the aim, varying polymerization potentials equaling 2.3, 2.2, 2.1, 2.0, and 1.9 V to -0.5 V were implemented. The best peak current for BPA was achieved with the prepared electrode under conditions where the electropolymerization process was provided between -0.5 and 2.0 V potential. The measurements were conducted at under the

optimum conditions 10 cycles and a scan rate of 50 mV/s, in the potential range -0.5 V to 2.0 V. The electrode obtained after this procedure was coded as PGA/PGE and washed by double-dipping in distilled water and dried at room temperature in a desiccator.

Electrochemical measurement

To investigate the electrochemical determination of the BPA, various voltammetric methods were performed. Cyclic voltammetric (CV) and differential pulse voltammetric (DPV) methods were used for the electrochemical characterization of PGA/PGE, determination and detection of BPA. The voltammetric measurements were actualized in 0.1 M pH 4.0 PBS containing 100 μ M BPA and were performed at room temperature. During the measurements, PGA/PGE was immersed in the analyte solution at a length of 1.0 cm in order to keep the surface area constant. CV and DPV signals were recorded in a potential range of 0.0 to 1.0 V. New electrodes were used for each measurement.

Preparation of real sample

In this study, real sample studies were made with plastic bottled drinking water samples bought from a local shop in Turkey and utilized with no pretreatment. For examination, 2.5 mL of the plastic bottled drinking water sample was diluted to 10.0 mL with PBS pH 4.0. Before the analysis, the water sample was freshly prepared. It was mixed in the ultrasonic bath for 10 minutes, and then analysis was carried out.

RESULTS AND DISCUSSION

Electro-polymerization of glutamic acid

The PGA/PGE was produced by immersing the bare PGE in a PBS pH 7.0 containing 10.0 mM GA

monomer and recording cyclic voltammograms taken at 50 mV/s scan rate and potential range of -0.5 to 2.0 V. In Figure 1, it is seen that the oxidation signal at 1.75 V in the first cycle decreases and disappears in after second cycle. This is thought to be related to the polymerization of the monomeric molecules. Here, it can be observed that the oxidation peak signals are increased with step by step each cycle the formation and development of an electroactive layer on the PGE surface. After the ninth cycle, the rise of this peak current is almost constant and more stable, indicating that the growth of polymerization has reached the saturation level. The reaction mechanism of the GA for the electropolymerization process is shown in Scheme 1 (28).

According to the experimental findings obtained, the thickness of the film had a significant effect on the electrocatalytic property of PGE (33). The degree of thickness was also adjusted. The coating was managed by changing the number of multiple cycles (3, 5, 7, 10, and 15 cycles) on PGE and the relevant electrocatalytic activity for the oxidation of 100 μ M BPA in PBS pH 4.0 was examined. As seen in Figure 2, the oxidation peak current of BPA has reached its peak in 10 cycles. Therefore, 10 cycles were selected for the electro-polymerization of GA. Initially, the electrocatalytic response of BPA also increased with an increase in the number of polymerization cycles. However, when the number of polymerization cycles was more than 10, the peak currents of the oxidation signal of BPA did not show a significant increase. This is because the film thickness hinders electron transfer after reaching certain saturation (34). Thus, electrodes with 10 cycles of film thickness were used for all electrochemical analyses.

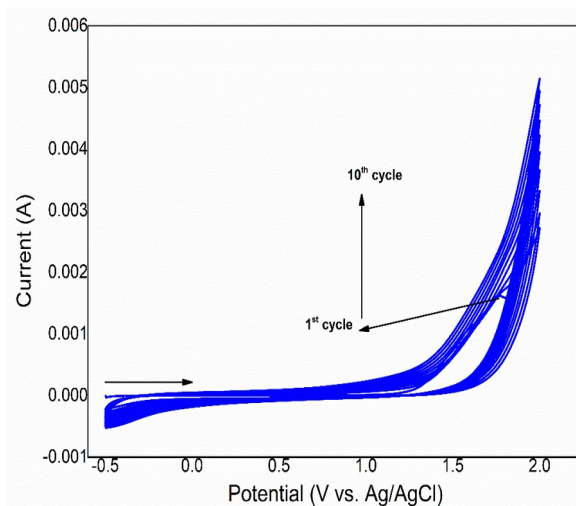
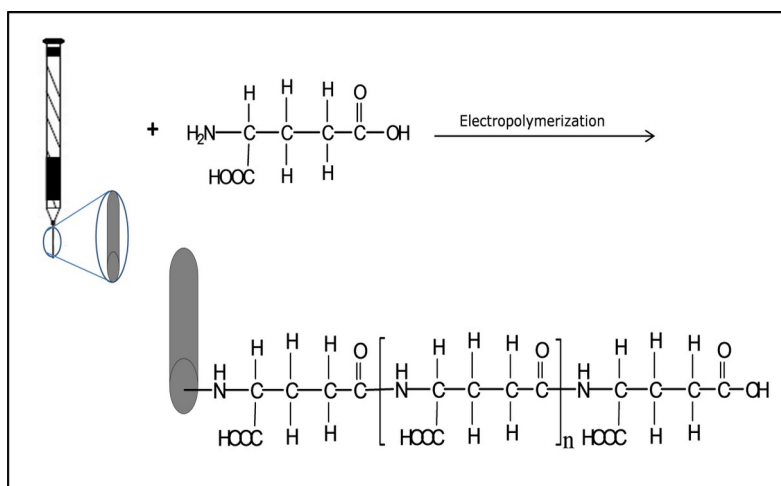


Figure 1: Cyclic voltammograms of electro-polymerization of GA on PGE in PBS pH 7.0 containing 10.0 mM L-glutamic acid at between -0.5-2.0 V potential range, 10 cycles, at scan rate of 50 mV/s.



Scheme 1: The reaction mechanism of the GA for the electropolymerization on the surface PGE.

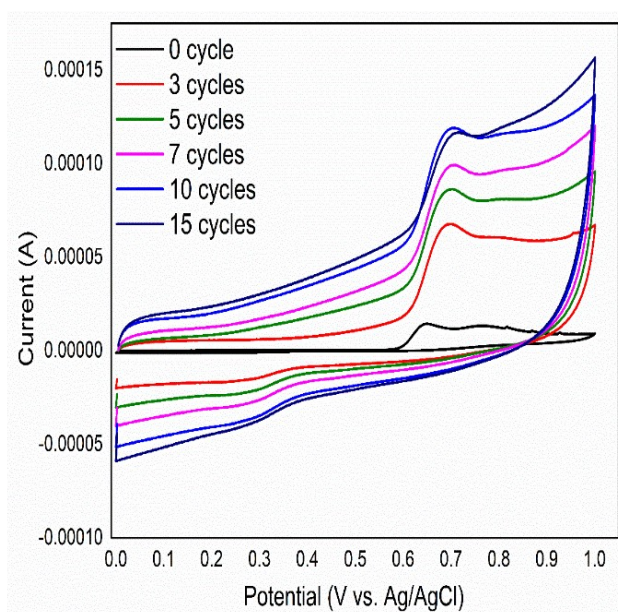


Figure 2: Cyclic voltammograms of PGA/PGEs with different number of cycles in PBS pH 4.0 containing 100 μM BPA at scan rate of 50 mV/s and the potential range of 0.0 V to 1.0 V.

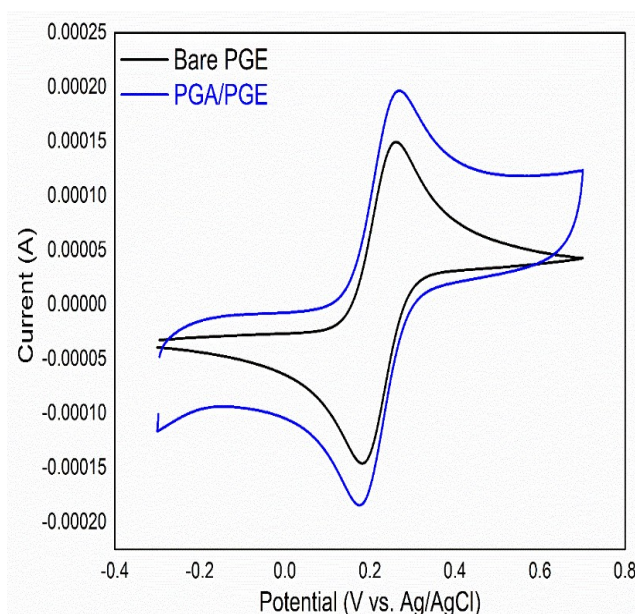


Figure 3: Cyclic voltammograms of bare PGE and PGA/PGE in 2.5 mM $\text{Fe}(\text{CN})_6^{3-/4-}$ + 0.1 M KCl, at potential range of -0.3-0.7 V, at scan rate of 50 mV/s.

Characterization studies

The redox types of $\text{Fe}(\text{CN})_6^{4-/3-}$ were selected for the electrochemical identification experiment. The cyclic voltammograms of $\text{Fe}(\text{CN})_6^{4-/3-}$ (2.5 mM) were acquired by bare PGE and PGA/PGE in Figure 3 (21). We determined well-identified oxidation and reduction peaks with the bare PGE at 0.27 and 0.19 V. Oxidation and its matching cathodic peak were seen with PGA/PGE at 0.28 and 0.18 V, respectively. As shown in Figure 3, the oxidation potential of $\text{Fe}(\text{CN})_6^{4-}$ redox species shifted to the anodic direction and the reduction potential of $\text{Fe}(\text{CN})_6^{3-}$ redox species shifted to the cathodic direction in the presence of PGA as modifiers according to bare PGE. Besides, in the case of PGA/PGE, peak currents were significantly raised, showing that the PGA/PGE has a high electroactive surface area, good

electrochemical properties, and ability to the electrostatic pull of the $\text{Fe}(\text{CN})_6^{4-/3-}$ redox pair (23).

EIS may provide useful information about the impedance alterations of the electrode surface to describe the sensor's construction procedure. The capacity of electron transfer of bare PGE and PGA/PGE was additionally investigated by utilizing EIS, as demonstrated in Figure 4. The Nyquist plots of the bare and modified electrodes were constructed in 1.0 mM $\text{K}_3[\text{Fe}(\text{CN})_6]$ + 0.1 M KCl solution. The spectra were matched in known corresponding circuit model as given in Figure 4 (inset), commonly given by the literature (35, 36). The greater electrocatalytic activity of PGA/PGE was shown by the drop in charge transfer resistance (Rct). The semicircle diameter at greater

frequencies corresponds to the R_{ct} , and the linear part at lower frequencies corresponds to the diffusion procedure (19). The values of charge transfer resistance were determined by fitting the data utilizing an appropriate corresponding circuit to

be 105 and 723 Ω for the bare PGE and PGA/PGE, respectively. The findings here show that PGA/PGE for $Fe(CN)_6^{4-/3-}$ had a higher electron transfer rate and capacity than the bare PGE (18).

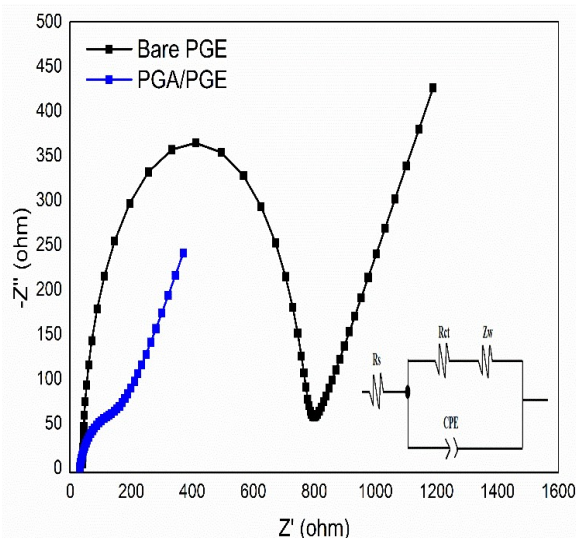


Figure 4: Nyquist plots of bare PGE and PGA/PGE in 5.0 mM $Fe(CN)_6^{3-/4-}$ + 0.1 M KCl solution. Inset: Simple circuit model utilized process (R_s , R_{ct} , Z_w , and CPE represent solution resistance, charge transfer resistance, Warburg impedance, and constant phase element, respectively).

SEM examinations were performed for determining the morphological properties of the PGA/PGE. Gold-palladium sputter coating was performed under 120 seconds and 100 \AA conditions before all images were taken. The SEM results from our previous studies show that the graphite layers on the bare PGE surface have a flat structure (18, 23). When the literature is examined, the SEM images obtained by electro-polymerization of amino acids on the surface of carbon-based electrodes are often similar, and the signs of modification are relatively mild (18, 19). In Figure 5, when examining the images of the modified electrode at different rates of

magnification, it is possible to say that the structures that are rough polymeric on the electrode surface come to the fore. The porous nano-dimensional polymeric structure formed on the electrode surface, providing high specific surface area and channels of ion diffusion and pathways of electron transport (28, 37). Here, the PGA films increased the surface area of the flat bare PGE which increases the sensitivity of the electrode for bisphenol A. In this context, it is possible to interpret the poly(glutamic acid) structure on the electrode surface from SEM micrographs.

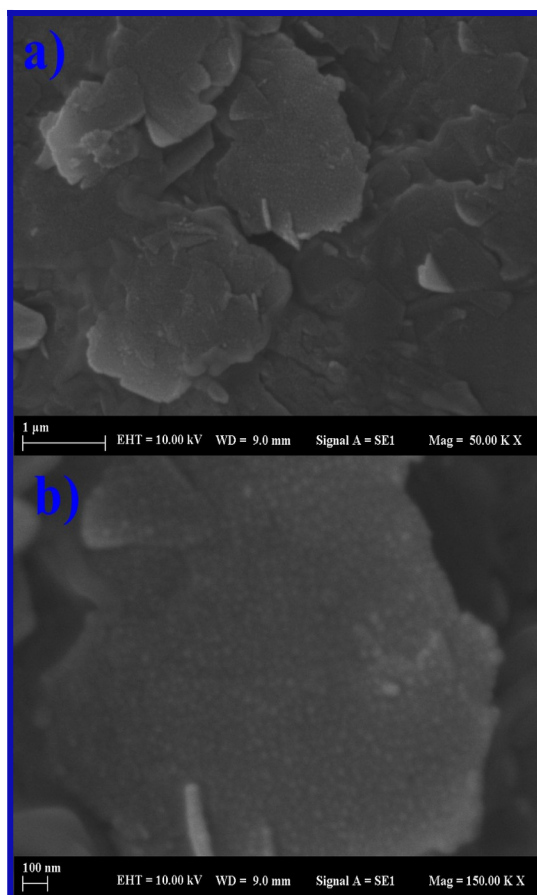


Figure 5: SEM micrographs of **a)** PGA/PGE (with 50000 magnifications) and **b)** PGA/PGE (with 150000 magnifications).

FTIR was used to characterize the presence of functional groups in the PGA/PGE composition. Thus, the formation of functional groups belonging to polyglutamic acid formed by electro-polymerization of GA on the electrode surface was examined (Figure 6). As seen in Figure 6, the bands that appear different from the bare PGE spectrum, the

broad peak at 3000-3500 cm^{-1} was the vibration stretching band of N-H and COOH; 1652 cm^{-1} was the vibration stretching band of carbonyl group (C=O); 1074 cm^{-1} was the most obvious peak representing the presence of aliphatic hydrocarbons, $-\text{CH}_2$ or $-\text{CH}_3$; proving that the electro-polymerization process was successful (38).

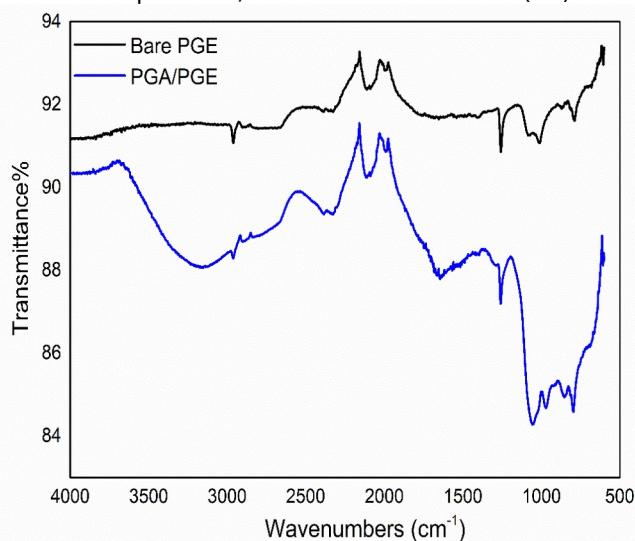


Figure 6: FTIR spectra of bare PGE and PGA/PGE.

Electrochemical oxidation of bisphenol A at PGA/PGE

As is known, BPA is an electroactive compound. Therefore, cyclic voltammograms were recorded on the surfaces of different electrodes in order to investigate the redox behavior and also evaluate the ability of the modifier agent to improve electrode performance for BPA determination. Both bare PGE and PGA/PGE have demonstrated oxidation responses that confirm the electroactive nature of BPA. Figure 7 displays the cyclic voltammograms obtained for 100 μM BPA at the bare PGE and PGA/PGE in PBS (0.1 M) pH 4.0 with a scanning rate of 50 mV/s. The BPA shows the oxidation current with a good response. The oxidation potential was seen at 0.65 V at a bare pencil graphite electrode.

However, in the same condition, PGA/PGE displayed significant improvement in the current signals, and the potential of oxidation was found at 0.70 V. It was observed that the oxidation signal of the BPA shifts in the anodic direction when the working electrode is PGA/PGE. Here, the noticeable enhancement of peak current demonstrates the electrocatalytic action of PGA/PGE towards the detection of bisphenol A (39). As a result, PGA/PGE showed the maximum intensity of the electrochemical signal, demonstrating that PGA exhibited higher electroconductivity, which could be resulted from the synergistic impact and good properties of modifiers, namely, high surface area, great electrical conductivity and much more sites for electroactive species.

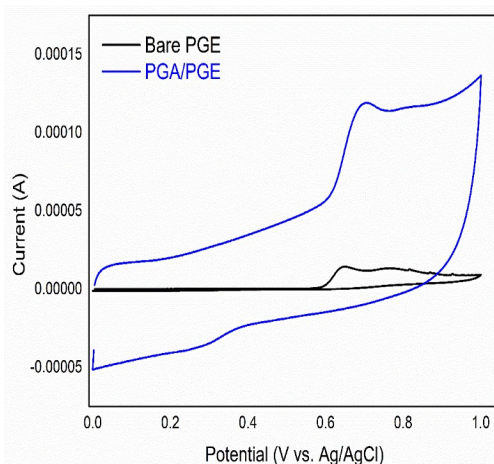


Figure 7: Cyclic voltammograms of bare PGE and PGA/PGE in PBS pH 4.0 containing 100 μM BPA, at potential range of 0.0-1.0 V, and scan rate of 50 mV/s.

Influence of pH on the detection of bisphenol A at PGA/PGE

The pH of the PBS has a considerable influence on the electrochemical response of BPA at the PGA/PGE by influencing peak potential and peak current. The influence of the PBS pH value on determining BPA at PGA/PGE was meticulously assessed in a wider pH interval of 4.0-8.0. Figure 8 shows cyclic voltammograms recorded for 100 μM BPA at PGA/PGE. The oxidation peak potential moves to a more negative potential by higher pH. The peak potential versus pH plot showed that the peak potential is linearly dependent on the pH value in

the interval of 4.0-8.0 with a slope of 0.0656 V/pH ($R^2=0.9957$) as demonstrated in Figure 9. This finding suggests there exists an equal quantity of protons and electrons taking part in the redox process. According to Bard and Faulkner (40), the transferred electron number in the BPA oxidation reaction was found as approximately 2 (41). Therefore, the reaction in Scheme 2, for the electro-oxidation of BPA on the surface of PGA/PGE can be suggested, where 2 electrons and 2 protons participate in the electrode reaction. This was in agreement with that stated in the literature (42).

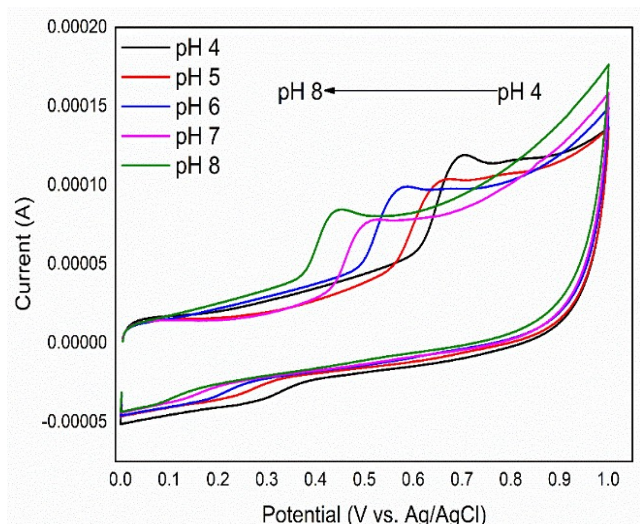


Figure 8: Cyclic voltammograms of PGA/PGE prepared at 10 polymerization cycles in the 4.0, 5.0, 6.0, 7.0, and 8.0 pH values PBS containing 100 μM BPA.

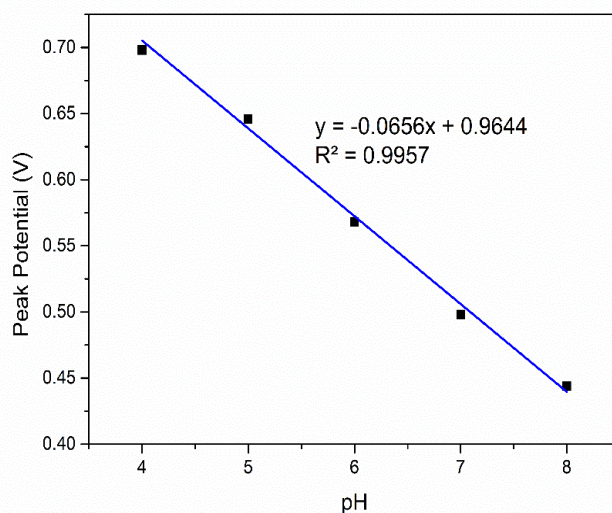
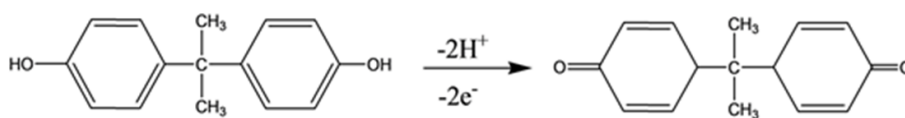


Figure 9: Graph showing the variation of the peak current responses of PBS containing 100 μM BPA with pH value.



Scheme 2: The possible oxidation mechanism of BPA at PGA/PGE.

Influence of potential scan rate on response oxidation peak current of BPA

The influence of changing the employed scan rate for 100 μM BPA in PBS pH 4.0 was examined by the CV technique at the PGA/PGE as demonstrated in Figure 10. The experiment findings acquired from the PGA/PGE displayed a rise in the peak currents with higher applied scanning rate, and they were proportional to each other based on the Randles-Sevcik equation (43). The finding suggested that

there was a shift of the oxidation peak potential towards the less negative side. To validate the electrode process, the plot of the peak current versus square roots of scanning rate was drawn, and the resulting plot was a straight line with satisfactory linearity in the interval from 25 to 500 mV/s as presented in Figure 11 with the correlation coefficient (R^2) of 0.9978. These results indicate that the electrode process is diffusion-controlled (28, 43).

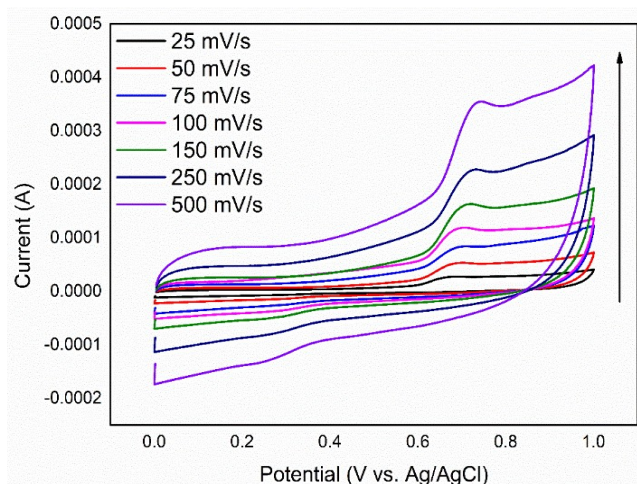


Figure 10: Cyclic voltammograms of the PGA/PGE at scan rates of 25 mV/s, 50 mV/s, 75 mV/s, 100 mV/s, 150 mV/s, 250 mV/s, and 500 mV/s in PBS pH 4.0 containing 100 µM BPA.

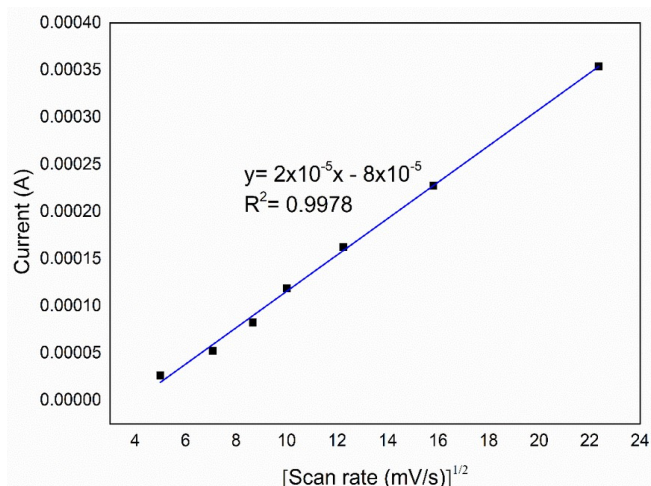


Figure 11: Graph showing the linear relationship between the square roots of the scan rate with oxidation peak current.

Analytical performance of the sensor toward BPA determination

A set of BPA solutions was created at a falling concentration starting from 1.0 µM to compute the identification and determination limit of the created PGA/PGE. The voltammograms acquired by differential pulse voltammetric method in the potential interval of 0.5 V to 1.0 V using the modified electrode in every solution are presented (Figure 12). By utilizing the voltammograms in Figure 12, a calibration plot that provides the current-concentration relationship shown in Figure 13 was obtained. As a consequence of the computations conducted from the calibration plot, the LOD value was found as 0.37 µM (S/N=3), and the LOQ value was found as 1.24 µM (S/N=10). The linear regression equation of PGA/PGE is $I(A) = 0.142C_{BPA}(M) + 2 \times 10^{-7}$, $R^2 = 0.9992$. The comparison of the analytical performances of some polymer-based electrodes in the literature is presented in Table 1.

Interference studies

Various compounds and ions like methanol, phenol, SO_4^{2-} , Na^+ , Cl^- , Cu^{2+} , Fe^{3+} , Pb^{2+} , K^+ and Cd^{2+} may be utilized in the synthesis and structure determination of packing materials (10). For identifying the influences of these materials on the electrochemical

determination of BPA, we investigated the variation in current by introducing these materials to the BPA solutions in the DPV analyses.

The interferent species were individually added to 5.0 µM of BPA solutions. When potassium chloride and sodium carbonate (500 µM each) were added, variations in the oxidation current of BPA in the DPV analysis were not seen. The concentration of every interference was more than at least 100 times higher than the BPA concentration in the detection of the interference influence in the DPV examination. Methanol (5000 µM) was also introduced to 5.0 µM BPA solutions, and a reduction in the anodic peak current was found, smaller than that of 5%. The effects of 1000 µM of Fe^{2+} , Cd^{2+} , K^+ , and Pb^{2+} , which have been utilized in several industrial procedures and are found in some water samples, were additionally examined for the analytical response of BPA utilizing the modified electrode in the DPV examination, shown in Table 2. This demonstrated that PGA/PGE has selectivity for BPA and may be utilized to electrochemically determine BPA in several real samples.

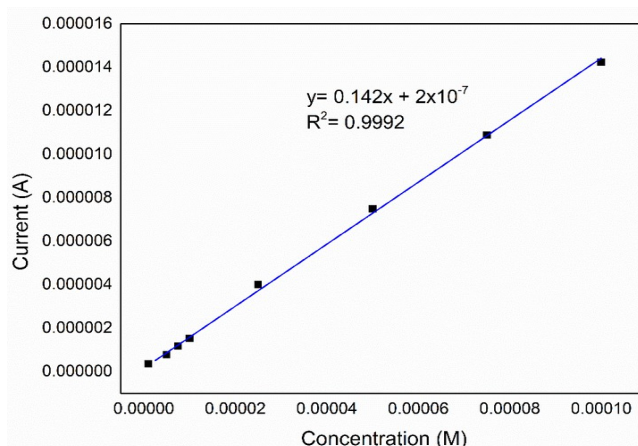
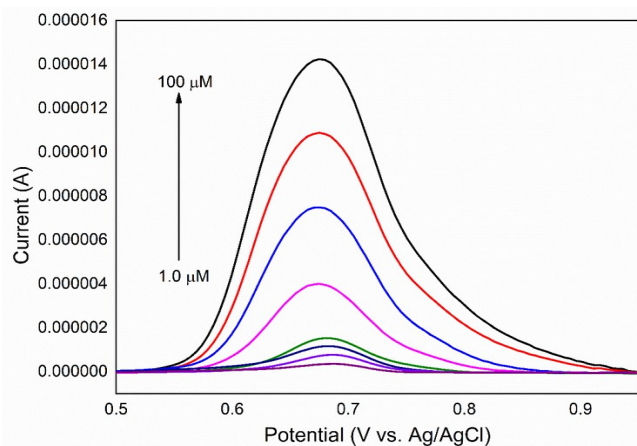


Figure 12: Differential pulse voltammograms of PGA/PGE in different concentrations of BPA solutions. **Figure 13:** Calibration graph of current-concentration (100, 75.0, 50.0, 25.0, 10.0, 7.5, 5.0, 1.0 μM concentrations of BPA in PBS pH 4.0).

Table 1: Comparison of some polymer-based sensor platforms in the literature for BPA determination.

Sensor	Electrochemical method	Linear range (μM)	Limit of detection (μM)	Reference
Tyrosinase/poly(thionine)/Glassy Carbon Electrode	Amperometry	400	23.0	(44)
Multi-walled Carbon Nanotubes/Poly (Crystal Violet)/Glassy Carbon Electrode	Linear Sweep Voltammetry	0.05-100	0.01	(45)
Poly(3,4 ethylenedioxythiophene) Glassy Carbon Electrode	Cyclic Voltammetry	90-140	55	(46)
Molecularly Imprinted Polymer-Modified Multiwalled Carbon Nanotube Paste Electrode	Differential Pulse Voltammetry	0.08-100	0.022	(47)
Poly(Chromotropic Acid)/Glassy Carbon Electrode	Square wave voltammetry	0.1-20	0.06	(48)
Polyglutamic acid/amino-functionalized carbon nanotubes/ Glassy Carbon Electrode	Differential Pulse Voltammetry	0.1-10	0.02	(49)
Poly(glutamic acid)/Pencil Graphite Electrode	Differential Pulse Voltammetry	1.0-100	0.37	This study

Table 2: Interference effects of some ion species on the oxidation peak response of 5.0 μM of BPA.

Species	Current (μA)	Current differences (μA)
N/A	1.08	0
Fe^{2+}	1.23	+0.15
K^+	1.19	+0.11
Cd^{2+}	1.21	+0.13
Pb^{2+}	0.98	-0.10

Reproducibility and stability of PGA/PGE

Intraday and interday measurements were recorded to examine the reproducibility of the PGA/PGE. To examine intraday repeatability performance, DPVs of 5.0 μM BPA were conducted using ten different

PGA/PGEs prepared just prior to the analysis. The percent relative standard deviation (RSD%) was found to be 2.63%. In order to investigate the repeatability performance interday, repeated measurements were made for ten days and the RSD

% was found to be 3.21%. These results demonstrated that the PGA/PGEs were replicable in their preparation. In addition, to examine the stability of the electrodes, DPV measurements were taken with electrodes held in a desiccator for 45 days. Hence, the difference between the starting and ending values was only 3.83%. In conclusion, these findings demonstrated that the PGA/PGE was quite stable.

Determination of BPA in real sample

The spike recovery method was used to examine the usability of the proposed sensor platform in real samples. Electrochemical measurements were performed with DPV method. In order to examine the analytical applicability of the method,

measurements were also recorded with another analytical method, namely ultraviolet-visible spectrophotometry (50). The plastic bottled drinking water sample was obtained from the local shop and it was used directly without any pretreatment. The 2.5 mL plastic bottled drinking water was diluted with phosphate buffer solution (10 mL, pH 4.0). Then, 10 and 20 μM standard BPA solutions were introduced to the diluted sample solution. Table 3 presents the obtained findings. Every measurement was replicated three times, and the RSD% was computed. The recovery values were determined to be in the range of 89.3 to 104.7%. The findings showed that the PGA/PGE could be applied to real sample analysis.

Table 3: Electrochemical detection of BPA in the plastic bottled drinking water sample with PGA/PGE.

Sample	Added concentration of bisphenol A (μM)	Found concentration of bisphenol A (μM) ^a	Found concentration of bisphenol A (μM) ^b	Relative standard deviation (%) ^b	Recovery (%) ^b
Plastic bottled drinking water	10.0	10.9 \pm 0.032	11.2 \pm 0.054	2.3	89.3
	20.0	21.3 \pm 0.034	19.1 \pm 0.031	2.6	104.7

^a UV-Vis spectrophotometric method.

^b PGA/PGE.

CONCLUSION

In this study, a modified electrode has been developed to determine BPA electrochemically. In the development phase of the electrode, the electropolymerization of glutamic acid was performed by CV method to obtain the PGA/PGE. The PGA/PGE was characterized by using the FTIR, SEM, EIS, and CV methods. Among the PGEs modified by the electropolymerization of glutamic acid, the most satisfactory findings were acquired with an electrode prepared by utilizing 10 electropolymerization cycles. Based on the measurement results taken at different pH values, the best peak current response was found at PBS pH 4.0. When the effect of scan rate on the oxidation mechanism of BPA is examined, it is concluded that the reaction is diffusion-controlled in the light of the findings obtained. BPA was electrochemically determined by utilizing the CV and DPV methods. The LOD and LOQ values for differential pulse voltammetric determination of BPA were 0.37 μM and 1.24 μM , respectively. The reproducibility and stability of the newly developed sensor platform were examined. Finally, the applicability of PGA/PGE to plastic bottled drinking water sample was assessed. The recovery values were found to be between 89.3 and 104.7%. The developed sensor platform stands out due to its low cost, easy and one-step preparation, and features such as good repeatability, sensitivity, and selectivity.

ACKNOWLEDGMENT

O. Gorduk especially thanks Prof. Dr. Yucel Sahin for his valuable contributions to this study.

REFERENCES

1. Alam AU, Deen MJ. Bisphenol A Electrochemical Sensor Using Graphene Oxide and β -Cyclodextrin-Functionalized Multi-Walled Carbon Nanotubes. *Anal Chem.* 2020; 92(7):5532-5539.
2. Ashraf G, Asif M, Aziz A, Wang Z, Qiu X, Huang Q, et al. Nanocomposites consisting of copper and copper oxide incorporated into MoS_4 nanostructures for sensitive voltammetric determination of bisphenol A. *Microchimica Acta.* 2019;186(6):337.
3. Gugoasa LA, Stefan-van Staden RI, van Staden JF, Coros M, Pruneanu S, editors. Voltammetric determination of bisphenol A with a silver-reduced graphene oxide composite paste microsensor. 2019 International Semiconductor Conference (CAS); 2019: IEEE.
4. Bolat G, Yaman YT, Abaci S. Highly sensitive electrochemical assay for Bisphenol A detection based on poly (CTAB)/MWCNTs modified pencil graphite electrodes. *Sens Actuators, B.* 2018;255:140-8.

5. Ezoji H, Rahimnejad M, Najafpour-Darzi G. Advanced sensing platform for electrochemical monitoring of the environmental toxin; bisphenol A. *Ecotoxicology and Environmental Safety*. 2020;190:110088.
6. Hu L, Fong C-C, Zhang X, Chan LL, Lam PK, Chu PK, et al. Au nanoparticles decorated TiO₂ nanotube arrays as a recyclable sensor for photoenhanced electrochemical detection of bisphenol A. *Environmental science & technology*. 2016;50(8):4430-8.
7. Bakirhan NK, Ozkan SA. The Recent Electrochemical Studies on Bisphenol A Detection in Beverages. *Safety Issues in Beverage Production*: Elsevier; 2020. p. 309-33.
8. Yaman YT, Abaci S. Sensitive adsorptive voltammetric method for determination of bisphenol A by gold nanoparticle/polyvinylpyrrolidone-modified pencil graphite electrode. *Sensors*. 2016;16(6):756.
9. Ji Y, Yin J, Xu Z, Zhao C, Huang H, Zhang H, et al. Preparation of magnetic molecularly imprinted polymer for rapid determination of bisphenol A in environmental water and milk samples. *Analytical and bioanalytical chemistry*. 2009;395(4):1125-33.
10. Koyun O, Gorduk S, Gencten M, Sahin Y. A novel copper (II) phthalocyanine-modified multiwalled carbon nanotube-based electrode for sensitive electrochemical detection of bisphenol A. *New J Chem*. 2019;43(1):85-92.
11. Malone E, Elliott C, Kennedy D, Regan L. Rapid confirmatory method for the determination of sixteen synthetic growth promoters and bisphenol A in bovine milk using dispersive solid-phase extraction and liquid chromatography-tandem mass spectrometry. *J Chromatogr B*. 2010;878(15-16):1077-84.
12. De Meulenaer B, Baert K, Lanckriet H, Van Hoed V, Huyghebaert A. Development of an enzyme-linked immunosorbent assay for bisphenol A using chicken immunoglobulins. *J Agric Food Chem*. 2002;50(19):5273-82.
13. Zhao W, Sheng N, Zhu R, Wei F, Cai Z, Zhai M, et al. Preparation of dummy template imprinted polymers at surface of silica microparticles for the selective extraction of trace bisphenol A from water samples. *J Hazard Mater*. 2010;179(1-3):223-9.
14. Kim Y, Jeon JB, Chang JY. CdSe quantum dot-encapsulated molecularly imprinted mesoporous silica particles for fluorescent sensing of bisphenol A. *J Mater Chem*. 2012;22(45):24075-80.
15. Gugoasa LA, Stefan-van Staden R-I, van Staden JF, Coroş M, Pruneanu S. Electrochemical Determination of Bisphenol A in Saliva by a Novel Three-Dimensional (3D) Printed Gold-Reduced Graphene Oxide (rGO) Composite Paste Electrode. *Anal Lett*. 2019;52(16):2583-606.
16. Özcan L, Altuntas M, Buyuksagis A, Türk H, Yurdakal S. Electrochemical determination of bisphenol A with pencil graphite electrodes modified with Co (II), Ni (II), Cu (II) and Fe (II) phthalocyaninetetrasulfonates. *Anal Sci*. 2016;32(8):881-6.
17. Messaoud NB, Lahcen AA, Dridi C, Amine A. Ultrasound assisted magnetic imprinted polymer combined sensor based on carbon black and gold nanoparticles for selective and sensitive electrochemical detection of bisphenol A. *Sens Actuators, B*. 2018;276:304-12.
18. Tahtaisleyen S, Gorduk O, Sahin Y. Electrochemical Determination of Tartrazine Using a Graphene/Poly (L-Phenylalanine) Modified Pencil Graphite Electrode. *Anal Lett*. 2020:1-21.
19. Dokur E, Gorduk O, Sahin Y. Differential Pulse Voltammetric Determination of Folic Acid Using a Poly (Cystine) Modified Pencil Graphite Electrode. *Anal Lett*. 2020;53(13): 1-19.
20. Koyun O, Gorduk S, Arvas M, Sahin Y. Electrochemically treated pencil graphite electrodes prepared in one step for the electrochemical determination of paracetamol. *Russ J Electrochem*. 2018;54(11):796-808.
21. Koyun O, Gursu H, Gorduk S, Sahin Y. Highly sensitive electrochemical determination of dopamine with an overoxidized polypyrrole nanofiber pencil graphite electrode. *Int J Electrochem Sci*. 2017;12:6428-44.
22. Koyun O, Gorduk S, Arvas MB, Sahin Y. Direct, one-step synthesis of molybdenum blue using an electrochemical method, and characterization studies. *Synth Met*. 2017;233:111-8.
23. Gorduk O. Differential Pulse Voltammetric Determination of Serotonin Using an Acid-Activated Multiwalled Carbon Nanotube-Over-Oxidized Poly (3, 4-ethylenedioxythiophene) Modified Pencil Graphite Electrode. *Anal Lett*. 2019;53(7):1034-52.
24. Santos DP, Zanoni MVB, Bergamini MF, Chiorcea-Paquim A-M, Diculescu VC, Brett A-MO. Poly (glutamic acid) nanofibre modified glassy carbon electrode: Characterization by atomic force microscopy, voltammetry and electrochemical impedance. *Electrochim Acta*. 2008;53(11):3991-4000.
25. Santos DP, Bergamini MF, Santos VA, Furlan M, Zanoni MVB. Preconcentration of rutin at a poly glutamic acid modified electrode and its determination by square wave voltammetry. *Anal Lett*. 2007;40(18):3430-42.

26. Liu X, Luo L, Ding Y, Ye D. Poly-glutamic acid modified carbon nanotube-doped carbon paste electrode for sensitive detection of L-tryptophan. *Bioelectrochemistry*. 2011;82(1):38-45.
27. Wang L, Huang P, Bai J, Wang H, Zhang L, Zhao Y. Direct simultaneous electrochemical determination of hydroquinone and catechol at a poly (glutamic acid) modified glassy carbon electrode. *International Journal of Electrochemical Science*. 2007;2(1):123-32.
28. Ganesh P, Swamy BK. Simultaneous electroanalysis of norepinephrine, ascorbic acid and uric acid using poly (glutamic acid) modified carbon paste electrode. *J Electroanal Chem*. 2015;752:17-24.
29. Yu A-M, Chen H-Y. Electrocatalytic oxidation and determination of ascorbic acid at poly (glutamic acid) chemically modified electrode. *Anal Chim Acta*. 1997;344(3):181-5.
30. Santos DP, Bergamini MF, Fogg AG, Zanoni MVB. Application of a glassy carbon electrode modified with poly (glutamic acid) in caffeic acid determination. *Microchimica Acta*. 2005;151(1-2):127-34.
31. Zhou X, Zheng X, Lv R, Kong D, Li Q. Electrodeposition of platinum on poly (glutamic acid) modified glassy carbon electrode for non-enzymatic amperometric glucose detection. *Electrochim Acta*. 2013;107:164-9.
32. Femenus JJ, Manikandan R, Narayanan SS, Deepa P. Determination of gallic acid using poly (glutamic acid): graphene modified electrode. *J Chem Sci*. 2019;131(2):11.
33. Özcan A, İlkbaş S. Preparation of poly (3, 4-ethylenedioxythiophene) nanofibers modified pencil graphite electrode and investigation of over-oxidation conditions for the selective and sensitive determination of uric acid in body fluids. *Anal Chim Acta*. 2015;891:312-20.
34. Özcan L, Şahin Y. Determination of paracetamol based on electropolymerized-molecularly imprinted polypyrrole modified pencil graphite electrode. *Sens Actuators, B*. 2007;127(2):362-9.
35. Koyun O, Sahin Y. Poly (L-Cysteine) modified pencil graphite electrode for determination of sunset yellow in food and beverage samples by differential pulse voltammetry. *Int J Electrochem Sci*. 2018;13:159-74.
36. Koyun O, Sahin Y. Voltammetric determination of nitrite with gold nanoparticles/poly (methylene blue)-modified pencil graphite electrode: application in food and water samples. *Ionics*. 2018;24(10):3187-97.
37. Li Y, Hsu P-C, Chen S-M, Lou B-S, Ali MA, Al-Hemaid F. Simultaneously Determination of Procaine and Catechol at Functionalized Multi-Walled Carbon Nanotube with Poly-Glutamic Acid Modified Electrode. *Journal of Biobased Materials and Bioenergy*. 2014;8(2):149-57.
38. Lin B, Li Z, Zhang H, Wu J, Luo M. Cloning and Expression of the γ -Polyglutamic Acid Synthetase Gene *pgsBCA* in *Bacillus subtilis* WB600. *BioMed Research International*. 2016; Article ID 3073949, 7 pages.
39. Li Y, Zhai X, Liu X, Wang L, Liu H, Wang H. Electrochemical determination of bisphenol A at ordered mesoporous carbon modified nano-carbon ionic liquid paste electrode. *Talanta*. 2016;148:362-9.
40. Bard AJ, Faulkner LR, Leddy J, Zoski CG. *Electrochemical methods: fundamentals and applications*: wiley New York; 1980.
41. Ulubay Karabiberoglu Ş. Sensitive Voltammetric Determination of Bisphenol A Based on a Glassy Carbon Electrode Modified with Copper Oxide-Zinc Oxide Decorated on Graphene Oxide. *Electroanalysis*. 2019;31(1):91-102.
42. Tian Y, Deng P, Wu Y, Li J, Liu J, Li G, et al. MnO₂ Nanowires-Decorated Reduced Graphene Oxide Modified Glassy Carbon Electrode for Sensitive Determination of Bisphenol A. *J Electrochem Soc*. 2020;167(4):046514.
43. Hu P, Zhu X, Luo X, Hu X, Ji L. Cathodic electrodeposited Cu-BTC MOFs assembled from Cu (II) and trimesic acid for electrochemical determination of bisphenol A. *Microchimica Acta*. 2020;187(2):145.
44. Dempsey E, Diamond D, Collier A. Development of a biosensor for endocrine disrupting compounds based on tyrosinase entrapped within a poly(thionine) film. *Biosensors and Bioelectronics*. 2004;20:367-377.
45. Wang W, Tang J, Zheng S, Ma X, Zhu J, Li F, Wang J. Electrochemical Determination of Bisphenol A at Multi-walled Carbon Nanotubes/Poly (Crystal Violet) Modified Glassy Carbon Electrode. *Food Anal. Methods*. 2017;10:3815-3824.
46. Mazzotta E, Malitesta C, Margapoti E. Direct electrochemical detection of bisphenol A at PEDOT-modified glassy carbon electrodes. *Anal Bioanal Chem*. 2013;405:3587-3592.
47. Chen Z, Tang C, Zeng Y, Liu H, Yin Z, Li L. Determination of Bisphenol A Using an Electrochemical Sensor Based on a Molecularly

Imprinted Polymer-Modified Multiwalled Carbon Nanotube Paste Electrode. *Analytical Letters*. 2014;47:996-1014.

48. Filik H, Avan AA. Electrochemical Determination of Bisphenol A Based on Poly(Chromotropic Acid) Modified Glassy Carbon Electrode. *Current Analytical Chemistry*. 2017;13(6):464-473.

49. Lin Y, Liu K, Liu C, Yin L, Kang Q, Li L, Li B. Electrochemical sensing of bisphenol A based on

polyglutamic acid/amino-functionalised carbon nanotubes nanocomposite. *Electrochimica Acta*. 2014;133:492-500.

50. Zhuang Y, Zhou M, Gu J, Li X. Spectrophotometric and high performance liquid chromatographic methods for sensitive determination of bisphenol A. *Spectrochimica Acta Part A: Molecular and Biomolecular Spectroscopy*. 2014;122:153-157.



Cytotoxic effects of Mannich bases via induction of caspase-3 pathway on human oral squamous cell carcinoma

Cem Yamali^{1,2*} , Halise Inci Gul^{1*} 

¹Ataturk University, Faculty of Pharmacy, Department of Pharmaceutical Chemistry, 25240, Erzurum, Turkey.

²Cukurova University, Faculty of Pharmacy, Department of Basic Pharmaceutical Sciences, 01330, Adana, Turkey.

Abstract: In the anticancer drug research, there is a need for the synthesis of compounds with selective cytotoxicity compared to the anticancer drugs in the market. The current study aimed to determine the cytotoxicities of the bis Mannich bases **1-9** towards human oral squamous cell carcinoma (OSCC). Mannich bases showed promising cytotoxicity in low micromolar in the range of 1.7-27 μ M against OSCC cell lines. The compounds **5** with the highest potency selectivity expression (PSE) value (318.1) and **7** with the highest tumor selectivity (TS) values (TS1:11.2, TS2:15.8) showed promising selective cytotoxicity towards cancer cell lines. Furthermore, Western blot analysis showed that the representative compound **7** induced the activation of caspase-3 in HSC-2 cells. These results may suggest that the apoptotic pathway may be one of the possible mechanisms of the action and the lead compound **7** can be subjected to the further bioassays and molecular design.

Keywords: Mannich base, anticancer, apoptosis, PARP

Submitted: October 27, 2020. **Accepted:** December 15, 2020.

Cite this: Yamali C, Gul HI. Cytotoxic effects of Mannich bases via induction of caspase-3 pathway on human oral squamous cell carcinoma. JOTCSA. 2021;8(1):187-94.

DOI: <https://doi.org/10.18596/jotcsa.817007>.

***Corresponding authors. E-mail:** (incigul@atauni.edu.tr)(c.yamali@yahoo.com)

INTRODUCTION

World Health Organization (WHO) cancer reports indicate that cancer is a principal health issue that causes deaths worldwide after cardiovascular system diseases. The most common types of cancer in men are lung, prostate, and colorectum, while those are the breast, colorectum, and lung in women (1). Among cancer types, oral cancers are part of head and neck cancers. According to the American Cancer Society, in 2020, 10.750 people will die from oral cancer in the US. It is indicated that tobacco, alcohol consumption, and several viral infections are primary risk factors (2). The main drawbacks of current chemotherapeutic drugs are known as selectivity deficiency, severe side effects, and multidrug resistance (3). Therefore, new and promising anticancer drug candidates for clinical trials is needed.

Mannich reaction is a useful way to obtain aminoalkylated compounds which are used as prodrugs in medicinal chemistry studies. Aminoalkylation of the compounds mostly affects the lipophilicity of the molecule, pKa, and absorption process through membranes (4). Besides, Mannich bases turn into α , β -unsaturated ketone moiety under suitable conditions and they act as thiol alkylators in cancer cells. This situation may provide advantages compared to available anticancer drugs since during the cell division thiol bearing glutathione levels were increased. Therefore, α , β -unsaturated ketones interact with the thiol group, except hydroxy and amine moieties that are available in proteins. Also, they may potentially show fewer side effects and selective cytotoxicity towards cancer cells except for normal cells (5-9). Large numbers of Mannich bases in different chemical structures such as ketonic, phenolic, and alkyne type compounds, etc were reported with anticonvulsant, analgesic,

antifungal, anticancer and antioxidant activities (4).

Chalcones having the structure of 1,3-diaryl-2-propen-1-one is one of the most privileged scaffolds in medicinal chemistry since they have a functional chemical skeleton to design many kinds of compounds, and they have also been reported with valuable bioactivities such as anticancer, anti-diabetic, antioxidant, anti-inflammatory, and anti-infective effects (10). Conversion of phenolic chalcones into the related Mannich bases generally increases their cytotoxic effects (6, 11-16). This promising behavior may be a result of additional alkylation centers formed by the chalcone to lead to excessive cytotoxic effects by interaction with more cellular thiols based on the sequential cytotoxicity hypothesis (5, 6, 17).

Mannich reaction as a powerful tool in medicinal chemistry is considered both for the synthesis of drug candidates and for the modification of physicochemical properties of the compound to direct its pharmacokinetic properties. In this study, cytotoxic/anticancer properties of Mannich bases, 1-(3,5-bis-aminomethyl-4-hydroxyphenyl)-3-(4-substituted phenyl)-2-propen-1-ones **1-9** (Table 1), were investigated *via* MTT test against human oral squamous cell carcinoma (OSCC) cell lines and human normal oral cells. Moreover, the mechanism of action of the representative compound was investigated *via* Western blot analysis to find out how the most potent compound affects cancer cells.

EXPERIMENTAL SECTION

Determination of the cytotoxicities *via* MTT and Western blot analysis

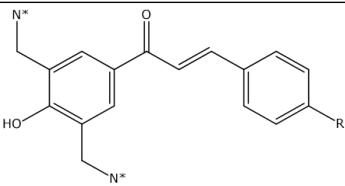
Cytotoxicity assay was realized according to our previous studies (13, 18, 19). Human oral

squamous cell carcinoma cell lines (Ca9-22, HSC-2, HSC-3, HSC-4) and human normal oral cells (HGF, HPLF, HPC) were used for 3-(4,5-dimethylthiazol-2-yl)-2,5-diphenyltetrazolium bromide (MTT) assay test in this study. Reference drugs were Doxorubicin and 5-Fluorouracil (5-FU). The mean value of CC_{50} for each cell type was calculated from triplicate assays. The selectivity index (SI) value was calculated by the quotient of the average CC_{50} value for non-malignant cells (HGF, HPLF, HPC) divided by the CC_{50} value for a specific tumor cell line (Ca9-22, HSC-2, HSC-3 or HSC-4). Tumor selectivity (TS) values (TS1) was calculated by dividing the average CC_{50} value towards normal cells into the average CC_{50} value towards cancer cell lines. (Column D/Column B, Table 2) and TS values (TS2) were generated for a compound by dividing the average CC_{50} value towards HGF cells into the CC_{50} value towards Ca9-22 cells (Column C/Column A, Table 2). A potency selectivity expression (PSE) values were calculated by dividing average CC_{50} values towards OSCC cell lines (a measure of potency) and the average SI figures towards these cell lines (a determination of tumor-selectivity) and expressed as a percentage. Western blot analysis was realized as described previously(20).

RESULTS AND DISCUSSION

The synthesis method of the compounds **1-9** (Table 1) was reported previously by our group (21). Target compounds **1-9** were obtained by the reaction of a suitable chalcone, paraformaldehyde, and suitable secondary amines such as piperidine (**1**, **4**, **7**) morpholine (**2**, **5**, **8**), and *N*-methyl piperazine (**3**, **6**, **9**) under microwave conditions and the chemical structures of the compounds were verified by 1H NMR, ^{13}C NMR, and HRMS (21).

Table 1. General chemical structure of the Mannich bases **1-9**.



Compound	R group	N* group
1		Piperidine
2	-CH ₃	Morpholine
3		<i>N</i> -methyl piperazine
4		Piperidine
5	-OCH ₃	Morpholine
6		<i>N</i> -methyl piperazine
7		Piperidine
8	-NO ₂	Morpholine
9		<i>N</i> -methyl piperazine

Cytotoxicities of the compounds **1-9** were presented in Table 2. The compounds showed remarkable cytotoxicities in the low micromolar concentration range of 1.7-27 μM against cancer cell lines. The compounds generally more powerful cytotoxic agents than 5-FU, even so, they were less effective compared to Doxorubicin. All compounds showed cytotoxic effect with the lowest average CC_{50} values of 2.5-12.9 μM against OSCC cell lines than reference drug 5-FU (16.9 μM), except the compounds **4** and **5**. When the results were considered, compound **7** (9.6 times, on Ca9-22), and compound **9** (7.7 times, on HSC-2; 6 times on HSC-3; 5.7 times on HSC-4) were found more cytotoxic compounds among others than 5-FU against the cell issued.

Selectivity index (SI), which is greater than the value of 1, indicates that the compound tested has selective cytotoxicity towards cancer cells, and that can be forwarded to further investigations (17, 22). Calculated SI values towards OSCC cell lines were in the range of 2.7-16.7. It seems that all compounds have selective cytotoxicity towards cancer cells. In addition, according to the average SI values (4.7-12.2) against OSCC cell lines, compound **7** drawn great attention, with the highest average SI value (12.2) against OSCC cell lines as a lead compound.

Tumor selectivity (TS) values (TS1 and TS2, Table 2) were calculated in two ways. According to TS1 values, compound **7** had the highest TS value (11.2), among others. HGF cells and Ca9-22 cell lines were produced from the same origin. Therefore, the calculation of TS2 values was done to understand tumor selectivity in terms of different aspects. The compounds **1**, **2**, and **7** had the highest TS2 values of 12.6, 13.6, and 15.8,

respectively. Two TS calculations indicated that compound **7** was a tumor-selective compound in series.

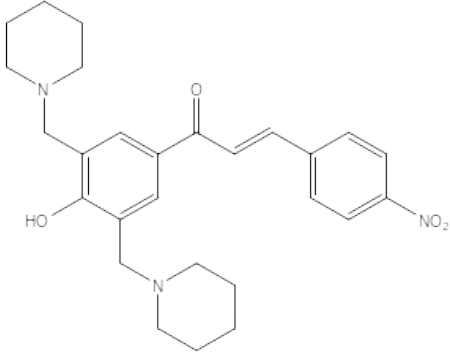
The lead compound, which has selective toxicity towards cancer cells, was determined according to potency selectivity expression (PSE) values in Table 2. PSE values were calculated in the range of 28-318.1. The compounds **1-3** having 4-methylphenyl and the compounds **4-6** having 4-methoxyphenyl had higher PSE values (197.5, 119.4, 118.8, 264.7, 318.1, 161.4, respectively) than **7-9** having 4-nitrophenyl (28, 65.1, 53.1, respectively). It can be concluded that the PSE values of the compounds prominently increased when electron-releasing groups were substituted on the phenyl ring. Furthermore, the promising lead (PL) concept (17, 23) was considered to determine the lead compound. Based on this concept, promising lead compounds have $\text{CC}_{50} < 10 \mu\text{M}$ and $\text{SI} > 10$. In this study, PL10 criteria have been achieved with the compounds **2** ($\text{CC}_{50}=8.8 \mu\text{M}$, $\text{SI}=10.2$) and **7** ($\text{CC}_{50}=2.6 \mu\text{M}$, $\text{SI}=14.7$) towards Ca9-22 and the compound **6** ($\text{CC}_{50}=3.7 \mu\text{M}$, $\text{SI}=10.8$) and **7** ($\text{CC}_{50}=2.3 \mu\text{M}$, $\text{SI}=16.7$) towards HSC-4 cell line.

According to results and evaluations, compound **7** made attraction, and also its drug-likeness properties were theoretically predicted, as shown in Table 3 using SwissADME web tool (24). The physicochemical properties of compound **7** such as the logarithm of the partition coefficient ($\log P$), molecular weight (MW), the number of hydrogen bond acceptors (HBA), hydrogen bond donors (HBD), rotatable bonds (RB), and total polar surface area (TPSA) were calculated to see if the compound **7** has drug-likeness properties. According to Lipinski and Veber filters, it can be expressed that compound **7** had a drug candidate potency with its compatible values.

Table 2. Cytotoxicities of the compounds 1-9 against OSCC cell lines.

Compounds	CC ₅₀ (μM)																			
	Human oral squamous cell carcinoma cell lines (OSCC)										Human normal oral cells									
	Ca9-22	SI	HSC-2	SI	HSC-3	SI	HSC-4	SI	Mean	SD	Mean	HGF	HPLF	HPC	Mean	SD	TS		PSE	logP
	(A)								(B)		(C)		(D)		(D)/(B)	(C)/(A)				
1	10.0	8.0	15.0	5.3	17.0	4.7	9.7	8.2	12.9	3.6	6.5	126.0	54.0	59.0	79.7	40.2	6.2	12.6	197.5	5.32
2	8.8	10.2	14.0	6.4	15.0	6.0	6.3	14.3	11.0	4.2	9.2	120.0	49.0	101.0	90.0	36.8	8.2	13.6	119.4	3.20
3	8.4	4.1	8.2	4.2	13.0	2.7	2.2	15.8	8.0	4.4	6.7	44.0	42.0	18.0	34.7	14.5	4.4	5.2	118.8	3.29
4	15.0	6.6	15.0	6.6	27.0	3.6	11.0	8.9	17.0	6.9	6.4	140.0	55.0	100.0	98.3	42.5	5.8	9.3	264.7	4.93
5	17.0	6.3	20.0	5.4	23.0	4.7	15.0	7.2	18.8	3.5	5.9	109.0	101.0	113.0	107.7	6.1	5.7	6.4	318.1	2.80
6	13.0	3.1	12.0	3.3	7.6	5.3	3.7	10.8	9.1	4.3	5.6	42.0	42.0	36.0	40.0	3.5	4.4	3.2	161.4	2.90
7	2.6	14.7	4.3	8.9	4.5	8.5	2.3	16.7	3.4	1.1	12.2	41.0	35.0	39.0	38.3	3.1	11.2	15.8	28.0	4.83
8	5.4	6.7	4.5	8.1	5.0	7.3	4.6	7.9	4.9	0.4	7.5	42.0	40.0	27.0	36.3	8.1	7.5	7.8	65.1	2.71
9	3.5	3.1	2.6	4.2	2.2	5.0	1.7	6.5	2.5	0.8	4.7	11.0	10.0	12.0	11.0	1.0	4.4	3.1	53.1	2.80
Doxorubicin	0.1	70.8	0.1	70.1	0.1	77.3	0.1	79.1	0.1	0.0	74.3	8.5	1.9	10.0	6.8	4.3	74.1	88.5	0.1	-
5-FU	25.0	38.4	20.0	48.0	13.0	73.8	9.7	98.9	16.9	6.9	64.8	1000.0	1000.0	879.0	959.7	69.9	56.7	40.0	26.1	-

Each value represents the mean ±S.D. of triplicate determinations. Human gingival fibroblast (HGF); Human periodontal ligament fibroblast (HPLF); Human pulp cell (HPC); Oral squamous cell carcinoma cell lines (OSCC: Ca9-22, HSC-2, HSC-3 and HSC-4); Tumor-selectivity index (TS); Potency-selectivity expression (PSE); Selective index (SI); 50% cytotoxic concentration (CC₅₀); SD standard deviation. logP values calculated by Molinspiration Cheminformatics online program.

Table 3. Druglikeness properties of the most potent lead compound **7**.


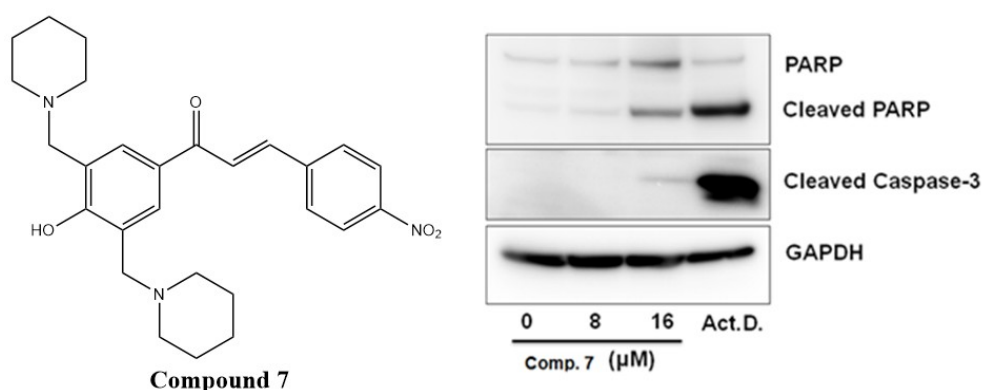
Compound	logP	MW	HBA	HBD	RB	TPSA
7	3,63	463,57	6	1	8	89,6
Druglike compound	<4.15	<500	<10	<5	<10	<140

Lipinski (Pfizer) filter: MW \leq 500, logP \leq 4.15, N or O \leq 10, NH, or OH \leq 5.
 Veber (GSK) filter: RB \leq 10, TPSA \leq 140

A partition coefficient (P) or its logarithmic value of logP is an indicator parameter of the solubility properties of the drug candidates. Among series, bis Mannich bases **1**, **4**, and **7**, which have piperidine, had the highest logP values of 5.32, 4.93, and 4.83, respectively, in series (Table 2). As for logP, CC₅₀, SI, and TS values of compound **7** were compared with other nitro derivatives, it can be stated that the piperidine ring led to having high logP value, and this situation resulted in increased cytotoxicity of the compound **7** against OSCC cell lines. It is known that lipophilicity enhances the absorption of the compounds through the cell membrane. Therefore,

the compound may easily accumulate in the cell and it may cause increased bioactivity.

Apoptosis, a programmed cell death process, has a role in regulating cell proliferation triggered by many anticancer drugs. Caspase-3 protein is known as one of the targets in the apoptotic process (25). Western blot analysis demonstrated that compound **7** induced the production of a cleaved product of PARP and the activation of caspase-3 in HSC-2 as potently as actinomycin-D, which was a positive control of apoptosis (Figure 1).

**Figure 1.** Western blot analysis of the representative compound **7** on HSC-2 cells.

CONCLUSION

In conclusion, this research was focused on to investigating the cytotoxic effects of Mannich bases on several cancer cell lines. The CC₅₀ values of the bis Mannich bases were found in the range of 1.7-27 μ M against OSCC cell lines. When tumor selectivity (TS1 and TS2) and potency selectivity expression (PSE) were considered, compound 5 with the highest PSE value (PSE=318.1) and compound 7 with the

highest TS values (TS1=11.2 and TS2=15.8) made great attraction. The most selective cytotoxic compound **7** induced apoptosis process in HSC-2 cells. The compound **7** can also be subjected to further bioassays on different cancer cells for future studies.

ACKNOWLEDGEMENTS

The authors are very thankful to Hiroshi Sakagami (Meikai University, Japan) and Noriyuki Okudaira (Meikai University, Japan) for bioassays. Research Foundation of Ataturk University, Erzurum, Turkey (Project Number: 2015-322) supported this study.

CONFLICT OF INTEREST

The authors declare that they have no conflict of interest.

REFERENCES

1. Siegel RL, Miller KD, Jemal A. Cancer statistics, 2019. *CA: A Cancer Journal for Clinicians*. 2019;69(1):7-34. Doi:10.3322/caac.21551
2. American Cancer Society. Cancer facts and figures 2020. 2020:1-76
3. Tewari D, Rawat P, Singh PK. Adverse drug reactions of anticancer drugs derived from natural sources. *Food and Chemical Toxicology*. 2019;123:522-35. Doi:10.1016/j.fct.2018.11.041
4. Roman G. Mannich bases in medicinal chemistry and drug design. *European Journal of Medicinal Chemistry*. 2015;89:743-816. Doi: 10.1016/j.ejmech.2014.10.076
5. Dimmock JR, Chamankhah M, Seniuk A, Allen TM, Kao GY, Halleran S. Synthesis and cytotoxic evaluation of some Mannich bases of alicyclic ketones. *Pharmazie*. 1995;50(10):668-71.
6. Dimmock JR, Kandepu NM, Hetherington M, Quail JW, Pugazhenthii U, Sudom AM, et al. Cytotoxic activities of Mannich bases of chalcones and related compounds. *Journal of Medicinal Chemistry*. 1998;41(7):1014-26. Doi: 10.1021/jm970432t
7. Gul M, Gul HI, Das U, Hanninen O. Biological evaluation and structure-activity relationships of bis-(3-aryl-3-oxo-propyl)methylamine hydrochlorides and 4-aryl-3-arylcarbonyl-1-methyl-4-piperidinol hydrochlorides as potential cytotoxic agents and their alkylating ability towards cellular glutathione in human leukemic T cells. *Arzneimittelforsch*. 2005;55(6):332-7. Doi: 10.1055/s-0031-1296868.
8. Gul M, Gul HI, Hanninen O. Effects of Mannich bases on cellular glutathione and related enzymes of Jurkat cells in culture conditions. *Toxicology in Vitro*. 2002;16(2):107-12. Doi: 10.1016/S0887-2333(01)00115-1
9. Gul M, Gul HI, Vepsalainen J, Erciyas E, Hanninen O. Effect of acetophenone derived Mannich bases on cellular glutathione level in jurkat cells - A possible mechanism of action. *Arzneimittelforsch*. 2001;51(8):679-82. Doi: 10.1055/s-0031-1300100
10. Mahapatra DK, Asati V, Bharti SK. An updated patent review of therapeutic applications of chalcone derivatives (2014-present). *Expert Opinion on Therapeutic Patents*. 2019;29(5):385-406, DOI: 10.1080/13543776.2019.1613374.
11. Yerdelen KO, Gul HI, Sakagami H, Umemura N. Synthesis and biological evaluation of 1,5-bis(4-hydroxy-3-methoxyphenyl)penta-1,4-dien-3-one and its aminomethyl derivatives. *Journal of Enzyme Inhibition and Medicinal Chemistry*. 2015;30(3):383-8. Doi: 10.3109/14756366.2014.940934
12. Yamali C, Gul HI, Sakagami H, Supuran CT. Synthesis and bioactivities of halogen bearing phenolic chalcones and their corresponding bis Mannich bases. *Journal of Enzyme Inhibition and Medicinal Chemistry*. 2016;31(sup4):125-31. Doi: 10.1080/14756366.2016.1221825.
13. Tugrak M, Yamali C, Sakagami H, Gul HI. Synthesis of mono Mannich bases of 2-(4-hydroxybenzylidene)-2,3-dihydroinden-1-one and evaluation of their cytotoxicities. *Journal of Enzyme Inhibition and Medicinal Chemistry*. 2016;31(5):818-23. Doi: 10.3109/14756366.2015.1070263
14. Gul HI, Yerdelen KO, Gul M, Das U, Pandit B, Li PK, et al. Synthesis of 4'-hydroxy-3'-piperidinomethylchalcone derivatives and their cytotoxicity against PC-3 cell lines. *Archiv der Pharmazie*. 2007;340(4):195-201. Doi: 10.1002/ardp.200600072
15. Gul HI, Tugrak M, Sakagami H. Synthesis of some acrylophenones with N-methylpiperazine and evaluation of their cytotoxicities. *Journal of Enzyme Inhibition and Medicinal Chemistry*. 2016;31(1):147-51. Doi: 10.3109/14756366.2015.1014474
16. Bilginer S, Gul HI, Mete E, Das U, Sakagami H, Umemura N, et al. 1-(3-aminomethyl-4-hydroxyphenyl)-3-pyridinyl-2-propen-1-ones: a novel group of tumour-selective cytotoxins. *Journal of Enzyme Inhibition and Medicinal Chemistry*. 2013;28(5):974-80. Doi: 10.3109/14756366.2012.700927
17. Das S, Das U, Sakagami H, Hashimoto K, Kawase M, Gorecki DK, et al. Sequential cytotoxicity: a theory examined using a series of 3,5-bis(benzylidene)-1-diethylphosphono-4-oxopiperidines and related phosphonic acids. *Bioorganic and Medicinal Chemistry Letters*. 2010;20(22):6464-8. Doi: 10.1016/j.bmcl.2010.09.051
18. Yamali C, Gul HI, Ece A, Bua S, Angeli A, Sakagami H, et al. Synthesis, biological evaluation and in silico modelling studies of 1,3,5-trisubstituted pyrazoles carrying benzenesulfonamide as potential anticancer agents and selective cancer-associated hCA IX isoenzyme inhibitors. *Bioorganic Chemistry*. 2019;92:103222. Doi: 10.1016/j.bioorg.2019.103222

19. Yamali C, Gul HI, Ozgun DO, Sakagami H, Umemura N, Kazaz C, et al. Synthesis and cytotoxic activities of difluoro-dimethoxy chalcones. *Anticancer Agents in Medicinal Chemistry*. 2017;17(10):1426-33. Doi: 10.2174/1871520617666170327123909
20. Yamali C, Ozmen Ozgun D, Gul HI, Sakagami H, Kazaz C, Okudaira N. Synthesis and structure elucidation of 1-(2,5/3,5-difluorophenyl)-3-(2,3/2,4/2,5/3,4-dimethoxyphenyl)-2-propen-1-ones as anticancer agents. *Medicinal Chemistry Research*. 2017;26(9):2015-23. Doi: 10.1007/s00044-017-1911-0
21. Yamali C, Gul HI, Cakir T, Demir Y, Gulcin I. Aminoalkylated phenolic chalcones: Investigation of biological effects on acetylcholinesterase and carbonic anhydrase I and II as potential lead enzyme inhibitors. *Letters in Drug Design and Discovery*. 2020;17(10):1283-92. Doi: 10.2174/1570180817999200520123510
22. Robles-Escajeda E, Das U, Ortega NM, Parra K, Francia G, Dimmock JR, et al. A novel curcumin-like dienone induces apoptosis in triple-negative breast cancer cells. *Cellular Oncology (Dordr)*. 2016;39(3):265-77. Doi: 10.1007/s13402-016-0272-x
23. Das U, Sakagami H, Chu Q, Wang Q, Kawase M, Selvakumar P, et al. 3,5-Bis(benzylidene)-1-[4-(2-(morpholin-4-yl)ethoxyphenylcarbonyl)]-4-piperidone hydrochloride: A lead tumor-specific cytotoxin which induces apoptosis and autophagy. *Bioorganic and Medicinal Chemistry Letter*. 2010;20(3):912-7. Doi: 10.1016/j.bmcl.2009.12.076
24. Daina A, Michielin O, Zoete V. SwissADME: A free web tool to evaluate pharmacokinetics, drug-likeness and medicinal chemistry friendliness of small molecules. *Scientific Reports*. 2017;7:42717. Doi: 10.1038/srep42717
25. Fink SL, Cookson BT. Apoptosis, pyroptosis, and necrosis: Mechanistic description of dead and dying eukaryotic cells. *Infection and Immunity*. 2005;73(4):1907-16. Doi:10.1128/IAI.73.4.1907-1916.2005



Modeling and Regeneration Studies for the Removal of Crystal Violet Using *Balanites aegyptiaca* Seed Shell Activated Carbon

Umar Yunusa^{1*} , Bishir Usman¹  and Muhammad Bashir Ibrahim¹ 

¹Department of Pure and Industrial Chemistry, Bayero University, P.M.B.3011, BUK, Kano-Nigeria.

Abstract: Activated carbon derived from *Balanites aegyptiaca* seed shell (ACBS) was employed to remove crystal violet (CV) from aqueous medium. The characterization of this ACBS has been conducted using analytical techniques such as SEM, EDS, and Brunauer-Emmett-Teller (BET) surface area analysis. The adsorption parameters investigated were as follows: contact time (5-120 min), temperature (303-333 K) and initial concentration (100-500 mg/L). The adsorption data were interpreted by using kinetic, isotherms and thermodynamic equations. The kinetic data matched the pseudo-second-order model well, and both external diffusion and internal diffusion influenced the adsorption of the dye onto the adsorbent. The isotherm data was in concurrence with the Freundlich model intimating the multilayer coverage of CV on the heterogeneous surface of the ACBS. The thermodynamic quantities like ΔS° , ΔH° and ΔG° were computed using Gibbs plot. The results implicated the practicability and endothermicity of the dye adsorption process. Regeneration studies show the effectiveness of CH_3COOH solution in CV recovery from ACBS than distilled water, H_2SO_4 , HCl , HNO_3 , and NaOH solutions. The regenerated ACBS was recycled five times and sustained an adsorption efficiency of 92.08%.

Keywords: Adsorption, *Balanites aegyptiaca*, crystal violet, modeling, regeneration.

Submitted: March 5, 2020. **Accepted:** December 21, 2020.

Cite this: Yunusa U, Usman B, Ibrahim M. Modeling and Regeneration Studies for the Removal of Crystal Violet Using *Balanites aegyptiaca* Seed Shell Activated Carbon. JOTCSA. 2021;8(1):195-208.

DOI: <https://doi.org/10.18596/jotcsa.698959>.

***Corresponding author. E-mail:** umaryunusa93@gmail.com.

INTRODUCTION

Water pollution is among the most terrible environmental problems globally and therefore needs pressing attention (1). Numerous toxic substances such as synthetic dyes, heavy metals, pesticides, and aromatic compounds are encountered in the wastewater emanating from various industries (2). The major source of industrial wastewater is the textile industry because of its high water utilization for dyeing and finishing processes (3). The presence of the aforementioned pollutants adversely affects water quality and is among the major cause of diseases and gives harm to human well-being (4,5). Among the different categories of pollutants, dyes are exclusively

noticeable to the bare eye even at minute concentrations. The adverse effects of dyes can be terrible depending on their class, concentration, and period of exposure (6). There are different classes of dyes (basic, direct, acidic, reactive, dispersive, sculpture, and metallic dyes) that fall into the neutral, anionic, and cationic categories. Basic dyes and diazo direct dyes have been observed to have the highest level of toxicity (7).

Crystal violet (CV), also referred to as Basic Violet 3, is a basic dye that belongs to a category of intensely colored compounds called triarylmethane dyes. CV is one of the most widely employed coloring agents in numerous application context (8). It is extensively

utilized in painting, textile dyeing, histological staining, printing, dermatology, and veterinary fields (9,10). However, the presence of CV in aqueous medium has deleterious effect on human health as it is proven as mutagenic, carcinogenic, and also causes skin irritation upon contact with the body (11,12). Therefore, adequate treatment is needed to remove it from wastewater before disposing in to the environment.

In the last decades, activated carbon has been widely employed in the reclamation of pollutant-bearing wastewater due to its high removal efficiency. However, the high cost of the commercial activated carbon makes it imperative to search for cheaper alternatives, mainly from agricultural biomass (13). *Balanites aegyptiaca* is an evergreen, multi-branched and spiny tree grown in the dry and savannah areas of Africa and southern Asia (14). It is widely used for different purpose in Nigeria and this lead to generation of colossal amount of waste as *Balanites aegyptiaca* seed shell (BESS). Relevant studies on the use of this agricultural waste are relatively few. Specifically, no report was documented on the removal of CV by this form of material.

The present work is aimed at probing the feasibility of using activated carbon derived from BESS as alternative adsorbent for CV removal from aqueous medium. In particular, the prepared adsorbent was characterized using scanning electron microscopy (SEM) interfaced with energy dispersive spectroscopy (EDS) and Brunauer-Emmett-Teller (BET) surface area analysis. The kinetic and isotherm data for CV adsorption on ACBS were analyzed using different mathematical models. Also, the thermodynamic quantities were computed in order to ascertain the feasibility of the removal process. Finally, regeneration study was conducted to establish the recovery and recycling of the ACBS.

MATERIALS AND METHODS

Preparation and characterization of activated carbon

The activated carbon preparation was mainly guided by the procedure described by (15), but substituting KOH for NaOH chemical activator. *Balanites aegyptiaca* seed shells were sourced locally, thoroughly washed, oven-dried and reduced to smaller particle size (1 mm). The sample was then subjected to first pyrolysis at 700 °C in a furnace for 90 min. A certain quantity of the resulting char was impregnated with NaOH with the impregnation ratio set at 2:1 (NaOH pellets: char). This was followed by second pyrolysis at 750 °C and activated for 90 min. The activated product was subsequently cooled, leached with 250 mL dilute HCl and then finally washed with

distilled water until the washing solution pH attained a neutral value.

The surface structure of the activated carbon and elemental composition were analyzed using scanning electron microscope interfaced with energy dispersive spectrometer (PRO: X: Phenom World 800-07334). The scanning of the sample was done at an accelerating voltage of 15.00 kV and 500 times magnification. The BET surface area, micropore volume, and average pore diameter of the ACBS was estimated by N₂ adsorption method at 77 K, using Quanta Chrome NOVA 2200e, surface area, and pore size analyzer.

Preparation of adsorbate solution

CV procured from E. Merck (Mumbai, India) was used as an adsorbate and was not subjected to any further purification prior to use. Stock solution (1000 mg/L) was prepared by dissolving 1.0 g of the dye into 1 L distilled water in a standard graduated flask. Working CV solution of different concentrations were prepared by employing successive dilution method. The aqueous phase initial pH was changed accordingly using 0.1 M NaOH or 0.1 M HCl solution and was monitored using pH meter (3510 model, Jenway).

Analysis of crystal violet

The final concentration of CV in the supernatant obtained after adsorption was analyzed using a UV/Vis spectrophotometer (Labda 35; Perkin Elmer) at maximum absorbance wavelength (λ_{max}) of 591 nm. Standard solutions (2-10 mg/L) of the adsorbate were prepared and absorbance values were recorded to obtain the calibration curve. The residual dye concentration was determined with reference to the linear calibration curve by interpolation.

Experimental protocol

Batch adsorption experiments were conducted in an Innova 4000 shaker (New Brunswick Scientific). The extent of CV dye removal was studied to assess the influence of varied operational parameters such as temperature (303-313 K), contact time (5-120 min), and initial adsorbate concentration (100-500 mg/L). The influence of each process parameter was investigated by altering that parameter while keeping alternate factors constant. Adsorbate solutions (50 mL) of fixed concentration were contacted with a fixed dose (0.15 g) of ACBS in 250 ml conical flasks. The pH of the aqueous solutions were adjusted to a predetermined optimum pH of 8.0. The contents were then agitated at 150 rpm under controlled temperature (30 ± 1 °C) in an incubator shaker. After pre-decided times, each sample was collected and then centrifuged at 5000 rpm for 10 min. Finally, the clear supernatant was decanted and analyzed for final dye concentration. To attest the correctness and reproducibility of the results, all the experiments were triplicated under same experimental conditions. The

extent of dye adsorption at equilibrium, q_e (mg/g), was computed using Eq. 1:

$$q_e = \left(\frac{C_0 - C_e}{m} \right) \times V \quad (1)$$

where C_0 and C_e (mg/L) stand for the initial and equilibrium liquid phase concentrations, respectively. V is the volume of the dye solution (L), and m is the dry mass of the adsorbent (g).

Kinetic studies

The protocol was essentially the same to those highlighted in the batch experiment. The difference is that the samples were collected after pre-decided times of 5, 10, 20, 30, 40, 60, 90, and 120 min. The supernatant obtained after adsorption was analyzed for concentration of the unadsorbed dye. The extent of dye uptake at time t , q_t (mg/g) was obtained using Eq. 2:

$$q_t = \left(\frac{C_0 - C_t}{m} \right) \times V \quad (2)$$

where C_0 and C_t (mg/L) are the aqueous-phase CV concentrations at initial and any time t , respectively. V is the dye solution volume (L), and m is the dry mass of the adsorbent (g). The kinetics of the CV removal was examined using the pseudo-first-order (16), and pseudo-second-order models (17). The linear equations representing the models are expressed by Eqs. 3-4, respectively:

$$\ln(q_e - q_t) = \ln q_e - k_1 t \quad (3)$$

$$\frac{t}{q_t} = \frac{1}{k_2 q_e^2} + \frac{t}{q_e} \quad (4)$$

where k_1 (1/min) and k_2 (g/mg min) represent the pseudo-first and pseudo-second-order rate constants, respectively. k_1 value can be computed from the gradient of the graph of $\ln(q_e - q_t)$ against t . Similarly, the k_2 and q_e values can be evaluated from the intercept and gradient of linear graph of t/q_t against t , respectively. The fitting and applicability of each kinetic model was verified using the coefficient of interrelationship (R^2) and sum of error squares (SSE, %) which was computed using Eq. 5 (18):

$$SSE (\%) = \sqrt{\frac{\sum (q_{e,exp} - q_{e,theo})^2}{N}} \quad (5)$$

where N is the data points number, $q_{e,cal}$ and $q_{e,exp}$ (mg/g) represent the calculated and experimental adsorption capacity, respectively.

Diffusion studies

The diffusion mechanisms of CV adsorption onto the ACBS were explored using intraparticle diffusion (19) and Boyd (20) models expressed mathematically by Eqs. 6 and 7, respectively. The fitting of the kinetic data into the models gives insight into the rate limiting step of the adsorption process.

$$q_t = k_{id} t^{1/2} + C \quad (6)$$

$$B_t = -0.4977 - \ln \left(1 - \frac{q_t}{q_e} \right) \quad (7)$$

where, k_{id} represent the intra-particle diffusion rate constant (mg/min^{1/2}g) and its value can be gotten from the gradient of the graph of q_t against $t^{1/2}$; C is the intercept which reflects the boundary layer thickness and B_t is the function of the fraction of adsorbate removed at time t .

Isotherms studies

Isotherm study was conducted with higher initial dye concentrations of 100, 200, 300, 400, and 500 mg/L. The isotherm data for CV adsorption on ACBS were modelled by fitting them to Freundlich, Langmuir, Elovich, Dubinin-Radushkevich, Jovanovic, and Temkin isotherm models. The linear equations representing the models are given by Eqs. 8-13 (21):

$$\log q_e = \log K_F + \frac{1}{n} \log C_e \quad (\text{Freundlich}) \quad (8)$$

$$\frac{C_e}{q_e} = \frac{C_e}{q_m} + \frac{1}{K_L q_m} \quad (\text{Langmuir}) \quad (9)$$

$$\ln \frac{q_e}{C_e} = \ln K_{e,qm} - \frac{q_e}{q_m} \quad (\text{Elovich}) \quad (10)$$

$$\ln q_e = \ln q_m - \beta \varepsilon^2 \quad (\text{Dubinin-Radushkevich}) \quad (11)$$

$$\ln q_e = \ln q_m - K_J C_e \quad (\text{Jovanovic}) \quad (12)$$

$$q_e = \frac{RT}{b} \ln C_e + \frac{RT}{b} \ln K_T \quad (\text{Temkin}) \quad (13)$$

where K_F , K_L , K_e , K_j , and K_T are Freundlich, Langmuir, Elovich, Jovanovic and Temkin isotherm constants, respectively; q_e and q_m represent the equilibrium and maximum monolayer adsorption capacity (mg/g) of the ACBS, respectively; C_e (mg/L) represent the equilibrium CV concentration, ϵ is the polanyi potential, β (mol^2/J^2) and b (J/mol) are constants associated with the adsorption energy. The suitability of the isotherm equation is assessed by comparing the coefficients of interrelationship, R^2 .

Thermodynamic studies

The thermodynamic experiments were similar to the kinetic study except that the experiment were performed at varying temperatures of 303, 313, 323 and 333 K. The values of the thermodynamic quantities such as entropy change (ΔS°), Gibbs free energy change (ΔG°), and enthalpy change (ΔH°) were computed using Eqs. 14-16 (22):

$$K_d = \frac{C_{ads}}{C_e} \quad (14)$$

$$\Delta G^\circ = -RT \ln K_d \quad (15)$$

$$\Delta G^\circ = \Delta H^\circ - T \Delta S^\circ \quad (16)$$

where, C_{ads} and C_e (mg/L) are equilibrium CV concentration of on the ACBS and in the liquid phase, respectively; K_d represents the equilibrium constant of adsorption, R represent the gas constant [$8.314 \text{ J} / (\text{K mol})$] and T represent the temperature (K). The values of ΔS° and ΔH° were obtained from the gradient and intercept of the plot of ΔG° against T , respectively.

Regeneration studies

Regeneration experiments were performed to investigate the feasibility of recycling the spent adsorbent and recovery of the dye from aqueous phase. The ACBS regeneration was explored by batch desorption using neutral, basic, and acidic desorbing solutions: distilled water, 0.1 M NaOH, 0.1 M H_2SO_4 , 0.1 M HCl, 0.1 M HNO_3 and 0.1 M CH_3COOH . CV-enriched adsorbent was prepared by shaking 0.15 g of adsorbent with 50 mL of 50 mg/L CV solution at 150 rpm for 120 in a shaker at 303 K. In desorption experiments, the CV-enriched adsorbent was added to 50 mL of 0.1 M of the aforementioned desorbing solutions. The contents were shaken at 150 rpm for 120 min and the supernatant was analyzed for the desorbed dye concentration. The desorbing solution concentration effect was investigated using the eluent

offering higher dye recovery. Similar protocol was applied but with different acetic acid concentration of 0.05, 0.1, 0.2, 0.3, 0.4, 0.5, and 1.0 M. The influence of contact time on desorption was also probed using 0.5 M CH_3COOH at varying time of 5, 10, 20, 30, 60, 90, and 120 min. The reusability of the ACBS was evaluated using 5 successive cycles of adsorption-regeneration and the amount adsorbed/desorbed at various cycles was recorded. The desorption efficiency was computed using the following equation:

$$\text{Desorption efficiency (\%)} = \frac{C_{des}}{C_{ads}} \times 100 \quad (17)$$

Where, C_{des} and C_{ads} stand for the concentration of CV desorbed and adsorbed in mg/L, respectively.

RESULTS AND DISCUSSION

SEM-EDS and BET analyses

The conversion of the precursor into activated carbon was normally associated with changes in morphology that were verified by conduction of pre- and post-activation SEM analysis of the sample. As observed in Figure 1(a), the surface of the BESS is rough and non-porous with some crevices. However, Figure 1(b) revealed variation in the surface texture of the precursor after the activation process with prominent pores existing on the ACBS surface. The development of pores was attributed to the breakdown of some lignocellulose at high activation temperature and subsequent loss of thermally labile compounds (23). The loaded adsorbent was also subjected to analysis and appreciable changes were observed as illustrated in Figure 1 (c). It can be seen that the number of pores diminished which might be ascribed to the occupation of the adsorbent surface by dye molecules. The EDS spectrum of the activated carbon was obtained to ascertain the elemental content (weight % of elements). Figure 2 illustrates that the EDS spectrum consist of peaks of C, O, N, P, S, and Cl. The results showed that the atomic percentages of the adsorbent before and after adsorption process as acquired by EDS quantification were C (82.98, 86.94%), O (13.16, 6.89%), N (2.78, 5.93%) P (0.95, 0.11%), S (0.13, 0.10%) and Cl (0.00, 0.04%), respectively. The changes in the atomic percentages are indication of the uptake of the CV by the adsorbent. The BET surface area, micropore volume, and average pore diameter were computed to be $700.29 \text{ m}^2 \text{ g}^{-1}$, $0.283 \text{ cm}^3 \text{ g}^{-1}$, and 19.41 nm, respectively. The higher surface area of ACBS is reflective of it good adsorption capability.

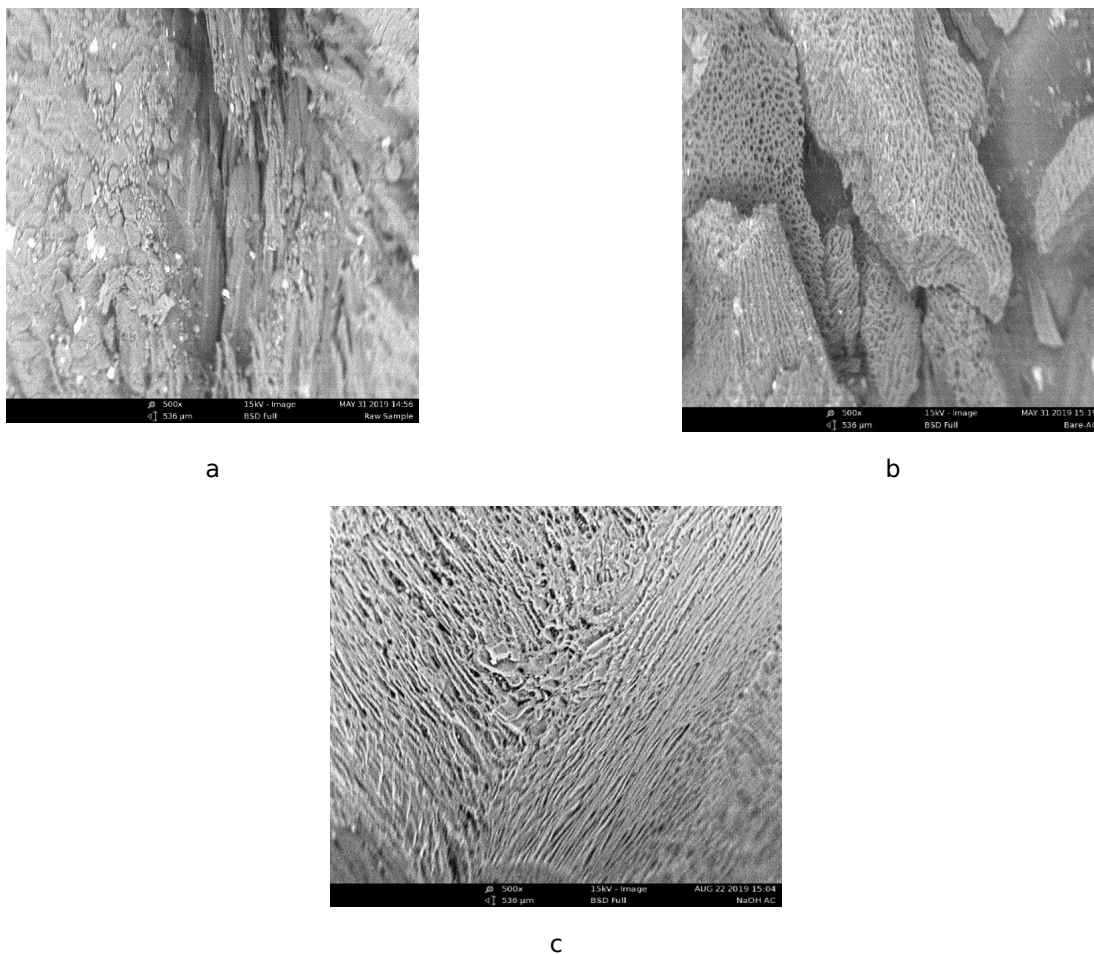


Figure 1: SEM micrograph of (a) BESS (b) ACBS (c) ACBS-CV.

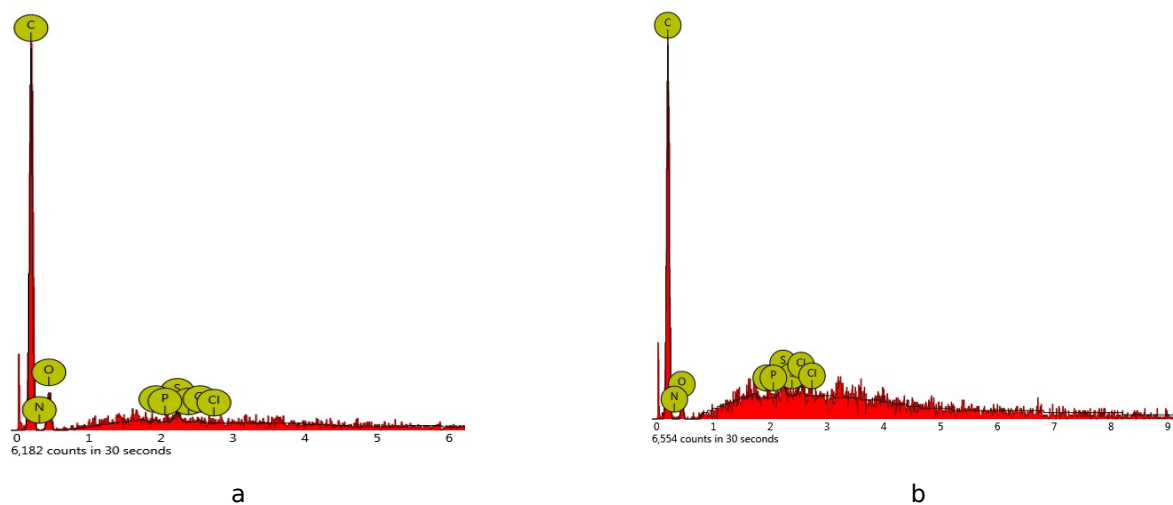


Figure 2: EDS spectra of ACBS (a) before and (b) after CV adsorption.

Kinetic studies

The graphs for pseudo-first-order and pseudo-second-order models are depicted in Figures 3 and 4, and the relevant parameters obtained from the plots are presented in Table 1. It is clear that the kinetic data align with the pseudo-second-order model ($R^2 = 0.9999$ for all initial CV concentrations). Also, the theoretical $q_{e,cal}$ value computed from the pseudo-second-order model was in conformity to the experimental value, which indicates the suitability of the model for the observed kinetics. Moreover, the pseudo-second-order model exhibited a relatively

lower value of the calculated sum of error squares (SSE, %) than the pseudo-first-order model as shown in Table 1. The pseudo-second-order rate constant k_2 , was observed to decline with increase in adsorbate concentration. This signifies slower adsorption rate at higher CV concentration. The results give a hint that chemisorption was the most favored mechanism in the uptake of the adsorbate by the adsorbent. Similar trend in kinetics was highlighted for the sorption of methylene blue onto *Terminalia catappa* and *Jatropha curcas* seed coats activated carbon (24).

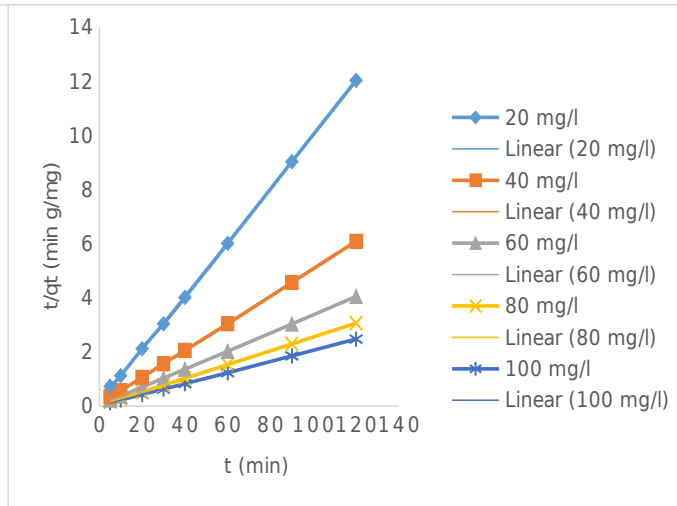
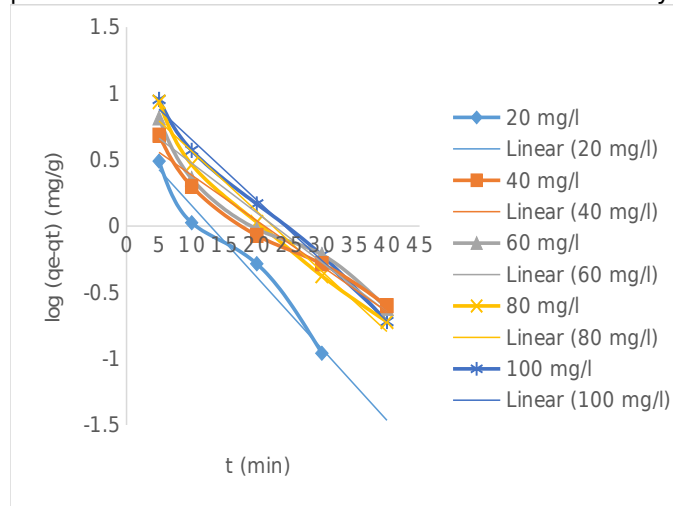


Figure 3: Pseudo-first-order fit for the adsorption of CV onto ACBS (N=5).

Figure 4: Pseudo-second-order fit for the adsorption of CV onto ACBS (N=8).

Table 1: Kinetic parameters for CV adsorption at various initial concentrations.

Kinetic model	Parameters	Initial CV concentration (mg/L)				
		20	40	60	80	100
Pseudo-first-order	k_1 (min^{-1})	0.124	0.078	0.086	0.104	0.105
	$q_{e,exp}$ (mg/g)	9.97	19.71	29.64	39.21	48.55
	$q_{e,cal}$ (mg/g)	4.96	5.34	7.06	10.45	12.84
	R^2	0.9708	0.9615	0.9529	0.9743	0.9915
	SSE (%)	2.51	6.43	10.09	12.86	15.97
Pseudo-second order	k_2 (g / mg min)	0.075	0.040	0.031	0.021	0.020
	$q_{e,exp}$ (mg/g)	9.97	19.71	29.64	39.21	48.55
	$q_{e,cal}$ (mg/g)	10.12	19.96	29.94	39.53	49.01
	R^2	0.9998	0.9999	0.9999	0.9999	0.9999
	SSE (%)	0.08	0.11	0.13	0.14	0.21

Diffusion studies

The adsorption process customarily involved four stages: (a) bulk movement of adsorbate from solution to the liquid film enclosing the adsorbent; (b) mass movement of adsorbate across the liquid film to the outer surface of the adsorbent, which is referred to as boundary layer diffusion (or film diffusion); (c) adsorbate transport from outer surface into the pores of the adsorbent, which is referred to as pore diffusion

(intraparticle diffusion or internal diffusion); (d) adsorption of adsorbate onto active sites in interior and exterior surfaces of adsorbent (25). To establish the rate-controlling step of the CV removal process, the intraparticle diffusion and Boyd models were engaged and the results were illustrated in Figures 5 and 6. As depicted in Figure 5, the intraparticle diffusion plot exhibited two different linear portions, implying two different steps in the CV uptake by the

adsorbent (26). The first portion is ascribed to the diffusion of the dye molecules into the pores of the ACBS, whereas the last portion represents the equilibrium phase where pore diffusion starts to drop-off due to low residual dye concentration in the solution (27). The boundary layer effect was observed to be significant as reflected by the large values of the intercept (Table 2). This indicates the involvement of film diffusion in the rate controlling step (28). The plot reveals that the boundary layer thickness is proportional to the dye concentration in solution. This implies that the more concentrated the dye solution, the more the time that will be required for the dye molecules to move from solution into the pores of the adsorbent.

The experimental kinetic data were further tested with the Boyd model in order to establish the rate-controlling step and the plot is exposed in Figure 6. It is observed that the plots in Figure 6 exhibited non-zero intercepts, confirming the participation of film diffusion in the adsorption process. However, the plots are non-linear, implying that film diffusion shows a relatively low control for dye adsorption onto ACBS (29).

Isotherm studies

The study of adsorption isotherms gives insight about the distribution of solute molecules between the aqueous and solid phases at equilibrium. Figures 7(a-f) typically illustrate the isotherms of the dye adsorption at 303 K, and the values of the characteristic empirical constants were given in Table 3. Examination of the interrelationship coefficients hint that the Freundlich model yielded the best matching of the isotherm data for CV adsorption onto ACBS. The order of the best matching is found to be: Freundlich > Elovich > Langmuir > Temkin > D-R > Jovanovic. The applicability of the Freundlich isotherm intimates the multilayer coverage of the adsorbate on the heterogeneous surface of the adsorbent (30). These findings were in accord with previous reports where the Freundlich isotherm gives better conformation for the sorption of CV by various adsorbents (31,32). Furthermore, the 1/n value (0.56) demonstrates higher heterogeneity and that physical adsorption administrates the uptake of the dye by the porous carbon (33). The Langmuir model also yield a relatively good match ($R^2 = 0.9869$), implying compatibility of the data to the model. This attest the partial involvement of monolayer type mechanism in the adsorption process (34). The value of R_L obtained (0.11) is illustrative of the favorability of the CV adsorption onto the activated carbon (35). The equilibrium data is also compatible with the Elovich model ($R^2 = 0.9875$), and this implies multilayer adsorption on the carbon surface (36). The data was also fit in the Temkin isotherm to determine the

energy associated with the CV-ACBS interaction. The obtained value of the Temkin constant, b (150.06 J/mol) is a signifier of the physical character of the adsorption (37) and this aligns with the multilayer principle. The energy of adsorption (E) from D-R model (1.29 kJ/mol) is less than 8 kJ/mol, testifying that the adsorption process is governed by weak physical forces (38). The poor matching of the data to the Jovanovic model recommend the non-suitability of the model in interpreting the results.

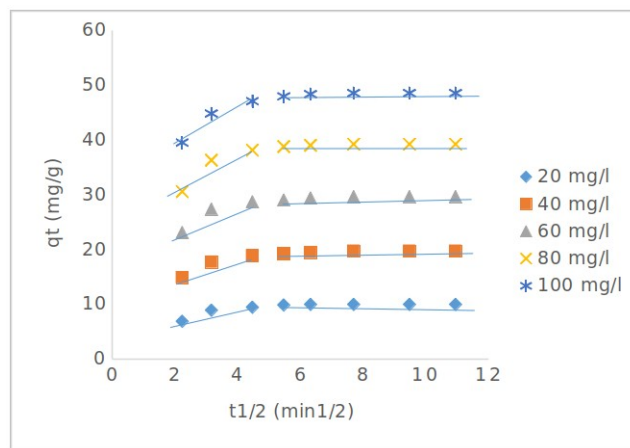


Figure 5: Intraparticle diffusion plot for CV adsorption onto ACBS.

Table 2: Intraparticle diffusion model parameters.

C_0 (mg/L)	K_{id} (g/mg min)	C
20	0.26	7.76
40	0.43	15.99
60	0.55	24.89
80	0.71	33.13
100	0.79	41.77

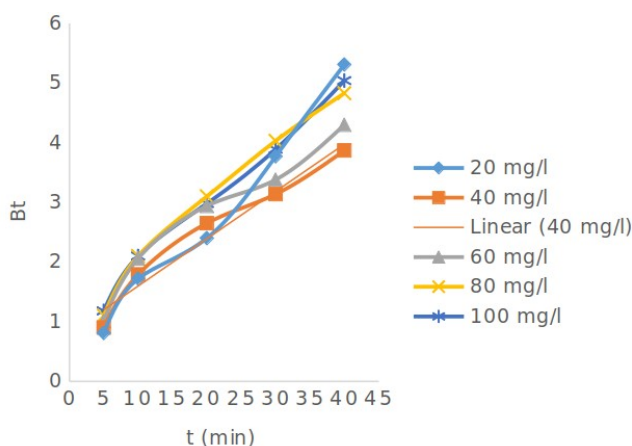
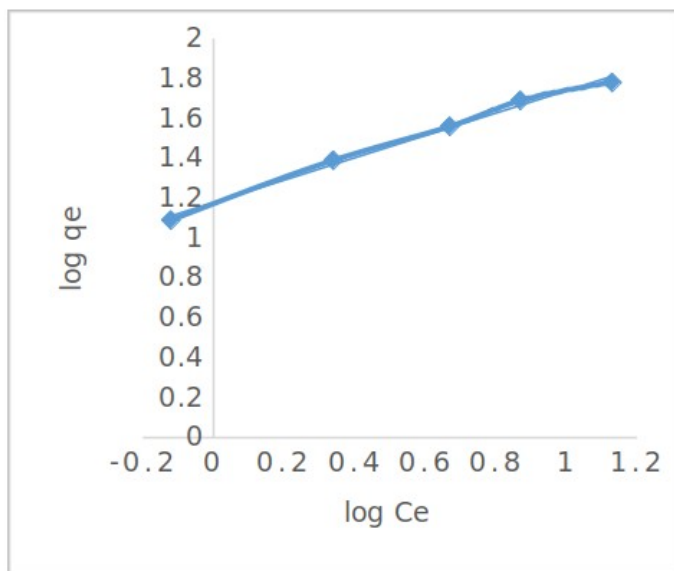
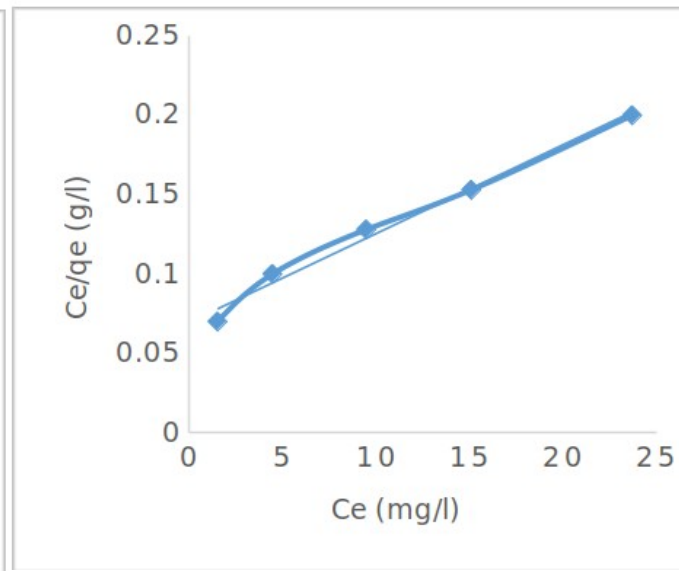


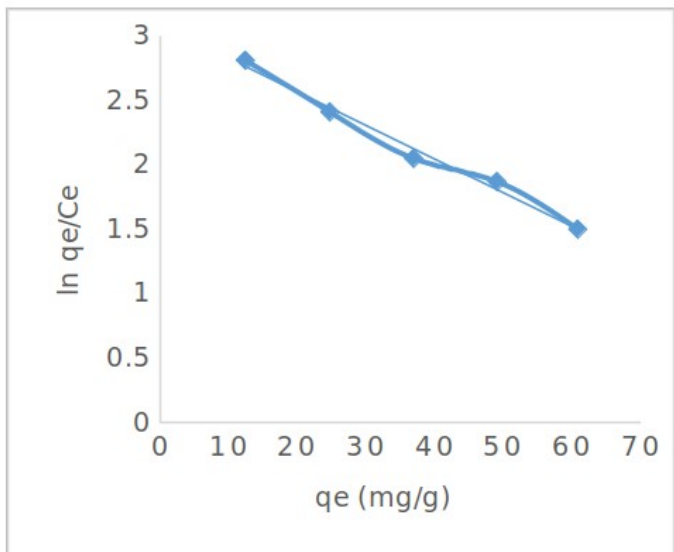
Figure 6: Boyd plot for CV adsorption onto ACBS.



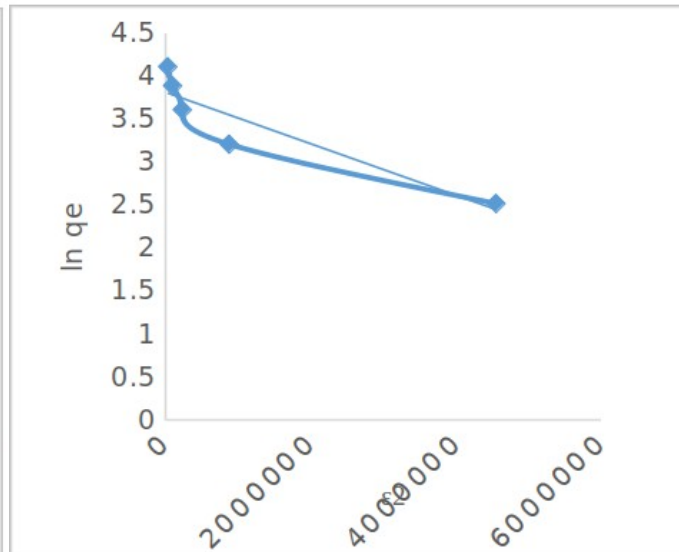
(a)



(b)



(c)



(d)

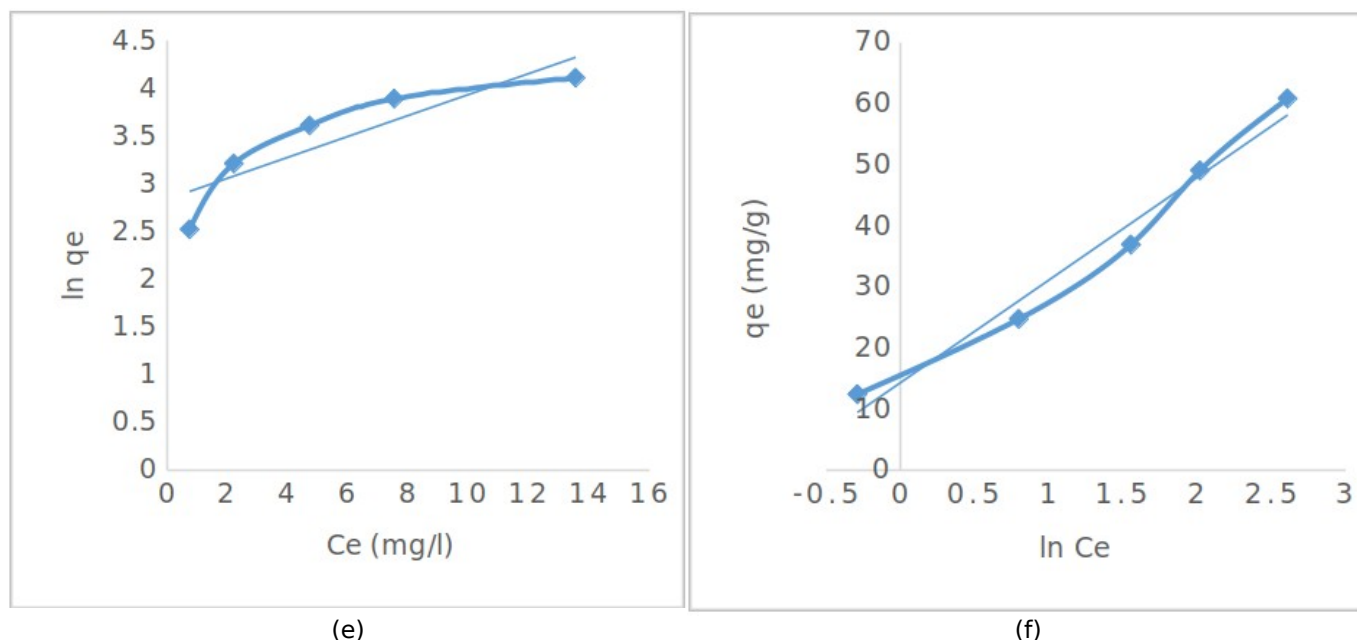


Figure 7: Isotherm fits for (a) Freundlich, (b) Langmuir, (c) Elovich, (d) Dubinin-Radushkevich, (e) Jovanovic, and (f) Temkin isotherm models.

Table 3: Isotherm parameters for CV adsorption onto ACBS.

Isotherm models	Parameters	Values
Langmuir	q_m (mg/g)	178.57
	K_L (dm ³ /mg)	0.08
	R_L	0.11
	R^2	0.9869
Freundlich	K_F (dm ³ /mg)	15.07
	$1/n$	0.56
	R^2	0.9916
Temkin	K_T (dm ³ /mg)	0.85
	b (J/mol)	150.06
	R^2	0.9742
D-R	q_m (mg/g)	45.37
	β (mol ² /J ²)	3×10^{-7}
	E (kJ/mol)	1.29
	R^2	0.8452
Elovich	q_m (mg/g)	38.31
	K_e	1.08
	R^2	0.9875
Jovanovic	q_m (mg/g)	17.03
	K_j	0.11
	R^2	0.7859

Thermodynamic studies

The thermodynamic parameters can shed more light on the energetic changes associated with the adsorption process. The values of the thermodynamic parameters like ΔG° , ΔH° and ΔS° were predicted using the Gibbs plot (Figure 8). From Table 4, the negative value of the Gibbs free energy intimates that the CV removal process is spontaneous. The increase in the negative value at elevated temperatures

indicates that the adsorbate uptake by the ACBS is enhanced at higher temperatures in the studied range. The positive value of the enthalpy change implies the endothermic nature of the CV adsorption by the adsorbent. The magnitude of enthalpic change may provide an insight about the kind of adsorption process involved. If the value of ΔH° is greater than 80 kJ/mol, the process is chemisorption which involves chemical bonding between the adsorbate and

adsorbent surface. Conversely, when ΔH° is lower than 80 kJ/mol, it signifies the adsorption process is physisorption (39). In this study, the value of ΔH° (45.24 kJ/mol) indicates physisorption of adsorbate onto ACBS. The positive value of the entropy change implies the easiness of the adsorbate removal by the adsorbent and that the adsorption phenomenon is entropy-controlled rather than enthalpy-controlled (40). Similar outcome in thermodynamics has been reported for the adsorption of crystal violet using activated carbon prepared from waste active sludge (41).

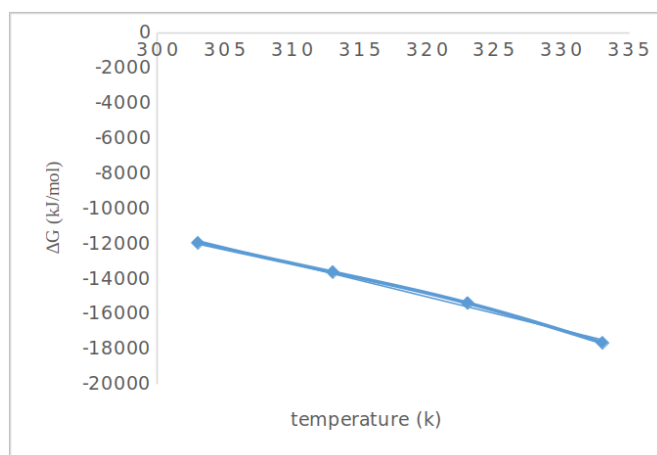


Figure 8: Gibbs plot for CV adsorption onto ACBS.

Table 4: Thermodynamic parameters of CV adsorption onto ACBS.

Temperature (K)	ΔH (kJ/mol)	ΔS (kJ/mol K)	ΔG (kJ/mol)
303	45.24	0.19	-11.96
313			-13.62
323			-14.38
333			-17.65

Regeneration studies

The exhausted adsorbent is not safe for disposal due to the consequent secondary pollution. It is therefore imperative to propose a method for regeneration and reuse of adsorbent so as to lessen the burden on environment in terms of disposal of the sludge. Furthermore, recovered valuable adsorbates can be employed as precursors for the industrial synthesis of vital chemicals after appropriate separation (42). For this reason, different regeneration solutions were assessed for achieving significant replenishment of the spent adsorbent. Figure 9 demonstrates that

maximum dye recovery (44.5%) was achieved with CH_3COOH . This is ascribed to the fact that CH_3COOH lowers the solution pH and the $\text{H}^+_{(\text{aq})}$ compete favorably with the cationic dye ion CV^+ for the adsorption sites of the ACBS (43). It is worthy of mention that addition of other acidic agents (HCl , H_2SO_4 and HNO_3) did not yield relatively effective recovery as compared to CH_3COOH . This is ascribed to the reaction of these strong acids with CV leading to the formation of colorless compound (44). Similarly, in a basic solution, OH^- ions attack the electrophilic carbon of the dye leading to its eventual discoloration (45). These findings were in concurrence with previous report on regeneration of CV-enriched adsorbent using different desorbing solutions (46).

The concentration of the best regeneration solution was also optimized in order to make the acetic acid regeneration solution technically viable for industrial application. The percent recovery was observed to increase with increasing concentration of CH_3COOH and maximum recovery of 85.55% was accomplished using 0.5 M solution (Figure 10). At high acid concentration, there was adequate H^+ in solution to compete with the CV^+ on the enriched-adsorbent (interference effect) and thus resulting in higher recovery. Similar phenomenon was highlighted for the desorption of malachite green using varying concentration of CH_3COOH (47).

The influence of contact time on CV desorption from the CV-enriched ACBS is illustrated in Figure 11. It may be observed that the dye desorbed very quickly in the first 20 min and then attained maximum elution of 85.29% in 30 min. The percent recovery remained nearly steady after this phase, signaling equilibrium of the process. Previous work on CV desorption from grapefruit peel also highlighted similar trend (48).

The reusability of the adsorbent is typically considered as a crucial character for making adsorption more operationally and economically advantageous (49). Figure 12 illustrates the results of the adsorption-desorption of CV for five successive cycles. It is seen that the adsorption efficiency for CV dropped from 97.87% in the first cycle to 92.08% in the fifth cycle. This gave a hint that the adsorbent can be consecutively utilized without appreciable decline in adsorption efficacy of CV. Similar phenomenon was reported for the recycling of activated carbon after five successive adsorption-desorption cycles (50).

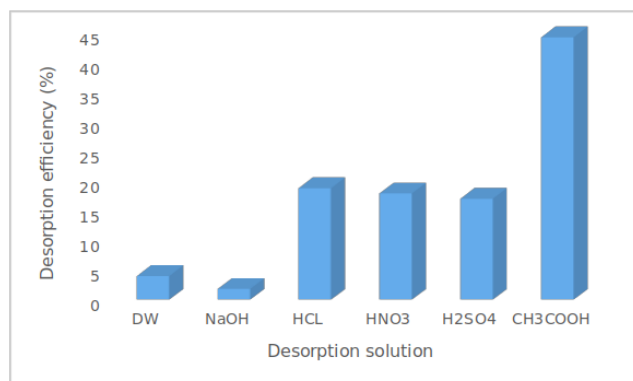


Figure 9: Screening of desorbing solutions for CV recovery.

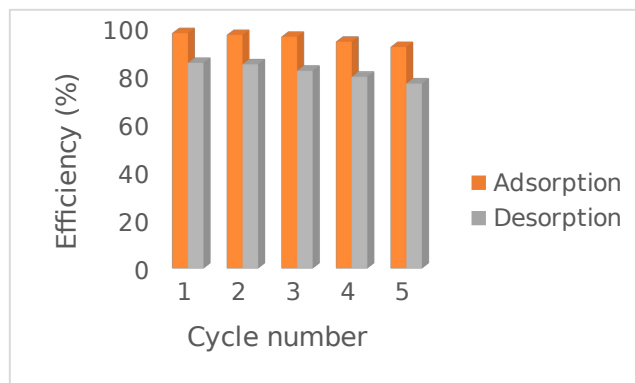


Figure 12: Reusability of ACBS for successive adsorption-desorption cycles of CV.

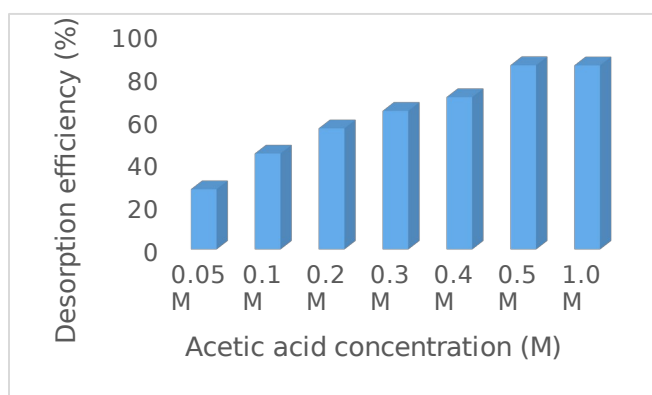


Figure 10: Influence of desorbing solution concentration on CV desorption from ACBS.

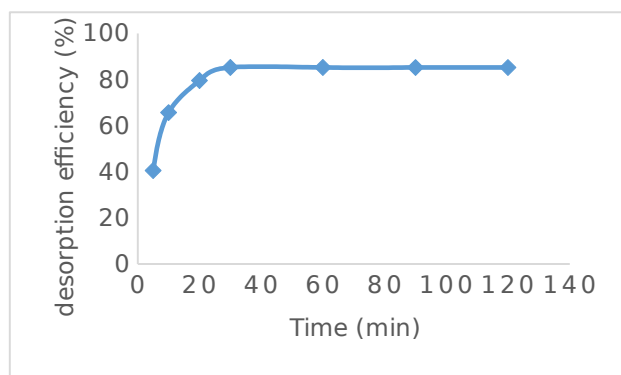


Figure 11: Influence of contact time on CV desorption from ACBS.

CONCLUSION

The activated carbon was prepared from *Balanites aegyptiaca* seed shell via a two-step chemical activation technique with sodium hydroxide. SEM analysis clearly reveals the variation in the morphology of the precursor and the prepared activated carbon. The EDS spectrum of the ACBS showed peaks for C, O, N, P, S, and Cl. Kinetics match well to pseudo-second-order model ($R^2 > 0.999$). The diffusion studies indicates the involvement of both external diffusion and internal diffusion in the CV adsorption process. The isothermal Freundlich model was the best to represent the equilibrium data ($R^2 = 0.9916$; $1/n = 0.56$), signifying the multilayer coverage of CV on the heterogeneous surface of the ACBS. The sequence of the best fitting isotherm model was found to be: Freundlich > Elovich > Langmuir > Temkin > D-R > Jovanovic. The data from thermodynamic study intimates the practicability ($\Delta G = -17.65$ kJ/mol), easiness ($\Delta S = 0.19$ kJ/mol K) and endothermicity ($\Delta H^\circ = 45.24$ kJ/mol) of the process. Regeneration studies reveals the effectiveness of CH_3COOH solution in CV recovery (85.55%). The findings affirmed the suitability of ACBS for crystal violet removal from aqueous medium.

REFERENCES

1. Abbas M, Harrache Z, Trari M. Removal of gentian violet in aqueous solution by activated carbon equilibrium, kinetics, and thermodynamic study. *Adsorption Science & Technology*. 2019;37(7-8):566-89.
2. Biçer G, Gönen F. Telon blue AGLF adsorption by NiO-based nanomaterials: equilibrium, kinetic, and thermodynamic approach. *Journal of the Turkish Chemical Society Section A: Chemistry*. 2017;4(3):675-90.

3. Yildiz A. Adsorption of acid red 114 onto Fe₃O₄@Caffeic acid recyclable magnetic nanocomposite. *Journal of the Turkish Chemical Society Section A: Chemistry*. 2017;4(1):327-40.
4. Jadhav JP, Kalyani DC, Telke AA, Phugare SS, Govindwar SP. Evaluation of the efficacy of a bacterial consortium for the removal of color, reduction of heavy metals, and toxicity from textile dye effluent. *Bioresource Technology*. 2010;101:165-73.
5. Jarup L. Hazards of heavy metal contamination. *British Medical Bulletin*. 2003;68:167-82.
6. Mashkoo F, Nasar A, Inamuddin, Asiri AM. Exploring the reusability of synthetically contaminated wastewater containing crystal violet dye using *Tectona grandis* sawdust as a very low-cost adsorbent. *Scientific Reports*. 2018;8:8314.
7. Robinson T, McMullan G, Marchant R, Nigam P. Remediation of dyes in textile effluent: A critical review on current treatment technologies with a proposed alternative. *Bioresource Technology*. 2001;77:247-55.
8. Dandil S, Sahbaz DA, Acikgoz C. High performance adsorption of hazardous triphenylmethane dye-crystal violet onto calcinated waste mussel shells. *Water Quality Research Journal*. 2019;54(3): 249-56.
9. Chackraborty S, Chowdhury S, Saha, PD. Adsorption of crystal violet from aqueous solution onto NaOH-modified rice husk. *Carbohydrate Polymers*. 2011;86:1533-41.
10. Mittal A, Mittal J, Kaur D, Gupta VK. Adsorption of hazardous crystal violet from wastewater by waste materials. *Journal of Colloid and Interface Science*. 2010; 343: 463-73.
11. Aljeboree A. Adsorption of crystal violet by Fugas sawdust from aqueous solution. *International Journal of ChemTech Research*. 2016; 9(3):412-23.
12. Nazifa, TA, Habba N, Aris A, Hadibarata T. Adsorption of procion red MX-5B and crystal violet dyes from aqueous solution onto corncob activated carbon. *Journal of the Chinese Chemical Society*. 2017;65(2):259-70.
13. Pehlivan E. Production and characterization of activated carbon from pomegranate pulp by phosphoric acid. *JOTCSA*. 2018;(5 sp. is. 1):1-8.
14. Hall JB, Walker DH. *Balanites aegyptiaca*-A monograph. School of Agricultural and Forest Sciences, University of Wales, Bangor, UK. 1991;1-65.
15. Wang X, Wang S, Yin X, Chen J, Zhu L. Activated carbon preparation from cassava residue using a two-step KOH activation: preparation, micropore structure and adsorption capacity. *Journal of Biobased Materials and Bioenergy*. 2014;8(20):1-8.
16. Langergren S. About the theory of so-called adsorption of soluble substances. *Band*. 1898; 24(4): 1-39.
17. Ho YS, McKay G. Pseudo-second-order model for sorption processes. *Process Biochemistry*. 1999;34: 451-65.
18. Hameed BH, Din ATM, Ahmad AL. Adsorption of methylene blue onto bamboo-based activated carbon: kinetics and equilibrium studies. *Journal of Hazardous Materials*. 2007;141:819-25.
19. Weber WJ, Morris JC. Kinetics of adsorption on carbon from solutions. *Sanitary Engineering Division ASCE*. 1963;89: 31-60.
20. Boyd GE, Adamson AW, Myers JLS. The exchange of ions from aqueous solution by organic zeolites, II: Kinetic. *Journal of the American Chemical Society*. 1947;69:2836-48.
21. Ayawei N, Ebelegi AN, Wankasi D. Modelling and interpretation of adsorption isotherms. *Journal of Chemistry*. 2017;3039817.
22. Wu J, Xia A, Chen C, Feng L, Su X, Wang X. Adsorption thermodynamics and dynamics of three typical dyes onto bio-adsorbent spent substrate of *Pleurotus eryngii*. *International Journal of Environmental Research and Public Health*. 2019;16(679):1-11.
23. Ahmad MA, Ahmad N, Bello OS. Adsorptive removal of malachite green dye using durian seed-based activated carbon. *Water Air Soil Pollution*. 2014;225:1-18.
24. Saheed IO, Adekola FA, Olatunji GA. Sorption study of methylene blue on activated carbon prepared from *Jatropha curcas* and *Terminalia catappa* seed coats. *JOTCSA*. 2017;4(1):375-94.
25. Nethaji S, Sivasamy A. Removal of hexavalent chromium from aqueous solution using activated carbon prepared from walnut shell biomass through alkali impregnation processes. *Clean Technologies and Environmental Policy*. 2014;16:361-8.
26. Ahmad MA, Afandi NS, Adegoke KA, Bello OS. Optimization and batch studies on adsorption of malachite green dye using rambutan seed activated

- carbon. *Desalination and Water Treatment*. 2015;57(45):21487-511.
27. Gorzin F, Abadi MMBR. Adsorption of Cr(VI) from aqueous solution by adsorbent prepared from paper mill sludge: kinetics and thermodynamic studies. *Adsorption Science & Technology*. 2017;36(1-2):149-69.
28. Al-Othman ZA, Ali R, Naushad M. Hexavalent chromium removal from aqueous medium by activated carbon prepared from peanut shell: adsorption kinetics, equilibrium and thermodynamic studies. *Chemical Engineering Journal*. 2012;184:238-47.
29. Ma J, Yu Fei, Zhou L, Jin L, Yang M, Luan J, Tang Y, Fan H, Yuan Z, Chen J. Enhanced adsorptive removal of methyl orange and methylene blue from aqueous solution by alkali-activated multiwalled carbon nanotubes. *Applied Materials and Interfaces*. 2012;4:5749-60.
30. Pakade VE, Nchoe OB, Hlungwane L, Tavengwa NT. Sequestration of hexavalent chromium from aqueous solution by activated carbon derived from macadamia nutshells. *Water Science and Technology*. 2017;75(1):196-206.
31. Ahsaine HA, Anfar Z, Zbair M, Ezahri M, El Alem N. Adsorptive removal of methylene blue and crystal violet onto micro-mesoporous Zr₃O/activated carbon composite: a joint experimental and statistical modeling considerations. *Journal of Chemistry*. 2018: 1-14.
32. Al-Azabi K, Al-Marog S, Abukrain A, Sulyman M. Equilibrium isotherm studies of dye adsorption onto orange peel powder. *Chemistry Research Journal*. 2018;3(1):45-59.
33. Akalin HA, Hicsonmez U, Yilmaz H. Removal of Cesium from aqueous solution by adsorption onto Sivas-Yildizeli (Türkiye) vermiculite: equilibrium, kinetic and thermodynamic studies. *Journal of the Turkish Chemical Society Section A: Chemistry*. 2018;5(1):85-116.
34. Kumar M, Tamilarasan R. Modeling studies for the removal of methylene blue from aqueous solution using *Acacia fumosa* seed shell activated carbon. *Journal of Environmental Chemical Engineering*. 2013;1:1108-16.
35. Experimental and DFT studies of the removal of pharmaceutical metronidazole from water using polypyrrole. *International Journal of Industrial Chemistry*. 2019;10:269-79.
36. Gubernak M, Zapala W, Kaczmarek K. Analysis of benzene adsorption equilibria on an RP-18e chromatographic column. *Acta Chromatographica*. 2003;13:38-59.
37. Kyziol-Komosińska J, Rosik-Dulewska C, Franus M, Antoszczyszyn-Szpicka P, Czupiol J, Krzyżewska I. Sorption Capacities of Natural and Synthetic Zeolites for Cu(II) Ions. *Polish Journal of Environmental Studies*. 2015;24:1111-23.
38. Foo KY, Hameed BH. Insights into the modeling of adsorption isotherm systems. *Chemical Engineering Journal*. 2010;156: 2-10.
39. Akar E, Altinisik A, Seki Y. Using of activated carbon produced from spent tea leaves for the removal of malachite green from aqueous solution. *Ecological Engineering*. 2013;52:19- 27.
40. Asadullah, Kaewsichan L, Tohdee K. Adsorption of hexavalent chromium onto alkali-modified biochar derived from *Lepironia articulata*: A kinetic, equilibrium, and thermodynamic study. *Water Environment Research*. 2019;1-14.
41. Sahbaz DA, Dandil S, Acikgoz C. Removal of crystal violet dye by a novel adsorbent derived from waste active sludge used in wastewater treatment. *Water Quality Research Journal*. 2019; 54(4):299-308.
42. Sharma K, Vyas RK, Dalai AK. Thermodynamic and kinetic studies of methylene blue degradation using reactive adsorption and its comparison with adsorption. *Journal of Chemical and Engineering Data*. 2017;62(11):3651-62.
43. Ogata F, Nakamura T, Kawasaki N. Adsorption capability of virgin and calcined wheat bran for molybdenum present in aqueous solution and elucidating the adsorption mechanism by adsorption isotherms, kinetics and regeneration. *Journal of Environmental Chemical Engineering*. 2018;6(4):4459-66.
44. Nidheesh PV, Gandhimathi R, Ramesh ST, Singh TSA. Adsorption and desorption characteristics of crystal violet in bottom ash column. *Journal of Urban and Environmental Engineering*. 2011;6(1):18-29.
45. Hassan MAE, Fayoumi LMA, El Jamal MM. Kinetic study of the discoloration of triphenylmethane dyes in function of pH, salt effect. *Journal of the University of Chemical Technology and Metallurgy*. 2011;46(4):395-400.
46. Neupane S, Ramesh ST, Gandhimathi R, Nidheesh PV. Pineapple leaf powder as a biosorbent for the removal of crystal violet from aqueous solution.

Desalination and water treatment. 2014;54(7):2041-54.

47. Yunusa U, Ibrahim MB. Reclamation of malachite green-bearing wastewater using desert date seed shell: adsorption isotherms, desorption and reusability studies. Chemsearch Journal. 2019;10(2):112-22.

48. Saeed A, Sharif M, Iqbal M. Application potential of grapefruit peel as dye sorbent: kinetics, equilibrium and mechanism of crystal violet adsorption. Journal of Hazardous Materials. 2010; 179:564-72.

49. Ali I, Peng C, Ye, T, Naz I. Sorption of cationic malachite green dye on phyto-genic magnetic nanoparticles functionalized by 3-mercaptopropanoic acid. Royal Society of Chemistry Advances. 2018;8:8878-97.

50. Azaman SAH, Afandi A, Hameed BH, Mohd Din AT. Removal of malachite green from aqueous phase using coconut shell activated carbon: adsorption, desorption, and reusability studies. Journal of Applied Science and Engineering. 2018;21(3):317-30.



Macroaggregated Albumin (MAA): Production, Size Optimization, Eu(III) and Tb(III) Complexes

Burcu UCAR^{1,*}   and Tayfun ACAR²  

¹Yildiz Technical University, Chemistry and Metallurgy Faculty, Department of Bioengineering, 34220, Istanbul, Turkey

Abstract: Herein, the synthesis of the macroaggregated albumin particles was carried out under different conditions for the size optimization that can be used in magnetic resonance, positron emission and fluorescence imaging. The size distribution analysis was performed with the Mastersizer and optimized MAA had 31.57 μm size and 0.36 PDI value. Morphological analysis was done with SEM. EDX and FT-IR analyzes were performed to study formed Eu^{3+} and Tb^{3+} complexes with optimized MAA. MAA complexes that can be used in lungs and liver imaging have been successfully obtained.

Keywords: MAA, Eu(III) complexes, Tb(III) complexes, Magnetic resonance imaging, Fluorescence imaging

Submitted: October 10, 2020. **Accepted:** December 23, 2020.

Cite this: Ucar B, Acar T. Macroaggregated Albumin (MAA): Production, Size Optimization, Eu(III) and Tb(III) Complexes. JOTCSA. 2021;8(1):209-16.

DOI: <https://doi.org/10.18596/jotcsa.808636>.

***Corresponding Author. E-mail:** brccr87@gmail.com, Telephone: +090-538-786-3200.

INTRODUCTION

Human serum albumin (HSA) is found in lymph, saliva, plasma (~60% of protein mass), cerebrospinal cord, and interstitial fluid. The secondary structure of HSA consists of 67% alpha-helix, 23% stretched chain, 10% beta-sheet, and folds. The change in the secondary and tertiary structures of HSA is due to the opening of this alpha-helical structure and the increase in beta-sheets. Protein aggregation occurs due to the partial opening of the tertiary structure and conformational changes of the secondary structure (1). The aggregation process of HSA consists of two steps: in the first step, as a result of the reversible nucleation occurring, proteins are thermodynamically incorporated in a reversibly growing nucleus sequentially. In the second step, after the

growing nucleus reaches a critical mass, protein molecules are added to the nucleus irreversibly. As a result, a large aggregate, which is very stable, is formed (1). In addition to the aggregation process, secondary structure changes occur due to the binding of metal complexes to a protein such as human serum albumin (HSA) (2).

Recently, some metal complexes bound to human serum albumin have shown high affinity toward DNA and have displayed various pharmacological properties (3). The development of metal complexes (especially Gallium, Gadolinium, and Lanthanides such as Europium and Terbium) that targeting cancerous cells under physiological conditions is of great current interest towards developing models for lots of pharmaceuticals from imaging

and contrast agents to metal-based radionuclide and chemotherapeutics agents (2, 4-6). These agents are of considerable interest as magnetic resonance imaging (MRI) agents, bioresponsive cellular imaging agents, luminescent bioprobes, and also in targeted radionuclide therapy before clinical application as simulating agents (2).

Terbium-149 (^{149}Tb), suggested as a potential alpha-emitter ($E_{\alpha} = 3.97 \text{ MeV}$; $I=17\%$) for targeted radionuclide therapy (TRT), has a relatively short half-life compared to ^{225}Ac , but four times longer than that of ^{213}Bi ($t_{1/2}$: 4.1 hours) and contains no daughter nuclides. ^{149}Tb can also be used in positron emission tomography (PET) of ^{149}Tb labeled radioligands, by reason of the co-emission of β^+ particles (positrons), and can be also stably coordinated with a DOTA chelator as a radiolanthanide. However, as it is assumed that ^{149}Tb is adsorbed on the surface of aggregates, there is no need to pre-conjugate the MAA with DOTA for labeling (7).

The PET or single-photon emission tomography (SPECT) tracer labeled MAA can accurately localize the tumor, determine the amount of perfusion, and provides better cross-sectional images for preoperative or pre-treatment planning, while providing intraoperative mapping through fluorescence or radioactive detection, using a hand probe or portable camera, and guides surgeons during tumor resection (8).

More than 80% of the administered albumin is retained in the pulmonary alveolar-capillary bed immediately after intravenous injection. Thus, the imaging procedure can be started immediately after injection. Since organ selectivity is a direct result of particle size, the sizes of labeled aggregates administered should be homogeneous and optimized. While aggregates below 1-10 micrometers are deposited by the reticuloendothelial system, aggregates above 10 micrometers are uptaken in the lung through a mechanical process. The erosion and fragmentation of the particles in the target organ reduced the particle size and thus, aggregates pass-through the pulmonary alveolar-capillary bed (9).

It is in the literature that MAA kits, which have been used in the clinic for radiolabeling with technetium-99m for many years, are used for labeling with metals such as lanthanides, gallium-68, and gadolinium (10). However, these kits are produced and optimized for labeling with technetium, so they contain many auxiliary substances that are not required for labeling with other metals. MAA, planned to be applied clinically in our study, was synthesized, optimized and labeled with relevant metals according to the purpose. This work forms the basis for manufacturing both a bioprobe, a contrast agent, and a radiotheranostic agent. The presented method and data will be used in the production of the agent to be applied in the mapping of liver and breast cancer, radio-guided occult lesion localization (11), and evaluation of regional perfusion in healthy and cancerous tissue.

We aim to prepare MAA particles that are sterile, free of pyrogens, with relatively long shelf-life, with a suitable range of particle size (30-80 μm) and higher radiochemical yields, showing diffusely increased tracer uptake in the lungs and liver.

MATERIAL AND METHODS

All reagents and solvents were commercial reagents of analytical grade and were used as received.

Production of the MAA Particles

0.4 or 0.8 mL of %20 HSA solution was diluted with 1 mL H_2O and 1.1 mL of %0.9 saline (NaCl). The obtained solution was sonicated in an ultrasonic bath (Bandeline) for 10 minutes or with a probe sonicator for a different time and amplitude. Then, 1 mL of %5 T80 was added to the HSA solution and the last volume was completed to 33.5 mL with 0.1M pH 5.8 PBS. The pH of the solution was controlled again. It is important that the pH is at the isoelectric point of HSA (pH 5.8-6.2). The mixture was stirred with a magnetic stirrer at 80 °C for 10 minutes. Next, it suddenly cooled to 25 °C. Heating and sudden cooling were performed twice (12, 13) and then it was lyophilized. Since the MAA obtained contains a large amount of salt, the salts were removed by washing and centrifugation three times and the MAA solution was lyophilized again.

Table 1: Synthesis parameters of the MAA particles.

	Amount of %20 HSA solution (mL)	Sonication Type	Sonication Conditions	T80
F1	0.4	Ultrasonic bath	10 min.	+
F2	0.4	Ultrasonic bath	10 min.	-
F3	0.4	Probe sonicator	30 sec., %50 W	+
F4	0.4	Probe sonicator	30 sec., %50 W	-
F5	0.4	Probe sonicator	45 sec., %50 W	-
F6	0.4	Probe sonicator	60 sec., %50 W	-
F7	0.4	Probe sonicator	45 sec., %60 W	-
F8	0.4	Probe sonicator	45 sec., %70 W	-
F9	0.8	Probe sonicator	45 sec., %50 W	-
F10	0.8	Probe sonicator	45 sec., %60 W	-
F11	0.4	Probe sonicator	45 sec., %60 W	-

Synthesis of Eu(III) and Tb(III) Complexes of the MAA Particles

5 mg of the MAA particles were dispersed in 1.5 mL of 1M AcONH₄ buffer solution at pH 4.8. 100 μ L of 4.11×10^{-5} M TbCl₃.6H₂O or 100 μ L of 5.35×10^{-5} M EuCl₃.6H₂O were added to 750 μ L of MAA solution. Complexing was carried out at 90°C at 300 rpm for 30 minutes. Washing was done in triplicate with 5 mL of 0.9% saline, and in triplicate with 5 mL dH₂O by centrifuge at 6000 rpm for 15 minutes. The excess metal remaining in the environment was removed. The complexes obtained were lyophilized and stored at -18 °C until reuse.

Size measurements of the MAA particles

The size distribution of the MAA particles was determined with Mastersizer (Hydro 2000MU, Malvern). After the production of the MAA particles, 10 mL of the emulsion was added to 250 mL of ultra-pure water until an obscuration rate of 5-15% was obtained. The samples were analyzed for the size distribution and particle size measurements were carried out in triplicate.

FT-IR Analysis of Eu(III) and Tb(III) Complexes of the MAA Particles

The molecular structure of the MAA, Eu(III)-MAA and Tb(III)-MAA were investigated by Fourier transform infrared (FT-IR) transmission spectra (IR-Prestige 21 FT-IR spectrophotometer, Shimadzu, Japan). MAA, Eu(III)-MAA, and Tb(III)-MAA were grounded into a fine powder. Then, the obtained powders were mixed with KBr powder and compacted into pellets for the FT-IR analysis. The spectra were examined in the wavenumber range of 400-4000 cm⁻¹ with a resolution of 4 cm⁻¹.

Scanning Electron Microscopy (SEM) Imaging and Energy dispersive X-Ray spectroscopy (EDX) Analysis

The surface morphology of the particles was viewed with scanning electron microscopy (SEM, EVO LS 10, Zeiss) with different magnification. To obtain SEM images, MAA particles were coated with a thin layer of Au-Pd at 10 mA for 60 seconds before observation (14).

Elemental analysis of Eu(III)-MAA and Tb(III)-MAA complexes were confirmed by EDX analysis.

RESULTS AND DISCUSSION

Size Distribution of the MAA Particles

MAA particles were produced in 11 formulations with different parameters (Table 1) to examine the effect of protein amount, stabilizer effect, sonication time and type on aggregate size. The size distribution and PDI values of the MAA particles were shown in Table 2. Size values of F1 and F2 formulations, made using ultrasonic bath, were found to be 191.75 and 131.91 microns, respectively. Due to the large size values, the sonication type was changed, and probe sonicator was used in other formulations. When T80 is used, it has been determined that the particle size is increased, and particles are obtained very far from the monodisperse, so no stabilizer was used in the F4-F12 formulations.

Subsequently, in the F4-F9 formulations, the power and duration of the probe sonicator were optimized. Three different times as 30, 45, and 60 seconds and three different powers 50, 60, and 70% watts were used. In the F4, F5, and F6 formulations, the size of the particles obtained with 50% watt power decreased from 59 microns to 16 microns by increasing the sonication time, but the PDI values were 0.3 for F4, 0.81 for F5 and 1.39 for F6. In other words, the increase in application time at constant power reduced the size and increased the PDI

values, causing the particles to have a polydisperse distribution.

Next, F7 (60% W) and F8 (70% W) was also produced at different sonication powers, together with the previously produced F5 (50% W). PDI values of 0.36 and 0.44 for F7 and F8, respectively, were accepted as monodispersed particles. The size of F7 was 31.57 microns, while F8 was measured as 14.13 microns. Finally, by varying the amount of HSA solution, F9 and F10 formulations were produced. While there was no significant difference in PDI values with the increase in protein amount, particle sizes increased by an average of 15-20 microns compared to F7. In line with these results, the F7 particles were determined as the optimized MAA particles. To show the reproducibility of this formulation, once again the F11 formulation was produced with the same parameters and its size was measured as 30.89 microns, and the PDI value as 0.43. F7 and F11 were consistent in size and PDI. The size distribution graph of the optimized MAA particles (F7) was given in Figure 1.

Table 2: The size distribution results of the MAA particles.

	Size (μm)	PDI
F1	191.75	0.42
F2	131.91	1.04
F3	56.12	0.37
F4	59.37	0.30
F5	34.28	0.81
F6	16.39	1.39
F7	31.57	0.36
F8	14.13	0.44
F9	44.83	0.38
F10	52.52	0.42
F11	30.89	0.43

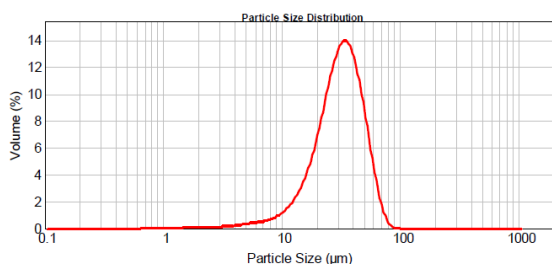


Figure 1: Size distribution graph of the optimized MAA particles (F7) (particle size distribution by volume).

Morphological Analysis of the MAA Particles

SEM images were taken from particles produced with the optimized formulation, F7. Morphological examination of F7 MAA particles was performed by SEM analysis as illustrated in Figure 2 and 3. SEM images confirmed the aggregation formation from the HSA. The images of aggregates taken at different magnifications were found to be compatible with the literature (15).

Synthesis of the Eu(III) and Tb(III) Complexes of the MAA Particles

Eu(III) and Tb(III) complexes of the F7 MAA particles were achieved. The complexes were analyzed by FT-IR and EDX.

FT-IR Analysis of the Eu(III) and Tb(III) Complexes of the MAA Particles

The Fourier Transform Infrared (FT-IR) analysis has been frequently applied for the recognition of organic and inorganic molecules. Figure 4 shows the FT-IR spectra of the Eu(III)-MAA and Tb(III)-MAA complexes comparatively with MAA. In the observed spectrum, the absorption bands of metal groups in the range of 500-700 cm^{-1} are clearly evident, differently from the MAA bands. Two sharp peaks of europium were seen at 534.7 and 621.7 cm^{-1} , while two sharp peaks for terbium at 626.9 and 533.6 cm^{-1} supported the presence of metals (16). A remarkable decrease in the peak intensities was determined in the spectra of the Eu(III)-MAA, and Tb(III)-MAA complexes, for the amide I band (1657.3 cm^{-1} , free MAA) and amide II band (1533.6 cm^{-1} , free MAA) area. It was thought that the decrease of the intensities was because of the interplay of metal ions with the C=O, C-N, and NH groups of HSA. The binding interactions between the MAA and the metal ions (Eu^{3+} and Tb^{3+}) were further evidenced by the spectral shifting of the amide I band from 1657.3 cm^{-1} in free MAA to 1651.8 cm^{-1} in the Eu(III)-MAA and 1651.4 cm^{-1} in the Tb(III)-MAA complexes. It has been noticed that the shift in this spectrum was due to the interplay of the Eu^{3+} and Tb^{3+} ions with the C=O and C-N groups of the MAA (17). In addition, a significant change was observed in the 1000-1200 cm^{-1} region. Unlike the spectrum of MAA, a double-headed broad peak appeared at 1076.0 and 1022.2 cm^{-1} for Eu(III)-MAA showed and at 1079.6 and 1024.4 cm^{-1} for Tb(III)-MAA. The changes in the three-dimensional structure of the aggregate due to the adsorption of the metal into the aggregate can be explained by the two vibration bands around 1075 and 1020 cm^{-1} of the threonine residue in the protein

structure (18, 19). These bands were compatible with the literature (20).

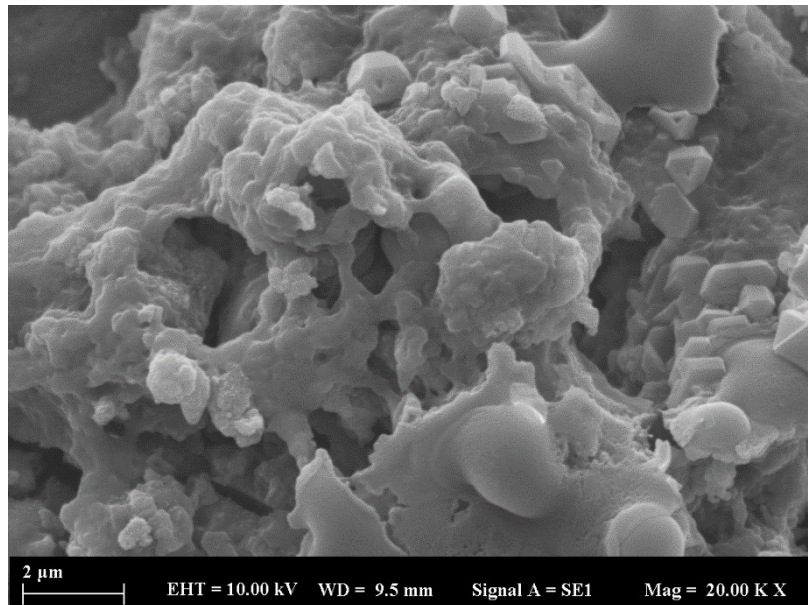


Figure 2: SEM image of the MAA particles (20.000).

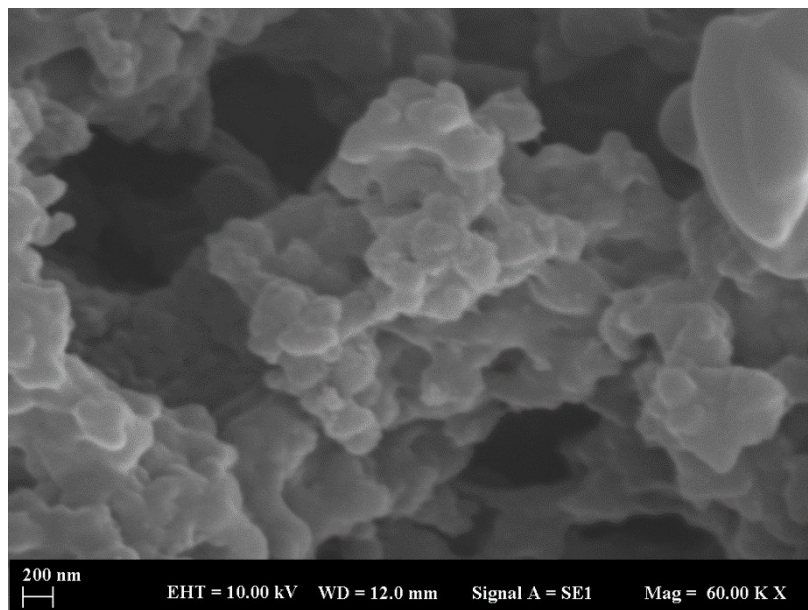


Figure 3: SEM image of the MAA particles (60.000).

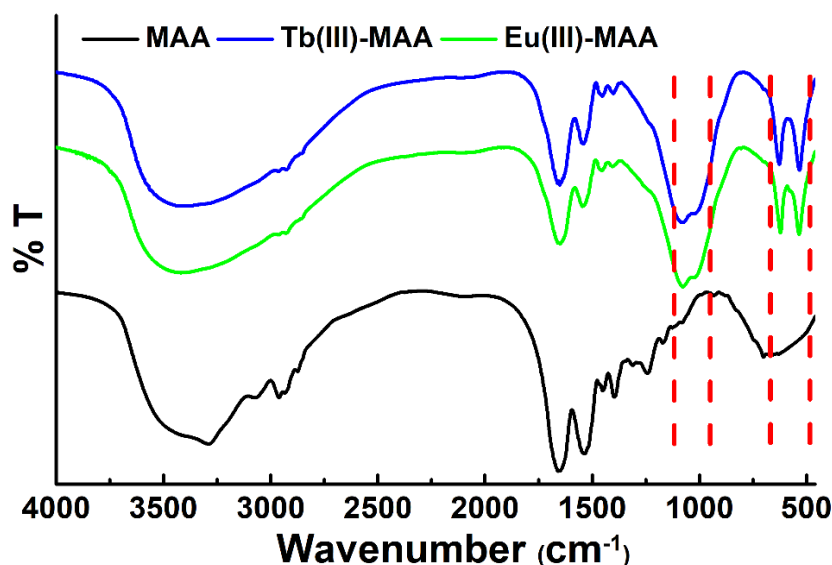
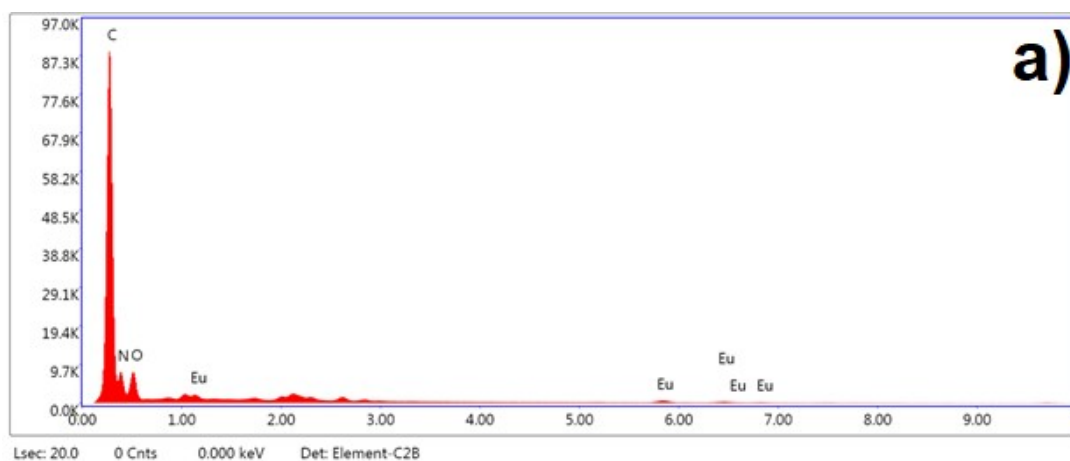


Figure 4: FT-IR spectra of the Eu(III)-MAA and Tb(III)-MAA complexes were given comparatively with MAA.

EDX Analysis of the Eu(III) and Tb(III) Complexes of the MAA Particles

EDX is a standard procedure for determining and measuring the fundamental composition of the area of samples from a few nanometers to micron size. The composition of the powder Eu(III)-MAA and Tb(III)-MAA samples were

measured using EDX. EDX spectra of the Eu(III)-MAA and Tb(III)-MAA complexes were given in Figure 5. The presence of Europium (Eu) and Terbium (Tb) in the resulting Eu(III)-MAA and Tb(III)-MAA complexes was evident in the corresponding EDX spectra in Figure 5a and 5b, respectively (21).



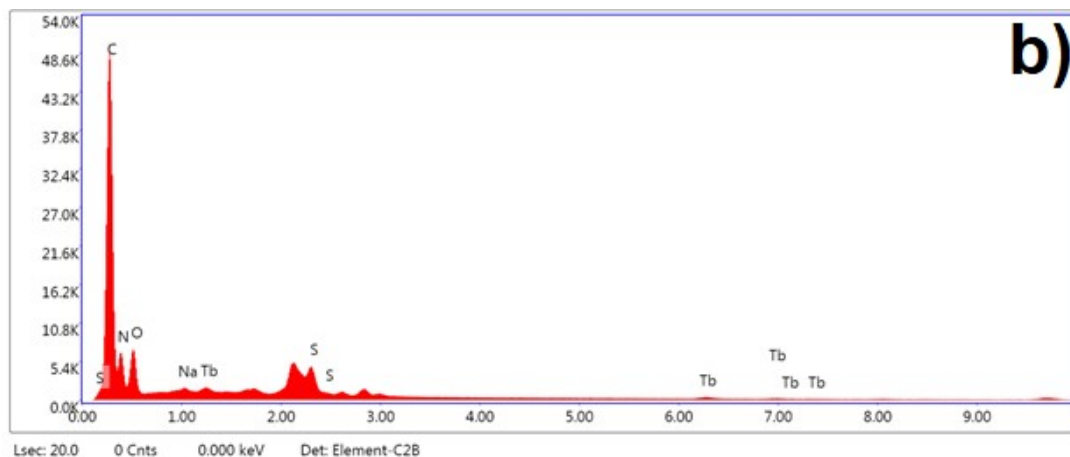


Figure 5: EDX spectra of the a) Eu(III)-MAA and b) Tb(III)-MAA complexes.

CONCLUSION

We have optimized the synthetic parameters of the MAA particles. Particles with an average size of 31 μm were chosen as optimized MAA. The structure of the metal complexes was evaluated by FT-IR analysis. The morphologies and qualitative analysis of the complexes were carried out using SEM-EDX. It is thought that the obtained Eu(III)-MAA and Tb(III)-MAA complexes can be used in magnetic resonance, positron emission and fluorescence imaging studies.

ACKNOWLEDGEMENT

The authors are grateful to Prof Dr. Tevfik Fikret CERMİK and Doç. Dr. Esra ARSLAN for critical revisions of the study. The authors also would like to thank M. Beşir ARVAS for all his support.

REFERENCES

- Maciążek-Jurczyk M, Janas K, Pożycka J, Szkudlarek A, Rogóż W, Owczarzy A, et al. Human serum albumin aggregation/fibrillation and its abilities to drugs binding. *Molecules*. 2020;25(3):618.
- Dasari S, Patra AK. Luminescent europium and terbium complexes of dipyridoquinoxaline and dipyridophenazine ligands as photosensitizing antennae: structures and biological perspectives. *Dalton Transactions*. 2015;44(46):19844-55.
- Asadi Z, Mosallaei H, Sedaghat M, Yousefi R. Competitive binding affinity of two lanthanum (III) macrocycle complexes toward DNA and bovine serum albumin in water. *Journal of the Iranian Chemical Society*. 2017;14(11):2367-85.
- Tikhonova TN, Shirshin EA, Budylin GS, Fadeev VV, Petrova GP. Assessment of the europium (III) binding sites on albumin using fluorescence spectroscopy. *The Journal of Physical Chemistry B*. 2014;118(24):6626-33.
- Amor-Coarasa A, Milera A, Carvajal DA, McGoron AJ, editors. 99mTc-MAA vs. 68Ga-MAA as Perfusion Agents. 2013 29th Southern Biomedical Engineering Conference; 2013: IEEE.
- Mathias CJ, Green MA. A convenient route to [68Ga] Ga-MAA for use as a particulate PET perfusion tracer. *Applied Radiation and Isotopes*. 2008;66(12):1910-2.
- Umbricht CA, Köster U, Bernhardt P, Gracheva N, Johnston K, Schibli R, et al. Alpha-PET for Prostate Cancer: Preclinical investigation using 149 Tb-PSMA-617. *Scientific reports*. 2019;9(1):1-10.
- Persico MG, Marengo M, De Matteis G, Manfrinato G, Cavenaghi G, Sgarella A, et al. 99mTc-68Ga-ICG-Labelled Macroaggregates and Nanocolloids of Human Serum Albumin: Synthesis Procedures of a Trimodal Imaging Agent Using Commercial Kits. *Contrast Media & Molecular Imaging*. 2020;2020.
- MAA D. Kit for the Preparation of Technetium Tc 99m Albumin Aggregated Injection 2017 [Available from: <https://www.draximage.com/pdf/MAA-PI-Oct-2017-1.pdf>].
- Mueller D, Kulkarni H, Baum RP, Odparlik A. Rapid Synthesis of 68Ga-labeled macroaggregated human serum albumin (MAA) for routine application in perfusion imaging

using PET/CT. *Applied Radiation and Isotopes*. 2017;122:72-7.

11. Dal F, Ökmen H, Yılmaz MK, Sarı S, Nazlı MA, Arslan E. Extraction of a foreign body from the breast using radio-guided occult lesion localization (ROLL): metallic foreign body in the breast. *European Journal of Breast Health*. 2017;13(3):159.

12. Al-Janabi M, Yousif Z, Kadim A, Al-Salem A. A new technique for the preparation of ready-to-use macroaggregated albumin (MAA) kits to be labelled with ^{99m}Tc for lung scanning. *The International journal of applied radiation and isotopes*. 1983;34(10):1473-8.

13. Ilyas M, Haider KH, Saeeda A, Javed M, Shams Z, Sameera C. In-House Preparation and Characterization of Ready-To-Use ^{99m}Tc-Sn-Macroaggregated Albumin Kit for Lung Perfusion Studies. *Medical Journal of Islamic Academy of Sciences*. 1998;11(4):131-8.

14. Arvas MB, Gorduk O, Gencten M, Sahin Y. Differential Pulse Voltammetric (DPV) Determination of Phosphomolybdenum Complexes by a Poly (Vinyl Chloride) Coated Molybdenum Blue Modified Pencil Graphite Electrode (PVC-MB-PGE). *Analytical Letters*. 2020:1-20.

15. Ament S, Maus S, Reber H, Buchholz H, Bausbacher N, Brochhausen C, et al. PET Lung Ventilation/Perfusion Imaging Using ⁶⁸Ga Aerosol (Galligas) and ⁶⁸Ga-Labeled Macroaggregated Albumin. *Theranostics, Gallium-68, and Other Radionuclides*: Springer; 2013. p. 395-423.

16. Maloubier M, Michel H, Solari PL, Moisy P, Tribalat M-A, Oberhaensli FR, et al. Speciation of americium in seawater and accumulation in the marine sponge *Aplysina cavernicola*. *Dalton Transactions*. 2015;44(47):20584-96.

17. Alhazmi HA. FT-IR spectroscopy for the identification of binding sites and measurements of the binding interactions of important metal ions with bovine serum albumin. *Scientia Pharmaceutica*. 2019;87(1):5.

18. Barth A. Infrared spectroscopy of proteins. *Biochimica et Biophysica Acta (BBA)-Bioenergetics*. 2007;1767(9):1073-101.

19. Liu X, Lee MJ, Coleman M, Rath P, Nilsson A, Fischer WB, et al. Detection of threonine structural changes upon formation of the M-intermediate of bacteriorhodopsin: evidence for assignment to Thr-89. *Biochimica et Biophysica Acta (BBA)-Bioenergetics*. 1998;1365(3):363-72.

20. Balamurugan A, Reddy M, Jayakannan M. Single polymer photosensitizer for Tb³⁺ and Eu³⁺ ions: An approach for white light emission based on carboxylic-functionalized poly (m-phenylenevinylene)s. *The Journal of Physical Chemistry B*. 2009;113(43):14128-38.

21. Dhanial SL, Chauhan A, Langyan R. Synthesis, characterization and photoluminescent properties of Eu (III) complexes with 5-hydroxy-2-hydroxymethyl-4H-4-pyranone and N, N'-donor heterocyclic coligands. *Rare Metals*. 2020:1-8.



Surface Assimilation and Corrosion Inhibition Characteristics of Water-Soluble Polyvinyl Alcohol on Mild Steel Surface in 0.5 M HCl Solution

Abhishek DWIVEDI¹ , Prem Kumar BHARTI¹ , Sudhish Kumar SHUKLA² 

¹Integral University, Lucknow, India.

²Manav Rachna University, Faridabad, India.

Abstract: As corrosion inhibitors for mild steel in acidic media, polymers are emerging materials due to its larger surface coverage area. This paper focuses on the characteristic of water-soluble solvent polyvinyl alcohol (PVA) at interface of mild steel under 0.5 M HCl, examined using electrochemical impedance spectroscopy, Tafel polarization, and weight reduction techniques. The findings of the study revealed that water-soluble polyvinyl alcohol as polymer inhibitor has restraint abilities, up to 93.7 percent for 3 hours in 0.5 M hydrochloric acid. An advanced form of high spatial resolution imaging of surface of mild steel at different stages was found by using scanning electron microscopy which shows that the sample immersed for 3 hrs in 0.5 M HCl with 100 ppm of water soluble PVA inhibitor provides good inhibition quality to corrosion on mild steel surface.

Keywords: Polymer inhibitor, Weight loss study, Langmuir adsorption isotherm, Polyvinyl Alcohol.

Submitted: September 22, 2020. **Accepted:** December 27, 2020.

Cite this: Dwivedi A, Bharti P, Shukla S. Surface Assimilation and Corrosion Inhibition Characteristics of Water-Soluble Polyvinyl Alcohol on Mild Steel Surface in 0.5 M HCl Solution. JOTCSA. 2021;8(1):219-30.

DOI: <https://doi.org/10.18596/jotcsa.794721>.

***Corresponding author.** E-mail: sudhishmru@gmail.com.

INTRODUCTION

Corrosion is formed due to the weakening and debasement of metal because of natural conditions. It causes due to the natural dampness, which prompts the oxidation of metal surface. Unadulterated metals or blends are isolated from a short of oxides, sulfates, carbonates, etc and significantly unpredictable and react viably within the sight of O₂ and H₂O likewise to CO₂ which leads because of metal degradation. So it very well might be treated as "A surface marvel alluded to be the assault on metals or composites by the climate like air, water or soil in a synthetic or electrochemical response to make more steady mixes."(1-3)

To lessen the impact of the destructive condition on metals, corrosion inhibitors are found in various natural and synthetic form, which diminishes the consumption rate when present in the corrosion framework at a reasonable focus without altogether

change in the convergence of some other destructive operator are utilized(4,5).

Metals can be prevented from the corrosion problems, through following precautionary procedures like (6-8).

A. Cathodic Protection: It is a successful strategy to rheostat corrosion on arrangements either enclosed or inundated in an electrolyte; as designated by the action mode, anodes are named dazzled present and peacemaking.

B. Assurance with anticorrosive casing: It is primarily cast off to shape a somatic interference between the destructive situations to secure the arrangement. it's far utilized for maximum element with metallic components present to the climate.

C. Corrosion Inhibitors: Inhibitors are added to the damaging domain of materials (in ppm) to avoid the corrosion effect in metals. Pipelines, vessels, and

types of gear are its primary application where soluble inhibitors are used successfully.

According to NACE, inhibitors are “a substance, which retards corrosion when added to an environment in appropriate concentration.”

It was found from the Langmuir adsorption isotherm that soluble polymers are efficient corrosion inhibitors as compared to the components like drugs, natural products, heterocyclic organic compounds, organic dyes, and so on, widely used as corrosion inhibitors, which covered the metal surface to repress the contact to the surface of metal and dampness (9,10).

Nowadays, various industries are using acids for the purpose of pickling, descaling, cleaning etc., (11-14). HCl is exceptionally destructive to the metals or mild steel (amalgam of unalloyed metals). In this way, the proficiency of water soluble polyvinyl alcohol as corrosion inhibitor has been evaluated using HCl solution of 0.5 M, 0.1 M, 1.5 M, etc. Productivity can be determined by gravimetric investigation, potentiodynamic polarization and electrochemical impedance spectroscopy. This is likewise bolstered by the surface examinations done by atomic power microscopy (10,15,16).

Pieces of literature show the majority of polymers like polyaniline, polyanthranilic, poly-diphenyl amine, and so on, as insoluble in nature, which limits their properties in interaction with the metal surface through the pi-bond present in the moiety. These polymeric materials are less utilized as corrosion inhibitors. However, polymeric materials can be sulfonated, to expand the solvability of polymeric material in an acidic medium. (1,2,16,17).

Principally polymers were utilized as covering material rather than inhibitors but due to the exceptionally insoluble nature of the majority of the polymers in aqueous medium, limit their use as a corrosion inhibitor. As of late, a few endeavors have been made to solubilize the polymers for the utilization of corrosion inhibitor (18-21). Polymers are magnificent consumption inhibitors for metallic antiques in corrosive condition. Nearness of a little amount of polymers might be powerful in hindering the consumption of metals in fluid acidic condition (22-26). Time is a champion factor while describing the corrosion inhibitor. Drenching time is a crucial factor to be considered in identifying the soundness of the inhibitor film and the rate of inhibitor adsorption. Weight reduction estimations were additionally used to contemplate the impact of temperature on the corrosion of mild steel with the nearness of consumption inhibitor (27-29).

Polyvinyl alcohol (PVA), commonly called as the green polymer, is a synthetic polymer and has been

considered as most commonly used water-soluble synthetic polymer due to its biologically accepted nature and biomedical applications (11-13,30,31).

Mild steel samples of 10 cm² surface zone in 0.5 M hydrochloric acid solution was examined with the inhibitive behavior of water soluble PVA using different methods for finding inhibitor efficiency and surface coverage of inhibitor over mild steel surface in corrosive environment using Atomic force microscopic techniques in this article.

MATERIAL AND METHODS

The acid was prepared by using the dilution formula to find out the volume of the acid required to prepare a solution.

Dilution formula;

$$C_1V_1 = C_2V_2 \quad (1)$$

where C= concentration, V= volume, 1= original solution, 2= the new solution.

Usually HCl is available in 12 M solution so; 12 M x V₁ = 0.5 M x 1000; V₁ = 41.6 mL must be taken in 1000 mL (1 L) flask with enough water added to form 1000 mL of 0.5 M solution (10,17,32,33).

The weight reduction and electrochemical examinations were done on mild steel segments submerged with the interface of water-soluble PVA and HCl (AR grade) both acquired from Merck India and twofold refined water was utilized for the weakening of forceful medium (15,16).

Weight Loss Studies

A 10 cm² surface zone of mild steel was immersed at 35 °C in 0.5 M HCl for 3 hours of time, examined and embraced to analyze the consumption conduct of certain metals in various corrosive arrangements utilizing weight reduction method. The total examinations were done in the funnel-shaped carafe having glass plug with various centralization of PVA inhibitor to acquire the ideal inhibitor fixation. Such investigations were directed for ideal convergence of soluble PVA at different temperature ranges, time interim, and grouping of corrosive. Inhibition efficiency (%) and surface coverage (Θ) of the PVA on mild steel were obtained by using the relation: (9,34-37)

$$I.E.(\%) = \frac{W_0 - W_i}{W_0} \times 100 \quad (2)$$

$$\Theta = \frac{W_0 - W_i}{W_0} \quad (3)$$

W₀ and W_i represent the weight loss of metal in the absence of PVA inhibitor and in the presence of PVA inhibitor concentration respectively (10).

The corrosion rate is calculated by dilution formula as

$$CR = \frac{87.6 \times \text{weight loss (mg)}}{\text{Surface area of the specimen (cm}^2\text{)} \times \text{Time (h)} \times \text{Density of the specimen (g cm}^{-3}\text{)}} \quad (4)$$

It has been found that fixation increment leads to a decrease corrosion rate.

Electrochemical Studies

Electrochemical systems are perfect for the investigation of the corrosion forms, as corrosion happens by means of electrochemical responses (34,36,38,39). In an electrochemical investigation process, a three-electrode assembly cell having a mild steel working electrode of 10 cm² in surface area is utilized to demonstrate the metal in a consuming framework of 1 cm² unpolished area facing the solution as working electrode. A saturated calomel electrode with large rectangular platinum foil was used as reference electrode and counter electrode respectively at 35 °C temperature (9,10,16,38,40). Acetone, water, and a variety of emery papers were employed on the working electrode preparation. An open circuit potential in circulated air through environment was directed in all electrochemical estimation using Potentiostat / galvanostat of Gamry instruments Inc. USA, (model G-300) and EIS programming. Tafel polarization, linear polarization resistance and electrochemical

impedance spectroscopy experiments (3,10,16,41-43) have been used for further study.

RESULT AND DISCUSSION

Weight-Loss Technique

Variation of PVA concentration in solution: Metal degradation technique was applied to study the behavior of soluble PVA concentration in absent and present condition has been listed in Table 1. The effect of inhibitor efficiency on the mild steel surface under 0.5 M HCl solutions at varying inhibitor concentration has been plotted in Figure. 1. The inhibitor efficiency has been indicated to be 93.70% at 100 ppm concentration of inhibitor in acidic solution. It was clearly found from the Table 1 that increasing the inhibitor concentration gradually decreases the weight loss and corrosion rate of metal while increases the inhibition efficiency. To achieve more accuracy in results all the examinations of sample has been performed in triplicate. To avoid statistical errors in graphical representation, an error bar has also been reported in Figure 1 (4,5,11,44).

Table 1. Range of data showing inhibitor efficiency of PVA at 10 cm² surface area of mild steel for 3 hours at 35 °C in 0.5 M HCl solution.

Inhibitor concentration (ppm)	Weight loss (mg)	IE (%)	CR (mmpy)
N/A	81.05	-	30.15
15	46.29	42.89	17.22
25	22.50	72.24	8.37
50	18.93	76.64	7.04
75	9.97	87.70	3.71
100	5.11	93.70	1.90

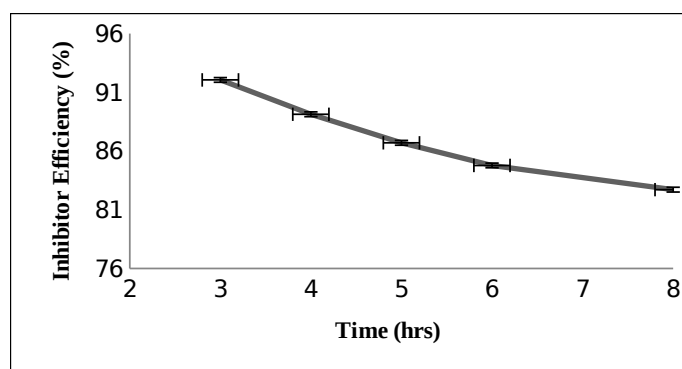


Figure 1. Change in PVA concentration lead to change in % inhibition efficiency at 35 °C for 3 hours of duration in 0.5 M HCl solution for exposed surface area of 10 cm² mild steel strip.

Variation of Immersion Time

In Figure 2, a graph with error bar represents the stability of inhibitor in the variable time interval. The data of weight loss of mild steel was recorded in 100 ppm concentration in 0.5 M HCl solution to the time range of 3 to 8 hrs at 35 °C. Figure 2 has been plotted to observe the inhibitor efficiency. The gradually increasing time of 3 to 8 hours of

immersion in mild steel specimen in 100 ppm inhibitor concentration with 0.5 M HCl solution decreases the inhibitor efficiency up to 82.71%. This plot discloses that the efficiency of inhibitor decreases with a slow rate due to the desorption of adsorbed layer of compound on mild steel surface (2,10).

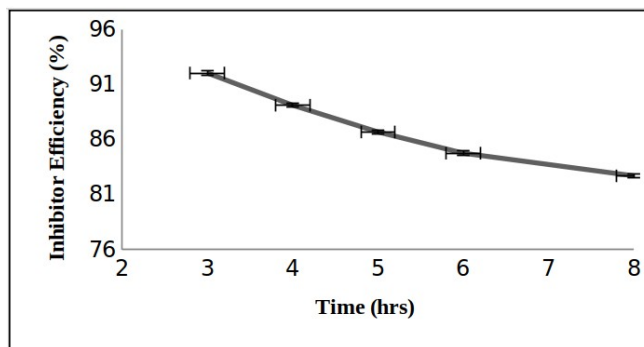


Figure 2. Change in immersion time of specimen leading to change in % inhibition efficiency at 35 °C for 3 hours duration in 0.5 M HCl solution for exposed surface area of 10 cm² mild steel strip.

Variation of Solution Temperature

A temperature variation at the range of 298 K to 328 K in 0.5 M HCl in 100 ppm inhibitor concentration has been plotted in Figure 3 and found that at increasing temperature, aqueous acid solution lowers the inhibitor efficiency up to 75.25%, which

represents that the adsorption process predominates over desorption up to 328 K where it takes place at 298 K and desorption of molecules of PVA on mild steel surface decreases due to high rate of heat of diluted HCl (45-47).

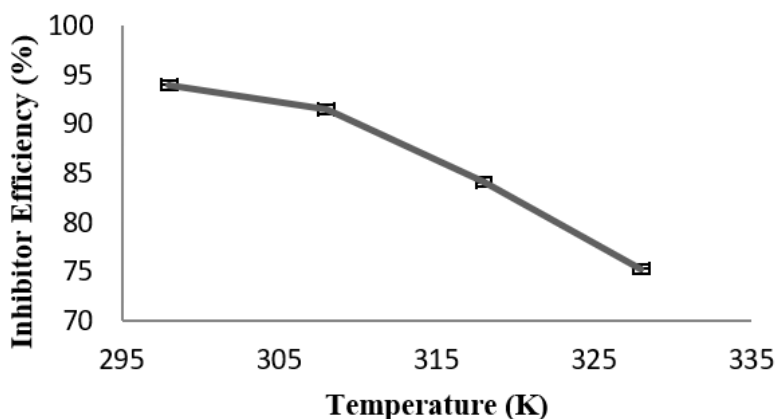


Figure 3. Temperature variation of acidic solution lead to change in % inhibition efficiency at 100 ppm inhibitor diluted for 3 hours duration in 0.5 M HCl solution for exposed surface area of 10 cm² mild steel strip.

Variation of Acid Concentration

An acidic concentration of 100 ppm PVA has been varied from 0.5 M to 2 M HCl for 3 hours at 35 °C on immersed mild steel structure and plotted in Figure 4. It has been observed that the increasing

concentration of acid in the solution decreases the inhibitor efficiency from 95.28% to 73.49%. Figure 4 has shown that the concentration level of 0.5 M HCl is very effective with a marginal decrease in inhibition efficiency (48).

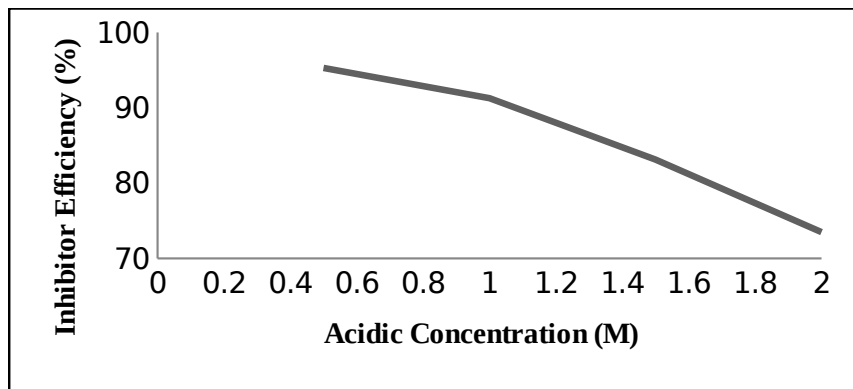


Figure 4. Variation of acidic solution lead to change in % inhibition efficiency at 100 ppm inhibitor diluted for 3 hours duration in 0.5 M HCl solution for exposed surface area of 10 cm² mild steel strip.

Adsorption Isotherm

Adsorption is the adherence of atoms, ions or molecules from a gas, liquid or dissolved solid to a surface (33). To support the adsorption isotherm study of the PVA molecule on the metal surface, Langmuir, Temkin, and Frumkin isotherms were employed. The Langmuir adsorption isotherm was found to be the best tool to explain the behavior of PVA molecule adsorption on the surface of the metal. This study defined the charge and the nature, electronic characteristics, adsorption of solvent of metal surface and other ionic species, on the electrochemical potential at solution interface (11). Langmuir adsorption isotherm expression (Formula 5) was used to calculate the adsorption isotherm by

fetching the value of surface coverage values (θ) from Table 1.

$$\frac{C_{inh}}{\theta} = \frac{1}{K_{ads}} + C_{inh} \quad (5)$$

where, C_{inh} is the concentration of PVA corrosion inhibitor employed and K_{ads} represents the equilibrium constant of adsorption in acid medium. Figure 5 represents the C_{inh} vs C_{inh}/θ graph having straight line with the migration coefficient (R) to be almost unity. Unit value of R represents that the adsorption of the inhibitor on mild steel surface follows the Langmuir adsorption isotherm (9,49,50).

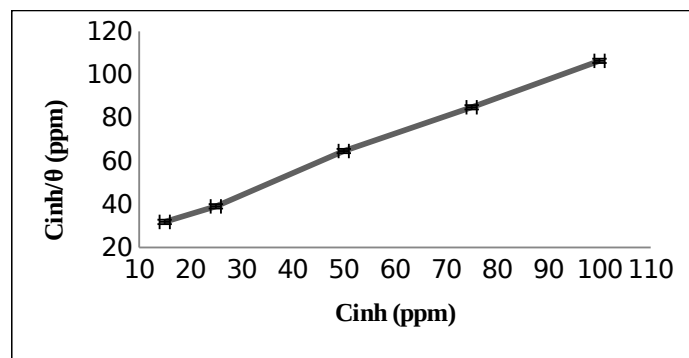


Figure 5. Adsorption of PVA inhibitor molecules on the mild steel surface in 0.5 M HCl solution using Langmuir's adsorption graph with error bar.

Tafel and Linear Polarization Study

To find the corrosion current density, Table 2 represents a free corroding potential system, corrosion potential (E_{corr}), anodic (ba) and cathodic (bc) Tafel slopes and corrosion current density (I_{corr}). These parameters are used to evaluate the efficiency of PVA polymer inhibitor in 0.5 M HCl solution at mild steel surface in presence and absence of PVA in the concentration. The variation in the range of corrosion potential (E_{corr}) while increasing the inhibitor concentration in the solution has been shown in Table 2. This indicates that the high rate of inhibitor may increase the current

density. The small amount of change between Tafel plots indicates the mix characteristic of inhibitor property (51). This corrosion current density (I_{corr}) shown in Table 2 indicates that increasing the inhibitor concentration will lead to a higher voltage than 85 mV with respect to zero solution concentration and resultant mixed type of inhibitor property. The calculated inhibition efficiency using tafel polarization study supports the Table 1 results stated above.

Calculation of Polarization resistance (R_p) from the slope of the potential current lines can be found by

the relation between working electrode surface area (A), and potential change dE and di, using Equation 6 as:

$$R_p = A \frac{dE}{di} \quad (6)$$

The results has been plotted in Figure 6 and states that PVA conquers the H₂ progression reaction on

cathode and found more polarized than the anodic reaction suspension.

The value of R_p increases while increasing the concentration of inhibitor to 100 ppm in 0.5 M HCl solution at same temperature and the good inhibitor efficiency was found to be 91.6%. From the value, as shown in Table 2, it was indicated that higher the concentration of the inhibitor may result in an increase in the efficiency of the inhibitor.

Table 2. Potentiodynamic polarization parameters for mild steel without and with PVA in 0.5 M hydrochloric acid

Inhibitor Conc.	Tafel data					Linear Polarization data	
	-E _{corr} (mV vs SCE)	b _a (mV dec ⁻¹)	b _c (mV dec ⁻¹)	I _{corr} (μA cm ⁻²)	IE (%)	R _p (Ω cm ²)	IE (%)
N/A	469	75	150	2140	-	20.1	-
25	472	74	152	410	80.8	120	83.2
50	470	70	157	265	87.6	180	88.8
75	466	73	149	225	89.5	206	90.2
100	471	74	161	190	91.1	240	91.6

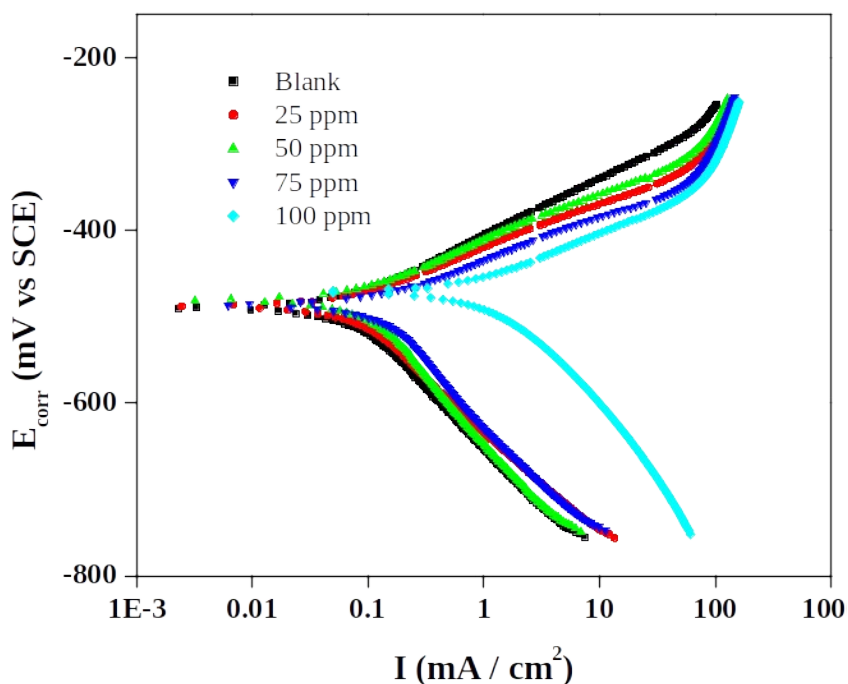


Figure 6. Tafel polarization curve in absence of inhibitor and presence of optimum concentration PAA inhibitor molecule on the surface of mild steel in 0.5 M HCl solution.

Electrochemical impedance spectroscopy and Surface morphology study

To study the experimental condition such as scan rate, voltage, frequency and the ionic species and concentration of electrolyte, the three regions of double layer i.e. space charge, compact layer, and diffuse layer is studied by modifying model of equation circuit reported by McDonald J.R. (9,20,50) for constant phase angle. Mansfeld’s A F. theoretical circuit is used to explain the interface model of HCl to mild steel phase angle (2,20). A Nyquist graph in

Figure 7 has been plotted to represent the behavior of corrosion on the surface of mild steel configuration in the presence and absence of inhibitor. All the experiment has been undertaken on mild steel surface at 0.5 M HCl solution at 35 °C, while varying the inhibitor concentrations. It has been observed from the electrochemical impedance spectroscopy plot that the semicircle diameter increases with increase in the concentration of inhibitor up to 100 ppm.

The basic electrochemical impedance parameter like solution resistance (R_s), admittance parameter (Y_0), total number of parts (n), resistance to charges transfers (R_t), and double electric layer capacitance (C_{dl}) was found to calculate the adsorption of metal and acid molecules interface due to the potential difference between solution and electrode at corrosion state using the equation 7.

$$C_{dl} = (Y_0 R_t^{1-n})^{1/n} \quad (7)$$

In the absence and presence of a PVA inhibitor at 0.5 M HCl concentration, Table 3 shows the values of R_s , Y_0 , n , and C_{dl} decreases with the addition of an inhibitor in concentrations, while R_t increased with the addition of an inhibitor. A protective film formed on the mixture and metal interface is due to the addition of more inhibitor molecules to the concentration, which resulted in an increase in the R_t value. The surface heterogeneity may increase and decrease as per the adsorption of inhibitor molecules on the adsorption of metal surface, which will affect the value of n . Equation 8 was used to plot the relation between protective layers thicknesses (d) and double layer capacitance (C_{dl}) by using the value of dielectric constant (ϵ) of protective layer and free space permittivity (ϵ_0) (52):

$$C_{dl} = \frac{\epsilon \epsilon_0}{d} \quad (8)$$

The result from the above plots revealed the percentage inhibitor efficiency to be 96.68% on mild steel surface in the presence of 100 ppm PVA in 0.5 M HCl, and this is in accordance with the data in the above studies. Surface study of all the samples was done to examine the impedance spectra, which were shown as depressed semicircle under real axis and appeared like a depressed capacitive loop using Figure 7 and Figure 8. The raising surface roughness and dislocation on metals property may lead to the heterogeneity on the mild steel surface due to dislocations or adsorption of the inhibitor molecules(14,53).

Surface morphology of the specimen represents the formation of adsorbed polymer film over the sample. The polished Figure 8(a) represents the smoother image of the surface whiles Figure 8(b) shows high roughness on the surface of the sample due to the effect of acid concentration. As compared to Figure 8(b), Figure 8(c) shows more perfect graph due to the impact of PVA inhibitors addition to the interface of mild steel strip.

Table 3. Electrochemical impedance parameters values of with and without PVA for mild steel corrosion in 0.5M HCl solution

Inhibitor concentration (ppm)	R_s ($\Omega \text{ cm}^2$)	R_p ($\Omega \text{ cm}^2$)	Y_0 ($\mu\text{F cm}^{-2}$)	n	C_{dl} ($\mu\text{F cm}^{-2}$)	IE (%)
N/A	1.23	8.3	1181.5	0.858	55	-
25	1.17	136.9	205.7	0.836	48	93.90
50	1.19	157.1	112.3	0.831	42	94.71
75	1.20	202.2	87.5	0.825	38	95.89
100	1.19	250.1	74.3	0.822	35	96.68

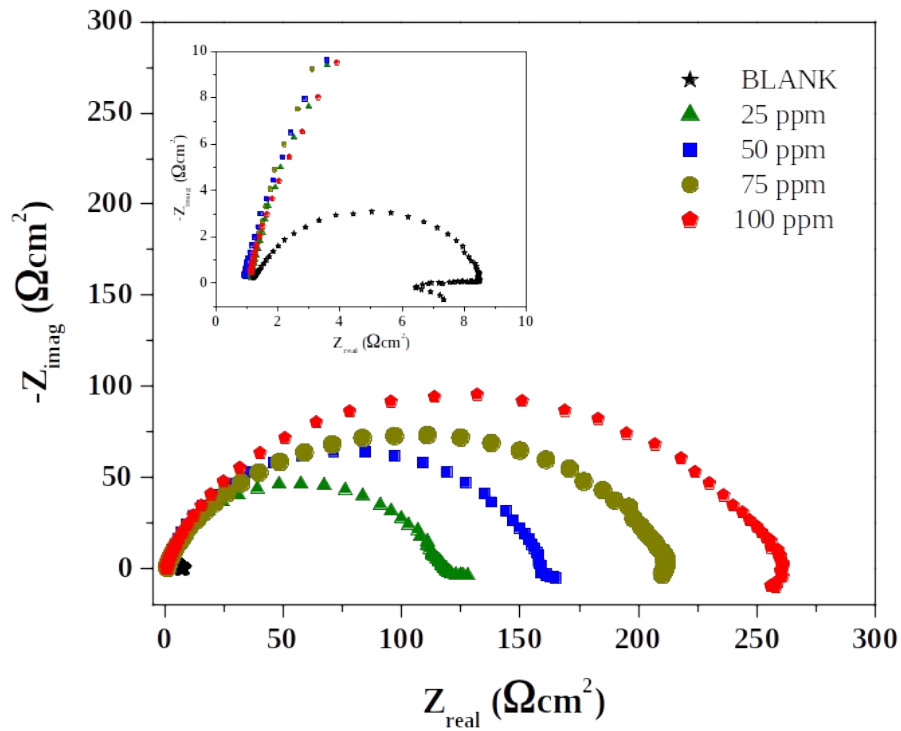


Figure 7. Nyquist plot of corrosion of mild steel in absence and presence of optimum concentration of PVA inhibitor in 0.5M hydrochloric acid solution

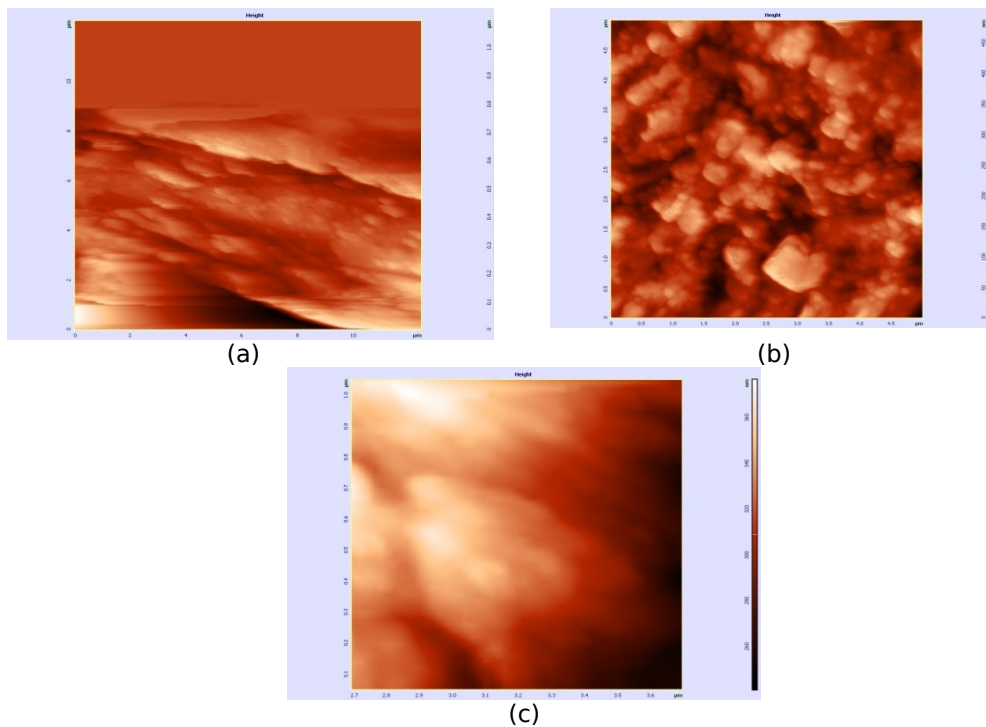


Figure 8. Surface morphological analysis through atomic force microscopy of mild steel sample. (a) Polished sample, (b) sample immersed for 3 hrs in 0.5 M HCl without inhibitor, (c) sample immersed for 3 hrs in 0.5 M HCl with 100 ppm PVA inhibitor.

CONCLUSIONS

It has been indicated that polymers, particularly the water soluble ones, are productive corrosion inhibitors in various aqueous media. (48-50). Tested water-soluble PVA exhibits outstanding corrosion inhibition properties against the surface of mild steel in a 0.5 M HCl solution. Impedance, polarization and gravimetric methodology findings suggest better effective water-soluble properties of PVA. The above study shows that the effectiveness of PVA as a corrosion inhibitor depends not only on the good results of the environmental conditions, but also on the steel surface flora and electrochemical potential at the tip, and also on the erection of the inhibitor itself. Polarization studies have shown that at 0.5 M HCl concentration at 100 ppm, PVA acts on both anodic and cathodic type reactions and shows that it is a mixed-type inhibitor. The PVA inhibitor efficiency was observed to be higher when the inhibitor concentration increased up to 100 ppm, with a dramatic change in the corrosion rate compared to the time of solution immersion.

The initiation boundaries mirror the endothermic metal disintegration process. The adsorption of PVA follows the Langmuir isotherm model and the estimations of the free vitality of adsorption show its unconstrained physical nature. The consequences of the arrangement of examinations have uncovered that the procedures engaged with corrosion inhibitors gives a uniform result as for all classes of mixes so far explored with one inhibitor in a given framework. The statement was supported by the results studied using characteristic atomic force microscopy.

ACKNOWLEDGMENT

The manuscript communication number provided by the Research and Development Cell, Integral University, Lucknow is: **IU/R&D/ 2020-MCN000976**.

REFERENCES

- Ji G, Shukla SKSK, Dwivedi P, Sundaram S, Ebenso EEEEE, Prakash R. Green Capsicum annum fruit extract for inhibition of mild steel corrosion in hydrochloric acid solution. *Int J Electrochem Sci*. 2012;7(12):12146-58.
- Singh AK, Shukla SK, Quraishi MA, Ebenso EE. Investigation of adsorption characteristics of N,N'-[(methylimino)dimethylidyne]di-2,4-xylylidene as corrosion inhibitor at mild steel/sulphuric acid interface. *J Taiwan Inst Chem Eng*. 2012;43(3):463-72.
- Singh AK, Shukla SK, Quraishi MA. Corrosion Behaviour of Mild Steel in Sulphuric Acid Solution in Presence of Ceftazidime. 2011;6:5802-14.
- Ameh PO, Eddy NO. Theoretical and experimental studies on the corrosion inhibition potentials of 3-nitrobenzoic acid for mild steel in 0.1 M H₂SO₄. *Cogent Chem [Internet]*. 2016;2(1):0-18. Available from: <http://dx.doi.org/10.1080/23312009.2016.1253904>
- Loto RT, Loto CA, Fedotova T. Electrochemical studies of mild steel corrosion inhibition in sulfuric acid chloride by aniline. *Res Chem Intermed*. 2014;40(4):1501-16.
- R. Winston Revie HHU. *Corrosion and Corrosion Control: An Introduction to Corrosion Science and Engineering [Internet]*. 4th ed. John Wiley & Sons; 2008. 512 p. Available from: https://books.google.co.in/books?id=HJHMHogrEiwC&dq=introduction+to+corrosion+formation&lr=&source=gbs_navlinks_s
- Gupta M, Mishra J, Pitre KS. Corrosion and inhibition effects of mild steel in hydrochloric acid solutions containing organophosphonic acid. *Int J Corros*. 2013;2013:1-6.
- Dwivedi A. A review on polymeric material used as a corrosion inhibitor for metals . 2012;
- Shukla SK. Corrosion inhibitive effect of N- (6-methoxyquinolin-8-yl) -pentane-1 , 4- diamine on mild steel / sulphuric acid solution interface. 2015;6(6):1779-86.
- Dwivedi A, Bharti PK, Shukla SK. Interaction of water soluble polyacrylic acid with mild steel / hydrochloric acid interface. *IOP Conf Ser Mater Sci Eng*. 2018;404(1).
- Kaviyarasu S, Anandakumar S, Vignesh K, Rampradheep GS. Development of inhibitor for the corrosion resistance in steel using polyvinyl alcohol. *Int J Sci Technol Res*. 2020;9(2):2888-93.
- Greco R, Samide A, Iacobescu GE, Cioateră N, Popescu A. Copper corrosion inhibitors based on polyvinyl alcohol and silver nanoparticles. *Chem Ind Chem Eng Q*. 2019;25(3):267-75.
- Srimathi M, Rajalakshmi R, Subhashini S. Polyvinyl alcohol-sulphanilic acid water soluble composite as corrosion inhibitor for mild steel in hydrochloric acid medium. *Arab J Chem [Internet]*. 2014;7(5):647-56. Available from: <http://dx.doi.org/10.1016/j.arabjc.2010.11.013>
- Karthikaiselvi R, Subhashini S, Rajalakshmi R. Poly (vinyl alcohol - aniline) water soluble composite as corrosion inhibitor for mild steel in 1 M HCl. *Arab J*

- Chem [Internet]. 2012;5(4):517-22. Available from: <http://dx.doi.org/10.1016/j.arabjc.2010.09.020>
15. Guo C, Zhou L, Lv J. Effects of expandable graphite and modified ammonium polyphosphate on the flame-retardant and mechanical properties of wood flour-polypropylene composites. *Polym Polym Compos*. 2013;21(7):449-56.
16. Shukla SK, Singh AK, Murulana LC, Kabanda MM, Ebenso EE. Inhibitive effect of azorubine dye on the corrosion of mild steel in hydrochloric acid medium and synergistic iodide additive. *Int J Electrochem Sci*. 2012;7(6):5057-68.
17. Murulana LC, Singh AK, Shukla SK, Kabanda MM, Ebenso EE. Experimental and Quantum Chemical Studies of Some Bis (trifluoromethyl-sulfonyl) Imide Imidazolium-Based Ionic Liquids as Corrosion Inhibitors for Mild Steel in Hydrochloric Acid Solution. *Ind Eng Chem Res*. 2012;51:13282-99.
18. Palou RM, Olivares-Xomelt O, Likhanova N V. Environmentally friendly corrosion inhibitors. *Green Corros Inhib theory Pract*. 2011;257-303.
19. Dahmani M, Et-Touhami A, Al-Deyab SS, Hammouti B, Bouyanzer A. Corrosion inhibition of c38 steel in 1 M HCl: A comparative study of black pepper extract and its isolated piperine. *Int J Electrochem Sci*. 2010;5(8):1060-9.
20. Perumal S, Muthumanickam S, Elangovan A, Sayee Kannan R, Mothilal KK. Inhibitive effect of Bauhinia tomentosa leaf extract on acid corrosion of mild steel. 2017;10(13):203-13. Available from: [http://www.sphinxesai.com/2017/ch_vol10_no13/2/\(203-213\)V10N13CT.pdf](http://www.sphinxesai.com/2017/ch_vol10_no13/2/(203-213)V10N13CT.pdf)
21. Gobara M, Zaghoul B, Baraka A, Elsayed M, Zorainy M, Kotb MM, et al. Green corrosion inhibition of mild steel to aqueous sulfuric acid by the extract of Corchorus olitorius stems. *Mater Res Express* [Internet]. 2017;4(4):046504. Available from: <http://stacks.iop.org/2053-1591/4/i=4/a=046504?key=crossref.c6c2ffa2531203e46e2b786b1417bf2e>
22. Alsingery RMD. Polypyrrole as a Perfect Corrosion Inhibitor for Mild Steel in Hydrochloric Acid Solution Cyclic Voltammetry. 2017;10(9):1058-65.
23. Lai C, Xie B, Zou L, Zheng X, Ma X, Zhu S. Adsorption and corrosion inhibition of mild steel in hydrochloric acid solution by S-allyl-O,O'-dialkyldithiophosphates. *Results Phys* [Internet]. 2017;7:3434-43. Available from: <https://doi.org/10.1016/j.rinp.2017.09.012>
24. Harabor I, Nechifor G, Branzoi V, Branzoi F, Carbon I. Investigation of Some Organic Polymers As Corrosion Inhibitors on Carbon Steel in. 2016;78.
25. Solomon MM, Umoren SA. Enhanced corrosion inhibition effect of polypropylene glycol in the presence of iodide ions at mild steel/sulphuric acid interface. *J Environ Chem Eng* [Internet]. 2015;3(3):1812-26. Available from: <http://linkinghub.elsevier.com/retrieve/pii/S2213343715001256>
26. Fidrushi A, Suryanto, Mahmood M. Ginger extract as green corrosion inhibitor of mild steel in hydrochloric acid solution. *IOP Conf Ser Mater Sci Eng*. 2018;290(1).
27. Deshmukh K, Basheer Ahamed M, Deshmukh RR, Khadheer Pasha SK, Bhagat PR, Chidambaram K. Biopolymer Composites With High Dielectric Performance: Interface Engineering. In: *Biopolymer Composites in Electronics* [Internet]. Elsevier; 2017. p. 27-128. Available from: <https://linkinghub.elsevier.com/retrieve/pii/B9780128092613000036>
28. Tsoeunyane MG, Makhatha ME, Arotiba OA. Corrosion Inhibition of Mild Steel by Poly(butylene succinate)-L-histidine Extended with 1,6-diisocynatohexane Polymer Composite in 1 M HCl. *Int J Corros* [Internet]. 2019 Mar 3;2019:1-12. Available from: <https://www.hindawi.com/journals/ijc/2019/7406409/>
29. Geethanjali R, Subhashini S. Synthesis and Kinetics of Corrosion Inhibition of Water-Soluble Terpolymer of Polyvinyl Alcohol Functionalized with Vinyl Sulfonate and p-Vinyl Benzene Sulfonate, in Molar HCl. *J Bio- Tribo-Corrosion* [Internet]. 2018 Dec 23;4(4):60. Available from: <http://link.springer.com/10.1007/s40735-018-0170-z>
30. Geethanjali R, Menaka R, Subhashini S. Gravimetric and Electrochemical Study of Temperature Effect of PVA Grafted Terpolymer on Corrosion Inhibition of Mild Steel in Hydrochloric Acid. *Mater Today Proc* [Internet]. 2018;5(8):16246-57. Available from: <https://linkinghub.elsevier.com/retrieve/pii/S221478531831071X>
31. Samide A, Merisanu C, Tutunaru B, Iacobescu GE. Poly (Vinyl Butyral-Co-Vinyl Alcohol-Co-Vinyl Acetate) Coating Performance on Copper Corrosion in Saline Environment. *Molecules* [Internet]. 2020 Jan 21;25(3):439. Available from: <https://www.mdpi.com/1420-3049/25/3/439>
32. Shukla SK, Quraishi MA, Prakash R. A self-doped conducting polymer "polyanthranilic acid": An efficient corrosion inhibitor for mild steel in acidic solution. *Corros Sci* [Internet]. 2008;50(10):2867-72. Available from: <http://dx.doi.org/10.1016/j.corsci.2008.07.025>

33. Shukla SK, Murulana LC, Ebenso EE. Inhibitive effect of imidazolium based aprotic ionic liquids on mild steel corrosion in hydrochloric acid medium. *Int J Electrochem Sci.* 2011;6(9):4286-95.
34. Shukla SK, Quraishi MA. 4-Substituted anilinomethylpropionate: New and efficient corrosion inhibitors for mild steel in hydrochloric acid solution. *Corros Sci.* 2009;51(9):1990-7.
35. Shukla SK, Quraishi MA. Ceftriaxone: A novel corrosion inhibitor for mild steel in hydrochloric acid. *J Appl Electrochem.* 2009;39(9):1517-23.
36. Ebenso EE, Kabanda MM, Arslan T, Saracoglu M, Kandemirli F, Murulana LC, et al. Quantum Chemical Investigations on Quinoline Derivatives as Effective Corrosion Inhibitors for Mild Steel in Acidic Medium. *Int J Electrochem Sci Int J Electrochem Sci [Internet].* 2012;7(7):5643-76. Available from: www.electrochemsci.org
37. Shukla SK, Singh AK, Quraishi MA. Triazines: Efficient corrosion inhibitors for mild steel in hydrochloric acid solution. *Int J Electrochem Sci.* 2012;7(April):3371-89.
38. Quraishi MA, Ahamad I, Singh AK, Shukla SK, Lal B, Singh V. N-(Piperidinomethyl)-3-[(pyridylidene)amino]isatin: A new and effective acid corrosion inhibitor for mild steel. *Mater Chem Phys.* 2008;112(3):1035-9.
39. Ji G, Shukla SK, Dwivedi P, Sundaram S, Ebenso EE, Prakash R. Green Capsicum annum fruit extract for inhibition of mild steel corrosion in hydrochloric acid solution. *Int J Electrochem Sci.* 2012;7(12):12146-58.
40. Shukla SK, Singh AK, Ebenso EE. Pharmaceutically active compound as corrosion inhibitor for mild steel in acidic medium. *Int J Electrochem Sci.* 2011;6(9):4276-85.
41. Singh AK, Shukla SK, Ebenso EE. Cefacetrile as corrosion inhibitor for mild steel in acidic media. *Int J Electrochem Sci.* 2011;6(11):5689-700.
42. Umoren SA, Banera MJ, Alonso-Garcia T, Gervasi CA, Mirífico M V. Inhibition of mild steel corrosion in HCl solution using chitosan. *Cellulose.* 2013;20(5):2529-45.
43. Shukla SK, Quraishi MA. Cefalexin drug: A new and efficient corrosion inhibitor for mild steel in hydrochloric acid solution. *Mater Chem Phys.* 2010;120(1):142-7.
44. Dos Pereira JDS, Neri JM, Emerenciano DP, De Freitas GRS, Felipe MBMC, De Souza MÂF, et al. Experimental and theoretical analysis of an oxazinoquinoxaline derivative for corrosion inhibition of AISI 1018 steel. *Quim Nova.* 2018;41(3):243-50.
45. Ji G, Shukla SK, Dwivedi P, Sundaram S, Ebenso EE, Prakash R. Parthenium hysterophorus plant extract as an efficient green corrosion inhibitor for mild steel in acidic environment. *Int J Electrochem Sci.* 2012;7(10):9933-45.
46. Shukla SK, Quraishi MA. The effects of pharmaceutically active compound doxycycline on the corrosion of mild steel in hydrochloric acid solution. *Corros Sci.* 2010;52(2):314-21.
47. Chakravarthy MP, Mohana KN. Adsorption and corrosion inhibition characteristics of some nicotinamide derivatives on mild steel in hydrochloric acid solution. *ISRN Corros.* 2014;2014(July):1-13.
48. Quraishi MA, Shukla SK. Poly(aniline-formaldehyde): A new and effective corrosion inhibitor for mild steel in hydrochloric acid. *Mater Chem Phys.* 2009;113(2-3):685-9.
49. Kannan P, Shukla SK, Rao TS, Rajendran N. Adsorption, thermodynamic and quantum chemical studies of 3-(4-Chlorobenzoylmethyl)benzimidazoliumbromide in inhibition effect on carbon steel. *J Mater Environ Sci.* 2016;7(4):1154-71.
50. Ji G, Shukla SK, Ebenso EE, Prakash R. Argemone mexicana leaf extract for inhibition of mild steel corrosion in sulfuric acid solutions. *Int J Electrochem Sci.* 2013;8(8):10878-89.
51. Kabanda MM, Shukla SK, Singh AK, Murulana LC, Ebenso EE. Electrochemical and quantum chemical studies on calmagite and fast sulphone black f dyes as corrosion inhibitors for mild steel in hydrochloric medium. *Int J Electrochem Sci.* 2012;7(9):8813-31.
52. Shukla SK, Ebenso EE. Corrosion inhibition, adsorption behavior and thermodynamic properties of streptomycin on mild steel in hydrochloric acid medium. *Int J Electrochem Sci.* 2011;6(8):3277-91.
53. Ji G, Shukla SK, Dwivedi P, Sundaram S, Ebenso EE, Prakash R. Parthenium hysterophorus plant extract as an efficient green corrosion inhibitor for mild steel in acidic environment. *Int J Electrochem Sci.* 2012;7(10):9933-45.



Effects of selected synthetic and biological insecticides on microbial population and microbial activities of soil samples

Sebiomo Adewole*  and Banjo Folake Mary 

Department of Biological Sciences, Tai Solarin University of Education, Ijagun, Nigeria.

Abstract: Modern agriculture depends upon the wide variety of natural and synthetically produced chemicals such as insecticides, fungicides, herbicides, and other pesticides. This work studied the effect of synthetic and biological insecticides on microbial population and microbial activities in soil samples. The insecticides used in this study are cypermethrin, chlorpyrifos, neem extracts, and ginger extracts. Bacteria and fungi were isolated and identified from the soil samples. TBC, TCC, and TFC were determined. Dehydrogenase activity, microbial respiration, and microbial biomass carbon in the soil samples were also examined. The control soil samples recorded the highest TBC, TFC, TCC, dehydrogenase activity, microbial respiration, and microbial biomass carbon. Soils treated with chlorpyrifos recorded the lowest total coliform count of $0.10 \times 10^5 \pm 0.00$ cfu/g, while cypermethrin treated soils recorded the lowest total bacterial count of $0.58 \times 10^5 \pm 0.025$ cfu/g. Cypermethrin-treated soils had the lowest effect on CO₂ respired in the soil with a value of 1687.50 ± 1.500 mg/kg. 500 g/mL Neem leaf extract had the highest microbial biomass carbon value of 9.40 ± 0.100 kgC/m². This work has shown that treatment with both synthetic and bio-insecticides resulted in significant drop in microbial population and microbial activity of soil samples.

Keywords: Microbial population, dehydrogenase activity, microbial respiration, microbial biomass carbon, cypermethrin, chlorpyrifos.

Submitted: May 03, 2020. **Accepted:** December 27, 2020.

Cite this: Sebiomo A, Banjo F. Effects of selected synthetic and biological insecticides on microbial population and microbial activities of soil samples. JOTCSA. 2021;8(1):229-38.

DOI: <https://doi.org/10.18596/jotcsa.731232>.

***Corresponding author.** E-mail: rev20032002@yahoo.com, Phone: +2348077675121 or +2347066468516.

INTRODUCTION

Mechanized agriculture depends heavily upon synthetically manufactured chemicals such as insecticides, fungicides, herbicides, and other pesticides (1). When pesticides are introduced into the soil about, it reaches the target organisms, interferes with metabolism in the environment, affects physicochemical properties or enzymatic activities of the soil, and also invariably affects human health. This has resulted in considerable public concern (2). Microorganisms are important parts of the food web in soils. Microbial biomass is a measure of potential microbiological and ecosystem activities. In order to understand the functioning of the ecosystem and examine soil disturbance because of various agricultural management

practices, microbial activities, and microbial biomass must be examined (3).

Insecticides are toxic substances which are used by farmers to kill insects which are liable to have a negative impact on crop production. Insecticides are used in agriculture, medicine, industry, and by consumers. They are an important factor behind the increase in agricultural productivity of the 20th century. Nearly all insecticides have the potential to significantly impact ecosystems; many are toxic to humans; while others accumulate in the environment (4). Residues of insecticides are broken down by a combination of environmental factors and microorganisms. Degradation products which are a result of microbial interactions leads to increased population sizes and microbial enzyme activities

which can in turn affect the transformation of plant nutrient elements in soil (5). There are insecticides which can only be degraded in soil by microorganisms through cometabolism. Other insecticides exert the deleterious effect on microorganisms. The use of insecticides in crops protects plants against different groups of insect pests. Although these chemicals are applied in low concentrations once in the soil, they can alter the chemical and biological properties of it and also affect soil microorganisms.

Das and Mukherjee (5) reported stimulatory effects of carbofuran at different doses under laboratory condition (5). Insecticides are used on crop plants to protect them from different group of harmful insects. Application of insecticides results in the decrease of the number of micro-organisms, alteration in biochemical activities, and quantitative and qualitative decrease of the microbial community of soil samples (6). Large-scale use of common pesticides can lead to soil toxicity, which may disturb several bio-chemical reactions and soil physicochemical properties. Due to high degree of toxicity, some pesticides particularly those that are persistent in soils, constitute a very important group of contaminants. Application of insecticides to plants and invariably reaching soils usually leads to their interaction with non-target soil micro-organisms and physio-chemical properties and hence exhibit chronic diverse effects on soil microflora (7). Hence this work studied the effect of synthetic and biological insecticides on microbial population and microbial activities (dehydrogenase activity, microbial respiration, and microbial biomass carbon) of soil samples.

MATERIALS AND METHODS

Soil sampling

Soil sampling were done in triplicate (in completely randomized design), using hand trowel to collect samples from the research field of Biological Sciences Department, Tai-Solarin University of Education, Ijagun, Ogun state, Nigeria. The samples were collected at 5 cm depth using the soil augur. The samples were then sieved with wire mesh (size <2 mm). Stones, plant debris and any visible soil fauna were removed from the soil samples by sorting after which they were thoroughly mixed with hand trowel. The soil was allowed to settle for seven days by incubating at 27 °C to allow the disturbances caused by sampling and sieving to stabilize. After the soil samples were allowed to settle, seeds of *Celosia argentia* were planted. Soil samples were collected 48 hours after treatment of *Celosia argentia* with the insecticides. The synthetic insecticides were applied according to manufacturer's instruction, in different plastic pots filled with 5 kg of soil and untreated soil samples were used as control. Neem and ginger extracts were also applied to different plastic pots filled with 5 kg soil samples. Soil samples were obtained from

the pots before and after incubation, after which they were analyzed.

Insecticides

The insecticides which were used in this study were obtained from local stores in Ijebu-Ode, Nigeria. The active ingredients are cypermenthrin 10% EC and chlorpyrifos 20% EC. Biological insecticides such as neem leaf extract and ginger extracts were also used in this study.

Preparation of plant extracts and insecticide sprays

Fresh neem leaves and ginger was soaked with water for three days, then they were cut into pieces, crushed, and blended using an electric blending machine. Thereafter, the following increasing quantities were prepared (100 g/mL, 200 g/mL, 300 g/mL, 400 g/mL, and 500 g/mL). After 24 h, the extract solutions were sieved with a cheese cloth to obtain a clear appearance. Cypermethrin and chlorpyrifos were prepared according to the manufacturer's specified instructions. The *Celosia argentia* plants were then sprayed with equal quantities of the insecticides.

Microbial analysis of soil samples

Total heterotrophic bacteria in soil samples were analyzed using Nutrient Agar (NA). Incubation was done at 30 °C for 24-48 h. Potato dextrose agar (PDA) was used for enumeration, isolation, and identification of fungi. Fungal isolates were incubated at 25 °C for 5-7 days. Bacterial isolates were characterized as based on cultural characteristics, staining reactions, and biochemical reactions and identifications were done using Bergey's Manual of Systemic Bacteriology (1984) as reference. Morphological and cultural characteristics were used to identify the fungi. The bacteria and fungi that emerged from plates were sub-cultured several times until pure cultures were obtained.

Determination of dehydrogenase activity

Six grams of soil and 6 mL of water samples were dispensed separately into 500 mL conical flasks. Thirty mL of glucose, 1 mL of 2,3,5-triphenyltetrazolium chloride (TTC) solution plus 2.5 mL of distilled water were added and shaken for 5 min. The mixtures were then filtered through a double layered filter paper into a 250 mL conical flask having formed 1,3,5-triphenyl formazan (TPF). The absorbances of sample extracts were read on a Cecil UV/Vis Spectrophotometer at a wavelength of 485 nm (20).

Determination of microbial respiration

The method of Klimek (8) was employed to determine soil microbial respiration. Soil samples were placed in glass jars containing 10 mL of 0.1 N NaOH solution. They were incubated in the dark at 25 ± 0.5 °C. Soil moisture content was maintained at 60% water holding capacity. Soil CO₂-evolution was regularly estimated during the twenty-five days incubation period and CO₂ released was measured

every 5 days. CO₂ recovered in each NaOH solution was measured by titration with HCl, after the addition of barium chloride. Percentage CO₂ evolved was then calculated.

Determination of microbial biomass carbon

Microbial biomass carbon was determined using the method of Vance et al. (9). Insecticide treated soils (5 g) were fumigated with 50 mL of 2:1 chloroform-

ethanol in a vacuum desiccator for 24 hrs. Soils that were not fumigated with chloroform-ethanol were used as control. The soil samples were extracted with 40 mL of 0.5 M K₂SO₄ for 30 min in an oscillator at 300 rpm. The control soil samples were also extracted with the 0.5 M K₂SO₄ and filtered through a Whatman No 42 Filter paper into a 250 mL conical flask. Microbial carbon was determined in a UV/Vis Spectrophotometer.

$$\text{Microbial biomass carbon} = \frac{\text{Absorbance of sample} \times \text{Gradient Factor} \times \text{Dilution factor}}{\text{Weight of sample}}$$

Statistical analysis

The data collected were subjected to analysis of variance (ANOVA). All analyses were carried out using the Statistical Package for Social Science (SPSS V.20).

RESULTS

Table 1 shows the biochemical and physicochemical properties of stabilized and un-stabilized soil samples.

Table 1. Microbiological, biochemical, and physicochemical properties of soils at the experimental site.

Soil characteristics	Unsettled soil	Settled soil
Soil type	Ferric luvisols	
Total nitrogen (%)	0.12	0.11
Available phosphorus (ppm)	12.04	11.51
Organic matter (%)	2.29	2.20
Soil electrical conductivity (µS/cm)	260.00	258.00
pH	6.90	6.70
Soil moisture (g)	19.21	19.00
Sand (g/kg)	640.00	639.00
Silt (g/kg)	160.00	158.00
Clay (g/kg)	169.50	167.00

Tables 2, 4, and 6 show the identified bacteria found in the soils treated with bio-insecticides and synthetic insecticides (neem leaf extract, ginger extract, cypermethrin and chlorpyrifos insecticides, respectively). *Pseudomonas aeruginosa* was commonly identified in all soil samples (Table 2,

Table 4 and Table 6). Fungi identified are shown in Tables 3, 5, and 7 (neem leaf extract, ginger extract, cypermethrin, and chlorpyrifos insecticides, respectively). *Aspergillus niger* was the most commonly occurring fungus in all soil samples (Tables 3, 5 and 7).

Table 2. Bacteria present in soils treated with neem leaf extract.

Treatment (g/mL)	Bacteria
Control	<i>Bacillus macerans</i> , <i>Pseudomonas chlororaphis</i> , <i>Pseudomonas aureginosa</i> , <i>Bacillus lincheniformis</i> , <i>Proteus vulgaricus</i> , <i>Bacillus macquariensis</i> , <i>Bacillus polymyxa</i> , <i>Streptococcus pyogenes</i> , <i>Micrococcus varians</i> , <i>Bacillus subtilis</i>
100	<i>Staphylococcus aureus</i> , <i>Pseudomonas aureginosa</i> , <i>Proteus mirabilis</i> , <i>Micrococcus luteus</i> , <i>Bacillus macerans</i> , <i>Pseudomonas putida</i> , <i>Pseudomonas putrefaciens</i> , <i>Bacillus subtilis</i> , <i>Staphylococcus aureus</i> , <i>Proteus vulgaricus</i> , <i>Serratia liquefaciens</i> .
200	<i>Micrococcus varians</i> , <i>Pseudomonas chlororaphis</i> , <i>Bacillus lincheniformis</i> , <i>Serratia marcescens</i> , <i>Streptococcus lactis</i> , <i>Micrococcus varians</i> , <i>Pseudomonas aureginosa</i> , <i>Bacillus subtilis</i> , <i>Serratia liquefaciens</i> , <i>Proteus Mirabilis</i> .
300	<i>Bacillus subtilis</i> , <i>Pseudomonas chlororaphis</i> , <i>Proteus mirabilis</i> , <i>Staphylococcus aureus</i> , <i>Serratia marcescens</i> , <i>Streptococcus pyogenes</i> , <i>Bacillus macerans</i> , <i>Pseudomonas aureginosa</i> , <i>B. macquariensis</i> , <i>Micrococcus varians</i> .
400	<i>Proteus morgani</i> , <i>Aeromonas hydrophilla</i> , <i>Bacillus subtilis</i> , <i>Streptococcus pyogenes</i> , <i>Bacillus subtilis</i> , <i>Serratia marcescens</i> , <i>Bacillus macerans</i> , <i>Bacillus subtilis</i> , <i>Streptococcus pyogenes</i> , <i>Pseudomonas aeruginosa</i> .
500	<i>Serratia marcescens</i> , <i>Aeromonas hydrophilla</i> , <i>Pseudomonas florescences</i> , <i>Staphylococcus aureus</i> , <i>Bacillus macerans</i> , <i>Bacillus subtilis</i> , <i>Pseudomonas chlororaphis</i> , <i>Proteus mirabilis</i> , <i>Staphylococcus aureus</i> , <i>Serratia marcescens</i> , <i>Streptococcus Pyogenes</i> .

Table 3. Fungi present in soils treated with neem leaf extract.

Treatment (g/mL)	Fungi
Control	<i>Rhizopus nigricans, Penicillium oxalicum, Aspergillus niger, Fusarium oxysporum</i>
100	<i>Aspergillus niger, Fusarium oxysporum, Penicillium oxalicum.</i>
200	<i>Aspergillus tamarii, Aspergillus fumigatus, Penicillium oxalicum, Rhizopus nigricans, Fusarium compacticum, Aspergillus niger</i>
300	<i>Aspergillus niger, Fusarium compacticum, Penicillium chrysogenum, Aspergillus fumigatus</i>
400	<i>Aspergillus niger, Fusarium oxysporum, Aspergillus tamarii</i>
500	<i>Penicillium chrysogenum, Fusarium oxysporum, Aspergillus niger, Aspergillus tamari</i>

Table 4. Bacteria present in soils treated with ginger extract.

Treatments (g/mL)	Bacteria
Control	<i>Bacillus macerans, Pseudomonas chlororaphis, Pseudomonas aureginosa, Bacillus lincheniformis, Proteus vulgaricus, Bacillus macquariensis, Bacillus polymyxa, Streptococcus pyogenes, Micrococcus varians, Pseudomonas chlororaphis, Bacillus subtilis.</i>
100	<i>Micrococcus luteus, Bacillus lincheniformis, Proteus mirabilis, Staphylococcus aureus, Pseudomonas floescences, Streptococcus pyogenes, Bacillus subtilis, Micrococcus varians, Bacillus lincheniformis, Streptococcus pyogenes, Pseudomonas putida, Staphylococcus aureus.</i>
200	<i>Pseudomonas aureginosa, Micrococcus varians, Bacillus subtilis, Staphylococcus aureus, Serratia marcences, Proteus mirabilis, Bacillus subtilis, Micrococcus varians, Bacillus lincheniformis, Staphylococcus aureus, Pseudomonas floescences, Proteus mirabilis.</i>
300	<i>Bacillus subtilis, Pseudomonas aureginosa, Bacillus macerans, Pseudomonas chlororaphis, Micrococcus varians, Proteus mirabilis, Bacillus macerans, Pseudomonas putida, Bacillus macerans, Pseudomonas chlororaphis, Micrococcus luteus, Proteus Mirabilis.</i>
400	<i>Bacillus lincheniformis, Pseudomonas aureginosa, Aeromonas hydrophilla, Serratia liquefaciens, Proteus mirabilis, Bacillus macerans, Pseudomonas floescences, Pseudomonas chlororaphis, Micrococcus luteus, Proteus mirabilis, Bacillus subtilis.</i>
500	<i>Bacillus macerans, Pseudomonas floescences, Aerobacter aerogenes, Staphylococcus aureus, Streptococcus pyogenes, Bacillus subtilis, Pseudomonas putida, Aerobacter aerogenes, Bacillus macerans, Proteus mirabilis.</i>

Table 5. Fungi present in soils treated with ginger extract.

Treatments (g/mL)	Fungi
Control	<i>Penicillium oxalicum, Aspergillus niger, Fusarium oxysporum.</i>
100	<i>Fusarium oxysporum, Aspergillus niger, Aspergillus tamari, Fusarium oxysporum, Aspergillus terreus</i>
200	<i>Penicillium oxalicum, Aspergillus fumigatus, Aspergillus niger, Penicillium oxalicum</i>
300	<i>Aspergillus terreus, Aspergillus tamarii, Aspergillus niger, Aspergillus terreus</i>
400	<i>Aspergillus niger, Aspergillus terreus, Penicillium oxalicum, Aspergillus. Fumigatus</i>
500	<i>Penicillium oxalicum, Aspergillus fumigatus, Aspergillus terreus, Penicillium chrysogenum, Aspergillus tamarii, Aspergillus niger</i>

Table 6. Bacteria present in soils treated with cypermethrin and chlopyrifos.

Treatments	Bacteria
Control	<i>Bacillus macerans, Pseudomonas chlororaphis, Pseudomonas aureginosa, Bacillus lincheniformis, Proteus vulgaricus, Bacillus macquariensis, Bacillus polymyxa, Streptococcus pyogenes, Micrococcus varians, Pseudomonas chlororaphis, Bacillus subtilis.</i>
Cypermethrin	<i>Bacillus subtilis, Pseudomonas floescences, Aerobacter aerogenes, Bacillus lincheniformis, Serratia liquefaciens, Bacillus macerans, Pseudomonas floescences, Aeromonas hydrophilla, Bacillus lincheniformis, Serratia marcences.</i>
Chlorpyrifos	<i>Pseudomonas purrefaciens, Pseudomonas floescences, Aeromonas hydrophilla, Bacillus macerans, Bacillus subtilis, Pseudomonas aureginosa, Pseudomonas putida, Aerobacter aerogenes, Bacillus lincheniformis, Bacillus subtilis.</i>

Table 7. Fungi present in soils treated with cypermethrin and chlorpyrifos.

Treatments	Fungi
Control	<i>Penicillium oxalicum, Aspergillus niger, Fusarium oxysporum</i>
Cypermethrin	<i>Penicillium oxalicum, Aspergillus niger, Aspergillus terreus, Fusarium Compacticum</i>
Chlorpyrifos	<i>Aspergillus terreus, Fusarium oxysporum, Aspergillus tamarii</i>

Effects of synthetic insecticides on soil microbial population

The TBC, TCC and TFC of the control soil samples were significantly higher ($P \leq 0.05$) than those of the insecticide treated soils (Table 8). Treatment with the synthetic insecticides caused significant changes ($P \leq 0.05$) in the population of microorganisms. Control soil samples recorded the highest bacterial, total coliform and total fungal counts of $1.30 \times 10^5 \pm 0.058$ cfu/g, $0.73 \times 10^5 \pm 0.048$ cfu/g and $0.60 \times 10^5 \pm 0.00$ cfu/g respectively. Soils

treated with chlorpyrifos recorded the lowest total coliform count of $0.10 \times 10^5 \pm 0.00$ cfu/g, while cypermethrin treated soils recorded the lowest total bacterial count of $0.58 \times 10^5 \pm 0.025$ cfu/g. The lowest total fungal count of $0.20 \pm 0.00 \times 10^5$ cfu/g were recorded in cypermethrin and chlorpyrifos treated soils respectively. There were significant differences ($P \leq 0.05$) in the total bacterial count, total coliform count and total fungi counts in Table 8.

Table 8. Effects of cypermethrin and chlorpyrifos on soil microbial population ($\times 10^5$ cfu/g).

Treatments	TBC	TCC	TFC
Control	1.30 ± 0.058^c	0.73 ± 0.048^b	0.60 ± 0.00^b
Cypermethrin	0.58 ± 0.025^a	0.20 ± 0.00^a	0.20 ± 0.00^a
Chlorpyrifos	0.78 ± 0.025^b	0.10 ± 0.00^a	0.20 ± 0.00^a

Control = Soil with *Celosia argentea* but without insecticides. ANOVA showed that values were significantly different at $P < 0.05$. Mean values with the same letters in a column are not significantly different ($P \geq 0.05$), while mean values with different letters in a column are significantly different ($P \leq 0.05$).

Effect of neem leaf extract on soil microbial population

In Table 9, the soil samples treated with insecticides caused significant changes ($P \leq 0.05$) in the microbial population. The highest TBC, TCC and TFC values of $1.30 \times 10^5 \pm 0.058$ cfu/g, $0.73 \times 10^5 \pm 0.048$ cfu/g

and $0.60 \times 10^5 \pm 0.00$ cfu/g respectively were obtained in control soil samples. Soils treated with neem leaf extract at 500 g/mL recorded the lowest total bacterial, total fungal, and total coliform counts of $0.38 \pm 0.025 \times 10^5$ cfu/g, $0.20 \pm 0.00 \times 10^5$ cfu/g and $0.20 \times 10^5 \pm 0.00$ cfu/g, respectively.

Table 9. Effects of neem leaf extracts on soil microbial population ($\times 10^5$ cfu/g).

Treatments (g/ml)	TBC	TCC	TFC
Control	1.30 ± 0.058^f	0.73 ± 0.048^c	0.60 ± 0.00^d
100	1.15 ± 0.29^e	0.68 ± 0.025^c	0.50 ± 0.00^c
200	0.93 ± 0.48^d	0.53 ± 0.025^b	0.35 ± 0.029^b
300	0.70 ± 0.00^c	0.45 ± 0.029^b	0.45 ± 0.029^c
400	0.55 ± 0.029^b	0.30 ± 0.00^a	0.28 ± 0.025^a
500	0.38 ± 0.025^a	0.20 ± 0.00^a	0.20 ± 0.00^a

Control = Soil with *Celosia argentea* but without insecticides. ANOVA showed that values were significantly different at $P < 0.05$. Mean values with the same letters in a column are not significantly different ($P \geq 0.05$), while mean values with different letters in a column are significantly different ($P \leq 0.05$).

Effect of ginger extract on soil microbial population

In Table 10, the control soil samples recorded the highest TBC, TCC and TFC values. Soil treated with ginger extract at 500 g/mL recorded the lowest TBC,

TCC and TFC values of $0.30 \pm 0.00 \times 10^5$ cfu/g and $0.20 \pm 0.00 \times 10^5$ cfu respectively. There were significant differences ($P \leq 0.05$) in the total bacterial count, total coliform count and total fungal count at different concentrations.

Table 10. Effects of ginger extracts on soil microbial population ($\times 10^5$ cfu/g)

Treatments (g/L)	TBC	TCC	TFC
Control	1.30 \pm 0.058 ^d	0.73 \pm 0.048 ^c	0.60 \pm 0.00 ^d
100	1.23 \pm 0.025 ^d	0.78 \pm 0.025 ^c	0.43 \pm 0.25 ^c
200	0.73 \pm 0.048 ^c	0.58 \pm 0.025 ^b	0.40 \pm 0.00 ^c
300	0.48 \pm 0.025 ^b	0.30 \pm 0.00 ^a	0.30 \pm 0.00 ^b
400	0.45 \pm 0.029 ^b	0.25 \pm 0.29 ^a	0.20 \pm 0.00 ^a
500	0.30 \pm 0.00 ^a	0.20 \pm 0.00 ^a	0.20 \pm 0.00 ^a

Control= Soil with *Celosia argentea* but without insecticides. ANOVA showed that values were significantly different at $P < 0.05$. Mean values with the same letters in a column are not significantly different ($P \geq 0.05$), while mean values with different letters in a column are significantly different ($P \leq 0.05$).

Effects of insecticides on microbial activities

Table 11 shows the effect of insecticides on dehydrogenase activity in the soils. Treatment of soil samples with the synthetic and biological insecticides resulted in significant drop in dehydrogenase activity. The control soil sample had the highest dehydrogenase activity value of $30.35 \pm$

$0.050 \mu\text{g g}^{-1} \text{h}^{-1}$, followed by 500 g/mL Neem leaf extract ($27.95 \pm 0.250 \mu\text{g g}^{-1} \text{h}^{-1}$). Chlorpyrifos treated soils had the lowest dehydrogenase activity value of $17.50 \pm 0.100 \mu\text{g g}^{-1} \text{h}^{-1}$. There were significant changes ($P \leq 0.05$) in the values of dehydrogenase activities in the insecticide treated soils.

Table 11. Effects of insecticides on dehydrogenase activities in the soil.

	Concentration (g/L)	DEH ($\mu\text{g g}^{-1} \text{h}^{-1}$)
Control		30.35 ± 0.050^1
Neem leaf	100	21.95 ± 0.150^{de}
	200	21.95 ± 0.150^{de}
	300	22.70 ± 0.100^f
	400	27.60 ± 0.100^h
	500	27.95 ± 0.250^h
Ginger	100	21.55 ± 0.050^{cd}
	200	21.25 ± 0.150^c
	300	22.20 ± 0.100^c
	400	26.35 ± 0.150^g
	500	26.70 ± 0.100^g
Concentration (mL)		DEH ($\mu\text{g g}^{-1} \text{h}^{-1}$)
Cypermethrin	13	18.35 ± 0.150^b
Chlorpyrifos	13	17.50 ± 0.100^a

ANOVA showed that values were significantly different at $P < 0.05$. Mean values with the same letters in a column are not significantly different ($P \geq 0.05$), while mean values with different letters in a column are significantly different ($P \leq 0.05$).

In Table 12, microbial biomass carbon of soil samples reduced significantly after treatment with the insecticides. It was observed that 500 g/mL Neem leaf had the highest microbial biomass carbon value of $9.40 \pm 0.100 \text{ kg C / m}^2$, followed by 400 g

Neem leaf ($8.40 \pm 0.200 \text{ kg C / m}^2$). Control soil samples recorded microbial biomass carbon value of $5.80 \pm 0.100 \text{ kg C / m}^2$. Meanwhile, cypermethrin recorded the lowest microbial biomass carbon value of $2.05 \pm 0.250 \text{ kg C / m}^2$.

Table 12. Effects of insecticides on microbial biomass carbon (kg C / m²) in soil samples.

	Concentration(g/L)	MBC(kg C / m ²)
Control		5.80±0.100 ^e
Neem leaf	100	5.35±0.150 ^{de}
	200	6.70 ± 0.200 ¹
	300	8.05 ± 0.250 ^{hi}
	400	8.40 ± 0.200 ⁱ
	500	9.40±0.100 ^j
Ginger	100	4.00±0.100 ^h
	200	4.55±0.150 ^{bc}
	300	5.05±0.150 ^{cd}
	400	7.45±0.150 ^g
	500	7.65 ± 0.1 50 ^{gh}
	Concentration (mL)	MBC(KgC/m ²)
Cypermethrin	13	2.05 ± 0.250 ^a
Chlorpyrifos	13	2.50±0.300 ^a

ANOVA showed that values were significantly different at $P < 0.05$. Mean values with the same letters in a column are not significantly different ($P \geq 0.05$), while mean values with different letters in a column are significantly different ($P \leq 0.05$).

Table 13 shows the effects of insecticides on microbial respiration (CO₂ respired). The insecticides also caused significant reduction in microbial respiration after treatment with the insecticides. 500 g/mL of Neem leaf extract had the highest microbial respiration value of 2288.00 ± 1.000 mg/kg. The control soil samples recorded a value of 1915.50 ± 1.500 mg/kg. 100 g of Neem leaf and 200 g of Ginger were observed to have a similar value of 1872.50 ± 1.500 mg/kg. Cypermethrin treated soils had the lowest effect on CO₂ respired in the soil with a value of 1687.50 ± 1.500 mg/kg. There were significant differences ($P \leq 0.05$) in the microbial respiration values of the insecticide treated soils.

DISCUSSION AND CONCLUSION

In this study, *Pseudomonas aeruginosa* and *Aspergillus niger* were the most commonly isolated microorganisms from the insecticide-treated soil samples. Iqbal and Bartakke (10) reported that they isolated *Acinetobacter radioresistens*, *Pseudomonas frederiksbergensis*, *Bacillus pumilus*, *Serratia liquefaciens*, *Serratia marcescens*, and *Burkholderia gladioli*. Treatment of soil samples with neem leaf

extracts resulted in significant reduction in soil microbes. This is supported by the finding of Nasim *et al.* (11) who also confirmed the same result for neem extracts. Neem extracts have been reported to possess antibacterial, antifungal, antimalarial, and antiviral properties.

Ajaz *et al.* (12) reported the isolation of chlorpyrifos resistant bacteria from cotton cultivated soil using conventional and API kit methods (12). In the present study, reduction in bacterial populations was observed after field treatment with chlorpyrifos. Liu *et al.* (13) reported reduced microbial populations which may affect the quantity of organic matter in soils. The extensive use of chlorpyrifos having a half-life from 10 to 120 days in soil has resulted in widespread environmental contamination affecting beneficial non-target soil microorganisms. Bera *et al.* (14) stated that microorganisms can cause breakdown of insecticides and utilize them as a source of nutrients. However, before degradation, insecticides have toxic effects on microorganisms, reducing their abundance, activity, and consequently, the diversity of their communities.

Table 13. Effects of insecticides on microbial respiration (CO₂ respired) in the soil.

	Concentration (g/mL)	CO ₂ respired (mg/kg)
Control		1915.50 ± 1.500 ^f
Neem leaf	100	1872.50 ± 1.500 ^d
	200	1877.00 ± 1.000 ^{de}
	300	1880.50 ± 1.500 ^e
	400	2184.50 ± 1.500 ^h
	500	2288.00 ± 1.000 ⁱ
Ginger	100	1867.50 ± 1.500 ^o
	200	1872.50 ± 1.500 ^o
	300	1865.50 ± 1.500 ^o
	400	1970.00 ± 2.000 ^g
	500	1974.00 ± 1.000 ^g
	Concentration (mL)	CO ₂ respired (mg/kg)
Cypermethrin	13	1687.50 ± 1.500 ^a
BTermicot	13	1694.00 ± 2.000 ^b

ANOVA showed that values were significantly different at $P < 0.05$. Mean values with the same letters in a column are not significantly different ($P \geq 0.05$), while mean values with different letters in a column are significantly different ($P \leq 0.05$).

The toxic effects of insecticides are initially noticed in soils by the reduction of microbial enzymic activities and microbial populations after application. After adaptation of microorganisms to these toxic environmental conditions, there is an increase in microbial enzymic activities and microbial population which in turn results in degradation of these toxic insecticides. In this study, the effects of insecticides on soil microbial enzymes (dehydrogenase and microbial respiration) showed reduction in microbial activity after treatment with the insecticides (synthetic and biological insecticide), the observed trends in relation to microbial enzymes in this research work were similar to the one we initially made (15). Rasool and Reshi (16) reported that several insecticides suppressed and reduced the activity of dehydrogenase enzymes in their study.

Caceres *et al.* (17) stated that pesticides have negative impacts of pesticides on soil enzymes such as hydrolases, oxidoreductases and dehydrogenase activities. Gundi (18) determined the effect of monochrotophos, quinalphos and cypermethrin on microbial populations in a black clay soil and demonstrated their synergistic effects at the lower levels and adverse effects at the highest level of the insecticides. According to Lopez (19) heterotrophic

mesophilic and psychrophilic aquatic bacteria as well as culturable phosphate-solubilizing microorganisms increased in lake water samples when treated with insecticides showing that sometimes, initially microbial population is affected by insecticide application but with time after adaptation to these insecticides, the population merely returns to normal or even increases. This indicates the changes in microbial catabolic capabilities as a result of induced insecticide degradation capabilities or due to a change within the microbial community.

The synthetic insecticides used in this study showed higher negative impacts on microbial activities (microbial biomass carbon, microbial respiration, dehydrogenase activity and microbial population) compared to the biological insecticides which were applied at different concentrations.

CONCLUSION

This work has shown that treatment with both synthetic and bio-insecticides resulted in significant drop in microbial population and microbial activity of soil samples. The synthetic insecticides used in this study has been shown to cause major reduction in microbial population and microbial activity. Hence

the use of synthetic insecticides is discouraged. Further research could be carried out to improve the usability of the biological insecticides.

REFERENCES

- Zhang B, Bai Z, Hoefel D, Tang L, Wang X, Li B, Li Z, Zhuang G. The impacts of cypermethrin pesticide application on the non-target microbial community of the pepper plant phyllosphere. *Science on Total Environment*. 2009; 407:1915-22.
- Ramudu A, Mohiddin G, Srinivasulu M, Rangaswamy V. Impact of fungicides chlorothalol oil and propiconazole on microbial activities in groundnut (*Arachis hypogaea* L.) soils. *International Scholarly Research Network Microbiology*. 2011; 623404, 1-7.
- Nannipieri P, Cervelli S, Pema A. Enzyme activities in some Italian soils. *Journal of Italian Agriculture*. 2012; 73: 367-76.
- Diplock EE, Mardlin DP, Killham KS, Paton G I. Predicting bioremediation of hydrocarbons: laboratory to field scale. *Environmental Pollution*. 2009; 157 (6): 1831-40.
- Das AC, Mukherjee D. Soil application of insecticides influences microorganisms and Plant Nutrient Applied Soil Ecology. 2007;14: 55-62.
- Vig K, Singh DK, Agrarwal HC, Dhawan AK, Dureja P. Soil micro- organisms in cotton fields sequentially treated with insecticides. *Ecotoxicology and Environmental Safety*. 2009; 69:263-76.
- Sarfraz H, Siddique T, Saleem M, Arshad M, Khalid A. Impact of pesticides on soil microbial diversity, enzymes and biochemical reactions. *Advances in Agronomy*. 2009; 102:159-200.
- Klimek B. Effect of Long-Term Zinc Pollution on Soil Microbial Community Resistance to Repeated Contamination. *Bulletin of Environmental Contamination and Toxicology*. 2012; 8(4): 617-22.
- Vance ED, Brookes PC, Jenkinson DS. An extraction method for measuring soil microbial biomass C. *Soil Biology and Biochemistry*. 1987; 17 (6): 837 - 42.
- Iqbal MA, Bartakke KV. Isolation of Pesticide Degrading Microorganisms from soil. *Advances in Bioresearch*. 2014; 5(4):164-8.
- Nasim G, Ilyas N, Shabbir A. Study of effect of organic pesticides: Endosulfan and Bifenthrin on growth of some soil fungi. *Mycopathology*. 2005; 3 (1&2): 27-31.
- Ajaz M, Jabeen N, Akhtar S, Rasool SA. Cloropyrifos resistant bacteria from Pakistani soils: isolation, identification, resistance profile and growth profile. *Pakistan Journal of Botany*. 2005; 37(2): 381-8.
- Liu J, Xie J, Chu Y, Sun C, Chen C, Wang Q. Combined effect of cypermethrin and copper on catalase activity in soil. *J. Soils Sed*. 2008; 8: 327-32.
- Bera S, Ghosh RK. Soil Microflora and Weed Management as Influenced by Atrazine 50 % WP in Sugarcane. *Universal Journal of Agricultural Research*. 2013; 1(2): 41-7.
- Sebiomo A, Ogundero VW, Bankole SA. Effect of four herbicides on microbial population, soil organic matter and dehydrogenase activity. *African Journal of Biology*. 2012; 10(5): 770-8.
- Rasool N, Reshi, ZA. Effect of the fungicide Mancozeb at different application rates on enzyme activities in a silt loam soil of the Kashmir Himalaya, India, *Trop. Ecol*. 2010; 51; 199-205.
- Caceres TP, He WX, Megharaj M, Naidu, R. Effect of insecticide fenamiphos on soil microbial activities in Australian and Ecuadorean soils. *Journal of Environmental Science*. 2009; 44: 13-7.
- Gundi V, Viswanath B, Chandra MS, Kumar VN, Reddy BR. Activities of cellulase and amylase in soils as influenced by insecticide interactions. *Ecotoxicology and Environmental Safety*. 2007; 68: 278-85.
- Lopez J. Growth and denitrifying activity of Xanthobacter in the presence of selected pesticides. *Applied Microbiology and Biotechnology*. 2006; 71: 563-7.
- Min H, Ye YF, Chen ZY, Wu WX, Du YF. Effects of butachlor on microbial populations and enzyme activities in paddy soil. *Journal of Environmental Science and Health*. 2001; 36: 581-95.



Monoamine Oxidase Inhibitory Effects of Medicinal Plants in Management of Alzheimer's Disease

Tuba Ege^{1*}  , Hayriye Deniz Şelimen²  

¹European University of Lefke, Faculty of Dentistry, Northern Cyprus TR-10 Mersin, Turkey.

²European University of Lefke, School of Health, Northern Cyprus TR-10 Mersin, Turkey.

Abstract: Alzheimer's disease is the most common progressive neurodegenerative disorder that affects large population of society, especially elderly people. Environmental and/or genetic factors contribute Alzheimer's disease to become a pivotal health problem but this relationship remains ambiguous. Globally growing prevalence of Alzheimer's disease requires to understand cellular pathways that lead to Alzheimer's disease and to develop new strategies for prevention and treatment. Elevated monoamine oxidase (MAO) enzymes activity with age is associated with etiology of Alzheimer's disease. Inhibition of monoamine oxidase enzyme can protect from neuronal damage, thus it became one of the key pathway for management of Alzheimer's disease. Using bioactive compounds from medicinal plants as potential monoamine oxidase inhibitors might be a better solution considering undesired side effects of synthetic drugs on human body. The purpose of this review is to implicate the importance of pharmacophore analysis which explains pharmacological properties of medicinal plants and interaction of bioactive compounds from plants with MAO enzyme.

Keywords: Monoamine oxidase, Alzheimer's disease, bioactive compounds, medicinal plants.

Submitted: November 10, 2020. **Accepted:** December 27, 2020.

Cite this: Ege T, Şelimen H. Monoamine Oxidase Inhibitory Effects of Medicinal Plants in Management of Alzheimer's Disease. JOTCSA. 2021;8(1):239-48.

DOI: <https://doi.org/10.18596/jotcsa.823874>.

Corresponding author. E-mail: tubacege@gmail.com. Phone: +90 392 660 2000 - 2921, Fax: +90 392 727 7528.

INTRODUCTION

Alzheimer's disease (AD) has been an important health problem that needs to be researched, as it affects the quality of life of millions of people. According to Alzheimer's Association Report (March 2020), the number of people living with Alzheimer's dementia in United States is 5,8 million and is expected to be 13,8 million by 2050 (1). According to the "Dementia in Europe Yearbook 2019 by Alzheimer Europe" report, in Turkey there were 528,547 citizens suffering from dementia in 2018 and due to the increase in the proportion of the 65-and-elder population each year, the number is estimated to be triplicated (1,745,679) by 2050 (2).

Alzheimer's disease is an irreversible age-dependent neurodegenerative disorder that is characterized as lessening the size of brain and

locally neuronal death in basal forebrain and hippocampus (3-5) of which common manifestations are progressive loss of memory, cognitive impairments, deterioration of learning and memory functions, disorientation and mood swings and communication problems (4,6-8).

ALZHEIMER PATHOPHYSIOLOGY

There are several hypotheses explaining risk factors (Figure 1) for developing AD such as long exposure to the environmental heavy metals, genetic factors, stress, depression, history of head injuries, hypertension and life styles, etc. but there is no clear consensus (9-11). Abnormal β -amyloid protein deposits outside of neurons and hyper-phosphorylated tau protein inside of neurons are two main factors which lead to develop AD because of misfolded protein accumulation (12).

The formation of senile plaques, (neuritic plaques) which are by products of biological aging, is associated with beta-amyloid protein deposits. β -amyloid precursor protein (APP) in the neuron cell membrane helps neurite outgrowth and repairs after injury (13). APP proteolysis contains two pathways as nonamyloidogenic and amyloidogenic. In nonamyloidogenic pathway, the product of cleavage APP by alpha and gamma secretase is soluble and is not causative agent of AD. However, amyloidogenic pathway produces amyloid beta monomer by beta and gamma secretase (3). In synaptic junction, insoluble sticky clumps of beta-amyloid monomer which form senile plaques-one of the major factors of AD-can block neuron-to-neuron signaling which eventually results in impaired memory and neuroinflammation (3,13). Also certain genetic analyses show that duplication and missense mutation in APP precursor causes certain AD cases. In some AD studies with Down syndrome (DS) showed that three copies of gene encoding amyloid precursor protein (APP) cause overexpression of APP, which is an another risk factor of AD (14,15).

Heat-stable and soluble tau protein in brain cell, which is a microtubule-associated protein (MAP) stabilizes microtubules. Hyper-phosphorylation by intracellular kinase such as cyclin-dependent kinase-5 (Cdk5), glycogen synthase kinase-3 β (GSK-3 β), Ca²⁺/calmodulin activated protein kinase II, casein kinase-I elicits paired-helical-filament (PHF) tau and neurofibrillary tangles (NFTs) (16). Abnormal hyper-phosphorylated tau protein inside of the AD patients' brain results in disruption of neuronal signaling and programmed cell death (17).

Besides these two main factors, studied complementary elements which lead developing AD are shown in Figure 1. In addition to amyloid precursor protein (APP) gene mutation, presenilin 1 (PSEN1)-presenilin 2 (PSEN2) and apolipoprotein E (APO E) gene mutations, respectively on chromosome 1 and 19, are involved in progression of AD (11). Patients with presenilin 1 and 2 missense gene mutations and apolipoprotein E (APO E) mutations are prone to develop beta amyloid plaques (18).

Many studies show that genetic polymorphisms of interleukin(19), alpha-antichymotrypsin (20), ATP-binding cassette transporter A1, synaptosomal-associated protein (SNAP-25) (21) and choline *O*-acetyltransferase (22) are recognized as pejorative factor in developing AD. Also insulin resistance and type-2 diabetes are important risk factor of AD (23). Moreover, some diseases like COVID-19 can prompt neurocognitive alterations and affects neurons and neuroglia (24). Since COVID-19 fatality rate

rises by approximately 11.2% per year of age (25) and this rate is higher in older age(26), patients with Alzheimer and dementia are at risk (27).

The cholinergic hypothesis demonstrates that impairment of cholinergic system contributes cognitive decline (28). Diminished concentration and function of acetylcholine (ACh) which is related with both memory and learning, is one of the marker of AD. While acetylcholinesterase (AChE) and butyrylcholinesterase (BuChE) hydrolyzes choline esters like acetylcholine, choline acetyltransferase (ChAT) synthesizes neurotransmitter acetylcholine (28,29). In AD patients' cerebral neocortex and hippocampus, it has been observed that the concentration of ACh and ChAT are decreased (30). Since cholinergic hypothesis is related with reduced ACh concentration, cholinesterase (acetylcholinesterase and butyrylcholinesterase) inhibitors are one of the ameliorating strategies for AD treatment (31).

Oxidative stress, high level reactive oxygen species, is admitted as pejorative factor in occurrence of AD. Oxidative stress in frontal cortex is accepted to be significant in cognitive impairment (3). Because of human brain's need for more energy than other tissues trigger more oxygen-consuming. This increases the possibility of free radicals production and tissue damage (32,33). In normal condition, excessive reactive oxygen level (ROS) can be eliminated by glutathione which is the most common endogenous antioxidant in brain. Attenuation of glutathione level is considered as a contributing factor to damage in hippocampus and frontal cortex (34). Also, ROS stimulates oxidation of lipids, proteins, and nucleic acids in neurons and deposition of amyloid beta and hyper-phosphorylated tau protein as well (32,33).

It is known that monoamine oxidase enzyme (MAO) interlink with oxidative stress mechanism. And it is related with monoaminergic pathway. Monoamine oxidase enzyme is flavin-dependent amine oxidase which include flavin adenine dinucleotide (FAD) in the active site (35). MAOs reside in the outer membrane of the mitochondria of the central nervous system, liver, lung, gastrointestinal tract, blood platelets, and placenta in mammals (36-38). Monoamine oxidase enzyme is responsible for oxidative deamination of several neurotransmitters and different exogenous and endogenous amines containing melatonin, serotonin, epinephrine, norepinephrine, dopamine, histamine, tryptamine, taurine and benzylamine (16,39). Monoamine oxidases exist in two isoforms (MAO-A and MAO-B), which have different substrates and different specific inhibitors on the other hand they have some overlapping substrates though (5). MAO-A and

MAO-B genes are located on X chromosome, and these two isoenzymes show 70% identity (40). MAO-A mainly catalyzes breakdown of serotonin, noradrenalin, norepinephrine, dopamine and tyramine while MAO-B catalyzes mainly breakdown of dopamine and phenylethylamine (38,41). In the brain, MAO-A is mainly expressed in catecholaminergic neurons but MAO B is expressed in serotonergic, histaminergic neurons and astrocytes (40). Both MAO A and B expression is regulated by diverse transcription factors and hormones and this expression increases with ages (42). Brain functions, regulation of concentration, emotional behaviors, adaption,

muscle coordination, protection of neurons from exogenous monoamines and storage of monoamines are regulated by monoamine oxidase enzymes subtypes. In recent studies, it shows that increase (or decrease) of MAO enzyme level which influences neurotransmitters metabolism leads to halting problems in brain and production of reactive oxygen species (ROS) (39). Furthermore, the importance of MAO enzymes is proved in several psychiatric conditions, including chronic stress, neurodegenerative disorders (Alzheimer's and Parkinson's diseases) and alcohol dependence (41,43).

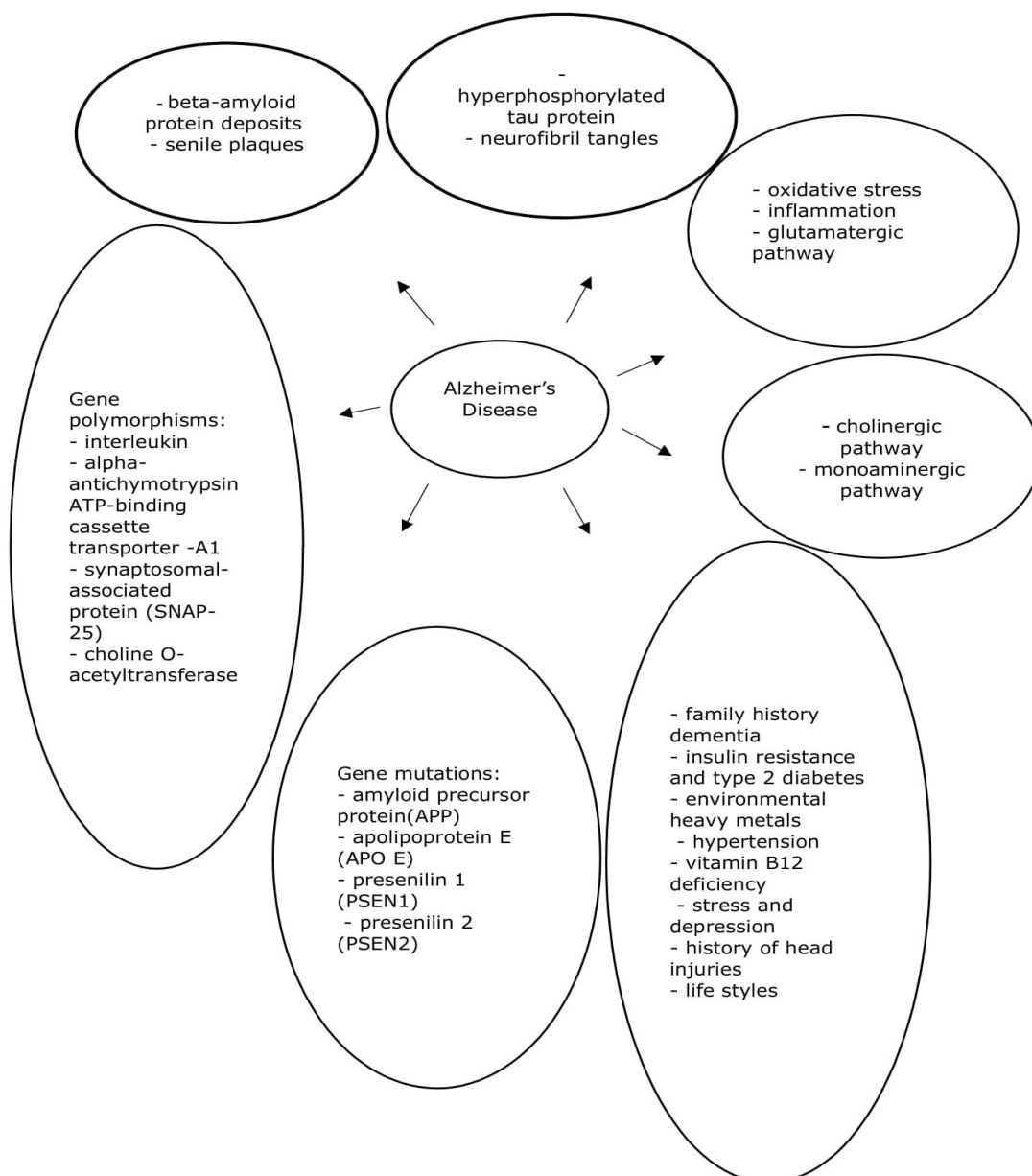


Figure 1. Risk Factors for developing Alzheimer's disease.

Neurotoxic byproducts of monoamine oxidase enzyme catalyzed reactions are aldehyde, ammonia, and hydrogen peroxide (H_2O_2) (16). Hydrogen peroxide can be converted to hydroxyl radical, an example of ROS, which leads to oxidative stress in brain (37,44). Hydroxyl radical produces an affliction in neuronal membrane and DNA of the mitochondria. Elevated H_2O_2 level activates cell acidosis resulting neuro-inflammation in brain. Immune cells produce interleukins which are a group of cytokines and they are linked to different diseases ranging from schizophrenia, major depression, and Alzheimer's disease (5). Also, throughout aging of brain, increased MAO enzyme activity produces more H_2O_2 which results in increased oxidative stress (31). Elevated oxidative stress has also an important function on progression of Alzheimer's disease (38). Recent discoveries demonstrate that both astrocytes and pyramidal neurons of AD brain include abnormal elevated level of MAO-B activity (39,45). It is stated that increased formation of beta plaque and ROS and dopamine metabolism is one of the hallmarks of monoamine oxidase activity and/or transcription rate (9,46).

The overexpression of MAO-B enhances amyloid β -peptide production and MAO-B is a main component of regulation of amyloid β -peptide by means of γ -secretase (45). High level of glucocorticoids is related with elevated MAO-B activity, which will increase amyloid- β and tau protein in rat model of AD (47). Neuropsychiatric disorders management is related with two isomers of MAO. Inhibition of MAO-A is widely used for clinical treatment of depression and anxiety since MAO-A possess high affinity to serotonin and norepinephrine, whilst MAO-B inhibition is an effective molecular target for AD (41,43).

There are several phytochemical analyses and pharmacological studies to research therapeutic potential and mechanism of folk medicinal plants about AD management. In this review, we will discuss plant-based MAO inhibitors that reveal anti-Alzheimer activity and neuroprotection. Studies suggest that bioactive compound from medicinal plants have promising multifunctional agent including monoamine oxidase inhibitors (MAOIs) for AD management to improve brain functions.

PLANTS AND DERIVATIVE COMPOUNDS WITH MAO INHIBITORY POTENTIAL

Phytochemicals are known as bioactive compounds in plants which have preventive and curative properties as enzyme inhibitory, antioxidant, anti-cancer and anti-inflammatory. Herbs which contain phenolic and polyphenolic bioactive compounds have been used

throughout human history to avert and treat disparate diseases (48).

Polyphenols, flavonoids and phenolic acids, have natural antioxidant activity to scavenge ROS and chelate metal ions, to inhibit different enzyme activities and to keep from protein aggregation (10). The phenolic hydroxyl groups (Phe-OH) are hydrogen donating antioxidants and they disrupt production of new radicals. Also, phenolics show high affinity to interact with protein due to their structure which includes hydrophobic benzenoid rings and hydrogen-bonding potential of Phe-OH groups. This unique structure provides possibility of inhibiting some enzymes related with ROS production such as MAOs and CYPs (49).

Quercetin, a flavonoid found in wine and green tea, is an inhibitor of monoamine oxidase A ($IC_{50} = 0.01 \mu\text{mol/L}$)/monoamine oxidase B ($IC_{50} = 10.89 \mu\text{mol/L}$) and a stonewall for amyloid beta and tau protein aggregation with $IC_{50} < 1 \mu\text{mol/L}$ (50-52).

Epigallocatechin gallate (EGCG) in green tea has anti-Alzheimer effect by displaying inhibitor function for amyloid beta aggregation ($IC_{50} = 0.18 \mu\text{mol/L}$) and MAO enzyme activity ($IC_{50} = 10 \mu\text{mol/L}$) (49,53).

Resveratrol, a popular phenol in wine, decreases amyloid beta production and inhibits monoamine oxidase A (MAO-A) with an IC_{50} of $26.6 \mu\text{mol/L}$ (49,54).

Curcumin (500.46 nM) and ellagic acid (412.24 nM) strongly inhibit MAO-B enzyme isolated from rat brain, compared to standard drug which is selegiline, MAO-B inhibitor. Both curcumin and ellagic acid inhibit MAO enzyme in a competitive and non-competitive way, but ellagic acid has more efficacious inhibitory effect on MAO-B than curcumin (55).

Curcumin, luteolin, apigenin, quercetin, and chlorogenic acid from medicinal plants have as good binding affinity as standard drugs due to having similar binding amino acid residue with drug rasagiline and selegiline, which are selective and irreversible MAO-B inhibitors (5).

MAO inhibitory potential of five coumarin derivatives from the roots of *Angelica gigas* Nakai (AG) and eight flavonoids from *Scutellaria baicalensis* Georgi (SB) is studied. Decursin isolated from AG strongly inhibits MAO-A with $IC_{50} = 1.89 \mu\text{M}$ but not MAO-B ($IC_{50} = 70.5 \mu\text{M}$), thus decursin is selective, reversible, and competitive inhibitor of human MAO-A. Wogonin isolated from SB is non-selective, reversible, and competitive inhibitor of MAO-A and moderate inhibitor of MAO-B ($IC_{50} = 6.35$ and 20.8 M , respectively). Decursinol angelate and

baicalein show selective and moderate inhibitory activity against MAO-A. Molecular docking analyses exhibit that decursin forms hydrogen bond with Asn116 residue of MAO-B and Asn181 residue of MAO-A, which H-bonds promote ligand binding affinity (56). Authors suggest that decursin and wogonin may be a remedy for Alzheimer disease, due to their reversible MAO-A inhibitor activity (57).

Berberine is an alkaloid which is found in many plants including goldthread, goldenseal, and oregon grape. It has been substantiated that berberine has distinct pharmacological properties such as being antioxidant, antidepressant, and anticancer. Berberine has a neuroprotective effect against long term exposure to heavy metals, which are aluminum, cadmium, and fluoride anion. After rats are orally exposed to these three metals (50 mg/kg, 5 mg/kg and 20 mg/kg, respectively) for three months, 50 mg/kg/day berberine is orally given for one month. Berberine penetrates blood-brain barrier, and inhibits AChE, BchE, and MAOs enzyme activities and also it reduces amyloid beta and neural fibril tangle production (9). It is observed that since berberine has a large hydrophobic surface, it has binding affinity to monoamine oxidase A and B because of their hydrophobic substrate recognition site (58). The inhibitory potential of berberine against MAO enzymes stems from these hydrophobic interactions. In drug design, hydrophobic interaction is very important by virtue of its ability to elevate binding affinity between target-drug interfaces (59). Both of their findings show that berberine can be used for anti-Alzheimer drug design.

Danshensu (salvianic acid A), a water-soluble compound, is a phenolic acid isolated from herbs. Scopolamine and amyloid- β ($A\beta$) protein-induced cognitive impairments in rat model, oral administration of danshensu (3 or 10 mg/kg) inhibits monoamine oxidase A (MAO-A) activity but not MAO-B and it elevates dopamine level and phosphorylation level of protein kinase A. It is suggested that danshensu may be a new therapeutic agent against cognitive dysfunction by MAO-A inhibition and dopamine level related PKA-CREB activation (7).

Another multi-target agent is sarsasapogenin (SRS) which is a steroidal saponin from *Asparagus racemosus*. *Asparagus racemosus* (satavar) spreads over Sri Lanka, India, and the Himalayas. Satavar has a wide range of biologically active compounds and shows pharmacological activities such as immunomodulatory activity, antihepatotoxic activity, antidepressant activity, aphrodisiac activity, and antioxidant effects. Satavar, one of the ancient ayurvedic medicine of India, has also been used to control AIDS symptoms (60).

Sarsasapogenin inhibits not only MAO-B but also acetylcholinesterase (AChE), butyrylcholinesterase (BuChE) and Beta-secretase 1 (BACE1). Their inhibition rates raise when concentration of sarsasapogenin is increased. Forty μ M SRS inhibits MAO-B enzyme by 68% as compared to control selegiline (85% inhibition). Molecular docking analysis carries out that SRS interacts only with hydrophobic residues (Tyr 326 and Gln206) of MAO-B (1).

Synthetic analogues synthesis of plants bioactive compounds is very important for drug production to combat neurodegenerative disease. Anti-Alzheimer's and anti-depressant benefits of dibenzylidene ketone derivatives (2,6-dibenzylidene cyclohexanone (A1K1) and 5-(2,3-dichlorophenyl)-1-(4-methoxyphenyl)-2-methylpenta-1,4-diene-3-one (A2K2)), which are analogues of curcumin, are evaluated in mice models. In mice, anti-Alzheimer activity are investigated by Y-maze test and Morris water maze test (MWM). Anti-depressant activity is investigated by forced swim test, tail suspension test and open field test. In the Y-maze test, administration of A1K1 and A2K2 (0.5 mg/kg and 1 mg/kg respectively for 3 days) intraperitoneally improves spontaneous alteration behavior, which increases cognitive performance. In Morris water maze test (MWM), mice are administered same concentrations as Y-maze test for 5 days instead of 3 days. Both doses (0.5 mg/kg and 1 mg/kg) of A1K1 and A2K2 minimize escape latency time as compared to control group. The molecular docking results reveal that both derivatives have high binding affinity to MAOB, which is related with hydrogen binding between ligand and protein (8).

Six synthetic α,β -unsaturated carbonyl-based tetralone derivatives (3f, 3o, 3u, 3ae, 3af, and 3ag) exhibit defense against $A\beta$ -induced cell death in pheochromocytoma cells (PC12 cell). One hundred μ m tetralone derivatives are treated to PC12 cells. These derivatives protect 88 percent of the cells from $A\beta$ -induced cell death. Compound 3f shows both MAO-B ($IC_{50} = 0.88 \pm 0.12 \mu$ m) and AChE ($IC_{50} = 0.045 \pm 0.02 \mu$ m) inhibitory potential. These α,β -unsaturated carbonyl-based tetralone derivatives have potency to develop multi-target-drugs (43).

Spondias mombin (*S. mombin*), also known as yellow mombin, has historically been used as an alternative medicine because of its polyphenol content. *S. mombin* leaves' chemical profile, phytochemical-protein mechanism and inhibitory properties on some enzymes (MAO-A, phosphodiesterase- 5, arginase, angiotensin I-converting enzyme, cholinesterase, ecto-5' nucleotidase, tyrosinase, and stimulated sodium-potassium ATPase) which are related with erectile and cognitive dysfunction are

analyzed. 3.125 µg/mL, 6.25 µg/mL, 12.5 µg/mL and 25 µg/mL of *S. mombim* fractions inhibit monoamine oxidase A (MAO). While the concentration increases, enzyme inhibition has also increased. HPLC/MS analysis proves that its chemical profile include lutein, zeaxanthin, β-cryptoxanthin, α-carotene, β-carotene, chlorogenic acid, and ellagic acid. Chlorogenic acid has the lowest binding score to MAO-A with lowest atomic contact energy (AtCE = -139.08). There are many studies associated with chlorogenic acid and ellagic acid consumption that provide a lot of benefits relevant to neurological degeneration (61).

Aloe vera (*Aloe barbadensis*-AV), a cactus-like plant, is a popular ingredient in pharmaceutical industry and cosmetics. Different alcohol extract concentrations of AV (0.001 M, 0.005 M, 0.01 M, 0.05 M, 0.1 M) exhibit good enzyme inhibition for MAO (4.46, 20.08, 43.91, 53.17, and 81.13%). The results have revealed that AV is an uncompetitive inhibitor for MAO. Owing to inhibition potential on MAO/AChE and reducing Alzheimer's disease symptoms and increasing cognition scores, AV can be recommended as a food supplement for treatment of Alzheimer's disease (62).

Ipomoea aquatica is known as water spinach. Meliorating effect of *Ipomoea aquatica* extracts is observed on mice with amyloid beta induced cognitive deficit. After 10 µL single intracerebroventricular injection of AB peptide, MAOs level increases in mice brain. Treatment with 200 mg/kg and 400 mg/kg of hydroalcoholic extract of *Ipomoea aquatica* (HAEIA) significantly increases neurotransmitter level, inhibits MAOs and AChE (acetylcholinesterase) enzyme activity and reduces glutamate level. In addition, both doses of HAEIA improve learning memory by reducing the negative effects of Alzheimer's disease (4).

Ammodaucus leucotrichus (*A. leucotrichus*) is a member of Apiaceae family. It is an endemic flowering plant found in North Africa, Morocco, Algeria, and Tunisia. It is traditionally used for cardiac diseases, stomach diseases, fever, vomits, and allergies. To illuminate the effects of *Ammodaucus leucotrichus* against neurological disorders, the anti-monoamine oxidase activities of the content of the essential oil that gathered from *A. leucotrichus* aerial parts is analyzed. Chemical analysis shows that perillaldehyde (58.3%) and limonene (23.33%) are the main components of essential oil. Essential oil and perillaldehyde have an inhibitory effect on both MAO-A with IC50 value 112.5 and 159.1 µg/mL respectively and MAO-B with IC50 values of 40.5 and 98.9 µg/mL in order. Essential oil and perillaldehyde show potent inhibitory activity for MAO-B than MAO-A (38).

Chinese herbal Naodesheng formula (ND) has been used as a therapeutic agent to treat mainly cardiovascular diseases. Naodesheng formula includes five different plants. Those are *Rhizoma Chuanxiong*, *Lobed Kudzuvine*, *Carthamus tinctorius*, *Radix Notoginseng* and *Crataegus pinnatifida*. When ND formula is studied for AD prevention, a biological pathway network is established. According to this network, it is found that albeit AChE is in the center, MAO-B is one of the nodes of this network and ND has drug-like properties. It can be utilized for treatment of central nervous system diseases by the virtual screening and network pharmacology methods (63).

Ethanol extract of arecanut (4-80 mg/kg) inhibits monoamine oxidase in albino rats (64). In mice brain, treatment of 200 and 400 mg/kg hydroalcoholic extract of arecanut reduce MAO level (65). The dichloromethane fraction of arecanut elevates serotonin and dopamine in the brain by inhibiting MAO-A (66).

In another study, methanol extract of *Plantago major* strongly inhibits MAO-A enzyme more than MAO-B with IC50 values 2.174 µg/mL and 21.051 µg/mL, respectively (67).

Ginkgo biloba has been utilized in alternative medicine and as a dietary supplement. EGb 761 is an extract isolated from *Ginkgo biloba* leaves. Main ingredients of EGb 761 are flavanol glycosides and terpene trilactones. Information related with its radical scavenger and antioxidant properties and low side effects supported that EGb741 can be regarded amenable to treatment for Alzheimer's disease (68). Long term daily administration (50 mg/kg oral) of EGb741 reduced cerebral MAO-A and MAO-B activity by down-regulation in age-induced and stress-induced mice (69).

Gardenia jasminoides is a member of Rubiaceae family that is grown in South Korea and Southern China. It is envisioned that ethyl acetate, methanol, and total extracts of *G. jasminosides* inhibit both monoamine oxidase-A (MAO-A) and monoamine oxidase-B (MAO-B) activities (70,71). To elucidate which components of *G. jasminoides* play a major role in MAO inhibition mechanism, bioactive compounds (protocatechuic acid, geniposide, 6'-O-trans-p-coumaroylgeniposide, 3,5-dihydroxy-1,7-bis(4-hydroxyphenyl) heptanes and ursolic acid) of ethyl acetate fraction *Gardenia jasminoides* are identified. 6'-O-trans-p-coumaroylgeniposide (127 mmol/L), 3,5-dihydroxy-1,7-bis (4-hydroxyphenyl) heptane (IC50 = 196 µmol/L), geniposide (IC50 = 223 µmol/L) and protocatechuic acid (IC50 = 300 µmol/L), are strong MAO-B inhibitors whereas ursolic acid (IC50=780 µmol/L) is a weak MAO-B

inhibitor. Protocatechuic acid has weak inhibition ($IC_{50} = 2411 \mu\text{mol/L}$), but 3,5-dihydroxy-1,7-bis(4-hydroxyphenyl)heptane ($IC_{50} = 400 \mu\text{mol/L}$) have modest inhibition against MAO-A. Ursolic acid does not exhibit any inhibition against MAO-A. Ursolic acid ($IC_{50} = 214 \mu\text{mol/L}$) and Protocatechuic acid ($IC_{50} = 334 \mu\text{mol/L}$) show significant inhibition against dopamine β -hydroxylase which converts dopamine into norepinephrine. 3,5-dihydroxy-1,7-bis(4-hydroxyphenyl) heptane exhibits more specific activity to MAO-B (16,129) than MAO-A (7,937), because it has a hydroxyl group and it makes it having great inhibitory potential on MAO-B over MAO-A. Protocatechuic acid shows about 8 times more specific activity on MAO-B (21,739) than on MAO-A (2,695). This decreases affinity to MAO-A related with protocatechuic acid structure which includes an additional hydroxy group at the ortho-position. Even if 6'-*O*-trans-p-coumaroylgeniposide has a hydroxy group, it has a lack of inhibition against MAO-A. It is explained with 6'-*O*-trans-p-coumaroylgeniposide structure which masking hydroxyl proton with methyl and glycosyl groups (72). The pharmacophore analysis gives an information interaction of bioactive compounds to the target protein (73). Determination of bioactive compounds of high binding affinity to MAOs is a useful approach for anti-Alzheimer drug development.

CONCLUSION AND FUTURE CONCERNS

The effects of known MAO inhibitor drugs (selective MAO-A, selective MAO-B, or nonselective MAO-A/B inhibitors, and reversible/irreversible MAOs) are limited. *In vivo* and *in vitro* investigations reveal that pharmaceutical properties of medicinal plants and their bioactive components support good opportunity as candidates for drug discovery and management for Alzheimer due to their MAOs inhibitory effects. Although phytochemical and pharmacological researches highlight promising MAO inhibitory potential of therapeutic medicinal plant and their rich content, it is needed further extensive research especially binding affinity between MAO enzyme and phytochemicals.

CONFLICT OF INTEREST

The authors declare no conflict of interest.

ACKNOWLEDGMENTS

The authors received no financial support for the research, authorship, and/or publication of this article.

REFERENCES

1. Kashyap P, Muthusamy K, Niranjana M, Tripathi S, Kumar S. Sarsasapogenin: A steroidal saponin from *Asparagus racemosus* as multi target directed ligand in Alzheimer's disease. *Steroids* [Internet]. 2020;153(October 2019):108529. Available from: <https://doi.org/10.1016/j.steroids.2019.108529>
2. Alzheimer Europe. Dementia in Europe Yearbook. Estimating the prevalence of dementia in Europe. 2019.
3. Patil P, Thakur A, Sharma A, Flora SJS. Natural products and their derivatives as multifunctional ligands against Alzheimer's disease. *Drug Dev Res*. 2020;81(2):165-83.
4. Sivaraman D, Panneerselvam P, Muralidharan P. Memory and brain neurotransmitter restoring potential of hydroalcoholic extract of *Ipomoea aquatica* forsk on amyloid beta A β (25-35) induced cognitive deficits in Alzheimer's mice. *Int J Pharmacol*. 2016;12(2):52-65.
5. Sivaraman D, Srikanth J. Discovery of novel monoamine oxidase-b inhibitors by molecular docking approach for Alzheimer's and Parkinson's disease treatment. *Int J Pharm Sci Rev Res*. 2016;40(1):245-50.
6. Alzheimer's Association. 2018 Alzheimer's disease facts and figures. *Alzheimer's Dement*. 2018;14(3):367-429.
7. Bae HJ, Sowndhararajan K, Park HB, Kim SY, Kim S, Kim DH, et al. Danshensu attenuates scopolamine and amyloid- β -induced cognitive impairments through the activation of PKA-CREB signaling in mice. *Neurochem Int* [Internet]. 2019;131(August):104537. Available from: <https://doi.org/10.1016/j.neuint.2019.104537>
8. Bashir MA, Khan A, Ullah, Badshah H, Rodrigues-Filho E, Din ZU, Khan A. Synthesis, characterization, molecular docking evaluation, antidepressant, and anti-Alzheimer effects of dibenzylidene ketone derivatives. *Drug Dev Res*. 2019;80(5):595-605.
9. Hussien HM, Abd-Elmegied A, Ghareeb DA, Hafez HS, Ahmed HEA, El-moneam NA. Neuroprotective effect of berberine against environmental heavy metals-induced neurotoxicity and Alzheimer's-like disease in rats. *Food Chem Toxicol* [Internet]. 2018;111(April 2017):432-44. Available from: <https://doi.org/10.1016/j.fct.2017.11.025>
10. Ji HF, Zhang HY. Multipotent natural agents to combat Alzheimer's disease. Functional spectrum and structural features. *Acta Pharmacol Sin*. 2008;29(2):143-51.
11. Riederer P, Danielczyk W, Grünblatt E. Monoamine Oxidase-B Inhibition in Alzheimer's Disease. *Neurotoxicology*. 2004;25(1-2):271-7.
12. Wang Y, Wang H, Chen H. AChE Inhibition-based Multi-target-directed Ligands, a Novel Pharmacological Approach for the Symptomatic and Disease-modifying Therapy of Alzheimer's Disease. *Curr Neuropharmacol*. 2016;14(4):364-75.

13. Cras P, Kawai M, Lowery D, Gonzalez-DeWhitt P, Greenberg B, Perry G. Senile plaque neurites in Alzheimer disease accumulate amyloid precursor protein. *Proc Natl Acad Sci U S A*. 1991;88(17):7552-6.
14. Tcw J, Goate AM. Genetics of β -Amyloid Precursor Protein in Alzheimer's Disease. *Cold Spring Harb Perspect Med*. 2017;7(6):1-12.
15. Wiseman FK, Al-Janabi T, Hardy J, Karmiloff-Smith A, Nizetic D, Tybulewicz VLJ, et al. A genetic cause of Alzheimer disease: Mechanistic insights from Down syndrome. *Nat Rev Neurosci*. 2015;16(9):564-74.
16. Fišar Z. Drugs related to monoamine oxidase activity. *Prog Neuro-Psychopharmacology Biol Psychiatry*. 2016;69:112-24.
17. Iqbal K, Liu F, Gong C-X, Tau in Alzheimer Disease and Related Tautopathies. *Curr Alzheimer Res*. 2010;8(7):656-64.
18. Hutton M, Hardy J. The presenilins and Alzheimer's disease. *Hum Mol Genet*. 1997;6(10 REV. ISS.):1639-46.
19. Mun MJ, Kim JH, Choi JY, Jang WC. Genetic polymorphisms of interleukin genes and the risk of Alzheimer's disease: An update meta-analysis. *Meta Gene [Internet]*. 2016;8:1-10. Available from: <http://dx.doi.org/10.1016/j.mgene.2016.01.001>
20. Ezquerro M, Blesa R, Tolosa E, Ballesta F, Oliva R. α -Antichymotrypsin gene polymorphism and risk for Alzheimer's disease in the Spanish population. *Neurosci Lett*. 1998;240(2):107-9.
21. Sumirtanurdin R, Thalib AY, Cantona K, Abdulah R. Effect of genetic polymorphisms on alzheimer's disease treatment outcomes: An update. *Clin Interv Aging*. 2019;14:631-42.
22. Xu X, Wang Y, Wang L, Liao Q, Chang L, Xu L, et al. Meta-Analyses of 8 Polymorphisms Associated with the Risk of the Alzheimer's Disease. *PLoS One*. 2013;8(9).
23. Qiu WQ, Folstein MF. Insulin, insulin-degrading enzyme and amyloid- β peptide in Alzheimer's disease: Review and hypothesis. *Neurobiol Aging*. 2006;27(2):190-8.
24. Steardo L, Steardo L, Zorec R, Verkhatsky A. Neuroinfection may contribute to pathophysiology and clinical manifestations of COVID-19. *Acta Physiol*. 2020;229(3):10-3.
25. Hall RE, Klenow PJ, Jones CI. Trading Off Consumption and COVID-19 Deaths. *Fed Reserv BANK Minneap Q Rev*. 2020;42(1).
26. Bulut C, Kato Y. Epidemiology of covid-19. *Turkish J Med Sci*. 2020;50(SI-1):563-70.
27. Brown EE, Kumar S, Rajji TK, Pollock BG, Mulsant BH. Anticipating and Mitigating the Impact of the COVID-19 Pandemic on Alzheimer's Disease and Related Dementias. *Am J Geriatr Psychiatry [Internet]*. 2020;28(7):712-21. Available from: <https://doi.org/10.1016/j.jagp.2020.04.010>
28. Francis PT, Palmer AM, Snape M, Wilcock GK. The cholinergic hypothesis of Alzheimer's disease: A review of progress. *J Neurol Neurosurg Psychiatry*. 1999;66(2):137-47.
29. Greig NH, Lahiri DK, Sambamurti K. Butyrylcholinesterase: An important new target in Alzheimer's disease therapy. *Int Psychogeriatrics*. 2002;14(SUPPL. 1):77-91.
30. García-Ayllón MS, Small DH, Avila J, Sáez-Valero J. Revisiting the role of acetylcholinesterase in Alzheimers disease: Cross-talk with β -tau and p-amyloid. *Front Mol Neurosci*. 2011;4(SEP):1-9.
31. Sharma K. Cholinesterase inhibitors as Alzheimer's therapeutics (Review). *Mol Med Rep*. 2019;20(2):1479-87.
32. Huang WJ, Zhang X, Chen WW. Role of oxidative stress in Alzheimer's disease (review). *Biomed Reports*. 2016;4(5):519-22.
33. Tönnies E, Trushina E. Oxidative Stress, Synaptic Dysfunction, and Alzheimer's Disease. *J Alzheimer's Dis*. 2017;57(4):1105-21.
34. Pocernich CB, Butterfield DA. Elevation of glutathione as a therapeutic strategy in Alzheimer disease. *Biochim Biophys Acta - Mol Basis Dis*. 2012;1822(5):625-30.
35. Kachalova G, Decker K, Holt A, Bartunik HD. Crystallographic snapshots of the complete reaction cycle of nicotine degradation by an amine oxidase of the monoamine oxidase (MAO) family. *Proc Natl Acad Sci U S A*. 2011;108(12):4800-5.
36. Fiedorowicz JG, Swartz KL. The role of monoamine oxidase inhibitors in current psychiatric practice. *J Psychiatr Pract*. 2004;10(4):239-48.
37. Rendu F, Peoc'h K, Berlin I, Thomas D, Launay JM. Smoking related diseases: The central role of monoamine oxidase. *Int J Environ Res Public Health*. 2011;8(1):136-47.
38. Sadaoui N, Bec N, Barragan-Montero V, Kadri N, Cuisinier F, Larroque C, et al. The essential oil of Algerian *Ammodaucus leucotrichus* Coss. & Dur. and its effect on the cholinesterase and monoamine oxidase activities. *Fitoterapia [Internet]*. 2018;130(June):1-5. Available from: <https://doi.org/10.1016/j.fitote.2018.07.015>
39. Duncan J, Johnson S, Ou XM. Monoamine oxidases in major depressive disorder and alcoholism. *Drug Discov Ther*. 2012;6(3):112-22.
40. Bortolato M, Chen K, Shih JC. Monoamine oxidase inactivation: From pathophysiology to therapeutics. *Adv Drug Deliv Rev*. 2008;60(13-14):1527-33.
41. Lee HW, Ryu HW, Kang MG, Park D, Lee H, Shin HM, et al. Potent inhibition of monoamine oxidase A by decursin from *Angelica gigas* Nakai and by wogonin from *Scutellaria baicalensis* Georgi. *Int J Biol Macromol [Internet]*. 2017;97:598-605. Available from: <http://dx.doi.org/10.1016/j.ijbiomac.2017.01.080>

42. Maggiorani D, Manzella N, Edmondson DE, Mattevi A, Parini A, Binda C, et al. Monoamine Oxidases, Oxidative Stress, and Altered Mitochondrial Dynamics in Cardiac Ageing. *Oxid Med Cell Longev*. 2017;2017(3).
43. Leng J, Qin HL, Zhu K, Jantan I, Hussain MA, Sher M, et al. Evaluation of multifunctional synthetic tetralone derivatives for treatment of Alzheimer's disease. *Chem Biol Drug Des*. 2016;88(6):889-98.
44. Gaweska H, Fitzpatrick PF. Structures and mechanism of the monoamine oxidase family. *Biomol Concepts*. 2011;2(5):365-77.
45. Schedin-Weiss S, Inoue M, Hromadkova L, Teranishi Y, Yamamoto NG, Wiehager B, et al. Monoamine oxidase B is elevated in Alzheimer disease neurons, is associated with γ -secretase and regulates neuronal amyloid β -peptide levels. *Alzheimer's Res Ther*. 2017;9(1):1-19.
46. Xie SS, Wang X, Jiang N, Yu W, Wang KDG, Lan JS, et al. Multi-target tacrine-coumarin hybrids: Cholinesterase and monoamine oxidase B inhibition properties against Alzheimer's disease. *Eur J Med Chem [Internet]*. 2015;95:153-65. Available from: <http://dx.doi.org/10.1016/j.ejmech.2015.03.040>
47. Green KN, Billings LM, Roozendaal B, McGaugh JL, LaFerla FM. Glucocorticoids increase amyloid- β and tau pathology in a mouse model of Alzheimer's disease. *J Neurosci*. 2006;26(35):9047-56.
48. Ege T. The Pharmacological and Therapeutic Potentials of *Epilobium hirsutum* L. *Int J Pharm Sci Rev Res*. 2019;57(2):20-3.
49. Pereira DM, Valentão P, Pereira JA, Andrade PB. Phenolics: From chemistry to biology. *Molecules*. 2009;14(6):2202-11.
50. Chimenti F, Cottiglia F, Bonsignore L, Casu L, Casu M, Floris C, et al. Quercetin as the active principle of *Hypericum hircinum* exerts a selective inhibitory activity against MAO-A: Extraction, biological analysis, and computational study. *J Nat Prod*. 2006;69(6):945-9.
51. Lee MH, Lin RD, Shen LY, Yang LL, Yen KY, Hou WC. Monoamine oxidase B and free radical scavenging activities of natural flavonoids in *Melastoma candidum* D. Don. *J Agric Food Chem*. 2001;49(11):5551-5.
52. Porat Y, Abramowitz A, Gazit E. Inhibition of amyloid fibril formation by polyphenols: Structural similarity and aromatic interactions as a common inhibition mechanism. *Chem Biol Drug Des*. 2006;67(1):27-37.
53. Mazzi EA, Harris N, Soliman KFA. Food constituents attenuate monoamine oxidase activity and peroxide levels in C6 astrocyte cells. *Planta Med*. 1998;64(7):603-6.
54. Zhou CX, Kong LD, Ye WC, Cheng CHK, Tan RX. *Veratrum taliense*. 2001;67:158-61.
55. Khatri D, Juvekar A. Kinetics of inhibition of monoamine oxidase using curcumin and ellagic acid. *Pharmacogn Mag*. 2016;12(46):116.
56. Chen D, Oezguen N, Urvil P, Ferguson C, Dann SM, Savidge TC. Regulation of protein-ligand binding affinity by hydrogen bond pairing. *Sci Adv*. 2016;2(3).
57. Lee HW, Kim YJ, Nam SJ, Kim H. Potent selective inhibition of monoamine oxidase a by alternariol monomethyl ether isolated from *alternaria brassicae*. *J Microbiol Biotechnol*. 2017;27(2):316-20.
58. Ji HF, Shen L. Molecular basis of inhibitory activities of berberine against pathogenic enzymes in Alzheimer's disease. *ScientificWorldJournal*. 2012;2012.
59. Varma AK, Patil R, Das S, Stanley A, Yadav L, Sudhakar A. Optimized hydrophobic interactions and hydrogen bonding at the target-ligand interface leads the pathways of Drug-Designing. *PLoS One*. 2010;5(8).
60. Alok S, Jain SK, Verma A, Kumar M, Mahor A, Sabharwal M. Plant profile, phytochemistry and pharmacology of *Asparagus racemosus* (Shatavari): A review. *Asian Pacific J Trop Dis*. 2013;3(3):242-51.
61. Ojo OA, Afon AA, Ojo AB, Ajiboye BO, Okesola MA, Aruleba RT, et al. *Spondias mombim* L. (Anacardiaceae): Chemical fingerprints, inhibitory activities, and molecular docking on key enzymes relevant to erectile dysfunction and Alzheimer's diseases. *J Food Biochem*. 2019;43(3):1-17.
62. Shakir MA. The effect of Aloe Vera extract on Acetylcholinesterase AchE and Monoamine Oxidase MAO enzymes. *Al-Mustansiriyah J Sci*. 2018;29(4):88-92.
63. PANG XC, KANG D, FANG JS, ZHAO Y, XU LJ, LIAN WW, et al. Network pharmacology-based analysis of Chinese herbal Naodesheng formula for application to Alzheimer's disease. *Chin J Nat Med*. 2018;16(1):53-62.
64. Dar A, Khatoon S, Rahman G, Atta-Ur-Rahman. Anti-depressant activities of *Areca catechu* fruit extract. *Phytomedicine*. 1997;4(1):41-5.
65. Kannan R, Sivaraman D, Muralidharan P, Deepakvenkataraman N. Neuroprotective effect of hydroalcoholic extract of *areca catechu* linn on β -amyloid (25-35) induced cognitive dysfunction in mice. *Int J Res Ayurveda Pharm*. 2013;4(5):747-53.
66. Khan S, Abbas G, Ahmed FS, Atta-Ur-Rahman, Dar A. Effect of dichloromethane fraction of *Areca catechu* nut on monoamines associated behaviors and tyramine pressor sensitivity in rodents. *Pak J Pharm Sci*. 2014;27(2):303-7.
67. Akıncioğlu, H., Akbaş, M. and Aydın T. Determination of Inhibition Effect of *Plantago Major* Plant Extract on Monoamine Oxidase Isoenzymes (MAO-A and MAO-B). In: 4th INTERNATIONAL CONFERENCE ON ADVANCES IN NATURAL & APPLIED SCIENCES. 2019.
68. Rojas C, Rojas-Castañeda J, Rojas P. Antioxidant properties of a *Ginkgo biloba* leaf extract (EGb 761) in animal models of Alzheimer's and Parkinson's diseases. *Curr Top Nutraceutical Res*. 2016;14(1):1-16.

69. Pardon MC, Joubert C, Perez-Diaz F, Christen Y, Launay JM, Cohen-Salmon C. In vivo regulation of cerebral monoamine oxidase activity in senescent controls and chronically stressed mice by long-term treatment with Ginkgo biloba extract (EGb 761). Mech Ageing Dev. 2000;113(3):157-68.

70. Hwang KH. Monoamine oxidase inhibitory activities of Korean medicinal plants classified to cold drugs by the theory of KIMI. Food Sci Biotechnol. 2003;12:238-41.

71. Park, T. K. and Hwang KH. Inhibitory activity of the fruit extract of Gardenia jasminoides on monoamine oxidase. Korean J Pharmacogn. 2007;38:108-12.

72. Kim JH, Kim GH, Hwang KH. Monoamine oxidase and dopamine β -hydroxylase inhibitors from the fruits of Gardenia jasminoides. Biomol Ther. 2012;20(2):214-9.

73. Pitchai D, Manikkam R, Rajendran SR, Pitchai G. Database on pharmacophore analysis of active principles, from medicinal plants. Bioinformation. 2010;5(2):43-5.



Characterization of the Alphabet Reform Painting

Yıldız CAKMAK¹  , Recep KARADAG^{2,3*}  , Nilhan KAYAMAN APOHAN⁴  ,
Ömer Yiğit ARAL¹   and Emrah CAKMAKCI⁴  

¹Department of Conservation and Restoration of Artworks, Faculty of Fine Arts, Mimar Sinan Fine Arts University, Bomonti Campus, Istanbul, Turkey

²Department of Fashion and Textile Design, Faculty of Fine Arts, Istanbul Aydın University, Florya Campus, Istanbul, Turkey

³TCF (Turkish Cultural Foundation) Istanbul, Turkey

⁴Department of Chemistry, Faculty of Science and Literature, Marmara University, Göztepe Campus, Istanbul, Turkey

Abstract: The Alphabet Reform painting which shows Atatürk teaching the new alphabet is important for the history of the Republic of Turkey. This painting was made by Nazmi Ziya GÜRAN in 1933. The painting is now maintained by the Ministry of Interior. In this work, the Alphabet Reform painting was analyzed for characterization and restoration purposes. The fabric of the canvas, pigments (organic-inorganic) and the binder of paint were characterized by Fourier Transform infrared spectroscopy-attenuated total reflectance (ATR-FTIR), scanning electron microscopy-energy dispersive X-ray spectroscopy (SEM-EDX) and high-performance liquid chromatography-coupled with diode array detection (HPLC-DAD) analysis methods. The CIEL*a*b* color parameters of the paint were determined by color measurement spectrophotometer. According to the results, the canvas was found to be of fibers of vegetable origin and the binders were determined to be linseed oil and dammar varnish. Red alizarin (madder lake organic pigment) and dark blue ultramarine pigments were detected as the organic pigments while CdS (yellow), Pb red (flesh color), PbCO₃ (white), ZnO (white), BaSO₄ (white), FeO (brown) and Cr₂O₃ (green color) were detected as the inorganic ones.

Keywords: Oil paintings, FTIR-ATR, SEM, HPLC, restoration.

Submitted: October 20, 2020. **Accepted:** January 05, 2021.

Cite this: Cakmak Y, Karadag R, Kayaman Apohan N. Characterization of the Alphabet Reform Painting. JOTCSA. 2021;8(1):249-62.

DOI: <https://doi.org/10.18596/jotcsa.813787>.

***Corresponding Author, Email:** recepkaradag@aydin.edu.tr / **GSM:** +90 532 525 02 82.

INTRODUCTION

There are a limited number of art pieces that survived to this day. It is inevitable that eventually there have been deteriorations or flaking on these pieces of art. Conservator-restorers are trying to restore these alterations developed over time. Restoration practices may be different for each art specimen. The successful restoration of artworks requires an in-depth analysis of the pieces. For instance, with the analysis of old paintings so much information can be attained such as the pigments used in the piece of art and changes that may occur in these pigments over time (1-6), organic and

inorganic substances (7-11), the binders (12-13), the areas with retouches or patches on these pieces, the areas with varnish, structural deteriorations (such as cracking, flaking, peeling, and tearing) (14-15), painting technique of the artist (16) and the types of the varnish (17-19) or the canvas that were used (such as silk, linen, hemp, cotton, jute) (20) which are of great importance for the restoration of these paintings. One can even have an idea about the palette of the artist given that he or she has the chance to analyze several pieces of art that belonged to that artist (21).

Today, many different methods are used in the analysis for restoration and preservation of artworks that are a part of cultural heritage in many countries around the world.

Fourier transform infrared spectroscopy (FTIR) and scanning electron microscopy, and energy dispersive x-ray spectroscopy (SEM-EDX) have proven themselves to be efficient methods for analysis in scientific examination of works of art over a long period of time (11).

Identification of pigments in artefacts can be a source of valuable information in concern with conversation and art history of the object. Numerous studies on the identification of pigments by FTIR analysis can be found in literature (2-5, 21-26). Regardless of the fact that many inorganic pigments such as ultramarine blue, lead white, malachite and Prussian blue fall into mid-IR region with their characteristic absorption bands, there are many that either do not absorb in that region at all or have absorptions that are at the low wave number end of the region and are not characteristic enough. However, through an extensive attenuated total reflectance - fourier transform infrared (ATR-FTIR) study, it was found that historically most widespread inorganic white, yellow, blue, green, brown and black pigments could be differentiated by examining their vibration bands in the region of 550-230 cm^{-1} (22).

High Performance Liquid Chromatography (HPLC) is also another useful technique for the used for the characterization of artworks. Many objects within a cultural heritage site may contain organic or inorganic materials. Many researchers have used HPLC analysis method to separate into components and to determine the dyestuff in the artwork (8-10, 27, 28).

These techniques along with others were used extensively in many studies for the characterization of old paintings. For instance, Jana Zelinska et al., investigated the main altar of the St. James Church in Slovakia (7). 25 inorganic pigments, substrate and organic binder samples which were taken from the wood panel were identified using FTIR, SEM-EDS and optical microscopy. FTIR findings led them to conclude that linseed oil was used as a binder whereas SEM-EDX results revealed the presence of azurite, chalk, and lead white (7).

Thiago G. Costa and his friends have examined Louis-Auguste's five paintings. They used UV-induced visible luminescence, SEM-EDX and FTIR spectroscopic techniques. As a result of FTIR analysis, they found carbonates, sulfates, alumina silicates, iron oxides, and Prussian blue as pigments and they found that an oil-based binder was used. According to EDX results, Pb element was found in all samples (15).

Milene Gil et al., studied Jose de Escovar's panel and mural painting by FTIR, SEM-EDX and technical photography (ultraviolet fluorescence-visible-Infrared) methods. They found Fe, lead white, red lead oxide, red mercury sulfide, calcium hydroxide, titanium, copper, zinc, and sulfur. They have identified the presence of an oil binder by the bands at 2926 cm^{-1} , 2854 cm^{-1} and 1703 cm^{-1} as a result of FTIR analysis and they have attained information about the artist's painting techniques (16).

In another research, Thiago G. Costa and his friends investigated the painting called "Primeira Missa no Brasil" which was originally made by Victor Meirelles in 1860 and its replica by Sebastiao Vieira Fernandes in 1929. This painting was also analyzed with FTIR, EDX and UV-induced visible luminescence methods. They identified the presence of prussian blue, lithopone, lead white, chrome yellow, cobalt blue pigments in the paintings. FTIR and EDS analyses showed a correlation between the elemental composition of pigments used by Meirelles and Fernandes, especially for lead (29).

In this work, we aimed to characterize the pigments and the binder of the Alphabet Reform painting. The painting was introduced to the Mimar Sinan Fine Arts University from the Ministry of Interior of Republic of Turkey to be restored. This painting was made by Nazmi Ziya GURAN who was influenced by the impressionist movement in Paris and who liked to reflect the opposite colors side by side, in 1933. This painting is of great importance for the history of Turkey for it shows Ataturk introducing the new alphabet reform to public. FTIR-ATR, SEM-EDX, and HPLC methods were used to characterize this painting.

MATERIALS AND METHODS

Materials

Purpurin and alizarin reference samples, and dimethylformamide were purchased from Sigma Aldrich. Acetonitrile, trifluoroacetic acid, hydrogen chloride, and methanol were purchased from Merck. The painting was obtained from the Ministry of Interior of Republic of Turkey.

Sample Collection

Samples were taken with a scalpel from paintings (11 samples) and also from the canvas. Samples (S1, S2, S3, S4, S5, S6, S7, S8, S9, S10 and S11) taken from the parts of the painting marked in Figure 1 (S1-S11) were examined.

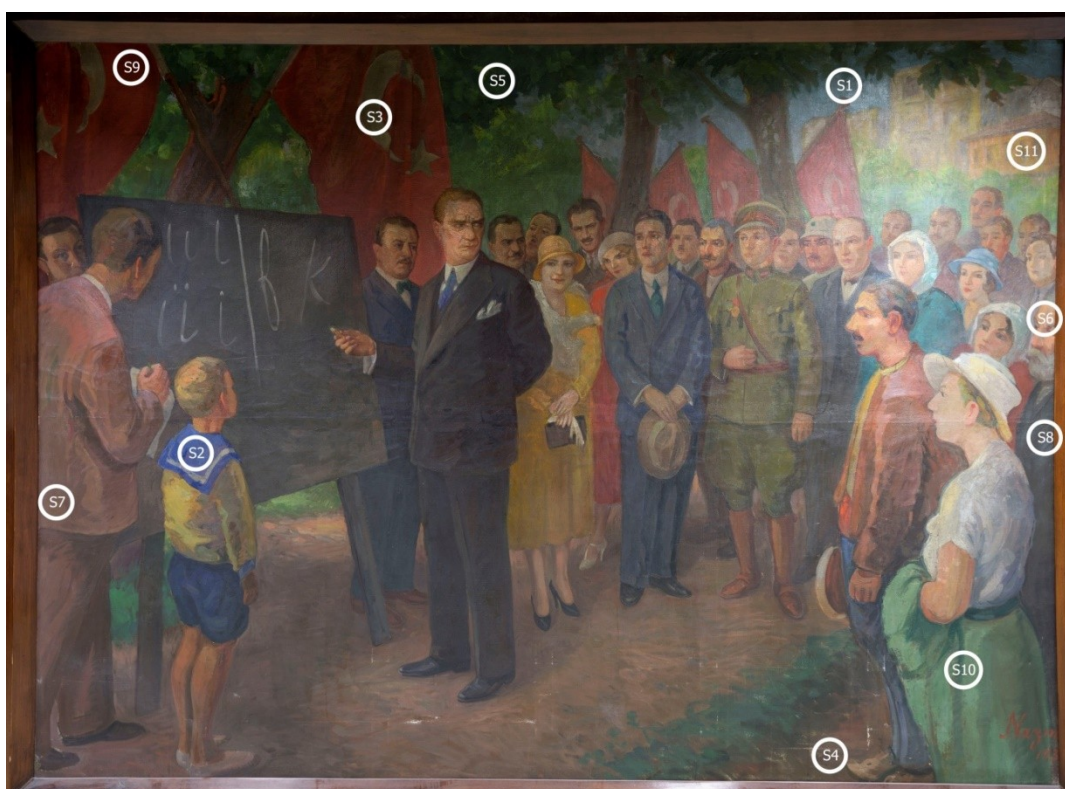


Figure 1. Alphabet Revolution oil paint (by the artist Nazmi Ziya GURAN, 1933).

Infrared-UV Imaging of the Painting

Infrared and UV authentications were as described in earlier reports (13-16, 30-31). Ambient light photograph of the oil painting was taken using a

Canon 5D Mark III camera. Infrared and ultraviolet images were acquired with an OptoLab camera for the documentation process. The images are shown in Figure 2a and 2b, respectively.

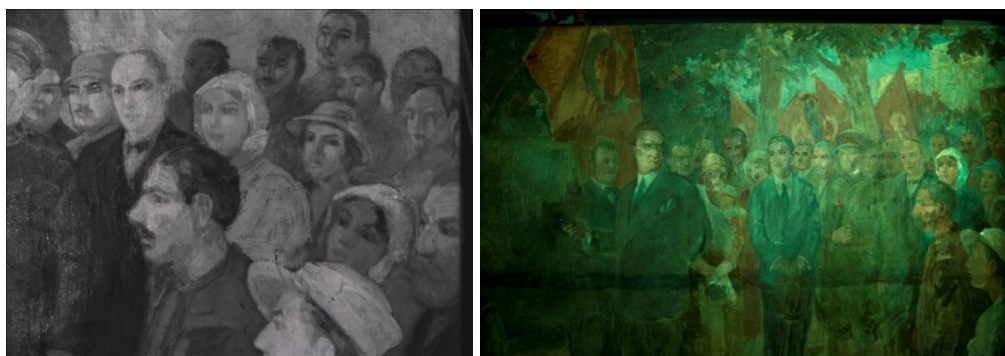


Figure 2. a) IR image (left) and b) UV image (right) of Alphabet Revolution oil paint.

Color Measurements

The color measurements were as described in earlier reports (32-35). The L^* , a^* and b^* values for the paintings were measured with a Konica Minolta CM 700d spectrophotometer.

HPLC

The HPLC analysis of the pigments was performed as described in earlier reports (36-39). Acetonitrile-water and water-trifluoroacetic acid were used as the mobile phase. Purpurin and alizarin were used as references.

SEM-EDX

SEM-EDX analysis was performed according to an earlier work (34). A Tescan Vega 3 Easy probe SEM with a Bruker 410-M EDX detector and Esprit 1.9 software was used to characterize the morphology of the canvas and other components. SEM-EDX instrumental conditions were a working distance of 8.05-16 mm and energies of 5-20 kV at a magnification of 100 to 800. Back scatter detectors were used for secondary electrons with a 30s collection time.

FTIR-ATR

The FTIR-ATR analysis was conducted as described in earlier reports (40-42). For the analyses of pigments and binders, the ATR-FTIR technique was applied. The analyses were performed with UATR Accessory for Spectrum Two, Diamond (1 Reflection) FTIR spectrometer (Perkin Elmer Diamond /ZnSe). A total of 60 scans were collected in the 4000 - 400 cm^{-1} spectral range, while the resolution employed was 4 cm^{-1} .

RESULTS AND DISCUSSION

Color Analysis

The color measurement results supply an important information of the color palette of the artist and it is vital for restorative purposes. During the restoration process, the color palette can be prepared according to the L^* , a^* and b^* values of the painting. Here L^* expresses white or black color (0-100); a^* expresses red ($a^>0$) or green ($a^<0$) color and b^* expresses yellow ($b^>0$) or blue ($b^<0$) color. The color measurement results of the painting samples with the CIE $L^*a^*b^*$ are shown in Table 1. When restorers and conservators need to restore artworks, these values can be used (18, 43, 44).

SEM-EDX Analysis

In order to determine the elemental components of cultural heritage artifacts, SEM-EDX technique is used. SEM images were obtained for the samples taken from the predetermined areas of the painting shown in Figure 1. Also SEM-EDX measurements were carried out. SEM image that belongs to the canvas of the painting is shown in Figure 3. It is seen that the canvas has fibers from plant origin either from flax or hemp (45). FTIR analysis was also carried out on the same canvas and standard flaxseed fibers as shown in Figure 4. As a result of comparison between the canvas and standard flax fibers, it was seen that the bands are in compliance with each other and it was decided that canvas was made of flax. According to the results of element analysis for the oil painting samples shown in Table 2, the main elements were found in these samples are Pb, Cd, Ba, Zn, Fe and Al metals.

Table 1. Color measurement results of all samples.

Sample	L^*	a^*	b^*
S1	60.68	-8.03	-2.65
S2	40.95	1.51	-25.51
S3	43.11	3.53	11.07
S4	34.80	2.87	7.00
S5	38.42	-12.26	12.50
S6	56.81	16.90	27.41
S7	40.20	6.01	8.30
S8	31.29	-1.82	1.64
S9	32.91	14.44	7.99
S10	41.41	-10.25	12.39
S11	59.28	7.87	20.12

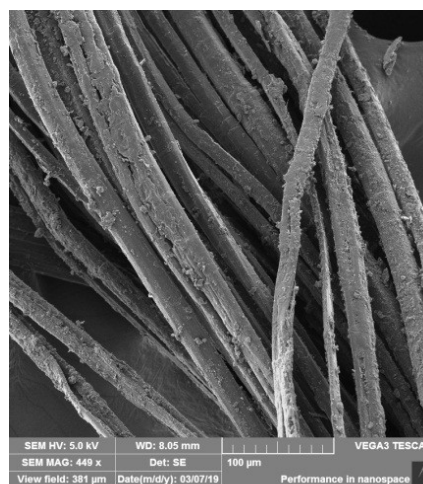


Figure 3. SEM image of the canvas in the Alphabet Revolution oil paint.

FTIR-ATR Analysis

FTIR was used to characterize the molecular composition of the selected paint samples and gain some information on the degree of hydrolysis of the paint. IR spectra of all samples are presented in Figure 5. The main bands detected in the FTIR-ATR spectra of the samples are summarized in Table 3. It can be seen from the FTIR spectra of the samples that the samples have organic and inorganic components which mean that the samples contain pigments and binder. Based on the FTIR data the binder of the painting was identified as linseed oil while it is thought that dammar resin was used as a varnish. The FTIR spectrum of reference linseed oil is presented in Figure 6. When Table 3 and the FTIR spectrum of the reference linseed oil in this figure are examined, the presence of common bands (2900-2800 cm^{-1} , 1700-1750 cm^{-1} , 1450-1550 cm^{-1} , 1000-1200 cm^{-1}) indicated that the binder in the samples is linseed oil. According to IR results of all samples -except canvas; the surface the painting layer is thought that covered by dammar varnish, as it is indicated by main absorption bands at 1700-1750, 1450-1550, 1350-1400 cm^{-1} (13,17-18).

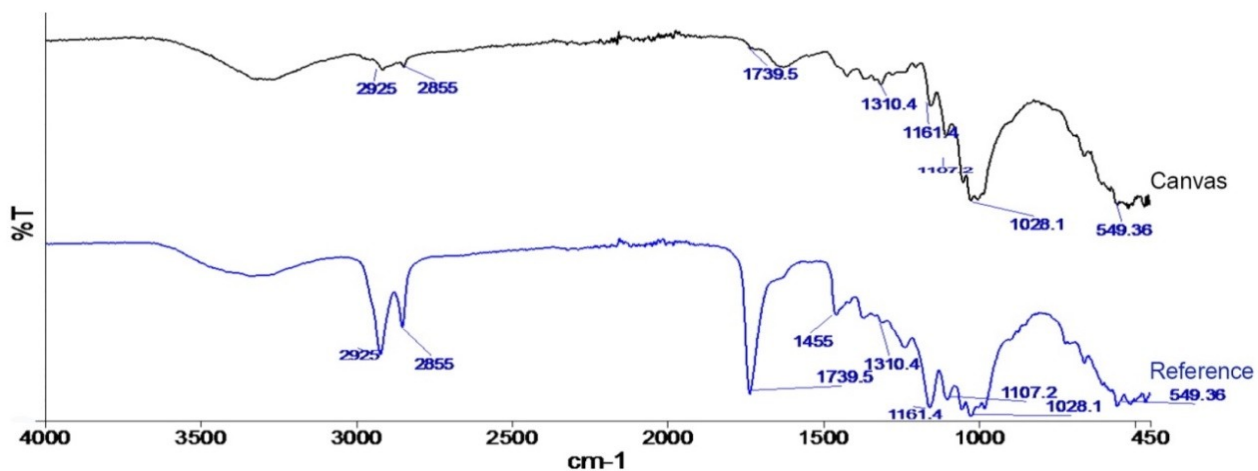
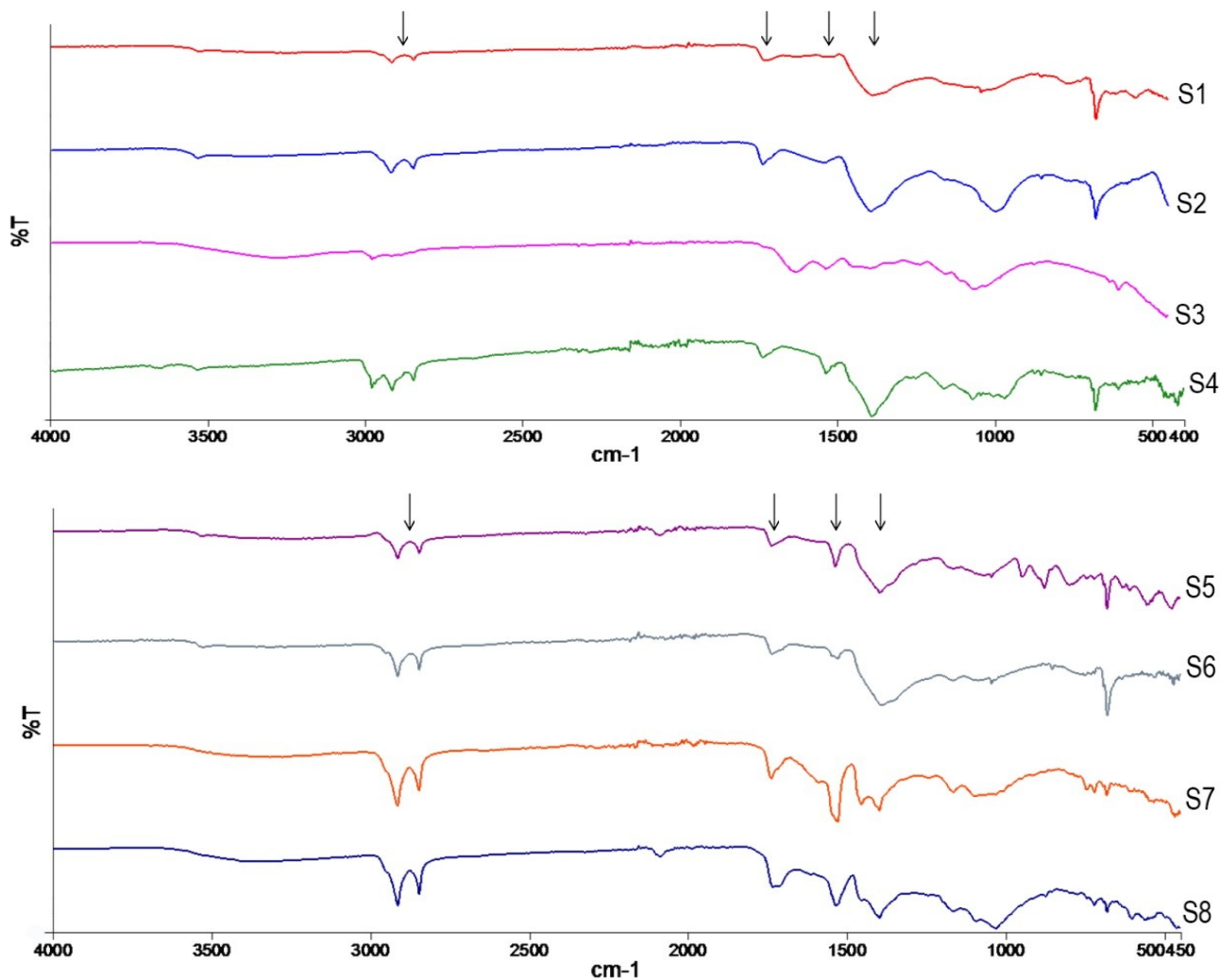


Figure 4. FTIR-ATR spectra of the canvas with paint on it in the Alphabet Revolution oil painting and the reference sample which was prepared by applying linseed oil on the linen canvas.



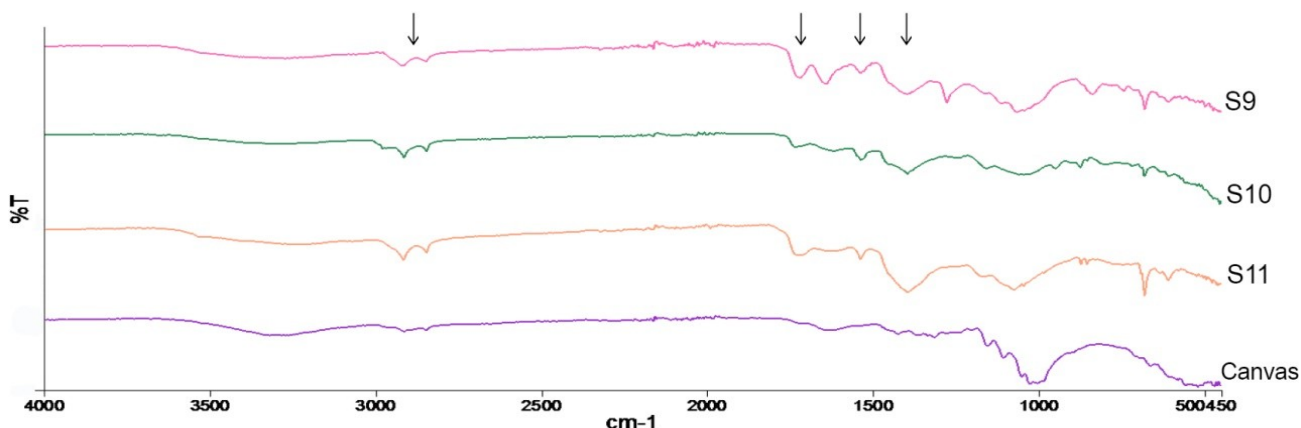


Figure 5. ATR-FTIR comparisons of all the samples in the Alphabet Revolution oil paint.

Table 3. FTIR analyses results: Characteristic bands in all samples in the 400-4000 region.

Sample	Bond type						
	O-H (cm ⁻¹)	C=O ester bond (cm ⁻¹)	C-H (cm ⁻¹)	C-O (cm ⁻¹)	CO ₃ ⁻² Carbonate (cm ⁻¹)	COOH Carboxylic acid (cm ⁻¹)	COO- carboxylate Fatty acid (cm ⁻¹)
S1	-	1729	2845-2917	1043	1389	-	-
S2	-	1734	-	997	1395	2500-3500	1535
S3	3537	1733	2848-2913	-	1393	-	1514
S4	-	1737	2848-2913	-	1391	-	1531
S5	-	1739	2848-2917	-	1395	-	1536
S6	3534	1738	2849-2917	-	1390	-	1530
S7	-	1736	2851-2917	-	1397	-	1529
S8	3300	1734	2849-2916	-	1397	-	1535
S9	3355	1734	2850-2923	1044	1402	-	1531
S10	-	1732	2851-2920	1040	1395	-	1542
S11	-	1727	2849-2918	-	1394	-	1539
Canvas	3265- 3320	-	2851-2920	1025	1312 1424	-	-

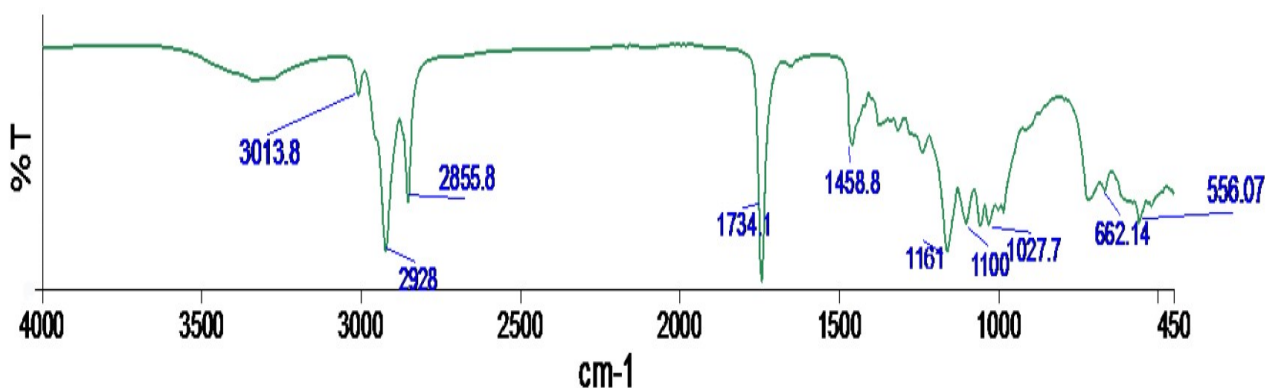


Figure 6. FTIR-ATR spectra of the reference Linseed Oil.

Table 2. SEM-EDX analysis results of all samples in the Alphabet Revolution oil paint.

Sample	Color	Elements and Percentages (%)																
		C	O	Na	Mg	Al	Si	P	S	K	Ca	Cr	Fe	Co	Zn	Cd	Ba	Pb
S1	Blue	21.95	20.08	0.51	-	0.32	-	-	-	-	-	0.91	-	-	1.33	-	-	54.91
S2	Blue	36.41	30.46	1.90	0.56	2.43	2.27	-	2.55	-	0.04	-	-	-	0.81	-	-	22.56
S3	White	37.56	26.76	-	-	0.23	0.10	-	2.97	0.03	0.29	--	-	-	26.97	-	4.97	0.72
S4	Brown	34.51	30.84	1.72	0.71	2.39	4.25	0.14	3.93	1.06	6.29	-	2.13	-	1.73	-	1.73	8.57
S5	Green	20.92	18.21	0.81	-	0.43	-	-	0.86	1.42	0.38	6.12	0.55	-	8.13	-	1.18	41.00
S6	Flesh color	9.99	11.63	0.33	-	0.86	-	-	1.25	0.02	0.31	-	-	-	1.29	1.17	0.04	72.80
S7	Brown	42.46	16.69	0.87	-	0.98	0.65	-	0.61	-	0.58	-	2.61	-	1.13	0.16	-	33.27
S8	Black	52.18	24.76	0.75	-	0.67	0.38	0.14	0.67	-	1.02	0.67	0.89	-	1.60	1.26	0.46	14.12
S9	Red	39.69	25.20	0.36	0.18	0.58	0.41	-	2.11	0.25	1.85	-	0.35	-	2.15	0.59	0.09	26.19
S10	Green	34.79	24.26	0.63	-	0.19	0.07	-	0.34	0.80	1.47	4.93	0.28	0.31	8.49	-	0.04	23.39
S11	Yellow	21.59	14.57	0.19	-	0.51	-	-	2.67	0.08	1.63	-	0.07	-	4.65	6.74	1.28	46.04

HPLC analysis

Samples 1, 2, and 9 were subjected to HPLC analysis. We could not be able to detect any organic dyes for samples 1 and 2. However, for sample 9 we successfully determined the presence of alizarine and purpurin pigments.

The full HPLC chromatogram of sample 9 is given in Figure 7 and the overlay spectra of alizarine and purpurin references with the corresponding spectra at 27.57 and 28.83 minutes in the HPLC chromatogram of sample 9 are presented in Figure 8 and 9, respectively.

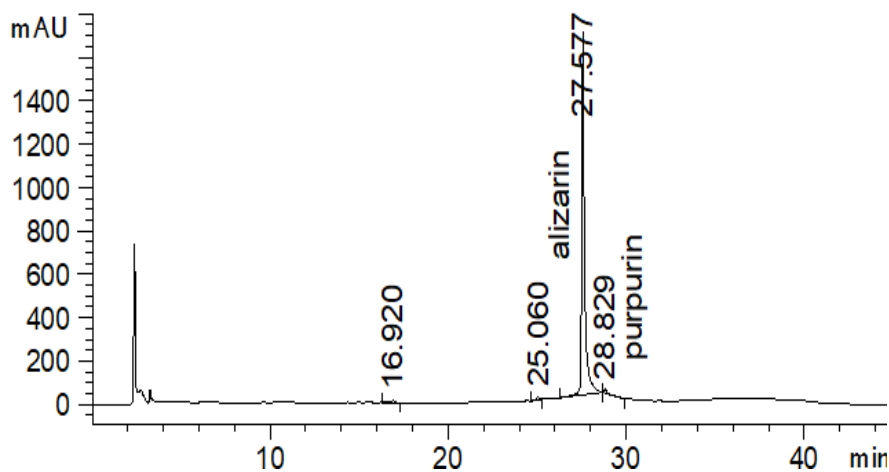


Figure 7. HPLC Chromatogram of sample 9.

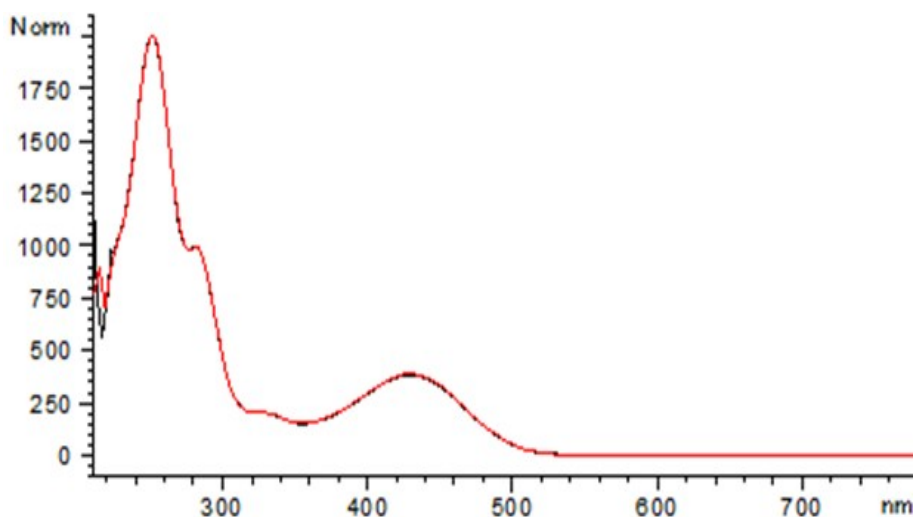


Figure 8. Comparison of the spectrum of alizarin dyestuff with the spectrum obtained at retention time at 27.57 minutes for sample 9. (red line: reference alizarin; black line: sample 9.)

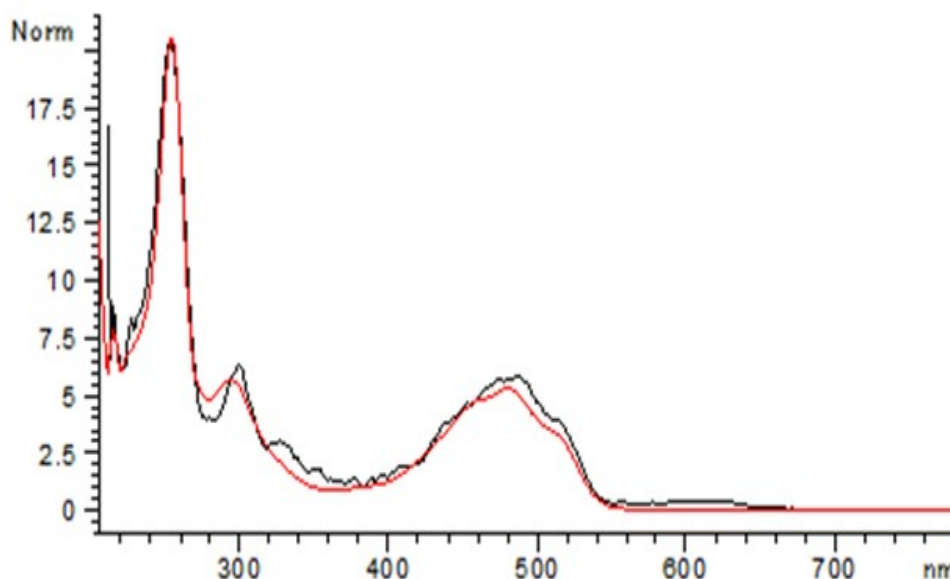


Figure 9. Comparison of the spectrum of purpurin dyestuff with the spectrum obtained at retention time at 28.83 minutes for sample 9. (**red line:** reference purpurin; **black line:** sample 9.)

General Evaluation of the Results

Based on the FTIR-ATR, HPLC analyses and the SEM-EDX results the main components of the samples were determined as follows:

Part S1: SEM-EDX results showed the presence of Pb, Zn, and Cr. Based on FTIR spectrum the presence of CO_3^{2-} vibrations at 1389 cm^{-1} and the green color of this section, the pigments in this region can be PbCO_3 , ZnO and Cr_2O_3 . The band at 678 cm^{-1} is also a characteristic peak for PbCO_3 (7). Moreover, band at 2917 and 2845 cm^{-1} which are attributed to stretching of C-H groups of the binder and a band at 1729 cm^{-1} which is due to characteristic ester carbonyl were detected in this sample. These findings show that an oil based binder could be used in the painting.

Part S2: In the FTIR spectrum of this sample, a broad band between 3500 and 2500 cm^{-1} indicates the presence of carboxylic acid groups which can be attributed the hydrolysis of the oil based binder (46) due to aging. Other important bands in this spectrum can be listed as follows: Ester (RCOOR) band at 1734 cm^{-1} , CO_3^{2-} band at 1395 cm^{-1} (PbCO_3), C-O at 997 cm^{-1} , which is a characteristic peak for ultramarine blue (21) and the band at 679 cm^{-1} (PbCO_3). According to the SEM-EDX result of sample 2; Na, Ca, Al, Si, S, O elements were found and no organic dyes were found according to HPLC analysis. The FTIR result of sample 2 is considered to be consistent with the FTIR results of reference ultramarine blue (21, 47) and the sample is thought to be synthetic ultramarine blue ($\text{Na}_{6-10}\text{Al}_6\text{Si}_6\text{O}_{24}\text{S}_{2-4}$) (24).

Part S3: The important bands in the FTIR spectrum for this sample were determined as follows: -OH band at 3537 cm^{-1} , C-H stretching vibrations at 2918 and 2848 cm^{-1} , ester

(RCOOR) band at 1733 cm^{-1} , carboxylate COO-band at 1514 cm^{-1} (which may suggest palmitate oil), 1393 cm^{-1} and 679 cm^{-1} for PbCO_3 , and Zn-O at 767 cm^{-1} (48). EDX revealed the existence of Pb, Zn, Ba elements in this sample. The white color and these findings suggest the presence of Zinc White (ZnO), Barium White (BaSO_4) and Lead White (PbCO_3) pigments.

Part S4: This sample produced a similar FTIR spectrum to samples above. It was found to contain Ca, Fe, Pb, Zn and Ba according to EDX results. The brown color of this region indicates the presence of Fe_2O_3 (hematite) (49) pigment in addition to others such as Zinc White (ZnO), Barium White (BaSO_4) and Lead White (PbCO_3). The presence of Ca could be attributed to presence of Gypsum ($\text{CaSO}_4 \cdot 2\text{H}_2\text{O}$).

Part S5: Different than other spectra Cr-O band 476 cm^{-1} was detected in this sample (22), and the presence of Cr was also confirmed by EDX measurements.

Part S6: In addition to organic groups the presence of lead was proved by FTIR analysis for this sample. Similar band were found for this sample as detailed above. EDX revealed the presence of S, Pb, Cd and Zn for this sample. Based on these findings we suggest that a blend of CdS yellow and Zn-Pb white were used to obtain flesh color.

Part S7: The FTIR and EDX results suggest that Fe_2O_3 , CdS yellow and white pigments were mixed to obtain the brown color on this region.

Part S8: The EDX results for this sample gave the highest carbon percentage among other samples. Therefore, the black color of this region is attributed to the presence of carbon black.

Part S9: HPLC result for this sample showed the presence of organic pigments. Madder lacquer dye (*Rubia tinctorum* L.) and a mixture of CdS yellow, Fe₂O₃ and Pb-Zn white inorganic pigments were found.

Part S10: The main pigment for this green colored region was found as Chromium oxide green. Other spectral evidence show that it is mixed with white pigments and gypsum as well as oil based binder.

Part S11: In addition to similar FTIR bands in all samples a band at 601 cm⁻¹ was detected in the fingerprint region of the FTIR spectrum of this sample. This band is consistent with the

reference band of CdS (3). Based on this FTIR result and EDX findings for this sample, it can be said that CdS yellow pigment and white pigments were used for the yellow color of this region.

Canvas: The following bands were detected in the FTIR spectrum of the canvas: at 3265-3320 cm⁻¹ (-OH band), 2851 cm⁻¹, 2920 cm⁻¹, 1621 cm⁻¹ (-C=O band), 1424-1321 cm⁻¹ (CO₃²⁻) and 1025 cm⁻¹ (C-O). As can be seen from Figure 4, this FTIR spectrum is very similar to the reference spectrum (linen).

Based on all these findings and evaluations the pigments found in the selected sections of the painting are listed in Table 4.

Table 4. Identified pigments in the Alphabet reform painting.

Sample	Color	Detected Pigments
S1	GREEN	Lead White (PbCO ₃) Zinc White (ZnO) Chromium oxide green (Cr ₂ O ₃)
S2	BLUE	Lead White (PbCO ₃) Zinc White (ZnO) Ultramarine blue (Na ₆₋₁₀ Al ₆ Si ₆ O ₂₄ S ₂₋₄)
S3	WHITE	Zinc White (ZnO) Barium White (BaSO ₄) Lead White (PbCO ₃)
S4	BROWN	Zinc White (ZnO) Barium White (BaSO ₄) Lead White (PbCO ₃) Gypsum (CaSO ₄ .2H ₂ O) Iron oxide (Fe ₂ O ₃)
S5	GREEN	Lead White (PbCO ₃) Zinc White (ZnO) Barium White (BaSO ₄) Chromium oxide green (Cr ₂ O ₃)
S6	FLESH COLOR	Lead Red (PbO ₂ .2PbO) Lead White (PbCO ₃) Zinc White (ZnO) Cadmium yellow (CdS)
S7	BROWN	Lead White (PbCO ₃) Zinc White (ZnO) Iron oxide (Fe ₂ O ₃) Cadmium yellow (CdS)
S8	BLACK	Lead White (PbCO ₃) Zinc White (ZnO) Barium White (BaSO ₄) Gypsum (CaSO ₄ .2H ₂ O) Chromium oxide green (Cr ₂ O ₃) Cadmium yellow (CdS) Iron oxide (Fe ₂ O ₃)
S9	RED	Madder (<i>Rubia tinctorum</i> L.) lake Lead White (PbCO ₃) Zinc White (ZnO) Gypsum (CaSO ₄ .2H ₂ O) Cadmium yellow (CdS) Iron oxide (Fe ₂ O ₃)
S10	GREEN	Lead White (PbCO ₃) Zinc White (ZnO) Gypsum (CaSO ₄ .2H ₂ O) Chromium oxide green (Cr ₂ O ₃) Iron oxide (Fe ₂ O ₃)
S11	YELLOW	Lead White (PbCO ₃) Zinc White (ZnO) Barium White (BaSO ₄) Gypsum (CaSO ₄ .2H ₂ O) Cadmium yellow (CdS)

CONCLUSION

In this work, the Alphabet Reform painting was analyzed by ATR-FTIR, SEM-EDX and HPLC-DAD analysis methods. The CIE L*a*b* values were also identified. Both organic and inorganic structures, pigments, binders (linseed oil), auxiliary driers (Ca and K elements) and the type of the canvas (linen) used were identified. Red alizarin (madder lake organic pigment) and dark blue ultramarine pigments were detected as the organic pigments while CdS (yellow), Pb red (flesh color), PbCO₃ (white), ZnO (white), BaSO₄ (white), FeO (brown) and Cr₂O₃ (green color) were detected as the inorganic ones.

These results will provide some guidelines for restorers and conservators during restoration and conservation processes. Restorers can apply patching according to the type of canvas. Retouch applications can be easily applied since dyes and pigments are identified. According to the chemical properties of organic and inorganic substances detected on the surface, this study also provides a guidance in the selection of suitable surfactants and solvents for cleaning.

Funding

This work was supported by Marmara University, Commission of Scientific Research Project (M.U. BAPKO) under grant FEN-C-DRP-101018-0537.

CONFLICT OF INTEREST : The authors declare no competing interests.

ACKNOWLEDGMENTS

We would like to thank to Instructor Abdulkadir Pars from the Faculty of Technology at Marmara University for his support on FTIR analysis.

REFERENCES

- Lomax SQ. Phthalocyanine and quinacridone pigments: their history, properties and use. *Studies in Conservation*. 2005 ; 50:sup-1. 19-29. doi: <https://doi.org/10.1179/sic.2005.50.Supplement-1.19>
- Weerd JV, Loon AV, Boon JJ. FTIR studies of the effects of pigments on the aging of oil. *Studies in conservation*. 2005; 50:1, 3-22. doi: <https://doi.org/10.1179/sic.2005.50.1.3>.
- Feller Robert L, editor. *Artists' Pigments A handbook of their history and characteristics* Volume 1. London: National Gallery of Art, Washington Archetype Publications; 2012.
- Roy A, editor. *Artists' Pigments A handbook of their history and characteristics* Volume 2. London: National Gallery of Art, Washington Archetype Publications; 2012.
- Fitzhugh EW, editor. *Artists' Pigments A handbook of their history and characteristics* Volume 3. London: National Gallery of Art, Washington Archetype Publications; 2012.
- Kasiri MB, Bbaylou AN, Zandkarimi H. Photo-oxidative stability of a series of red acrylic paints. *Progress in color, colorants and coatings*. 2014; 177-85. doi: <https://doi.org/https://dx.doi.org/10.30509/pccc.2013.75834>.
- Zelinska J, Kopecka I, Svobodova E, Milovska S, Hurai V. Stratigraphic EM-EDS, XRF, Raman and FT-IR analysis of multilayer paintings from the Main Altar of the St. James Church in Levoca (Slovakia). *Journal of Cultural Heritage*. 2018; 33:90-9. doi: <https://doi.org/10.1016/j.culher.2018.03.006>.
- Nasa J, Nodari L, Nardelli F, Sabatini F, Degano I, Modugno F, et al. Chemistry of modern paint media: The strained and collapsed painting by Alexis Harding. *Microchemical Journal*. 2020 June ; 155:104659. doi: <https://doi.org/10.1016/j.microc.2020.104659>.
- Claro A, Melo MJ, Melo JSS, Berg KJ, Burnstock A, Montague M, et al. Identification of red colorants in van Gogh paintings and ancient Andean textiles by microspectrofluorimetry. *Journal of Cultural Heritage*. 2010; 11(1) :27-34. doi: <https://doi.org/10.1016/j.culher.2009.03.006>.
- Benetti F, Perra G, Damiani D, Atrei A, Marchettini N. ToF-SIMS characterization of proteinaceous binders in the wall painting "Madonna and Child enthroned with Saints" by Ambrogio Lorenzetti in the St. Augustine Church (Siena, Italy). *International Journal of Mass Spectrometry*. 2015 Dec;392:111-7. doi: <https://doi.org/10.1016/j.ijms.2015.09.018>.
- Kaszowska Z, Malek K, Panczyk M, Mikolajaska A. A joint application of ATR-FTIR and SEM imaging with high spatial resolution: Identification and distribution of painting materials and their degradation products in paint cross sections. *Vibrational Spectroscopy*. 2013; 65: 1-11. doi: <https://doi.org/10.1016/j.vibspec.2012.11.018>.
- Melo HP, Cruz AJ, Valadas S, Cardoso AM, Candeias A. The use of glass particles and its consequences in late 16th century oil painting: A Portuguese case based on the analytical results and the technical treatises. *Journal of Cultural Heritage*. 2020 May;43:261-70. Doi: <https://doi.org/10.1016/j.culher.2019.11.001>.
- Iwanicka M, Moretti P, Oudheusden SV, Sylwestrzak M, Cartechini L, Jan van den Berg K, et al. Complementary use of Optical Coherence

- Tomography (OCT) and Reflection FTIR spectroscopy for in-situ non-invasive monitoring of varnish removal from easel paintings. *Microchemical Journal*. 2018; 138: 7-18. doi: <https://doi.org/10.1016/j.microc.2017.12.016>.
14. Rodriguez S H, Appoloni C R, Campos PHOV, Gonçalves B, Kajiya EAM, Molari R, et al. Non-Destructive and portable analyses helping the study and conservation of a Saraceni copper plate painting in the Sao Paulo museum art. *Microchemical Journal*. 2020; 104787. doi: <https://doi.org/10.1016/j.microc.2020.104787>.
15. Costa TG, Silva BFP, Mattos LP, Escorteganha MR, Ritcher FA, Correia MDM, et al. Analysis of the constituent materials of 19th century paintings attributed to Louis-Auguste Moreaux belonging to the Historical Museum of Santa Catarina-Florianopoli, Brazil. *Forensic Chemistry*. 2019; 100177. doi: <https://doi.org/10.1016/j.forc.2019.100177>.
16. Gil M, Manso M, Pessanha S, Manhita A, Cardoso A, Nunes M, et al. Old masters under the microscope. Technical and material comparison of a 17th c. mural and panel painting assigned to Jose de Escovar in Southern Portugal. *Microchemical Journal*. 2020; 104396. <https://doi.org/10.1016/j.microc.2019.104396>.
17. Nevin A, Comelli D, Osticioli I, Toniolo L, Valentini G, Cubeddu R. Assessment of the ageing of triterpenoid paint varnishes using fluorescence, Raman and FTIR spectroscopy. *Analytical and Bioanalytical Chemistry* 2009; 395:2139-2149. doi: <https://doi.org/10.1007/s00216-009-3005-4>.
18. Ciofini D, Striova J, Camaiti M, Siano S. Photo-oxidative kinetics of solvent and oil-based terpenoid varnishes. *Polymer Degradation and Stability*. 2015; 30124-5. doi: <https://doi.org/10.1016/j.polymdegradstab.2015.11.002>.
19. Rie E. The Influence of varnishes on the appearance of paintings. *Studies in Conservation*. 1987; pp.1-13. doi: <https://doi.org/10.1179/sic.1987.32.1.1>.
20. Karadag R, Dolen E. Examination of Historical Textiles With Dyestuff Analyses by TLC and Derivative Spectrophotometry. *Turkish Journal of Chemistry*. 1997; 21: 126-33. Url: <https://journals.tubitak.gov.tr/chem/issues/kim-97-21-2/kim-21-2-9-96058.pdf>.
21. Doleżyńska-Sewerniak E, Klisińska-Kopacz A. A characterization of the palette of Rafał Hadziewicz (1803-1886) through the following techniques: Infrared false colour (IRFC), XRF, FTIR, RS and SEM-EDS. *Journal of Cultural Heritage*. 2019 Mar;36:238-46. doi: <https://doi.org/10.1016/j.culher.2018.09.001>.
22. Vahur S, Teearu A, Leito I. ATR-FT-IR spectroscopy in the region 550-230 cm⁻¹ for identification of inorganic pigments. *Spectrochimica Acta Part A: Molecular and Biomolecular Spectroscopy*. 2010; 75: 1061-72. doi: <https://doi.org/10.1016/j.saa.2009.12.056>.
23. Van Loon A, Boon J.J. Characterization of the deterioration of bone black in the 17th century Oranjezaal paintings using electron-microscopic and micro-spectroscopic imaging techniques. *Spectrochimica Acta Part B* 59. 2004; 1601-9. doi: <https://doi.org/10.1016/j.sab.2004.03.021>.
24. Monico L, Rosi F, Miliani C, Daveri A, Brunetti B. G. Non-invasive identification of metal-oxalate complexes on polychrome artwork surfaces by reflection mid-infrared spectroscopy. *Spectrochimica Acta Part A: Molecular and Biomolecular Spectroscopy* 116. 2013; 270-80. doi: <https://doi.org/10.1016/j.saa.2013.06.084>.
25. Vetter W, Schreiner M. Characterization of pigment-binding media systems-comparison of non-invasive in-situ reflection FTIR with transmission FTIR microscopy. *www.e-PRESERVATIONScience.org* 2011; 8, 10-22. url: https://www.researchgate.net/profile/Manfred_Schreiner/publication/312415149_Identification_and_Preservation_of_Cultural_Heritage/links/5a4f528daca2726172bc8a95/Identification-and-Preservation-of-Cultural-Heritage.pdf.
26. Newman R. Some application of Infrared Spectroscopy in the examination of painting materials. *Journal of the American Institute for Conservation*. 1980;19: 42-62. doi: <https://doi.org/10.1179/019713679806028977>.
27. Zangrando R, Piazza R, Cairns W. R. L, Izzo F.C, Vianello A. Quantitative determination of un-derivatised amino acids in artistic mural paintings using high-performance liquid chromatography/electrospray ionization triple quadrupole mass spectrometry. *Analytica Chimica Acta*. 2010; 675: 1-7. doi: <https://doi.org/10.1016/j.aca.2010.06.045>.
28. Marras S, Pojana G, Ganzerla R, Marcomini A. Study and characterization of mural paintings from XIX century in a noble Venetian (Italy) palace. *Microchemical Journal*. 2010;96: 397-405. doi: <https://doi.org/10.1016/j.microc.2010.07.003>.
29. Costa TG, Ritcher FA, Correia M, Escorteganha MR, Santiago AG. Multi-technical analysis as a tool to investigate structural species in the “replica” of First Mass in Brazil

- painting by Sebastião Vieira Fernandes. *Journal of Molecular Structure*. 2016; 196-204. doi: <https://doi.org/10.1016/j.molstruc.2016.05.019>.
30. Saverwyns S, Currie C, Lamas-Delgado E. Macro X-ray fluorescence scanning (MA-XRF) as tool in the authentication of paintings. *Microchemical Journal*. 2018;137: 139-47. doi: <https://doi.org/10.1016/j.microc.2017.10.008>.
31. Giorgi L, Nevin A, Nodari L, Comelli D, Alberti R. In-situ technical study of modern paintings part 1: The evolution of artistic materials and painting techniques in ten paintings from 1889 to 1940 by Alessandro Milesi (1856-1945). *Spectrochimica Acta Part A: Molecular and Biomolecular Spectroscopy*. 2019;219: 530-8. doi: <https://doi.org/10.1016/j.saa.2019.04.083>.
32. Deveoglu O, Torgan E, Karadag R. The characterization by liquid chromatography of lake pigments prepared from European buckthorn (*Rhamnus cathartica* L.). *Pigment & Resin Technology*. 2012 ; 41: 331-8. doi: <https://doi.org/10.1108/03699421211274234>.
33. Deveoglu O, Erkan G, Torgan, E, Karadag R. The evaluation of procedures for dyeing silk with buckthorn and walloon oak on the basis of colour changes and fastness characteristics. *Coloration Technology*. 2013; 129: 223-31. doi: <https://doi.org/10.1111/cote.12023>.
34. Deveoglu O, Karadag R, Torgan E, Yildiz Y. Examination of dyeing properties of the dyed cotton fabrics with barberry (*Berberis vulgaris* L.). *Journal of Natural Fibers*. 2018;1809-98. 1544-0478. doi: <https://doi.org/10.1080/15440478.2018.1558143>.
35. Yasukava Akemi, Chida Ayumi, Yoji Kato, Kasai Miki. Dyeing silk and cotton fabrics using natural blackcurrants. *Sage Journals*. 2017; 87:2379-87. doi: <https://doi.org/10.1177%2F0040517516671125>.
36. Deveoglu O, Karadag R, Yurdu T. Qualitative HPLC determination of main anthraquinone and lake pigment contents from *dactylopius coccus* dye insect. *Chemistry of Natural Compounds*. 2011; 47: No.1. doi: <https://doi.org/10.1007/s10600-011-9842-3>.
37. Deveoglu O, Torgan E, Karadag R. Identification by RP-HPLC-DAD of natural dyestuffs from lake pigments prepared with a mixture of weld and dyer's oak dye plants. *Journal of Liquid Chromatography & Related Technologies*. 2012; 35: 331-42. doi: <https://doi.org/10.1080/10826076.2011.601487>.
38. Deveoglu O, Cakmakci E, Taskopru T, Torgan E, Karadag R. Identification by RP-HPLC-DAD, FTIR, TGA and FESEM-EDAX of natural pigments prepared from *Datisca cannabina* L. *Dyes and Pigments*. 2012; 94: 437-42. doi: <https://doi.org/10.1016/j.dyepig.2012.02.002>.
39. Karadag R, Torgan E, Taskopru T, Yildiz, Y. Characterization of dyestuffs and metals from selected 16-17th- century ottoman silk brocades by RP-HPLCDAD and FESEM-EDX. *Journal of Liquid Chromatography & Related Technologies*. 2015; 38:5 591-9. doi: <https://doi.org/10.1080/10826076.2014.922476>.
40. Pintus V, Wei S, Schreiner M. Accelerated UV ageing studies of acrylic, alkyd, and polyvinyl acetate paints: Influence of inorganic pigments. *Microchemical Journal*. 2016; 124: 949-61. doi: <https://doi.org/10.1016/j.microc.2015.07.009>.
41. Rosi F, Daveri A, Moretti P, Brunetti BG, Miliani C. Interpretation of mid and near-infrared reflection properties of synthetic polymer paints for the non-invasive assessment of binding media in twentieth-century pictorial artworks. *Microchemical Journal*. 2016; 124: 898-908. doi: <https://doi.org/10.1016/j.microc.2015.08.019>.
42. Banti A, La Nasa J, Tenorio AL, Modugno F, Jan KVD, Ormsby B, et al. A molecular study of modern oil paintings: investigating the role of dicarboxylic acids in the water sensitivity of modern oil paints. *Royal Society of Chemistry Advances*. 2018; 8: 6001-12. doi: <https://doi.org/10.1039/C7RA13364B>.
43. Şahinbaşkan B. Y, Karadag R, Torgan E. Dyeing of silk fabric with natural dyes extracted from cochineal (*Dactylopius coccus* Costa) and gall oak (*Quercus infectoria* Oliver). *Journal of Natural Fibers*. 2017. doi: <https://doi.org/10.1080/15440478.2017.1349708>.
44. Karadag R, Yurdu T. Dyestuff and Colour Analyses of the Seljuk Carpets in Konya Ethnography Museum. The International Institute for Conservation of Historic & Artistic Works. 2010. doi: <https://doi.org/10.1179/sic.2010.55.Supplement-2.178>.
45. Nayak R, Houshyar S, Khandual A, Padhye R, Fergusson S. *Handbook of Natural Fibres (Second Edition) Volume 1: Types, Properties and Factors Affecting Breeding and Cultivation* In: Kozlowski R. M, Talarczyk M. M. (editors). Chapter 14: Identification of natural textile fibres . 2020; pp. 503-34. doi: <https://doi.org/10.1016/B978-0-12-818398-4.00016-5>.
46. Sanches D, Ramos AM, Coelho JFJ, Costa CSF, Vilarigues M, Melo MJ. Correlating thermophysical properties with the molecular composition of 19th century chrome yellow oil paints. *Polymer Degradation and Stability*. 2017; 138: 201-11. doi:

<https://doi.org/10.1016/j.polymdegradstab.2017.02.010>.

47. Izzo FC. 20th Century Artist's Oil Paints; A Chemical-Physical Survey. Thesis for: PhD in Chemical Science-Conservation Science. 2011May. Url: <http://hdl.handle.net/10579/1100>.

48. Maryse M. dottorato di ricerca Application of FTIR microscopy to cultural heritage materials.

2009. doi:

<https://doi.org/10.6092/unibo/amsdottorato/1404>.

49. Delamare F, Guineau B. Les matériaux de la couleur. Paris: Gallimard; 1999. 159 p. (Découvertes Gallimard). Url: <https://www.bcin.ca/bcin/detail.app?id=192315>.



Optimization and Selection of Mobile Phase for the Determination of Multiple Pesticide Standards Using Liquid Chromatography-Tandem Mass Spectrometry

Abubakar Lawal^{1,2*}  and Richard Chee Seng Wong¹ 

¹Department of Chemistry, University of Malaya, Kuala Lumpur, Malaysia.

²Department of Pure and Industrial Chemistry, Umaru Musa Yar'adua University Katsina, Nigeria.

Abstract: The selection of the best mobile phase setup is one of the most important factors to be considered prior to quantitative instrumentation of multiple pesticides. Usually, mobile phases comprises of water (A) and an organic solvent (B) are the setup used in liquid chromatography instruments for the analysis of pesticide residues in various samples. Unfortunately, most of the analyses are being carried out without optimization and selection of the best mobile phase setup to improve the sensitivity of the instrument. For that reason, the comparative analysis of the reportedly used mobile phases and some few suggested ones was carried out on the multi-pesticide mixture of 0.1 mg/kg (100 µg/kg) standard solutions and quantified with liquid chromatography-tandem mass spectrometry (LC-MS/MS) instrument. Consequently, the best mobile phases setup that resulted in the sum of average total chromatographic peak areas (ATCPAs) and average total chromatographic peak heights (ATCPH) for the total ion chromatography (TIC) scans as an index that correspond to the concentration levels was selected [0.1% formic acid in H₂O (A) and 0.1% formic acid in acetonitrile (ACN) (B)]. And further optimization was successfully carried out on the selected mobile phase-A and the resulted setup [1% ACN and 0.1% formic acid in Milli-Q-water (mobile phase A) coupled with 0.1% formic acid in ACN (mobile phase-B)] improved the instrumental sensitivity on the targeted analytes. Thus, this justify the potential benefits of optimizing setup of the mobile phases prior to LC-MS/MS instrumentation of multi-pesticide analytes.

Keywords: Mobile phase, Analysis of multi-pesticide residues, Liquid chromatography-tandem mass spectrometry, Total ion chromatography, Total chromatographic peak areas.

Submitted: August 10, 2020. **Accepted:** January 06, 2021.

Cite this: Lawal A, Wong R. Optimization and Selection of Mobile Phase for the Determination of Multiple Pesticide Standards Using Liquid Chromatography-Tandem Mass Spectrometry. JOTCSA. 2021;8(1):263-78.

DOI: <https://doi.org/10.18596/jotcsa.778786>.

***Corresponding Author. E-mail:** abubakarlawa1360@yahoo.com.

INTRODUCTION

Foods are contaminated through various activities performed by man such as the accidental or intentional discharge of chemicals or waste substances from domestic, industrial and agricultural sites into the environment (1, 2). However, most of these contaminants are non-biodegradable, which can be easily transferred from the ground surface to the underground water because of their ability in dissolving sparingly in water (3, 4). At the long run, the contaminants pollute the foods through their respective circulatory movements in the environment (5). The contaminants include inorganic matters such as

heavy metals (6-8), as well as organic chemicals such as heat-generated compounds [polycyclic aromatic hydrocarbons (PAHs) and acrylamide] (9), organic polymers (bromodiphenyl ethers, chlorobiphenyls, chlorodibenzodioxins, chlorodibenzofurans, etc), mycotoxins (aflatoxins), perfluoroalkyl acids (10-12). Other contaminants with emerge-concerns include phthalates, bisphenol A, alkylphenols (13), phytosterols, estrogens, phytoestrogens (14), pharmaceuticals/veterinary drugs, synthetic dyes and pesticides (15-18).

Advantageously, pesticides have been used in domestic and agricultural practices for decades increasing the gross domestic products (GDP) of

many countries around the globe. But their dangers in handling and excessive usage have been the issues of concern due to their residual accumulations in food chain resulting in many health problems that include cancers, etc. However, there are challenges experienced in the determination of multiple residue of pesticide analytes in food samples. These could be due to extensive ranges of their chemical properties such as neutral, acidic and basic (19), vapor pressure/Henry's law constant (20), solubility (21), partition coefficient in octanol/water ($\log P$) (22) and acid dissociation constant (pK_a) (23). Besides, the analytical samples also play challenging roles for pesticides extraction during sample preparation because of their features that include non-polar, polar, fatty and waxy samples (24, 25).

Even though the conventional methods such as liquid-liquid extraction (LLE), liquid-phase microextraction (LPME) as well as solid phase extraction (SPE) techniques were previously used as the sample preparation methods for the multiple pesticides analysis (16), they possess poor efficiency and selectivity of the targeted, which were their major drawbacks (26). Also, many detectors and quantification instruments were used previously for the analyses of multiple pesticide residues (26). These instruments include the gas chromatography-atomic emission detector (GC-AED) (27) and the high performance liquid chromatography (HPLC) (28). Other instruments include gas chromatography-tandem mass spectrometry (GC-MS/MS) (29) and liquid chromatography-tandem mass spectrometry (LC-MS/MS) (30). Unfortunately, the poor sensitivity of these instruments is their major setbacks. Fortunately, the shortcomings of the conventional sample preparation techniques and that of the detecting and quantifying instruments could be corrected through optimization such as the use of response surface methodology (RSM) (26, 31).

Accordingly, these compel food safety analysts to improve better ways of analyzing multi-pesticide residues in food samples through effective sample preparations and instrumentation techniques. For instance, RSM optimization of the instrumental parameters for LC-MS/MS (advanced) instrument such as the setup of the mobile phases could provide better results of pesticides determination at the lower concentration levels.

Usually, mobile phases comprise of Milli-Q-water (A) and an organic solvent (B) setup are used in the liquid chromatography instruments for the analyses of pesticide residues in various samples of food materials (26, 32, 33). In fact, the organic solvents such as acetonitrile (ACN) and methanol are significantly used in the reverse-phase of liquid chromatography (LC) due to their excellent compatibility (34).

Thus, the aim of this research is to comparatively study the most recently used (reported) setup of mobile phases and some few suggested ones (Table 2). The best mobile phases setup that provided highest average total chromatographic peak area (ATCPA) as an index that correspond to the concentration of analytes in the multi-pesticide mixture of standard solutions was selected after the LC-MS/MS instrumentation.

However, the multi-pesticides mixture of standard solutions of Dursban, Diazinon, Thiamethoxam, Metalaxyl, Thiobencarb, Baycarb, Carbaryl and Propamocarb (Figure 1) were analyzed for the purpose of the mobile phase optimization.

It is, therefore, hoped that the result of this study would serve as a reference guide for the future studies, and the optimized mobile phase setup would be routinely used in LC-MS/MS for the determination of multiple pesticide residues in various food samples.

Table 1: Auto-tuning and Mass-Hunter optimization results of the instrument using the multi-pesticides mixture of standard solutions

Pesticide	MF	MIM	TOP	COC	IM (ESI)	PI	MRM ₁ /MRM ₂	CE ₁ /CE ₂	ART
Dursban (Chlorpyrifos)	C ₉ H ₁₁ Cl ₃ NO ₃ PS	349	Insecticide & Nematicide	Organophosphorus	[M+H] ⁺	350	96.8/197.9	34/22	11.36
Diazinon	C ₁₂ H ₂₁ N ₂ O ₃ PS	304	Insecticide	Organophosphorus	[M+H] ⁺	305	96.9/169.1	42/22	10.22
Thiamethoxam	C ₈ H ₁₀ ClN ₅ O ₃ S	292	Insecticide	Neonicotinoid	[M+H] ⁺	292	132/211	26/10	2.68
Metalaxyl	C ₁₅ H ₂₁ NO ₄	279	Fungicide	Xylylalanine	[M+H] ⁺	280	160.1/220.1	26/10	7.33
Thiobencarb	C ₁₂ H ₁₆ ClNOS	257	Herbicide	Thiocarbamate	[M+H] ⁺	258	89.1/125	54/26	10.34
Baycarb (Fenobucarb)	C ₁₂ H ₁₇ NO ₂	207	Insecticide	Carbamate	[M+H] ⁺	208	77/95	42/10	8.34
Carbaryl	C ₁₂ H ₁₁ NO ₂	201	Insecticide & Nematicide	N-Methyl Carbamate	[M+H] ⁺	202	127.1/145	30/6	7.16
Propamocarb	C ₉ H ₂₀ N ₂ O ₂	188	Fungicide	Other Carbamate	[M+H] ⁺	189	74/102.1	26/14	1.36

PIN, pesticide identity number; MF, molecular formula; MIM, mono-isotopic mass; TOP, type of pesticide; COC, class of chemical; IM, ionization mode; ESI, electrospray ionization; PI, precursor ion (m/z); MRM, multiple reactions monitoring; CE, collision energy (eV); ART, average retention time (min)

Table 2: The list of suggested and reported mobile phases used for the optimization

	References	Water (A)	Organic Mobile Phase (B)
1.	1 st suggested mobile phase	A	ACN
2.	Rajski, Lozano (35), Pérez-Ortega, Gilbert-López (54)	A + 0.1% FA	ACN
3.	, Economou, Botitsi (56) and Lucas (57)	A + 0.1% FA	ACN + 0.1% FA
4.	Vázquez, Lozano (36)	A + 0.1% FA	ACN + 0.1% FA + 5% A
5.	2 nd suggested mobile phase	A	MeOH
6.	Golge and Kabak (58)	A + 5 mM AF	MeOH + 5 mM AF
7.	Zanella, Munaretto (43)	A + 2% MeOH + 0.1% FA + 5 mM AF	MeOH + 0.1% FA + 5 mM AF
8.	3 rd suggested mobile phase	A	MeOH/ACN (1:1)
9.	4 th suggested mobile phase	A + 5 mM AF + 0.1%FA	MeOH/ACN (1:1) + 0.1% FA + 5 mM AF

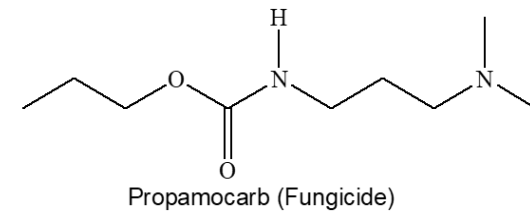
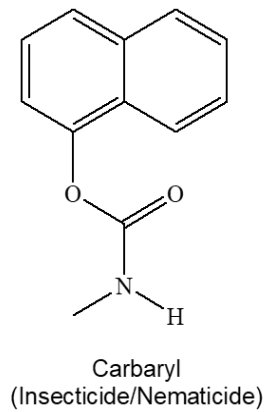
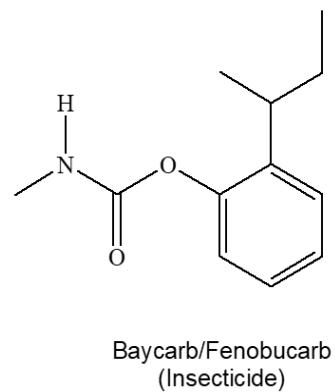
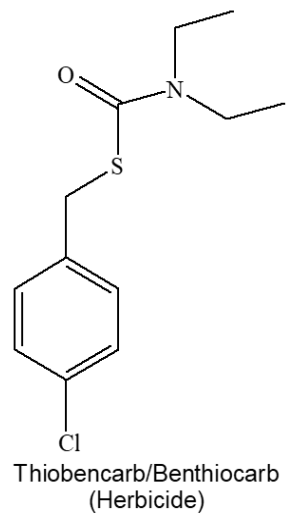
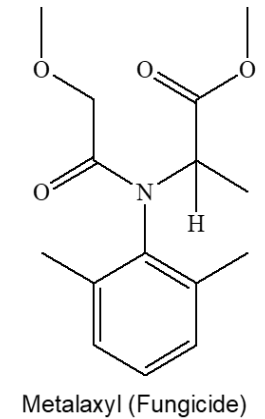
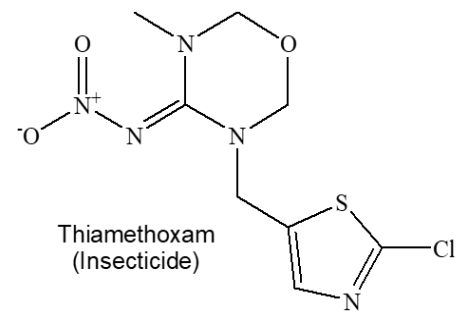
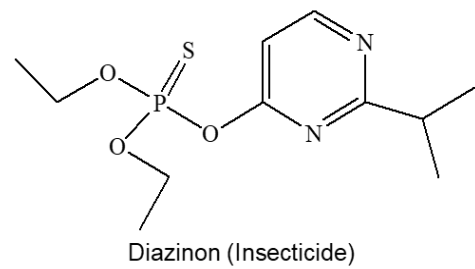
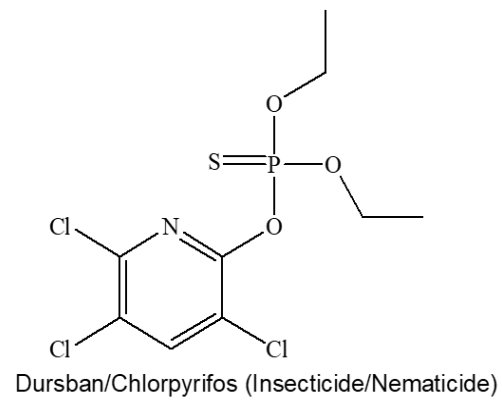


Figure 1: Structural formula of the analyzed pesticide residues

MATERIAL AND METHODS

The chemicals and reagents such as the stock standard solution (100 mg/kg) for pesticide Baycarb,

Carbaryl, Diazinon, Dursban, Metalaxyl, Propamocarb, Thiamethoxam and Thiobencarb were purchased from AccuStandard® (New Haven, USA). The LC-MS grade organic solvents that include ACN and methanol were purchased from Merck (Germany). The formic acid was purchased from Fisher Scientific. The Millipore-filtered (deionized) water was obtained using Merck Millipore water purification system (Billerica, USA). While, the apparatus and equipments that include the 100 and 500 µL microsyringe were purchased from Agilent (Australia). The pH meter PB was purchased from Sartorius group (Germany). The HPLC autosampler vials were purchased from Agilent Technologies (USA). The Supelco HPLC column [Ascentis® Express C₁₈ (5 cm x 2.1 mm, 2.7 µm)] was purchased from Sigma-Aldrich (USA). And the liquid chromatography-tandem mass spectrometry (LC-MS/MS) [triple quadrupole (G6490A) built in Electrospray ESI (±) MS/MS Sensitivity and Jet stream Technology] instrument was purchased from Agilent (Singapore).

Conditioning of the LC-MS/MS

The following contributory parameters of the LC-MS/MS instrument were setup initially that include; analyte injection volume (5 µL), flow rate (0.1 mL/min), column temperature (30 °C), gas temperature (200 °C), nebulizer gas (45 psi), gas flow (14 L/min), sheath gas temperature (400 °C), capillary voltage (3000 V), sheath gas flow (11 L/min), and delta⁽⁺⁾ EMV (200 V). However, these factors contributed in determining optimum fragmentor voltage and the four-fragmentor product ions with their respective retention time (RT) and collision energy (CE) (Table 1). Moreover, the instrumental default settings were further used for the development of the best gradient program runs for the mobile phase-B elution time by adopting and modifying the methods used by Rajski, Lozano (35) and Vázquez, Lozano (36) for analysis of similar multi-pesticide compounds. This results in the best shortest elution time, which provided the best total ion chromatography (TIC) peaks resolution for the LC-MS/MS instrumentation (Figure 2). However, TIC resolution provided an optimum condition for the attainment of higher total chromatographic peak area (TCPA) (37) and mathematically expressed in Equation 1 (38).

Therefore,

$$TCPA = \sum CPA \quad (\text{Eq. 1})$$

Where

TCPA is the total chromatographic peak area and CPA is the chromatographic peak area.

Notably, the best setup of mobile phases were also selected using the initial settings of the instrument. Therefore, the TCPA obtained from LC-MS/MS analysis serves as an index used for estimating the number of target analytes that are present in the analyzed samples (31). It is because of the close similarities range of the resulted peak areas due to the log*P* of targeted analytes. Moreover, the peak areas maybe correlated and categorically suitable for multiple pesticides analysis using the LC-MS/MS instrument (39).

Sample Treatment and Methodology

The stock standard solution of 100 µg/mL that is equivalent to 100 mg/kg (i.e. 100,000 µg/kg) or parts per million (ppm) (40) for each pesticide was diluted to 10, 1 and 0.1 mg/kg (100 µg/kg) with appropriate volumes of methanol. The appropriate volumes were calculated using the dilution formula as expressed in Equation 2 (41), separately. Afterward, the prepared working standard solutions were preserved in a refrigerator at 4 °C before carrying out the LC-MS/MS analysis.

$$C_1 C_2 = V_1 V_2 \quad (\text{Eq. 2})$$

Where

C₁: The concentration of the stock standard solution,

C₂: The concentration of the working standard solution

V₁: The volume of the stock standard solution

V₂: The volume of the working standard solution.

Meanwhile, the selection of the LC-MS/MS mobile phase was carried out by optimization technique using one factor or variable at a time (OFAT or OVAT) based on the documentation of Sherma (42). However, the multivariate optimization technique was not favorable for the selection because responses for each of the mobile phase is required individually without interaction to estimate the actual effect of the mobile phase setup. Moreover, the two setups of mobile (organic and aqueous) phases are involved with interactive percentage flow of organic/aqueous changes to create an optimum condition of analytes detection.

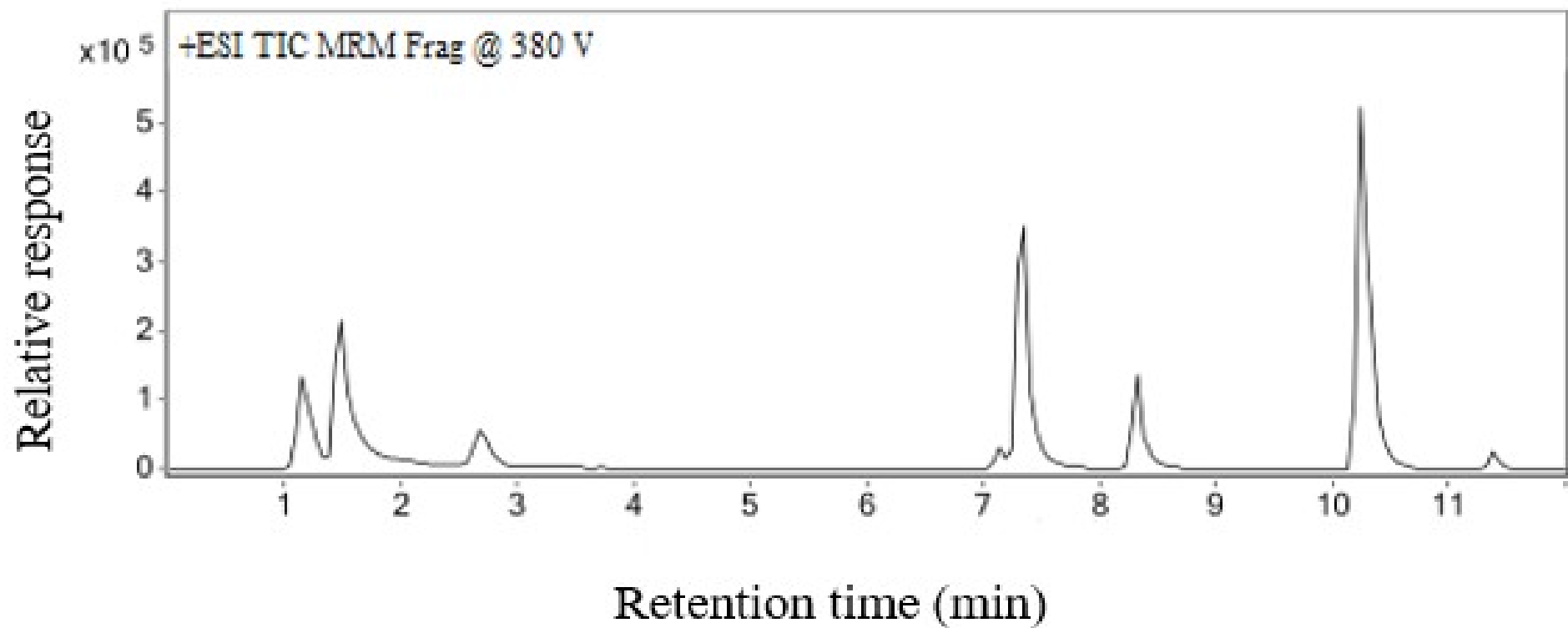


Figure 2: The total ion chromatography (TIC) of the analyzed pesticide standards.

Table 1: Auto-tuning and Mass-Hunter optimization results of the instrument using the multi-pesticides mixture of standard solutions

Pesticide	MF	MIM	TOP	COC	IM (ESI)	PI	MRM ₁ /MRM ₂	CE ₁ /CE ₂	ART
Dursban (Chlorpyrifos)	C ₉ H ₁₁ Cl ₃ NO ₃ PS	349	Insecticide & Nematicide	Organophosphorus	[M+H] ⁺	350	96.8/197.9	34/22	11.36
Diazinon	C ₁₂ H ₂₁ N ₂ O ₃ PS	304	Insecticide	Organophosphorus	[M+H] ⁺	305	96.9/169.1	42/22	10.22
Thiamethoxam	C ₈ H ₁₀ ClN ₅ O ₃ S	292	Insecticide	Neonicotinoid	[M+H] ⁺	292	132/211	26/10	2.68
Metalaxyl	C ₁₅ H ₂₁ NO ₄	279	Fungicide	Xylylalanine	[M+H] ⁺	280	160.1/220.1	26/10	7.33
Thiobencarb	C ₁₂ H ₁₆ ClNOS	257	Herbicide	Thiocarbamate	[M+H] ⁺	258	89.1/125	54/26	10.34
Baycarb (Fenobucarb)	C ₁₂ H ₁₇ NO ₂	207	Insecticide	Carbamate	[M+H] ⁺	208	77/95	42/10	8.34
Carbaryl	C ₁₂ H ₁₁ NO ₂	201	Insecticide & Nematicide	N-Methyl Carbamate	[M+H] ⁺	202	127.1/145	30/6	7.16
Propamocarb	C ₉ H ₂₀ N ₂ O ₂	188	Fungicide	Other Carbamate	[M+H] ⁺	189	74/102.1	26/14	1.36

PIN, pesticide identity number; MF, molecular formula; MIM, mono-isotopic mass; TOP, type of pesticide; COC, class of chemical; IM, ionization mode; ESI, electrospray ionization; PI, precursor ion (m/z); MRM, multiple reactions monitoring; CE, collision energy (eV); ART, average retention time (min)

Thus, comparative analysis was carried out on some assumed and selected mobile phases reportedly used for analysis of pesticides in various samples. Experimentally, the comparative analysis was carried out on the multi-pesticide mixture of 0.1 mg/kg multi-pesticide mixture of standard solutions. Consequently, the TIC of the instrumental runs for each of the mobile phases resulted in chromatographic peak heights (ATCPH), and areas (ATCPAs) as presented in Table 3. Then again, the addition of organic solvent into aqueous mobile phase could provide the optimum condition of $\log P$, which contributes to the attainment of good condition for the multi-pesticide residues analysis in food samples using LC-MS/MS instrument as revealed (43). For this reason, optimization was carried out by serial addition of ACN into the aqueous mobile phase (0.1% FA milli-Q-water). Thus, the mobile phase setup that provided the best separation of analytes and the highest TCPA was selected for further optimization by adding 0, 0.5, 1.0, 1.5, 2.0, 2.5, 3.0, 3.5, 4.0, 4.5, 5.0, 7.5 and 10% ACN in mobile phase A. Moreover, the best pH solution was selected based on the results of the average TCPA responses of the LC-MS/MS instrument.

RESULTS AND DISCUSSION

The responses of the screened mobile phases were compared and recorded. The mobile phase setup [0.1% formic acid in Milli-Q-water (A) and 0.1% formic acid in ACN (B)] was the best based on the highest results obtained [ATCPAs \pm standard deviation (STDEV) as well as ATCPH \pm STDEV] in triplicates as tabulated and illustrated in Table 3 and Figure 3, respectively. This result was also supported by other findings using the mobile phase for pesticides analysis (44, 45). Meanwhile, further optimization result of mobile phase-A after addition of ACN (0 - 10%) revealed that the addition of 1% ACN into 0.1% FA Milli-Q-water at an average pH of 3.50 ± 0.07 STDEV (mobile phase A) coupled with 0.1% FA in ACN at pH 6.56 ± 0.04 STDEV (mobile phase-B) provided the highest ATCPA (Table 4).

The results were supported by their respective pH readings as shown in Table 4 and Figure 4, respectively. Moreover, the retention time (min) of the pesticide analytes were less than the results reported by some literatures such as thiamethoxam, $2.68 < 2.87$ (46); propamocarb, $1.36 < 1.47$ (47); carbaryl, $7.16 < 16.0$ (48); metalaxyl, $7.33 < 17.90$ (49); thiobencarb $10.34 < 10.76$ (50), and dursban, $11.36 < 12.30$ (51). But the retention time (min) of baycarb (8.34) and diazinon (10.22) were more than 6.73 (52) and 7.09 (53) respectively. Fortunately, the optimized mobile phase contributes towards shortening the total run time (min) for the multiple pesticides analysis using the LC-MS/MS instrument.

CONCLUSION

The selection and optimization of the best mobile phase setup was successfully carried out. Eventually, the optimized mobile phase setup [1% ACN and 0.1% FA in Milli-Q-water (mobile phase-A) coupled with 0.1% FA in ACN (mobile phase-B)] improved the instrumental sensitivity on the targeted analytes. Thus, this justify the potential benefits of optimizing setup of the mobile phases prior to LC-MS/MS instrumentation of multi-pesticide analytes. Also, the selected and optimized mobile phase setup could be used for the analysis of other contaminants with similar properties to the analyzed pesticide compounds.

ACKNOWLEDGMENT

The authors acknowledge the Postgraduate Research Project (IPPP) for supporting this research under the grant no. PG 174-2014B, University of Malaya Kuala Lumpur, Malaysia.

CONFLICT OF INTEREST

The authors of this research agreed with no conflicts of interest.

Table 3: The ATCPH and ATCPA Instrumental responses for the selection of mobile phase

Ref codes	References	Water (A)	Organic M/Phase (B)	% M/Phase B	ATCPH \pm STDEV	ATCPA \pm STDEV
A	1 st suggested mobile phase	A	ACN	25	$(361 \pm 2) \times 10^5$	$(47 \pm 3) \times 10^7$
B	Rajski, Lozano (35), Pérez-Ortega, Gilbert-López (54)	A + 0.1% FA	ACN	30	$(349 \pm 3) \times 10^5$	$(46 \pm 1) \times 10^7$
C	, Economou, Botitsi (56) and Lucas (57)	A + 0.1% FA	ACN + 0.1% FA	15	$(50 \pm 1) \times 10^6$	$(72 \pm 9) \times 10^7$
D	Vázquez, Lozano (36)	A + 0.1% FA	ACN + 0.1% FA + 5% A	30	$(31 \pm 2) \times 10^6$	$(38 \pm 1) \times 10^7$
E	2 nd suggested mobile phase	A	MEOH	30	$(17 \pm 1) \times 10^6$	$(23 \pm 2) \times 10^7$
F	Golge and Kabak (58)	A + 5 mM AF	MEOH + 5 mM AF	30	$(26 \pm 2) \times 10^6$	$(30 \pm 1) \times 10^7$
G	Zanella, Munaretto (43)	A + 2% MEOH + 0.1% FA + 5 mM AF	MEOH + 0.1% FA + 5 mM AF	10	$(58 \pm 3) \times 10^6$	$(60 \pm 7) \times 10^7$
H	3 rd suggested mobile phase	A	MEOH/ACN (1:1)	30	$(27 \pm 1) \times 10^6$	$(30 \pm 4) \times 10^7$
I	4 th suggested mobile phase	A + 5 mM AF + 0.1%FA	MEOH/ACN (1:1) + 0.1% FA + 5 mM AF	25	$(36 \pm 5) \times 10^6$	$(32 \pm 3) \times 10^7$

ATCPH, average total chromatographic peak height; ATCPA, average total chromatographic peak area; RT, retention time; AF, ammonium formate; FA, formic acid; STDEV, standard deviation; Ref, reference

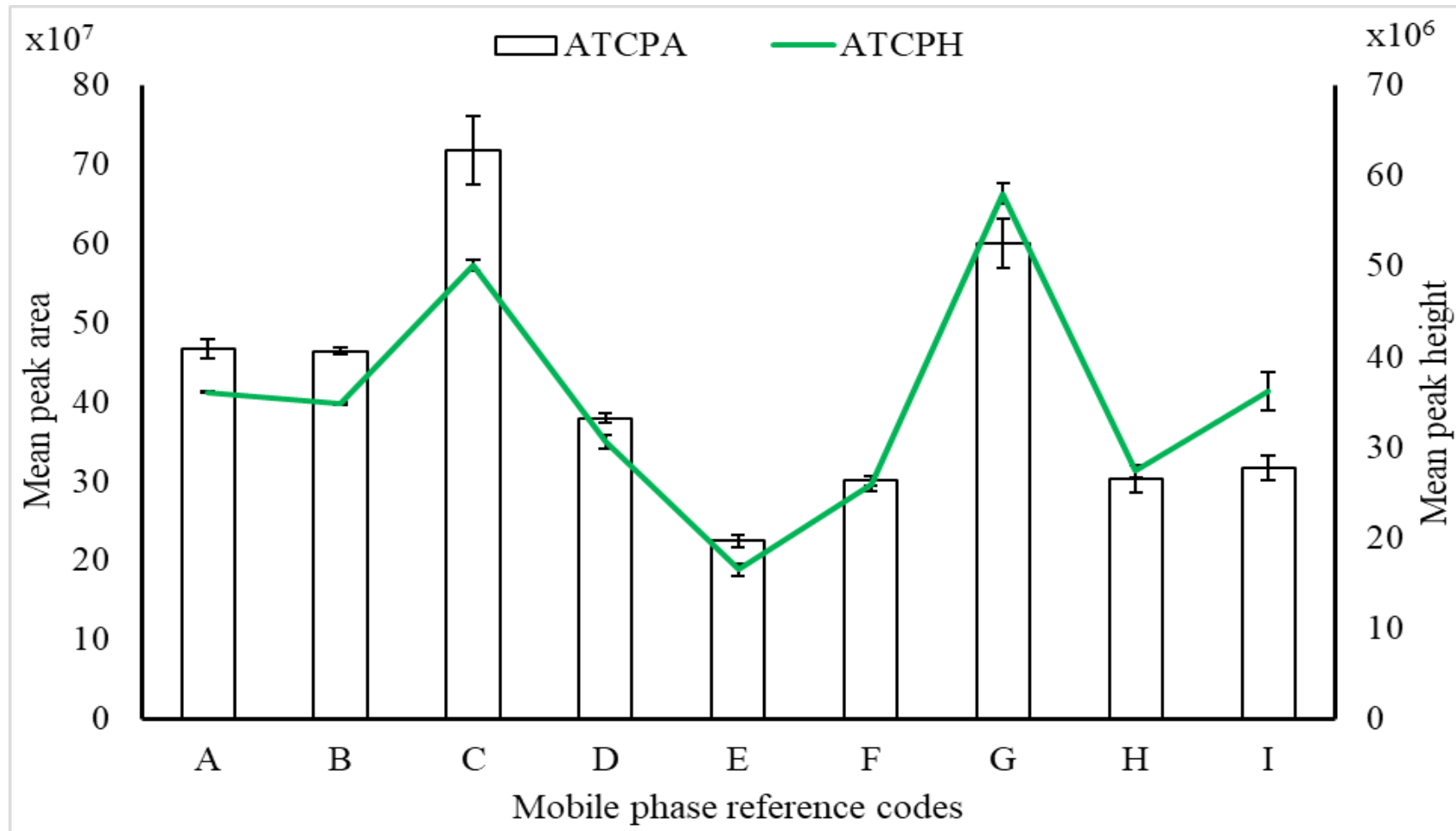


Figure 3: The comparative studies of ATCPA and ATCPH results for the analyzed mobile phases

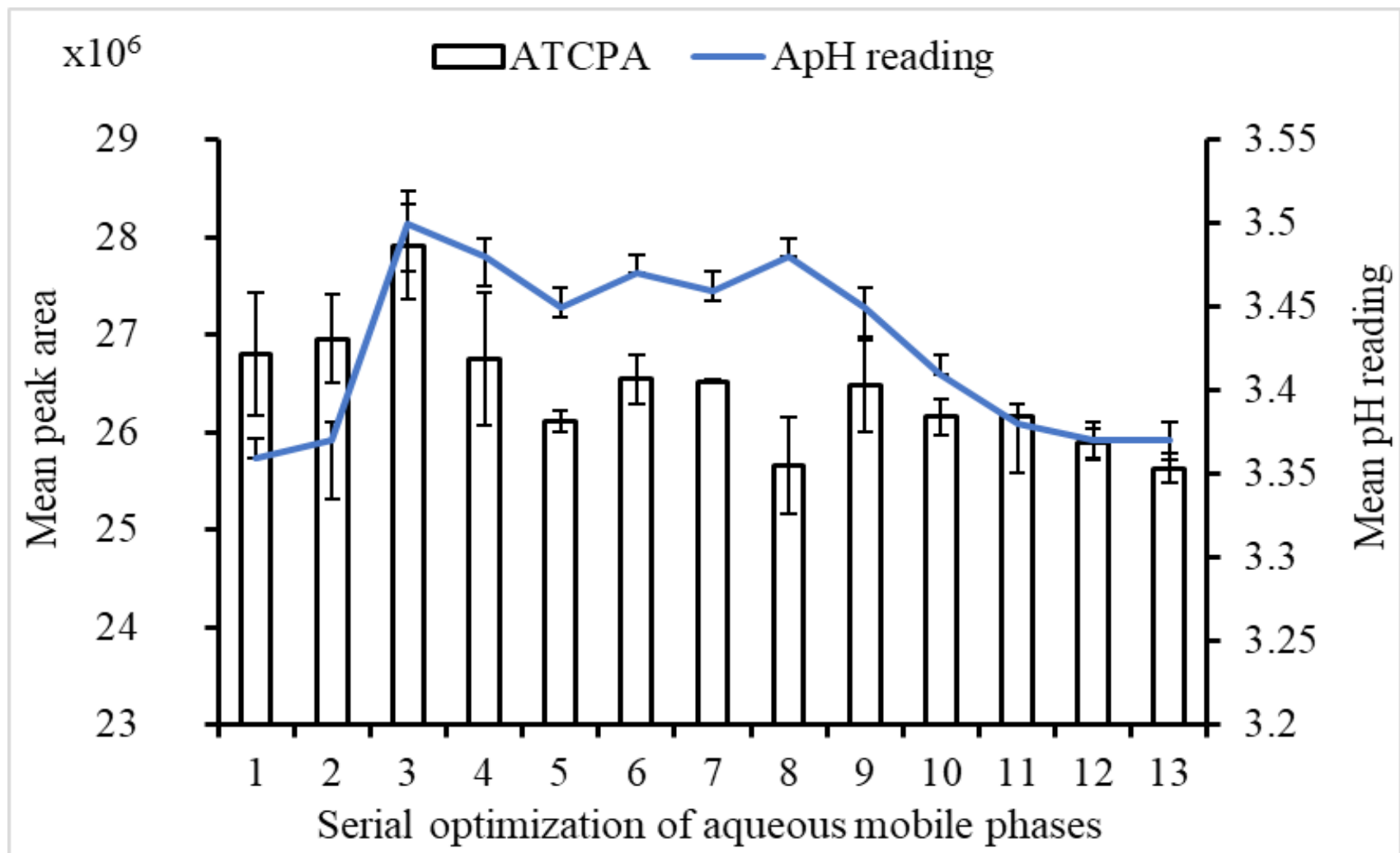


Figure 4: Comparative illustration for the optimization of the selected aqueous mobile phase by ATCPA and ApH readings

Table 4: The Instrumental responses for the optimization of the selected mobile phase

Solution	% ACN in Aqueous Mobile Phase	ApH reading \pm STDEV	Organic Mobile Phase	ATCPA \pm STDEV
1	H ₂ O + 0.1% FA + 0% ACN	3.36 \pm 0.00	ACN + 0.1% FA	(27 \pm 2) \times 10 ⁶
2	H ₂ O + 0.1% FA + 0.5% ACN	3.37 \pm 0.08	ACN + 0.1% FA	(27 \pm 1) \times 10 ⁶
3	H ₂ O + 0.1% FA + 1.0% ACN	3.50 \pm 0.07	ACN + 0.1% FA	(28 \pm 2) \times 10 ⁶
4	H ₂ O + 0.1% FA + 1.5% ACN	3.48 \pm 0.04	ACN + 0.1% FA	(27 \pm 2) \times 10 ⁶
5	H ₂ O + 0.1% FA + 2.0% ACN	3.45 \pm 0.01	ACN + 0.1% FA	(261 \pm 3) \times 10 ⁵
6	H ₂ O + 0.1% FA + 2.5% ACN	3.47 \pm 0.00	ACN + 0.1% FA	(265 \pm 6) \times 10 ⁵
7	H ₂ O + 0.1% FA + 3.0% ACN	3.46 \pm 0.01	ACN + 0.1% FA	(2652 \pm 4) \times 10 ⁴
8	H ₂ O + 0.1% FA + 3.5% ACN	3.48 \pm 0.00	ACN + 0.1% FA	(26 \pm 1) \times 10 ⁶
9	H ₂ O + 0.1% FA + 4.0% ACN	3.45 \pm 0.04	ACN + 0.1% FA	(26 \pm 1) \times 10 ⁶
10	H ₂ O + 0.1% FA + 4.5% ACN	3.41 \pm 0.00	ACN + 0.1% FA	(262 \pm 5) \times 10 ⁵
11	H ₂ O + 0.1% FA + 5.0% ACN	3.38 \pm 0.07	ACN + 0.1% FA	26 \times 10 ⁶ \pm 0
12	H ₂ O + 0.1% FA + 7.5% ACN	3.37 \pm 0.03	ACN + 0.1% FA	(259 \pm 4) \times 10 ⁵
13	H ₂ O + 0.1% FA + 10.0% ACN	3.37 \pm 0.03	ACN + 0.1% FA	(256 \pm 4) \times 10 ⁵

FA, formic acid; ApH, average pH reading; ATCPA, average total chromatographic peak area; STDEV, standard deviation

REFERENCES

1. Chapman PM. Determining when contamination is pollution—weight of evidence determinations for sediments and effluents. *Environment International*. 2007;33(4):492-501.
2. Prasad KD, Ramteke P. Microbial contamination of important food borne pathogens in the production of an aseptically processed mango drink. *Asian Journal of Dairy and Food Research*. 2013;32(1):56-64.
3. McCarthy JF, Zachara JM. Subsurface transport of contaminants. *Environmental science & technology*. 1989;23(5):496-502.
4. Gong Y, Tang J, Zhao D. Application of iron sulfide particles for groundwater and soil remediation: A review. *Water research*. 2016;89:309-20.
5. Lake IR, Hooper L, Abdelhamid A, Bentham G, Boxall AB, Draper A, et al. Climate change and food security: health impacts in developed countries. *Environmental Health Perspectives*. 2012;120(11):1520.
6. Koki IB, Lawal A, Taqui SN. Source identification and evaluation of surface water quality using factor and discriminant analysis. *Bajopas*. 2018;11(2):169-75.
7. Baba A, Garba ST, Bello HS. Bioremediation Potential of Immobilized *Corynebacterium kutscheri* in the Treatment of Tannery Industry Effluent from Challawa Industrial Estate, Kano State, Nigeria. *JOTCSA*. 2020;7(2):335-50.
8. Lawal A. Comparative analysis on selected bulb species. Sokoto, Nigeria: Usmanu Danfodiyo University; 2011.
9. Mohammed AA, Iniaghe PO, Abu TO, Bello MO, Abdulkadir MD. Source Analysis of Heavy Metals and Polycyclic Aromatic Hydrocarbons from a Popular Dumpsite, Lagos State, Nigeria. *JOTCSA*. 2020;7(2):489-504.
10. Chan-Hon-Tong A, Charles M-A, Forhan A, Heude B, Sirot V. Exposure to food contaminants during pregnancy. *Science of the Total Environment*. 2013;458:27-35.
11. Alsharif AMA, Tan GH, Choo YM, Lawal A. Liquid Phase Microextraction for Analysis of Mycotoxins in Food Samples: REVIEW. *Research Journal of Chemical and Environmental Sciences*. 2015;3(6):5-21.
12. Alsharif AMA, Tan GH, Choo Y-M, Lawal A. Efficiency of hollow fiber liquid-phase microextraction chromatography methods in the separation of organic compounds: A review. *Journal of Chromatographic Science*. 2016;1-14.
13. Meador JP, Yeh A, Young G, Gallagher EP. Contaminants of emerging concern in a large temperate estuary. *Environmental Pollution*. 2016;213:254-67.
14. Ribeiro AR, Maia A, Santos M, Tiritan ME, Ribeiro CMR. Occurrence of Natural Contaminants of Emerging Concern in the Douro River Estuary, Portugal. *Archives of environmental contamination and toxicology*. 2016;70(2):361-71.
15. McGrath T, Elliott C, Fodey T. Biosensors for the analysis of microbiological and chemical contaminants in food. *Analytical and bioanalytical chemistry*. 2012;403(1):75-92.
16. Lawal A, Tan GH, Alsharif AMA. Recent Advances in Analysis of Pesticides in Food and Drink Samples Using LPME Techniques Coupled to GC-MS and LC-MS: a Review. *Journal of AOAC International*. 2016;99(6):1383-94.
17. Lawal A, Wong RCS, Tan GH, Abdulra'uf LB, Alsharif AMA. Recent modifications and validation of QuEChERS-dSPE Coupled to LC-MS and GC-MS instruments for determination of pesticide/agrochemical residues in fruits and vegetables. *Journal of chromatographic science*. 2018:1-14.
18. Lawal A, Gwaram NS, Suraj Abdulkarim S. Spectrophotometric determination of Tartrazine in some selected beverages: A case study of Katsina town, Nigeria. *FUDMA Journal of Sciences*. 2020;4(3):685-9.
19. Yang XJ, Du Z, Lin A, Yuan Q, Wan P, Wong C. Simultaneous determination of neutral, basic and acidic pesticides in aquatic environmental matrices by solid-phase extraction and liquid chromatography electrospray ionization mass spectrometry. *Anal Methods*. 2013;5:2083-92.
20. Jantunen LM, Bidleman TF. Temperature dependent Henry's law constant for technical toxaphene. *Chemosphere-Global Change Science*. 2000;2(2):225-31.
21. Hijosa-Valsero M, Bécares E, Fernández-Aláez C, Fernández-Aláez M, Mayo R, Jiménez JJ. Chemical pollution in inland shallow lakes in the Mediterranean region (NW Spain): PAHs, insecticides and herbicides in water and sediments. *Science of the Total Environment*. 2016;544:797-810.
22. Mamy L, Patureau D, Barriuso E, Bedos C, Bessac F, Louchart X, et al. Prediction of the Fate of Organic Compounds in the Environment From Their Molecular Properties: A Review. *Critical Reviews in*

- Environmental Science and Technology. 2015;45:1277-377.
23. Kortum G, Vogel W, Andrussov K. Dissociation constants of organic acids and bases. CRC hand book of chemistry and physics. 2000.
24. Orso D, Martins ML, Donato FF, Rizzetti TM, Kemmerich M, Adaime MB, et al. Multiresidue determination of pesticide residues in honey by modified QuEChERS method and gas chromatography with electron capture detection. *Journal of the Brazilian Chemical Society*. 2014;25(8):1355-64.
25. Majors RE. QUEChERS-a new technique for multiresidue analysis of pesticides in foods and agricultural samples. Advanstar Communications 131 W First ST, Duluth, MN 55802 USA; 2007.
26. Lawal A, Wong RCS, Tan GH, Abdulra'uf LB. Determination of Pesticide Residues in Fruit and Vegetables by High-Performance Liquid Chromatography-Tandem Mass Spectrometry with Multivariate Response Surface Methodology. *Analytical Letters*. 2018:1-18.
27. Cook J, Engel M, Wylie P, Quimby B. Multiresidue screening of pesticides in foods using retention time locking, GC-AED, database search, and GC/MS identification. *Journal of aoac international*. 1998;82(2):313-26.
28. Aulakh J, Malik A, Kaur V, Schmitt-Kopplin P. A Review on solid phase micro extraction—high performance liquid chromatography (SPME-HPLC) analysis of pesticides. *Critical Reviews in Analytical Chemistry*. 2005;35(1):71-85.
29. Chang C, Luo J, Chen M, Wu K, Dong T, He X, et al. Determination of twenty organophosphorus pesticides in blood serum by gas chromatography-tandem mass spectrometry. *Analytical Methods*. 2016;8(22):4487-96.
30. Qin Y, Chen L, Yang X, Li S, Wang Y, Tang Y, et al. Multi-residue Method for Determination of Selected Neonicotinoid Insecticides in Traditional Chinese Medicine Using Modified Dispersive Solid-phase Extraction Combined with Ultra-performance Liquid Chromatography Tandem Mass Spectrometry. *Analytical Sciences*. 2015;31(8):823-30.
31. Lawal A, Wong RCS, Tan GH, Abdulra'uf LB, Alsharif AMA. Multi-pesticide Residues Determination in Samples of Fruits and Vegetables Using Chemometrics Approach to QuEChERS-dSPE Coupled with Ionic Liquid-Based DLLME and LC-MS/MS. *Chromatographia*. 2018;81(5):759-68.
32. Lawal A, Koki IB. Determination of Multi - Pesticide Residues in Coconut Water by QuEChERS - dSPE Ionic Liquid - Based DLLME Couple with High Performance Liquid Chromatography-Tandem Mass Spectrometry (LCMS/MS). *ChemSearch Journal*. 2019;10(1):87-93.
33. Lawal A, Abdulra'uf LB. Chemometrics Approach to QuEChERS-dSPE for Multi-Standard Determination of Pesticides in Blank Samples of Milli-Q-Water Using High-Performance Liquid Chromatography-Tandem Mass Spectrometry (LC-MS/MS). *ChemSearch Journal*. 2020;11(1):66 - 73.
34. Anastassiades M, Lehotay SJ, Štajnbaher D, Schenck FJ. Fast and easy multiresidue method employing acetonitrile extraction/partitioning and "dispersive solid-phase extraction" for the determination of pesticide residues in produce. *Journal of AOAC international*. 2003;86(2):412-31.
35. Rajski Ł, Lozano A, Uclés A, Ferrer C, Fernández-Alba AR. Determination of pesticide residues in high oil vegetal commodities by using various multi-residue methods and clean-ups followed by liquid chromatography tandem mass spectrometry. *Journal of Chromatography A*. 2013;1304:109-20.
36. Vázquez PP, Lozano A, Uclés S, Ramos MG, Fernández-Alba A. A sensitive and efficient method for routine pesticide multiresidue analysis in bee pollen samples using gas and liquid chromatography coupled to tandem mass spectrometry. *Journal of Chromatography A*. 2015;1426:161-73.
37. Scientific C. The theory of HPLC. Chromatographic parameters. e-Learning for the Analytical Chemistry Community, LC/GC, Chromacademy. 2014:1-21.
38. Bramston-Cook R. Peak detection with varian star work station for varian 3800 and 450 gas chromatographs Lotus Consulting 5781 Campo Walk Long Beach, USA: Lotus Flower, Inc. ; 2009. p. 1-24.
39. Lazartigues A, Fratta C, Baudot R, Wiest L, Feidt C, Thomas M, et al. Multiresidue method for the determination of 13 pesticides in three environmental matrices: water, sediments and fish muscle. *Talanta*. 2011;85(3):1500-7.
40. Units and concentrations [Internet]. Environmental Protection (Water) Policy 2009. 2018 [cited 24-09-2018]. Available from: <https://www.ehp.qld.gov.au/water/monitoring/sampling-manual/pdf/data-handling-units-and-concentrations.pdf>.
41. How To Find Dilution In Chemistry - Calculate Dilution [Internet]. 2010 [cited 24-09-2018]. Available from: <http://www.tutapoint.com/knowledge-center/view/calculating-dilution/>.
42. Sherma J. Recent advances in thin-layer chromatography of pesticides. *Journal of AOAC International*. 2001;84(4):993-9.

43. Zanella R, Munaretto JS, Martins ML. Determination of Pesticide Multiresidues in Apple, Pear and Grape using modified QuEChERS and analysis by LC-QTOF-MS. Agilent Technologies, Inc. 2013;1-12.
44. Chen M, Yi Q, Hong J, Zhang L, Lin K, Yuan D. Simultaneous determination of 32 antibiotics and 12 pesticides in sediment using ultrasonic-assisted extraction and high performance liquid chromatography-tandem mass spectrometry. *Analytical Methods*. 2015;7(5):1896-905.
45. Pastor-Belda M, Garrido I, Campillo N, Viñas P, Hellín P, Flores P, et al. Determination of spirocyclic tetronic/tetramic acid derivatives and neonicotinoid insecticides in fruits and vegetables by liquid chromatography and mass spectrometry after dispersive liquid-liquid microextraction. *Food chemistry*. 2016;202:389-95.
46. Friedrich MT, Martins ML, Prestes OD, Zanella R. Use of factorial design in the development of multiresidue method for determination of pesticide residues in wheat by liquid chromatography-tandem mass spectrometry. *Food Analytical Methods*. 2016;9(9):2541-51.
47. Martínez-Domínguez G, Nieto-García AJ, Romero-González R, Frenich AG. Application of QuEChERS based method for the determination of pesticides in nutraceutical products (*Camellia sinensis*) by liquid chromatography coupled to triple quadrupole tandem mass spectrometry. *Food chemistry*. 2015;177:182-90.
48. Morais DC, Collins EH, Jardim CH, Fontes ICS. Pesticide determination in sweet peppers using QuEChERS and LC-MS/MS. *Food chemistry*. 2018;249:77-83.
49. Miliadis G, Tsiantas P, Siragakis G. Problems encountered in LC-MS/MS analysis for the determination of pesticide residues in food. *Journal of the Hellenic Veterinary Medical Society*. 2017;68(4):635-40.
50. Rebelo AM, Dolzan MD, Heller M, Deschamps FC, Abate G, Micke GA, et al. Simultaneous determination of herbicides in rice by QuEChERS and LC-MS/MS using matrix-matched calibration. *Journal of the Brazilian Chemical Society*. 2016;27(1):186-93.
51. Bordin AB, Minetto L, Filho IDN, Beal LL, Moura S. Determination of Pesticide Residues in Whole Wheat Flour Using Modified QuEChERS and LC-MS/MS. *Food Analytical Methods*. 2016:1-9.
52. Zheng W, Park J-A, Zhang D, El-Aty AA, Kim S-K, Cho S-H, et al. Determination of fenobucarb residues in animal and aquatic food products using liquid chromatography-tandem mass spectrometry coupled with a QuEChERS extraction method. *Journal of Chromatography B*. 2017;1058:1-7.
53. Lopez SH, Lozano A, Sosa A, Hernando MD, Fernandez-Alba AR. Screening of pesticide residues in honeybee wax comb by LC-ESI-MS/MS. A pilot study. *Chemosphere* 2016;163 44-53.
54. Pérez-Ortega P, Gilbert-López B, García-Reyes JF, Ramos-Martos N, Molina-Díaz A. Generic sample treatment method for simultaneous determination of multiclass pesticides and mycotoxins in wines by liquid chromatography-mass spectrometry. *Journal of Chromatography A*. 2012;1249:32-40.
55. Núñez O, Gallart-Ayala H, Ferrer I, Moyano E, Galceran MT. Strategies for the multi-residue analysis of 100 pesticides by liquid chromatography-triple quadrupole mass spectrometry. *Journal of Chromatography A*. 2012;1249:164-80.
56. Economou A, Botitsi H, Antoniou S, Tsipi D. Determination of multi-class pesticides in wines by solid-phase extraction and liquid chromatography-tandem mass spectrometry. *Journal of Chromatography A*. 2009;1216(31):5856-67.
57. Lucas D. Optimizing Sample Preparation for LC/MS/MS of Pesticide Residues in Herbal Teas. Agilent Technologies, Inc, . 2013:1-14.
58. Golge O, Kabak B. Determination of 115 pesticide residues in oranges by high-performance liquid chromatography-triple-quadrupole mass spectrometry in combination with QuEChERS method. *Journal of Food Composition and Analysis*. 2015;41:86-97.



Investigation of Singlet Oxygen Production Property of Peripherally Tetra-substituted In(III)Cl Phthalocyanine for Photodynamic Therapy

Semih Gorduk*  

Yildiz Technical University, Faculty of Arts and Science, Department of Chemistry, 34210 Istanbul, Turkey.

Abstract: Phthalocyanines (Pcs) are macrocyclic compounds of great importance. Different metals and ligands can be used in the synthesis of Pc compounds and they give different properties to Pcs. Thus, the applications of Pcs have been increasing every day. One of the most important areas of use of Pcs is photodynamic therapy (PDT) application. The scope of this study is synthesis, characterization, and investigation of singlet oxygen generation property of new peripherally tetrakis(benzodioxane) substituted indium(III) chloride phthalocyanine (**InClPc**). The compound may be used as a potential photosensitizer for PDT applications. The new compound was characterized by various techniques such as elemental analysis, FT-IR, ^1H NMR, MS, and UV-Vis techniques. Furthermore, photophysical and photochemical properties of the synthesized Pc were investigated for PDT studies. At the same time, the effect of combination of heavy indium atom and benzodioxane groups bearing oxygen atom on solubility and photophysicochemical properties was discussed. The results showed that this compound exhibits good solubility in DMSO and shows high singlet oxygen production (Φ_{Δ} : 0.76). According to the displayed properties and singlet oxygen production, we can say that this compound is a potential candidate for PDT applications.

Keywords: Photodynamic therapy; phthalocyanine; singlet oxygen; indium(III) ion; photophysicochemical properties.

Submitted: October 19, 2020. **Accepted:** January 07, 2021.

Cite this: Gorduk S. Investigation of Singlet Oxygen Production Property of Peripherally Tetra-substituted In(III)Cl Phthalocyanine for Photodynamic Therapy. JOTCSA. 2021;8(1):279-88.

DOI: <https://doi.org/10.18596/jotcsa.812081>.

***Corresponding author.** E-mail: sgorduk@yildiz.edu.tr, semih_grdk@hotmail.com

INTRODUCTION

Today, cancer is one of the most serious health problems. It is a disease that causes death of millions of people every year despite many completed and ongoing research and millions of people get this disease every year and unfortunately, most of them die (1). Many researchers and research institutions have been working intensively for the treatment of this disease (2). The disease occurs as a result of uncontrolled division and proliferation of cells and therefore it is gene-based. Since all living things have different gene structures, cancer is basically an individual disease (3). Therefore, it is not possible to talk about a single and definitive treatment method. Today, conventional methods such as surgical intervention,

chemotherapy and radiotherapy are used (4, 5). As an alternative to these studies, photodynamic therapy (PDT) has become one of the important methods used in cancer treatment (6). It is important to design photosensitizers that will make PDT applications more effective (7, 8). Phthalocyanines (Pcs) are also used as a photosensitizing agent for this treatment method (9-11).

Pcs are of great importance both in application and science and there are many studies in the literature on Pc derivatives (12, 13). Pcs, which have physical and chemical properties that can be changed according to the purpose, are used in many application areas (13). The effective use of Pcs in

Langmuir-Blodgett films, chemical sensors, nonlinear optical and electrode materials, electrochemistry, biomedical agents for imaging and PDT, and solar cell applications has led to increased interest in them (14-17). The properties that make Pcs attractive are their π -electron systems and their physical and chemical behavior. Pcs to be used for PDT applications have primarily high singlet oxygen production, displays selectivity for cancerous cells, show absorption in long wavelengths, prevent aggregation and should be soluble (18, 19). The major disadvantage of unsubstituted Pcs, which is insoluble in organic solvents, is overcome by the addition of various substituents to non-peripherally and peripherally positions of Pc compounds. The solubility of Pcs can be increased by binding some functional groups (crown ethers, alkyl, alkoxy, carboxylate, alkythio and the donor atoms such as N and O etc.) to peripherally position of Pc ring or by adding some metal ions (Zn, Mg, In etc.) to the interior of Pcs (20-26). Therefore, in this study, benzodioxane ligand containing alkyl and oxygen atoms, which can increase the solubility of Pc compound, was chosen. Pc compounds containing benzodioxane ligand have been reported previously (27-32). Kantekin and co-workers also investigated the photophysical and photochemical properties including singlet oxygen quantum yield of the same Pc molecule bearing different metals (Zn and Mg) (31). However, indium(III) metal ion containing derivative of the same Pc has not been reported. Also, indium(III) Pcs show the potential to be used as a photosensitizer in PDT because of their ideal singlet oxygen quantum yield caused by the heavy atom effect of indium(III) atom (33, 34). Accordingly, indium(III) metal ion was chosen as the central atom in the ring of Pc compound.

Within the scope of this study, chloroindium(III) Pc compound, which can be used as a photo-sensitizing agent for PDT, containing benzodioxane groups was synthesized and its structure was characterized by various techniques. Herein, we aimed to increase the efficiency of the ideal photosensitizer by binding substituents containing oxygen atoms to Pc ring and to increase singlet oxygen production due to the heavy atom effect of indium(III) atom and thus absorption at long wavelengths was provided. These results have been supported with fluorescence, singlet oxygen production, photodegradation, and aggregation properties.

EXPERIMENTAL SECTION

Materials and Equipments

The used chemicals, equipments, materials, photochemical, and photophysical parameters and formulas were given in the supplementary information file.

Synthesis of the Compound

The 4-((2,3-dihydrobenzo[b][1,4]dioxin-2-yl)methoxy)phthalonitrile compound used as a starting compound in this study was reported in our previous study (27). The new 2(3),9(10),16(17),23(24)-tetrakis-((2,3-dihydrobenzo[b][1,4]dioxin-2-yl)methoxy)phthalocyaninato chloroindium(III) (**InCIPc**) compound was synthesized for the first time according to given procedure in our previous works (27). As the only difference, anhydrous indium(III) chloride (34.5 mg, 0.156 mmol) for **InCIPc** were used in the synthesis. The detailed experimental procedure is given in supplementary information file.

2(3),9(10),16(17),23(24)-tetrakis-((2,3-dihydrobenzo[b][1,4]dioxin-2-yl)methoxy)phthalocyaninato indium(III) chloride (InCIPc)

The THF: MeOH (100:6) solvent system was chosen for column chromatography. Yield: 35% (59.18 mg), Mp: >300 °C, Anal. calc. for C₆₈H₄₈ClInN₈O₁₂: C, 61.90; H, 3.67; N, 8.49; Found: C, 61.70; H, 3.50; N, 8.22%. FT-IR (ATR, cm⁻¹): 3045-3010 (Ar-CH), 2927-2875 (Aliphatic-CH, CH₂), 1622 (C=N), 1587-1485 (C=C), 1250 (C-O-C). ¹H-NMR (400 MHz, CDCl₃), (δ : ppm): 7.76-7.65 (bm, 6H, Ar-H), 7.42-7.13 (bm, 6H, Ar-H), 6.93-6.40 (bm, 16H, Ar-H), 4.90 (bs, 4H, Aliphatic-CH), 4.51-4.13 (bm, 16H, Aliphatic-CH₂). UV-Vis (DMSO, 1×10⁻⁵ M): λ_{max}/nm (log ϵ): 709 (4.80), 638 (3.78), 368 (4.40). MS (MALDI-TOF), (m/z): Calc.: 1318.216, Found: 1318.425 [M]⁺.

RESULT AND DISCUSSION

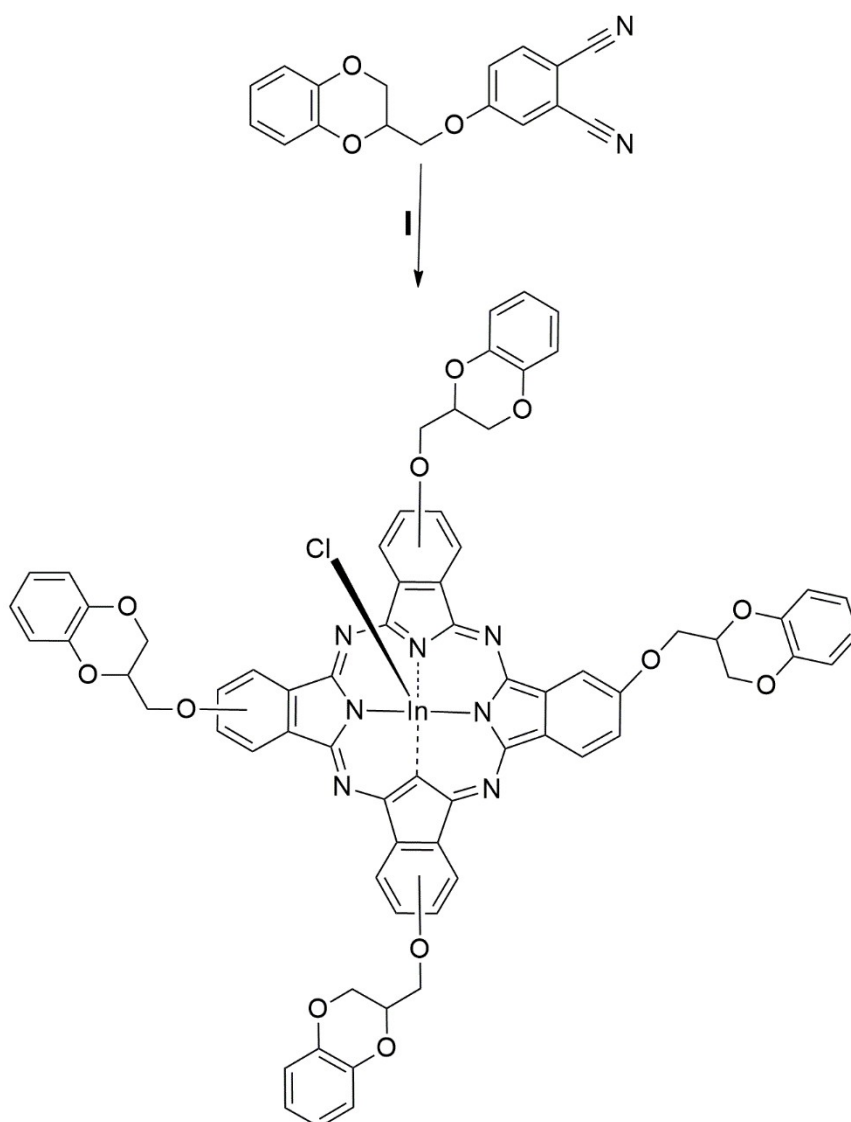
Synthesis and characterization studies

The synthesis procedure for the compound is presented in Scheme 1. The synthesis and characterization studies of 4-((2,3-dihydrobenzo[b][1,4]dioxin-2-yl)methoxy)phthalonitrile compound used as a starting compound in this study were given in our previous work (27). On the other hand, **InCIPc** derivative in scope of this study was synthesized for the first time. We carried out nucleophilic substitution reactions between 2-hydroxymethyl-1,4-benzodioxane and 4-nitrophthalonitrile in order to obtain substituted phthalonitrile compound. **InCIPc** compound was obtained by cyclotetramerization of this compound in the presence of anhydrous indium(III) chloride and DBU as a catalyst. Purification of **InCIPc** was achieved by column chromatography (silica gel) with THF/MeOH solvent mixture. The compound was obtained with 35% yield and exhibited good solubility in DMSO. Various techniques such as FT-IR, elemental analysis, NMR, and MS were used to elucidate the structure of the compound.

In the FT-IR spectrum of **InCIPc** formed as a result of the cyclotetramerization of the phthalonitrile compound, the disappearance of the peak of the C≡N group at 2230 cm⁻¹ of the phthalonitrile and the

formation of the C=N group at 1622 cm^{-1} of Pc ring support the structure. In addition, vibrational bands of aromatic-CH ($3045\text{-}3010\text{ cm}^{-1}$), aliphatic-CH, -CH_2 groups ($2927\text{-}2875\text{ cm}^{-1}$) and C=C ($1587\text{-}1485\text{ cm}^{-1}$) and C-O-C (1250 cm^{-1}) bands of the Pc ring and substituted groups support the structure. The NMR spectrum of **InCIPc** compound is similar to the phthalonitrile derivative, which is the starting material. Due to the aggregation in Pc ring and deuterio solvent, a broad spectrum was obtained according to the NMR spectrum of the phthalonitrile derivative. In the ^1H NMR spectrum, the signals of the aromatic protons were observed at around 7.76-

6.40 ppm and the signals of aliphatic protons were observed at around 4.90-4.13 ppm. These signals prove the formation of the expected structure. In the MALDI-TOF spectrum of the **InCIPc** compound, the presence of the peak at 1318.425 [M]^+ confirms the structure. The theoretical and experimental elemental analysis results are compatible with the targeted structure. The spectral data are compatible with the spectral data of previously published Pc compounds (27, 30-32). It is seen that the data obtained from elemental analysis, FT-IR, mass, and ^1H NMR analyses of **InCIPc** compound are compatible with the synthesized structure.



Scheme 1: General synthesis scheme for **InCIPc** (I: InCl_3 , DBU, n-pentanol, $160\text{ }^\circ\text{C}$, 24 h).

UV-Vis and Aggregation Studies

Generally, UV-Vis spectroscopy is the most specific method used in the characterization of Pcs. Pcs are highly colored compounds thanks to their π electron system originating from benzene rings. This chromaticity causes them to give characteristic absorption bands in the visible and ultraviolet

region. There are two characteristic bands in UV-Vis measurements of Pcs. The first of these is observed between 300-400 nm. The band formed in this region is called as B-band or Soret band. The characteristic second band is observed around 600-750 nm and is called the Q band (35). The Q band is

caused by $\pi\text{-}\pi^*$ transitions and therefore the absorption density is high. The shoulder in Q band gives information about whether Pc is metal or metal-free. Namely, while the only band observed in Q band indicates that the structure is a metallo Pc, the presence of two bands approximately equal to each other indicates that the structure is a metal-free Pc (36). At the same time, UV-Vis measurements help us to understand whether Pc is aggregated in the solvent from which the spectrum was taken. There are many factors that affect the absorption properties of Pcs. These can be listed as the substituents attached to Pc, the central metal atom, the position of the substituents, the solvent used to dissolve Pc, the aggregation, the conjugation and the symmetry of molecule. When looking the presence of these two bands in the UV-Vis spectrum of the obtained compound, it is seen that **InCIPc** is formed (Figure 1). When the UV-Vis spectrum of the compound was examined, Q band at 709 nm and B band at 368 nm were observed. No aggregation was observed in the UV-Vis spectrum of the compound taken in DMSO. The Q band of this compound appears to have shifted to red in the wavelength when compared to other peripherally tetra substituted Pcs containing benzodioxane (27). The important factor in the red shift of the Q band is due to the used heavy indium metal which binds the chlorine atom in the axial position in Pc ring. The red shift of Q band has significant effects on photochemical and photophysical properties.

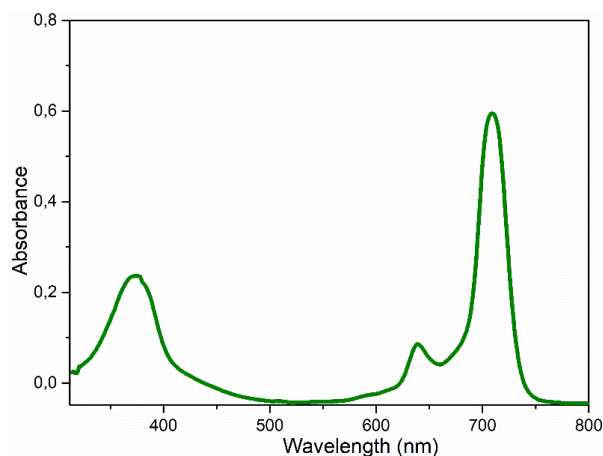


Figure 1: Electronic absorption spectrum of **InCIPc** in DMSO (Concentration: 1.0×10^{-5} M)

Aggregation is a problem in PDT. Aggregation is not a desirable situation in the application areas of Pcs, as it causes widening and low resolution in the Q band seen in the UV-Vis spectrum of Pcs (37). The UV-Vis spectra of the compound in different

concentrations (2.00×10^{-6} - 1.20×10^{-5} mol/L) of DMSO are given in Figure 2. When the UV-Vis spectrum of the compound was examined, it was observed that the synthesized compound did not show aggregation in DMSO. In addition, it is seen that the molar concentration and the absorption intensity of the Q band change in direct proportion. This result is in accordance with the Lambert-Beer's Law.

Photophysical and photochemical Properties

The photochemical and photophysical properties of the compound in DMSO were investigated to determine whether it is suitable for PDT using UV-Vis and fluorescence spectrophotometers. Photochemical measurements include photodegradation quantum yield (Φ_d) and singlet oxygen quantum yield (Φ_Δ), while photophysical measurements include fluorescence quantum yield (Φ_F) and spectra.

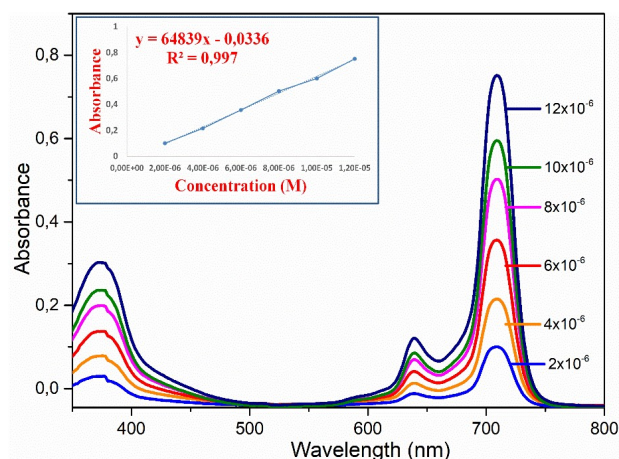


Figure 2: UV-Vis spectra of **InCIPc** compound in DMSO and at different concentrations for aggregation properties (Inset: Absorbances versus concentrations)

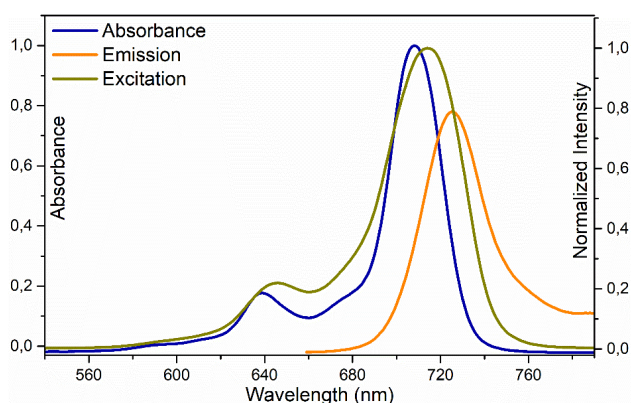
Fluorescence spectra and quantum yield (Φ_F) properties

The absorbance, emission, and excitation values and spectra of the compound in DMSO are given in Table 1 and Figure 3. According to literature, these fluorescence properties are characteristic for indium(III) Pcs in DMSO (29, 30, 38, 39). According to these values, it has been predicted that the excitation spectra of **InCIPc** differ from the absorption spectra because of the loss of symmetry (34) and this demonstrates that the nuclear configuration was changed. Fluorescence spectra were observed at 725 nm for emission and at 713 nm for excitation in DMSO. The Stokes shift value ($\lambda_{\text{ems}} - \lambda_{\text{exc}}$) of the compound was found as 12 nm.

Table 1: Spectral, photophysical and photochemical data for **InCIPc** in DMSO.

Solvent	Q band λ_{\max} (nm)	Extinction coefficient (cm ⁻¹ /M)	log ϵ	Excitation λ_{Ex} (nm)	Emission λ_{Em} (nm)	Stokes Shift Δ_{Stokes} (nm)	Φ_{F}	Φ_{Δ}	Φ_{d} (10 ⁻⁵)
DMSO	709	63150	4.80	713	725	12	0.09	0.76	2.55

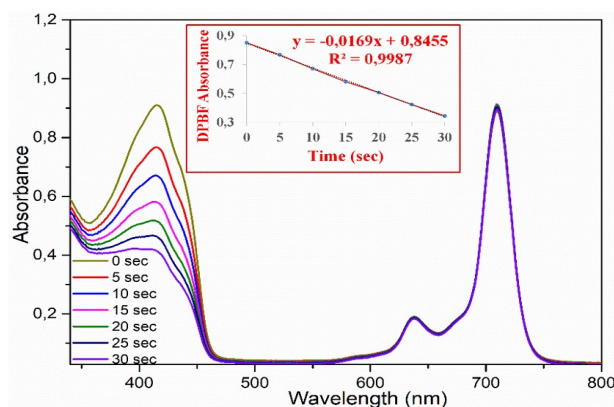
Ideal photosensitizers should show some fluorescent behavior in order to be able to follow them in the body. Therefore, it is important to investigate their fluorescent quantum yield (Φ_{F}) characteristics for PDT applications. The Φ_{F} of **InCIPc** is calculated according to current literature with reference to standard ZnPc (40). Table 1 presents Φ_{F} value of **InCIPc**. The Φ_{F} efficiency was calculated as 0.09 for **InCIPc** in DMSO. The fluorescence efficiency reduces since increasing the atomic number causes more intersystem crossing (41, 42). Therefore, **InCIPc** exhibits low values because of the heavy metal effect. **InCIPc** displays lower fluorescence quantum values compared to unsubstituted ZnPc (Φ_{F} =0.20 in DMSO) and Zn(II) and Mg(II) derivatives of the same Pc (31). Owing to the enhancement of inter-system crossing by the presence of a heavy indium atom in **InCIPc**, Φ_{F} value is low as expected (43). This Φ_{F} value is also similar to other studied InPc compounds (29, 30). The fluorescent behavior of this photosensitizer is appropriate for determination and quantification of photosensitizer in PDT studies.

**Figure 3:** Fluorescent spectra of **InCIPc** in DMSO.

Singlet oxygen production properties

The singlet oxygen generation is an important condition used in PDT. Singlet oxygen generation is the most important behavior of photosensitizer. The singlet oxygen quantum yield (Φ_{Δ}) which is amount of the produced singlet oxygen is the most important indicator for using of molecules as photosensitizers in PDT applications (44). The Φ_{Δ} depends on the used solvent. A suitable solvent was biocompatible DMSO. DMSO as a solvent meets the conditions required for the photosensitizers and it is already used as a solvent in the literature for determination of the Φ_{Δ} (41). The Φ_{Δ} are found via 1,3-diphenylisobenzofuran (DPBF) compound, which has an absorption at 417 nm, as a quencher. Also, the standard ZnPc is used as reference. The

absorbance of DPBF was monitored using UV-Vis spectroscopy after each 5 s of light irradiation. The compound did not degrade against light irradiation, since the compound is resistant to light. The results showing the absorbance change of DPBF are given in Figure 4 and the calculated Φ_{Δ} value is listed in Table 1. The Φ_{Δ} value of **InCIPc** is 0.76 in DMSO. While **InCIPc** showed higher Φ_{Δ} value than unsubstituted ZnPc and Mg(II) derivative of the same Pc, it showed lower Φ_{Δ} value than Zn(II) derivative of the same Pc (31). **InCIPc** exhibited good singlet oxygen production and it can be potential candidate as potential photosensitizer in PDT. Thanks to the enhancement of intersystem crossing by the heavy atom effect of large In(III) atom, **InCIPc** generates high singlet oxygen. When Φ_{F} and Φ_{Δ} are evaluated in terms of the heavy atom effect for **InCIPc**, decrease in Φ_{F} value accompanied by increase in Φ_{Δ} value. **InCIPc** demonstrated higher Φ_{Δ} values than **Std-ZnPc** which means that the substitution of 4-((2,3-dihydrobenzo[b][1,4]dioxin-2-yl)methoxy) groups to the macrocycle increased singlet oxygen generation. The singlet oxygen generation of this compound is similar with Pc containing different substituents on the Pc ring and In(III) metal ion in Pc cavity (34, 45, 46). The synthesized compound has sufficient singlet oxygen generation for PDT.

**Figure 4:** UV-Vis spectral changes of **InCIPc** during singlet oxygen production measurements in DMSO (Inset: Plot of DPBF absorbance versus time).

Photodegradation properties

Photodegradation is generally used to determine the stability of Pcs, which is important in photocatalytic application reactions as well as in PDT. Photodegradation is the oxidative decomposition of the photosensitizer under light irradiation and this photodegradation is studied by quantum efficiency. The photodegradation quantum yield (Φ_{d}) of

photosensitizer play a key role in PDT. The Φ_d value gives the stability of the compound against the light irradiation. After exposure to light for every 5 min of the compound, the photodegradation studies in DMSO were performed by monitoring the decrease of the absorbance of the compound. Figure 5 presents the changes in Q band of the compound. The Q band intensity of compound was not disturbed in DMSO under light irradiation. As we know from the literature, the Φ_d of the stable photosensitizer are between 10^{-3} and 10^{-6} (47). The Φ_d value of compound presents in Table 1 and it showed about the same stability with order of 10^{-5} . The Φ_d value of **InCIPc** in DMSO was calculated as 2.55×10^{-5} . The obtained Φ_d value of **InCIPc** are similar with Zn(II) and Mg(II) derivatives of the same Pc (31). **InCIPc** demonstrated lower Φ_d values than **Std-ZnPc** which means that the substitution of 4-((2,3-dihydrobenzo[b][1,4]dioxin-2-yl)methoxy)groups to the macrocycle increased the stability of this phthalocyanine against light irradiation. The results indicate that this compound has moderate stability to photochemical degradation. The photodegradation quantum yields (Φ_d) are in harmony with other InPcs (30, 33, 48) and the stability of the compound are suitable for PDT.

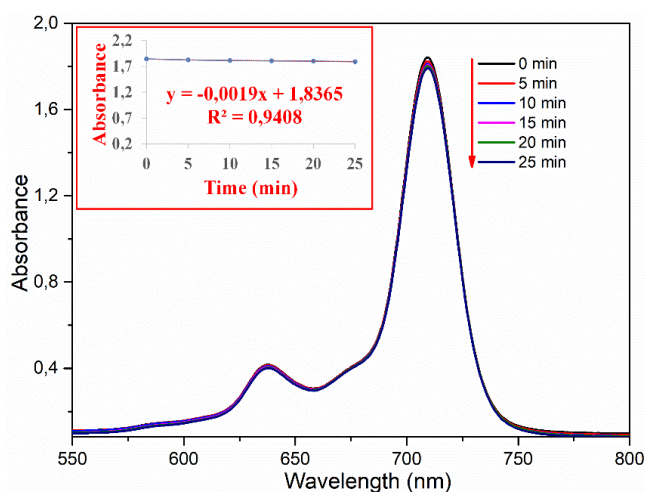


Figure 5: UV-Vis spectral change of **InCIPc** during photodegradation measurements in DMSO (Inset: plot of Q band absorbance versus time)

CONCLUSIONS

In this study, new tetra-substituted chloroindium(III) Pc bearing benzodioxane groups was synthesized and characterized by using elemental analysis, UV-Vis, FT-IR, ^1H NMR and MALDI-TOF MS techniques. At the same time, the photophysical properties of the compound were researched in order to understand whether it is suitable for PDT. According to the UV-Vis measurements, we observed that this compound dissolves very well in DMSO, does not aggregate, and gives Q band around 709 nm and B band around 368 nm. In addition, we observed that

the ratio between absorption and concentration in the Q band changes in accordance with the Lambert-Beer law. The fluorescence spectral results show that the excitation spectrum of this compound differs from the absorption spectra and this demonstrates that the nuclear configuration was changed. The fluorescence quantum yield of the obtained compound (0.09) is lower than the unsubstituted ZnPc compound. When singlet oxygen quantum yield was examined, we observed that the compound show higher result than unsubstituted ZnPc. This situation is due to indium(III) ion being a heavy atom and increasing the transition between systems. In addition, the used benzodioxane substituted groups may have an effect on high singlet oxygen production compared to unsubstituted ZnPc compound. According to the photodegradation results, it is seen that the synthesized compound is stable to light. As a result, with this study, a candidate molecule that can be used as a potential photosensitizer in PDT applications has been reported in the literature.

Conflict of interest: The authors declare that they have no conflict of interest.

REFERENCES

1. Siegel RL, Miller KD, Jemal A. Cancer statistics, 2020. *Ca-Cancer J. Clin.* 2020;70(1):7-30.
2. Miller KD, Siegel RL, Lin CC, Mariotto AB, Kramer JL, Rowland JH, et al. Cancer treatment and survivorship statistics, 2016. *Ca-Cancer J. Clin.* 2016;66(4):271-89.
3. Thompson CB. Apoptosis in the pathogenesis and treatment of disease. *Science.* 1995;267(5203):1456-62.
4. Vanneman M, Dranoff G. Combining immunotherapy and targeted therapies in cancer treatment. *Nat. Rev. Cancer.* 2012;12(4):237-51.
5. Miller A, Hoogstraten B, Staquet M, Winkler A. Reporting results of cancer treatment. *cancer.* 1981;47(1):207-14.
6. Dougherty TJ, Gomer CJ, Henderson BW, Jori G, Kessel D, Korbek M, et al. Photodynamic therapy. *J. Natl. Cancer Inst.* 1998;90(12):889-905.
7. Dolmans DE, Fukumura D, Jain RK. Photodynamic therapy for cancer. *Nat. Rev. Cancer.* 2003;3(5):380.
8. Li X, Kolemen S, Yoon J, Akkaya EU. Activatable photosensitizers: agents for selective photodynamic therapy. *Adv Funct Mater.* 2017;27(5):1604053.
9. Lukyanets EA. Phthalocyanines as photosensitizers in the photodynamic therapy of cancer. *J Porphyrins Phthalocyanines.* 1999;3(6):10.

10. Ogura S-i, Tabata K, Fukushima K, Kamachi T, Okura I. Development of phthalocyanines for photodynamic therapy. *J Porphyrins Phthalocyanines*. 2006;10(09):1116-24.
11. Lo P-C, Rodríguez-Morgade MS, Pandey RK, Ng DK, Torres T, Dumoulin F. The unique features and promises of phthalocyanines as advanced photosensitisers for photodynamic therapy of cancer. *Chem Soc Rev*. 2020;49(4):1041-56.
12. Gorduk S, Altindal A. Non-peripherally tetra substituted phthalocyanines bearing carboxylic acid anchoring groups as photosensitizer for high efficient dye-sensitized solar cells. *J Mol Struct*. 2020;1204:127636.
13. Gregory P. Industrial applications of phthalocyanines. *J Porphyrins Phthalocyanines*. 2000;4(4):432-437.
14. Claessens CG, Hahn U, Torres T. Phthalocyanines: From outstanding electronic properties to emerging applications. *The Chemical Record*. 2008;8(2):75-97.
15. Gounden D, Nombona N, van Zyl WE. Recent advances in phthalocyanines for chemical sensor, non-linear optics (NLO) and energy storage applications. *Coord Chem Rev*. 2020;420:213359.
16. Karaca H. Synthesis of Novel Chalcone Substituted Metallophthalocyanines: Electrochemistry, Spectroelectrochemistry and Catalytic Oxidation of 2-mercaptoethanol. *J Turk Chem Soc, Sect A: Chem*. 2018;5(2):701-18.
17. Wöhrle D, Schnurpfeil G, Makarov SG, Kazarin A, Suvorova ON. Practical applications of phthalocyanines—from dyes and pigments to materials for optical, electronic and photo-electronic devices. *Macrocyclic Chem*. 2012;5(3):191-202.
18. Rosenthal I. Phthalocyanines as photodynamic sensitizers. *Photochem Photobiol*. 1991;53(6):859-70.
19. Liu MO, Tai C-h, Sain M-z, Hu AT, Chou F-i. Photodynamic applications of phthalocyanines. *J Photochem Photobiol, A*. 2004;165(1-3):131-36.
20. Kliesch H, Weitemeyer A, Müller S, Wöhrle D. Synthesis of phthalocyanines with one sulfonic acid, carboxylic acid, or amino group. *Liebigs Annalen*. 1995;1995(7):1269-73.
21. Ogunsipe A, Nyokong T. Effects of substituents and solvents on the photochemical properties of zinc phthalocyanine complexes and their protonated derivatives. *J Mol Struct*. 2004;689(1-2):89-97.
22. Günsel A. Comparative Studies of Photophysicochemical Properties of Non-Peripherally Anisole/Thioanisole-Tetrasubstituted Gallium(III) Phthalocyanines Containing Oxygen/Sulfur Bridge. *J Turk Chem Soc, Sect A: Chem*. 2017;5(1):269-82.
23. Gorduk S. Ferulic Acid Substituted Zn(II) Phthalocyanine: Synthesis, Characterization and Investigation of Photophysical and Photochemical Properties. *J Turk Chem Soc, Sect A: Chem*. 2018;5(2):903-18.
24. Temizel S, Sevim AM. Synthesis and photophysical properties of A3B-type non-symmetrically substituted anthracene-based zinc(II) phthalocyanine. *J Turk Chem Soc, Sect A: Chem*. 2020;7(1):107-16.
25. Güzel E. Preparation and investigation of aggregation, fluorescence and singlet oxygen generation properties of gallium and metal-free phthalocyanines. *J Turk Chem Soc, Sect A: Chem*. 2019;5(3):1051-60.
26. Özçeşmeci M. Aromatik azo grupları ile modifiye edilmiş, yakın-IR bölgede soğurma yapan metallsiz ve çinko(II) ftalosiyeninlerin sentezi ve karakterizasyonu. *J Turk Chem Soc, Sect A: Chem*.; 2015; 2(4):32-41.
27. Gorduk S, Koyun O, Avciata O, Altindal A, Avciata U. Synthesis of Peripherally Tetrasubstituted Phthalocyanines and Their Applications in Schottky Barrier Diodes. *J. Chem*. 2017;2017:1-9.
28. Gorduk S, Avciata O, Avciata U. Photocatalytic degradation of methylene blue under visible light irradiation by non-peripherally tetra substituted phthalocyanine-TiO₂ nanocomposites. *Inorg Chim Acta*. 2018;471:137-47.
29. Gorduk S. Investigation of photophysicochemical properties of non-peripherally tetra-substituted metal-free, Mg(II), Zn(II) and In(III) Cl phthalocyanines. *Polyhedron*. 2020;189:114727.
30. Gorduk S. Octa-substituted metallophthalocyanines bearing (2,3-dihydrobenzo-1,4-benzodioxin-2-yl) methoxy and chloro groups: Synthesis, characterization and photophysicochemical studies. *J Porphyrins Phthalocyanines*. 2020;24(4):548-62.
31. Demirbaş Ü, Ömeroğlu İ, Akçay HT, Durmuş M, Kantekin H. Synthesis, characterization, photophysical and photochemical properties of peripherally tetra benzodioxane substituted metal-free phthalocyanine and its zinc(II) and magnesium(II) derivatives. *J Mol Struct*. 2020;1223:128992.
32. Demirbaş Ü, Akyüz D, Akçay HT, Koca A, Kantekin H. Non-peripherally tetra substituted phthalocyanines bearing benzodioxane moieties: Synthesis, characterization and investigation of

- electrochemical and spectroelectrochemical properties. *J Mol Struct.* 2019;1189:234-39.
33. Uslan C, Köksoy B, Durmuş M, İşleyen ND, Öztürk Y, Çakar ZP, et al. The synthesis and investigation of photochemical, photophysical and biological properties of new lutetium, indium, and zinc phthalocyanines substituted with PEGME-2000 blocks. *J. Biol. Inorg.* 2019:1-20.
34. Yanık H, Aydın D, Durmuş M, Ahsen V. Peripheral and non-peripheral tetrasubstituted aluminium, gallium and indium phthalocyanines: Synthesis, photophysics and photochemistry. *J Photochem Photobiol, A.* 2009;206(1):18-26.
35. Nyokong T. Electronic spectral and electrochemical behavior of near infrared absorbing metallophthalocyanines. *Functional Phthalocyanine Molecular Materials: Springer;* 2010. p. 45-87.
36. Kadish K, Smith KM, Guillard R. The porphyrin handbook: phthalocyanines: properties and materials: Elsevier; 2000.
37. Snow AW. Phthalocyanine Aggregation. *The Porphyrin Handbook: Phthalocyanines: Properties and Materials.* 2000;17:129.
38. Can OS, Kaya EN, Durmuş M, Bulut M. High photosensitized singlet oxygen generating zinc(II) and indium(III) acetate phthalocyanines containing 6,8-di-tert-butyl-3-(p-oxyphenyl) coumarin groups. *J Photochem Photobiol, A.* 2016;317:56-67.
39. Sindelo A, Osifeko OL, Nyokong T. Synthesis, photophysicochemical and photodynamic antimicrobial chemotherapy studies of indium pyridyl phthalocyanines: Charge versus bridging atom. *Inorg Chim Acta.* 2018;476:68-76.
40. Ogunsipe A, Chen J-Y, Nyokong T. Photophysical and photochemical studies of zinc(II) phthalocyanine derivatives—effects of substituents and solvents. *New J Chem.* 2004;28(7):822-27.
41. Ogunsipe A, Maree D, Nyokong T. Solvent effects on the photochemical and fluorescence properties of zinc phthalocyanine derivatives. *J Mol Struct.* 2003;650(1-3):131-40.
42. Simone BCD, Mazzone G, Russo N, Sicilia E, Toscano M. Metal atom effect on the photophysical properties of Mg(II), Zn(II), Cd(II), and Pd(II) tetraphenylporphyrin complexes proposed as possible drugs in photodynamic therapy. *Molecules.* 2017;22(7):1093.
43. Durmuş M, Nyokong T. Synthesis, photophysical and photochemical properties of aryloxy tetra-substituted gallium and indium phthalocyanine derivatives. *Tetrahedron.* 2007;63(6):1385-94.
44. Lovell JF, Liu TW, Chen J, Zheng G. Activatable photosensitizers for imaging and therapy. *Chem Rev.* 2010;110(5):2839-57.
45. Chauke V, Durmuş M, Nyokong T. Photochemistry, photophysics and nonlinear optical parameters of phenoxy and tert-butylphenoxy substituted indium(III) phthalocyanines. *J Photochem Photobiol, A.* 2007;192(2-3):179-87.
46. Ali HEA, Pişkin M, Altun S, Durmuş M, Odabaş Z. Synthesis, characterization, photophysical, and photochemical properties of novel zinc(II) and indium(III) phthalocyanines containing 2-phenylphenoxy units. *J Lumin.* 2016;173:113-19.
47. Durmuş M. Photochemical and photophysical characterization. *Photosensitizers in medicine, environment, and security: Springer;* 2011. p. 135-266.
48. Çapkin A, Pişkin M, Durmuş M, Bulut M. Spectroscopic, photophysical and photochemical properties of newly metallo-phthalocyanines containing coumarin derivative. *J Mol Struct.* 2020;1213:128145.

SUPPORTING INFORMATION

Investigation of Singlet Oxygen Production Property of Peripherally Tetra-substituted In(III)Cl Phthalocyanine for Photodynamic Therapy

Semih Gorduk*

Yildiz Technical University, Faculty of Arts and Science, Department of Chemistry, 34210 Istanbul, Turkey
 *Corresponding Author: Semih Gorduk, E-mail: sgorduk@yildiz.edu.tr, Tel: +90 212 383 42 19.

EXPERIMENTAL SECTION

Materials

N,N-dimethylformamide (DMF), Dimethyl sulfoxide (DMSO), chloroform (CHCl₃), diethylether, methanol (MeOH), tetrahydrofuran (THF), ethanol (EtOH), dichloromethane (DCM), *n*-hexane, *n*-pentanol, and acetone were purchased from MERCK. 4-Nitrophthalonitrile, 2-hydroxymethyl-1,4-benzodioxan, 1,8-diazabicyclo[5.4.0]undec-7-ene (DBU), potassium carbonate (K₂CO₃), anhydrous indium(III) chloride were purchased from Aldrich. All chemicals were of reagent grade. All solvents were dried and stored over molecular sieves. The progress of the reactions was monitored by thin layer chromatography (TLC).

Equipments

Melting points of compounds were determined via an electrothermal Gallenkamp device. The UV-vis measurements were made on a Shimadzu UV-2001 UV-Vis spectrophotometer. Elemental analysis studies were performed by a LECO TRUSPEC CHN 932 instrument. The IR spectra of the compounds were registered using a Thermo Fisher scientific NICOLET IS10 spectrometer (ATR sampling accessory). A Bruker Avance III 400 MHz spectrometer was used for ¹H-NMR analyses. MALDI-TOF mass measurements were carried out by a Bruker Microflex LT MALDI-TOF-MS. Fluorescence spectra, were registered by Varian Eclipse spectrophotometer using 1 cm path length cuvettes at room temperature. General electric quartz line lamp (300 W) was used to perform photochemical measurements. Ultraviolet and infrared radiations were filtered using A 600 nm glass cut off filter (Schott) and a water filter, respectively. An extra interference filter (Intor, 670 or 700 nm with a band width of 40 nm) was placed through the light path before the sample. A POWER MAX5100 (Molelectron detector incorporated) power meter was utilized to determine light intensities.

Photophysical and Photochemical Measurements

Fluorescence quantum yield (Φ_F) measurements

The Φ_F values were calculated by the comparative method (Eq. 1) [1, 2] using unsubstituted ZnPc as the reference. The Φ_F value of unsubstituted ZnPc is 0.20 in DMSO [3, 4]. Both the synthesized Pcs and the standard were excited at convenient wavelength.

$$\Phi_F = \Phi_F(\text{Std}) \frac{F \times A_{\text{Std}} \times n^2}{F_{\text{Std}} \times A \times n_{\text{Std}}^2} \quad (\text{Eq. 1})$$

In Eq. 1, *F* and *F*_{Std} are the areas under the fluorescence emission curves of the synthesized Pc and standard unsubstituted ZnPc, respectively. *A* and *A*_{Std} are the absorbances of the synthesized Pc and standard unsubstituted ZnPc at the excitation wavelengths, respectively. The η and η_{std} are the refractive indices of used solvents for the synthesized Pc and standard unsubstituted ZnPc, respectively.

Singlet oxygen quantum yield (Φ_Δ) measurements

The Φ_Δ measurements were performed using the experimental setup described in previous studies [4, 5] with standard unsubstituted ZnPc (in DMSO) as the reference. 2 mL of the synthesized Pc solution (*C*=1.0×10⁻⁵ M) containing the singlet oxygen scavenger was irradiated in the Q-band region using the photoirradiation setup described in the literature. The Φ_Δ values were calculated via the relative method with DPBF (singlet oxygen chemical scavenger) in DMSO using Eq. 2.

$$\Phi_\Delta = \Phi_\Delta^{\text{Std}} \frac{R \cdot I_{\text{abs}}^{\text{Std}}}{R^{\text{Std}} \cdot I_{\text{abs}}} \quad (\text{Eq. 2})$$

$\Phi_{\Delta}^{\text{std}}$ is Φ_{Δ} for the standard unsubstituted ZnPc ($\Phi_{\Delta}^{\text{std}} = 0.67$ in DMSO) [1, 6]. R and R_{Std} are DPBF photobleaching rates in the presence of the synthesized Pc and standard unsubstituted ZnPc, respectively. I_{abs} and $I_{\text{abs}}^{\text{std}}$ are the rates of light absorption by the synthesized Pc and standard unsubstituted ZnPc, respectively. The concentration of DPBF was lowered to $\sim 3 \times 10^{-5}$ M to avoid chain reactions formed by DPBF in the presence of singlet oxygen [7]. Solutions of the photosensitizer including DPBF were prepared in the dark environment and irradiated in the Q-band region using the described setup in the measurements part. Degradation of DPBF at 417 nm was monitored. The used light intensity in Φ_{Δ} value measurements is 7.05×10^{15} photons. $s^{-1} \cdot \text{cm}^{-2}$.

Photodegradation quantum yield (Φ_{Δ}) measurements

The Φ_{Δ} measurements were performed by the experimental setup described in previous studies [8]. Φ_{Δ} values of the synthesized Pcs were calculated via **Eq. 3**.

$$\Phi_{\Delta} = \frac{(C_0 - C_t) \times V \times N_A}{I_{\text{abs}} \times S \times t} \quad (\text{Eq. 3})$$

In Equation 3, S is the irradiated cell area, t is the irradiation time, C_0 and C_t are the sample concentration before and after irradiation, respectively, V is the used volume of solution in measurement, N_A is the Avogadro's constant and I_{abs} is the overlap integral of the radiation source light intensity and the absorption of the synthesized Pc. The used light intensity in Φ_{Δ} value measurements is 2.20×10^{16} photons. $s^{-1} \cdot \text{cm}^{-2}$.

Synthesis of 2(3),9(10),16(17),23(24)-tetrakis-((2,3-dihydrobenzo[b][1,4]dioxin-2-yl)methoxy)phthalocyaninato chloro indium(III) (InClPc)

The compound was synthesized according to given procedure in our previous works [9]. The mixture of 4-((2,3-dihydrobenzo[b][1,4]dioxin-2-yl)methoxy)phthalonitrile compound (0.2 g, 0.69 mmol), n-pentanol (4 mL), 1,8-diazabicyclo[4.5.0]undec-7-ene (DBU) (5 drops), equivalent amounts of anhydrous InCl_3 heated to 160 °C and stirred for 24 h at this temperature under N_2 atmosphere. Then cooling to room temperature, the reaction mixture was precipitated by the addition of n-hexane and filtered off. After washing with hot MeOH and hot EtOH, the product was purified with column chromatography by using silica gel and THF/MeOH solvent system. Solvent system for column chromatography was THF/MeOH (100:6).

REFERENCES

1. S. Fery-Forgues, D. Lavabre, Are fluorescence quantum yields so tricky to measure? A demonstration using familiar stationery products, *J. Chem. Educ.* 76(9) (1999) 1260.
2. M.D. Maree, T. Nyokong, K. Suhling, D. Phillips, Effects of axial ligands on the photophysical properties of silicon octaphenoxypthalocyanine, *J. Porphyrins Phthalocyanines* 6(06) (2002) 373-376.
3. A. Ogunsipe, J.-Y. Chen, T. Nyokong, Photophysical and photochemical studies of zinc(II) phthalocyanine derivatives—effects of substituents and solvents, *New J. Chem.* 28(7) (2004) 822-827.
4. I. Gürol, M. Durmuş, V. Ahsen, T. Nyokong, Synthesis, photophysical and photochemical properties of substituted zinc phthalocyanines, *Dalton Trans.* (34) (2007) 3782-3791.
5. A. Ogunsipe, T. Nyokong, Effects of substituents and solvents on the photochemical properties of zinc phthalocyanine complexes and their protonated derivatives, *J. Mol. Struct.* 689(1-2) (2004) 89-97.
6. A. Ogunsipe, D. Maree, T. Nyokong, Solvent effects on the photochemical and fluorescence properties of zinc phthalocyanine derivatives, *J. Mol. Struct.* 650(1-3) (2003) 131-140.
7. W. Spiller, H. Kliesch, D. Wöhrle, S. Hackbarth, B. Röder, G. Schnurpfeil, Singlet oxygen quantum yields of different photosensitizers in polar solvents and micellar solutions, *J. Porphyrins Phthalocyanines* 2(2) (1998) 145-158.
8. A. Ogunsipe, T. Nyokong, Photophysical and photochemical studies of sulphonated non-transition metal phthalocyanines in aqueous and non-aqueous media, *J. Photochem. Photobiol., A* 173(2) (2005) 211-220.
9. S. Gorduk, O. Koyun, O. Avciata, A. Altindal, U. Avciata, Synthesis of Peripherally Tetrasubstituted Phthalocyanines and Their Applications in Schottky Barrier Diodes. *Journal of Chemistry.* 2017 (2017) 1-9.



Synthesis of Polyaniline/Biochar Composite Material and Modeling with Nonlinear Model for Removal of Copper (II) Heavy Metal Ions

Halime YAKIŞIK¹  , Uğur ÖZVEREN^{2*}  

¹University of Marmara, Faculty of Engineering, Department of Chemical Engineering, 34722, İstanbul, TURKEY.

²University of Marmara, Faculty of Engineering, Department of Chemical Engineering, 34722, İstanbul, TURKEY.

Abstract: In recent years, the pollution of water sources has become an important concern for industrial development. Especially, contamination with heavy metal ions leads to serious environmental problems and water-borne diseases. Therefore, the synthesis of different low-cost adsorbent materials with high removal efficiency are being researched extensively. In this study, biochar was obtained from torrefied hazelnut shell and used during polyaniline synthesis to obtain Polyaniline/Biochar composite for removal of copper(II) ions from wastewater. During the study, optimal temperature, pH, adsorbent amount and contact time parameters were investigated. The removal efficiency of developed novel composite adsorbent was found to be 89.23% under the optimum experimental conditions. Kinetic studies also confirmed the adsorption performance. The morphological analysis of adsorbent was characterized with thermal gravimetric analysis (TGA). A new nonlinear model was developed for removal efficiency prediction of Polyaniline/Biochar composite adsorbent since the adsorption behavior has been found to be highly complex. The batch experiments of Polyaniline/Biochar were studied to train the model. The consistency between experimental targets and model outputs gives a high correlation coefficient ($R^2=0.9943$) and shows that the proposed model can estimate the Cu(II) removal efficiency of adsorbent accurately. Modeling the behavior of Cu(II) adsorption will be helpful to describe a set of operating conditions for amplifying water treatment technology at the industrial level. Moreover, it can be supposed that the modeling approach developed in this study will expedite the advancement of material science in various application fields for a data-driven future wherein the knowledge can be aggregated.

Keywords: Heavy metal removal, Copper(II), Biochar, Polymeric composite material, Modeling

Submitted: October 20, 2019. **Accepted:** January 07, 2021.

Cite this: Yakışık H, Özveren U. Synthesis of Polyaniline/Biochar Composite Material and Modeling with Nonlinear Model for Removal of Copper (II) Heavy Metal Ions. JOTCSA. 2021;8(1):289-302.

DOI: <https://doi.org/10.18596/jotcsa.635073>.

***Corresponding author.** ugur.ozveren@marmara.edu.tr, GSM: +90 535 883 77 01.

INTRODUCTION

With rapid population and industrial growth, many types of contaminants including dyestuff, pharmaceutical compounds, heavy metals can be found in water sources and considerably damage the environment (1). Long-term exposure of heavy metal ions occurs water-borne environmental pollution that causes serious health problems thanks to high-level toxin accumulation in human bodies (2, 3). In particular, copper is a common pollutant

needed in various industries (automotive, pipes, valves, power plants, and electronics, etc.) due to its high electrical and thermal conductivity. However copper is widely used in different technologies, the toxicity of overload Cu uptake especially influences the liver as a target organ and causes acute poisoning. These environmental concerns have boosted the investigation of alternative recovery technologies for the Cu(II) removal.

To date, a number of water treatment technologies have been employed for the removal of contaminants from water sources including coagulation-flocculation, biological oxidation, ionic exchange, electrochemical oxidation, adsorption, and membrane filtration (4-8). It is thought that the adsorption technique provides the most suitable alternative recovery to other treatment methods due to its more economical and simple application (8, 9). This recovery method is a well-known technology for heavy metal removal even at a very low ion concentration with a wide range of raw materials availability and low energy requirement (10). Researchers also have studied a set of adsorbents such as activated carbon (11), zeolites (12, 13), fly ash (14), polymers (15-20), clays (21, 22) and agricultural wastes (6, 23, 24) in the removal of heavy metal ions. Nonetheless, the production of effective adsorbents for acceptable water treatment mechanisms is still a challenge.

Biochar can be generated from almost all carbonaceous materials as a promising adsorbent for wastewater treatment with its remarkable chemical properties. As a waste management technique, the conversion of biomass waste into biochar has attracted attention because of its reusable properties. In addition, biomass sources have been identified as suitable adsorbent materials for different adsorption applications due to their enriched surface properties, cost-effective properties, and porous structures providing a wide surface area. Therefore, recent studies have been focused on the production of biochar using a wide variety of biomass wastes as a carbon source (straw, husk, sawdust, sludge residue, etc.) (25-28). On the other hand, application of biochar for wastewater recovery has been limited due to its low mechanical durability (29, 30). In studies where biomass wastes consisted only of lignin and cellulose, adsorbents showed low selectivity and mechanical resistance to heavy metal ions (31, 32). Therefore, recent studies have been focused on improving its potential practical applications for heavy metal removal through incorporation with various sorbent materials.

Modifying biochar with polymer matrices overcome the drawbacks of biochar and improve adsorption efficiency. In current decades, electroactive polymeric adsorbents such as polythiophene (PTh), polypyrrole (PPy) and polyaniline (PANI), find applications in multiple fields such as rechargeable batteries, microelectronics, composite materials, optics, biosensors, electronic devices, and adsorbents for wastewater recovery due to their doping and de-doping abilities (33-36). Among these polymeric composites, polyaniline (PANI) and its derivatives have attracted attention because of their specific characteristic properties including good redox reversibility, low-cost synthesis in aqueous solution, and ecological stability. Furthermore, PANI conducting polymer has shown high removal

efficiency for heavy metal ions due to its ion exchange properties, and porous structure (37). Therefore, PANI adsorbents with their remarkable properties have been studied by researchers for the removal of heavy metal ions extensively due to functional amine and imine groups in their chains (38, 39).

On the other hand, the large swelling during charge–discharge process often disrupts the mechanical stability of PANI (40). Therefore, carbon-based materials were utilized to support the mechanical structure and improve the electrochemical stability of PANI due to synergetic effect between PANI and carbon materials (41-43). However, some typical carbon-based materials used for PANI composites (such as carbon nanotubes, fullerene, and graphene) were synthesized via complex processes with limited and high-cost material sources (44-46). This is a crucial obstacle for commercial adsorbent applications of PANI-carbon based composites. Therefore, more attention requires to be focused on synthesis of PANI-carbon based composite adsorbent materials with comparable removal efficiency by using environmental, low-cost, and highly effective carbon rich materials as raw materials. On that note, biochar produced from different biomass sources have been considered as a promise to maintain significant characteristics such as high surface area, and excellent conductivity to the polyaniline structure (47). In current years, the utilization of PANI polymer onto the lignocellulosic biomass surface has been also examined to improve the properties and applicability of PANI (48). The PANI-based composites such as PANI/sawdust (49), and PANI/Argan-nut-shell (50) have indicated high removal capacity for aqueous pollutants. However, according to the best of our knowledge, no study has been reported for investigating the synergistic effect between biochar and Polyaniline as a carbon-based PANI composite adsorbent for wastewater treatment applications. Herein we synthesized a novel Polyaniline/Hazelnut Shell Biochar (PANI/BC) via in-situ chemical polymerization as a PANI-carbon based composite.

Beyond these, working conditions have a strong influence on adsorption capacity, which is largely dependent on all process variables. But evaluating the removal efficiency of synthesized adsorbent under different experimental conditions is a highly time-consuming and expensive method. Because, the wastewater treatment process is highly complex which are depended on all process variables and removal mechanisms. Therefore, aside from the experimental researches regarding adsorption studies, research is nowadays underway that seeks to employ modeling approach to understand which operational condition improves the removal efficiency. To our best knowledge, limited researches have been announced that concern the modeling and optimization of the removal process of

adsorbent materials created in laboratories. Modeling of the adsorption process to understand the adsorption behavior is developed with an experimental run. The determination of removal percentage is the main factor that indicates the goodness of adsorption. Thus, it is essential to estimate the removal percentage in different experimental conditions. Therefore, the removal percentage was assigned as an output variable of the proposed model to clear the effect of each experimental parameters on the removal process.

The current study includes the development of a new nonlinear regression model that describes Cu(II) removal along with various operating conditions. The objective of this study is to develop and evaluate a novel predictive model for exploring the impact of different experimental parameters on Cu(II) removal efficiency using experimental datasets. The affecting parameters include the following: adsorbent dosage, pH, adsorption time, and temperature, and all of which were preferred as input parameters and the model was developed by using model input parameters. The proposed model can estimate the removal efficiency of PANI/BC composite adsorbent as an output parameter. The validation of the proposed model was determined by investigating the adjustment of calculated and experimental results. A comparison between the calculated and experimental results gives the best fit for the adsorption efficiency prediction. This indicates the model is feasible for predicting the behavior of removal efficiency of Cu(II) ions. Finally, the nonlinear regression model we suggested in this study may improve the understanding of adsorption nature and may ease the conducting of adsorbent designs with increasing the selectivity towards specified heavy metal ions. According to our

assumptions, the findings of this study also endow a new report on the modeling approach to demonstrate the opportunities of this technology having an advancement on material synthesis for various complex engineering approaches involving life and basic sciences in future.

EXPERIMENTAL SECTION

Preparation of the biochar

The hazelnut shells in the Black Sea region of Turkey were used for the preparation of the biochar. The biochar production from hazelnut shell samples was carried out under argon atmosphere using a vacuum oven (51). Biochar was produced at 200°C for 3 days. At the end of 3 days, the produced biochar samples were soaked in 50% H₂SO₄ for 24 hours and then filtered using vacuum filtration technique. Sulfuric acid used during biochar synthesis increases the surface area of biochar, removes the ash content, and helps make biochar as a more effective adsorbent. Then, the biochar was purified with distilled water and dried at 110 °C. The dried biochar was ground with RETSCH ZM 200 Grinder device and was sieved using RETSCH AS 200 with grain size below 250 μm for adsorption experiments.

Synthesis of PANI/BC composite

For the synthesis of PANI/BC composite hybrid material, 5 mL of aniline and 1 g of prepared biochar sample was dissolved in 70 mL of HCl (2 M) solution for 12 hours with stirring to prevent any particle aggregation. After 12 hours, 5 g of APS (Ammonium Persulfate) was dissolved in 20 mL of distilled water and slowly added to the solution for 10 minutes at constant stirring speed. Reaction mechanism of aniline polymerization through chemical oxidation was represented in Figure 1.

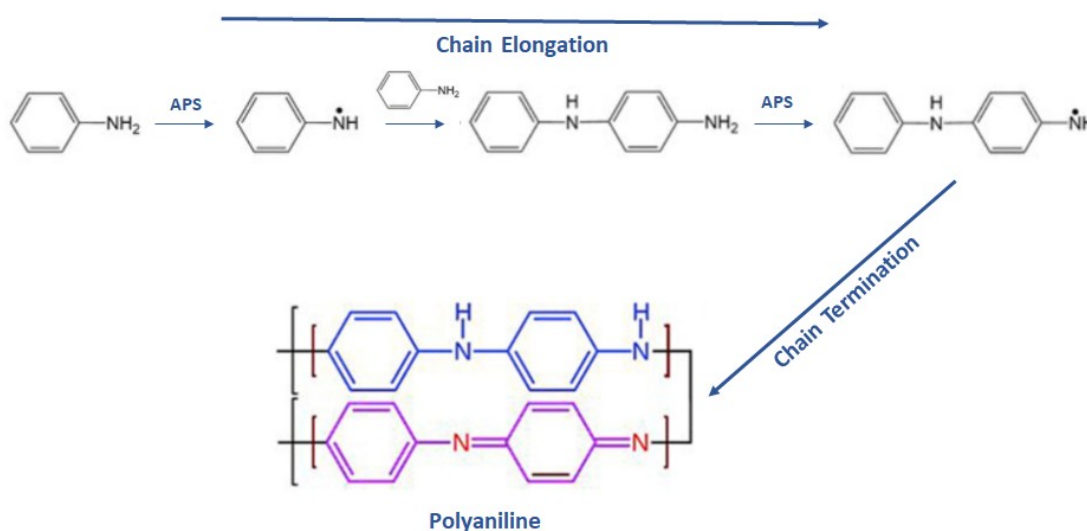


Figure 1. Polymerization mechanism of polyaniline (52, 53).

The polymerization was continued for 12 hours at a constant heating rate of 30°C and a constant stirring rate of 200 rpm. The Polyaniline/Biochar (PANI)/BC

composite material was obtained as a result of the reaction and then was filtered. After filtration, the hybrid material samples were washed first with HCl

(2M) solution, then with distilled water, and adsorbent samples were dehydrated in a vacuum oven at 90°C for 1 day (54, 55).

Batch experiments for adsorption of Cu(II) ions

To determine the adsorption features of Polyaniline/Biochar (PANI/BC) composite, heavy metal adsorption experiments were carried out by using Cu(II) adsorption stock solutions. Chemicals and reagents were used of analytical grade. Cu(II) stock solutions (1000 mg/L) were prepared by dissolving copper(II) nitrate, $\text{Cu}(\text{NO}_3)_2$, in distilled water. The solutions were prepared by diluting the stock solutions to specific concentrations.

Adsorption experiments were performed adding certain amounts of adsorbent material into tubes containing 50 mL of metal ion solution. Adsorption process was conducted by mixing these solutions at different temperatures and at a constant stirring speed of 200 rpm. The pH values of the solutions were adjusted using HCl (1 M) or NaOH (1 M). On the other hand, the constant temperature of the adsorbent solutions was provided with a water bath. Adsorbents were removed from the solutions by using vacuum filtration technique at different time intervals (5, 15, 30, 60, 120, 180, 240, 300, and 360 min) and adsorption capacities were calculated to make kinetic calculations. Copper removal experiments from aqueous solution was conducted by using batch experiments according to various experimental conditions such as pH (2-8), temperature (18, 20, 25, 30 °C), contact time (5-360 min), and adsorbent dosage (5-150 mg) to observe the effect of operational parameters on the removal efficiency.

At the end of the experiments, the adsorbents were removed from the solutions and filtered. The concentration of metal ions remaining in the solutions were determined using SHIMADZU, Double Beam UV-VIS Spectrophotometer/UV-2600 device. The percentage of metal ions was computed using the following equation.

$$\text{Removal \%} = \frac{C_0 - C_e}{C_0} \times 100 \quad (1)$$

Adsorption capacities were also computed using the following equation.

$$q_e = \frac{(C_0 - C_e) \times V}{W} \quad (2)$$

Where C_0 and C_e are initial ion concentration of heavy metal ions (mgL^{-1}) and equilibrium concentration of heavy metal ions (mgL^{-1}) respectively. V represents the volume of adsorbate solution (mL) and W is the adsorbent amount in (mg).

RESULT and DISCUSSION

Characterization

Thermal gravimetric analysis: The thermal stability of pure polyaniline, and Polyaniline/Biochar (PANI/BC) composite were determined with thermogravimetric analysis. Figure 2 indicates the thermal gravimetric plots of pure PANI (a) and PANI/BC composite (b). The TGA characterization curve of pure PANI (Figure 2) shows three steps of mass loss: the first one takes place at around 100-200 °C with 6.98 % weight loss accounting to the loss of adsorbed water molecules and dopant HCl molecules from polymer chains; second step at about 200-400 °C with a mass decline of 12.12 % which was likely due to the discharge of protonic acid groups and the third step at about 400-750 °C with a weight decline of 37.22 % is due to thermal decomposition of PANI chains and the fracture of the polymer chain (56). The thermogravimetric analysis of PANI/BC composite (Figure 2) demonstrates three phases of mass loss: the first step initiating at about 100-200 °C with a mass loss of 3.84 %, regarded as dehydration step of the adsorbed water molecules; second step occurred at about 200-380°C with a mass decrease of 11.41 % as an outcome of the protonic acid groups removal and the final stage observed in between 380-700°C with a weight loss of 33.12 % as a result of the fracture of polymer chain that governs the gas production.

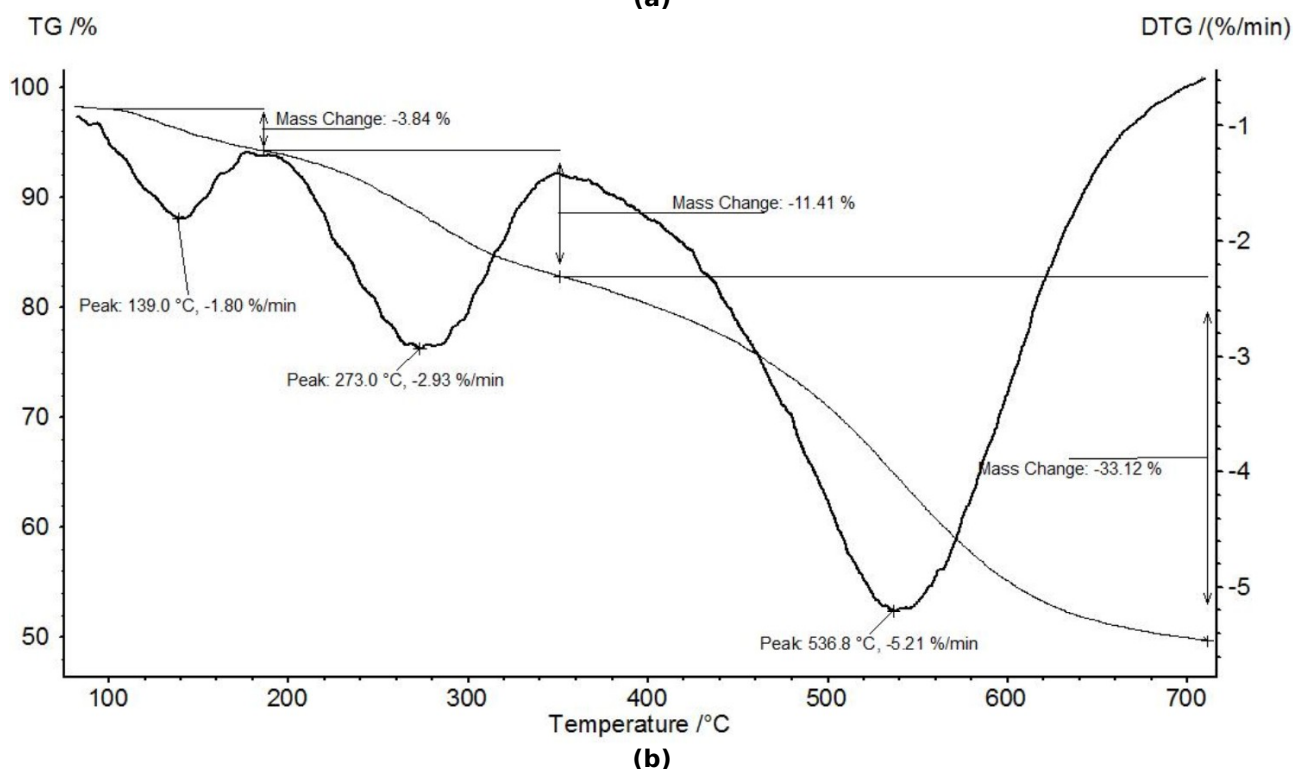
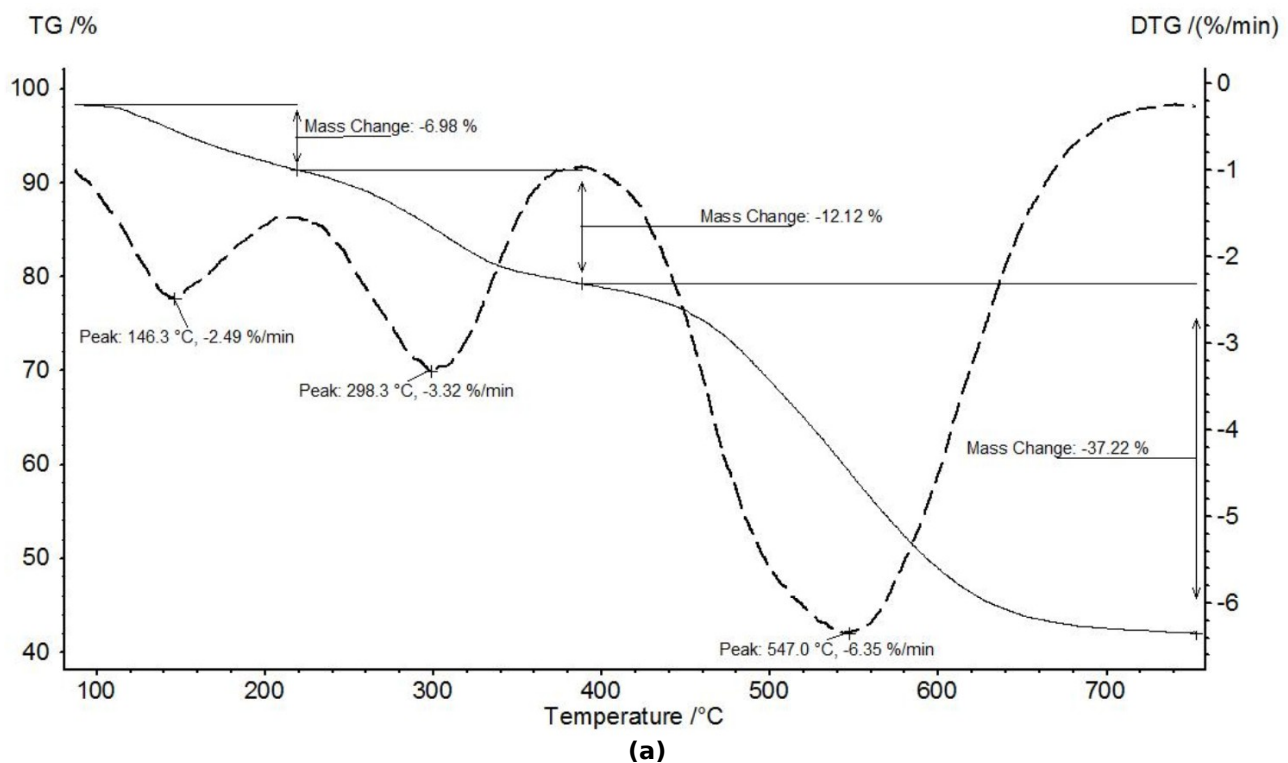


Figure 2. TGA thermograms of PANI (a), and PANI/BC composite (b).

It has been conducted that PANI is not much thermally stable as an organic polymer. In contrast, the PANI/BC composite showed a lower weight loss at every thermal step that can be related to improved thermal stability. This indicates that biochar particles enhanced the thermal stability of

PANI making it favorable in high temperature applications.

UV/Vis absorbance analysis

In the literature, it is discovered that the removal percentages of Cu(II) ions increase with an increase of initial ion concentration between 50-600 ppm

(57). However, a higher concentration of Cu(II) has been found to reduce the adsorption capacity due to the saturation of the adsorption sites. Therefore, in this study the initial ion concentration of Cu(II) ions was determined as 200 ppm as reported from literature (57, 58). 10 working solutions (20, 40, 60, 80, 100, 120, 140...200 mg/L) were prepared by diluting the stock solutions of copper(II) nitrate using distilled water.

The absorbance values were determined by using SHIMADZU, Double Beam UV-Vis Spectrophotometer/UV-2600 device at proper wavelength for Cu²⁺ ions (450 nm). These absorbance values were plotted with the concentrations of solutions as shown in Figure 3.

UV/Vis spectroscopy is widely performed available technique for adsorption characterization of prepared adsorbent samples. Adsorption capacities of prepared adsorbents for heavy metal ions can be studied by using UV/Vis spectroscopy. Spectral analysis was applied with a SHIMADZU, Double

Beam UV-Vis Spectrophotometer/UV-2600 device as collecting spectra from 200–1100 nm. Deuterium and tungsten lamps are preferred to obtain illumination across the ultraviolet, visible, and near-infrared electromagnetic spectrum.

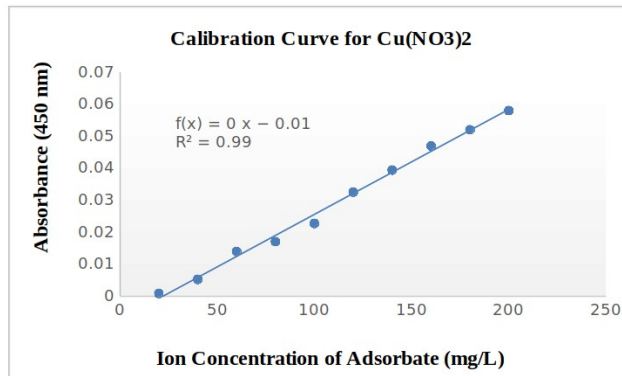


Figure 3. The calibration equation and calibration curve.

Table 1. Removal percentages determined with UV spectrometry.

pH	T (°C)	Adsorbent Dosage (mg)	Contact Time (min)	Removal (%)
2	30	20	60	62.76
3	30	20	60	80.31
4	30	20	60	84.66
5	30	20	60	84.57
6	30	20	60	82.40
7	30	20	60	83.12
8	30	20	60	81.70
4	18	20	60	79.85
4	20	20	60	87.72
4	25	20	60	86.66
4	30	20	60	84.69
4	20	5	60	88.17
4	20	10	60	89.23

Batch experiments

pH effect: The solute pH is important in adsorption experiments and generally the influence of pH parameter was examined prior to the other experimental parameters. The higher removal efficiencies of Cu(II) ions were founded when the pH of solution is greater than 4 since the decomposition rate occurred more slowly on the adsorbent surface under pH 4. The decrease in solute pH showed the lower tendency of removal efficiency for the PANI/BC composite adsorbents that can be associated with

4	20	15	60	87.72
4	20	20	60	87.72
4	20	30	60	86.66
4	20	40	60	86.51
4	20	50	60	86.66
4	20	100	60	86.51
4	20	150	60	85.30
4	20	10	5	85.45
4	20	10	15	86.21
4	20	10	30	83.34
4	20	10	60	88.17
4	20	10	120	87.42
4	20	10	180	88.33
4	20	10	240	88.03
4	20	10	300	88.48
4	20	10	360	88.33

higher acidic conditions due to the protonation of the groups.

In usual, water adsorption can occur easily on the surface of biochar, which is due to the covered eventual adsorbent surface layer with hydroxyl groups. These hydroxyls groups can take and leave protons to the water as making the adsorbent surface positively or negatively charged (59).

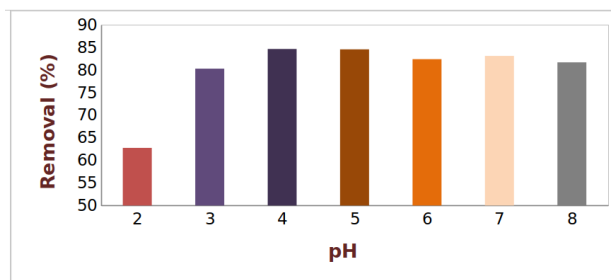


Figure 4. At 30°C, the pH effect examination for 20-mg amounts of PANI/BC composite adsorbent for 60 min of contact time.

If the acidic properties of the adsorbent surface are higher than the solute, the surface is charged negatively since the surface release protons to the solvent. In contrast, the surface is charged positively since the particle receives protons from the solvent due to the basic characteristic of the adsorbent surface (59).

As shown in Figure 4, it can be concluded that the pH values between 3 and 6 promote the adsorption

mechanism of Cu(II) ions due to nitrogen-containing functional groups in the polymeric chain including amine, imine, and protonated imine as responsible sites for adsorption.

Temperature effect: Temperature is a vital parameter for both adsorption rate and equilibrium conditions as it is changing the molecular interactions and solubility (60).

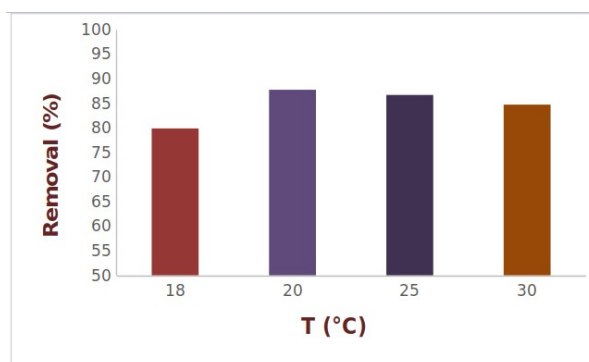


Figure 5. At pH 4 the temperature effect examination for 20-mg amounts of PANI/BC composite adsorbents for 60 min of contact time.

The adsorption of Cu(II) ions on PANI/BC composite adsorbent was examined at temperatures of 18, 20, 25, and 30 °C. As shown in Figure 5, the removal efficiency of adsorbent samples at 20 °C is higher than the removal efficiency at 18 °C, which can be associated with the increment of adsorption rate with temperature effect. The increase of temperature accelerates the mobility of Cu(II) ions on the adsorbent surface. The increase of removal efficiency of adsorbent from 18 to 20 °C also shows the spontaneous and feasibility of the adsorption mechanism. Adsorption efficiency can also decrease with the decrease of temperature effect in physical adsorption process due to the endothermic nature of mechanism. However, it was observed that the removal efficiency decreased with the increasing of temperature from 20 to 30°C may be due to the

physical adsorption behavior. In physical adsorption with increasing temperature, weaker physical attractions occur between the adsorbent surface and aqueous solution(61).

Dosage effect: Experimental studies were repeated with different dosages of PANI/BC to examine the effect of adsorbent dosage on removal efficiency and the results are given in Figure 6. The adsorbent amount is a very effective parameter as it defines the extent of removal. Increasing the adsorbent amount from 5 to 100 mg resulted in a sharp decrease in the percentage removal for Cu(II) ions. This behavior can be also observed probably due to overlapping functional sites at higher adsorbent amounts.

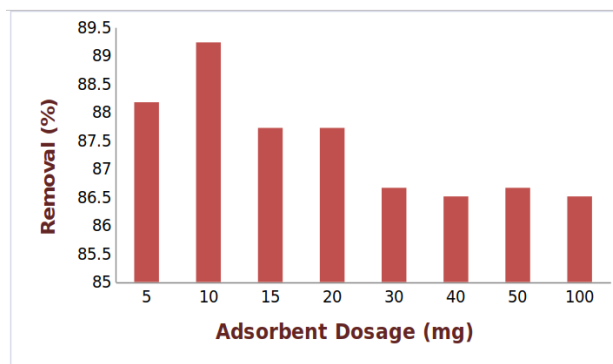


Figure 6. At pH 4, the adsorbent dosage effect examination of PANI/BC composite adsorbents for 20°C temperature and 60 min contact time.

Besides, the driven forces between adsorbent surface and solution physically obstruct available adsorption sites as leading to adsorption capacity decrease. In general, decreasing effective binding sites can be associated with the agglomeration of exchange particles (62).

On the other hand, the removal efficiency of Cu(II) increased from 88.17% to 89.23% with an increase of the adsorbent amount from 5 mg to 10 mg for 1 h of contact time. This increase in the adsorption can be related more availability of binding sites on the adsorbent surface to yield complexes with metal ions. The copper removal almost remains unchanged after (0.3 g) dosage of adsorbent is added since the adsorption equilibrium is reached. The maximum removal efficiency for PANI/BC

composite was found at an adsorbent dosage of 10 mg of the composite at 20°C and for 1 h of contact time in the adsorption batch experiment as can be seen from Figure 6.

The effect of contact time: The contact time explains the rate of the binding possibility of metal ions on the adsorbent surface and gives the optimum contact time for removal process completion of the metal ions. Figure 7 indicates the contact time effect on the removal efficiency of PANI/BC composite adsorbent. The removal efficiency increases with time and achieves equilibrium within 180 min. The metal ion adsorption changes with time increase thanks to saturation, considering that the possibility of monolayer covering of metal ions on the adsorbent surface.

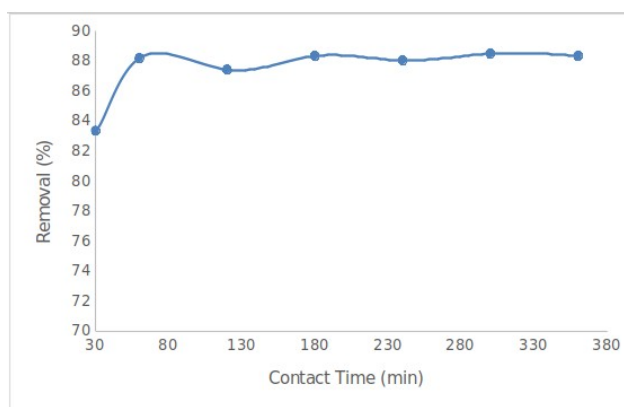


Figure 7. At pH 4, the contact time effect examination for 10-mg amounts of PANI/BC composite adsorbents for 20°C temperature.

As shown in figures, the relationship between the effecting experimental variables such as pH, contact time, temperature, and their related removal abilities contains highly non-linear complex behavior for various adsorbent substances. Therefore, it is generally very difficult to estimate the most promising operational conditions of different adsorbent types for improving the adsorption capacity. Besides, the experimental set up of these mechanisms can be time-consuming and highly costly. However, models are one of the best alternatives to avoid these limitations.

Kinetic analysis of PANI/BC composite adsorbent

The kinetic studies show the rate of the chemical reaction during the adsorption processes and define the effecting parameters of these reactions for the equilibrium access with an acceptable amount of time. The simulations of kinetic models give also hints about for the adsorption mechanisms and adsorption capacities.

One of the most preferred kinetic models are the Linearized Pseudo First-Order and Pseudo Second Order models. The linearised pseudo-first-order kinetic model formulation can be expressed as the following statement (63):

$$\ln(q_e - q_t) = \ln q_e - k_1 t \quad (3)$$

Where k_1 (min^{-1}) denotes the pseudo-first-order adsorption rate constant, whereas the q_e and q_t are the expressions of the adsorbed mass amounts of adsorbent (mg/g) at equilibrium time and t (min) time, respectively. In general, the pseudo-first-order kinetic models which change significantly according to the adsorption mechanism are appropriate for only the first 20 and 30 contact minutes of adsorbents.

The linearized Pseudo second-order kinetic model can also be formulated as the following statement (64):

$$\frac{t}{q_t} = \frac{1}{k_2 q_e^2} + \frac{1}{q_e} \times t \quad (4)$$

Where k_2 (min^{-1}) refers to the pseudo-second-order kinetic model rate constant as can be related to the experimental conditions including the initial solute pH, temperature, etc. When k_2 decreases the required time is increased for reaching the equilibrium conditions. The main assumption of the pseudo-second-order kinetics is the adsorption rate-limiting step occurs due to the valency forces of interactions between adsorbent surface and heavy metal ions. k_2 (min^{-1}) and q_e (mg/g) values can be calculated from the intercept and slope of the plotted curves that were generated by plotting t/q_t versus t (min). If the adsorption process follows these kinetic model results, the plotted curve would be straight line. One of the big advantages of this type of kinetic model is the estimating q_e parameters with a relatively small experimental error.

These two different kinetic models were utilized for PANI/BC composite adsorbent material for its predetermined operational conditions such as pH 4 of solute and 20°C to investigate the compatibility of the synthesized adsorbent samples with both kinetic models.

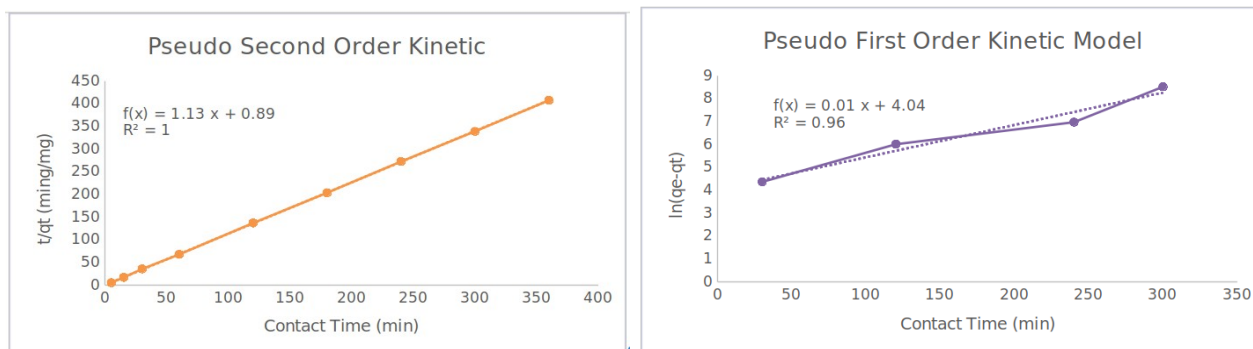


Figure 8. The comparison of PANI/BC composite adsorbent results with Pseudo Second Order Kinetic Model (top) and with Pseudo First Order Kinetic Model (bottom).

As seen in Figure 8, the pseudo-second-order model fits better with the experimental results because it gives a higher determination coefficient factor (1) than the pseudo-first-order model result (0.9612). Pseudo-second-order kinetic model can be considered as the proper model for the adsorption process of Cu(II) onto the PANI/BC composite adsorbent due to its high determination coefficient value and its validity for almost every contact time variety.

For the pseudo-first-order kinetic model, the k_1 and q_e values can be determined from the slope and intercept of curves obtained by plotting of t/q_t versus t whereas the k_2 and q_e values were also obtained using the same method for the pseudo-second model. The determined parameter values were given in Table 2.

Table 2. Kinetic model parameters for adsorption of Cu(II) ions onto PANI/BC composite.

Pseudo First Order Kinetic Model			Pseudo Second Order Kinetic Model		
k_1 (min^{-1})	q_e (mg/g)	R^2	k_2 (min^{-1})	q_e (mg/g)	R^2
0.0141	4.036	0.9612	1.1295	0.8861	1

Nonlinear regression model

Samples: The effect of five variables on the efficiency of Cu(II) adsorption including; pH, adsorbent dosage, contact time, and temperature were selected as input parameters and utilized to develop the model. All experimental results were divided into training and testing sets. Samples were randomly selected by using the MATLAB software. The training dataset was employed to develop a non-linear regression model and a testing dataset was applied for validation of the proposed model.

Model: Modeling is a proven and accepted engineering approach to design and optimize removal processes by using a nonlinear combination of experimental parameters. This combination is defined as highly complex, which is affected by different operational conditions and adsorption mechanisms. Thus, modeling of removal processes is encouraged by using nonlinear regression. Non-linear regression technique is a kind of regression analysis in which observational data are modeled by a function that is a nonlinear combination of the model parameters and depends on one or more independent variables.

In this study, an innovative approach is implemented to improve the accuracy of the nonlinear regression and its estimation ability of removal efficiency. The aim is to define optimum operational conditions as input variables associated with removal efficiency and to perform an exponential and logarithmic regression on developed model. The developed model that is used for the estimation of Cu(II) removal, is the following:

$$\text{Removal Efficiency Prediction for Cu(II)} = (-0.0061916) \times (x_1) + ((-0.034073) \times (x_2)) + ((0.30832) \times (x_3)) + ((-13272) \times (x_4)) + ((-7.8883 \times 10^{-10}) \times (x_5)) + ((-4.5737 \times 10^{-09}) \times (x_6))$$

where x_1 is $(\text{temp}^3/\text{ph}^3)$, x_2 is $((\text{time}/\text{ph}) \times \cos(\text{ph}))$, x_3 is $(\cos(\text{mass}^2) \times \cot(\text{time}/\sin(\text{ph}^{0.5})))$, x_4 is $(\text{ph}^3/\text{temp}^2)/\text{temp}^2$, x_5 is $(\text{temp}^7/\cos(\text{time}^2))/\text{ph}$, x_6 is (mass^4) , respectively, and the coefficients from γ_1 to γ_6 denote the regression coefficients.

The comparison between the model results and experimental datasets gave a high correlation coefficient (0.9494) as indicating the Cu(II) removal estimation ability of the model for PANI/BC composite adsorbent.

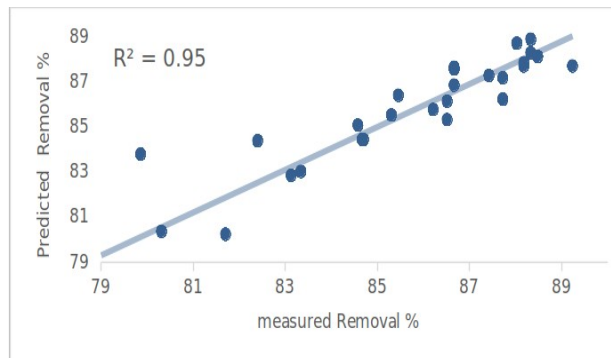


Figure 9. The comparison between the experimental results and the predicted results obtained from the developed non-linear model.

Regression analysis was used to define the consistency of the model output results and the target values showing whether the training network is acceptable or not (Figure 9). In addition, to obtain a better understanding of the model ability, optimal operating parameters obtained from experimental studies were tested with model simulation results. According to experimental results, pH of the adsorbate solution 4, the adsorbent dosage of 10 mg, and temperature of 20 °C were determined as the optimum experimental conditions with a removal efficiency of % 89.23 for PANI/BC composite adsorbent. This value is quite high as considering the many removal percentages obtained from copper removal studies in the literature (65-69). The results demonstrated that the PANI/BC composite was found to be an ideal adsorbent material for the removal of copper metals.

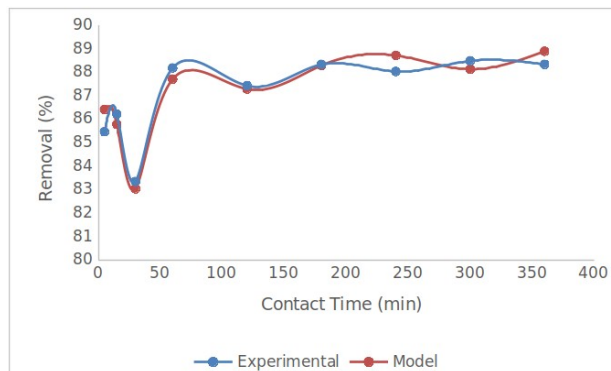


Figure 10. Agreement between the non-linear model and experimental results as a function of contact time.

The impacts of experimental parameters on Cu(II) ions removal ability were utilized to comprehend the process when the other factors were fixed at the optimum value that conducted in experimental studies. As can be seen in Figure 10, the prediction ability of the proposed model was validated by using the corresponding model simulation results with the experimental outcomes of PANI/BC composite adsorbent.

CONCLUSION

In this study, the removal of Cu(II) toxic heavy metal ions from aqueous solution using a novel Polyaniline/Biochar (PANI/BC) composite adsorbents was conducted in batch experiments. The effects of operational parameters such as adsorbent dosage, pH, contact time, and temperature were investigated on the Cu(II) removal process. The kinetic results showed that the Cu(II) removal occurs in the 30 min of contact time, which implies a high affinity of adsorbent toward ions, probably due to the functional adsorption sites such as hydroxyl, carboxyl, and amine groups on the adsorbent surface. It was also found that the utilization of a non-linear regression modeling approach is a very effective, economic, and eco-friendly method for comprehending of removal mechanism. Moreover, the optimal conditions of PANI/BC composite for Cu(II) adsorption experiments showed good agreement with our proposed model. Modeling results were compared with experimental results to verify the predictive accuracy and applicability of the model. According to our expectations, large applicable information about composite materials gained with ease of modeling approach will increase the discovery of advanced materials for future green synthesis components and clean energy systems.

REFERENCES

- Rashid N, Rehman MSU, Han J-I. Recycling and reuse of spent microalgal biomass for sustainable biofuels. *Biochemical engineering journal*. 2013;75:101-7.
- Patra J, Panda S, Dhal N. Biochar as a low-cost adsorbent for heavy metal removal: A review. *Int J Res Biosci*. 2017;6:1-7.
- Sardar K, Ali S, Hameed S, Afzal S, Fatima S, Shakoor MB, et al. Heavy metals contamination and what are the impacts on living organisms. *Greener Journal of Environmental Management and Public Safety*. 2013;2(4):172-9.
- Galil N, Rebhun M. Primary chemical treatment minimizing dependence on bioprocess in small treatment plants. *Water Sci Technol*. 1990;22(3-4):203-10.
- Kurniawan TA, Chan GY, Lo W-H, Babel S. Physico-chemical treatment techniques for wastewater laden with heavy metals. *Chem Eng J*. 2006;118(1-2):83-98.
- O'Connell DW, Birkinshaw C, O'Dwyer TF. Heavy metal adsorbents prepared from the modification of cellulose: A review. *Bioresource technology*. 2008;99(15):6709-24.
- Wang Y-H, Lin S-H, Juang R-S. Removal of heavy metal ions from aqueous solutions using various low-cost adsorbents. *Journal of Hazardous Materials*. 2003;102(2-3):291-302.
- Fu F, Wang Q. Removal of heavy metal ions from wastewaters: a review. *Journal of environmental management*. 2011;92(3):407-18.
- Khezami L, Capart R. Removal of chromium (VI) from aqueous solution by activated carbons: kinetic and equilibrium studies. *Journal of hazardous materials*. 2005;123(1-3):223-31.
- Ali I. New generation adsorbents for water treatment. *Chemical reviews*. 2012;112(10):5073-91.
- Uzun I, Güzel F. Adsorption of some heavy metal ions from aqueous solution by activated carbon and comparison of percent adsorption results of activated carbon with those of some other adsorbents. *Turkish Journal of Chemistry*. 2000;24(3):291-8.
- Biškup B, Subotić B. Kinetic analysis of the exchange processes between sodium ions from zeolite A and cadmium, copper and nickel ions from solutions. *Sep Purif Technol*. 2004;37(1):17-31.
- Cincotti A, Mameli A, Locci AM, Orrù R, Cao G. Heavy metals uptake by Sardinian natural zeolites: Experiment and modeling. *Ind Eng Chem Res*. 2006;45(3):1074-84.
- Gupta VK, Ali I. Removal of lead and chromium from wastewater using bagasse fly ash - a sugar industry waste. *J Colloid Interf Sci*. 2004;271(2):321-8.
- Haroun AA, El-Halawany NR. Preparation and Evaluation of Novel Interpenetrating Polymer Network-Based on Newspaper Pulp for Removal of Copper Ions. *Polym-Plast Technol*. 2011;50(3):232-8.
- Haroun AA, Mashaly HM, El-Sayed NH. Novel nanocomposites based on gelatin/HPET/chitosan with high performance acid red 150 dye adsorption. *Clean Technol Envir*. 2013;15(2):367-74.
- Kardam A, Raj KR, Srivastava S, Srivastava MM. Nanocellulose fibers for biosorption of cadmium, nickel, and lead ions from aqueous solution. *Clean Technol Envir*. 2014;16(2):385-93.
- Huang Q, Liu MY, Mao LC, Xu DZ, Zeng GJ, Huang HY, et al. Surface functionalized SiO₂ nanoparticles with cationic polymers via the combination of mussel inspired chemistry and surface initiated atom transfer radical polymerization: Characterization and enhanced removal of organic dye. *J Colloid Interf Sci*. 2017;499:170-9.
- Huang QA, Liu MY, Chen JY, Wan Q, Tian JW, Huang L, et al. Facile preparation of MoS₂ based polymer composites via mussel inspired chemistry and their high efficiency for removal of organic dyes. *Appl Surf Sci*. 2017;419:35-44.
- Zhang XY, Huang Q, Liu MY, Tian JW, Zeng GJ, Li Z, et al. Preparation of amine functionalized carbon nanotubes via a bioinspired strategy and their application in Cu²⁺ removal. *Appl Surf Sci*. 2015;343:19-27.
- Gier S, Johns WD. Heavy metal-adsorption on micas and clay minerals studied by X-ray photoelectron spectroscopy. *Applied Clay Science*. 2000;16(5-6):289-99.
- Koppelman M, Dillard J. A study of the adsorption of Ni (II) and Cu (II) by clay minerals. *Clays and Clay Minerals*. 1977;25(6):457-62.

23. Dang V, Doan H, Dang-Vu T, Lohi A. Equilibrium and kinetics of biosorption of cadmium (II) and copper (II) ions by wheat straw. *Bioresource technology*. 2009;100(1):211-9.
24. Hadi B, Margaritis A, Berruti F, Bergougnou M. Kinetics and equilibrium of cadmium biosorption by yeast cells *S. cerevisiae* and *K. fragilis*. *Int J Chem React Eng*. 2003;1(1).
25. Sharma YC, Uma, Gode F. Engineering Data for Optimization of Preparation of Activated Carbon from an Economically Viable Material. *J Chem Eng Data*. 2010;55(9):3991-4.
26. Yang T, Lua AC. Textural and chemical properties of zinc chloride activated carbons prepared from pistachio nut shells. *Mater Chem Phys*. 2006;100(2-3):438-44.
27. Foroushani FT, Tavanai H, Hosseini FA. An investigation on the effect of KMnO₄ on the pore characteristics of pistachio nut shell based activated carbon. *Microporous and Mesoporous Materials*. 2016;230:39-48.
28. Zheng W, Guo MX, Chow T, Bennett DN, Rajagopalan N. Sorption properties of greenwaste biochar for two triazine pesticides. *Journal of Hazardous Materials*. 2010;181(1-3):121-6.
29. Anderson N, Jones J, Page-Dumroese D, McCollum D, Baker S, Loeffler D, et al. A comparison of producer gas, biochar, and activated carbon from two distributed scale thermochemical conversion systems used to process forest biomass. *Energies*. 2013;6(1):164-83.
30. Liu W-J, Zeng F-X, Jiang H, Zhang X-S. Preparation of high adsorption capacity bio-chars from waste biomass. *Bioresource technology*. 2011;102(17):8247-52.
31. Nagarale R, Gohil G, Shahi VK. Recent developments on ion-exchange membranes and electro-membrane processes. *Advances in colloid and interface science*. 2006;119(2-3):97-130.
32. Zhou Y, Gao B, Zimmerman AR, Fang J, Sun Y, Cao X. Sorption of heavy metals on chitosan-modified biochars and its biological effects. *Chemical Engineering Journal*. 2013;231:512-8.
33. Wang L-X, Li X-G, Yang Y-L. Preparation, properties and applications of polypyrroles. *Reactive and Functional Polymers*. 2001;47(2):125-39.
34. Taghizadeh A, Taghizadeh M, Jouyandeh M, Yazdi MK, Zarrintaj P, Saeb MR, et al. Conductive polymers in water treatment: A review. *Journal of Molecular Liquids*. 2020;113447.
35. Das TK, Prusty S. Review on conducting polymers and their applications. *Polymer-plastics technology and engineering*. 2012;51(14):1487-500.
36. Laabd M, Hallaoui A, Aarb N, Esseki A, Eljazouli H, Lakhmiri R, et al. Removal of polycarboxylic benzoic acids using polyaniline-polypyrrole copolymer: experimental and DFT studies. *Fibers and Polymers*. 2019;20(5):896-905.
37. Jiang Y, Liu Z, Zeng G, Liu Y, Shao B, Li Z, et al. Polyaniline-based adsorbents for removal of hexavalent chromium from aqueous solution: a mini review. *Environmental Science and Pollution Research*. 2018;25(7):6158-74.
38. Wang J, Zhu W, Zhang T, Zhang L, Du T, Zhang W, et al. Conductive polyaniline-graphene oxide sorbent for electrochemically assisted solid-phase extraction of lead ions in aqueous food samples. *Analytica Chimica Acta*. 2020;1100:57-65.
39. Yang Y, Wang W, Li M, Wang H, Zhao M, Wang C. Preparation of PANI grafted at the edge of graphene oxide sheets and its adsorption of Pb (II) and methylene blue. *Polymer Composites*. 2018;39(5):1663-73.
40. Xia C, Chen W, Wang X, Hedhili MN, Wei N, Alshareef HN. Highly stable supercapacitors with conducting polymer core-shell electrodes for energy storage applications. *Advanced Energy Materials*. 2015;5(8):1401805.
41. Shao D, Chen C, Wang X. Application of polyaniline and multiwalled carbon nanotube magnetic composites for removal of Pb (II). *Chemical Engineering Journal*. 2012;185:144-50.
42. Kim MK, Sundaram KS, Iyengar GA, Lee K-P. A novel chitosan functional gel included with multiwall carbon nanotube and substituted polyaniline as adsorbent for efficient removal of chromium ion. *Chemical Engineering Journal*. 2015;267:51-64.
43. Ansari MO, Kumar R, Ansari SA, Ansari SP, Barakat M, Alshahrie A, et al. Anion selective pTSA doped polyaniline@ graphene oxide-multiwalled carbon nanotube composite for Cr (VI) and Congo red adsorption. *Journal of colloid and interface science*. 2017;496:407-15.
44. Patel N, Okabe K, Oya A. Designing carbon materials with unique shapes using polymer blending and coating techniques. *Carbon*. 2002;40(3):315-20.
45. Li X, Cai W, An J, Kim S, Nah J, Yang D, et al. Large-area synthesis of high-quality and uniform graphene films on copper foils. *science*. 2009;324(5932):1312-4.
46. Liu D, Xia L-J, Qu D, Lei J-H, Li Y, Su B-L. Synthesis of hierarchical fiberlike ordered mesoporous carbons with excellent electrochemical capacitance performance by a strongly acidic aqueous cooperative assembly route. *Journal of Materials Chemistry A*. 2013;1(48):15447-58.
47. Jin H, Wang X, Shen Y, Gu Z. A high-performance carbon derived from corn stover via microwave and slow pyrolysis for supercapacitors. *Journal of Analytical and Applied Pyrolysis*. 2014;110:18-23.
48. Qiu B, Xu C, Sun D, Wang Q, Gu H, Zhang X, et al. Polyaniline coating with various substrates for hexavalent chromium removal. *Applied Surface Science*. 2015;334:7-14.
49. Mansour M, Ossman M, Farag H. Removal of Cd (II) ion from waste water by adsorption onto polyaniline coated on sawdust. *Desalination*. 2011;272(1-3):301-5.
50. Laabd M, Chafai H, Esseki A, Elamine M, Al-Muhtaseb S, Lakhmiri R, et al. Single and multi-component adsorption of aromatic acids using an eco-friendly polyaniline-based biocomposite. *Sustainable materials and technologies*. 2017;12:35-43.

51. Novak JM, Lima I, Xing B, Gaskin JW, Steiner C, Das K, et al. Characterization of designer biochar produced at different temperatures and their effects on a loamy sand. *Annals of Environmental Science*. 2009.
52. Karri RR, Tanzifi M, Yarakı MT, Sahu J. Optimization and modeling of methyl orange adsorption onto polyaniline nano-adsorbent through response surface methodology and differential evolution embedded neural network. *Journal of environmental management*. 2018;223:517-29.
53. Alonso PEdG. Alternative synthesis methods of electrically conductive bacterial cellulose-polyaniline composites for potential drug delivery application 2017.
54. Mi H, Yang X, Li F, Zhuang X, Chen C, Li Y, et al. Self-healing silicon-sodium alginate-polyaniline composites originated from the enhancement hydrogen bonding for lithium-ion battery: A combined simulation and experiment study. *Journal of Power Sources*. 2019;412:749-58.
55. Yakışık H. Polymer nanocomposites: synthesis, characterization and application in heavy-metal removal. 2019.
56. Guo Y, Zheng M, Chen J. Chemical synthesis, characterization and thermal analysis of polyaniline/copper composite powder. *Journal of composite materials*. 2008;42(14):1431-8.
57. Dandil S, Sahbaz DA, Acikgoz C. Adsorption of Cu (II) ions onto crosslinked Chitosan/Waste Active Sludge Char (WASC) beads: Kinetic, equilibrium, and thermodynamic study. *International journal of biological macromolecules*. 2019;136:668-75.
58. Ma J, Li T, Liu Y, Cai T, Wei Y, Dong W, et al. Rice husk derived double network hydrogel as efficient adsorbent for Pb (II), Cu (II) and Cd (II) removal in individual and multicomponent systems. *Bioresource technology*. 2019;290:121793.
59. Hosokawa M, Nogi K, Naito M, Yokoyama T. *Nanoparticle technology handbook*: Elsevier; 2012.
60. Ahmaruzzaman M, Sharma D. Adsorption of phenols from wastewater. *Journal of Colloid and Interface Science*. 2005;287(1):14-24.
61. Aksu Z, Tatlı Aİ, Tunç Ö. A comparative adsorption/biosorption study of Acid Blue 161: Effect of temperature on equilibrium and kinetic parameters. *Chemical Engineering Journal*. 2008;142(1):23-39.
62. Rahmani A, Mousavi HZ, Fazli M. Effect of nanostructure alumina on adsorption of heavy metals. *Desalination*. 2010;253(1-3):94-100.
63. Ho YS, Wase DJ, Forster C. Kinetic studies of competitive heavy metal adsorption by sphagnum moss peat. *Environmental Technology*. 1996;17(1):71-7.
64. Ho Y-S, McKay G. Pseudo-second order model for sorption processes. *Process biochemistry*. 1999;34(5):451-65.
65. Ali MB, Wang F, Boukherroub R, Lei W, Xia M. Phytic acid-doped polyaniline nanofibers-clay mineral for efficient adsorption of copper (II) ions. *Journal of colloid and interface science*. 2019;553:688-98.
66. Kubilay Ş, Gürkan R, Savran A, Şahan T. Removal of Cu (II), Zn (II) and Co (II) ions from aqueous solutions by adsorption onto natural bentonite. *Adsorption*. 2007;13(1):41-51.
67. Wu S, Li F, Xu R, Wei S, Li G. Synthesis of thiol-functionalized MCM-41 mesoporous silicas and its application in Cu (II), Pb (II), Ag (I), and Cr (III) removal. *Journal of Nanoparticle Research*. 2010;12(6):2111-24.
68. Ghaemi N. A new approach to copper ion removal from water by polymeric nanocomposite membrane embedded with γ -alumina nanoparticles. *Applied Surface Science*. 2016;364:221-8.
69. Betiha M, Moustafa Y, Mansour A, Rafik E, Elshahat M. Nontoxic polyvinylpyrrolidone-propylmethacrylate-silica nanocomposite for efficient adsorption of lead, copper, and nickel cations from contaminated wastewater. *Journal of Molecular Liquids*. 2020:113656.



Usage of Cellulose Acetate Butyrate Based Oligomeric Structures on Cotton Fabric Coatings

Zehra Yıldız^{1*}  , H. Ayşen Önen²  , Ozan Gazi Dehmen³  ,
and Atilla Güngör⁴  

¹ Marmara University, Faculty of Technology, Department of Textile Engineering, Kadıköy, İstanbul, 34722, Türkiye

² Istanbul Technical University, Faculty of Science and Letters, Department of Chemistry, Maslak, İstanbul, 34467, Türkiye

³ Istanbul Technical University, Institute of Science and Technology, Polymer Science and Technology, Maslak, İstanbul, 34467, Türkiye

⁴ Marmara University, Faculty of Science and Letters, Department of Chemistry, Kadıköy, İstanbul, 34722, Türkiye

Abstract: In this study, the hydroxyl groups of cellulose acetate butyrate (CAB) oligomer were reacted with toluene diisocyanate-hydroxyethyl methacrylate (TDI-HEMA) adduct, in order to improve properties of CAB such as flexibility, thermal stability, etc. Then the obtained modified CAB oligomer was characterized by FTIR and ¹H NMR analysis. UV-curable coating formulations were prepared by using the modified CAB oligomer, and then applied on cotton fabrics in order to reinforce cotton fabrics and make them durable in outdoor environments. Cotton fabrics were treated with a commercial washing detergent, alkaline solution, and an enzyme prior to the UV-coating, in order to increase the adhesion between the cotton fabric and coating layer. Washed and coated fabrics were evaluated in terms of absorbency, tensile, and adhesion properties, respectively. Light microscopy was employed to observe the effects of washing processes on fiber, and to show the abrasion deformation on coated fabric. Results proved that the best washing process in fibrillation was found as enzymatic washing due to the highest adhesion strength and the least deformation against abrasion.

Keywords: UV-Curing; Cellulose Acetate Butyrate; Cotton Fabric; Pectinase Enzyme; Peel Test.

Submitted: October 20, 2019. **Accepted:** January 09, 2021.

Cite this: Yıldız Z, Önen HA, Dehmen OG, Güngör A. Usage of Cellulose Acetate Butyrate Based Oligomeric Structures on Cotton Fabric Coatings. JOTCSA. 2021;8(1):303-10.

DOI: <https://doi.org/10.18596/jotcsa.634996>.

***Corresponding author. E-mail:** zehra.yildiz@marmara.edu.tr.

INTRODUCTION

Cellulose is a biopolymer that is the most abundant, easily accessible, and cheap raw material and is widely used in many commercial applications. The hydroxyl groups of cellulose allow its conversion into regenerated cellulose via the formation of ester and ethers by the reaction with various chemical species. This modification process gives the desired physical/chemical properties that are required for the usage area. The most important commercially available cellulose ester derivatives are as follows; cellulose acetate, cellulose acetate propionate and

butyrate, and carboxymethyl cellulose acetate butyrate. Among all cellulose derivatives, cellulose acetate butyrate (CAB) has some superior properties such as high scratch resistance and being economical. The inelastic rod-like structure of CAB crystals causes a high viscosity of CAB in a molten state that restricts the processability of CAB. Besides, the low thermal stability of polysaccharide structures of CAB, leads to a narrow processability range between the melting and decomposition temperatures, thus lowers the thermal stability of CAB. In order to overcome the mentioned problems, some researches based on the modification of CAB

have been performed but there is no research considering the modification of the CAB by using the urethane-based oligomers (1-3).

UV-curing technology is favored due to the requirement of less solvent or none (environment friendly), processability at low temperatures (economical), and saving of time with a rapid crosslinking mechanism just in a few seconds (mass production). UV-curable coatings can be used as varnishes, adhesives, inks, functional coating materials in many industries such as automotive, printing, dentistry, furniture, micro-electronics, biomedical, optical, and packaging products. The reaction of toluene diisocyanate-hydroxyethyl methacrylate (TDI-HEMA) is often performed in literature, to prepare UV-sensitive coating formulations. Here, the UV-curable acrylate groups are provided by HEMA, which supplies the usage of solvent/waste-free process and provides time and cost-efficiency. Whereas the isocyanate groups of TDI gives an elastic behavior to the oligomer due to the formation of carbamate ester units. In TDI-HEMA reaction, some isocyanate functional groups are left unreacted intentionally in order to give additional functionalities by introducing other active species in further reactions. For instance, TDI-HEMA-functionalized carbon nanotubes, TDI-HEMA-epoxy acrylate oligomers, TDI-HEMA-butyl acrylate oligomers have all been manufactured via the usage of TDI-HEMA adduct in the literature (4-9).

Due to the hydrophobic impurities on cotton fibers such as waxes, pectin, grease, hemicellulose, protein etc., the solution uptake and wettability properties of fibers negatively affected during the finishing processes. Therefore, cotton fibers need to be scoured in order to enhance the hydrophilicity and dyestuff uptake, to improve the compatibility between fiber/finishing agent, and to increase the adhesion strength between the fiber/coating layer. In this study, a commercial washing process with standard ECE washing powder, alkali treatment with concentrated sodium hydroxide (NaOH) solution, and enzymatic washing with pectinase enzyme were all employed for cotton fabric scouring. The ECE washing powder is a non-ionic, phosphated, without optical brightening agent and used in textile fastness tests. It helps to remove the water/detergent soluble impurities from the fiber surface. In alkali treatment, concentrated NaOH solution helps to dissolve the impurities such as lignin, hemicellulose, grease, and waxes on the fiber surface. During the alkaline treatment, the surface area of fibers increases due to the fibrillation which supplies a better penetration of the coating layer. The enzymatic washing step presents, some advantages over the other washing steps such as being sustainable and eco-friendly, requiring less energy, and giving less deformation to the fiber surface. Pectinase enzyme was chosen to decompose the pectinic impurities on cotton fabric. In literature, PET fabrics have been treated with

cutinase enzyme and NaOH solution, respectively. Accordingly, the enzymatic washing process showed a better performance in the fibrillation of PET fabric compared to the alkaline treatment (10-18).

In this study, the hydroxyl groups on CAB structure were modified by TDI-HEMA adduct in order to enhance the undesired properties of CAB. Then the modified CAB oligomers obtained were included in UV-curable coating formulations on cotton fabrics. In order to improve the adhesion between the cotton fiber and coating layer, fabrics were treated with an alkaline solution, pectinase enzyme, and ECE washing powder, respectively. The abrasion, tensile, and adhesion properties of washed and coated fabrics were all investigated.

EXPERIMENTAL

Materials

CAB (Eastman 551-0.01, 53 % wt. butyryl, 2 % wt. acetyl, 1.5 % wt. hydroxyl content), 1,6-hexanediol diacrylate (HDDA, Merck, reactive diluent), tetrahydrofuran (THF, Merck), toluene diisocyanate (TDI, Merck), 2-hydroxyethyl methacrylate (HEMA, Merck), sodium hydroxide (NaOH, Merck), dibutyltin dilaurate (DBTDL, T12 catalyst, Merck), 1-hydroxycyclohexyl phenyl ketone (Irgacure® 184, photo initiator, Ciba Specialty Chemicals), non-ionic wetting agent (Uniwett HGA Alfa Kimya), ECE phosphated, without optical brightening agent (SDL Atlas) were all used as received. Cotton fabrics (115 g/m², 30 warp/cm, 22 weft/cm) were obtained from Tavsanlı Tekstil Co.

Preparation and Application of Coating Formulations

Figure 1 shows the synthesis steps of TDI-HEMA modified CAB oligomer. Firstly, TDI-HEMA in an equimolar ratio, HDDA (30 % wt.), T12 catalyst, and THF were all loaded to a round bottomed flask, under nitrogen atmosphere, equipped with a condenser and magnetic stirrer. THF and HDDA were used to dissipate a sudden temperature increase and to dilute the reaction media, respectively. The reaction was performed for the first half an hour in an ice bath, another half an hour at 25 °C, then 1 h at 70 °C. The decrease in the intensity of isocyanate peak was followed by FTIR spectroscopy during the reaction. In the second step, certain amounts of CAB, allowing to react only 50 % of hydroxyl groups on it, was dissolved in THF and included into the reaction flask. The temperature was raised to 90 °C and ended in half an hour by checking the disappearance of isocyanate peak in FTIR spectra. The rest of the hydroxyl groups on CAB were intentionally left unreacted in order to give flexibility to the oligomer. Due to the differences in reactivity of isocyanates in para and ortho positions, at first isocyanates in para position react with the hydroxyl groups of HEMA, whereas the isocyanates in ortho position reacts with the hydroxyl groups of CAB in the second step, at a higher temperature.

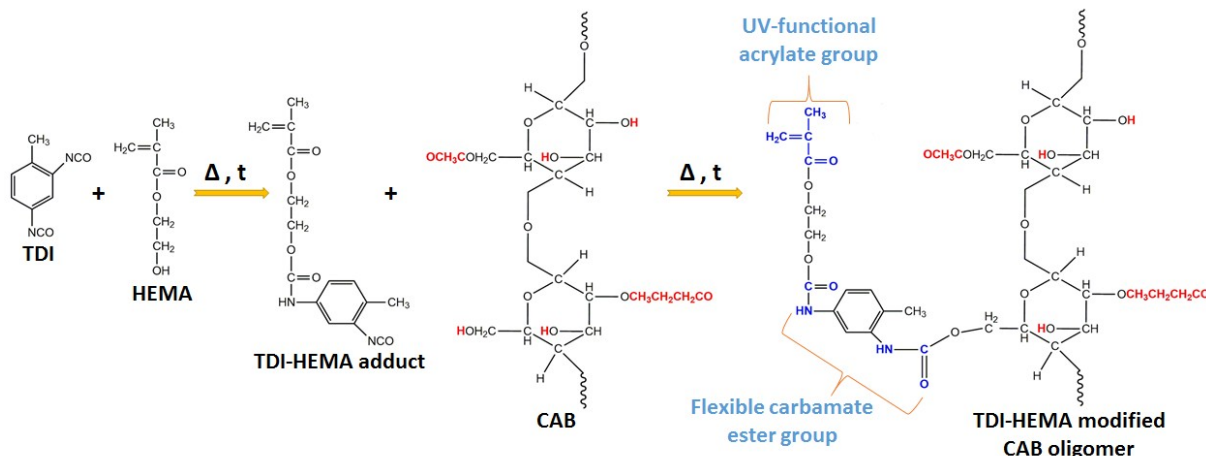


Figure 1. Synthesis of TDI-HEMA modified CAB oligomer.

Cotton fabrics were cut in 15x20 cm dimensions that are needed to make the T-peel test. The process parameters of each washing processes can be seen in Figure 2. The washing processes were all performed on an enclosed Pyrex glass with 25 cm diameter, equipped with a magnetic stirrer. Fabrics were immersed in the washing media and were laid out on the bottom of Pyrex. Distilled water was used on each rinsing step.

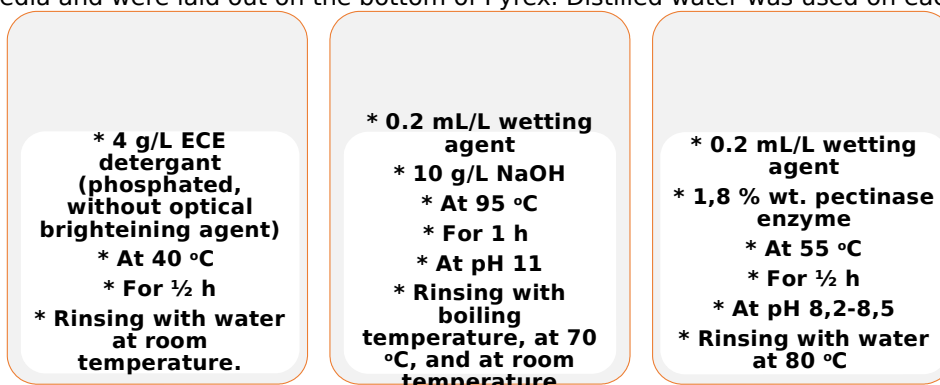


Figure 2. Parameters of each washing processes.

Fabric samples with various washing processes were dipped into the coating formulation containing 3% wt. photoinitiator for 3 min. After that fabrics were put between two PE films and pressed by a squeezing roller to dissipate the excess resin from the fabric. Then fabrics were exposed to UV-light for

3 min from both sides of the fabric between two glass plates. The fabric coating process was performed in both one layer and two layers of fabric in order to make the tensile testing and T-peel test, respectively. Figure 3 illustrates the fabric coating and curing processes.

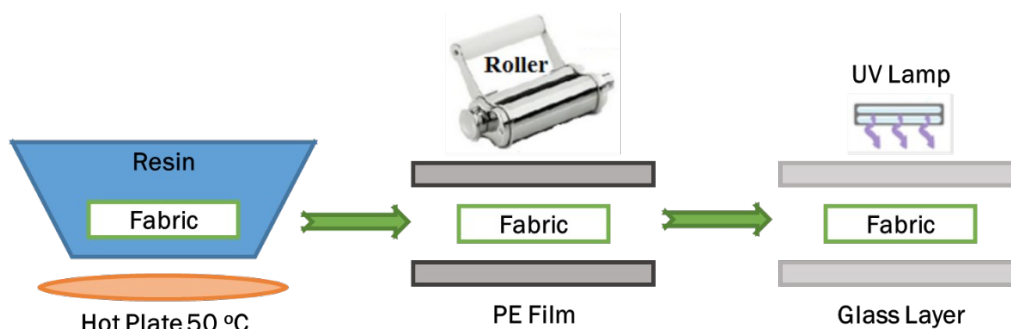


Figure 3. Application of coating formulations and UV-curing.

Characterization

The synthesized TDI-HEMA adduct and modified CAB

oligomer were characterized by FTIR (Perkin Elmer Spectrum 100 FTIR equipped with a ZnSe ATR

crystal) and ^1H NMR spectroscopic methods (Agilent VNMRS 500 MHz, with deuterated dimethylsulfoxide (DMSO-d_6) as solvent and tetramethylsilane (TMS) as an internal standard). In order to evaluate the hydrophilicity property of fabrics after washing steps, an absorbency test (AATCC-79-2004) was employed (19). Tensile testing (TS EN ISO 13934-1) (20) and abrasion test (TS EN ISO 12947-2 for fabrics without coating layer, TS EN ISO 5470-2 for fabrics with coating layer) (21, 22) were performed in Instron 4411 tensile testing machine, and Martindale pilling and abrasion instrument, respectively. The adhesion strength in double layered coated fabrics was measured by the T-peel test (ASTM D1876-08) also in Instron 4411 tensile testing machine (23).

RESULTS AND DISCUSSION

FTIR Analysis

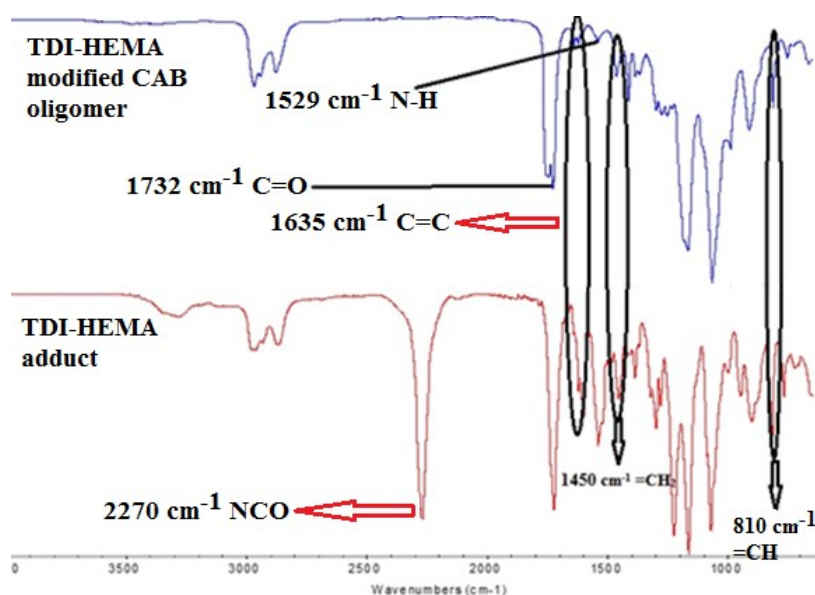


Figure 4. FTIR spectra of TDI-HEMA adduct and modified CAB oligomers.

^1H NMR Spectra

The ^1H NMR spectra of TDI-HEMA modified CAB oligomer was given in Figure 5. The characteristic methacrylic proton peaks of HEMA can be followed from the peaks at 4.27-4.35 ppm ($-\text{O}-\text{CH}_2-\text{CH}_2-\text{O}$), at 6.10-6.18 ppm ($\text{C}(\text{CH}_3)=\text{CH}_2$ *cis*), and 5.59-5.60 ppm ($\text{C}(\text{CH}_3)=\text{CH}_2$ *trans*), respectively. At 2.14-2.17 ppm

The FTIR spectra of TDI-HEMA adduct and modified CAB oligomers can be seen in Figure 4. Accordingly, in the spectra of TDI-HEMA adduct, the isocyanate peak at 2270 cm^{-1} disappeared with the reaction of CAB. This result can be explained by the reactivity differences of isocyanate groups. Due to the steric hindrance of methyl groups, the isocyanate groups of TDI in ortho-position are four times less reactive than the isocyanate groups in para-position. Thus in the first step, the isocyanates in para-position react with the hydroxyl groups of HEMA. Whereas the isocyanates in ortho-position react with the hydroxyl groups of CAB in the second step due to the increased temperature. The characteristic HEMA peaks of $\text{C}=\text{C}$, $=\text{CH}_2$, and $=\text{CH}$ were observed at 1635 cm^{-1} , 1450 cm^{-1} , and 810 cm^{-1} , respectively. The characteristic carbamate ester peaks of N-H bending and $\text{C}=\text{O}$ stretching were observed at 1529 cm^{-1} and 1732 cm^{-1} in the spectra of modified CAB oligomer (24-26).

region, the methyl proton peak of TDI can be observed. The existence of carbamate ester groups ($-\text{NH}-\text{COO}$) in the structure can be seen with the proton peak at 5.01 ppm. The proton peaks of the cellulose structure can be all observed at 3.32-4.18 ppm region (25, 27-29).

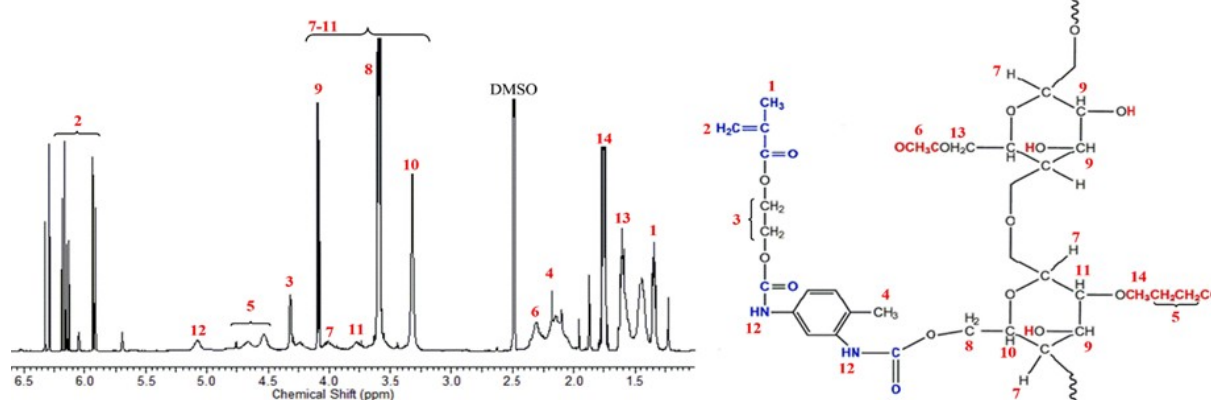


Figure 5. ^1H NMR spectra of TDI-HEMA modified CAB oligomer.

Absorbency Test

The hydrophilicity behavior of fabrics after various washing processes was investigated by using an absorbency test according to the AATCC TM79-2018 standard (19). The absorbency test is performed by following a complete disappearance of a distilled water droplet, which is dripped from a certain height, on the fabric surface, by using a chronometer. Accordingly, the absorbency test value of 142 seconds was recorded on the unwashed fabric surface. After washing processes, the

absorbency test result was recorded as 3 seconds for each washing procedure. When the fabric was coated with the UV-curable formulation, the absorbency test result was obtained as more than 24 hours, which means the water droplet cannot be immersed into the fabric surface. The decline on the absorbency test results from the 142 seconds to the 3 seconds after washing is due to the fibrillation of fibres. Fibrillation causes a rougher look (Figure 6) and the formation of more surface area among fiber structure which means more points are formed to bond the liquid on the fabric surface.

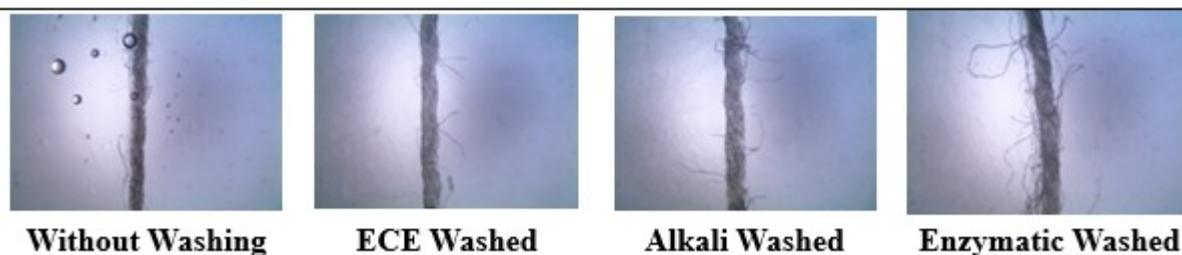



Figure 6. Light microscopy images of single fiber from the fabric without washing and fabrics after each washing processes.

Abrasion Resistance Test

The abrasion resistance values of pure fabric, fabrics after washing, and fabrics after UV-coating with their light microscopy images were all given in Table 1. The abrasion resistance test for uncoated washed fabrics was recorded according to the TS EN ISO 13934-1 standard. Fabrics were cut in 5 cm diameter and allowed to be abraded towards a standard wool fabric. When a yarn was a break in both warp and weft directions, the test is ended. Results are given in terms of "cycle". Pure cotton fabric showed a 38,000 cycle before damaged. The smooth surfaces are more durable against abrasion than corresponding rough surfaces. After washing steps, due to the fibrillation on fiber surface, fabrics gained a rougher look, thus the abrasion resistance values were all decreased. It was recorded as 34,000 cycle (ECE washed), 32,000 cycle (alkaline-washed), and 30,000 cycle (enzymatically washed), respectively.

After UV-coating process, another abrasion test which is suitable for resin coated fabrics were performed according to the TS EN ISO 5470-2 standard. On this test, coated fabrics were cut into 5 cm diameter and allowed to be abraded by a sandpaper. The evaluation was made in terms of the weight loss percentage after 100 cycle abrasion. Accordingly, after UV-coating process, the unwashed fabric showed a 20.3% weight loss in abrasion test. Whereas when the fabrics are washed prior to the UV-coating process, the abrasion results were all decreased. And the least weight loss value of 11.6% was recorded in the case of enzymatically washed UV-coated fabric sample. This result is due to the highest fibrillation level of enzymatic washing, resulting a better bonding between the fiber surface and the coating layer. The light microscopy images of UV-coated fabrics after 100 cycle abrasion were also supported this result.

Table 1. Abrasion resistance values of fabrics before/after washing and UV-coating.

	Without Washing	ECE-Washed	Alkaline-Washed	Enzymatically Washed	
Abrasion Resistance (cycle)	38,000	34,000	32,000	30,000	Uncoated
Abrasion Resistance (weight loss, %)	20.3	16.4	14.1	11.6	Coated
					
Light Microscopy Images After Abrasion Test					

Tensile and Peel Testing

Table 2 shows the tensile strength values of pure fabric and fabrics after each washing processes. Also the peel strength values of double layered UV-coated fabrics were given in Table 2. An increase in tensile strength values were observed due to the fibrillation after washing processes. This result is stemming from the increase in surface roughness with fibrillation, more adherence points are formed on the fiber surfaces (Figure 6). Thus fabrics become more durable after washing. The highest tensile strength value of 1080 N was recorded on the sample with pectinase enzyme washing. Considering

the peel testing results, as in tensile testing, due to the increase in surface roughness the adherence between the coating layer and fiber surface increases. Thus the highest peel test value of 27.8 N was also recorded in the sample with enzymatic washing. Figure 7 illustrates the possible bonding mechanism between the UV-coating layer and cotton fabric surface. The strong hydrogen bondings between the hydroxyl groups of cellulose and hydroxyl groups of CAB, carbonyl groups of carbamate esters and HEMA, and NH groups in carbamate esters are all responsible for the bonding mechanism.

Table 2. The tensile strength and peel test values of washed and UV-coated fabrics.

	Without Washing	ECE-Washed	Alkaline-Washed	Enzymatic-Washed	
Tensile Strength (N)	950	1001	1070	1080	Uncoated
Peel Test (N)	16.3	20.2	23.6	27.8	Double Layered UV-Coated

CONCLUSIONS

In this study, the hydroxyl groups on CAB structure were modified by TDI-HEMA adduct in order to enhance the undesired properties of CAB such as high viscosity due to the inelastic structure, low thermal stability etc. The obtained TDI-HEMA adduct and modified CAB oligomer were chemically characterized by FTIR and ^1H NMR spectroscopies. By using the modified CAB oligomer, UV-coating formulations were prepared and applied on double-layered cotton fabrics. In order to increase the adhesion strength between UV-coating layer and cotton fabric surface, the ECE, alkaline, and enzymatic washing processes were applied on cotton fabrics prior to the UV-coating. All results are consistent that the washing step with pectinase

enzyme showed the highest performance in the fibrillation of cotton fibers. Thus the highest absorbency and the least abrasion resistance by means of cycle were recorded in the case of enzymatic washed sample. After double-layered UV-coating process, the least abrasion resistance by means of weight loss percentage after 100 cycle and the highest peel strength were also recorded for enzymatic washed sample. Considering the industrial usage, a commercial tarpaulin fabric properties are as follows; flame resist, water-proof, and 850 g/m² in weight. The double-layered UV-coated fabric proposed in this paper is also water-proof, and having a lower weight of 524 g/m². Thus it can be suggested that the proposed UV-coated fabric can be used as light-weighted tarpaulin. Further studies are now in progress modifying the

oligomeric structure by incorporation of phosphorus- containing flame resistant functional groups.

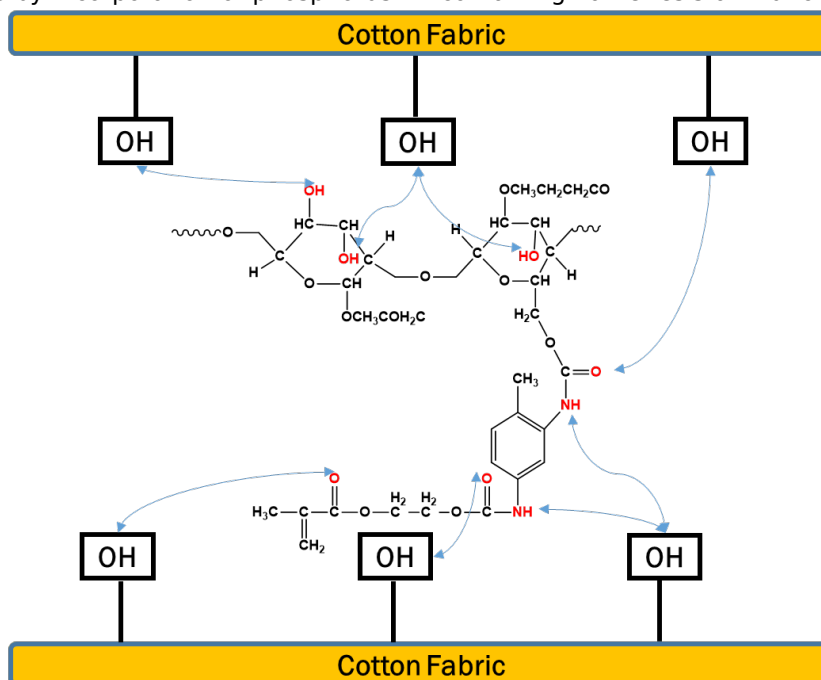


Figure 7. The bonding mechanism between the UV-coating layer and cotton fabric surface.

ACKNOWLEDGEMENT

The extended abstract of this study was orally presented in 31th National Chemistry Congress on 10-13 September 2019, İstanbul (31. Ulusal Kimya Kongresi 10-13 Eylül, 2019, İstanbul).

REFERENCES

- Çakmakçı E, Güngör A, Kayaman-Apohan N, Kuruca SE, Çetin MB, Dar KA. Cell growth on in situ photo-cross-linked electrospun acrylated cellulose acetate butyrate. *Journal of Biomaterials Science, Polymer Edition*. 2012;23(7):887-99.
- Wang X, Huang S, Wang Y, Wei P, Chen Y, Xia Y, et al. Eco-friendly cellulose acetate butyrate/poly (butylene succinate) blends: crystallization, miscibility, thermostability, rheological and mechanical properties. *Journal of Polymer Research*. 2017;24(2):16.
- Biniaś W, Biniaś D. Formation of Microfibres from Cellulose Acetate Butyrate by Electrospinning with a Surface Modified in Low-temperature Plasma. *Fibres & Textiles in Eastern Europe*. 2014.
- Barszczewska-Rybarek IM. Characterization of urethane-dimethacrylate derivatives as alternative monomers for the restorative composite matrix. *Dental Materials*. 2014;30(12):1336-44.
- Lei G, Angeli S, Kristol D, Snyder W. Preparation of new blocked diisocyanate for dental application. *Journal of Polymer Science Part A: Polymer Chemistry*. 1987;25(2):607-15.
- Wang SJ, Wang YL, Yang PF, Li TD, editors. Preparation of polyurethane-poly (butyl acrylate) hybrid latexes via miniemulsion polymerization. *Applied Mechanics and Materials*; 2012: Trans Tech Publ.
- Wang F, Hu J, Tu W. Study on microstructure of UV-curable polyurethane acrylate films. *Progress in organic coatings*. 2008;62(3):245-50.
- Xie J, Zhang N, Guers M, Varadan VK. Ultraviolet-curable polymers with chemically bonded carbon nanotubes for microelectromechanical system applications. *Smart materials and structures*. 2002;11(4):575.
- Liu X-D, Sheng D-K, Gao X-M, Li T-B, Yang Y-M. UV-assisted surface modification of PET fiber for adhesion improvement. *Applied Surface Science*. 2013;264:61-9.
- Eker P. Farklı Hammaddeler İçeren Lycralı Dokuma Kumaşlarda Biyo-Parlatma ve Biyo-Parlatmanın Kumaş Performansına Etkileri. Adana 2012 (In Turkish).
- Ozgen H. Farklı Yöntemlerle Pamuklu Örme Kumaşın Enzimatik Hidrofilleştirilmesi. Bartın 2018 (In Turkish).
- Stanescu MD, Dochia M, Radu D, Sirghie C. Green solution for cotton scouring. *Fibres & Textiles in Eastern Europe*. 2010;18(3):80.
- SANCAR B, PAKSOY N, BALCI O, KURTOĞLU N.

Pamuklu Dokuma Kumaşların Boyamaya Hazırlık İşlemlerinde Enzim Kullanım Olanaklarının İncelenmesi ve Kombine Proses Geliştirilmesi. *Tekstil ve Mühendis*. 2012;19(86) (In Turkish).

14. Toprak T. Pamuklu Kumaşlarda Kombine Enzim Proseslerinin Geliştirilmesi. Bursa 2014 (In Turkish).

15. Davulcu A. Pamuklu Kumaşların Ön Terbiye Proseslerinin Enzimatik Yöntemlerle Kombine Edilmesi Üzerine Bir Araştırma. Bursa 2008 (In Turkish).

16. Duran K, Bozacı E, Karahan H. Protein Esaslı Mamüllerin Enzimatik ÖnTerbiyesi. *Tekstil ve Konfeksiyon*. 2007;3:187-92.

17. Yılmaz B. Selülozik Materyallerin Tek Banyoda Kombine Proses ile Boyanmasında Optimizasyon. İstanbul 2004 (In Turkish).

18. Donelli I, Freddi G, Nierstrasz VA, Taddei P. Surface structure and properties of poly-(ethylene terephthalate) hydrolyzed by alkali and cutinase. *Polymer Degradation and Stability*. 2010;95(9):1542-50.

19. AATCC TM79-2018, Absorbency of Textiles. 2018.

20. TS EN ISO 13934-1:Tekstil - Kumaşların gerilme özellikleri - Bölüm 1:En büyük kuvvetin ve en büyük kuvvet altında boyca uzamanın şerit yöntemiyle tayini. 2013 (In Turkish).

21. TS EN ISO 5470-2:Lastik veya plastik kaplı kumaşlar-Aşınma dayanımının tayini-Böllüm 2:Martindale aşındırıcı. 2004 (In Turkish).

22. TS EN ISO 12947-2:Tekstil - Martindale metoduyla kumaşların aşınmaya karşı dayanımının

tayini- Bölüm 2: Numune kopmasının tayini. 2017 (In Turkish).

23. ASTM D1876-08: Standard Test Method for Peel Resistance of Adhesives (T-Peel Test). ASTM International: West Conshohocken, PA; 2015.

24. Grepinet B, Pla F, Hobbes P, Swaels P, Monge T. Modeling and simulation of urethane acrylates synthesis. I. Kinetics of uncatalyzed reaction of toluene diisocyanate with a monoalcohol. *Journal of applied polymer science*. 2000;75(5):705-12.

25. Liao F, Zeng X-r, Li H-q, Lai X-j, Zhao F-c. Synthesis and properties of UV curable polyurethane acrylates based on two different hydroxyethyl acrylates. *Journal of Central South University*. 2012;19(4):911-7.

26. Tan SZ, Wang Y, Zhang YF, Zhou WL, editors. Preparation of a novel prepolymer of polyurethane acrylate. *Advanced Materials Research*; 2012: Trans Tech Publ.

27. Dong Y, Edgar KJ. Imparting functional variety to cellulose ethers via olefin cross-metathesis. *Polymer Chemistry*. 2015;6(20):3816-27.

28. Dong Y, Mosquera-Giraldo LI, Troutman J, Skogstad B, Taylor LS, Edgar KJ. Amphiphilic hydroxyalkyl cellulose derivatives for amorphous solid dispersion prepared by olefin cross-metathesis. *Polymer Chemistry*. 2016;7(30):4953-63.

29. Kunwong D, Sumanochitraporn N, Kaewpirom S. Curing behavior of a UV-curable coating based on urethane acrylate oligomer: the influence of reactive monomers. *Sonklanakarın Journal of Science and Technology*. 2011;33(2):201.



A Novel Conjugated Pyrene-BODIPY Dyad: Synthesis, Characterization and Properties

Husniye Ardic Alidagi^{*} , Seda Cetindere 

Gebze Technical University, Faculty of Science, Department of Chemistry, 41400, Kocaeli, Turkey.

Abstract: In the present work, a novel highly conjugated pyrene-boron dipyrromethene (Py-BODIPY) **4** with a donor-acceptor (D-A) skeleton small molecule was synthesized by Sonogashira cross-coupling reaction between 1-ethynylpyrene (**2**) as a donor group and BODIPY **3** as an acceptor group. The new compound was characterized by fourier transform-infrared (FT-IR), nuclear magnetic resonance spectroscopy (NMR), mass spectrometry (MALDI-TOF) and elemental analysis. The photophysical and electrochemical properties of the compound **4** were investigated by UV-vis absorption, fluorescence emission spectroscopy, and cyclic voltammetry (CV) in dichloromethane. It was found from the optical and electrochemical measurements that the target compound has highest occupied molecular orbital energy level (E_{HOMO}) at -5.70 eV, lowest unoccupied molecular orbital energy level (E_{LUMO}) at -3.27 eV, and the band gap was calculated as 2.43 eV. In addition, theoretical computational studies was also carried out via density functional theory (DFT) for investigation of molecular structure and energy levels of the compound. On the basis of these results, the novel Pyrene-BODIPY compound **4** could be potential candidate for organic light emitting diodes (OLEDs).

Keywords: Pyrene, BODIPY, optoelectronic device.

Submitted: November 20, 2020. **Accepted:** January 12, 2021.

Cite this: Ardic Alidagi H, Cetindere S. A Novel Conjugated Pyrene-BODIPY Dyad: Synthesis, Characterization and Properties. JOTCSA. 2021;8(1):311-20.

DOI: <https://doi.org/10.18596/jotcsa.819632>.

***Corresponding author.** E-mail: hardic@gtu.edu.tr.

INTRODUCTION

Two or more chromophore containing supramolecular systems have attracted the interest of the world of science, because of their potential for significant applications ranging from energy transfer to optoelectronic devices and sensors (1,2). This interest have caused the synthesis and characterization of a wide range of molecules placed with different chromophores chosen for their characteristic photophysical and electrochemical features. Investigation of photophysical properties of such compounds is especially fascinating and extremely dependent on the functional dye systems (3). Among many organic dyes, boron dipyrromethene (BODIPY) dyes have an importance as a fluorophore with many advantages including high quantum yield, high extinction coefficient, narrow emission bandwidth, and so, insensitivity to pH and solvent polarity, and considerable chemical and photochemical stabilities in solid state and in

solution (4-6). BODIPYs are widely applied as fluorophores and, if combined with an appropriate electron donor or acceptor units like as pyrenes exhibit efficient electron or energy transfer (7-9). In addition, BODIPYs are excellent candidates as a π -acceptor building block for optoelectronic applications due to the planar dipyrromethene core may ensure π - π stacking with delocalized HOMO-LUMO orbitals, large dipole moment in the range of 3-5 Debye, oriented toward the fluorine groups, could enhance thin film ordering by strong dipolar interactions, and also α , β or meso positions are easily functionalized for enhancing the conjugation or solution processibility (10).

Pyrenes are also an important part of the fluorophore family because of their unique photophysical properties and abilities to create an excimer caused to common use as a fluorescent label in different macromolecules (11-13). In the UV region, it has a high molar extinction coefficient and

absorption spectra are possessed by the transition to S_2 state because S_1 state is just about forbidden (14,15). Fluorescence is emitted from S_1 state, causing an extremely obvious Stokes shift because internal conversion from S_2 to S_1 is ultrafast (75–85 fs) (16,17). Because of the low oscillator strength, S_1 lifetime is quite long which makes pyrene beneficial for non-radiant energy transfer (18). Conjugated pyrene derivatives are one of the significant organic functional intermediates as an organic semiconductor for application in photovoltaic devices such as OLEDs, OFETs, OLEFETs, and solar cells. For this purpose, studies were carried out to improve the electronic and optical properties of pyrene derivatives by changing their molecular structure by substituting electron donor or acceptor groups (19-22). Although many photoactive supramolecular systems containing two or more chromophores have been reported up to date, only a few articles about boron dipyrromethene-pyrene systems have been published (23-27).

In this contribution, we herein have designed and synthesized a solution processible D-A π -conjugated small molecule which could be used as a semiconductor in the application of organic optoelectronics based on a BODIPY acceptor unit and pyrene donor unit that is linked via an alkyne spacer. The strategies designing the molecular structure were; π -donor pyrene unit substituted through the meso position of π -acceptor BODIPY unit for facilitating electron-transfer, methyl groups on BODIPY unit ensure good solubility in many organic solvents, so this solution processibility serves easy purification and thin film formation which is necessary for the semiconductor. The new semiconductor shows a large dipole moment calculated from the density functional theory program provides intramolecular charge transfer. The new molecule was characterized by mass spectrometry, FT-IR, $^1\text{H}/^{13}\text{C}$ NMR, elemental analysis, and thermogravimetric analysis (TGA). The optical and electrochemical properties of the new molecule were examined by UV-Vis absorption, fluorescence emission spectroscopies, and CV. Also, the photophysical and electrochemical properties of the molecule were studied by DFT program to calculate the photophysical and electrochemical parameters (28-30).

EXPERIMENTAL SECTION

Materials and Equipments

All reagents and solvents were bought through a trading agent and used as received unless mentioned. The reactions were done under argon gas unless otherwise noted. Analytical thin layer chromatography (TLC) for monitoring the reactions was used on silica gel plates (Merck, Kieselgel 60, 0.25 mm thickness) with an F_{254} indicator. Silica gel (Merck, Kieselgel 60, 230–400 mesh) was used in column chromatography. ^1H and ^{13}C NMR spectra were taken in CDCl_3 solution on Varian INOVA 500

MHz spectrometer. Elemental analysis was performed using a Thermo Finnigan Flash 1112 Instrument. Mass spectra were recorded on a Bruker Daltonics Microflex LT MALDI-TOF mass spectrometer. Infrared spectra were measured on a Perkin Elmer Spectrum 100 Optica FT-IR Spectrometer. UV-Vis spectra were measured with a Shimadzu 2101 UV spectrophotometer. Fluorescence excitation and emission spectra were measured on a Varian Eclipse spectrofluorometer by using 1 cm path length cuvettes at 25 °C. Thermal properties of the compound were investigated on Mettler Toledo TGA/SDTA 851 TGA at a heating rate of 10 °C min^{-1} under nitrogen flow. The electrochemical experiments were acquired using a CHI842B electrochemical workstation (CH Instruments).

Electrochemical Calculations

The electrochemical measurements were carried out by CV under argon at 25 °C with a scanning rate of 100 mVs^{-1} . The experiments were performed in anhydrous dichloromethane with 0.1 M tetrabutylammonium hexafluorophosphate (TBAPF_6) as an electrolyte. A standard three-electrode system in an electrochemical cell was used where a glassy carbon electrode served as the working electrode, a platinum wire electrode was the counter electrode, and an Ag/AgCl (saturated KCl) electrode was used as the reference electrode. The results are adjusted versus the Fc/Fc^+ redox couple potential. The HOMO energy level of the compound was calculated from the onset oxidation potential (E_{ox}) in CV, using the equation of $\text{HOMO} = -[E_{\text{ox}} - E_{1/2}(\text{ferrocene}) + 4.8]$ V, where $E_{1/2}(\text{ferrocene})$ is the onset oxidation potential of ferrocene vs. Ag/AgCl reference electrode and 4.8 eV is the energy level of ferrocene below vacuum level. The LUMO energy level was calculated from the onset reduction potential in cyclic voltammetry, using the equation of $\text{LUMO} = -[E_{\text{red}} - E_{1/2}(\text{ferrocene}) + 4.8]$ V. The band gap (E_g) was calculated using the equation of $E_g = E_{\text{LUMO}} - E_{\text{HOMO}}$.

Synthesis

The necessary compound **1**, **2** and **3** for the successful preparation of novel Py-BODIPY **4** were synthesized and characterized according to literature procedure (31, 32).

Synthesis of trimethyl(pyren-1-ylethynyl)silane (1)

1-Bromopyrene (100 mg, 3.6 mmol) was added to triethylamine (Et_3N) (40 mL) and toluene (6 mL) and then, tetrakis(triphenylphosphine)palladium(0) ($\text{Pd}(\text{PPh}_3)_4$) (210 mg, 0.18 mmol), copper(I)iodide (69 mg, 0.36 mmol), triphenylphosphine (PPh_3) (94 mg, 0.36 mmol) were added under argon atmosphere, respectively. Then the reaction mixture was heated to 60 °C and trimethylsilylacetylene (TMSA) (700 mg, 7.2 mmol) was injected through a septum. After 15 min the reaction was heated to 80 °C and stirred overnight. The cooled reaction mixture was extracted with dichloromethane and water. The

collected organic phase was dried over Na_2SO_4 , and the solvent was evaporated under reduced pressure. The residue was purified by column chromatography, and petroleum ether was used as the eluent. ^1H NMR (in CDCl_3) δ (ppm) = 8.58 (d, 1H, $J=8.5$ Hz), 8.16-8.02 (m, 8H), 0.43 (s, 9H). MS (MALDI-TOF) ($\text{C}_{21}\text{H}_{18}\text{Si}$) m/z : Calc. 298.12, found 299.067 $[\text{M}+\text{H}]^+$.

Synthesis of 1-ethynylpyrene (2)

Compound **1** (370 mg, 1.2 mmol) was suspended in methanol (25 mL). K_2CO_3 (330 mg, 2.4 mmol) was added and the reaction mixture stirred at room temperature (rt) overnight and then poured into water (100 mL) and filtered. The filter was washed with water until the filtrate was neutral. Compound **2** was obtained as a brown solid (230 mg, 85%). ^1H NMR (in CDCl_3) δ (ppm) = 8.60 (d, 1H, $J=8.8$ Hz), 8.25-8.02 (m, 8H), 3.63 (s, 1H). MS (MALDI-TOF) ($\text{C}_{18}\text{H}_{10}$) m/z : Calc. 226.08, found 226.089 $[\text{M}]^+$.

Synthesis of 1,3,5,7-tetramethyl-8-(4-bromophenyl)-4,4-difluoro-4-bora-3a,4a-diaza-s-indacene (3)

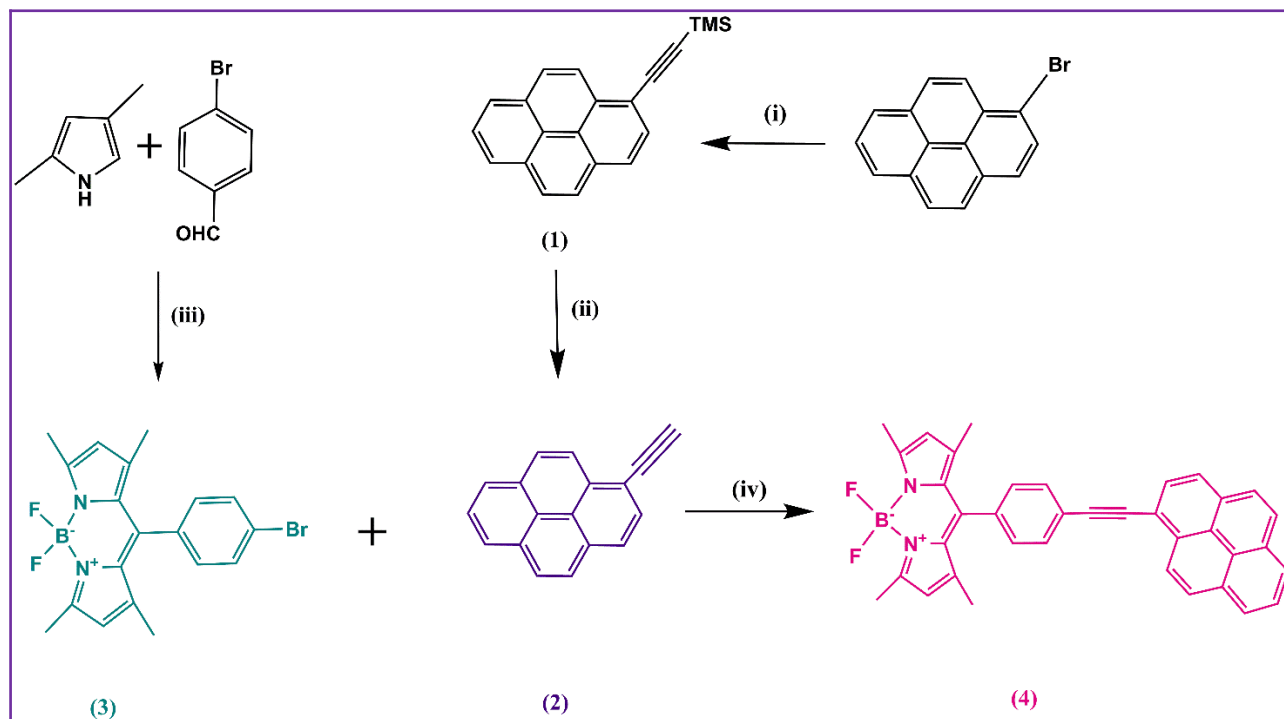
4-Bromobenzaldehyde (1.0 g, 5.4 mmol), 2,4-dimethylpyrrole (1.0 g, 10.5 mmol) and trifluoroacetic acid (TFA) (16 μL , 0.2 mmol) were dissolved in dry dichloromethane (250 mL) under argon, and the reaction mixture was stirred at rt for 18h. The disappearance of the benzaldehyde was controlled via TLC and then a solution of 2,3-dichloro-5,6-dicyano-1,4-benzoquinone (DDQ) (1.2 g, 5.3 mmol) in dry tetrahydrofuran (THF) (20 mL) was added slowly to the reaction mixture and stirred for an additional 4 h. The mixture was then cooled to 0 °C, Et_3N (16 mL) was added, and then the mixture was warmed to rt. After stirring for 2h, boron trifluoride diethyl etherate ($\text{BF}_3\cdot\text{OEt}_2$) (16 mL) was added, and the reaction mixture stirred for an additional 18 h at rt. A saturated sodium bicarbonate solution (200 mL) was then added to the mixture. The organic layer was separated and concentrated under reduced pressure to approximately 50 mL followed by the addition of 200 mL water. The mixture was extracted with diethyl ether (3 times of 200 mL), the collected organic extracts were dried over anhydrous Na_2SO_4 and the solvent was evaporated under reduced pressure. The raw product was purified by flash column chromatography on silica gel eluting with dichloromethane/n-hexane (1:1) to obtain the product as a dark-orange solid (101 mg, 25% yield). ^1H NMR (in CDCl_3) δ (ppm) = 7.63 (d, 2H, $J=8.0$ Hz), 7.20 (d, 2H, $J=8.0$ Hz), 5.94 (s, 2H), 2.52 (s, 6H), 1.45 (s, 6H); MS (MALDI-TOF) ($\text{C}_{19}\text{H}_{18}\text{BF}_2\text{N}_2\text{Br}$) m/z : Calc. 402.071, found 403.064 $[\text{M}+\text{H}]^+$.

Synthesis of 1,3,5,7-tetramethyl-8-(4-(pyren-1-ylethynyl)phenyl)-4,4-difluoro-4-bora-3a,4a-diaza-s-indacene (4)

Compound **3** (100 mg, 0.25 mmol) was dissolved in Et_3N (1.2 mL) and it was bubbled with argon for 15 min. Later on, bis(triphenylphosphine)palladium dichloride ($\text{Pd}(\text{PPh}_3)_2\text{Cl}_2$) (5.26 mg, 0.0075 mmol), CuI (3.09 mg, 0.016 mmol), PPh_3 (3.3 mg, 0.013 mmol), and 1-ethynylpyrene (**2**) (57 mg, 0.25 mmol) were added to the solution under argon. The reacted product was heated to 60 °C and stirred for 24 h. It was cooled to rt and concentrated under reduced pressure. The pure product was obtained as a reddish solid (27 mg, 20% yield) after silicagel-filled column chromatography with using n-hexane/dichloromethane (10:1) solvent system. ^1H NMR (in CDCl_3) δ (ppm) = 8.70 (d, 1H, $J=8.6$ Hz), 8.27-8.23(m, 4H), 8.15 (dd, 2H, $J=16.1$ Hz, $J=8.3$ Hz), 8.07 (m, 2H), 7.86 (d, 2H, $J=8.2$ Hz), 7.38 (d, 2H, $J=7.4$ Hz), 6.02 (s, 2H), 2.58 (s, 6H), 1.51 (s, 6H); ^{13}C NMR (in CDCl_3) δ (ppm) = 157.52, 155.72, 150.73, 142.85, 141.73, 138.53, 137.12, 135.44, 135.10, 131.72, 131.11, 129.77, 129.59, 129.33, 128.95, 128.64, 128.25, 127.69, 126.68, 125.25, 119.20, 116.25, 110.25, 87.96, 87.10, 15.88, 14.89. Elemental analysis: Calc. for $\text{C}_{37}\text{H}_{27}\text{BF}_2\text{N}_2$: C, 81.03; H, 4.96; N, 5.11. Found: C, 80.79; H, 5.13; N, 5.18%. MS (MALDI-TOF) m/z : Calc. 548.44, found 548.74 $[\text{M}]^+$.

RESULTS AND DISCUSSION

The synthetic route for the synthesis of **4** was outlined in Scheme 1. The intermediates (**1**, **2**, and **3**) which were used in the synthesis of the target compound were carried out according to the literature procedures. Briefly, **1** was obtained from a Sonogashira cross-coupling reaction of 1-bromopyrene and TMSA, using palladium pre-catalyst and copper co-catalyst system, following this reaction trimethylsilyl group of **1** was eliminated with K_2CO_3 in methanol, and **2** was obtained in high yield of 85%. On the other hand, **3** was prepared by sequential reactions. For this purpose first, the condensation reaction of 2,4-dimethylpyrrole with 4-bromobenzaldehyde in the presence of TFA was performed to obtain dipyrromethane, then it was oxidized with DDQ and then coordinated with $\text{BF}_3\cdot\text{OEt}_2$ using Et_3N as the base to afford **3** intermediate. Conjugated pyrene-BODIPY target compound **4** was obtained by the Sonogashira reaction in the presence of $\text{Pd}(\text{PPh}_3)_2\text{Cl}_2/\text{CuI}$ catalyst system and Et_3N (acted as base and solvent) of the prepared intermediates. Encouragingly, the good solubility of the target compound in many organic solvents helped easy purification and analysis of pyrene-BODIPY **4**. Despite of good solubility the pure compound **4** was obtained in 20% yield only.



Scheme 1: The synthetic route to compound **4**. (i) TMSA, Et₃N, Toluene, CuI, Pd(PPh₃)₄, PPh₃; (ii) K₂CO₃, MeOH; (iii) TFA, THF, DDQ, Et₃N, BF₃·OEt₂; (iv) Et₃N, CuI, Pd₂(PPh₃)₂Cl₂, PPh₃.

The structures of the molecules were determined with general spectroscopic methods, such as mass spectrometry, NMR spectroscopy, FT-IR spectra, and elemental analysis. The results received were matched with the expected structures as seen in the experimental part. In Figure 1, the molecular ion peak of the target compound was seen at m/z 548, additional peak which was seen at m/z 529 was attributed to the separation of fluorine, which is common in BODIPY compounds (33). The characteristic carbon-carbon triple bond and acetyl-CH stretch bands of the acetylene group were seen at 3292 and 2100 cm^{-1} on FT-IR spectra of EthyPy compound. However, the disappearance of the band at 3292 cm^{-1} while the band at 2100 cm^{-1} only shifted to 2200 cm^{-1} , confirmed the structure of **4** (Figure 3). The ¹H NMR spectra of **4** is shown in Figure 2. The pyrene protons were located in the region of $\delta=8.22-8.71$ ppm, and the phenyl protons were shown at 7.86 and 7.38 as two sets of a doublet. The proton signals of two CH-groups and the four CH₃-groups on the pyrrole ring were monitored at $\delta=6.02$ ppm and $\delta=2.58, 1.51$ ppm, respectively.

The thermal behavior of the compound **4** was carried out using TGA. The decomposition

temperature (Td) of the compound was estimated in the temperature scale from 25 °C to 700 °C at a heating rate of 10 °C/min and TGA observed that the compound has good stability in nitrogen, with the 5% of Td of 227 °C. Remained char yield was 52% at 700 °C (Figure 4).

As shown in Figure 5a, UV-Vis absorption and normalized fluorescence emission spectra of dye **4** and its sub-units **2** and **3** chromophores were measured at rt in dichloromethane for comparison. **2** and **3** exhibit absorption maxima at 358 and 502 nm which were attributed $\pi-\pi^*$ transitions of pyrene and BODIPY moieties, respectively (31,34). The dye **4** exhibits a strong absorption peak at a low energy band (502 nm) which is appointed to the S₀-S₁ transition of BODIPY unit and, the broad absorption peak at high energy band region (347- 384 nm) is appointed to S₀-S₂ transitions of the pyrene unit and also S₀-S₁ transition of BODIPY unit, which are consistent with previously reported pyrene and BODIPY chromophores (35-39). The optical energy gap width (E_g^{opt}) obtained from the absorption spectra in solution is 2.43 eV which consistent with the experimental result from the CV.

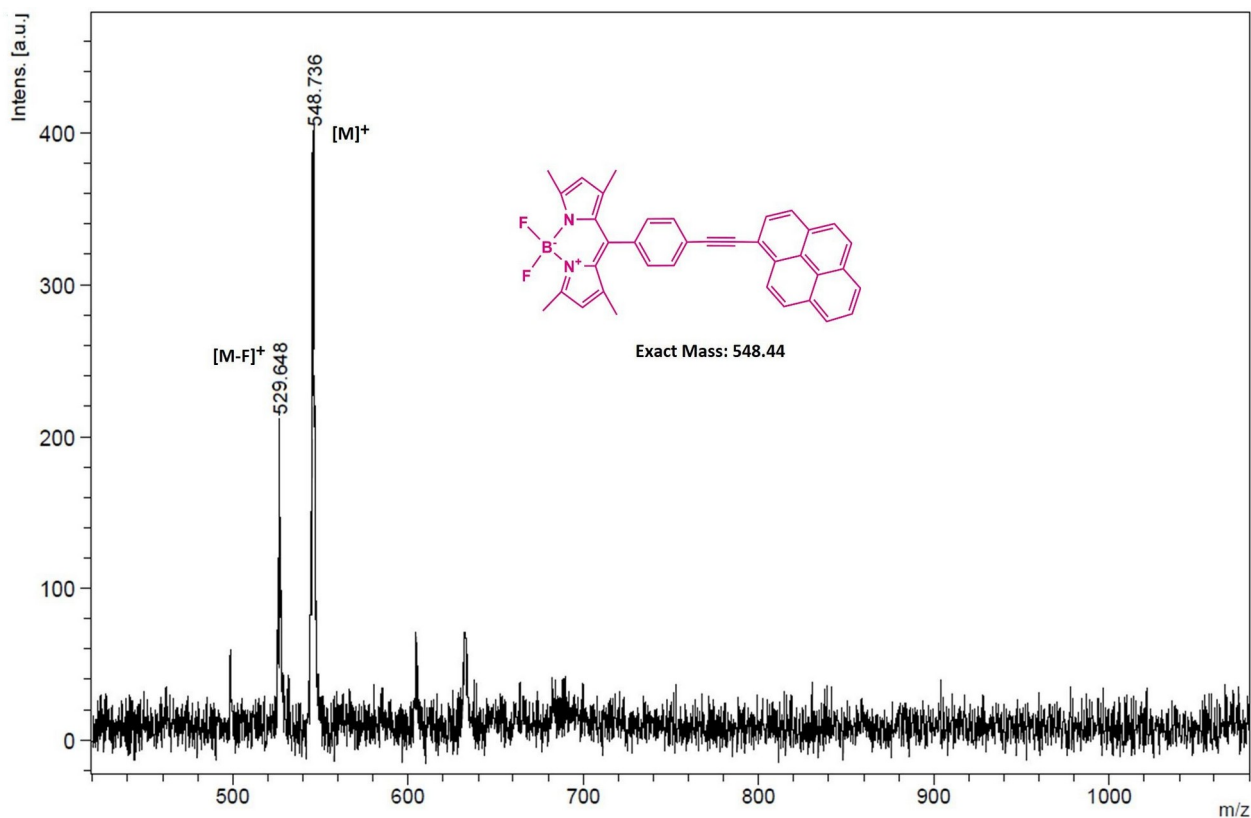


Figure 1: MALDI-MS spectra of **4**.

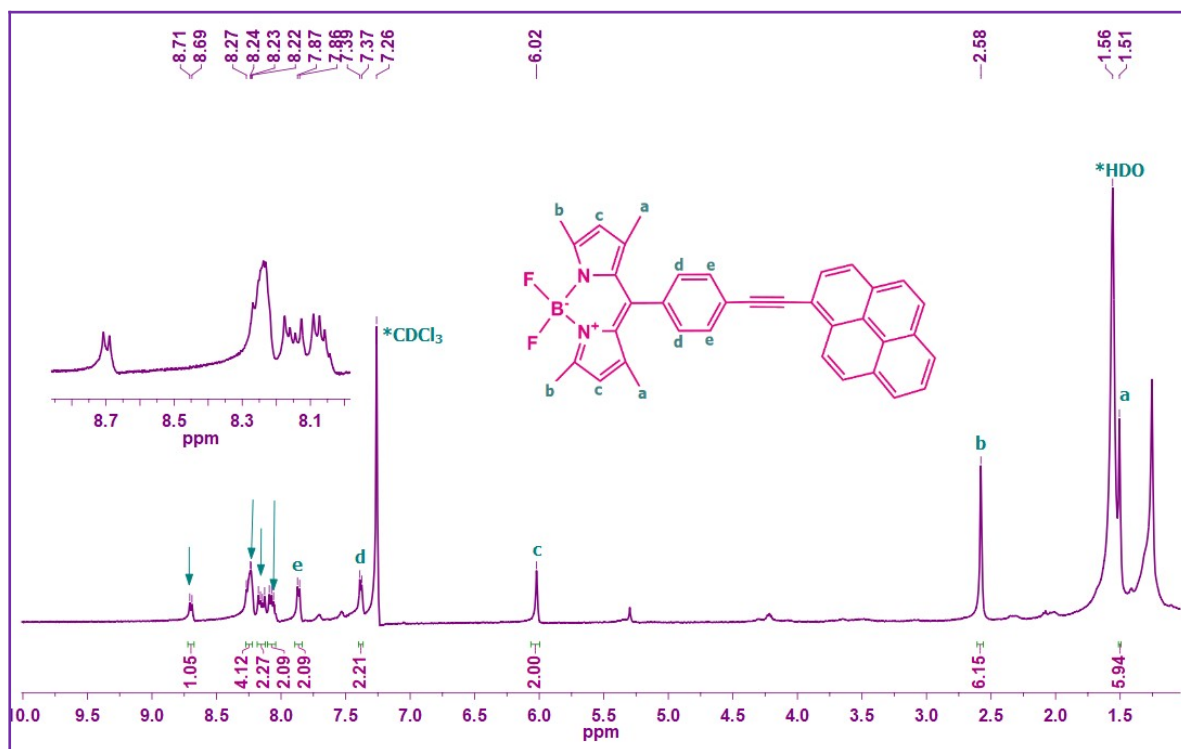


Figure 2: ¹H NMR spectra of **4** in CDCl₃.

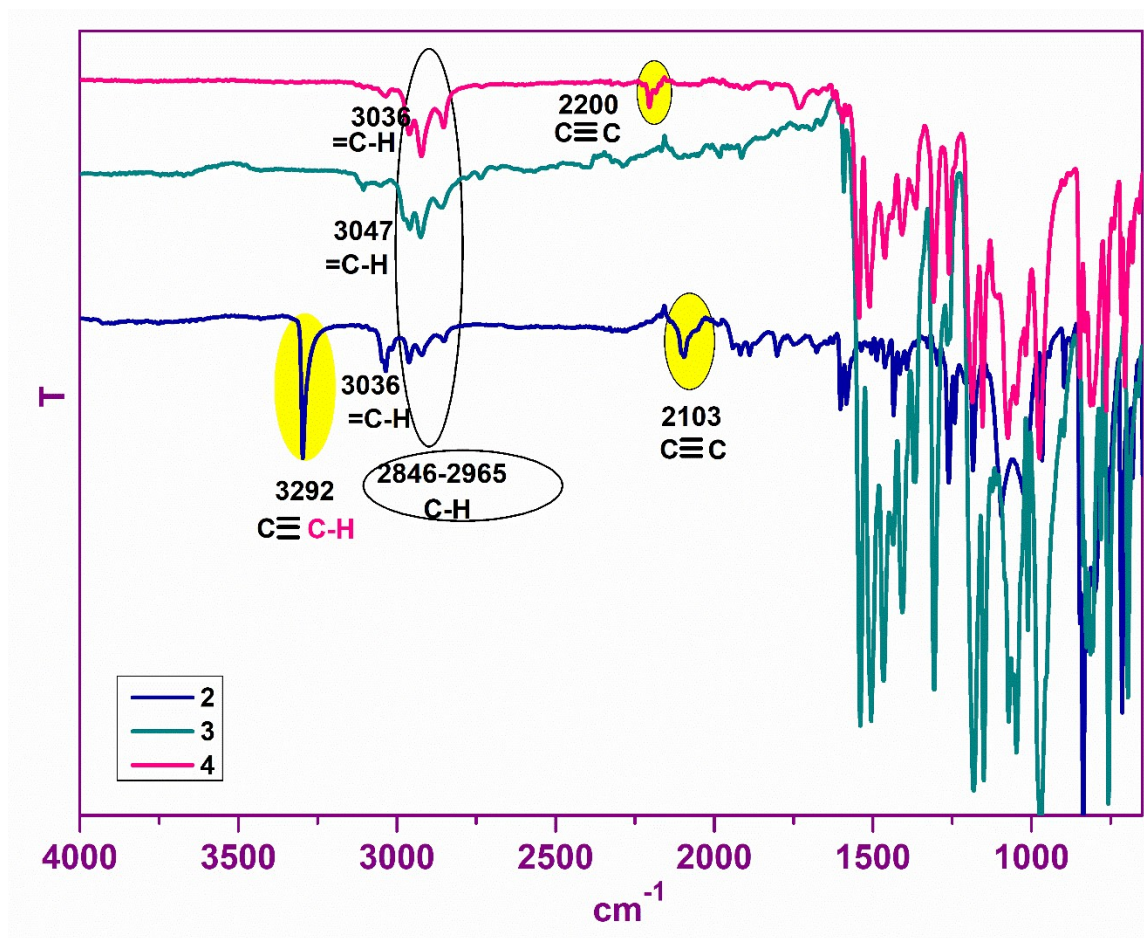


Figure 3: FT-IR spectra of 2, 3, and 4.

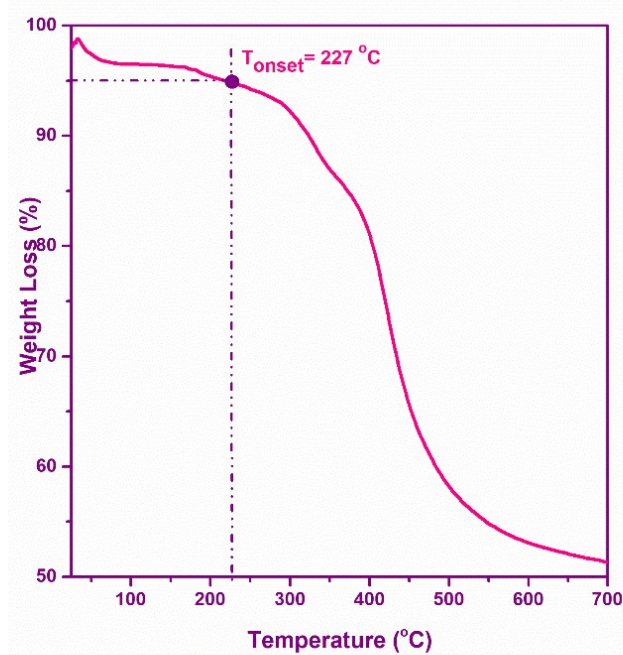


Figure 4: TGA thermogram of 4 at a temperature ramp of 10 $^{\circ}\text{C}/\text{min}$ under N_2 .

Fluorescence emission spectra for all compounds obtained upon excitation at 350 nm for comparison. The emission spectra of compounds show good mirror symmetry with the corresponding absorption bands except one that corresponds to pyrene on BODIPY unit is at the range of 350-390 nm are no longer present. (Figure 6a). Also, the lifetime of the compounds was studied at 310 nm excitation and observed 16 ns for **2**, 2.78 ns for **3** and, 1.78 ns for **4** (Figure 6b).

Cyclic voltammety in dichloromethane solution demonstrates a reversible reduction for **4** with the half-wave potential ($E_{1/2}$ red) located at -1.13 V (vs Ag/AgCl). This shows a high LUMO energy level of -3.27 eV for **4** shows reversible oxidation for **4** with the half-wave potential ($E_{1/2}$ ox) located at 1.30 V (vs Ag/AgCl) and the HOMO energy level of -5.70 eV for **4** (Figure 5b).

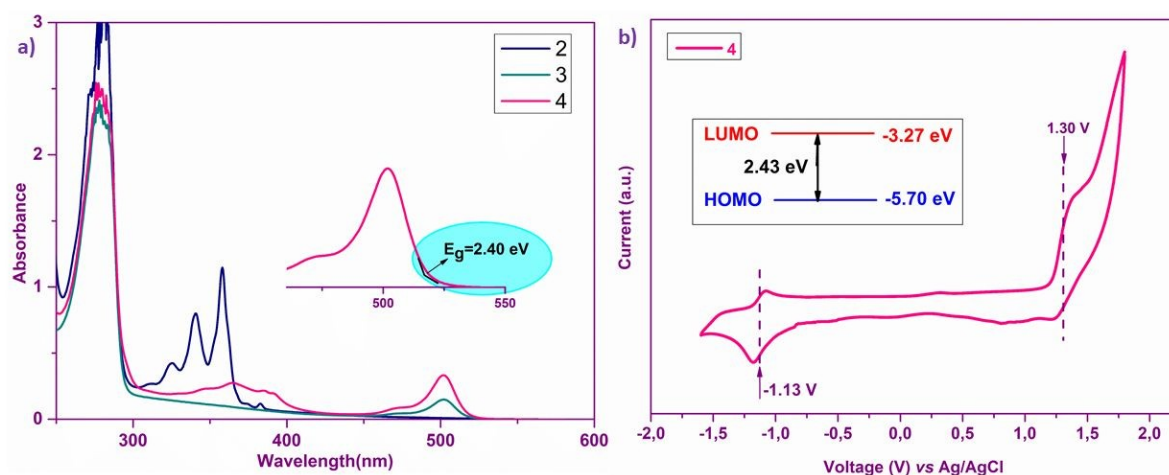


Figure 5: a) Optical absorption spectra of **4** in dichloromethane solution, and the corresponding optical band gap (E_g). b) Cyclic voltammogram of **4** in dichloromethane (0.1 M $\text{Bu}_4\text{N}^+\text{PF}_6^-$, scan rate = 100 mV/s) and experimental HOMO-LUMO energy levels.

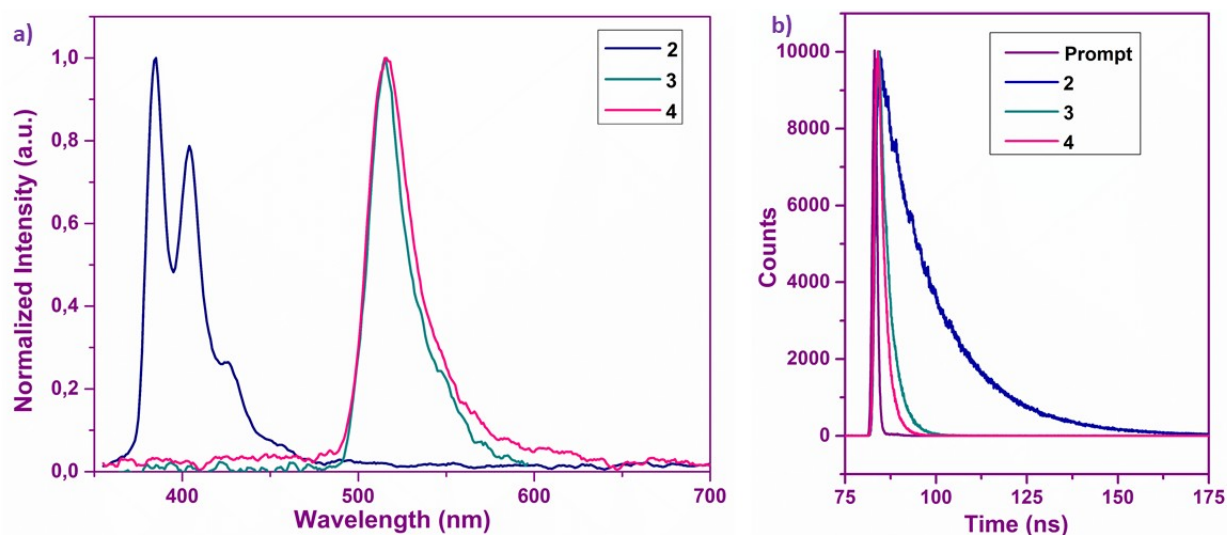


Figure 6: a) Fluorescence spectra b) Lifetime spectra of compounds (**2**, **3**, and **4**).

To understand more about the structural and electronic properties of the compound **4**, DFT analysis was performed at the B3LYP/6-31G* basis set. DFT calculations show that the phenyl ring is orthogonal to the BODIPY ring plane at a 90° dihedral angle. The reason is thought to be due to the steric impediment of methyl groups located at β -positions of pyrrole unit, so this impediment

prevents the free rotation of the phenyl ring (40). The molecule exhibits a large dipole moment of 4.90 D that enables higher intramolecular charge-transfer rates (41). The dipole moment is higher than that previously reported a similar molecule in the literature (42). The calculations indicate that both HOMO and LUMO levels are placed on the BODIPY unit (Figure 7).

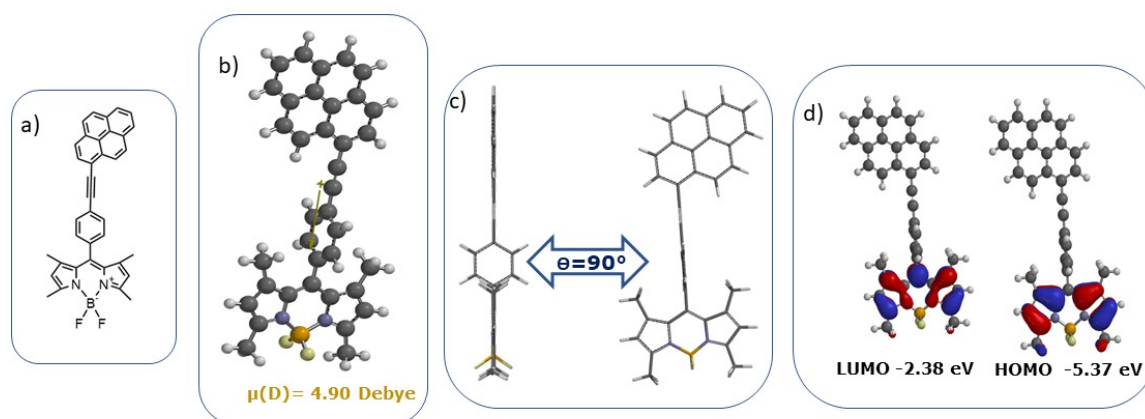


Figure 7: a) Molecular structure of compound **4**, b) Optimal geometry along with calculated dipole moment, c) Optimized molecular geometry showing inter-ring dihedral angle, d) DFT calculated frontier molecular orbital (HOMO and LUMO energy levels).

CONCLUSION

A new conjugated BODIPY dyad **4** consisting of pyrene as a donor group and BODIPY as an acceptor group linked via ethyne spacer was designed, synthesized, and successfully characterized. For a better understanding of its molecular nature, energy levels (HOMO/LUMO), and optical/electrochemical features were also examined by theoretical calculations, absorption and emission spectroscopies, and cyclic voltammetry. Based on all the studies, it can be concluded that the newly synthesized pyrene-BODIPY, a molecule having a relatively low band gap, could be of promising interest in future OLEDs.

ACKNOWLEDGMENTS

It is our pleasure to present this study consisting of selected papers based on poster presentations from the 2020 meeting of the 32nd National Chemistry Congress held on September 17-19 by Turkish Chemical Society, Turkey.

REFERENCES

1. Ward MD. Photo-induced electron and energy transfer in non-covalently bonded supramolecular assemblies. *Chemical Society Reviews*. 1997; 26:365-75.
2. Balzani V, Bergamini G, Ceroni P. From the photochemistry of coordination compounds to light-powered nanoscale devices and machines. *Coordination Chemistry Reviews*. 2008; 252:2456-69.
3. Guldi DM. Fullerene-porphyrin architectures; photosynthetic antenna and reaction center models. *Chemical Society Reviews*. 2002; 31:22-36.
4. Haugland RP. *Handbook of Fluorescent Probes and Research Chemicals*, 10th ed.; Molecular Probes: Eugene, OR, 2005.
5. Thoresen LH, Kim H, Welch MB, Burghart A, Burgess K. Synthesis of 3,5-diaryl-4,4-difluoro-4-bora-3a,4a-diaza-s-indacene (BODIPY) dyes. *Synlett*. 1998; 1276-1278.
6. Rurack K, Kollmannsberger M, Daub J. A highly efficient sensor molecule emitting in the near infrared (NIR): 3,5-distyryl-8-(p-dimethylaminophenyl)difluoroboradiaza-s-indacene. *New Journal of Chemistry*. 2001; 25: 289-292.
7. Loudet A, Burgess K. BODIPY Dyes and Their Derivatives: Syntheses and Spectroscopic Properties. *Chemical Reviews*. 2007; 107:4891-4932.
8. Ulrich G, Ziesel R, Harriman A. *The Chemistry of Fluorescent Bodipy Dyes: Versatility Unsurpassed*. *Angewandte Chemie International Edition*. 2008; 47: 1184-201.
9. Kowada T, Maeda H, Kikuchi K. BODIPY-based probes for the fluorescence imaging of biomolecules in living cells. *Chemical Society Reviews*. 2015; 44: 4953-972.
10. Ho D, Ozdemir R, Kim H, Earmme T, Usta H, Kim C. BODIPY-Based Semiconducting Materials for Organic Bulk Heterojunction Photovoltaics and Thin-Film Transistors. *ChemPlusChem*. 2019; 84: 18-37.
11. Winnik FM. Photophysics of preassociated pyrenes in aqueous polymer solutions and in other organized media. *Chemical Reviews*. 1993; 93:587-614.
12. Duhamel J. New insights in the study of pyrene excimer fluorescence to characterize

- macromolecules and their supramolecular assemblies in solution. *Langmuir*. 2012; 28:6527-38.
13. Yeşilot S, Çoşut B, Ardiç Alidağı H, Haciveliöğlü F, Altınbaş Özpınar G, Kılıç A. Intramolecular excimer formation in hexakis-(pyrenyloxy)cyclotriphosphazene: photophysical properties, crystal structure, and theoretical investigation. *Dalton Transaction*. 2014; 43: 3428-33.
14. Lambert C, Ehbets J, Rausch D, Steeger M. Charge-Transfer Interactions in a Multichromophoric Hexaarylbenzene Containing Pyrene and Triarylamines. *Journal of Organic Chemistry*. 2012; 77: 6147-54.
15. Merz J, Fink J, Friedrich A, Krummenacher I, Al Mamari HH, Lorenzen S, Haehnel M, Eichhorn A, Moos M, Holzapfel M, Braunschweig H, Lambert C, Steffen A, Ji L, Marder TB. Pyrene Molecular Orbital Shuffle—Controlling Excited State and Redox Properties by Changing the Nature of the Frontier Orbitals. *Chemistry European Journal*. 2017; 23:13164-80.
16. Raytchev M, Pandurski E, Buchvarov I, Modrakowski C, Fiebig T. Bichromophoric Interactions and Time-Dependent Excited State Mixing in Pyrene Derivatives. A Femtosecond Broad-Band Pump–Probe Study. *Journal of Physical Chemistry A*. 2003; 107: 4592-600.
17. Krebs N, Pugliesi I, Hauer J, Riedle E. Two-dimensional Fourier transform spectroscopy in the ultraviolet with sub-20 fs pump pulses and 250-720 nm supercontinuum probe. *New Journal of Physics*. 2013; 15: 085016.
18. Rodriguez-Cordoba W, Sierra CA, Puentes CO, Lahti PM, Peon J. Photoinduced energy transfer in bichromophoric pyrene-PPV oligomer systems: the role of flexible donor-acceptor bridges. *Journal of Physical Chemistry B*. 2012; 116: 3490-503.
19. Lee OP, Yiu AT, Beaujuge PM, Woo CH, Holcombe TW, Millstone JE, Douglas JD, Chen MS, Frechet JM. Efficient small molecule bulk heterojunction solar cells with high fill factors via pyrene-directed molecular self-assembly. *Advanced Materials*. 2011; 23: 5359-63.
20. Oniwa K, Kikuchi H, Shimotani H, Ikeda S, Asao N, Yamamoto Y, Tanigaki K, Jin T. 2-Positional pyrene end-capped oligothiophenes for high performance organic field effect transistors. *Chemical Communications*. 2016; 52: 4800-03.
21. Ardiç Alidağı H, Cosut B, Kılıç A, Yesilot S. Synthesis and spectral properties of a hexameric pyrene-fluorene chromophore based on cyclotriphosphazene. *Polyhedron*. 2014; 81: 436-41.
22. Figueira-Duarte TM, Mullen K. Pyrene-based materials for organic electronics. *Chemical Reviews*. 2011; 111: 7260-314.
23. Callaghan S, Filatov MA, Savoie H, Boyle RW, Senge MO. In vitro cytotoxicity of a library of BODIPYanthracene and -pyrene dyads for application in photodynamic therapy. *Photochemical & Photobiological Sciences*. 2019; 18: 495-504.
24. Ziesel R, Goze C, Ulrich G, Cesario M, Retailleau P, Harriman A, Rostron JP. Intramolecular energy transfer in pyrene-BODIPY molecular dyads and triads. *Chemistry A European Journal*. 2005; 11: 7366-78.
25. Yang Y, Zhang L, Gao C, Xu L, Bai S, Liu X. Pyrene-based BODIPY: synthesis, photophysics and lasing properties under UV-pumping radiation. *RSC Advances*. 2014; 4: 38119-23.
26. Fakis M, Beckwith JS, Seintis K, Martinou E, Nançoz C, Karakostas N, Petsalakis I, Pistolis G, Vauthey E. Energy transfer and charge separation Dynamics in photoexcited pyrene-bodipy molecular dyads. *Physical Chemistry Chemical Physics*. 2018; 20: 837-49.
27. Porcu P, Vonlanthen M, González-Méndez I, Ruiu A, Rivera E. Design of Novel Pyrene-Bodipy Dyads: Synthesis, Characterization, Optical Properties, and FRET Studies. *Molecules*. 2018; 23: 2289.
28. Matin MM, Chakraborty P, Alam MS, Islam MM, Haneef U. Novel mannopyranoside esters as sterol 14 α - demethylase inhibitors: Synthesis, PASS predication, molecular docking, and pharmacokinetic studies. *Carbohydrate Research*. 2020; 496: 108130.
29. Özkınalı S, Çavuş MS, Sakin B. Synthesis, Characterisation and DFT Calculations of Azo-Imine Dyes. *Journal of the Turkish Chemical Society Section A: Chemistry*. 2018; 5(1): 159-78.
30. Matin MM, Bhattacharjee SC, Chakraborty P, Alam MS. Synthesis, PASS predication, in vitro antimicrobial evaluation and pharmacokinetic study of novel n-octyl glucopyranoside esters. *Carbohydrate Research*. 2019; 485: 107812.
31. Bernhardt S, Kastler M, Enkelmann V, Baumgarten M, and Müllen K. Pyrene as Chromophore and Electrophore: Encapsulation in a Rigid Polyphenylene Shell. *Chemistry A European Journal*. 2006; 12: 6117 - 28.
32. Sun J, Zhong F, Yi X, Zhao J. Efficient Enhancement of the Visible-Light Absorption of Cyclometalated Ir(III) Complexes Triplet Photosensitizers with Bodipy and Applications in Photooxidation and Triplet–Triplet Annihilation

Upconversion. *Inorganic Chemistry*. 2013; 52: 6299–6310.

33. Çetindere S, Tümay SO, Şenocak A, Kılıç A, Durmuş M, Demirbaş E, Yeşilot S. Novel pyrene-BODIPY dyes based on cyclotriphosphazene scaffolds: Synthesis, photophysical and spectroelectrochemical properties. *Inorganica Chimica Acta*. 2019; 494: 132–40.

34. Cosut B. Highly efficient energy transfer in BODIPY-pyrene decorated cyclotriphosphazene. *Dyes and Pigments*. 2014; 100:11–16.

35. Cetindere S. Photophysics of BODIPY Dyes: Recent Advances. *Intech Open*. Chapter, 2020.

36. Mahapatra AK, Maji R, Maiti K, Manna SK, Mondal S, Ali SS, Manna S, Sahoo P, Mandal S, Uddin MR, Mandal D. A BODIPY/pyrene-based chemodosimetric fluorescent chemosensor for selective sensing of hydrazine in the gas and aqueous solution state and its imaging in living cells. *RSC Advances*. 2015; 5: 58228–36.

37. Karolin J, Johansson LBA, Strandberg L, Ny T. Fluorescence and Absorption Spectroscopic Properties of Dipyrometheneboron Difluoride (BODIPY) Derivatives in Liquids, Lipid Membranes, and Proteins. *Journal of American Chemical Society*. 1994; 116: 7801–6.

38. Toele P, Zhang H, Trieflinger C, Daub J, Glasbeek M. Femtosecond fluorescence upconversion study of a boron dipyrromethene dye in solution. *Chemical Physics Letters*. 2003; 368: 66–75.

39. Harriman A, Hissler M, Zissel R. Photophysical properties of pyrene-(2,2'-bipyridine) dyads. *Physical Chemistry Chemical Physics*. 1999; 1: 4203–11.

40. Zhou XF. 4,4-Difluoro-1,3,5,7-tetramethyl-8-pentafluorophenyl-4-bora-3a,4a-diaza-s-indacene. *Acta Crystallographica Section E*. 2010; E66: o757.

41. Dobkowski J, Rettig W, Waluk J. Intramolecular Charge- Transfer Properties of a Molecule with a Large Donor Group: The Case of 4'-(Pyren-1-yl)Benzonitrile. *Physical Chemistry Chemical Physics*. 2002; 4: 4334–9.

42. Sultati A, Verykios A, Panagiotakis S, Armadorou KK, Haider MI, Kaltzoglou A, Drivas C, Fakharuddin A, Bao X, Yang C, Rashid bin Mohd Yusoff A, Evangelou EK, Petsalakis I, Kennou S, Falaras P, Yannakopoulou K, Pistolis G, Argitis P, Vasilopoulou M. Suppressing the Photocatalytic Activity of Zinc Oxide Electron-Transport Layer in Nonfullerene Organic Solar Cells with a Pyrene-Bodipy Interlayer. *ACS Applied Materials & Interfaces*. 2020; 12(19): 21961–73.



Antimicrobial Activity Evaluation of Newly Synthesized *N,N*-Disubstituted Taurinamidobenzenesulfonamide Derivatives

Özlem AKGÜL^{1*}, Ayşegül ATEŞ², Şafak ERMERTCAN²

¹Department of Pharmaceutical Chemistry, Faculty of Pharmacy, Ege University, İzmir-Turkey.

²Department of Pharmaceutical Microbiology, Faculty of Pharmacy, Ege University, İzmir-Turkey.

Abstract: Herein we synthesized 6 new *N,N*-disubstituted taurinamidobenzenesulfonamide derivatives and characterized their structures by means of ¹H and ¹³C NMR, HR-MS analysis. In addition, their *in vitro* antibacterial and antifungal activities were tested against two gram-positive, two gram-negative bacteria, and two fungal strains by using broth microdilution method. Compounds **1** (methoxy substitution) and **2** (methyl substitution) displayed the best antibacterial activity against *Escherichia coli* and *Staphylococcus aureus*, respectively. *E. faecalis* was affected by compounds **1**, **2**, **4**, and **6**, becoming the most susceptible pathogen compared to other tested bacterial and fungal strains. Interestingly, changing fluoro atom in compound **6** with the chloro atom, as in compound **5**, deteriorated the antibacterial activity against all bacterial strains. As a result, these results provide us to investigate the relationship between structural changes and antibacterial/antifungal activity, which can be further used to develop more effective taurine derivatives.

Keywords: Taurine, taurinamidobenzenesulfonamide, antibacterial, antifungal, microdilution.

Submitted: December 01, 2020. **Accepted:** January 12, 2021.

Cite this: Akgül Ö, Ateş A, Ermertcan Ş. Antimicrobial Activity Evolution of Newly Synthesized *N,N*-Disubstituted Taurinamidobenzenesulfonamide Derivatives. JOTCSA. 2021;8(1):321-28.

DOI: <https://doi.org/10.18596/jotcsa.834579>.

*Corresponding author. E-mail: ozlem.akgul@ege.edu.tr.

INTRODUCTION

Sulfanylamide was first established as a selective toxic agent against bacteria in the 1930s, which ushered in a new era in antibacterial drug development studies. As the sulfonamide and amine parts of the molecule can be functionalized by different groups, a wide range of sulfanylamide derivatives with diverse pharmacokinetic and pharmacodynamic properties have been synthesized (Figure 1). In addition, the clinically useful sulfa drug class of antibacterials was discovered. However, the emerging bacterial resistance against these drugs limits their usage in treatment (1).

Sulfanylamide is a competitive inhibitor of *p*-aminobenzoic acid and exerts its bacteriostatic action via binding to dihydropteroate synthase (DHPS). Although the structure-activity relationship of sulfa drugs indicates that the amino part should

be free of substitution in order to show an antimicrobial effect, modification of the amine part might also result in active molecules. A study replacing the amino group in sulfanylamide with the methyl, nitro, or chloro group and substituting the sulfonamide moiety with various heterocycles resulted in compounds with promising *in vitro* antibacterial activity against various bacterial strains (Figure 1) (2).

Recently, it was reported that bacteria encode genetically different carbonic anhydrases (CAs) which are involved in their virulence and growth abilities. In addition, various *N*-substituted sulfanylamide derivatives were found to be potential inhibitors of bacterial CAs. Therefore, CAs considered as druggable targets that serve a new mechanism of action devoid of resistance mechanism (3-5). All these findings support the idea that sulfanylamide derivatives will protect their place in drug development studies in the future, too.

Amino acids with their nontoxic profile and biocompatibility properties represent an interesting tool for constructing new, biologically active molecules (6, 7). Taurine, 2-aminoethanesulfonic acid, is the only free and nonproteogenic amino acid in mammals (8–11). Despite its negatively charged sulfonic acid, it can be transported inside cells with TauT transporters in humans and contributes to various important physiological events. Also, it passes through bacterial membranes with the help of TauABC transporters to be used as a sulfur, carbon, and nitrogen source (12). There is also evidence that bacteria use taurine to biosynthesize natural products. For example, a newly investigated antibiotic bulgecin-A with taurine in its structure was isolated from a gram-negative bacterium *Paraburkholderia acidophila*, which inhibits lytic transglycosylases of bacterial cell wall biosynthesis (13). In contrast to its role in bacteria, taurine shows antibacterial, antifungal, and antiviral activity in humans (14, 15). The mechanism underlying the antibacterial activity of taurine depends on the formation of taurinechloramine from the attack of

toxic HOCl on the amine group of taurine during inflammation (Figure 2) (16–18).

In our previous study, we designed a group of taurine derivative by using molecular hybridization method and tested for their antimicrobial and antifungal properties. Among the final compounds, the derivative comprising a sulfanylamide group showed moderate antibacterial activity only against the gram-positive *Enterococcus faecalis* with a minimum inhibitory concentration (MIC) of 128 µg/mL (Figure 2) (19). In order to find more effective sulfanylamide derivatives and extend our knowledge of antimicrobial taurine derivatives, in this study, we decided to keep the taurinamidobenzenesulfonamide part of the previously investigated molecule unchanged and replace the phthalimide part with a hydrophobic benzyl group in order to obtain *N,N*-disubstituted derivatives with benzyl groups decorated with different electron-withdrawing and electron-donating groups (Figure 3). This modification strategy will give us an opportunity to investigate the contribution of disubstitution to antimicrobial activity.

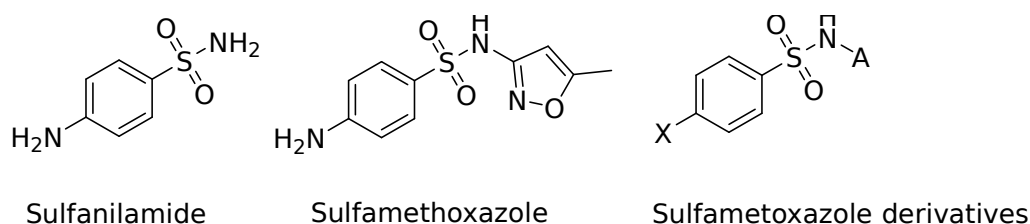


Figure 1. Structures of sulfanylamide, sulfamethoxazole, and previously investigated sulfamethoxazole derivatives

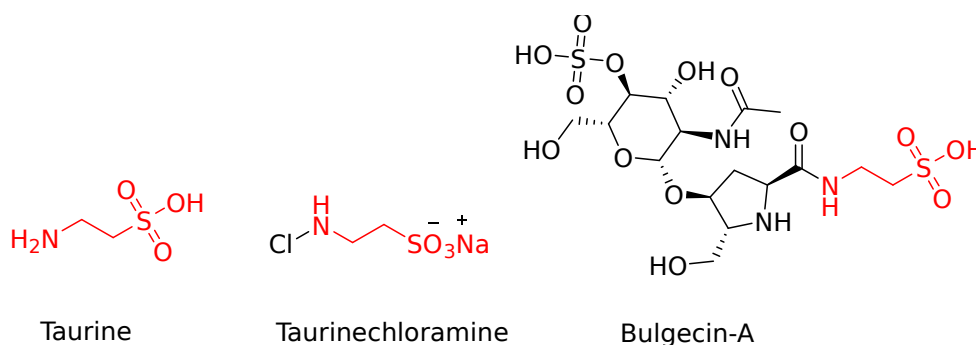


Figure 2. Structures of taurine and its biologically active derivative, and the antibiotic bulgecin-A with taurine in its structure.

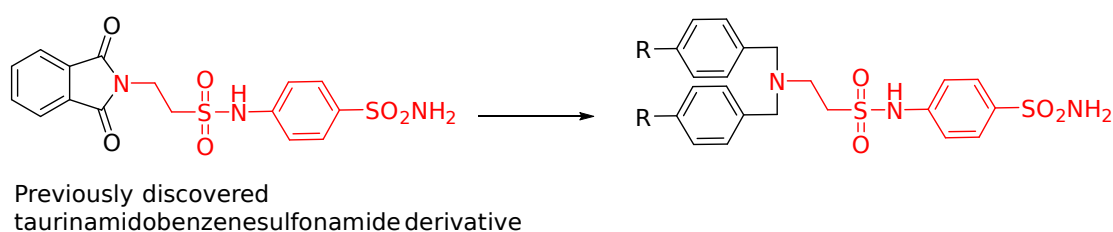
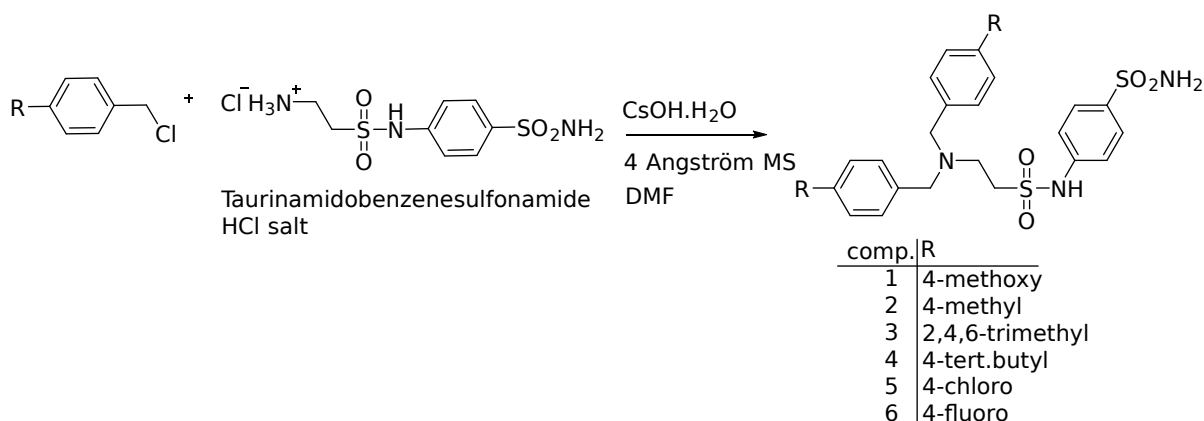


Figure 3. Drug design strategy.**Figure 4.** General synthesis of the final compounds **1-6**.

MATERIAL AND METHODS

Chemistry

Anhydrous solvents and all reagents were purchased from Sigma-Aldrich and Interlab (Germany). All reactions were performed under an argon atmosphere. ^1H and ^{13}C NMR spectra were performed in $\text{DMSO-}d_6$ on an Agilent 600 MHz PremiumCOMPACT NMR spectrometer. Chemical shifts and coupling constants (J) were reported in parts per million (ppm) and in Hertz (Hz) respectively. Merck silica gel F-254 plates were used for TLC analyses and the products were visualized by UV detection. The products were purified by flash chromatography employing Merck silica gel 60 (230–400 mesh ASTM) as stationary phase. Stuart® (SMP30) melting point apparatus was used to measure melting points in open capillary tubes and the results were uncorrected. High-resolution mass spectrometry (HR-MS) analyses were recorded on Agilent Technologies 6530 Accurate-Mass Q-TOF LC/MS.

General Procedure for the Synthesis of the Final Compounds

Taurinamidobenzenesulfonamide hydrochloride salt was prepared by following the reaction conditions previously described by us (19, 20). For obtaining final compounds; various benzyl chloride (2 mmol) and taurinamidobenzenesulfonamide.HCl (1.7 mmol) was added to a mixture of cesium hydroxide monohydrate ($\text{CsOH.H}_2\text{O}$, 1.7 mmol), activated powdered 4 Angström molecular sieves (500 mg) in anhydrous N,N -dimethyl formamide (DMF, 8.3 mL) and stirred at room temperature for 18 hr (21, 22). After the completion of the reaction the mixture was filtered, and the solvent was evaporated under reduced pressure. The residue was subjected to flash chromatography eluting with ethyl acetate: n-hexane (EtOAc: Hxn) and the obtained residue was crystallized with ethanol: water to afford the desired compounds **1-6** as white powders.

4-((2-(Bis(4-methoxybenzyl)amino)ethyl)sulfonamido)benzenesulfonamide **1**

Elution with EtOAc: Hxn (25%) and crystallized with ethanol: water afforded **1** as a white solid (yield 3%); Mp: 120.2°C; ^1H NMR (400 MHz, $\text{DMSO-}d_6$, δ , ppm): 2.76-2.78 (m, 2H, CH_2), 3.41-3.43 (m, 2H, CH_2), 3.48 (m, 4H, benzylic- CH_2), 3.75 (s, 6H, OCH_3), 6.85 (d, $J = 8.2$ Hz, 4H, Ar-H), 7.16 (d, $J = 8.2$ Hz, 4H, Ar-H), 7.23 (d, $J = 8.8$ Hz, 2H, Ar-H), 7.35 (s, 2H, SO_2NH_2), 7.79 (d, $J = 8.1$ Hz, 2H, Ar-H), 10.28 (brs, 1H, $\text{SO}_2\text{NH-}$); ^{13}C NMR (100 MHz, $\text{DMSO-}d_6$, δ , ppm): 159.1 (2 \times Ar-C), 142.2, 139.4, 131.2 (2 \times Ar-C), 130.6 (4 \times Ar-C), 128.1 (2 \times Ar-C), 118.8 (2 \times Ar-C), 114.5 (4 \times Ar-C), 57.0 (2 \times benzylic-C), 55.9 (2 \times OCH_3), 48.5, 46.5; ESI-HRMS (m/z) $[\text{M}+\text{H}]^+$, calculated for $\text{C}_{24}\text{H}_{30}\text{N}_3\text{O}_6\text{S}_2$ 520.1571; found 520.15743.

4-((2-(Bis(4-methylbenzyl)amino)ethyl)sulfonamido)benzenesulfonamide **2**

Elution with EtOAc: Hxn (25%) and crystallized from ethanol: water afforded **2** as a white solid (yield 20%); Mp: 177.8°C; ^1H NMR (400 MHz, $\text{DMSO-}d_6$, δ , ppm): 2.30 (s, 6H, CH_3), 2.79-2.77 (m, 2H, CH_2), 3.43-3.41 (m, 2H, CH_2), 3.51 (s, 4H, benzylic- CH_2), 7.10 (d, $J = 7.7$ Hz, 4H, Ar-H), 7.15 (d, $J = 7.9$ Hz, 4H, Ar-H), 7.21 (d, $J = 8.6$ Hz, 2H, Ar-H), 7.36 (s, 2H, SO_2NH_2), 7.77 (d, $J = 8.6$ Hz, 2H, Ar-H), 10.27 (1H, brs, $\text{SO}_2\text{NH-}$); ^{13}C NMR (100 MHz, $\text{DMSO-}d_6$, δ , ppm): 142.2, 139.4, 136.9 (2 \times Ar-C), 136.3 (2 \times Ar-C), 129.7 (4 \times Ar-C), 129.4 (4 \times Ar-C), 128.1 (2 \times Ar-C), 118.8 (2 \times Ar-C), 57.6 (2 \times benzylic-C), 48.6, 46.8, 21.6 (2 \times alip-C); ESI-HRMS (m/z) $[\text{M}+\text{H}]^+$, calculated for $\text{C}_{24}\text{H}_{30}\text{N}_3\text{O}_4\text{S}_2$ 488.1672; found 488.16769.

4-((2-(Bis(2,4,6-trimethylbenzyl)amino)ethyl)sulfonamido)benzenesulfonamide **3**

Elution with EtOAc: Hxn (25%) and crystallized from ethanol: water afforded **3** as a white powder (yield 24%). Mp: 229.0°C; ^1H NMR (400 MHz, $\text{DMSO-}d_6$, δ , ppm): 2.15 (m, 12H, CH_2), 2.21 (m, 6H, CH_2), 2.76-

2.73 (m, 2H, CH₂), 3.25-3.22 (m, 2H, CH₂), 3.47 (s, 4H, benzylic-CH₂), 6.77 (s, 4H, Ar-H), 7.13 (d, *J* = 8.2 Hz, 2H, Ar-H), 7.35 (m, 2H, SO₂NH₂), 7.74 (d, *J* = 9.0 Hz, 2H, Ar-H), 10.28 (1H, brs, SO₂NH-); ¹³C NMR (100 MHz, DMSO-*d*₆, δ, ppm): 142.0, 139.5, 138.4 (4 × Ar-C), 136.6 (2 × Ar-C), 132.1 (2 × Ar-C), 129.6 (4 × Ar-C), 128.0 (2 × Ar-C), 118.9 (2 × Ar-C), 52.4 (2 × benzylic-C), 50.3, 47.8, 21.4 (2 × aliph-C), 20.5 (4 × aliph-C); ESI-HRMS (*m/z*) [M+H]⁺, calculated for C₂₈H₃₈N₃O₄S₂ 544.2298; found 544.23027.

4-((2-(Bis(4-(tert-butyl)benzyl)amino)ethyl)sulfonamido)benzenesulfonamide 4

Elution with EtOAc: Hxn (25%) and crystallized from ethanol: water afforded **4** as a white powder (yield 2%). Mp:172.2°C; ¹H NMR (400 MHz, DMSO-*d*₆, δ, ppm): 1.31 (m, 18H, CH₃), 2.84-2.81 (m, 2H, CH₂), 3.59-3.57 (m, 4H, CH₂), 4.79 (s, 2H, benzylic-CH₂), 7.14 (d, *J* = 8.4 Hz, 2H, Ar-H), 7.22 (d, *J* = 8.0 Hz, 2H, Ar-H), 7.33-7.31 (m, 4H, Ar-H), 7.35 (m, 2H, SO₂NH₂), 7.42 (d, *J* = 8.0 Hz, 3H, Ar-H), 7.69 (d, *J* = 8.3 Hz, 1H, Ar-H); ¹³C NMR (100 MHz, DMSO-*d*₆, δ, ppm): 150.8, 150.3 (2 × Ar-C), 136.7 (2 × Ar-C), 134.1, 129.2 (2 × Ar-C), 128.8, 128.7, 128.3 (2 × Ar-C), 127.2, 126.1 (2 × Ar-C), 126.0 (2 × Ar-C), 125.9, 57.4 (benzylic-C), 53.6 (benzylic-C), 40.9, 35.1, 32.1 (6 × aliph-C), 32.0 (2 × aliph-C); ESI-HRMS (*m/z*) [M+H]⁺, calculated for C₃₀H₄₂N₃O₄S₂ 572.2611; found 572.26138.

4-((2-(Bis(4-chlorobenzyl)amino)ethyl)sulfonamido)benzenesulfonamide 5

Elution with EtOAc: Hxn (25%) and crystallized from ethanol: water afforded **5** as a white powder (yield 23%). Mp:119.4°C; ¹H NMR (400 MHz, DMSO-*d*₆, δ, ppm): 2.78-2.80 (m, 2H, CH₂), 3.47-3.49 (m, 2H, CH₂), 3.55 (s, 4H, benzylic-CH₂), 7.22 (d, *J* = 8.7 Hz, 2H, Ar-H), 7.30 (d, *J* = 8.7 Hz, 4H, Ar-H), 7.36-7.37 (m, 6H, Ar-H, SO₂NH₂), 7.79 (d, *J* = 8.7 Hz, 2H, Ar-H), 10.30 (brs, 1H, SO₂NH-); ¹³C NMR (100 MHz, DMSO-*d*₆, δ, ppm): 142.1, 139.5, 138.5 (2 × Ar-C), 132.5 (2 × Ar-C), 131.2 (4 × Ar-C), 129.1 (4 × Ar-C), 128.1 (2 × Ar-C), 118.8 (2 × Ar-C), 56.9 (2 × benzylic-C), 48.4, 46.9; ESI-HRMS (*m/z*) [M+H]⁺, calculated for C₂₂H₂₄Cl₂N₃O₄S₂ 528.0580; found 528.05806.

4-((2-(Bis(4-fluorobenzyl)amino)ethyl)sulfonamido)benzenesulfonamide 6

Elution with EtOAc: Hxn (25%) and crystallized from ethanol: water afforded **6** as a white powder (yield 7%). Mp:110.1°C; ¹H NMR (400 MHz, DMSO-*d*₆, δ, ppm): 2.77-2.79 (m, 2H, CH₂), 3.46-3.49 (m, 2H, CH₂), 3.55 (s, 4H, benzylic-CH₂), 7.13 (t, *J* = 8.7 Hz, 4H, Ar-H), 7.22 (d, *J* = 8.7 Hz, 2H, Ar-H), 7.29-7.31 (m, 4H, Ar-H), 7.36 (m, 2H, SO₂NH₂), 7.78 (d, *J* = 8.7 Hz, 2H, Ar-H), 10.28 (1H, brs, SO₂NH-); ¹³C NMR (100 MHz, DMSO-*d*₆, δ, ppm): 162.2 (d, *J* = 237.6 Hz, 2 × Ar-C), 142.1, 139.4, 135.6 (d, *J* = 2.9 Hz, 2 × Ar-C), 131.3 (d, *J* = 8.2 Hz, 3 × Ar-C), 128.1 (3 × Ar-C), 118.7 (3 × Ar-C), 115.9 (d, *J* = 21.2 Hz, 3 × Ar-C), 56.8 (2 × benzylic-C), 48.4, 46.7; ESI-HRMS (*m/z*) [M+H]⁺, calculated for C₂₂H₂₄F₂N₃O₄S₂ 496.1171; found 496.11818.

Antimicrobial Activity

Establishment of minimum inhibitory concentration (MIC)

The microorganisms that were used in study (*Staphylococcus aureus* (ATCC 29213), *Enterococcus faecalis* (ATCC 29212), *Escherichia coli* (ATCC 25922), *Pseudomonas aeruginosa* (ATCC 27853), *Candida albicans* (ATCC 90028) and *Candida parapsilosis* (ATCC 22019) were stored in Brain-Heart Infusion Broth (Merck, Germany) with 10% glycerol at -80 °C. Titled compounds were screened for their antimicrobial activity against each strain employing broth microdilution method and MICs of synthesized compounds were determined according to the European Committee on Antimicrobial Susceptibility Testing (EUCAST) document (23). The solid growth medium Mueller-Hinton Agar (Merck, Germany) and Sabouraud Dextrose Agar (Oxoid, UK) were exploited for the bacteria and yeasts grown at 37 °C for 24 h, respectively. Then, bacteria and yeasts were suspended in saline. The turbidity of bacterial and fungal inocula was fixed to 0.5 McFarland by densitometer (Biosan, DEN-1), and the suspensions were diluted 100-fold and 10-fold for bacteria and yeasts, respectively. Mueller-Hinton broth (Merck, Germany) (50 μL) and RPMI (Sigma, UK) with 2% of glucose (RPMI 2% G) were added into the each well of sterile 96-well microdilution plates for bacteria and yeasts, respectively. 50 μL from each of the tubes containing the corresponding concentration of 6 new compounds were included into first wells each column of the microdilution plate and serial dilutions were accomplished. Bacterial and yeast inoculum suspensions were inoculated each well of plate with 50 μL, and the plates were incubated for 24 h at 37 °C. Growth control for each organisms and sterility control for medium were also tested. The final concentrations of the compounds were ranged from 2048 to 512 μg/ml. The MIC value was defined as the lowest concentration of the compound that entirely inhibited the microbial growth. The well-known antibiotic ciprofloxacin (Santa Cruz, US) and antifungal drug fluconazole (Sigma, UK) were used as reference drugs. Also, the study was performed by using the quality control ranges that were recommended by EUCAST. All test conditions were carried out at least in triplicate and DMSO was also tested independently for its antimicrobial activity.

RESULTS AND DISCUSSION

Synthesis and Characterization of the Final Compounds

Herein, 6 new 4-((2-(bis(4-substituted benzyl)amino)ethyl)sulfonamido)benzenesulfonamide derivatives have been prepared. The starting compound taurinamidobenzenesulfonamide hydrochloride salt was established by a 4 step reaction, as previously described (19,20). To obtain the final compounds, taurinamidobenzene-sulfonamide hydrochloride salt was reacted with

various benzyl chlorides in the presence of a 4 Å molecular sieve and cesium hydroxide monohydrate in *N,N*-dimethylformamide solution at room temperature for 18 h (Figure 4). Final compounds **1-6** were achieved in yields of 2%-24%, as described in the Experimental Section. All six compounds were characterized by ¹H and ¹³C NMR and high-resolution mass spectrometric (HR-MS) analysis, and all spectral data obtained were consistent with the proposed structures (see the Experimental section for details).

In the ¹H NMR spectra, the aromatic protons located at the amine part of compound **4** were observed as a singlet signal having four proton integration while the other compounds displayed the same protons as two signals with four-proton integration. Together with these protons, the signals of the benzylic protons (3.47-4.79 ppm) were indicative for the formation of disubstitution. On the other hand, the hydrogens of sulfanylamide displayed two separate signals, indicating the AA'BB' aromatic system. All aromatic proton signals were detected at 6.77-7.79 ppm region. The protons of the taurine scaffold exhibited two separate signals in aliphatic field at 2.76-3.59 ppm. The primary and secondary sulfonamide peaks were assigned as singlet at 7.22-

7.31 ppm and 10.38-10.42 ppm respectively, though secondary sulfonamide hydrogen of compound **4** did not have any signal. The signals corresponding to methoxy, methyl, trimethyl and *tert*-butyl groups were located in the expected regions which also verified the disubstitution, since these substitutions were doubled. In ¹³C NMR spectra, aromatic carbon signals were detected in the range of 115.88-162.2 ppm. Benzylic carbon signals were detected at 52.4-57.6 ppm region. In addition, the alkyl substitutions and taurine carbon atoms were observed in the expected regions. The splitting of carbon-fluoro atoms were also detected in ¹³C NMR. On the other hand, HR-MS data were consistent with the proposed molecular weights.

Biological Activity

Antimicrobial activity

Final compounds were tested for their *in vitro* antibacterial and antifungal activities against two gram-positive bacteria; two gram-negative bacteria and two fungal strains using broth microdilution method with ciprofloxacin and fluconazole as reference drugs. Table 1 summarizes the structure-activity relationship from biological activity results.

Table 1. *In vitro* antibacterial and antifungal activity (MIC, µg/mL) of compounds **1-6** compared to ciprofloxacin and fluconazole.

Compound	Gram (+) bacterial strains				Gram (-) bacterial strains				Fungal strains	
	R	<i>S. a.</i>	<i>E. f.</i>	<i>E. c.</i>	<i>P. a.</i>	<i>C. a.</i>	<i>C. p.</i>			
1	2 4-OCH ₃	3 2048	4 512	5 512	6 1024	7 >2048	8 >2048			
9	10 4-CH ₃	11 512	12 512	13 1024	14 2048	15 1024	16 1024			
17	18 2,4,6-(CH ₃) ₃	19 1024	20 1024	21 >2048	22 2048	23 >2048	24 >2048			
25	26 4-C(CH ₃) ₃	27 1024	28 512	29 1024	30 1024	31 >2048	32 >2048			
33	34 4-Cl	35 2048	36 2048	37 >2048	38 >2048	39 >2048	40 >2048			
41	42 4-FI	43 1024	44 512	45 1024	46 1024	47 >2048	48 >2048			
Ciprofloxacin	0.25	1	0.008	0.5	nt	nt				
Fluconazole	nt	nt	nt	nt	32	2				

S. a., *Staphylococcus aureus*; *E. f.*, *Enterococcus faecalis*; *E. c.*, *Escherichia coli*; *P. a.*, *Pseudomonas aeruginosa*; *C. a.*, *Candida albicans*; *C. p.*, *Candida parapsilosis*; nt, not tested.

Compound **2** comprising an electron-donating methyl group as a substituent on the phenyl ring showed the highest MIC (512 µg/mL) against the gram-positive *Staphylococcus aureus*. Adding two methyl groups to the ortho position, as in compound **3**, or replacing the methyl group with a bulky *tert*-butyl group, as in compound **4**, yielded a twofold decrease in the MIC (1024 µg/mL). Halogenation of the phenyl ring with a fluoro (compound **6**) or a chloro (compound **5**) atom also resulted in a two- and fourfold decrease in antibacterial activity compared to compound **2**.

The other gram-positive bacterium *E. faecalis* displayed higher susceptibility to all compounds **1-6** compared to other tested bacterial and fungal strains. Substitution with an electron-donating methyl, methoxy, or even bulky *tert*-butyl group (compounds **1**, **2**, and **4**) resulted in the same activity profile with an MIC of 512 µg/mL (Table 1). Interestingly, replacement of the methyl group with a halogen like a fluoro atom, as in compound **6**, restored the activity (MIC = 512 µg/mL), while

chloro substitution, as in compound **5**, deteriorated antibacterial activity (MIC = 2048 µg/mL).

The gram-negative bacterium *Escherichia coli* was inhibited with the methoxy-substituted compound **1** with a MIC of 512 µg/mL, showing the best antibacterial activity profile among the tested compounds. The increased affinity of compound **1** against gram-negative bacteria might be ascribed to the hydrogen-bonding capability of the methoxy substituent. Replacing the methoxy group (compound **1**) with other electron-donating methyl or bulky *tert*-butyl groups or with an electron-withdrawing atom like fluoro decreased the antibacterial activity twofold, resulting in an MIC of 1028 µg/mL, while the other substitutions decreased the antibacterial activity against *E. coli*.

Among the bacterial strains, *Pseudomonas aeruginosa* was the least susceptible pathogen against the tested compounds **1-6**. Compounds **1**, **4**, and **6** showed twofold better antibacterial activities compared to compounds **2**, **3**, and **5** with an MIC of 1024 µg/mL.

Interestingly, only compound **2** showed antifungal activity against *Candida albicans* and *C. parapsilosis*. Introduction of other substitutions rather than a methyl group deteriorated antifungal activity.

CONCLUSION

In this study, we synthesized six new taurinamidobenzenesulfonamide derivatives and evaluated their *in vitro* antibacterial and antifungal activity against two gram-positive bacteria (*S. aureus* and *E. faecalis*), two gram-negative bacteria (*E. coli* and *P. aeruginosa*), and two fungal strains (*C. albicans* and *C. parapsilosis*) using broth microdilution method. All compounds showed significantly poor antibacterial activity (MIC = 512–2048 µg/mL), while only compound **2** showed antifungal activity with an MIC of 1024 µg/mL. The poor inhibition profile of the compounds may be explained by their low water solubility which probably prevent their diffusion from the lipid membrane to the hydrophilic cytoplasmic environment. It can be concluded that changing phthalimido with substituted benzyl groups did not increase the antibacterial/antifungal activity of taurinamidobenzenesulfonamide core structure.

ACKNOWLEDGMENT

The authors are grateful for financial support from The Scientific and Technological Research Council of Turkey [TUBITAK; Project number: SBAG- 117S516] and Ege University Scientific Research Projects Coordination Unit [Project number: 16-ECZ-012].

CONFLICT OF INTERESTS

The authors have declared no conflict of interest.

REFERENCES

- Sui Y-F, Li D, Wang J, Bheemanaboina RRY, Ansari MF, Gan L-L, et al. Design and biological evaluation of a novel type of potential multi-targeting antimicrobial sulfanilamide hybrids in combination of pyrimidine and azoles. *Bioorg Med Chem Lett*. 2020 Mar;30(6):126982. Doi: 10.1016/j.bmcl.2020.126982.
- Naaz F, Srivastava R, Singh A, Singh N, Verma R, Singh VK, et al. Molecular modeling, synthesis, antibacterial and cytotoxicity evaluation of sulfonamide derivatives of benzimidazole, indazole, benzothiazole and thiazole. *Bioorg Med Chem*. 2018 Jul;26(12):3414–28. Doi: 10.1016/j.bmc.2018.05.015.
- Ali M, Angeli A, Bozdog M, Carta F, Capasso C, Farooq U, et al. Benzylaminoethylureido-Tailed Benzenesulfonamides Show Potent Inhibitory Activity against Bacterial Carbonic Anhydrases. *ChemMedChem*. 2020 Oct 28;cmdc.202000680. Doi: 10.1002/cmdc.202000680.
- Supuran CT, Capasso C. Antibacterial carbonic anhydrase inhibitors: an update on the recent literature. *Expert Opin Ther Pat*. 2020 Sep 3;0(0):1–20. Doi: 10.1080/13543776.2020.1811853.
- Supuran CT, Capasso C. Carbonic anhydrases from pathogens. In: *Carbonic Anhydrases*. Elsevier; 2019. p. 387–417. Doi: 10.1016/B978-0-12-816476-1.00020-4.
- Küçükbay H, Buğday N, Küçükbay FZ, Berrino E, Bartolucci G, Del Prete S, et al. Synthesis and carbonic anhydrase inhibitory properties of novel 4-(2-aminoethyl)benzenesulfonamide-dipeptide conjugates. *Bioorg Chem*. 2019;83(September 2018):414–23. Doi: 10.1016/j.bioorg.2018.11.003.
- Ibrahim MA, Panda SS, Birs AS, Serrano JC, Gonzalez CF, Alamry KA, et al. Synthesis and antibacterial evaluation of amino acid-antibiotic conjugates. 2014; Doi: 10.1016/j.bmcl.2014.01.065.
- Grygorenko OO, Biiitseva A V., Zherish S. Amino sulfonic acids, peptidosulfonamides and other related compounds. *Tetrahedron*. 2018 Mar;74(13):1355–421.
- Chung M, Malatesta P, Bosquesi P, Yamasaki P, Santos JL dos, Vizioli E. *Advances in Drug Design Based on the Amino Acid Approach: Taurine Analogues for the Treatment of CNS Diseases*. Pharmaceuticals. 2012 Oct 23;5(10):1128–46.
- Gupta RC. Taurine Analogues and Taurine Transport: Therapeutic Advantages. In: S.S. O, P. S, editors. *Taurine 6*. New York: Springer US; 2006. p. 449–67.

11. Ripps H, Shen W. Review: taurine: a “very essential” amino acid. *Mol Vis*. 2012;18(November):2673-86.
12. Cook AM, Denger K. Metabolism of taurine in microorganisms: A primer in molecular biodiversity? In: *Advances in Experimental Medicine and Biology*. Springer New York; 2006 [cited 2020 Nov 22]. p. 3-13.
13. Tomoshige S, Dik DA, Akabane-Nakata M, Madukoma CS, Fisher JF, Shrout JD, et al. Total Syntheses of Bulgecins A, B, and C and Their Bactericidal Potentiation of the β -Lactam Antibiotics. *ACS Infect Dis*. 2018 Jun 8;4(6):860-7.
14. Chen K, Zhang Q, Wang J, Liu F, Mi M, Xu H, et al. Taurine protects transformed rat retinal ganglion cells from hypoxia-induced apoptosis by preventing mitochondrial dysfunction. *Brain Res*. 2009 Jul;1279:131-8.
15. Vanitha MK, Baskaran K, Periyasamy K, Saravanan D, Ilakkia A, Selvaraj S, et al. A Review on the Biomedical Importance of Taurine. *Int J Pharma Res Heal Sci*. 2015 [cited 2016 Apr 15];3(3):680-6.
16. Gottardi W, Debabov D, Nagl M. N-Chloramines, a Promising Class of Well-Tolerated Topical Anti-Infectives. *Antimicrob Agents Chemother*. 2013;57(3):1107-14.
17. Jekle A, Yoon J, Zuck M, Najafi R, Wang L, Shiau T, et al. NVC-422 Inactivates *Staphylococcus aureus* Toxins. *Antimicrob Agents Chemother*. 2013;57(2):924-9.
18. Darouiche D, Najafi R, Krantz K, Debabov D, Friedman L, Khosrovi B, et al. NVC-422. *Drugs Future*. 2011;36(9):651.
19. Akgül Ö, Öztürk İ, Aygül A, Ermertcan Ş. Synthesis and Antimicrobial Activity of Some Taurinamide Derivatives. *Marmara Pharm J*. 2017; 21(2):361-361.
20. Akgül Ö, Angeli A, Vullo D, Carta F, Supuran CT. Unconventional amino acids in medicinal chemistry: First report on taurine merged within carbonic anhydrase inhibitors. *Bioorg Chem*. 2020 Oct 1;103:104236.
21. Salvatore RN, Yoon CH, Jung KW. Synthesis of secondary amines. *Tetrahedron*. 2001 Sep [cited 2016 Jul 28];57(37):7785-811.
22. Salvatore RN, Nagle AS, Schmidt SE, Jung KW. Cesium Hydroxide Promoted Chemoselective N - Alkylation for the Generally Efficient Synthesis of Secondary Amines. *Org Lett*. 1999 Dec;1(12):1893-6. Doi: 10.1021/ol9910417.
23. European Committee on Antimicrobial Susceptibility Testing. Routine and extended internal quality control for MIC determination and disk diffusion as recommended by EUCAST. *Eucast*. 2020;Version 10:1-20.



Analysis of Trace Elements, Cholinesterase Inhibitory Activity, and ADME/Tox Profiling of some *Achillea* Species

Duygu Taskin^{*1} , Talip Sahin² , Mucahit Ozdemir³ , and Bahattin Yalcin³ 

^{1*} Department of Analytical Chemistry, Faculty of Pharmacy, University of Health Sciences, Istanbul, Turkey

² Institute of Health Sciences, Marmara University, 34854-Maltepe, Istanbul, Turkey.

³ Department of Chemistry, Faculty of Science, Marmara University, 34722 Istanbul, Turkey.

Abstract: In this study, the anti-cholinesterase activities of different extracts of *Achillea lycaonica*, *A. vermicularis* and *A. nobilis* L. subsp. *neilreichii* (Kerner) Formanek species were examined and then trace elements (Al, V, Cr, Mn, Fe, Co, Ni, Cu, Zn, As, Se, Cd, and Pb) of the plants were analyzed by ICP-MS. The pharmacokinetic properties of the phenolic compounds of these plants previously analyzed by us and the ADME-Tox (absorption, distribution, metabolism, excretion, and toxicity) profiles of the trace elements we identified in this study were estimated. According to the data obtained, it was determined that all three plants showed high acetyl-cholinesterase inhibitory activity. The concentration of trace elements was lower than that declared by WHO, except for the *A. lycaonica*. It was determined that V, Cr, Fe, Co, and As metals in *A. lycaonica* exceeded the limit values determined by WHO. According to ADMET estimates, it is thought that the toxic values of all three plants are not high, and therefore the use of *A. nobilis* and *A. vermicularis* plants does not pose any health risk but *A. lycaonica* should be used carefully due to the presence of heavy metals.

Keywords: Phenolic compounds, ADMET, cholinesterase inhibitory, ICP-MS.

Submitted: December 29, 2020. **Accepted:** January 17, 2021.

Cite this: Taskin D, Sahin T, Ozdemir M, Yalcin B. Analysis of Trace Elements, Cholinesterase Inhibitory Activity, and ADME/Tox Profiling of some *Achillea* Species. JOTCSA. 2021;8(1):329-42.

DOI: <https://doi.org/10.18596/jotcsa.849654>.

***Corresponding Author. E-mail:** duygu.taskin@sbu.edu.tr.

INTRODUCTION

The genus *Achillea* is widely found in Europe, temperate areas of Asia, and North America. *Achillea* sp. is one of the most valuable and economic plants of Anatolia. In Turkey, the *Achillea* genus is used in wound healing, abdominal pain, stomachache, symptomatic relief of colds, ulcers, and diarrhea (1).

Herbal teas prepared from aerial parts of different *Achillea* species have traditionally been used as an anti-inflammatory agent for the treatment of spasmolytic and rheumatic pain. The aerial parts of different *Achillea* species are widely used in folk medicine for the preparation of drugs with anti-inflammatory spasmolytic, hemostatic, digestive, and collagic effects. The dried flower heads of the *Achillea nobilis* L. subsp. *neilreichii* (Kerner)

Formanek are used as a diuretic and an emmenagog for wound healing, for abdominal pain, and against diarrhea in Turkey (2). *Achillea lycaonica* Boiss. et Heldr. is a plant native to Turkey and are known to have antioxidant, wound healing, and cytotoxic effects (3). The flowers of *Achillea vermicularis* Trin. are used in the treatment of diarrhea and renal pain. In addition, the plant's capitulum is used in the treatment of asthma (4,5).

Trace elements play an essential role in the formation of chemical components in plants. Some metals such as zinc, iron, copper, chromium, and cobalt are required at certain levels for living things and are toxic in high concentrations. On the other hand, mercury, lead, and cadmium metals are harmful to the body even at low concentrations, and no beneficial properties are known. Medicinal herbs are known to be used in traditional therapy for

certain symptoms due to their low side effects. Plants may pose health risks due to toxic elements that may be contained due to environmental pollution, etc. Therefore, it is very important to know medicinal plants in terms of trace element content (6-9). Inductively coupled plasma-mass spectrometry ICP-MS is a technique frequently used in trace element analysis of medicinal plants due to its high sensitivity and wide linear dynamic range (10-13).

Anticipating the pharmacokinetic properties of pharmaceutical molecules increases the likelihood of reaching the target faster and more guaranteed. The word ADMET is an abbreviation for absorption, distribution, metabolism, excretion, and toxicity. These criteria define the pharmaceutical activities of the drug candidates (14).

In this study, trace metal analysis and anticholinesterase activities were determined depending on the medicinal use of plants. In addition, the ADMET profiles of the phenolic compounds we analyzed in our previous studies and the trace elements we detected in this study were estimated.

MATERIAL AND METHODS

Identification of Plant Material

The taxonomic identity of the *A. lycaonica* was confirmed by Prof. Dr. Turan Arabaci. The voucher specimens were deposited in the herbarium of the Faculty of Pharmacy, İnönü University; herbarium number: T. Arabacı 2969. The *A. vermicularis* Trin. was authenticated by Dr. Ahmet Dogan, and a voucher specimen (MARE-18071) was deposited at the Marmara University Pharmacy herbarium for future reference. The taxonomic identity of the *A. nobilis* L. subsp. *neilreichii* (Kerner) Formanek was confirmed by Assist. Prof. Dr. Ismail Senkardes. The voucher specimens were deposited in the herbarium of the Faculty of Pharmacy, Marmara University; herbarium numbers: MARE-18074.

Preparation of Plants Extracts

The dried aerial parts of plants were extracted chloroform, ethyl acetate, and ethanol by using the soxhlet and maceration methods. All extracts were filtered and evaporated to dryness under reduced pressure at 45°C in a rotary evaporator. The crude extracts were then transferred to vials and kept at +4 °C for future analysis.

Determination of AChE Inhibitory Activities of Different Extracts

Inhibition of cholinesterases was evaluated using a 96-well microplate reader based on the method of Ellman (1961) with some modifications. Spectrophotometric data were recorded by Shimadzu UV-1800 spectrophotometer. Experiments have been carried out at least in triplicate, and galantamine was used as a reference (15).

Inductively Coupled Plasma-Mass Spectrometry (ICP-MS) Analysis

An Agilent 7700 ICP-MS and ASX-500 autosampler was used to determine the trace elements in the samples. The internal standard was used for each element to be analyzed. The collision reaction cell was used to eliminate spectral and non-spectral interference, and the required mode for each element was determined by the collision reaction cell. It was noted that the abundance rates were higher in elements with more than one isotope and no interference-effect. Accordingly, the mass of the studied elements is shown in Table 1.

For trace element determination, *Achillea* samples were accurately weighed and placed in teflon containers to be dissolved in a microwave oven (Berghoff). A mixture of HNO₃: H₂O₂, 3:1 (v:v) was prepared, and 10 mL of this mixture was added to the samples and placed in the microwave oven incinerator. The dissolution process was carried out by adjusting the temperature (0- 180 °C) and time (35 minutes) of the microwave oven program. After dissolution, all samples were filtered and completed to 25 mL with ultrapure water and read in Agilent 7700 ICP-MS device.

Table 1. ICP-MS operating conditions.

Element	Mass	ISTD* mass	Tune Mode	Time (sec)
Al	27	45 ^a	He	0.30
V	51	45	He	0.10
Cr	52	45	He	1.00
Mn	55	45	He	0.10
Fe	56	45	He	0.10
Co	59	45	He	0.10
Ni	60	45	He	1.00
Cu	63	45	He	0.30
Zn	66	72 ^b	He	0.20
As	75	72	He	0.30
Se	78	72	He	5.00
Cd	111	115 ^c	No Gas	1.00
Pb	208	209 ^d	No Gas	0.30

*Internal Standards: ^aSc ^bGe ^cIn ^dBi

ADME/Tox Prediction

Anticipating the pharmacokinetic properties of pharmaceutical molecules increases the likelihood of reaching the target faster and more guaranteed. The ADMET criteria define the pharmaceutical activities of the drug candidates. pkCSM, a free online web server (<http://structure.bioc.cam.ac.uk/pkcsm>) was used to predict the properties of the previously analyzed compounds and trace elements from *A. lyconica*, *A. nobilis*, and *A. vermicularis*. Toxtree-v3.1.0.1851 software was used to estimate toxicity analysis of substituents of structures according to Cramer's rules. Cramer's rules are divided into three categories. Low (Class I), Substances with simple chemical structures and for which efficient modes of metabolism exist, suggesting a low order of oral toxicity. Intermediate (Class II), Substances which possess structures that are less innocuous than class I substances, but do not contain structural features suggestive of toxicity like those substances in class III. High (Class III), Substances with chemical structures that permit no strong initial presumption of safety or may even suggest significant toxicity or have reactive functional groups.

Molecular polar surface area (PSA) is a very useful parameter for the prediction of drug transport properties. Polar surface area is defined as a sum of surfaces of polar atoms (usually oxygens, nitrogens, and attached hydrogens) in a molecule. This parameter has been shown to correlate very well with the human intestinal absorption, Caco-2 monolayers permeability, and blood-brain barrier penetration. Molecular lipophilicity potential (MLP) is useful property to rationalize various molecular ADME characteristics (like membrane penetration or plasma-protein binding). Analysis of the 3-D distribution of hydrophobicity on the molecular surface is particularly helpful when explaining differences in observed ADME properties of molecules with the same logP, since the 3D parameter contains much more information than logP expressed by just a single value. Molecular polar surface area and molecular lipophilicity potential calculated using Molinspiration cheminformatics (www.molinspiration.com/cgi-bin/properties) (14,16).

In this study, ADMET properties of 18 phenolic compounds and 13 trace metals that we analyzed from these three plants with our previous studies (17-19) were measured by a computer, and the partition coefficients (log P) of the related phenolic compounds were found.

RESULTS AND DISCUSSION

Concentrations of Trace Elements in *Achillea* Species

The accumulation levels of heavy metals resulting from natural or human-induced activities should be

regularly measured and monitored in terms of environment and human health. For this, the ICP-MS (Inductively coupled plasma-mass spectrometer) device has been used in recent years, which has advantages such as being economical, fast, and working even at very low concentrations. Accordingly, in this study, trace metal analysis of three different *Achillea* species whose phenolic content we analyzed in previous publications were performed with ICP MS. It is aimed to determine the concentrations of Al, V, Cr, Mn, Fe, Co, Ni, Cu, Zn, As, Se, Cd, and Pb quantitatively as trace metals, and the results were presented in Table 2. The vanadium content was determined in the range of 0.24-1.58 ng/mg. When compared to each other of *Achillea* species, the most high level of V in AL. The Aluminium and chromium contents were detected in the range of 190.16-638.40 ng/mg and 0.91-2.71 ng/mg, respectively. In Yener's study, the Al and Cr contents were found 1424 and 4.8 mg/kg in *Malvella sherardiana* (20). In another study, heavy metal analysis of 20 medicinal plants was performed, and the highest chromium value was found to be 33.75 µg/g (21). In another study, the heavy metal content of the most used medicinal plants in Sudan was analyzed, and as a result, the highest chromium values were found in *Ammi visnaga* L (2.6 mg/kg) and *Foeniculum vulgare* P. Mill (3.6 mg/kg) (22). In a study by Khan et al., the maximum amount of Mn in *Artemisia vulgaris* L. was 52.94 ppm and the amount of Fe in *Withania somnifera* L., was 206.69 ppm (23). In Karahan et al., that taken 17 medicinal plants collected from Turkey was founded the Fe levels in the range of 78.96- 907.062 mg/kg. And also in that study, they were detected Mn levels in the range of 12.11-362.57 mg/kg (24). In another study, cobalt, nickel, copper, and arsenic were studied in 26 plants, and these heavy metal content ranges were found to be 0.57- 2.86, 3.47-10.83, 5.12- 17.90, and 0.08- 3.03, respectively (25). In another review study, the cadmium content range of medicinal plants analyzed was 0.051- 704.39 µg/g, while the selenium content was 0.3-41.3 µg/g. While the zinc range of medicinal plants analyzed in the same study was found to be 0.14-7695.4 µg/g, the lead range was found to be 0.09-22.95 µg/g (26). The WHO maximum permissible limits of chromium and lead in medicinal herbs are 2 and 10 ppm, respectively (27). In addition, in literature reviews, this value has been reported to be 0.3 ppm in terms of cadmium and 50 ppm for zinc (28,29). The limit values of Fe and Cu accepted by FAO / WHO for edible vegetables are 450 and 40 ppm, respectively (30). Ni limit value accepted by FAO / WHO for plants is 5 ppm (31). Among the analyzed plants, all species are within this limit value While the limit value determined by FAO / WHO for vanadium is 0.03 ppm, it has been reported that these values are 0.50 and 0.01 for arsenic and cobalt, respectively (32).

Table 2. Quantification of trace elements in *Achillea* species by ICP-MS. Concentrations of the analyzed trace elements [mean (ng/mg) \pm SD. n=4]

Plant samples	<i>A. vermicularis</i>	<i>A. nobilis subsp. neilreichii</i>	<i>A. lyconica</i>
Al	190.16 \pm 12.89	520.39 \pm 35.28	638.40 \pm 43.28
V	0.24 \pm 0.01	0.55 \pm 0.02	1.58 \pm 0.06
Cr	0.91 \pm 0.05	2.54 \pm 0.13	2.710 \pm 0.001
Mn	18.97 \pm 1.09	45.96 \pm 2.64	24.73 \pm 1.42
Fe	125.57 \pm 1.31	319.23 \pm 3.32	584.55 \pm 6.08
Co	0.095 \pm 0.005	0.25 \pm 0.01	0.39 \pm 0.02
Ni	1.05 \pm 0.04	1.83 \pm 0.07	2.26 \pm 0.08
Cu	4.09 \pm 0.32	6.46 \pm 0.51	6.04 \pm 0.47
Zn	30.17 \pm 1.13	40.99 \pm 1.54	43.20 \pm 1.62
As	0.08 \pm 0.01	0.51 \pm 0.03	0.565 \pm 0.04
Se	0.09 \pm 0.01	0.045 \pm 0.003	0.052 \pm 0.003
Cd	0.06 \pm 0.01	0.19 \pm 0.01	0.150 \pm 0.006
Pb	0.68 \pm 0.03	4.43 \pm 0.20	3.135 \pm 0.140

When the amounts of all metals detected in plants are examined, it is seen that Co and V metals are above the limit values determined in all three plants. In addition, it was determined that the amount of Cr, Fe, and most importantly As, besides V and Co, was above the allowed value in *A. lycanica*. No disease has been detected in humans due to vanadium deficiency. In general, the toxicity of vanadium compounds is also low. In this regard, the possible damage of vanadium excess in plants can be ignored. When all results were examined, it was determined that *A. lycanica* contained higher amounts of heavy metals than the allowed values among the other species. The most important of these heavy metals is As. Considering that arsenic is classified as "Group 1" in terms of being carcinogenic when examining the criteria of the International Cancer Research Agency, it is a natural conclusion that it is necessary to be careful in the use of *A. lycanica*.

Determination of Anticholinesterase Activities of Plants

In the current study, cholinesterase enzyme activities of different extracts obtained from the

plants by two extraction methods were compared. It was determined that both the maceration (74.64%) and soxhlet (69.23%) ethanol extracts of *A. lycanica* showed potent anti-cholinesterase activity compared to other extracts. It was also observed that the chloroform extracts from both extraction methods did not have any enzyme inhibition ability. It was found that both the maceration ethanol (82.11%) and soxhlet ethanol (55.04%) extracts of *A. nobilis L. subsp. neilreichii* exhibited strong anti-cholinesterase activity compared to other extracts. When the results of the *A. vermicularis* were compared, it was found that maceration ethanol (79.49%) and soxhlet ethanol (76.92%) extracts had the highest inhibition of cholinesterase enzyme. As the results, maceration ethanol extracts of all three plants were determined to have the highest enzyme inhibition ability in this study. When all data are compared with the standard compound, galantamine, all extracts were found to have lower activity than the standard compound (95.52%) at 500 µg/mL concentration (Table 3).

Table 3. AChE inhibitory activities of different extracts from plants

Enzyme inhibition (%) (500 µg/mL)			
Extracts	<i>A. lycanica</i>	<i>A. nobilis L. subsp. neilreichii</i>	<i>A. vermicularis</i>
Maceration chloroform	NA*	44.62±1.63	NA
Maceration ethyl acetate	44.62±1.85	30.20±1.69	36.87±1.97
Maceration ethanol	74.64±1.78	82.11±0.84	79.49±0.34
Soxhlet chloroform	NA	26.21±1.64	26.27±0.099
Soxhlet ethyl acetate	54.42±1.04	NA	64.10±0.64
Soxhlet ethanol	69.23±2.05	55.04±2.52	76.92±1.48
Galanthamine		95.52±1.15	

*NA: no activity

In silico ADME/Tox profiling of phenolics and trace elements

The pharmacokinetics of phenolic compounds and trace metals in plants were predicted by the parameters of absorption, distribution, metabolism, excretion, and toxicity as shown in Table 4-7 and Figure 1. The Caco-2 permeability values (>0.90) of caffeic acid, salicylic acid, 8-hydroxy-salvigenin,

naringenin, and apigenin compounds were predicted to be high. Chlorogenic acid, rutin, dicaffeoylquinic acid, apigenin 6,8-di-C-glucoside, and luteolin-3',7-di-O-glucoside were predicted to have poorly intestinal absorption (human) compared to other compounds. Salicylic acid has low skin permeability properties (log Kp>-2.5).

Table 4. The ADMET parameters of the following compounds from plants via pkCSM software.

Property	Predicted Value									
	Caffeic acid	Chlorogenic acid	Quercetin	Salicylic acid	Rutin	8-Hydroxy-salvigenin	Luteolin	Dicaffeoylquinic acid	Naringenin	Apigenin
Absorption										
Water solubility (log mol/L)	-4.30	-2.75	-3.37	-1.66	-2.89	-3.84	-3.09	-2.92	-3.22	-3.33
Caco2 permeability	0.96	-0.62	0.59	1.13	-0.66	1.15	0.10	-1.16	1.03	1.01
Intestinal absorption (% A)	96.1	17.1	74.9	77.7	28.3	68.8	81.1	16.3	91.3	93.2
Skin Permeability (log Kp)	4	6	9	1	0	7	3	6	1	5
Skin Permeability (log Kp)	-2.79	-2.74	-2.74	-2.32	-2.74	-2.74	-2.74	-2.74	-2.74	-2.74
P-glycoprotein substrate	No	Yes	Yes	No	Yes	Yes	Yes	Yes	Yes	Yes
P-glycoprotein I inhibitor	No	No	No	No	No	No	No	No	No	No
P-glycoprotein II inhibitor	Yes	No	No	No	No	Yes	No	No	No	No
Distribution										
VDss ^a	-0.14	-0.85	0.24	-0.47	-0.07	0.01	1.15	1.96	-0.02	0.82
Fraction unbound	0.08	0.40	0.02	0.53	0.30	0.08	0.17	0.29	0.06	0.15
BBB permeability ^b (log BB)	-0.14	-1.44	-1.36	-0.31	-2.10	-0.40	-0.91	-2.13	-0.58	-0.73
CNS permeability ^c log PS	-2.06	-4.03	-3.43	-2.91	-5.75	-3.20	-2.25	-3.80	-2.22	-2.06
Metabolism										
CYP2D6 substrate	No	No	No	No	No	No	No	No	No	No
CYP3A4 substrate	Yes	No	No	No	No	No	No	Yes	No	No
CYP1A2 inhibitor	Yes	No	Yes	No	No	Yes	Yes	No	Yes	Yes
CYP2C19 inhibitor	Yes	No	No	No	No	Yes	No	No	No	Yes
CYP2C9 inhibitor	Yes	No	No	No	No	Yes	Yes	No	No	No
CYP2D6 inhibitor	No	No	No	No	No	No	No	No	No	No
CYP3A4 inhibitor	Yes	No	Yes	No	No	Yes	No	No	No	No
Excretion										
Total Clearance (log mL/min/kg)	0.80	0.37	0.58	0.66	-0.27	0.73	0.50	-0.06	0.06	0.57
Renal OCT2 substrate	No	No	No	No	No	No	No	No	No	No
Toxicity										
AMES toxicity	No	No	Yes	No	Yes	No	No	No	No	No
Max. tolerated dose (log mg/kg/day)	0.29	1.22	1.06	0.61	0.43	0.85	0.50	0.44	-0.18	0.33
hERG I inhibitor	No	No	No	No	No	No	No	No	No	No
hERG II inhibitor	Yes	No	No	No	Yes	Yes	No	No	No	No
Oral Rat Acute ^d Toxicity	2.57	2.11	2.30	2.05	2.44	2.06	2.46	2.54	1.79	2.45
Oral Rat Chronic ^e Toxicity	1.59	3.37	3.03	2.21	5.46	2.54	2.41	3.89	1.94	2.30
Hepatotoxicity	Yes	Yes	No	No	No	No	No	No	No	No
Skin Sensitization	No	No	No	No	No	No	No	No	No	No
<i>T. Pyriformis</i> toxicity (log µg/L)	0.57	0.29	0.30	-0.23	0.29	0.30	0.33	0.29	0.37	0.38
Minnow toxicity (log mM)	-0.03	3.70	1.41	2.10	2.78	0.06	3.17	3.35	2.14	2.43

^aVolume of Distribution (log L/kg)^bBBB (Blood-brain Barrier)^cCNS (Central Nervous System)^dOral Rat Acute Toxicity unit is (mol/kg) and these values are lethal dose, 50% (LD₅₀)^eOral Rat Chronic Toxicity unit is (log mg/kg bw/day)

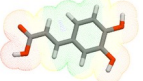
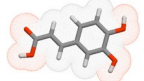
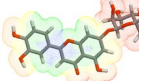
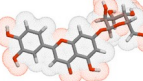


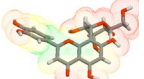
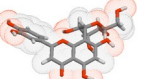
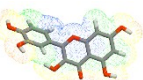

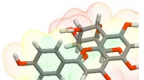
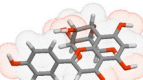
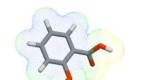
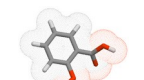
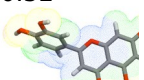
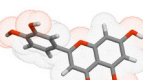
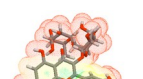
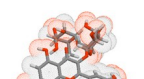
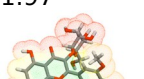
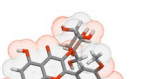
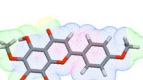
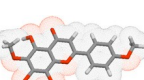
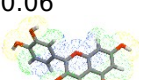
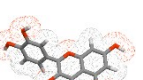
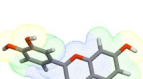
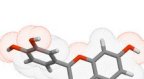
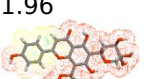
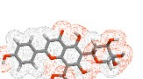




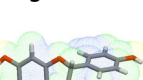
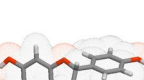
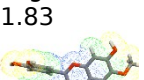

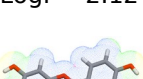
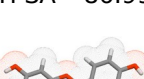
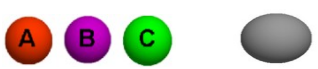
Table 5. The ADMET parameters of the following compounds from plants via pkCSM software.

Property	Predicted Value							
	Luteolin-7-glucoside	Orientin	Vitexin	isorhamnetin-3-O-glucoside	3-O-Methylquercetin	Apigenin 6,8-di-C-glucoside	Luteolin-3',7-di-O-glucoside	Axillarin
Absorption								
Water solubility	-2.72	-2.91	-2.85	2.91	-3.16	-2.84	-2.60	-3.17
Caco2 permeability	0.25	-1.25	-0.96	0.33	-0.62	-1.13	-0.77	-0.52
Intestinal absorption	37.56	43.73	46.70	49.71	76.07	14.66	0	82.65
Skin Permeability	-2.74	-2.74	-2.74	2.74	-2.74	-2.74	-2.74	-2.74
P-glycoprotein substrate	Yes	Yes	Yes	Yes	Yes	Yes	Yes	Yes
P-glycoprotein I inhibitor	No	No	No	No	No	No	No	No
P-glycoprotein II inhibitor	No	No	No	No	No	No	No	Yes
Distribution								
VDss	0.88	1.49	1.07	1.25	0.22	0.57	-0.02	0.78
Fraction unbound	0.22	0.26	0.24	0.11	0.07	0.28	0.29	0.12
BBB permeability	-1.56	-1.64	-1.45	1.72	-1.16	-1.93	-2.3	-1.52
CNS permeability	-3.93	-4.09	-3.83	4.22	-3.27	-4.77	-4.94	-3.48
Metabolism								
CYP2D6 substrate	No	No	No	No	No	No	No	No
CYP3A4 substrate	No	No	No	No	No	No	No	No
CYP1A2 inhibitor	No	No	No	No	Yes	No	No	Yes
CYP2C19 inhibitor	No	No	No	No	No	No	No	No
CYP2C9 inhibitor	No	No	No	No	No	No	No	No
CYP2D6 inhibitor	No	No	No	No	No	No	No	No
CYP3A4 inhibitor	No	No	No	No	No	No	No	No
Excretion								
Total Clearance	0.48	0.37	0.44	0.49	0.46	-0.11	-0.13	-0.13
Renal OCT2 substrate	No	No	No	No	No	No	No	No
Toxicity								
AMES toxicity	No	No	No	No	No	No	No	No
Max. tolerated dose	0.58	0.57	0.58	0.64	0.52	0.46	0.27	0.27
hERG I inhibitor	No	No	No	No	No	No	No	No
hERG II inhibitor	No	No	No	Yes	No	Yes	Yes	Yes
Oral Rat Acute Toxicity	2.55	2.57	2.595	2.55	2.53	2.48	2.50	2.50
Oral Rat Chronic Toxicity	4.28	4.39	4.635	4.45	2.26	5.86	6.35	6.35
Hepatotoxicity	No	No	No	No	No	No	No	No
Skin Sensitisation	No	No	No	No	No	No	No	No
<i>T. Pyriformis</i> toxicity	0.29	0.29	0.29	0.29	0.3	0.29	0.29	0.29
Minnow toxicity	6.34	6.13	4.90	6.55	2.37	11.61	8.83	8.83

Table 6. The ADMET parameters of following trace metals in plants via pkCSM software.

Property	Predicted Value												
	Al	V	Cr	Mn	Fe	Co	Ni	Cu	Zn	As	Se	Cd	Pb
Absorption													
Water solubility	0.15	-0.05	-0.03	-0.03	-0.03	-0.03	-0.02	-0.03	-0.07	0.14	0.16	-0.20	-0.01
Caco2 permeability	1.38	1.38	1.38	1.38	1.38	1.38	1.38	1.38	1.38	1.38	1.38	1.38	1.38
Intestinal absorption	100	100	100	100	100	100	100	100	100	100	100	100	100
Skin Permeability	-2.65	-2.59	-2.59	-2.59	-2.59	-2.59	-2.59	-2.59	-2.59	-2.65	-2.65	-2.57	-2.64
P-glycoprotein substrate	Yes	Yes	Yes	Yes	Yes	Yes	Yes	Yes	Yes	Yes	Yes	Yes	Yes
P-glycoprotein I inhibitor	No	No	No	No	No	No	No	No	No	No	No	No	No
P-glycoprotein II inhibitor	No	No	No	No	No	No	No	No	No	No	No	No	No
Distribution													
VDss	-0.06	-0.05	-0.05	-0.05	-0.05	-0.05	-0.05	-0.05	-0.05	-0.06	-0.06	-0.04	-0.04
Fraction unbound	0.80	0.79	0.79	0.79	0.79	0.79	0.79	0.79	0.79	0.80	0.80	0.78	0.80
BBB permeability	0.03	0.03	0.03	0.03	0.03	0.03	0.03	0.03	0.03	0.03	0.03	0.01	0.02
CNS permeability	-2.30	-2.30	-2.30	-2.30	-2.30	-2.30	-2.30	-2.30	-2.30	-2.30	-2.30	-2.30	-2.30
Metabolism													
CYP2D6 substrate	No	No	No	No	No	No	No	No	No	No	No	No	No
CYP3A4 substrate	No	No	No	No	No	No	No	No	No	No	No	No	No
CYP1A2 inhibitor	No	No	No	No	No	No	No	No	No	No	No	No	No
CYP2C19 inhibitor	No	No	No	No	No	No	No	No	No	No	No	No	No
CYP2C9 inhibitor	No	No	No	No	No	No	No	No	No	No	No	No	No
CYP2D6 inhibitor	No	No	No	No	No	No	No	No	No	No	No	No	No
CYP3A4 inhibitor	No	No	No	No	No	No	No	No	No	No	No	No	No
Excretion													
Total Clearance	0.52	0.52	0.51	0.51	0.51	0.51	0.51	0.51	0.53	0.52	0.52	0.58	0.58
Renal OCT2 substrate	No	No	No	No	No	No	No	No	No	No	No	No	No
Toxicity													
AMES toxicity	No	No	No	No	No	No	No	No	No	No	No	No	No
Max. tolerated dose	1.18	1.19	1.19	1.19	1.19	1.19	1.19	1.19	1.19	1.18	1.19	1.16	1.16
hERG I inhibitor	No	No	No	No	No	No	No	No	No	No	No	No	No
hERG II inhibitor	No	No	No	No	No	No	No	No	No	No	No	No	No
Oral Rat Acute Toxicity	2.22	2.28	2.29	2.29	2.29	2.30	2.30	2.29	2.28	2.22	2.22	2.22	2.15
Oral Rat Chronic Toxicity	0.96	1.09	1.13	1.15	1.15	1.16	1.17	1.15	1.05	0.94	0.97	0.74	0.57
Hepatotoxicity	No	No	No	No	No	No	No	No	No	No	No	No	No
Skin Sensitisation	No	No	No	No	No	No	No	No	No	No	No	No	No
<i>T. Pyriformis</i> toxicity	-0.68	-0.70	-0.72	-0.73	-0.73	-0.73	-0.74	-0.73	-0.69	-0.67	-0.68	-0.54	-0.49
Minnow toxicity	2.45	2.32	2.36	2.37	2.37	2.38	2.38	2.37	2.29	2.43	2.46	2.04	2.14

Table 7. Molecular Lipophilicity Potential (MLP) and Topological Polar Surface Area (TPSA) 3D structures of compounds from plants based on Molinspiration Cheminformatics.

Compound	MLP	TPSA	Compound	MLP	TPSA
Caffeic acid	 LogP= 0.94	 TPSA= 77.75	Luteolin-7-glucoside	 LogP= 0.19	 TPSA= 190.28
Chlorogenic acid	 LogP= -0.45	 TPSA= 164.74	Orientin	 LogP= 0.03	 TPSA= 201.27
Quercetin	 LogP= 1.68	 TPSA= 131.24	Vitexin	 LogP= 0.52	 TPSA= 181.04
Salicylic acid	 LogP= 1.87	 TPSA= 57.53	Luteolin	 LogP= 1.97	 TPSA= 111.12
Rutin	 LogP= -1.06	 TPSA= 269.43	Isorhamnetin-3-O-glucoside	 LogP= -0.06	 TPSA= 199.51
8-Hydroxy-salvigenin	 LogP= 3.23	 TPSA= 98.39	3-O-Methylquercetin	 LogP= 1.96	 TPSA= 120.36
Luteolin	 LogP= 1.97	 TPSA= 111.12	Apigenin 6,8-di-C-glucoside	 LogP= -2.10	 TPSA= 271.19
Dicaffeoylquinic acid	 LogP= 1.21	 TPSA= 211.28	Luteolin-3',7-di-O-glucoside	 LogP= -1.83	 TPSA= 269.43
Naringenin	 LogP= 2.12	 TPSA= 86.99	Axillarin	 LogP= 1.98	 TPSA= 129.59
Apigenin	 LogP= 2.46	 TPSA= 90.89	Trace Metals	 LogP= n/a* TPSA= 0.00	

In the surface representation of the molecular lipophilicity potential, the hydrophobic surface is coded with purple and blue colors and the hydrophilic surface is coded with orange and red colors.

A= Al, V, Cr, Mn, Co, Ni, Fe, Cu, Cd, Zn, As; B= Se; C= Pb

TOXIC HAZARD

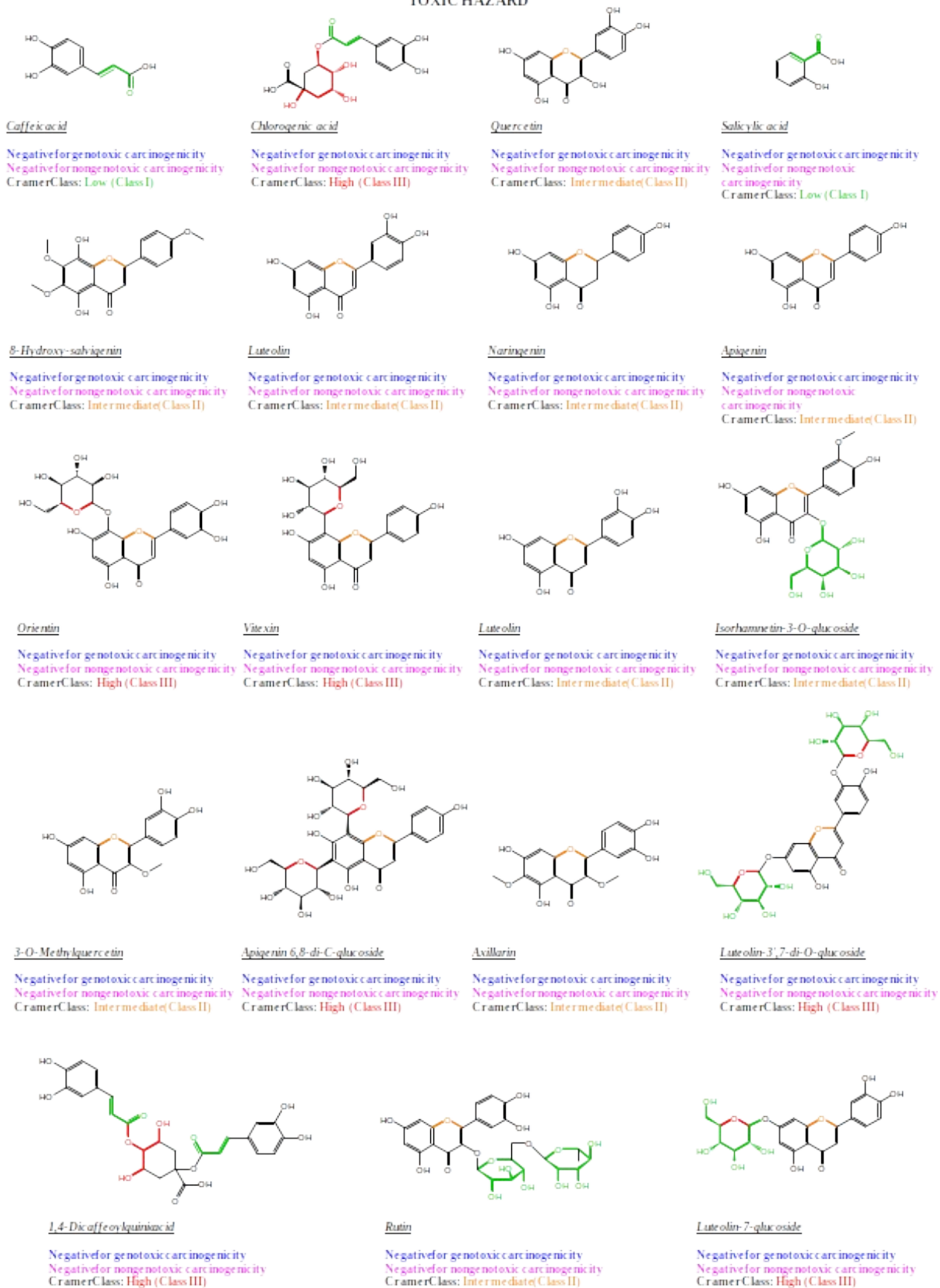


Figure 1. The Carcinogenicity and mutagenicity prediction test of all compounds in this study by Toxtree software.

Chlorogenic acid, quercetin, rutin, 8-Hydroxy-salvigenin, luteolin, dicaffeoylquinic acid, naringenin, apigenin, luteolin-7- glucoside, orientin, vitexin, isorhamnetin-3-O-glucoside, 3-O-methyl quercetin, apigenin 6,8-di-C-glucoside, luteolin-3',7-di-O-glucoside and axillarin compounds have the property of P-glycoprotein substrate. Caffeic acid, 8-hydroxy-salvigenin, and axillarin compounds have only P-glycoprotein II inhibitory properties, while all other compounds do not have P-glycoprotein I inhibitory properties. Chlorogenic acid and salicylic acid had low the volume of distribution (VDs) while luteolin, dicaffeoylquinic acid, apigenin, luteolin-7-glucoside, orientin, vitexin, luteolin, isorhamnetin-3-o-glucoside, apigenin 6,8-di-c-glucoside, and axillarin had high VDs (human) values.

Chlorogenic acid, quercetin, rutin, dicaffeoylquinic acid, luteolin-7-glucoside, orientin, vitexin, isorhamnetin-3-O-glucoside, 3-O-methyl quercetin, apigenin 6,8-di-C-glucoside, luteolin-3',7-di-O-glucoside, and axillarin compounds were predicted to be poorly distributed to the Blood-brain barrier. All compounds were predicted to be unable to penetrate the Central Nervous System (CNS). While caffeic acid and dicaffeoylquinic acid compounds are substrates to the CYP3A4 enzyme, all other compounds do not show the feature of substrates to the enzymes CYP3A4 and CYP2D6. It has been predicted that not all compounds inhibit the CYP2D6 enzyme, but some compounds have an inhibitory effect on CYP1A2 CYP2C19 CYP2C9 and CYP3A4 other enzymes. Not all compounds are predicted to have Renal OCT2 substrate.

Quercetin and rutin compounds were predicted to show AMES toxicity. Caffeic acid chlorogenic acid compounds have a Hepatotoxicity effect. All compounds were predicted to be not Skin Sensitization. All compounds were predicted to be not Minnow toxicity.

Caffeic acid, rutin, 8-Hydroxy-salvigenin, isorhamnetin-3-O-glucoside, apigenin 6,8-di-C-glucoside, luteolin-3',7-di-O-glucoside, and axillarin compounds have hERG II inhibitory effects.

All heavy metals were predicted to have high Caco-2 permeability, Intestinal absorption, and Skin Permeability All heavy metals were predicted to have the property of P-glycoprotein substrate but not P-glycoprotein I and II inhibitory effects. It was predicted that all metals have no effect on metabolic enzymes. All metals were predicted to have no AMES toxicity, Hepatotoxicity, Minnow toxicity, and Skin Sensitization effects. Not all metals were predicted to have hERG I inhibitor and hERG II inhibitory effects.

The parameters selected for estimating the in-silico bioavailability of phenolic compounds and trace metals contained in plants were lipophilicity (LogP) and topological polar surface area. Molecules with

a log P value of less than 1 are hydrophilic; 1 to 5 are strongly lipophilic. In QSAR (quantitative structure-activity relationship) studies, LogP (octanol-water partition coefficient), i.e., lipophilicity (fat solubility) and hydrophilicity (water solubility) are important parameters. A negative value for LogP means the compound has a higher affinity for the aqueous phase (it is more hydrophilic); when LogP= 0, the compound is equally partitioned between the lipid and aqueous phases; a positive value for LogP denotes a higher concentration in the lipid phase (i.e., the compound is more lipophilic). Hydrophobicity affects drug absorption, bioavailability, drug-receptor interactions, metabolism of molecules, and their toxicity. Topological polar surface area (TPSA) is a parameter used in the estimation of drug transport properties. The polar surface area is defined as the sum of the surfaces of polar atoms on the molecule (33).

The LogP values of metals are -0.71 for Aluminum (Al), Vanadium (V), Chromium (Cr), Manganese (Mn), Cobalt (Co), Nickel (Ni); -1.39 for Iron (Fe); -1.11 for Copper (Cu) and Cadmium (Cd); 0.39 for Zinc (Zn); -0.61 for Arsenic (As); 0.79 for Selenium (Se) and 2.93 for Lead (Pb), respectively. The most hydrophilic metal is Iron (Fe), the most lipophilic metal is lead.

When Figure 1 is examined, it is estimated that seven compounds will be highly toxic, although the mutagenic and carcinogenic effects of most of the phenolic compounds we have analyzed in relevant publications were predicted at low and medium levels. It has been proven in previous studies that these 7 compounds contain the *Achillea nobilis* plant. It is understood from Table 7 that most of these toxic compounds are hydrophilic. However, hydrophilic chemicals are easier to destroy by the body than lipophilic toxic substances, and lipophilic toxic substances can accumulate in the body at dangerous levels. In addition to this literature information, it is seen in Table 7 that the log P predicted values of the compounds in this plant except caffeic acid are less than 1. These data show us that these compounds, which are thought to be highly toxic, are hydrophilic. Hence, these results suggested that this plant will not pose a very high risk for human health in the use as food/ medicine.

CONCLUSION

The success rate of drug development from phytochemicals is low due to their poor pharmacokinetics. There is an increasing trend, an imperative for *in vitro* testing and *in silico* prediction before *in vivo* and clinical stages in drug discovery. Therefore, determining the ADMET profile of phytocompounds also provides a preliminary idea for determining their usability as drug substance or raw material. In this study, we investigated computationally the drug candidate

potential of phytochemicals and heavy metals analyzed in some *Achillea* species, using physicochemical and pharmacokinetic approaches.

According to the ADME/Tox profile, caffeic acid, salicylic acid, 8-hydroxy-salvigenin, naringenin, and apigenin are easily absorbable; luteolin, dicaffeoylquinic acid, apigenin, luteolin-7-glucoside, orientin, vitexin, isorhamnetin-3-O-glucoside, apigenin 6,8-di-c-glucoside, and axillarin are dispersible; caffeic acid and dicaffeoylquinic metabolized and excreted and almost all compounds (excluding quercetin, rutin, caffeic and chlorogenic acid) were found to be non-toxic. Therefore, this study reveals that the plants examined have reliable ADME properties in terms of phenolic compounds and trace metals they contain.

ACKNOWLEDGEMENTS

Thanks to Dr. Ismail Senkardes, Dr. Ahmet Dogan, and Dr. Turan Arabaci, who identified the plants.

COMPLIANCE WITH ETHICS REQUIREMENTS

Conflict of Interest: No conflict of interest exists in the submission of this manuscript, and all authors approve the manuscript for publication. This work described was an original research that has not been published previously and not under consideration for publication elsewhere, in whole or in part. All the authors listed have approved the manuscript that is submitted. Duygu Taşkın, Talip Şahin, Mücahit Özdemir, and Bahattin Yalçın have no conflict of interest.

Ethical Approval: This article does not contain any studies with human or animal subjects.

REFERENCES

- 1 Turkmengolu FP, Agar OT, Akaydin G, Hayran M, Demirci B. Characterization of volatile compounds of eleven *Achillea* species from Turkey and biological activities of essential oil and methanol extract of *A. hamzaoglu* Arabacı & Budak. *Molecules*. 2015;20(6):1432-58.
- 2 Karabay-Yavasoglu NU, Karamenderes C, Baykan S, Apaydin S. Antinociceptive and anti-inflammatory activities and acute toxicity of *Achillea nobilis* subsp. *neilreichii* extract in mice and rats. *Pharmaceutical Biology*. 2007;45(2):162-8.
- 3 Azaz AD, Arabacı T, Sangun MK, Yıldız B. Composition and the in vitro antimicrobial activities of the essential oils of *Achillea wilhelmsii* C. Koch. and *Achillea lycanica* Boiss. & Heldr. *Asian Journal of Chemistry*. 2008;20(2):1238-44.
- 4 Behçet L, Arık M. An ethnobotanical investigation in east Anatolia (Turkey). *Turkish Journal of Agricultural and Natural Sciences*. 2013;2(1):1-89.
- 5 Bulut G, Biçer M, Tuzlacı E. The folk medicinal plants of Yüksekova (Hakkari- Turkey). *Journal of Faculty of Pharmacy of Istanbul University*. 2016;46(2):115-24.
- 6 Abugassa IO, Bashir AT, Doubali K, Etwir RH, Abu-Enawel M, Abugassa SO. Characterization of trace elements in medicinal herbs by instrumental neutron activation analysis. *Journal of Radioanalytical and Nuclear Chemistry*. 2008;278(3):559-63.
- 7 Karadas C, Kara D. Chemometric approach to evaluate trace metal concentrations in some spices and herbs. *Food Chemistry*. 2012;130(1):196-202.
- 8 Tokalioglu S. Determination of trace elements in commonly consumed medicinal herbs by ICP-MS and multivariate analysis. *Food Chemistry*. 2012;134(4):2504-8.
- 9 Klaric DA, Klaric I, Mornar A, Velic D, Velic N. Blackberry wines mineral and heavy metal content determination after dry ashing: multivariate data analysis as a tool for fruit wine quality control. *International Journal of Food Sciences and Nutrition*. 2016;67(5):514-23.
- 10 Basgel S, Erdemoglu SB. Determination of mineral and trace elements in some medicinal herbs and their infusions consumed in Turkey. *Science of The Total Environment*. 2006;359(1-3):82-9.
- 11 AL-Oud SS. Heavy metal contents in tea and herb leaves. *Pakistan Journal of Biological Sciences*. 2003;6(3):208-12.
- 12 Nookabkaew S, Rangkadilok N, Satayavivad J. Determination of trace elements in herbal tea products and their infusions consumed in Thailand. *Journal of Agricultural and Food Chemistry*. 2006;54(18):6939-44.
- 13 Bora T, Aksoy C, Tunay Z, Aydın F. Determination of trace elements in illicit spice samples by using ICP-MS. *Microchemical Journal*. 2015;123:179-84.
- 14 Pires DEV, Blundell TL, Ascher DB. pkCSM: predicting small-molecule pharmacokinetic and toxicity properties using graph-based signatures. *Journal of Medicinal Chemistry*. 2015;58(9):4066-72.
- 15 Ellman GL, Courtney KD, Andress V, Featherstone RM. A new and rapid colorimetric determination of acetylcholinesterase activity. *Biochemical Pharmacology*. 1961;7(2):88-95.

- 16 Patlewicz G, Jeliaskova N, Safford RJ, Worth AP, Aleksiev B. An evaluation of the implementation of the Cramer classification scheme in the Toxtree software. SAR and QSAR in Environmental Research. 2008;19(5-6):495-524.
- 17 Taşkın T, Taşkın D, Rayaman E, Dikpınar T, Selçuk SS, Arabacı T. Characterization of the Biological Activity and Phenolics in *Achillea lycanica*. Analytical Letters. 2018;51(1-2):33-48.
- 18 Taşkın D, Taşkın T, Rayaman E. Phenolic composition and biological properties of *Achillea nobilis* L. subsp. *neireichii* (Kerner) Formanek. Industrial Crops & Products. 2018; 11: 555-62.
- 19 Taşkın T, Balkan IE, Taşkın D, Dogan A. Characterization of Phenolic Constituents and Pharmacological Activity of *Achillea vermicularis*. Indian Journal of Pharmaceutical Sciences. 2019;81(2):293-301.
- 20 Yener I. Trace Element Analysis in Some Plants Species by Inductively Coupled Plasma Optical Emission Spectrometry (ICP-OES). Journal of the Institute of Science and Technology. 2019;9(3):1492-502.
- 21 Abou-Arab AAK, Abou-Donia MA. Heavy metals in Egyptian spices and medicinal plants and the effect of processing on their levels Journal of Agricultural and Food Chemistry. 2000;48(6):2300-4.
- 22 Ebrahim AM, Eltayeb MH, Khalid H, Mohamed H, Abdalla W, Grill P, Michalke B. Study on selected trace elements and heavy metals in some popular medicinal plants from Sudan. Journal of Natural Medicines. 2012;66:671-9.
- 23 Khan SA, Khan L, Hussain I, Marwat KB, Akhtar N. Profile Of Heavy Metals In Selected Medicinal Plants. Pakistan Journal of Weed Science Research. 2008;14(1-2):101-10.
- 24 Karahan F, Ozyigit II, Saracoglu IA, Yalcin IE, Hocaoglu-Ozyigit A, Ilcim A. Heavy Metal Levels and Mineral Nutrient Status in Different Parts of Various Medicinal Plants Collected from Eastern Mediterranean Region of Turkey. Biological Trace Element Research. 2020;197:316-29.
- 25 Baye H, Hymete A. Levels of Heavy Metals in Common Medicinal Plants Collected from Environmentally Different Sites. Middle-East Journal of Scientific Research. 2013;13 (7):938-43.
- 26 Sarma H, Deka S, Deka H, Saikia RR. Accumulation of Heavy Metals in Selected Medicinal Plants. Reviews of Environmental Contamination and Toxicology. 2011;214:63-86.
- 27 WHO. WHO Guidelines for Assessing Quality of Herbal Medicines with Reference to Contaminants and Residues. World Health Organization, Geneva, Switzerland, 2006.
- 28 Dghaim R, Khatib SA, Rasool H, Khan MA. Determination of Heavy Metals Concentration in Traditional Herbs Commonly Consumed in the United Arab Emirates. Journal of Environmental and Public Health. 2015;2015(4):1-6.
- 29 Zamir R, Hosen A, Ullah MO, Nahar N. Microbial and Heavy Metal Contaminant of Antidiabetic Herbal Preparations Formulated in Bangladesh. Journal of Evidence-Based Complementary and Alternative Medicine. 2015;2015(3).1-9.
- 30 Singh NM, Singh NR. A Quantitative Analysis of Heavy Metals in Vegetables Grown At Kakching-Wabagai Area, Thoubal District Manipur. Indian Journal Of Research. 2014;3(6).1-3.
- 31 Hayta Ş, Avcil N. Bitlis Katı Atık Tesisi Çevresindeki *Hypericum scabrum* L., *Achillea vermicularis* Trin, *Anchusa azurea* Miller var. *azurea* Gard. Dict. Bitkilerinin Ağır Metal İçeriklerinin Belirlenmesi. Bitlis Eren University Journal of Science and Technology. 2019;8(4):1533-44. (In Turkish)
- 32 Shir Khanloo H, Mirzahassemi SAH, Shir Khanloo N, Moussavi-Najarkola SA, Farahani H. The evaluation and determination of heavy metals pollution in edible vegetables, water and soil in the south of Tehran province by GIS. Archives of Environmental Protection. 2015;41(2):64-74.
- 33 Grabowski T, Jaroszewski JJ. Bioavailability of veterinary drugs in vivo and in silico. Journal of Veterinary Pharmacology and Therapeutics. 2009; 32: 249-57.



Corrosion Inhibitive Potentials Of (E)-5-((4-Benzoylphenyl)Diazenyl)-2-Hydroxybenzoic Acid On Mild Steel Surface In 0.5 M HCl- Experimental and DFT Calculations

Justinah Solayide Amoko^{1,2,4}  , Olawale Folorunso Akinyele³  ,
Oluwatoba Emmanuel Oyeyeyin^{1,4*}  , and Samson Dare Olayanju³  

¹Department of Chemical Sciences, Adekunle Ajasin University, Akungba-Akoko, Ondo State, Nigeria.

²Department of Chemistry, Adeyemi College of Education, Ondo, Ondo State, Nigeria.

³Department of Chemistry, Obafemi Awolowo University, Ile-Ife, Nigeria.

⁴Theoretical and Computational Chemistry Unit, Department of Chemical Sciences, Adekunle Ajasin University, Akungba-Akoko, Ondo State, Nigeria.

Abstract: One of the ways of reducing metal corrosion and its devastating effects is by using organic corrosion inhibitors. This is because of the π -conjugation in their moieties, their ability to donate electrons to the metal's vacant d -orbitals, and their low lying LUMO orbitals for accepting electrons as well from the metal, all these improve their adsorption on the metal surface. (E)-5-((4-benzoylphenyl)diazenyl)-2-hydroxybenzoic acid (AD4) was synthesized via the coupling reaction of *p*-aminobenzophenone and Salicylic acid, characterized via FTIR, UV/Vis, ¹H-NMR, and ¹³C-NMR spectroscopy. The melting point of AD4 is 103 °C–106 °C indicating that it is thermally stable and pure. Gravimetric and potentiodynamic polarization techniques were employed to obtain the corrosion rates (C_r) and percentage inhibition efficiency (%IE) at different concentrations of the inhibitor and at different temperatures. The thermodynamic parameters like Enthalpy, ΔH°_{ads} , Entropy, ΔS°_{ads} and free energy of adsorption (ΔG°_{ads}) of Adsorption were calculated. The Langmuir adsorption isotherm was used to describe the adsorption of AD4 molecules on mild steel. Quantum mechanical calculations were employed to calculate the electronic properties and global reactivity descriptors of AD4. The theoretical results are broadly consistent with experimental results. From the results obtained AD4 could be used as a corrosion inhibition agent in the oil and gas industries.

Keywords: Corrosion; Corrosion inhibitors; Adsorption isotherm; Density functional theory; (E)-5-((4-benzoylphenyl)diazenyl)-2-hydroxybenzoic acid

Submitted: November 05, 2020. **Accepted:** January 17, 2021.

Cite this: Amoko JS, Akinyele OF, Oyeyeyin OE, Olayanju SD. Corrosion Inhibitive Potentials Of (E)-5-((4-Benzoylphenyl)Diazenyl)-2-Hydroxybenzoic Acid On Mild Steel Surface In 0.5 M HCl- Experimental and DFT Calculations. JOTCSA. 2021;8(1):343-62.

DOI: <https://doi.org/10.18596/jotcsa.821488>.

***Corresponding author:** emmanueltooba90@gmail.com.

INTRODUCTION

Metals corrode when they come in contact with their environment like those that happen when metal parts come in contact with acids used in acid pickling and descaling (1) in the industries. Loss of lives and properties, increased the cost of production while replacing or repairing damaged parts and reduction in the duration of equipment amongst others are some of the dangers posed by

corrosion of metals (2). Also, metallic parts of household equipment like burglary proof, office equipment like tables and chairs, electronic devices, etc would last longer if protected from corrosion. Combating this menace, therefore, is very important, although it is more achievable to reduce it than to total removal. Corrosion occurs when the surface of metals are being attacked by a series of chemical reactions like the formation of oxides (3). Corrosion inhibitors have been employed over the

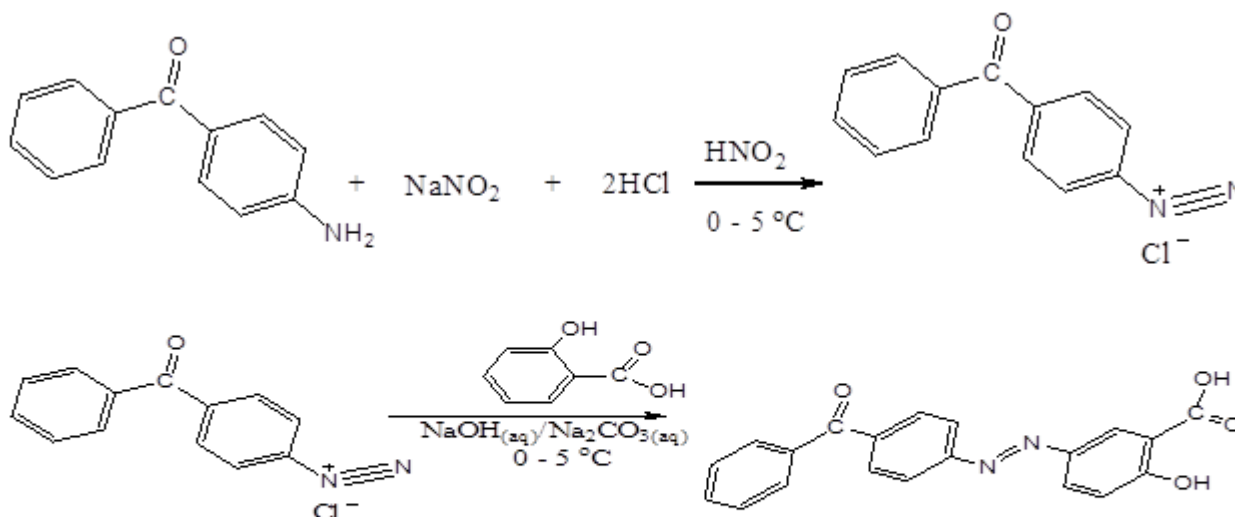
past few decades and in recent times to achieve this (4), (5), (6). Heteroatomic organic inhibitors are used because they are usually extensively conjugated, the lone pairs of electrons on the heteroatomic O, N, and S present in their moieties make available electrons to the metal's vacant *d*-orbitals (7), (8), (9). These inhibitors are adsorbed and as such serve as a protective shield on the surface of the metals, with polar functional groups acting as the reaction centers (10). These organic inhibitors, including azo compounds, are preferred to inorganic salts because they are less toxic. (11), (12). In our previous works, the corrosion inhibitive properties of (E)-3-(2-p-tolyldiazenyl)-1-nitrosonaphthalen-2-ol (13) and (E)-4-hydroxy-3-[(2,4,6-tribromophenyl)diazenyl]benzaldehyde (5) were investigated, both were adsorbed on the surface of the metal and reduced the rates of corrosion. Quantum mechanical calculations have been employed in conjunction with experimental techniques in a bid to get clearer pictures about the mode and mechanisms of reactions and chemical processes (10), (8), (14). They have also been used as a guide to experiments, predictive tools for reactions and to obtain molecular properties of existing and hypothetical molecular entities (15), (16), (17), (18). Against this background, (E)-5-((4-

benzoylphenyl)diazenyl)-2-hydroxybenzoic acid (Scheme 1) was synthesized and characterized using the Fourier transform infrared (FTIR). Ultraviolet/visible (UV/Vis), Nuclear magnetic resonance (¹H-NMR and ¹³C-NMR) spectroscopic techniques and melting point determination. The investigation of corrosion inhibition was carried out, using gravimetric and potentiodynamic polarization techniques. The surface of the metal was characterized using scanning electron microscopy (SEM). The electronic properties and reactivity descriptors were calculated using the density functional theory (DFT) method. The results obtained were compared to experimental results.

EXPERIMENTAL

Synthesis of (E)-5-((4-benzoylphenyl)diazenyl)-2-hydroxybenzoic acid (AD4)

All reagents and solvents used are of analytical grade, purchased, and used as supplied. Compound AD4 was synthesized by *p*-aminobenzophenone and coupling it with Salicylic acid (Scheme 1), following the same procedure described for NAD (13) with the same molar ratio of the reagents to give brick red solid. Melting point 103°C-106°C, yield 41 %. Other physical properties are presented in Table 1.



Scheme 1: Synthesis of AD4.

Table 1: Physical Properties of AD4.

compound	molecular formula	molecular weight	color	melting point (°C)	%yield
AD4	C ₂₀ H ₁₄ N ₂ O ₄	346.342	Brick Red	103-106	41

Spectral Measurements

Infrared spectra

The Infrared spectra (using KBr disc) of AD4 were recorded on Shimadzu FTIR 8000 Spectrometer at the Redeemer's University, Ede, Nigeria (Supp. 1, Table 2). The IR spectrum in Figure 1 showed a band at 3435 cm⁻¹ which is attributed to ν O-H_{str}, while the band at 3061 cm⁻¹ is for ν C-H_{str} (aromatic sp²), band

at 1600 cm⁻¹ is assigned to ν C=C_{str}, band at 1448 cm⁻¹ assigned to ν N=N_{str}, band at 1678 cm⁻¹ is assigned to ν C=O_{str} and band at 1296 cm⁻¹ is assigned to ν C-O_{str}. The spectrum showed the expected functional groups especially the azo (-N=N-), aromatic -C=C-, -C=O- and the hydroxyl groups (Table 2), signifying the formation of the dye.

Table 2: Important IR Absorption Bands (cm⁻¹) of AD4.

Compound	OH str	-CH	-C=C-	-N=N-	-C=O- str	-C-O-str
AD4	3435	3061	1600	1448	1678	1296

Electronic spectra

The electronic spectra of AD4 were determined in ethanol using Shimadzu UV-Vis Spectrometer at the Central Laboratory Science, Obafemi Awolowo University, Ile-Ife, Osun State, Nigeria (Supp. 2,

Table 3). The UV/Visible spectrum (Figure 2) showed peaks at 280 nm, 325 nm, 380 nm attributed to π - π^* aromatic, π - π^* (IMCT from the entire molecule via the -N=N- group), and n- π^* (from the heteroatoms present in the molecule), respectively.

Table 3: Electronic spectra data of AD4.

Compound	λ_{max} (nm)	Assignment
AD4	280, 325, 380	π - π^* aromatic, π - π^* (IMCT) and n- π^* respectively

Nuclear Magnetic Resonance spectra

The NMR of AD4 was recorded in dimethyl sulfoxide (DMSO) *d*₆/ Bruker Avance 400 MHz using deuterated solvents and tetramethyl silane (TMS) as an internal standard at the Department of Chemistry, Friedrich-Schiller University, Jena, Germany (Supp. 3 and 4, Table 4). The Signal at 3.40 ppm for the ¹H NMR spectrum is due to hydroxyl proton, H_a of the carboxylic acid group (Figure 3 and Table 4) while the peak at 11.50 ppm is due to the proton on the free hydroxyl group, H_b. The Signals at 7.50 - 9.50 ppm are attributed to the different protons of the phenyl rings. The ¹³C NMR spectrum (Figure 4) showed signals at 118, 119, 123, 127-129, 132, 134, 136, 137, 138, 150, 161, 191, and 197 ppm corresponding to different carbons in the molecule, with 136 for carbonyl carbon and 191 for carboxylic acid carbon.

Materials and method for corrosion studies**Gravimetric method**

The coupons were weighed. The experiment was conducted in a thermostated water bath with the coupons dipped in 0.5 M HCl (100 mL) test solutions-one without the inhibitor AD4 (blank), and the others with different concentrations of AD4 (2.89 x 10⁻⁴ - 1.444 x 10⁻³ M) for 6 hours and at different temperatures (298 -338 K). The metals were recovered from the test solutions, rinsed with acetone, dried and reweighed. This experiment was done in triplicate to ensure consistency in the results obtained. Equations 1-3 were obtained from the resulting data (Table 4).

$$C_R = \frac{W_0 - W_1}{A_t} \quad (\text{Eq. 1})$$

$$\theta = 1 - \frac{C_r^I}{C_r^0} \quad (\text{Eq. 2})$$

C_R is the corrosion rate, θ , the degree of freedom and %IE, the percentage inhibition efficiency of AD4. W_0 (weight loss in the blank solution), W_1 (weight loss of mild steel with the inhibitor) in grams. A (area in cm²), t (time in hrs). C_r^I (rate of corrosion with inhibitor), and C_r^0 (rate of corrosion without inhibitor) in g cm⁻² h⁻¹.

The Langmuir adsorption isotherm (Eq. 4) was employed to describe the mode of adsorption of AD4 on the surface of the metal.

$$\frac{C}{\theta} = \left[\frac{1}{K_{ads}} \right] + C$$

With C being the concentration of AD4, K_{ads} , the equilibrium adsorption constant and θ , the extent of surface coverage. The thermodynamic parameters were also calculated to further explain the adsorption process. The standard Gibb's free energies of adsorption (ΔG_{ads}^0) were calculated in equation 5.

$$K_{ads} = \frac{1}{55} e^{\frac{-\Delta G_{ads}^0}{RT}} \quad (\text{Eq. 5})$$

ΔG_{ads}^0 are the free energy of adsorption, R being the gas constant, and 55.5, the isocratic contribution of water in the solution. The enthalpy, ΔH^0 and entropy ΔS^0 were obtained from the plots of ΔG_{ads}^0 against temperature (Equation 6).

$$\Delta G_{ads}^0 = \Delta H^0 - T \Delta S^0 \quad (\text{Eq. 6})$$

This was accompanied by the kinetic model which was used to obtain the activation energies, E_a , and the pre-exponential factors from the plot of $\ln C_R$ against $1/T$ (Figure 9) with the application of the Arrhenius equations 7 and 8, as presented in Table 5.

$$C_R = A \times e^{\frac{-E_a}{RT}} \quad (\text{Eq. 7})$$

$$\ln C_R = \ln A - \frac{E_a}{RT} \quad (\text{Eq. 8})$$

Enthalpy, ΔH^* and entropy, ΔS^* of activation values were calculated (Equation 8) and Table 6.

$$C_R = \left(\frac{RT}{Nh} \right) \exp \left(\frac{\Delta S^0}{R} \right) \exp \left(\frac{-\Delta H^0}{RT} \right) \quad (\text{Eq. 9})$$

h is the Planck's constant, N the Avogadro's number, T the absolute temperature, and R the universal gas constant.

Potentiodynamic polarization technique

This experiment was conducted as it was in (13). The %IE was calculated from the data extracted from the Tafel curves (Equation 10).

$$\%IE = \frac{I_{corr}^0 - I_{corr}}{I_{corr}^0} \times 100 \quad (\text{Eq. 10})$$

where, I_{corr}^0 and I_{corr} are the corrosion densities in the absence and presence of the inhibitor, respectively.

Surface morphology

The surface architecture of the mild steel before and after immersion in acid solution (both in the blank and inhibitor solutions) was imaged using Scanning Electron Microscope (SEM) Phenom Prox by Phenomworld Eindhoven, The Netherlands.

Quantum chemical calculations

Quantum chemical calculations were carried out with complete geometric optimization on the best conformer (obtained by the molecular mechanics' force field) using DFT with a large polar 6-31G* basis set for all atoms (19). Electronic properties such as the energies of the frontier molecular orbitals, FMOs [energies of the highest occupied molecular orbital (E_{HOMO}) and energy of the lowest unoccupied molecular orbital (E_{LUMO})], ionization potential (I) in equation 11, electron affinity (A) in equation 12, energy bandgap (E_g) in equation 13, global reactivity descriptors like chemical hardness (η) in equation 14, softness (δ) in equation 15, electronegativity (χ) in equation 16, chemical potential (C_p) in equation 17, global electrophilicity index (ω) in equation 18 and the fraction of electrons transferred (ΔN) in equation 19 were calculated, all on Spartan 14 computational chemistry software (20). The FMOs maps of AD4 were also plotted together with its electrostatic potential map.

$$I = -E_{HOMO} \quad (\text{Eq. 11})$$

$$A = -E_{LUMO} \quad (\text{Eq. 12})$$

$$E_g = E_{LUMO} - E_{HOMO} \quad (\text{Eq. 13})$$

$$\eta = \frac{\Delta E}{2} \quad (\text{Eq. 14})$$

$$\delta = \frac{1}{\eta} \quad (\text{Eq. 15})$$

$$\chi = \frac{(I+A)}{2} \quad (\text{Eq. 16})$$

$$C_p = -\chi \quad (\text{Eq. 17})$$

$$\omega = \frac{\chi^2}{E_g} \quad (\text{Eq. 18})$$

$$\Delta N = \frac{\chi_{Fe} - \chi_{inh}}{2(\eta_{Fe} + \eta_{inh})} \quad (\text{Eq. 19})$$

To account for the directions of electrons flow (predicting electrophilic and nucleophilic atoms), the Fukui parameters were calculated using a dual descriptor (defined within [-1; 1]) to determine individual sites within the molecule (7) (equations 20 and 21).

$$f_k^+ = [q_k(N+1) - q_k(N)] \quad \text{for nucleophilic attack (Eq. 20)}$$

$$f_k^- = [q_k(N) - q_k(N-1)] \quad \text{for electrophilic attack (Eq. 21)}$$

$$\Delta f_k(r) = f_k^+ - f_k^- \quad (\text{Eq. 22})$$

$q_k(N+1)$ is the charges on the atoms in the molecule's anionic ($N+1$) state, $q_k(N)$ is the charges on the atoms in the molecule's neutral (N) state and $q_k(N-1)$ is the charges on the atoms in the molecule's cationic ($N-1$) state (equations 20-22). f_k^+ and f_k^- are the nucleophilic and electrophilic Fukui functions, respectively.

RESULTS AND DISCUSSION

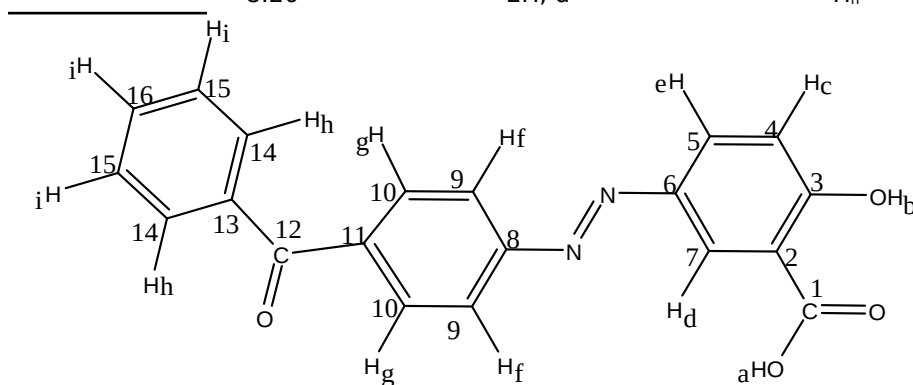
Gravimetric analysis

Variation of IE with Concentration and Temperature

The data obtained for the gravimetric experiments are recorded in Table 4. The variations of the %IE with concentration and temperature were considered. Generally, %IE increases with an increase in concentration while it decreases as the temperature increases (Table 4 and Figures 5 and 6). This is expected because as more of the inhibitor is used (increased concentration), more of its molecules are adsorbed on the metal surface thereby reducing the rate of corrosion. Also, as we move to higher temperatures, some of the inhibitor molecules are easily desorbed, thereby decreasing the inhibition efficiency. The optimum adsorption took place at 318 K where a %IE of 95 was observed, beyond this there is desorption of AD4 molecule at the metal's surface. This was also observed by previous researchers (21) and in our previous works (5). The %IE of 4,5,6,7-tetrahydro-1,3-benzothiazole was reported to be 81.53 % by Mallikarjuna and coworkers (12) while it was 80.39 % in our previous work with (E)-4-hydroxy-3-[(2,4,6-tribromophenyl)diazonyl]benzaldehyde (5).

Table 4: ^1H NMR and ^{13}C NMR spectral data of AD4 in DMSO.

Compound	^1H NMR			^{13}C NMR	
	δ ppm	Integration, Multiplicity	Assignment	δ ppm	Assignment
AD4	3.40	1H, s	H _a	118	C ₂
	11.50	1H, s	H _b	119	C ₅
	8.20	1H, d	H _e	123	C ₈
	7.80	2H, d	H _f	127 - 129	C ₃ , C ₁₄ , C ₉ , C ₁₃
	7.50	3H, m	H _i	132	C ₄
	7.70	2H, d	H _g	134	C ₁₅
	7.75	1H, s	H _d	136	C ₁₂
	9.50	1H, d	H _c	137	C ₁₀
	8.20	2H, d	H _h	138	C ₁₆
				150	C ₇
			161	C ₆	
			191	C ₁	
			197	C ₁₁	



(E)-5-((4-benzoylphenyl)diazenyl)-2-hydroxybenzoic acid (AD4), d = doublet, s = singlet, m = multiplet

Adsorption and Thermodynamic Considerations

A plot of C/θ vs C (298 - 338 K) generated the data in Table 6 and their plots (Figure 7). The adsorption obeys the Langmuir adsorption isotherm given their R^2 values. ΔG values show that the adsorption process is spontaneous (Table 6), these values are between -28 to -36 kJ/mol, indicating that the adsorption of AD4 molecules on the mild steel is through physisorption. The value of ΔS obtained (-0.101 kJ/mol) showed the molecules or AD4 are not as free to move as they are being trapped on the surface of the metal. The positive value of ΔH_{ads}^0 obtained indicated an endothermic reaction. ΔH_{ads}^0 around -40 kJ/mol⁻¹ is a physisorption process while it is a chemisorption process when it tends to -100 kJ/mol⁻¹. The adsorption of AD4 a physisorption process ($\Delta H_{\text{ads}}^0 = 0.14$ kJ/mol⁻¹).

Values of apparent activation energies may increase in the presence of AD4 than that of a pure acidic medium, if it is so like it is in this work, it implies that the AD4 is absorbed physically (physisorption) (22). The larger values of A in the presence of AD4 compared to that of the blank solution (Table 7) implied that most of the active sites are blocked by AD4.

The larger ΔH^* and ΔS^* values in the presence of AD4 (Table 8) is a consequence of the increase in energy barrier of the corrosion process in the presence of AD4 as also seen from the activation energies, E_a . The interaction of AD4 and mild steel is endothermic in nature, owing to the positive ΔH^* values in the blank and in the presence of AD4 while the negative ΔS^* values implied that there is the formation of the activated complex in the rate-determining step which is dissociative, hence an observable increase in disorderliness (23).

Table 5: Parameters obtained from gravimetric analysis.

Compound	Temp. (K)	Concentration (M)	Weight loss (g)	Corrosion rate($\text{gcm}^{-2}\text{h}^{-1}$)	%IE	Θ
AD4	298	Blank	0.041	0.00213	-	-
		0.000289	0.0180	0.0011	50	0.4947
		0.000577	0.0150	0.0008	64	0.6371
		0.000866	0.0120	0.0007	68	0.6746
		0.001155	0.0110	0.0007	69	0.6871
		0.001444	0.0090	0.0005	78	0.7765
	308	Blank	0.036	0.00209	-	-
		0.000289	0.0250	0.0015	29	0.2887
		0.000577	0.0210	0.0013	39	0.3901
		0.000866	0.0160	0.0008	60	0.5978
		0.001155	0.0120	0.0007	65	0.6515
		0.001444	0.0118	0.0007	67	0.6701
	318	Blank	0.048	0.00253	-	-
		0.000289	0.0230	0.0012	52	0.5241
		0.000577	0.0100	0.0006	78	0.7791
		0.000866	0.0090	0.0005	80	0.7967
		0.001155	0.0080	0.0005	81	0.8046
		0.001444	0.0020	0.0001	95	0.9540
	328	Blank	0.061	0.00312	-	-
		0.000289	0.0370	0.0022	29	0.2869
		0.000577	0.0370	0.0019	38	0.3751
		0.000866	0.0210	0.0013	59	0.5909
		0.001155	0.0160	0.001	69	0.6850
		0.001444	0.0140	0.0008	74	0.7494
	338	Blank	0.15	0.00912	-	-
		0.000289	0.0310	0.0016	83	0.4887
		0.000577	0.0220	0.0013	85	0.5731
		0.000866	0.0200	0.0012	87	0.6080
0.001155		0.0240	0.0013	86	0.5923	
0.001444		0.0200	0.0012	87	0.6168	

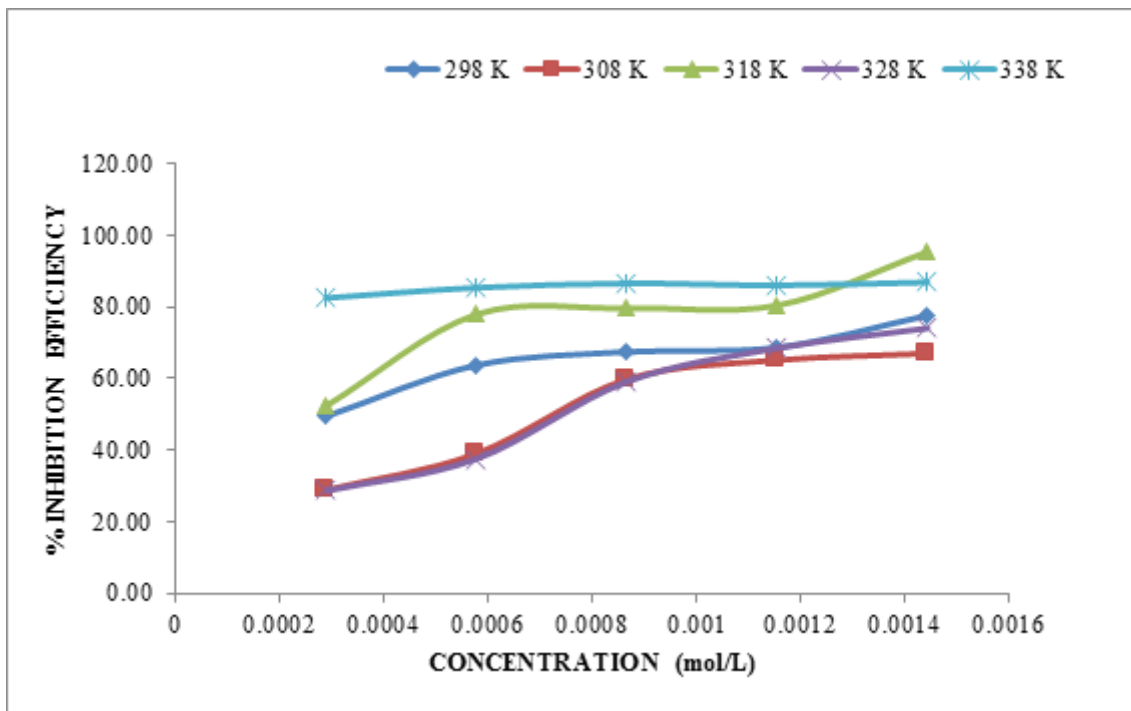


Figure 5: Variation of IE of AD4 with concentration.

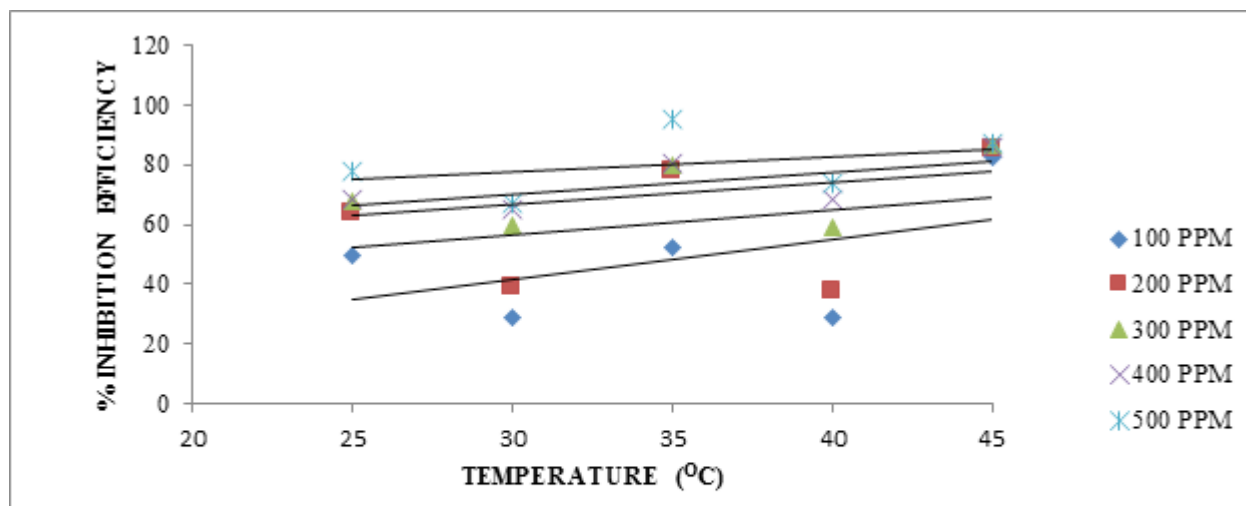


Figure 6: Variation of IE of AD4 with temperature.

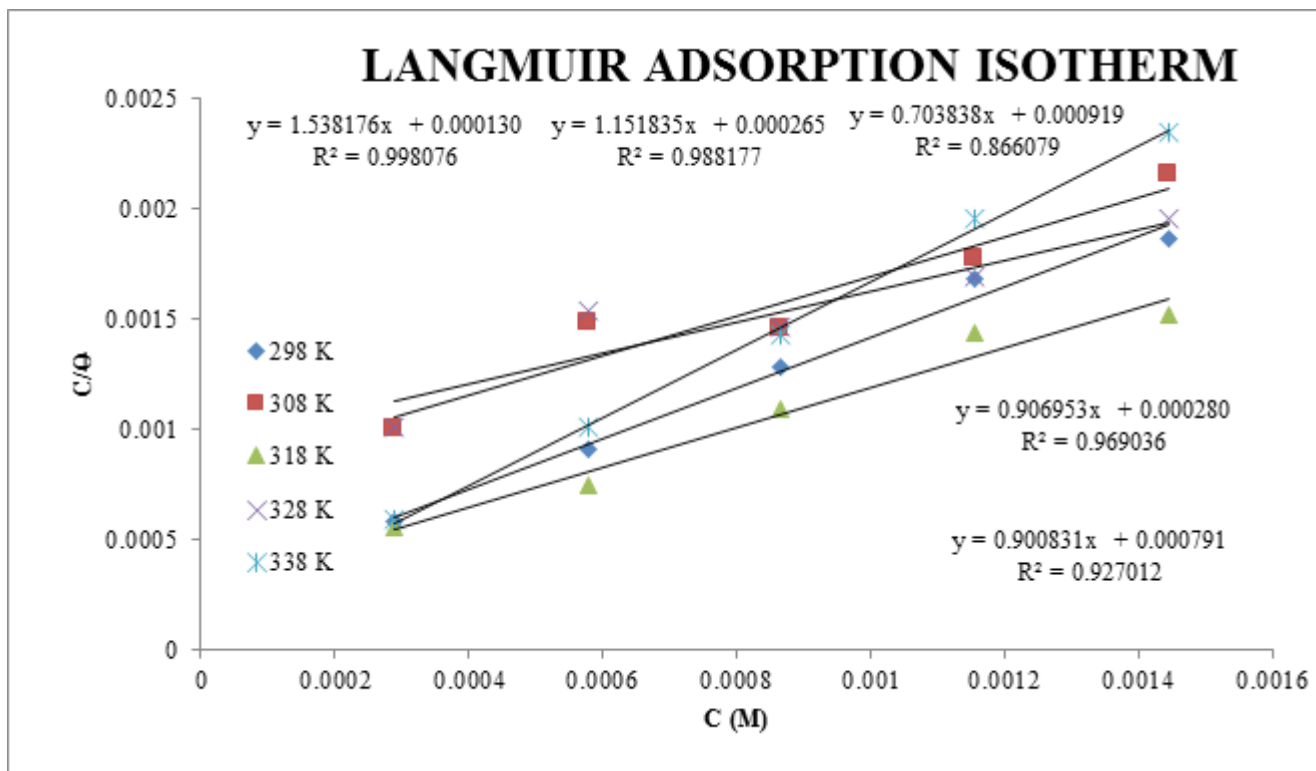


Figure 7: Langmuir isotherm for AD4 adsorption.

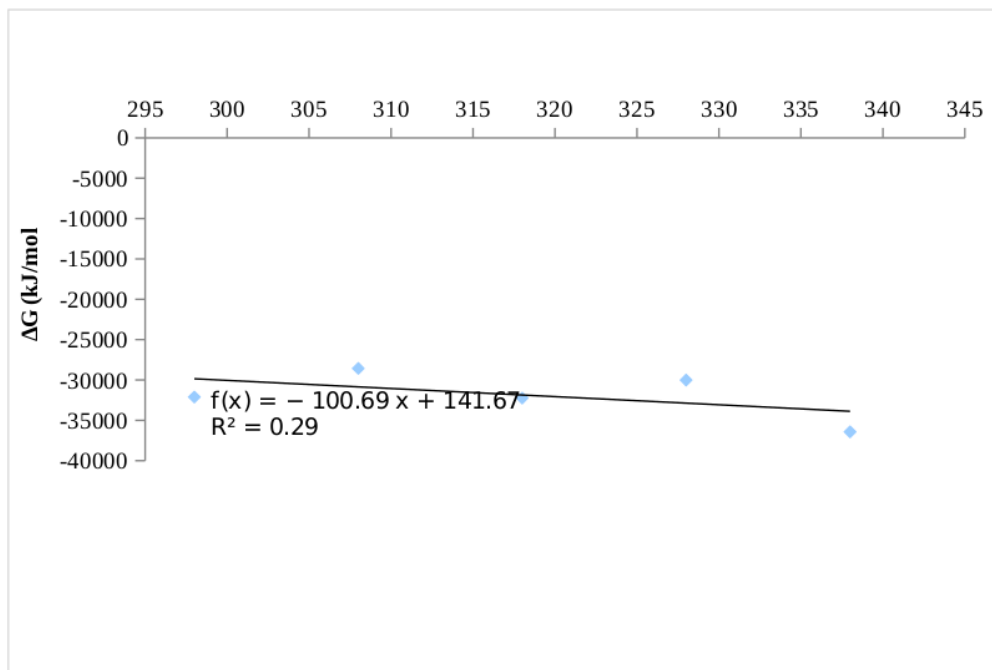


Figure 8: Determination of ΔH°_{ads} and ΔS°_{ads} , of AD4.

Table 6: Thermodynamic parameters of AD4.

Comp.	Temp. (K)	R ²	Intercept	K	ΔG (kJmol ⁻¹)	ΔS(kJ/mol ⁻¹ K ⁻¹)	ΔH (kJmol ⁻¹)
AD4	298	0.9981	0.00013	7692.31	-32.120	-0.10069	0.14167
	308	0.927	0.000791	1264.22	-28.578		
	318	0.969	0.00028	3571.43	-32.247		
	328	0.8661	0.000919	1088.14	-30.020		
	338	0.9981	0.00013	7695.31	-36.432		

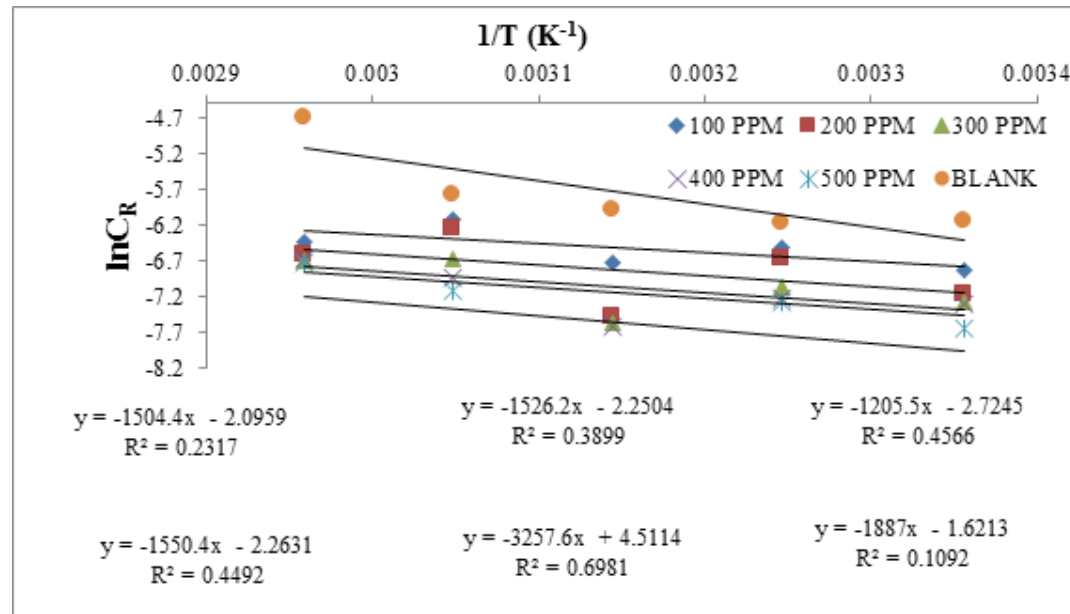


Figure 9: Activation energy plot.

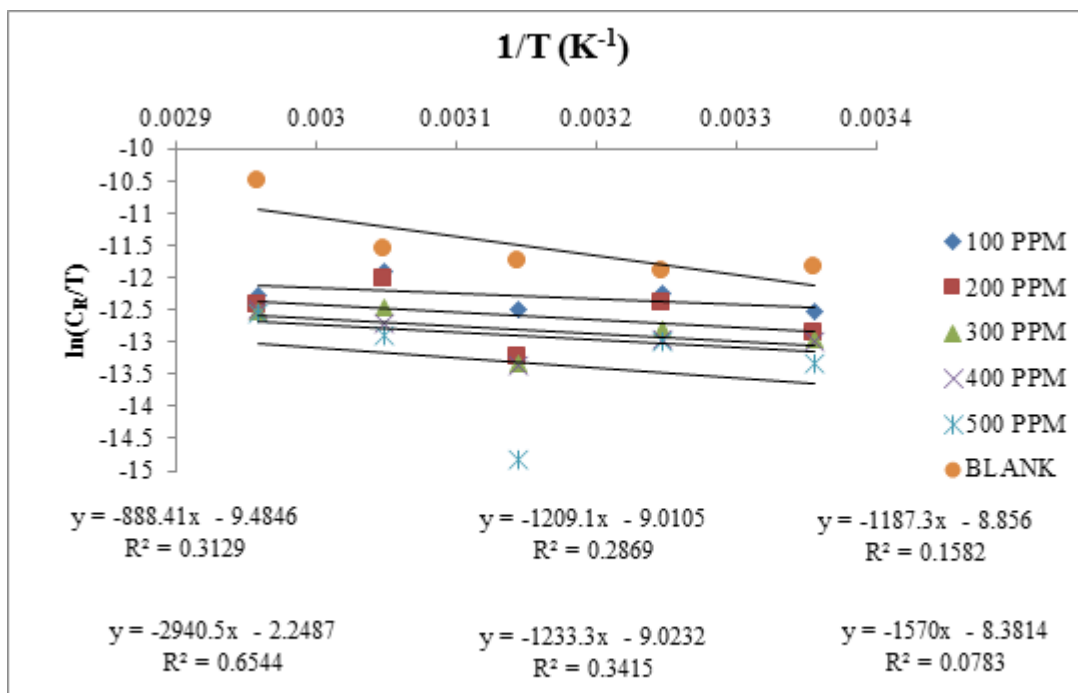


Figure 10: Transition state determination.

Table 7: Activation energy and pre-exponential factor for the process .

Compound	Concentration(M)	Slope	Ea (Jmol ⁻¹)	In A	A
AD4	BLANK	-3257.6	27078.69	4.5114	91.05
	0.000289	-1205.5	10022.53	2.7245	0.656
	0.000577	-1504.4	12507.58	2.0959	0.1230
	0.000866	-1526.2	12688.83	2.2504	0.1054
	0.000116	-1550.4	12890.03	2.2631	0.1040
	0.000144	-1887.0	15688.52	1.6213	0.1976

Table 8: Values for the transition state parameters

Compound	Concentration (M)	Slope	Intercept	Enthalpy(Jmol ⁻¹)	Entropy(Jmol ⁻¹ K ⁻¹)
AD4	BLANK	-2940.5	-2.2487	24447.4	-216.236
	0.000029	-888.41	-9.4846	7386.241	-276.395
	0.000058	-1187.3	-8.856	9871.212	-271.169
	0.000087	-1209.1	-9.0105	10052.457	-272.453
	0.000116	-1233.3	-9.0232	10253.656	-272.559
	0.000145	-1570	-8.3814	13052.980	-267.223

Tafel plots

AD4 is a mixed-type inhibitor (Fig. 11), that is, it is both cathodic and anodic. The corrosion rate decreases as AD4 concentration increases (Table 9),

this is because more of the AD4 molecules covers more surface of the mild steel concentration increases from 0.015 g to 0.075 g.

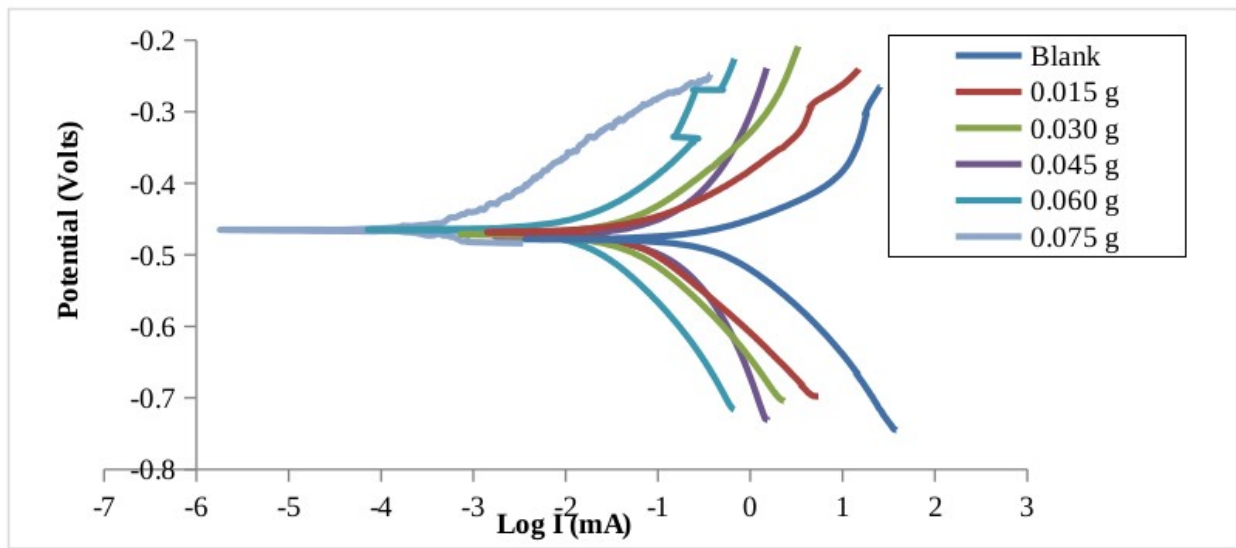


Figure 11: Potentiodynamic polarization curve for AD4 adsorption.

Surface analysis

The unused mild steel (Figure 11a) showed little or no scratch on its surface, however, Figure 11b (mild steel immersed in 0.5 M HCl for six hours) showed an aggressive attack by the acid. Figure 11c (mild

steel in the presence of the inhibitor and acid) is not as smooth as in Figure 11a but smoother than 11b, this is a consequence of the action of the inhibitor molecule on the surface of the mild steel.

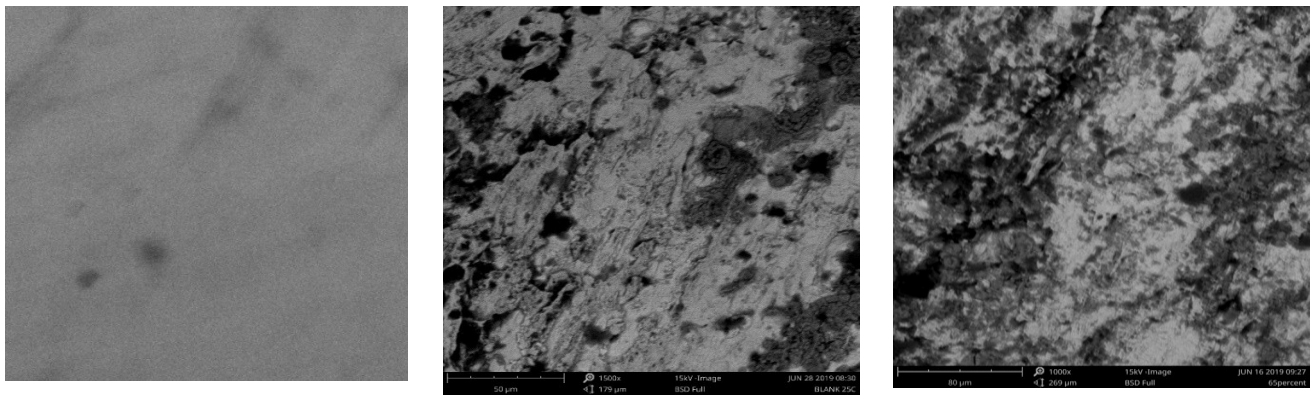


Figure 12: (a) SEM image of polished mild steel (b) SEM image of mild steel exposed to 0.5M HCl (c) SEM image of mild steel in the presence of AD4 molecule.

Table 9: Polarization Parameters and Inhibition Efficiencies of AD4 on Mild Steel.

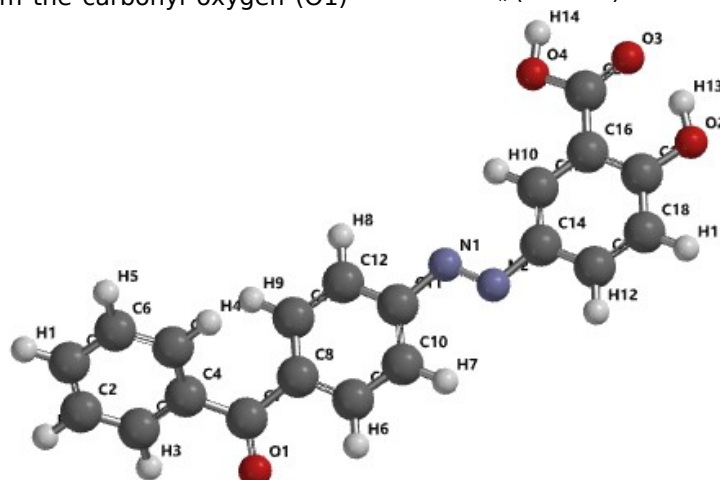
	Conc. (g)	$-\beta_c$ (mV)	β_a (mVdec ⁻¹)	C_R mpy	$-E_{corr}$ (mV)	I_{corr} (μ mA)	%IE
AD4	Blank	143.5	107.7	7.51724	478.624	740.062	-
	0.015	126.3	130.2	1.41638	501.093	139.441	81
	0.030	141.7	121.3	1.33159	471.568	131.093	82
	0.045	189	171.8	1.14625	474.886	112.847	85
	0.060	159.9	152.4	0.237362	465.244	23.368	96
	0.075	34.6	71.7	0.002936	464.899	0.289	99.9

b_c & b_a = Tafel slopes, $C_R = b_c$ & b_a = Tafel slopes, C_R = corrosion rate, E_{corr} = corrosion potential, I_{corr} = corrosion current density, IE = inhibition efficiency

Quantum mechanical analysis

HOMO, LUMO, and E_g values of AD4 are presented in Table 10. The low E_g value of AD4 suggests that electrons are easily transferred from the compound to the metal surface while the high E_{HOMO} value and low-lying LUMO orbitals indicate that the molecule accepts electrons readily from, while at the same time, donate electrons to the metal's d orbitals, this shows that the mechanism of adsorption here is of electron donation and back-donation as supported by the values of other descriptors calculated. Softness value for example shows that AD4 would react readily with the metal, as also supported by the values of χ , ω , and μ . The high inhibition efficiency is associated with the electron-donating ability, evidenced by the ΔN value which is ≈ 3.6 (24), (25). The HOMO plot of AD4 (Fig. 12b) shows that the orbitals with abundant electron spread across the molecule from the carbonyl oxygen (O1)

to the other part of the molecule, and all the heteroatoms in the process, save for the hydroxyl oxygen on the carboxylic acid group, this shows the part of the molecule donating electrons to the metal, the LUMO (Fig. 12c) orbitals spread over almost the same region as it was in the HOMO map. This confirms that there is an intramolecular charge transfer (ICT) in the molecule. The donor-acceptor (D-A) charge distribution on the electrostatic potential map (Fig. 12d) confirms the charge transfer. These further support the good inhibitory property of AD4. From Table 11, atoms having $f_k > 0$ are electrophilic while those with $f_k < 0$ are the nucleophiles. C14 is the preferred site for the nucleophilic attack as its maximum value of f_k^+ is 0.036 and positive value of Δf (0.048) while C5 is the preferred site for electrophilic attack as it has a maximum value of f_k^- (0.002) and the negative value of f_k (-0.005).

**Figure 12a:** Optimized structure of AD4.

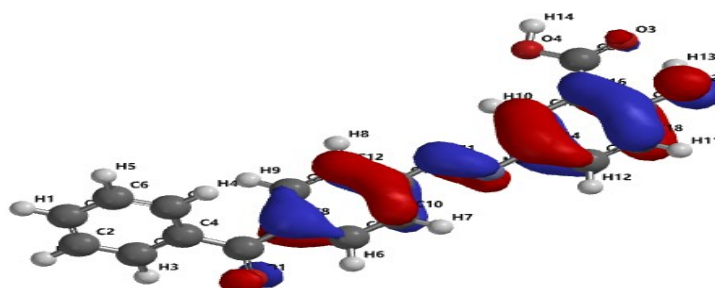


Figure 12b: HOMO map of AD4

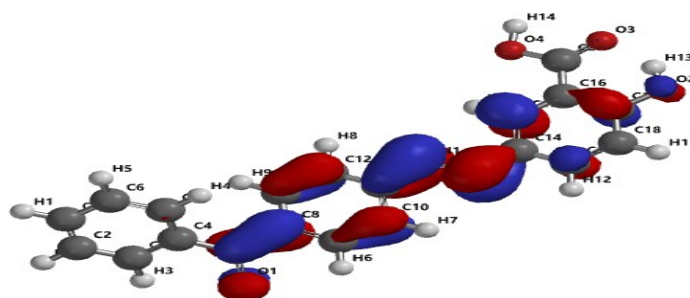


Figure 12c: LUMO map of AD4.

Table 10: Quantum chemical parameters for AD4 dye.

Parameters	E_{HOMO} (eV)	E_{LUMO} (eV)	A (eV)	I (eV)	ΔE (eV)	η (eV)	δ (eV ⁻¹)	χ (eV)	ω (eV)	μ (eV)	ΔN
AD4	-6.12	-2.58	2.58	6.12	3.54	1.77	0.56	4.35	5.35	3.64	0.75

Table 11: Fukui functions and Mulliken atomic charges of AD4 atoms (excluding hydrogen atoms).

AD4	$q_k(N+1)$	$q_k(N)$	$q_k(N-1)$	f_k^+	f_k^-	Δf
C1	-0.13	-0.119	-0.112	-0.011	-0.007	-0.004
C2	-0.138	-0.135	-0.132	-0.003	-0.003	0
C3	-0.156	-0.151	-0.145	-0.005	-0.006	0.001
C4	0.086	0.072	0.072	0.014	0	0.014
C5	-0.18	-0.177	-0.179	-0.003	0.002	-0.005
C6	-0.14	-0.137	-0.134	-0.003	-0.003	0
C7	0.279	0.32	0.331	-0.041	-0.011	-0.03
C8	0.071	0.082	0.088	-0.011	-0.006	-0.005
O1	-0.545	-0.463	-0.428	-0.082	-0.035	-0.047
C9	-0.204	-0.171	-0.168	-0.033	-0.003	-0.03
C10	-0.166	-0.129	-0.121	-0.037	-0.008	-0.029
C11	0.301	0.284	0.282	0.017	0.002	0.015
C12	-0.156	-0.151	-0.116	-0.005	-0.035	0.03
C13	-0.179	-0.187	-0.15	0.008	-0.037	0.045
N1	-0.408	-0.317	-0.225	-0.091	-0.092	0.001
N2	-0.416	-0.31	-0.219	-0.106	-0.091	-0.015
C14	0.304	0.268	0.28	0.036	-0.012	0.048
C15	-0.227	-0.178	-0.153	-0.049	-0.025	-0.024
C16	0.03	0.013	0.012	0.017	0.001	0.016
C17	0.287	0.324	0.355	-0.037	-0.031	-0.006
C18	-0.177	-0.172	-0.157	-0.005	-0.015	0.01
C19	-0.146	-0.13	-0.11	-0.016	-0.02	0.004
C20	0.555	0.585	0.624	-0.03	-0.039	0.009
O2	-0.676	-0.636	-0.572	-0.04	-0.064	0.024
O3	-0.566	-0.532	-0.498	-0.034	-0.034	1.110E-16
O4	-0.573	-0.569	-0.559	-0.004	-0.01	0.006

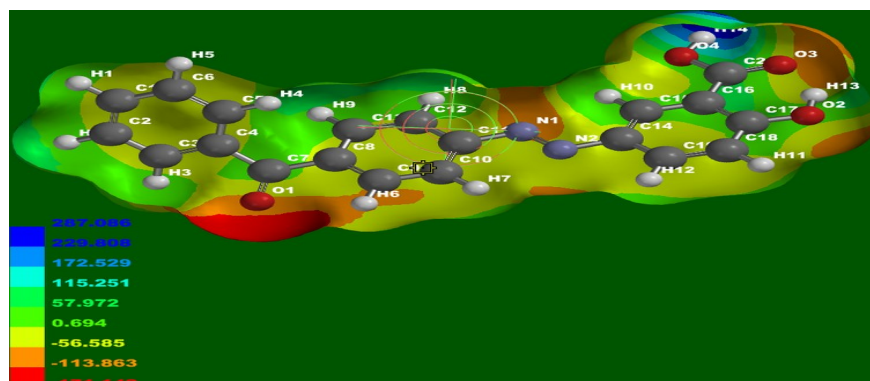


Figure 12d: Electrostatic potential map of AD4.

CONCLUSIONS

The corrosion inhibitive potential of (E)-5-((4-benzoylphenyl)diazenyl)-2-hydroxybenzoic acid (AD4) on mild steel in acidic medium was investigated. The inhibition efficiency increases with increased concentration of AD4 but decreases with increase in temperature. The inhibition is a spontaneous process that obeyed Langmuir isotherm. The result from the Tafel plot proved that the inhibitor is a mixed type inhibitor (cathodic and anodic inhibitor). From the calculated thermodynamic and kinetic parameters, AD4 adsorption followed the physisorption mechanism. The results obtained from quantum chemical calculations agreed with the experiments. AD4 could be used in the oil, gas, and steel industry as anti-corrosive agent.

ACKNOWLEDGMENT

We would like to thank Adeyemi College of Education and Adekunle Ajasin University for creating enabling environments for this research work.

REFERENCES

1. Society AE and SF. Proceedings AESF SUR/FIN 2002: Annual International Technical Conference. In: Proceedings AESF SUR/FIN 2002: Annual International Technical Conference. 2002.
2. Verma C, Quraishi MA, Ebenso EE. Microwave and ultrasound irradiations for the synthesis of environmentally sustainable corrosion inhibitors: An overview. *Sustain Chem Pharm* [Internet]. 2018;10:134-47. Available from: <https://doi.org/10.1016/j.scp.2018.11.001>
3. Jadhav N, Kasisomayajula S, Gelling VJ. Polypyrrole/Metal Oxides-Based Composites/Nanocomposites for Corrosion Protection. *Front Mater*. 2020;7:1-7.
4. Albrakaty RH, Wazzan NA, Obot IB. Theoretical Study of the Mechanism of Corrosion Inhibition of Carbon Steel in Acidic Solution by 2-aminobenzothiazole and 2-Mercatobenzothiazole. *Int J Electrochem Sci*. 2018;13:3535-54.
5. Amoko SJ, Akinyele OF, Oyenehin OE, Olayanju DS, Aboluwoye CO. Experimental and theoretical investigation of corrosion inhibitive potentials of (E)-4-hydroxy-3-[(2,4,6-tribromophenyl)diazenyl] benzaldehyde on mild steel in acidic media. *Phys Chem Res*. 2020 Jun 1;8(3):399-416.
6. Fouda AS, Abdallah M, Eissa M. Corrosion inhibition of Aluminum in 1 M phosphoric acid solutions using some Chalcones derivatives and synergistic action with halide ions. *African J Pure Appl Chem*. 2013;7(12):394-404.
7. Yao N, Diki S, Gondo G, Diomandé D, Akpa SJ, Ouédraogo A. Aluminum Corrosion Inhibition by 7-(Ethylthiobenzimidazolyl) Theophylline in 1M Hydrochloric Acid: Experimental and DFT Studies. *Int J Appl Pharm Sci Res*. 2018;3(4):41-53.
8. Oyenehin OE, Obadawo BS, Ojo FK, Akerele DD, Akintemi EO, Ejelonu BC, et al. Experimental and Theoretical Study on the Corrosion Inhibitive Potentials of Schiff Base of Aniline and Salicylaldehyde on mild steel in 0.5M HCl. *Adv J Chem B* [Internet]. 2020;2(4):197-208. Available from: <http://www.ajchem-b.com/>
9. Ogunyemi BT, Latona DF, Adejoro IA. Molecular modeling and quantitative structure - property relationships (QSPRs) of purine derivatives as corrosion inhibitor in acid medium. *Sci African* [Internet]. 2020;8:e00336. Available from: <https://doi.org/10.1016/j.sciaf.2020.e00336>
10. Nwankwo HU, Olasunkanmi LO, Ebenso EE. Electrochemical and Computational Studies of Some Carbazole Derivatives as Inhibitors of Mild Steel Corrosion in Abiotic and Biotic Environments. *J Bio-Tribo-Corrosion* [Internet]. 2018;4(13):1-17.

Available from: <https://doi.org/10.1007/s40735-018-0130-7>

11. Abboud Y, Abourriche A, Saffaj T, Berrada M, Charrouf M, Bennamara A, et al. A novel azo dye, 8-quinolinol-5-azoantipyrine as corrosion inhibitor for mild steel in acidic media. Desalination [Internet]. 2009;237(1-3):175-89. Available from: <http://dx.doi.org/10.1016/j.desal.2007.12.031>

12. Mallikarjuna NM, Keshavayya J, Prasanna BM, Praveen BM, Tandon HC. Synthesis, Characterization, and Anti-corrosion Behavior of Novel Mono Azo Dyes Derived from 4,5,6,7-Tetrahydro-1,3-benzothiazole for Mild Steel in Acid Solution. J Bio-Tribo-Corrosion [Internet]. 2020;6(1):1-17. Available from: <https://doi.org/10.1007/s40735-019-0306-9>

13. Amoko SJ, Akinyele OF, Oyenehin OE, Olayanju DS, Aboluwoye CO. Synthesis , characterization and computational studies on the corrosion inhibitive potentials of (e) -3- (2-p-tolyldiazenyl) -1-nitrosophthalen-2-ol. Leonardo J Sci. 2018; (33):29-48.

14. Rbaa M, Dohare P, Berisha A, Dagdag O, Lakhri L, Galai M, et al. New Epoxy sugar based glucose derivatives as eco friendly corrosion inhibitors for the carbon steel in 1 . 0 M HCl: Experimental and theoretical investigations. J Alloys Compd [Internet]. 2020;833:154949. Available from: <https://doi.org/10.1016/j.jallcom.2020.154949>

15. Kumar A, Satya M, Tewari P. Density functional theory calculations of spectral , NLO , reactivity , NBO properties and docking study of Vincosamide - N - Oxide active against lung cancer cell lines H1299. SN Appl Sci [Internet]. 2020;2:1021. Available from: <https://doi.org/10.1007/s42452-020-2842-9>

16. M. Muthukkumar, T. Bhuvaneshwari, G.Venkatesh, C.Kamal, P. Vennila, Stevan Armaković, Sanja J. Armaković, Y. Sheena Mary CYP. Synthesis, characterization and computational studies of semicarbazide derivative. J Mol Liq [Internet]. 2018; Available from: <https://doi.org/10.1016/j.molliq.2018.09.123>

17. Oyenehin OE, Ajibade A, Esan TO. Substituent Effects on the Structural and Nonlinear Optical Properties of 1-[4-((E)-[4-(methylsulfanyl)phenyl]methylidene)amino]phenyl] ethanone and Some of its Substituted Derivatives- a Theoretical Method. Phys Chem Res. 2018;6(3):667-83.

18. Adejoro IA, Oyenehin OE, Ogunyemi BT. Computational Investigation on Substituent and Solvent Effects on the Electronic, Geometric and Spectroscopic Properties of Azobenzene and Some Substituted Derivatives. Int J Comput Theor Chem. 2015;3(6):50-7.

19. AD B. Density - functional thermochemistry. III. The role of exact exchange. J Chem Phys. 1993;98:5648-52.

20. Shao Y, Molnar LF JY et al. SPARTAN 14', build 1.01. Irvine (CA); 2014.

21. Obot IB, Obi-egbedi NO, Umoren SA. Antifungal drugs as corrosion inhibitors for aluminium in 0 . 1 M HCl. Corros Sci [Internet]. 2009;51(8):1868-75. Available from: <http://dx.doi.org/10.1016/j.corsci.2009.05.017>

22. Obot IB, Umoren S, Obi-egbedi NO. Corrosion inhibition and adsorption behaviour for aluminium by extract of Aningeria robusta in HCl solution: Synergistic effect of iodide ions. J Mater Environ Sci. 2011;2(1):60-71.

23. Saliyan R. AA V. Inhibition of corrosion of mild steel in acid media by N'- benzylidene-3-(quinolin-4-ylthio) propanohydrazide. Bull Mater Sci. 2008;31(4):699-711.

24. Lukovits I., Kalman E. ZF. Corrosion Inhibitors: Correlation between the electronic structures and efficiency. Corros Sci. 2001;57(1):3-8.

25. Oyenehin OE. Structural and Solvent Dependence of the Electronic Properties and Corrosion Inhibitive Potentials of 1,3,4-thiadiazole and Its Substituted Derivatives- A Theoretical Investigation. Phys Sci Int J. 2017;16(2):1-8.

SUPPLEMENTARY INFORMATION

Corrosion Inhibitive Potentials Of (E)-5-((4-Benzoylphenyl)Diazenyl)-2-Hydroxybenzoic Acid On Mild Steel Surface In 0.5 M HCl- Experimental and DFT Calculations

Justinah Solayide Amoko^{1,2,4}  , Olawale Folorunso Akinyele³  ,
Oluwatoba Emmanuel Oyeneyin^{1,4*}  , and Samson Dare Olayanju³  

FTIR, UV-VIS, ¹H-NMR, and ¹³C-NMR spectra of AD4

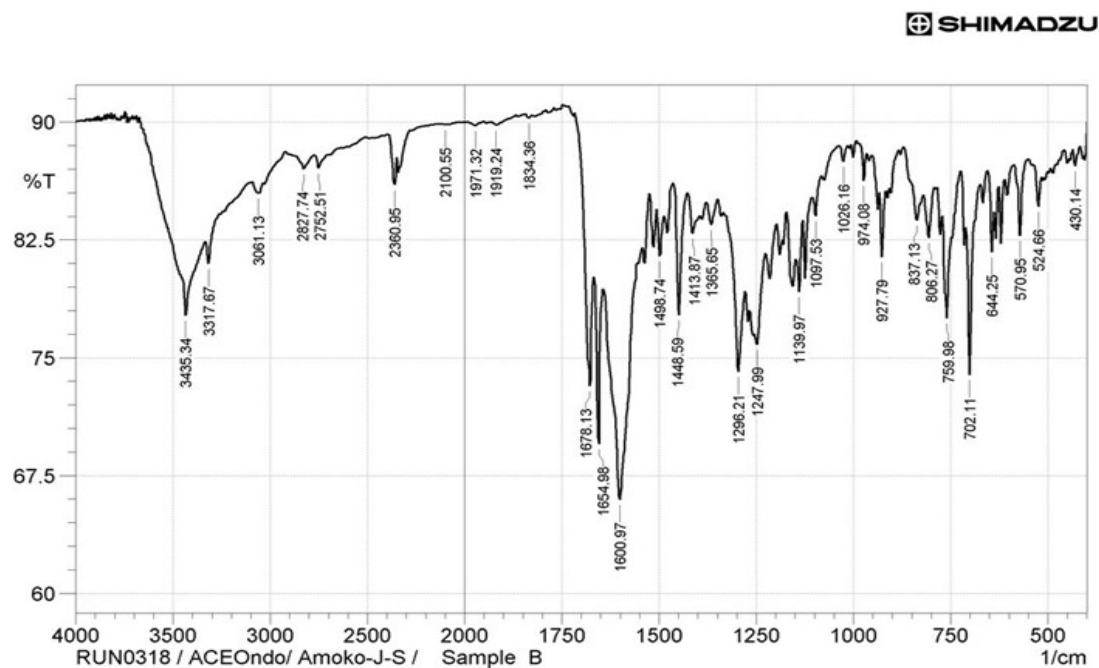


Figure S1: FTIR spectrum of AD4

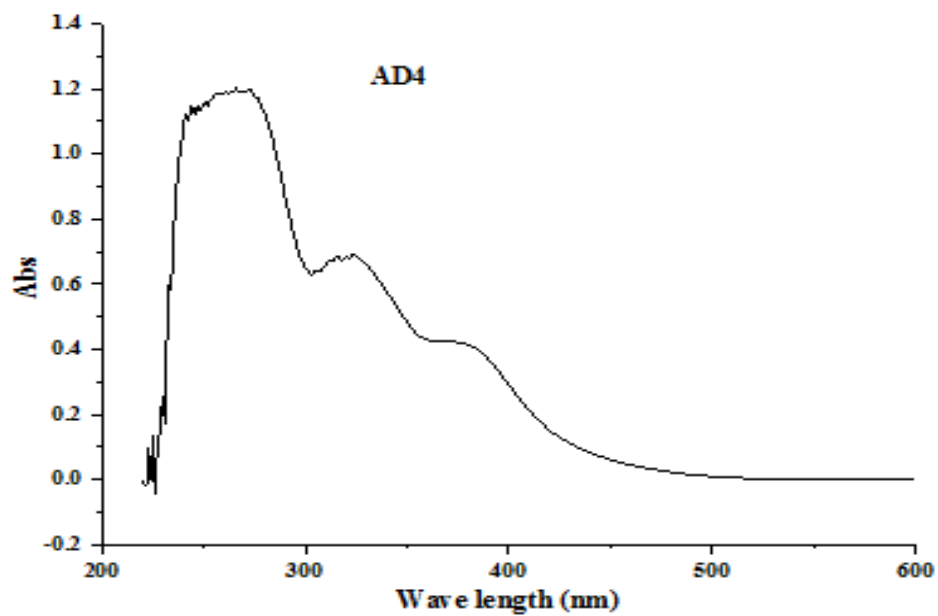


Figure S2: UV/Vis absorption spectrum of AD4

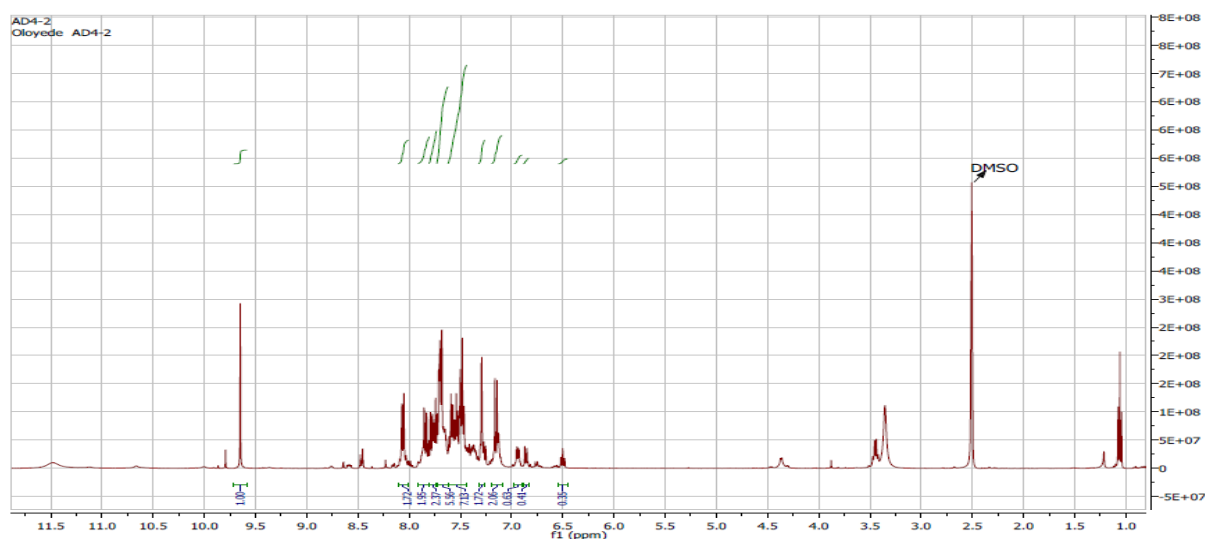


Figure S3: ¹H NMR spectrum of AD4

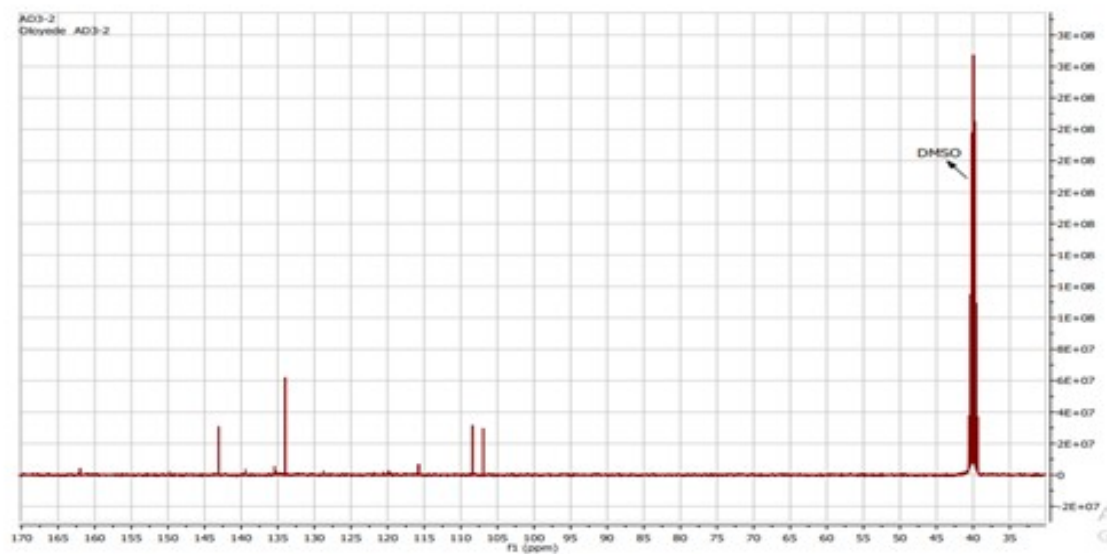


Figure S4: ¹³C-NMR spectrum of AD4



Regioselective Synthesis of Some Rhamnopyranoside Esters for PASS Predication, and ADMET Studies

Mohammed Mahbubul Matin^{1*}, Naimul Islam¹, Aysha Siddika¹, and Sreebash C. Bhattacharjee^{1,2}

¹University of Chittagong, Faculty of Science, Department of Chemistry, 4331, Chattogram, Bangladesh.

²Bangladesh Council of Scientific & Industrial Research (BCSIR), Chemical Research Division, 4220, Chattogram, Bangladesh.

Abstract: Notable biological activities including brains protective activities have made carbohydrate esters as a topic of great interest over the past several decades. In this context, unimolecular treatment of methyl α -L-rhamnopyranoside with dibutyltin oxide gave the corresponding 2,3-*O*-(dibutylstannylene) derivative which was then allowed to react with 3-chlorobenzoyl chloride. The reaction regioselectively furnished the 3-*O*-substitution product in excellent yield. To get newer rhamnopyranoside esters chlorobenzoate was further converted into four 2,4-di-*O*-substituted products with other acylating agents using direct acylation technique. Moreover, thermodynamic properties indicated that these sugar esters (SEs) possess better stability, suitable polar nature and higher binding affinity than the non-ester rhamnopyranoside. Prediction of Activity Spectra for Substances (PASS) predication showed that these SEs should be more potent against fungal pathogens than the bacterial organisms. With these encouraging results absorption, distribution, metabolism, excretion, and toxicity (ADMET) and drug-likeness properties of the SEs are also discussed.

Keywords: Dibutyltin oxide (DBTO) method, Methyl α -L-rhamnopyranoside, Regioselectivity, PASS predication, AdmetSAR.

Submitted: November 23, 2020. **Accepted:** January 18, 2021.

Cite this: Matin MM, Islam N, Siddika A, Bhattacharjee SC. Regioselective Synthesis of Some Rhamnopyranoside Esters for PASS Predication, and ADMET Studies. JOTCSA. 2021;8(1):363-74.

DOI: <https://doi.org/10.18596/jotcsa.829658>.

***Corresponding author.** E-mail: mahbubchem@cu.ac.bd, Tel: +880-1716-839689, Fax: +880-31-2606014.

INTRODUCTION

Sugar esters (SE) are composed of a sugar moiety and one or more acyl group(s) (1). Due to the presence of both hydrophilic and lipophilic moieties, SEs are biodegradable, environmentally friendly, non-toxic, non-allergic, and non-irritating (2-3). Their good stabilizing properties render them to use in the food, cosmetics, pharmaceutical formulations, and bioremediation of pollutants (4-6). In addition to their surfactant properties, SEs possess anticancer, insecticidal and antimicrobial activities (7-9). Some SEs are used as intermediate for the synthesis of many natural and synthetic biomolecules including glycosylation (10). Hence, SEs are getting more attention as a vivid field of research to the organo-synthetic and biological chemists (11).

Among SEs, rhamnopyranoside based esters got special interest as they are active in many natural products (12-13) and showed cytotoxic activity against several different cell lines. For instance, brasilicardin A (**1**, Figure 1) was isolated from the broth of actinomycete *Nocardia brasiliensis* IFM0406 which contains two rhamnopyranosyl moieties. Addition of 3-hydroxybenzoate esters in the 3- and 4-positions of its rhamnose unit(s) is responsible for immunosuppressive activities (14). *S. buergeriana* derived 2-*O*-acetyl-3,4-di-*O*-(*E*)-*p*-methoxycinnamoyl- α -L-rhamnopyranoside exerted significant protective effects against glutamate-induced neurodegeneration (15). In 2020, Elmaidomy *et al.* (16) isolated four novel rhamnopyranose esters (**2a-d**, Figure 1) from the

stem of *P. odorata* which exhibited triple-negative breast cancer suppressive activities along with antioxidant properties. We reported in our previous studies that the incorporation of ester group(s) at different position of rhamnose enhanced its

antimicrobial functionality (17-18) like other SEs (19). Some of the SEs were found promising against SARS-CoV-2 main protease than the hydroxychloroquine (HCQ) (20).

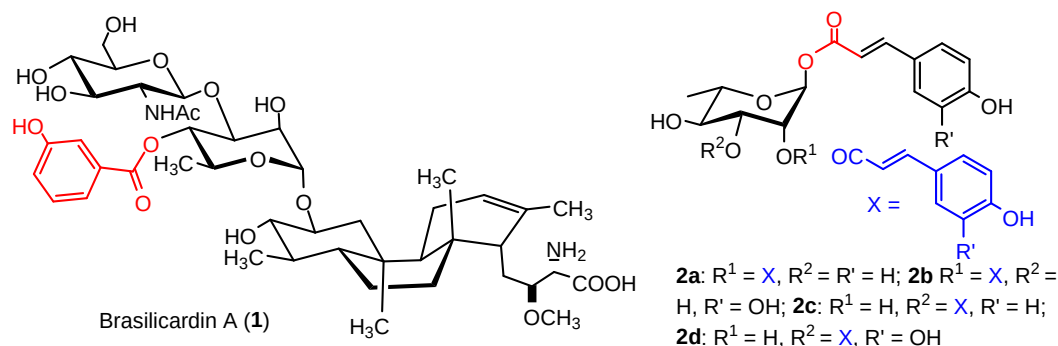


Figure 1. Naturally occurring rhamnopyranose esters.

The chemical synthesis of carbohydrate esters by hydroxyl group protection/deprotection strategies is essential for the synthesis of oligosaccharides and carbohydrate-conjugates. This needs regio- and stereochemical control to get desired SEs. However, selective and regioselective esterification (acylation) of monosaccharide molecules is a difficult task due to the presence of multiple 2° hydroxyl groups of similar reactivity (21). Hence, development of selective esterification methods for sugar modification is highly desired. Several methods (22-23) with different reaction conditions (21) were developed where dibutyltin oxide (DBTO) method was found to be promising (24). In this paper, the regioselective synthesis of 3-*O*-(3-chlorobenzoyl)rhamnopyranosides from methyl α -L-rhamnopyranoside (**3**) employing DBTO method is described with DFT based thermodynamic properties, PASS prediction, and drug-likeness (ADMET) studies.

EXPERIMENTAL

Materials and general methods

Methyl α -L-rhamnopyranoside (**3**) and related reagents/solvents were commercially available (Merck, Germany), and were used as received, unless otherwise specified. TLC (thin layer chromatography) was conducted on plates coated with Kieselgel GF₂₅₄, and the spots were detected by spraying the plates with 1% H₂SO₄ and heating at 150–200 °C until blackish coloration took place. CC (column chromatography) was conducted with silica gel G₆₀. In both the cases solvent system employed was *n*-hexane/ethyl acetate (EA) in different ratios. Reduced pressure using a bath temperature below 40 °C was maintained for evaporations. FT-IR spectra were recorded on a FT-IR spectrophotometer (Shimadzu, IR Prestige-21) in CHCl₃ technique. ¹H NMR (400 MHz) spectra were recorded for solutions in CDCl₃ using tetramethylsilane (TMS) as an internal standard with a Bruker DPX-400 spectrometer at the

Bangladesh Council of Scientific and Industrial Research (BCSIR) Laboratories, Dhaka, Bangladesh.

Synthesis of methyl 3-*O*-(3-chlorobenzoyl)- α -L-rhamnopyranoside (**4**)

A suspension of methyl α -L-rhamnopyranoside (**3**) (200 mg, 1.122 mmol) and dibutyltin oxide (307 mg, 1.1 molar eq) in anhydrous methanol (10 mL) was heated under gentle reflux in nitrogen atmosphere until a clear solution was obtained (~4 h). After refluxing for an additional hour, the solvent was removed, and the resulting intermediate tin complex (**3a**) was obtained as a white solid. A stirred suspension of the tin complex (**3a**) in dry dioxane (10 mL) was treated with 3-chlorobenzoyl chloride (0.15 mL, 1.1 molar eq) and stirring was continued at room temperature overnight. Removal of solvent and silica gel column chromatography (with *n*-hexane-EA, 1:4 as eluent) furnished the title compound **4** (317 mg, 89%) as needles, mp 140-142 °C (ethyl acetate-*n*-hexane) (25). *R*_f = 0.46 (with *n*-hexane/EA = 1/2); FT-IR (CHCl₃) ν_{\max} (cm⁻¹): 3360-3560 (OH), 1695 (CO); ¹H NMR (400 MHz, CDCl₃) δ_{H} ppm: 8.15 (s, 1H, Ar-*H*), 8.05 (d, *J* = 7.9 Hz, 1H, Ar-*H*), 7.65 (d, *J* = 8.0 Hz, 1H, Ar-*H*), 7.50-7.54 (m, 1H, Ar-*H*), 5.15 (dd, *J* = 9.4 and 3.3 Hz, 1H, H-3), 4.65 (d, *J* = 1.5 Hz, 1H, H-1), 3.72-3.76 (m, 3H, H-2, H-4 and H-5), 3.40 (s, 3H, OCH₃), 1.33 (d, 3H, *J* = 5.7 Hz, CH₃).

Synthesis of methyl 3-*O*-(3-chlorobenzoyl)-2,4-di-*O*-methanesulfonyl- α -L-rhamnopyranoside (**5**)

To a solution of the **4** (50 mg, 0.158 mmol) in dry pyridine (1 mL) was added methanesulfonyl chloride (40 mg, 0.349 mmol) slowly at 0 °C followed by addition of a catalytic amount of DMAP (4-*N,N*-dimethylaminopyridine). The reaction mixture was allowed to attain room temperature and stirring was continued for 5 h. A small amount of ice-water (0.2 mL) was added to the reaction mixture to decompose excess mesyl chloride, and extracted

with DCM (dichloromethane, 3×3 mL). The combined DCM extract was washed successively with 5% hydrochloric acid, saturated aqueous sodium hydrogen carbonate solution and brine. The DCM layer was dried over Na₂SO₄, and concentrated under reduced pressure. The residue was then purified by CC (elution with *n*-hexane/EA, 12:1) and furnished the 2,4-di-*O*-mesyl esters **5** (68 mg, 91%) as a pale yellow oil. *R*_f = 0.49 (*n*-hexane/EA = 5/1); FT-IR (CHCl₃) ν_{\max} (cm⁻¹): 1703 (CO), 1370, 1365 (SO₂); ¹H NMR (400 MHz, CDCl₃) δ_{H} ppm: 7.91 (s, 1H, Ar-*H*), 7.76 (d, *J* = 7.8 Hz, 1H, Ar-*H*), 7.47 (d, *J* = 8.0 Hz, 1H, Ar-*H*), 7.33-7.37 (m, 1H, Ar-*H*), 5.46 (dd, *J* = 9.3 and 3.3 Hz, 1H, H-3), 5.35 (d, *J* = 3.3 Hz, 1H, H-2), 5.25 (t, *J* = 9.4 Hz, 1H, H-4), 4.70 (s, 1H, H-1), 3.90-3.95 (m, 1H, H-5), 3.42 (s, 3H, OCH₃), 3.31 (s, 3H, SO₂CH₃), 3.15 (s, 3H, SO₂CH₃), 1.28 (d, *J* = 6.0 Hz, 3H, CH₃).

Synthesis of methyl 3-*O*-(3-chlorobenzoyl)-2,4-di-*O*-pivaloyl- α -L-rhamnopyranoside (**6**)

To a rapidly stirred and cooled (0 °C) solution of the diol **4** (50 mg, 0.158 mmol) in anhydrous pyridine (2 mL) was slowly added pivaloyl chloride (42 mg, 0.348 mmol), and stirring was continued at this temperature for 10 h. Conventional work-up procedure as described earlier followed by CC purification (*n*-hexane-EA, 10:1) provided the di-*O*-pivaloate **6** (72 mg, 94%) as clear needles, mp 85-87 °C. *R*_f = 0.53 (*n*-hexane/EA = 5/1); FT-IR (CHCl₃) ν_{\max} (cm⁻¹): 1738, 1732, 1701 (CO); ¹H NMR (400 MHz, CDCl₃) δ_{H} ppm: 7.96 (s, 1H, Ar-*H*), 7.79 (d, *J* = 7.8 Hz, 1H, Ar-*H*), 7.46 (d, *J* = 8.1 Hz, 1H, Ar-*H*), 7.34-7.38 (m, 1H, Ar-*H*), 5.43 (dd, *J* = 9.6 and 3.4 Hz, 1H, H-3), 5.36 (d, *J* = 3.4 Hz, 1H, H-2), 5.27 (t, *J* = 9.6 Hz, 1H, H-4), 4.68 (s, 1H, H-1), 3.88-3.91 (m, 1H, H-5), 3.42 (s, 3H, OCH₃), 1.27 (d, *J* = 5.9 Hz, 3H, CH₃), 1.20 (s, 9H, C(CH₃)₃), 1.18 (s, 9H, C(CH₃)₃).

Synthesis of methyl 3-*O*-(3-chlorobenzoyl)-2,4-di-*O*-pentanoyl- α -L-rhamnopyranoside (**7**)

A stirred and cooled solution of the diol **4** (50 mg, 0.158 mmol) in dry pyridine (2 mL) was treated with pentanoyl chloride (42 mg, 0.348 mmol) and stirring was continued at this temperature for 12 h. The reaction was stopped by adding ice-water. Usual work-up followed by column chromatography furnished the di-*O*-pentanoate **7** (66 mg, 86%) as a clear syrup which resisted crystallization. *R*_f = 0.52 (*n*-hexane/EA = 5/1); FT-IR (CHCl₃) ν_{\max} (cm⁻¹): 1748, 1742, 1698 (CO); ¹H NMR (400 MHz, CDCl₃) δ_{H} ppm: 7.93 (s, 1H, Ar-*H*), 7.80 (d, *J* = 7.6 Hz, 1H, Ar-*H*), 7.45 (d, *J* = 8.0 Hz, 1H, Ar-*H*), 7.33-7.37 (m, 1H, Ar-*H*), 5.42 (dd, *J* = 9.5 and 3.2 Hz, 1H, H-3), 5.34 (d, *J* = 3.2 Hz, 1H, H-2), 5.27 (t, *J* = 9.5 Hz, 1H, H-4), 4.65 (s, 1H, H-1), 3.89-3.94 (m, 1H, H-5), 3.41 (s, 3H, OCH₃), 2.27-2.36 (m, 4H, 2×CH₃(CH₂)₂CH₂CO), 1.53-1.64 (m, 4H, 2×CH₃CH₂CH₂CH₂CO), 1.28 (d, *J* = 6.0 Hz, 3H, CH₃), 1.19-1.31 (m, 4H, 2×CH₃CH₂(CH₂)₂CO), 0.84-0.94 (m, 6H, 2×CH₃(CH₂)₃CO).

Synthesis of methyl 3-*O*-(3-chlorobenzoyl)-2,4-di-*O*-hexanoyl- α -L-rhamnopyranoside (**8**)

Hexanoyl chloride (47 mg, 0.349 mmol) was slowly added to an ice-cooled suspension of diol **4** (50 mg, 0.158 mmol) in pyridine (2 mL). The reaction mixture was allowed to attain the room temperature and stirred for additional 12 h when TLC indicated the formation of a faster-moving single product. The reaction was stopped by adding ice-water (0.2 mL) and extracted with DCM (3×3 mL). The combined DCM extract was treated successively with 5% hydrochloric acid, saturated aqueous sodium hydrogen carbonate solution, and brine. The organic layer was dried over Na₂SO₄, and concentrated under diminished pressure. The residue was then subjected to CC (elution with *n*-hexane/EA, 12:1), and gave the 2,4-di-*O*-hexanoate **8** (71 mg, 88%) as a thick liquid. *R*_f = 0.55 (*n*-hexane/EA = 5/1); FT-IR (CHCl₃) ν_{\max} (cm⁻¹): 1754, 1745, 1698 (CO); ¹H NMR (400 MHz, CDCl₃) δ_{H} ppm: 7.94 (s, 1H, Ar-*H*), 7.83 (d, *J* = 7.8 Hz, 1H, Ar-*H*), 7.44 (d, *J* = 8.0 Hz, 1H, Ar-*H*), 7.37 (t, *J* = 4.6 Hz, 1H, Ar-*H*), 5.40 (dd, *J* = 9.8 and 3.3 Hz, 1H, H-3), 5.33 (d, *J* = 3.3 Hz, 1H, H-2), 5.28 (t, *J* = 9.8 Hz, 1H, H-4), 4.64 (s, 1H, H-1), 3.85-3.904 (m, 1H, H-5), 3.42 (s, 3H, OCH₃), 2.25-2.35 (m, 4H, 2×CH₃(CH₂)₃CH₂CO), 1.54-1.64 (4H, m, 2×CH₃(CH₂)₂CH₂CH₂CO), 1.26 (d, *J* = 6.2 Hz, 3H, CH₃), 1.18-1.32 (m, 8H, 2×CH₃(CH₂)₂(CH₂)₂CO), 0.88-0.94 (m, 6H, 2×CH₃(CH₂)₄CO).

Thermodynamic properties calculation

For thermodynamic properties calculation quantum mechanical based density functional theory (DFT) was used. Initial geometry of the rhamnopyranoside **3** was taken from the Chemspider website. Necessary modification for other compounds **4-8** was conducted using the the GaussView (5.0) program (26). All the compounds were then optimized by Lee, Yang, and Parr's (LYP) correlation functional under 3-21G basis set with Gaussian 09 program (26). The optimized structures were used to calculate their thermodynamic properties.

PASS Predication

For the prediction of activity spectra for substances (PASS) the freely accessible web resource PASS Online (<http://www.way2drug.com/passonline/>) was used (27). This *in silico* generated results are suitable for understanding pharmacological profile of drug related compounds. Initially, the structures of **3-8** were drawn with ChemDraw 16.0, and then converted into their SD file format, and applied to predict the biological spectrum like antibacterial, antifungal, anticarcinogenic and antioxidant properties using this software. Generally, predicted results are expressed as Pa (probability for active substance) and Pi (probability for inactive substance). With the increasing value of Pa and decreasing value of Pi, the chance of experimentally finding of a given activity increases. That is Pa should be greater than Pi and the considered scale is 0.000 to 1.000.

ADMET calculation

Absorption, distribution, metabolism, excretion, and

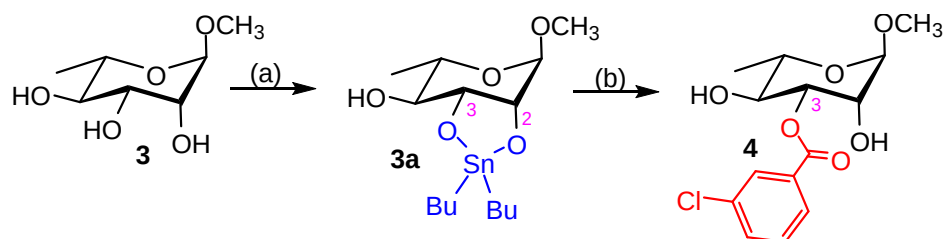
toxicity (ADMET) prediction could avoid the huge cost and time associated with the *in vivo* experiments during drug discovery. In the present investigation, *in silico* ADMET was calculated using pkCSM program (<http://biosig.unimelb.edu.au>) (28). Appropriate stereochemical structures of the SEs **3-8** were converted to the corresponding SMILES (simplified molecular-input line-entry system) and SD file formats, and used for the calculation of pkCSM-pharmacokinetics. The similar SMILES and SD file formats were also used to predict drug-likeness properties using SwissADME free web tools (<http://www.swissadme.ch>) (29). Overall drug-likeness score was also predicted (<http://www.molsoft.com/mprop/mprop.cgi>) (30).

RESULTS AND DISCUSSION

Regioselective 3-chlorobenzoylation of methyl α -L-rhamnopyranoside (**3**)

Initially, methyl α -L-rhamnopyranoside (**3**) was transformed into the intermediate tin complex **3a** by treatment with the dibutyltin oxide in anhydrous methanol under reflux condition. The formation of the tin complex **3a** may be explained by considering

the mechanism proposed by Tsuda *et al.* (31), which states that in cases of glycoses or glycosides where there is a *cis*-vicinal glycol system present, formation of a highly stable five-membered stannylene ring is more favorable between an axial-equatorial pair. Tin complex **3a**, on unimolecular reaction with 3-chlorobenzoyl chloride, furnished a solid (mp 140-142 °C) in good yield (Scheme 1). The appearance of absorption bands at 3360-3560 and 1695 cm^{-1} in its FT-IR spectrum suggested the presence of carbonyl and hydroxyl groups in the molecule i.e. partial chlorobenzoylation of the molecule. In the ^1H NMR spectrum, appearance of four aromatic protons at δ 8.15 (s, 1H), 8.05 (d, 1H), 7.65 (d, 1H) and 7.50-7.54 (m, 1H) clearly indicated the addition of one chlorobenzoyl group in the molecule. A doublet at δ 4.65 with small coupling constant (1.5 Hz) was assigned for equatorially oriented H-1. We noticed huge downfield shift of H-3 to δ 5.15 from its usual value (δ 4.00 ppm) (32) which suggested the incorporation of 3-chlorobenzoyl group at C-3 position. Thus, the compound was assigned as methyl 3-*O*-(3-chlorobenzoyl)- α -L-rhamnopyranoside (**4**).



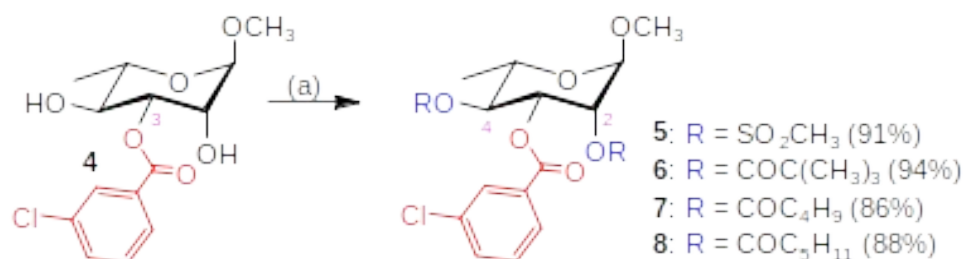
Scheme 1. Regioselective chlorobenzoylation of rhamnopyranoside **3**. *Reaction conditions:* (a) Bu_2SnO , MeOH, reflux, 4 h; (b) 3-Cl. $\text{C}_6\text{H}_4\text{COCl}$, 1,4-dioxane, rt, 12 h, 89%.

The regioselective 3-*O*-(3-chlorobenzoylation) of rhamnopyranoside **3** may be rationalized by assuming that a highly stable five-membered stannylene ring **3a** was formed between the *cis*-vicinal glycol system (2-OH and 3-OH) of the rhamnoside **3** (Scheme 1). The formation of the tin complex **3a** was in conformity with the mechanism proposed by Tsuda *et al.* (31). The equatorial hydroxyl group at position C-3 of **3a** was activated most during acylation (31), thereby, forming solely the 3-*O*-substitution product with the unimolar 3-chlorobenzoyl chloride. The structure of the 3-*O*-(3-

chlorobenzoyl) derivative **4** was also further confirmed by the preparation and characterization of its four 2,4-di-*O*-acyl derivatives **5-8**.

Synthesis of 2,4-di-*O*-acyl esters **5-8** of chlorobenzoylrhamnopyranoside **4**

To get newer rhamnopyranoside esters as well as to confirm the structural information of chlorobenzoyl **4**, four 2,4-di-*O*-acyl esters **5-8** were synthesized and characterized. Initially, treatment of diol **4** with dimolar mesyl chloride at low temperature furnished a pale yellow oil (Scheme 2).



Scheme 2. 2,4-Di-*O*-acylation of chlorobenzoyl **4**. *Reaction conditions:* (a) $\text{CH}_3\text{SO}_2\text{Cl}/(\text{CH}_3)_3\text{CCOCl}/\text{C}_4\text{H}_9\text{COCl}/\text{C}_5\text{H}_{11}\text{COCl}$, dry Py, 0 °C-rt, 5-12 h.

Appearance of two new bands at 1370 and 1365 cm^{-1} in addition to carbonyl stretching (1703 cm^{-1}), and disappearance of hydroxyl band in the FT-IR spectrum clearly indicated the complete mesylation of the molecule. This fact was further confirmed by its ^1H NMR spectrum where two new three-proton singlets were found at δ 3.31 and 3.15 ppm corresponding to two mesyl groups. The C-6 methyl protons appeared at δ 1.28, and C-1 OCH_3 appeared at δ 3.42. However, considerable downfield shift of H-2 (δ 5.35) and H-3 (δ 5.25) as compared to its precursor chlorobenzoate **4** (δ 3.72-3.76 as multiplet) confirmed the attachment of mesyl groups at C-2 and C-4 positions. On the basis of spectroscopic evidences, the structure of the molecule was established as methyl 3-*O*-(3-chlorobenzoyl)-2,4-di-*O*-methanesulfonyl- α -L-rhamnopyranoside (**5**).

In the subsequent step, reaction of the diol **4** with pivaloyl chloride for 10 h followed by chromatography furnished clear needles (mp 85-87 $^\circ\text{C}$) in excellent yield (Scheme 2). Disappearance of hydroxyl bands and presence of three carbonyl stretching bands at 1738, 1732 and 1701 cm^{-1} in its FT-IR spectrum clearly indicated the complete pivaloylation of the compound. ^1H NMR also supported the above fact where two nine-proton singlets appeared at δ 1.20 and 1.18 corresponding to two pivaloyl groups. In addition, H-2 (δ 5.36) and H-4 (δ 5.27) appeared downfield than the diol **4** (δ 3.72-3.76) affirming the attachment of pivaloyl groups at C-2 and C-4 positions. So, the structure of the compound was established as methyl 3-*O*-(3-chlorobenzoyl)-2,4-di-*O*-pivaloyl- α -L-rhamnopyranoside (**6**).

Reaction of diol **4** with excess pentanoyl chloride in

dry pyridine followed by chromatography furnished a faster-moving syrup in 86% (Scheme 2). Its FT-IR spectrum showed the absence of hydroxyl stretching, and the presence of carbonyl bands at 1748, 1742 and 1698 cm^{-1} indicating the attachment of pentanoyl groups in the molecule. The fact was confirmed by analyzing its ^1H NMR spectrum where extra eighteen protons appeared at δ 2.27-2.36 (m, 4H), 1.53-1.64 (m, 4H), 1.19-1.31 (m, 4H) and 0.84-0.94 (m, 6H). Also, H-2 and H-4 shifted considerable downfield as compared to its precursor **4**. Hence, the compound was assigned as methyl 3-*O*-(3-chlorobenzoyl)-2,4-di-*O*-pentanoyl- α -L-rhamnopyranoside (**7**).

Finally, dimolar hexanoylation of the 2,4-diol **4** with hexanoyl chloride followed by chromatography gave a thick liquid in good yield (Scheme 2). Its FT-IR spectrum exhibited characteristic carbonyl bands at 1754, 1745 and 1698 cm^{-1} , and band related to hydroxyl group was disappeared. In the ^1H NMR spectrum additional twenty-two protons appeared in the aliphatic region which confirmed the attachment of two hexanoyl groups in the molecule. Downfield shift of H-2 (δ 5.33) and H-4 (δ 5.28) as compared to the diol **4** indicated the attachment of hexanoyloxy groups at C-2 and C-4 positions. Thus, the compound was established as methyl 3-*O*-(3-chlorobenzoyl)-2,4-di-*O*-hexanoyl- α -L-rhamnopyranoside (**8**).

Thermodynamic properties of rhamnopyranosides

Having successful preparation of rhamnose based SEs **4-8** we have calculated their thermodynamic properties based on quantum mechanical DFT optimization (26). The optimized structures (298.15 K, 1.0 atm) of **3-8** are shown in Figure 2.

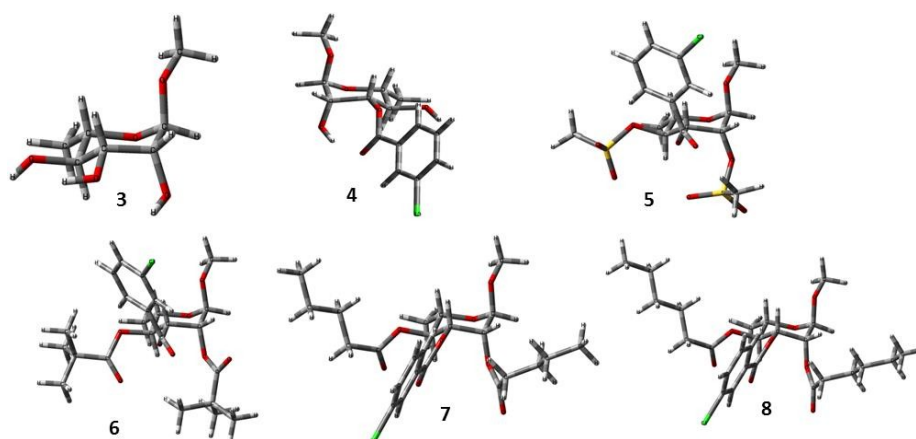


Figure 2. DFT optimized (B3LYP/3-21G) conformational structures of **3-8**.

It was found that these SEs possess $^1\text{C}_4$ conformation with similar C1 symmetry (Figure 2) which are in consistence with their ^1H NMR spectral data. Thermodynamic properties such as electronic energy (EE), enthalpy (ΔH), Gibbs' free energy (G) and dipole moment (μ) of the optimized

rhamnopyranosides **3-8** are summarized in Table 1. With the increase of the negative energy value, the electrons become more tightly bound with the nucleus. It is worth mentioning that addition of ester group(s) increased electron binding tendency (-1447 to -2631 Hartree) than the parent

rhamnopyranoside **3** (-651.2403 Hartree). The highest electron binding was observed for dimesylate **5** (-2631.008 Hartree) indicating the more stability of the compound. This fact was further supported by the lower ΔH values (more negative values) of SEs than the non-ester sugar **3** (Table 1). Gibbs free energy (G) of the SEs (-1447.2685 to -2630.6936 Hartree) was found very much lower than the non-ester **3** (-651.0598

Hartree) which indicated their spontaneous binding, and interaction with other substrates. In addition, dipole moment (μ) of a molecule signifies the measure of net molecular polarity and binding affinity. It was observed that the addition of ester group(s) gradually increased μ as compared to non-ester rhamnopyranoside **3**. This suggested the more polar nature and higher binding affinity with target enzyme of the SEs **4-8** (3, 23).

Table 1: Thermodynamic properties of the synthesized rhamnopyranoside based SEs.

Molecule	MF	MW	EE (Hartree)	ΔH (Hartree)	G (Hartree)	μ (Debye)
3	C ₇ H ₁₄ O ₅	178.18	-651.2403	-651.0075	-651.0598	2.6783
4	C ₁₄ H ₁₇ ClO ₆	316.73	-1447.5915	-1447.2685	-1447.3395	3.8598
5	C ₁₆ H ₂₁ ClO ₁₀ S ₂	472.90	-2631.0080	-2630.5985	-2630.6936	8.1775
6	C ₂₄ H ₃₃ ClO ₈	484.19	-1985.8611	-1985.2751	-1985.3785	7.2095
7	C ₂₄ H ₃₃ ClO ₈	484.19	-1985.8379	-1985.2501	-1985.3593	8.4353
8	C ₂₆ H ₃₇ ClO ₈	513.02	-2064.0407	-2063.3925	-2063.5082	8.5241

PASS Predicted biological activities

The basic aim of the biological activity spectrum was to describe the properties of biologically active substances. In this respect online-based Prediction of Activity Spectrum for Substances (PASS) software (<http://www.way2drug.com/passonline/>) is efficiently used to find novel targets for biological activities (33). PASS results, as shown in Table 2, indicated that the synthesized SEs **4-8** possess better antifungal activity (0.70>Pa>0.42) than

antibacterial property (0.54>Pa>0.47). Incorporation of ester group(s) increased antifungal potentiality of rhamnopyranoside molecule **3** except methanesulfonyl ester **5**. Antifungal potentiality of pentanoyl (**7**) and hexanoyl (**6**) esters were comparable to the standard antibiotic tetracycline and fluconazole. However, incorporation of ester moieties did not increase anti-carcinogenic and antioxidant properties (Table 2).

Table 2: PASS predicted biological activities of rhamnopyranoside **3-8**.

Drug	Antibacterial		Antifungal		Anti-carcinogenic		Antioxidant	
	Pa	Pi	Pa	Pi	Pa	Pi	Pa	Pi
3	0.574	0.010	0.650	0.013	0.662	0.010	0.650	0.004
4	0.537	0.013	0.665	0.012	0.571	0.014	0.400	0.012
5	0.470	0.019	0.421	0.045	0.339	0.045	0.249	0.036
6	0.533	0.014	0.667	0.012	0.406	0.030	0.309	0.021
7	0.545	0.013	0.700	0.010	0.449	0.024	0.315	0.021
8	0.545	0.013	0.700	0.010	0.449	0.024	0.315	0.021
TC	0.694	0.005	0.523	0.023	-	-	-	-
FCZ	-	-	0.726	0.008	-	-	-	-

TC = tetracycline; FCZ = fluconazole; Pa = Probability to be active; Pi = Probability to be inactive.

ADMET and drug-likeness properties

For the drug development, pharmacokinetics, and safety properties such as absorption, distribution, metabolism, excretion, and toxicity (ADMET) play a significant role. We have used pkCSM predictive model (28, 34) to rapidly evaluate pharmacokinetic and toxicity properties. As shown in Table 3, these SEs **4-8** have good absorption [Caco-2 (colon cancer cell line) permeability and human intestinal absorption (HIA)] with better permeability through BBB (blood brain barrier) and CNS (central nervous system) comparable to the standard antibiotic fluconazole. Metabolism is predicted based on the CYP model (CYP3A4) which indicated that esters **5-8** (except **4**) are the CYP3A4 substrate. The *in silico* pkCSM also indicated that these rhamnopyranoside esters **4-8** are safer drug candidate with low toxicity as they are non-inhibitor of the human ether-a-go-go-related gene (hERG). It should be noted that

inhibition of hERG by drugs causes long QT syndrome and sudden death of patients with cardiac ischemia.

Drug-likeness (35) and medicinal chemistry friendliness of these compounds were predicted by SwissADME predictor (35) and Molsoft's chemical fingerprints (30). The results are presented in Table 4, and indicated that all the SEs (except dimesylate **5**) have good topological polar surface area (TPSA, below 140 Å²) which is in agreement with the most important rule of drug-likeness. Also, these SEs **4-8** did not violate pan-assay interference compounds (PAINS). PAINS are chemical compounds that often give false positive results in high-throughput screens. However, we observed that drug-likeness model scores as predicted by MolSoft were in the borderline (>-0.99) (Figure S6).

Table 3. ADMET calculation of rhamnopyranoside derived SEs **3-8**.

Drug	Absorption		Distribution		Metabolism	Excretion	Toxicity		
	C2P	HIA (%)	P-gpl	BBB permeability	CNS	CYP3A4 substrate	Total clearance	hERG inhibitor	LD ₅₀
3	0.648	75.31	No	-0.67	-3.162	No	0.628	No	1.403
4	0.635	72.84	No	-0.679	-3.041	No	0.350	No	2.562
5	0.97	60.62	No	-2.058	-3.101	Yes	0.518	No	2.284
6	1.161	93.19	Yes	-1.188	-2.511	Yes	0.021	No	2.411
7	0.938	86.23	No	-1.38	-2.889	Yes	0.361	No	2.457
8	0.938	81.98	Yes	-1.417	-2.76	Yes	0.423	No	2.192
FCZ	1.191	87.82	No	-1.200	-3.221	No	0.386	No	2.210

*C2P is Caco-2 permeability (log Papp in 10⁻⁶ cm/s, >0.90 indicates high permeability); HIA = Human intestinal absorption (% absorbed, >30% is better absorbed); P-gpl = P-glycoprotein inhibitor; BBB (blood brain barrier) is mentioned as logBB (logBB >-1.0 is moderately cross blood brain barrier); CNS is expressed as logPS (logPS>-2.0 can easily penetrate the CNS); Total clearance is expressed in log mL/min/kg; Toxicity is calculated as hERG inhibitor, and oral rat acute toxicity (mol/kg); FCZ = fluconazole.

Table 4. Calculation of drug-likeness properties using SwissADME and Molinspiration.

Drug	HBA	HBD	TPSA Å ²	Inhibitors					PAINS alerts	Drug likeness score
				CYP1A2	CYP2C19	CYP2C9	CYP2D6	CYP3A4		
3	5	3	79.15	No	No	No	No	No	0	-0.48
4	6	2	85.22	No	No	No	No	No	0	-0.19
5	10	0	148.26	No	No	No	No	No	0	-0.99
6	8	0	97.36	No	Yes	No	Yes	Yes	0	-0.64
7	8	0	97.36	No	Yes	Yes	Yes	Yes	0	-0.42
8	8	0	97.36	No	No	Yes	Yes	Yes	0	-0.51

*HBA = Hydrogen bond acceptor, HBD = Hydrogen bond donor, TPSA = Topological polar surface area, PAINS = Pan-assay interference compounds.

CONCLUSION

Dibutyltin oxide (DBTO) method was successfully applied for the regioselective esterification of rhamnopyranoside **3**, and obtained monosubstitution single product **4**, indicating regioselectivity at C-3 position. Compound **4** was further converted into four novel 2,4-di-*O*-acyl esters **5-8** with four non-traditional acylating agents. The high selectivity, the cleanness of the reactions, easy work-up procedures, and high yields proved the use of these reagents highly encouraging in comparison to other traditional reagents employed for selective acylation of carbohydrate derivatives. Thermodynamic properties based on DFT optimization, PASS predication and drug-likeness molecular properties of these novel rhamnopyranoside esters are also discussed. Thus, it is expected that the present study provide future prospect of rhamnopyranoside-based biodegradable and ecofriendly drugs especially antimicrobial agents.

ACKNOWLEDGMENT

We are grateful to the Ministry of Education, Bangladesh and BANBEIS for financial support (grant no. PS 201660, 2016-17) to conduct this research work.

REFERENCES

- Matin MM, Bhattacharjee SC, Chakraborty P, Alam MS. Synthesis, PASS predication, *in vitro* antimicrobial evaluation and pharmacokinetic study of novel *n*-octyl glucopyranoside esters. Carbohydrate Research. 2019;485:107812. Doi: 10.1016/j.carres.2019.107812
- Pöhnlein M, Slomka C, Kukharenko O, Gärtner T, Wiemann LO, Sieber V, Syldatk C, Hausmann R. Enzymatic synthesis of amino sugar fatty acid esters. European Journal of Lipid Science and Technology. 2014;116:423. Doi: 10.1002/ejlt.201300380
- Matin MM, Hasan MS, Uzzaman M, Bhuiyan MMH, Kibria SM, Hossain ME, Roshid MHO. Synthesis, spectroscopic characterization, molecular docking, and ADMET studies of mannopyranoside esters as antimicrobial agents. Journal of Molecular Structure. 2020;1222:128821. Doi: 10.1016/j.molstruc.2020.128821
- Neta NS, Teixeira JA, Rodrigues LR. Sugar ester surfactants: Enzymatic synthesis and applications in food industry. Critical Reviews in Food Science and Nutrition. 2015;55(5):595-610, Doi: 10.1080/10408398.2012.667461

5. Lou X. Antimicrobial structure-efficacy relationship of sugar fatty acid esters. *Journal of Chemical and Pharmaceutical Research*. 2014;6(5):944-946.
6. Akanbi TO, Barrow CJ. Enzymatic production of antioxidants and their applications. In: *Encyclopedia of Food Chemistry*; Elsevier; 2019, pp 92-96. Doi: 10.1016/B978-0-08-100596-5.21646-6
7. Traxler P, Fritz H, Fuhrer H, Richter WJ. Papulacandins, a new family of antibiotics with antifungal activity. Structures of papulacandins A, B, C and D. *Journal of Antibiotics*. 1980;33(9):967-978. Doi: 10.7164/antibiotics.33.967
8. Watanabe T, Katayama S, Matsubara M, Honda Y, Kuwahara M. Antibacterial carbohydrate monoesters suppressing cell growth of *Streptococcus mutans* in the presence of sucrose. *Current Microbiology*. 2000;41:210-213. Doi: 10.1007/s002840010121
9. Matin MM, Bhuiyan MMH, Kabir E, Sanaullah AFM, Rahman MA, Hossain ME, Uzzaman M. Synthesis, characterization, ADMET, PASS predication, and antimicrobial study of 6-*O*-lauroyl mannopyranosides. *Journal of Molecular Structure*. 2019;1195:189-197. Doi: 10.1016/j.molstruc.2019.05.102
10. Matin MM. One step intramolecular cyclization of diol via mesylation: Efficient synthesis of sugar derived [1,4]oxazepanes. *Journal of Bangladesh Chemical Society*. 2008;21(2):179-183.
11. Dhavale DD, Matin MM. Piperidine homoazasugars: Natural occurrence, synthetic aspects and biological activity study. *ARKIVOC*. 2005;2005(3):110-132. Doi: 10.3998/ark.5550190.0006.314
12. Yang L-J, Yang X-D, Yang S, Zhao J-F, Zhang H-B, Liang Li. Two new benzoyl esters of glucose from *Lagotis yunnanensis*. *Chemistry of Natural Compounds*. 2006;42(6):649-651. Doi: 10.1080/1028602031000093366
13. Jung ME, Koch P. An efficient synthesis of the protected carbohydrate moiety of brasilicardin A. *Organic Letters*. 2011;13(14):3710-3713. Doi: 10.1021/ol2013704
14. Komatsu K, Tsuda M, Tanaka Y, Mikami Y, Kobayashi J. SAR studies of brasilicardin A for immunosuppressive and cytotoxic activities. *Bioorganic & Medicinal Chemistry*. 2005;13(5):1507-1513. Doi: 10.1016/j.bmc.2004.12.029
15. Kim SR, Kim YC. Neuroprotective phenylpropanoid esters of rhamnose isolated from roots of *Scrophularia buergeriana*. *Phytochemistry*. 2000;54(5):503-509. Doi: 10.1016/S0031-9422(00)00110-2
16. Elmaidomy AH, Mohammed R, Owis AI, Hetta MH, AboulMagd AM, Siddique AB, Abdelmohsen UR, Rateb ME, Sayed KAE, Hassan, HM. Triple-negative breast cancer suppressive activities, antioxidants and pharmacophore model of new acylated rhamnopyranoses from *Premna odorata*. *RSC Advances*. 2020;10:10584. Doi: 10.1039/d0ra01697g
17. Matin MM. Synthesis and antimicrobial study of some methyl 4-*O*-palmitoyl- α -L-rhamnopyranoside derivatives. *Orbital: The Electronic Journal of Chemistry*. 2014;6(1):20-28. Doi: 10.17807/orbital.v6i1.553
18. Uddin MT, Kabir AKMS, Manchur MA. Synthesis and antimicrobial activities of some derivatives of L-rhamnose. *Pakistan Journal of Biological Sciences*. 2004;7(12):2192-2197. Doi: 10.3923/pjbs.2004.2192.2197
19. Matin MM, Chakraborty P, Alam MS, Islam MM, Haneer U. Novel mannopyranoside esters as sterol 14 α -demethylase inhibitors: Synthesis, PASS predication, molecular docking, and pharmacokinetic studies. *Carbohydrate Research*. 2020;496:108130. Doi: 10.1016/j.carres.2020.108130
20. Matin MM, Uzzaman M, Chowdhury SA, Bhuiyan MMH. *In vitro* antimicrobial, physicochemical, pharmacokinetics, and molecular docking studies of benzoyl uridine esters against SARS-CoV-2 main protease. *Journal of Biomolecular Structure and Dynamics*. 2020 (in press). Doi: 10.1080/07391102.2020.1850358
21. Jäger M, Minnaard AJ. Regioselective modification of unprotected glycosides. *Chemical Communications*. 2016;52:656-664. Doi: 10.1039/C5CC08199H
22. Ren DB, Zhang L, Zhang M. Progress on selective acylation of carbohydrate hydroxyl groups. *Asian Journal of Organic Chemistry*. 2019;8(10): 1813-1823. Doi: 10.1002/ajoc.201900400
23. Matin MM, Chakraborty P. Synthesis, spectral and DFT characterization, PASS predication, antimicrobial, and ADMET studies of some novel mannopyranoside esters. *Journal of Applied Science & Process Engineering*. 2020;7(2):572-586. Doi: 10.33736/jaspe.2603.2020
24. Kiyoshima K, Sakamoto M, Ishikura T, Fukagawa Y, Yoshioka T, Naganawa H, Sawa T, Takeuchi T. Application of dibutyltin oxide method to regioselective acylation and alkylation of tylosin at C-4". *Chemical and Pharmaceutical Bulletin*. 1989;37(4):861-865. doi: 10.1248/cpb.37.861

25. Kabir AKMS, Alauddin M, Matin MM, Battacharjee SC. Regioselective monobenzoylation of methyl α -L-rhamnopyranoside. *Chittagong University Studies, Part II: Science*. 1997;21(2):59-63.
26. Frisch MJ, Trucks GW, Schlegel HB, Scuseria GE, Robb MA, Cheeseman JR, Scalmani G, Barone V, Petersson PA, Nakatsuji H. Gaussian 09, 2013, Gaussian Inc. (Wallingford CT).
27. Filimonov DA, Lagunin AA, Glorizova TA, Rudik AV, Druzhilovskii DS, Pogodin PV, Poroikov VV. Prediction of the biological activity spectra of organic compounds using the PASS online web resource. *Chemistry of Heterocyclic Compounds*. 2014;50(3):444-457. Doi: 10.1007/s10593-014-1496-1
28. Pires, DEV, Blundell TL, Ascher DB. pkCSM: predicting small-molecule pharmacokinetic properties using graph-based signatures. *Journal of Medicinal Chemistry*. 2015;58(9):4066-4072.
29. Daina A, Michielin O, Zoete V. SwissADME: a free web tool to evaluate pharmacokinetics, drug-likeness and medicinal chemistry friendliness of small molecules, *Scientific Report*. 2017;7:42717.
30. Kilic-Kurt Z. Synthesis of novel oxadiazole derivatives, molecular properties prediction, and molecular docking studies. *Journal of Turkish Chemical Society, Section A: Chemistry*. 2020;7(3):753-74. Doi: 10.18596/jotcsa.705951
31. Tsuda Y, Haque ME, Yoshimoto K. Regioselective monoacylation of some glycopyranosides via cyclic tin intermediates. *Chemical and Pharmaceutical Bulletin*. 1983;31:1612-1624. Doi: 10.1248/cpb.31.1612
32. Matin MM, Ibrahim M. Synthesis of 2,3-di-*O*-substituted derivatives of methyl 4-*O*-acetyl- α -L-rhamnopyranoside. *The Chittagong University Journal of Science*. 2006;30(2):67-76.
33. Lagunin A, Stepanchikova A, Filimonov D, Poroikov V. PASS: prediction of activity spectra for biologically active substances. *Bioinformatics*. 2000;16(8):747-748. Doi: 10.1093/bioinformatics/16.8.747
34. Tok F, Kaymakçioğlu B, İlhan R, Yılmaz S, Kırmızıbayrak P, Tok T. Design, synthesis, biological evaluation and molecular docking of novel molecules to PARP-1 enzyme. *Turkish Journal of Chemistry*. 2019;43(5):1290-1305.
35. Emen FM, Demirdöğen RE, Avşar G, Kılıç D. 2-Chlorobenzoylthiourea-modified MCM-41 for drug delivery. *Journal of the Turkish Chemical Society Section A: Chemistry*. 2019;6(1):29-34.

SUPPLEMENTARY DATA

Regioselective Synthesis of Some Rhamnopyranoside Esters for PASS Predication, and ADMET Studies

Mohammed M. Matin^{1*}, Naimul Islam¹, Ayesha Siddika¹, Sreebash C. Bhattacharjee^{1,2}

¹University of Chittagong, Faculty of Science, Department of Chemistry, 4331, Chattogram, Bangladesh.

²Bangladesh Council of Scientific & Industrial Research (BCSIR), Chemical Research Division, 4220, Chattogram, Bangladesh.

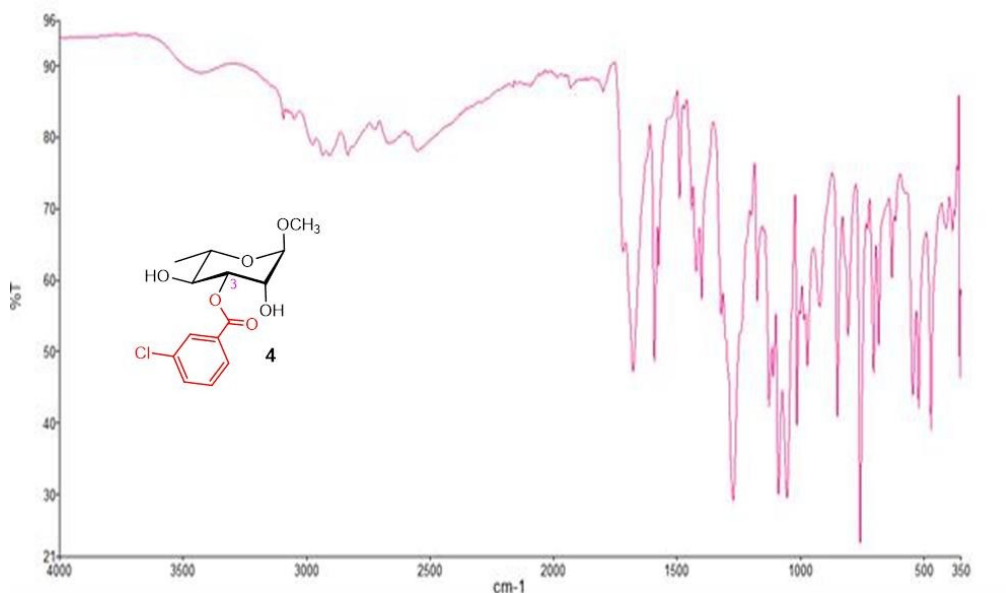


Figure S1. FT-IR spectrum of 4.

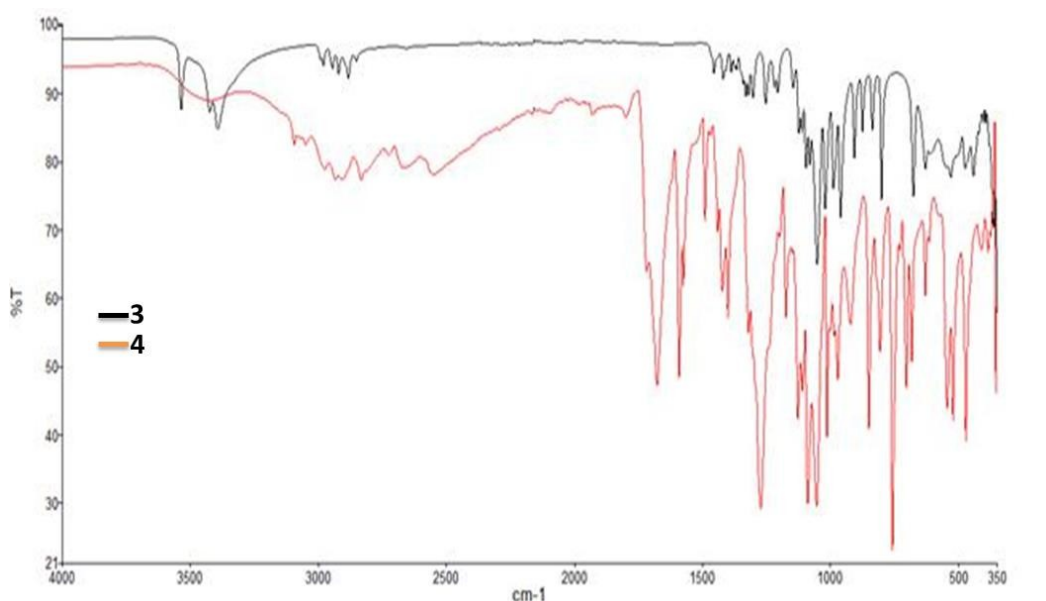


Figure S2. Comparative FT-IR spectra of compound 3 and 4.

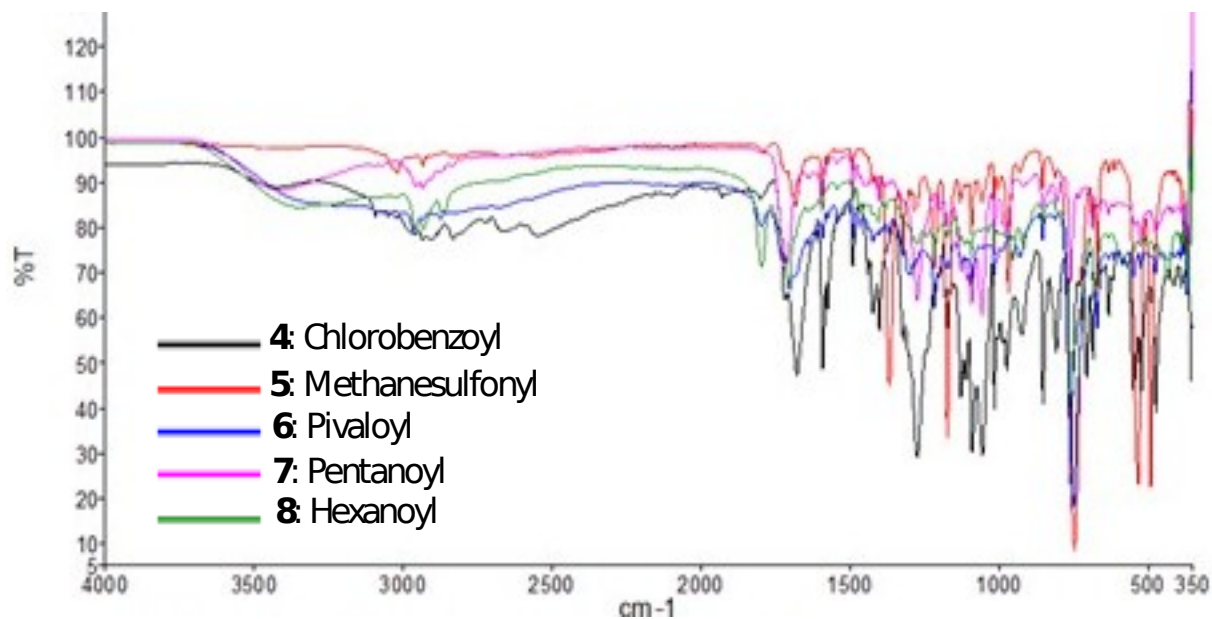


Figure S3. Comparative FT-IR spectra of compound 4-8.

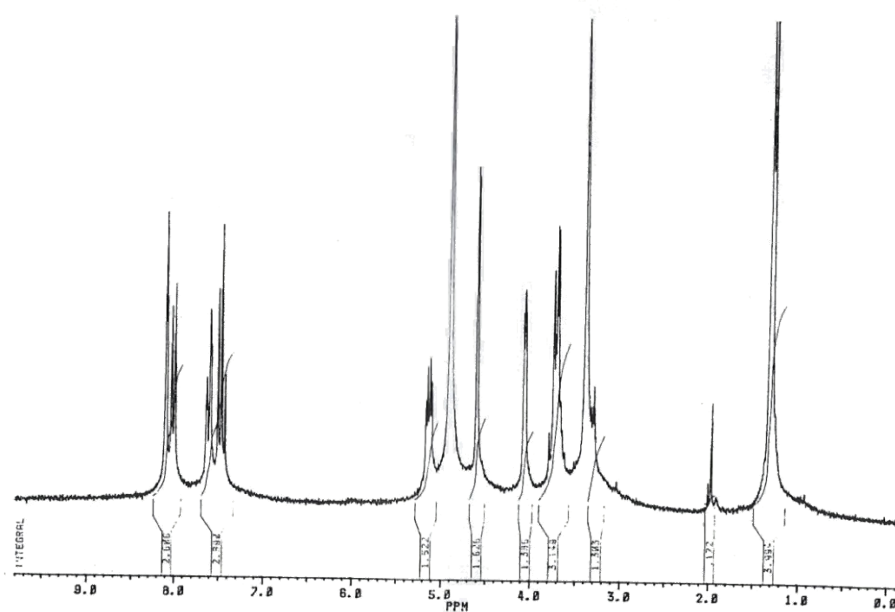


Figure S4. ¹H NMR (400 MHz, CDCl₃) spectrum of 4.

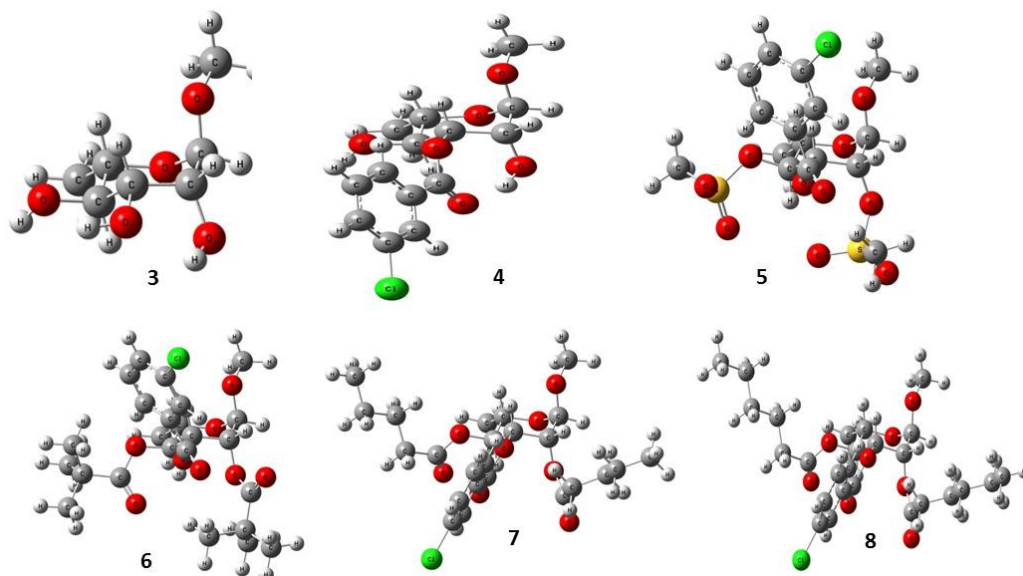


Figure S5. DFT optimized (B3LYP/3-21G) structures of rhamnopyranoside **3-8** (ball and stick model).

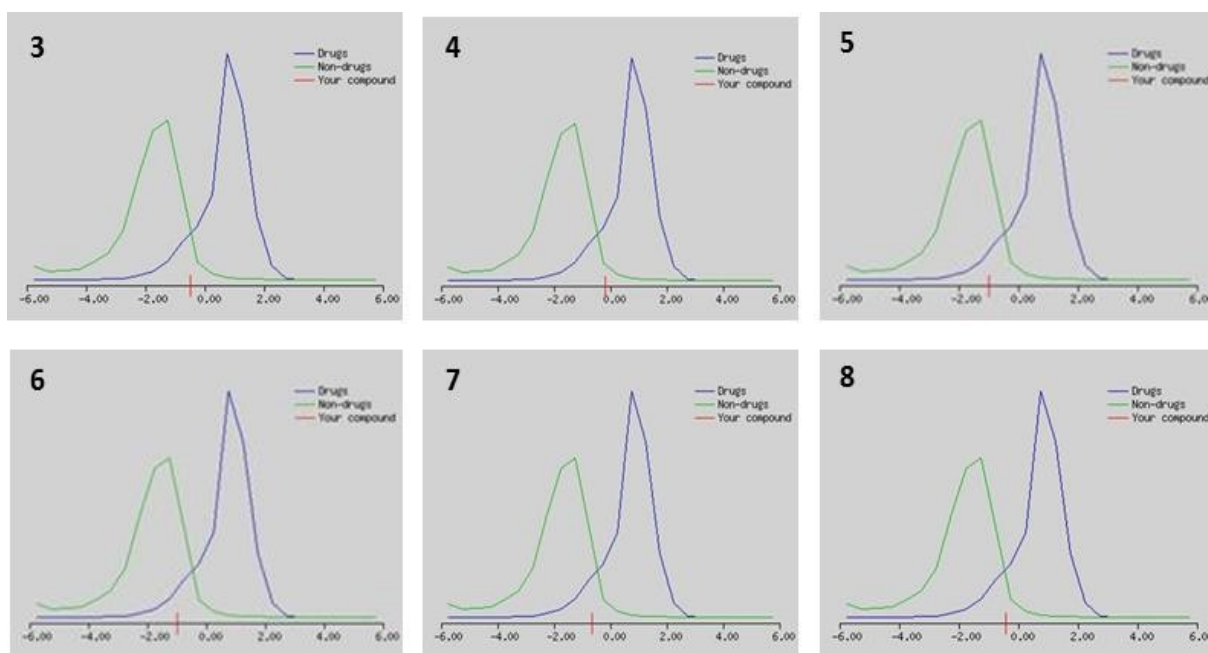


Figure S6. Druglikeness model score of SEs **4-8** predicted by MolSoft software.